Imagerie Radar de la Surface Océanique : de l'Estimation de l'Etat de Mer à la Caractérisation de Pollution Marine

Sebastien Angelliaume

Ecole doctorale n°548 : Mer et Sciences

MIO (UM 110 UTLN/AMU/CNRS-INSU/IRD)

THESE présentée par :

Sébastien ANGELLIAUME

soutenue le : **11 décembre 2020**

pour obtenir le grade de Docteur en Physique

Spécialité : Télédétection Radar

Imagerie Radar de la Surface Océanique : de l'Estimation de l'Etat de Mer à la Caractérisation de Pollution Marine

Directeur de thèse : Charles-Antoine Guérin – Université de Toulon-MIO

Jury

Mme. HAUSER DANIELE,	Directrice de Recherche CNRS – LATMOS	Rapporteur
M. ROUEFF ANTOINE,	Maître de conférences HDR – Ecole Centrale de Marseille	Rapporteur
M. SOUYRIS JEAN-CLAUDE,	Docteur Ingénieur – CNES	Examinateur
M. POTTIER ERIC,	Professeur des Universités – Université de Rennes-IETR	Examinateur
Mme. BAKLOUTI MELIKA,	Professeur des Universités – Aix-Marseille Université-MIO	Examinateur
M. GUERIN CHARLES-ANTOINE,	Professeur des Universités – Université de Toulon-MIO	Directeur de thèse

REMERCIEMENTS

Mes premiers mots seront en destination de ma famille, ma femme que j'aime passionnément et mes deux magnifiques enfants. C'est avec vous, au jour de jour, que ces travaux de recherche ont été accomplis. Mes parents bien évidemment et toute ma famille.

Je tiens à remercier chaleureusement C.-A. Guérin, bien sûr pour avoir accepté d'encadrer ma *Validation des Acquis par l'Expérience*, mais également pour son implication exemplaire tout au long des deux sujets de thèses que nous avons encadrés. Ce fut pour moi deux aventures passionnantes, pendant lesquelles j'ai énormément appris, scientifiquement bien sûr mais également humainement incontestablement. Merci C.-A..

Je suis arrivé en juin 2006 à l'ONERA, dans l'équipe RIM. J'ai découvert une équipe d'ingénieurs remarquables, passionnés et investis … ainsi que l'aventure des essais en vol, et quelle aventure ! Merci à tous de m'avoir accueilli et les jolis résultats présentés dans ce manuscrit sont aussi les vôtres. Un merci tout particulier à Olivier et à Jean-Marc de m'avoir accordé toute leur confiance, source de mon épanouissement dans votre équipe.

Merci à toutes les Directions de l'ONERA pour m'avoir laissé la liberté d'aboutir dans cette *Validation des Acquis par l'Expérience* : la Direction des Ressources Humaines, la Direction Scientifique et la Direction du Département ElectroMagnétisme et Radar.

Et puis, … Pascale !

RESUME

L'imagerie radar est utilisée depuis plus de 40 ans pour l'observation de la Terre. Elle permet l'acquisition de données à haute résolution spatiale, sur l'ensemble du globe, de jour comme de nuit et quasi indépendamment des conditions atmosphériques et météorologiques. Même si la réponse radar des surfaces océaniques est en général bien caractérisée dans la littérature, il demeure à ce jour un certain nombre de verrous scientifiques. Les travaux de recherche exposés dans ce manuscrit ont pour vocation à faire progresser la caractérisation de la surface océanique dans la bande des micro-ondes : deux volets ont été explorés, l'extension des modèles de rétrodiffusion et la télédétection des pollutions marines. Une originalité importante des résultats présentés est qu'ils s'appuient simultanément sur des travaux expérimentaux et sur des développements théoriques.

Une meilleure compréhension de l'interaction entre l'onde EM et la surface de mer nous a permis d'étendre le domaine d'emploi des modèles analytiques de rétrodiffusion. Une distribution adaptée des pentes des vagues permet de restituer qualitativement les asymétries directionnelles observées expérimentalement. L'utilisation d'un modèle de Bragg composite corrigé du rapport de polarisation permet quant à lui de restituer la distribution de fouillis de mer en polarisation directe.

Traditionnellement restreinte à la détection des nappes d'hydrocarbures en mer, nous avons exploré l'usage de l'imagerie radar pour le suivi des pollutions par produits chimiques. Au-delà de la détection, nous avons également démontré la pertinence des données SAR pour la caractérisation et la quantification des pollutions marines, à condition de disposer d'un instrument dont le niveau de bruit est suffisamment faible.

ABSTRACT

Radar imagery has been used for more than 40 years for Earth observation. It enables the acquisition of high spatial resolution data, over the entire globe, day and night and in almost all weather conditions. Even though the radar response backscattered from the ocean surfaces is generally well characterized in the literature, there remain a number of scientific issues. The aim of this dissertation is to report on progresses in the characterization of the ocean surface in the microwave regime: two aspects have been investigated, namely the extension of ocean backscattering models and the remote sensing of marine pollution. An important originality of these works is the combined utilization of both experimental data and theoretical developments.

A better understanding of the interaction of EM waves at the sea surface has allowed to extend the validity domain of analytical backscattering models. An appropriate distribution of wave slopes makes the predictions of directional asymmetries in qualitative agreement with the experimental observations. The use of a composite Bragg model corrected for the polarization ratio makes it possible to model accurately the statistical distribution of sea clutter intensity in both co-polarizations.

Traditionally restricted to the detection of mineral oil slicks at sea, we have explored the use of radar imagery to monitor hazardous and noxious substances over the ocean surface. Beyond detection, we have also demonstrated its relevance for the characterization and quantification of marine pollution, provided data were collected by an instrument with a sufficiently low noise floor.

TABLE DES MATIERES

1. INTRODUCTION

Ce manuscrit expose les travaux de recherche que j'ai réalisés tout au long de mon parcours professionnel. Il s'inscrit dans une démarche personnelle de Validation des Acquis de l'Expérience (VAE) afin d'obtenir le diplôme de Doctorat en Physique, spécialité *Télédétection micro-ondes*.

Je suis titulaire d'une Maîtrise de Mathématiques obtenue avec la mention *bien* à l'Université d'Aix-Marseille III en 2001, d'un DEA *Signal Image et Acoustique* obtenu en 2003 à l'ENSEEIHT (Ecole Nationale Supérieure d'Electrotechnique, d'Electronique, d'Informatique, d'Hydraulique et des Télécommunications) et je suis diplômé de l'école d'ingénieur ENSICA (Ecole Nationale Supérieure d'Ingénieurs de Constructions Aéronautiques), promotion 2003.

Mon parcours professionnel est jusqu'à ce jour composé de deux étapes successives. Tout d'abord de 2003 à 2006 au sein de la société Thales à Massy-Palaiseau (92) j'ai développé une chaîne de traitement radar interférométrique complète (du recalage automatique du couple d'images au déroulement de la phase interférométrique). J'ai ensuite intégré l'ONERA (Office National d'Etudes et de Recherches Aérospatiales) en juin 2006 et depuis je suis en charge de la définition, de la programmation et de la réalisation de campagnes de mesure radar expérimentales aéroportées ainsi que de l'analyse des signaux radar acquis. Mes activités me permettent d'aborder à la fois un volet expérimental avec la réalisation d'essais en vol ainsi qu'un volet théorique avec l'exploitation et l'analyse des données collectées. La dualité entre ces activités théoriques et expérimentales est pour moi fondamentale dans la conduite de mes travaux.

Au cours de mes cinq premières années à l'ONERA, j'ai principalement mené des activités de recherche sur la caractérisation des zones forestières. J'ai participé aux premiers travaux sur l'apport de la polarisation compacte (mode $\pi/4$) et initié les développements algorithmiques pour l'exploitation de données SAR acquises en mode tomographique, tout d'abord en collectant des données expérimentales depuis une nacelle puis à partir de mesures aéroportées. Ces travaux s'inscrivaient dans le cadre de la préparation de la mission spatiale BIOMASS de l'Agence Spatiale Européenne (ESA) et ont été publiés dans des journaux scientifiques à comité de relecture [1][2].

Ensuite et depuis maintenant une dizaine d'années, mes activités de recherche se sont principalement focalisées sur la télédétection de la surface océanique. Tout au long de ces travaux [58][62][65][80][82][83][85][96][107][110][112][115], je me suis intéressé à la confrontation entre mesures expérimentales et modèles électromagnétiques de rétrodiffusion, pour en analyser les limitations et proposer des extensions et améliorations, notamment au travers de collaboration avec l'Institut Méditerranéen d'Océanologie (MIO) de l'Université de Toulon. Différentes publications scientifiques sont venues couronner ces travaux, dont certaines en collaboration avec des organismes de recherches internationaux [65][85][96][110][115].

Au cours de ces cinq dernières années, je me suis consacré à la télédétection de pollutions marines à travers deux projets de recherche de grande envergure. Le premier, POLLUPROOF (02/2014 – 12/2017), est un projet financé par l'Agence Nationale de la Recherche (ANR) et qui avait comme principal objectif de proposer aux Douanes Françaises des moyens de télédétection pour la surveillance des pollutions en mer par déversements de produits chimiques. Les travaux réalisés ont permis d'ouvrir la voie à des moyens d'investigations novateurs adaptés aux pollutions par substances liquides nocives en mer difficilement atteignables jusqu'alors. Le second projet, New Advanced Observation Methods Integration (NAOMI), est un programme de recherche en collaboration entre l'ONERA et TOTAL (05/2014 – 07/2019). J'étais en charge du volet Offshore, pendant lequel j'ai pu étendre l'utilisation classique de l'imagerie radar en proposant des méthodes innovantes de caractérisation et de quantification des pollutions marines par hydrocarbures.

Même si la réponse radar des surfaces océaniques est en général bien caractérisée dans la littérature, il demeure à ce jour un certain nombre de verrous scientifiques. Les travaux de recherche exposés dans ce manuscrit ont pour vocation de faire progresser les connaissances sur la caractérisation de la surface océanique dans la bande des micro-ondes. Une originalité importante des travaux présentés est qu'ils s'appuient systématiquement à la fois sur des travaux expérimentaux et sur des développements théoriques.

Ce manuscrit est consacré à mes activités de recherche sur la caractérisation des surfaces océaniques uniquement. Après une première partie introductive, les principes de l'imagerie radar sont présentés dans un second chapitre. Le troisième chapitre présente un bref état de l'art sur l'interaction entre le signal radar et la surface océanique. Un quatrième porte sur la caractérisation de la réponse radar d'une surface de mer, le cinquième et dernier chapitre est quant à lui dédié à la télédétection micro-ondes des pollutions marines. Une sélection de mes publications dans des revues scientifiques les plus marquantes est fournie en Annexe.

2. IMAGERIE RADAR

2.1. Introduction

L'imagerie radar est utilisée depuis plus de 40 ans pour l'observation de la Terre. Elle permet l'acquisition de données à haute résolution spatiale, sur l'ensemble du globe, de jour comme de nuit et quasi indépendamment des conditions atmosphériques et météorologiques. La télédétection radar est utilisée dans un grand nombre d'applications, tant sur les surfaces continentales qu'océaniques. Parmi celles-ci, on peut citer le suivi des surfaces agricoles, la mesure de la biomasse forestière à l'échelle globale, la cartographie de précision en gestion de crise, l'étude des courants marins, l'estimation des conditions de mer ou encore la détection et le suivi des pollutions marines.

Seasat [3] est le premier satellite d'observation de le Terre civil à embarquer un instrument radar imageur (Fig. 1). Lancé en 1978 par le JPL et la NASA, il n'a malheureusement fonctionné que pendant 105 jours à cause d'un grave disfonctionnement interne. Dédié à l'observation des océans, les images radar acquises par cet instrument ont permis de mettre en évidence des phénomènes océanographiques macroscopiques complexes comme les courants, les ondes internes ou la formation des glaces de mer.

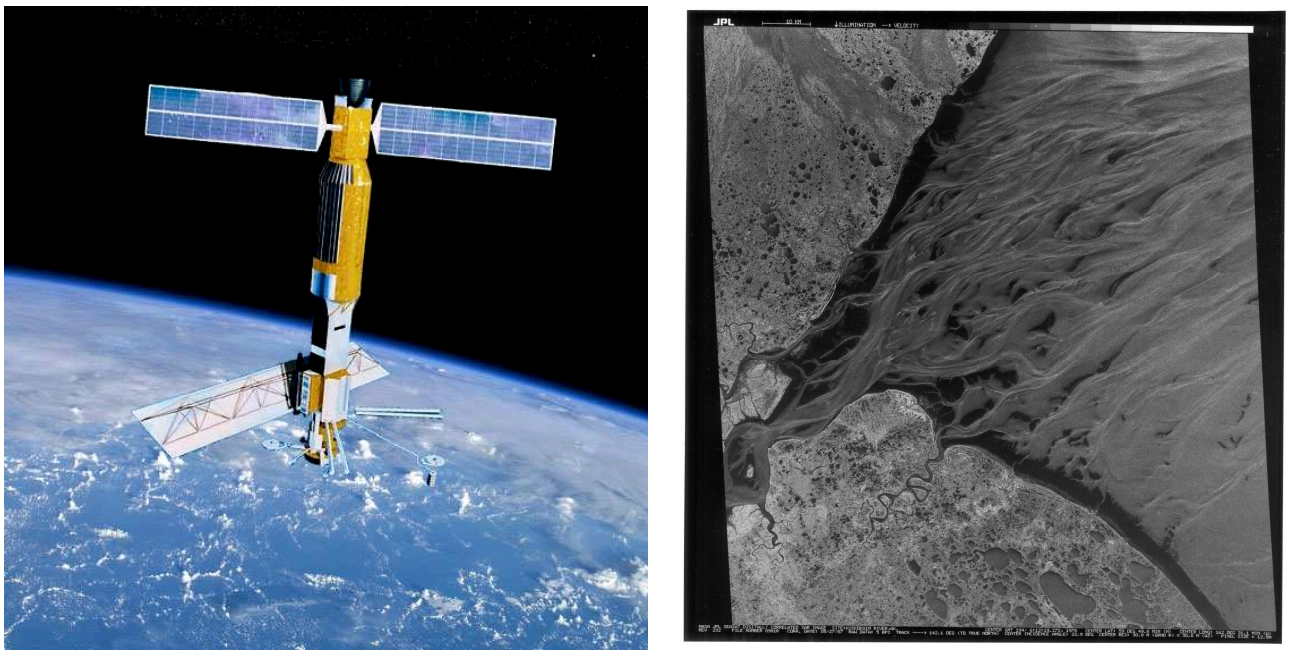

(a) Vue d'artiste du satellite Seasat – source : https://www.jpl.nasa.gov/missions/seasat/

(b) Image du delta de Kuskokwim en Alaska SAR bande L polarisation HH

Fig. 1: (a) Vue d'artiste du satellite Seasat et (b) image SAR acquise en bande L polarisation HH sur le delta de la rivière Kuskokwim en Alaska en 1978

L'Agence Spatiale Européenne (ESA) a ensuite lancé les satellites ERS-1/2 [4], respectivement en 1991 et 1995, embarquant un instrument radar imageur à synthèse d'ouverture (RSO ou SAR pour « *Synthetic Aperture Radar* » en anglais) en bande C (cf. 2.2.3). D'une durée de vie exceptionnelle (respectivement 9 et 16 ans), ces capteurs ont permis de nombreuses avancées scientifiques, notamment lors de la phase de vol en tandem des deux instruments. En parallèle, le satellite JERS-1 [5] de l'agence spatiale japonaise (JAXA) a permis l'acquisition d'images SAR en bande L (cf.

2.2.3). D'avril à octobre 1994, a eu lieu l'unique expérience de mise en orbite d'un instrument SAR multifréquences. Né d'une collaboration entre JPL/NASA, DLR et ASI les radars SIR-C/X-SAR [6] ont été embarqués à bord de la navette Endeavour et ont acquis des images radar en bandes X (cf. 2.2.3), C et L. En 1995, le Canada a lancé son premier satellite radar d'observation de la Terre, RADASAT-1 [7], avec notamment un mode ScanSAR large fauchée (~ 500 km). La mission Shuttle Radar Topography Mission (SRTM) [8] a ensuite permis les premières acquisitions par radar interférométrique depuis l'espace en février 2000 et la création d'un modèle numérique de terrain (MNT) à l'échelle du globe, toujours largement utilisé de nos jours. Suite aux succès majeurs de ces missions spatiales pionnières, de nombreux instruments radar imageurs ont ensuite été lancés par différentes agences spatiales. On notera en particulier les missions RADARSAT-2 [9] dotée d'un mode polarimétrique complet et d'un niveau de bruit instrumental très bas ou encore TerraSAR-X [10], le premier radar civil bande X haute résolution dans l'espace lancé par l'Allemagne en 2007. Un changement de paradigme a ensuite été enclenché par l'ESA avec le programme COPERNICUS. Il consiste en la planification à long terme de différentes missions spatiales d'observation de la Terre et en la mise en accès libre de toutes ces données. Il en résulte une démocratisation et utilisation massive des données spatiales de télédétection avec comme principal objectif de permettre aux différents pays européens d'assurer le contrôle et la surveillance de leur environnement. De nombreux autres projets de missions spatiales sont actuellement à l'étude ou en phase de lancement. On peut citer la mission BIOMASS [11] de l'ESA qui doit être lancée en 2022 et qui sera le premier radar imageur en basse fréquence (bande P) dans l'espace ou encore la mission NiSAR [12], développée de manière conjointe par les agences spatiales américaine (JPL/NASA) et indienne (ISRO), qui doit embarquer deux radars imageurs opérant simultanément en bandes L et S.
Un moteur majeur du développement des instruments spatiaux a toujours été la technologie aéroportée, qui est généralement en avance de plusieurs années sur les capacités des capteurs spatiaux [13]. Les instruments aéroportés d'aujourd'hui sont capables de fournir des données radar de haute qualité avec une résolution spatiale décimétrique, voir centimétrique, et permettent le développement de nouvelles approches dans l'analyse des données et l'extraction des informations accessibles par imagerie radar. Parmi les différents systèmes aéroportées toujours en opération actuellement, on peut citer l'instrument UAVSAR [14] de JPL/NASA qui embarque un radar bande L à très faible niveau de bruit instrumental sous un Gulfstream-III, le système d'imagerie radar multifréquence F-SAR [15] développé par le DLR à bord d'un Dornier DO228 et SETHI [16] et le système de télédétection optique et radar aéroporté développé par l'ONERA, embarqué sous les ailes d'un Falcon 20.

2.2. Principe de fonctionnement d'un radar imageur

Un radar imageur est un système hyperfréquence **actif** qui produit des images d'une zone d'intérêt à partir du rayonnement micro-ondes **rétrodiffusé** par la surface illuminée. L'instrument est embarqué à bord d'une plateforme mobile (satellite, avion, hélicoptère, drone, voiture …) et opère en visée latérale (*Side-Looking Airborne Radar - SLAR*) perpendiculairement à la direction d'avancement. Contrairement à un instrument optique qui, dans le cas général, fonctionne en visée nadir (direction de la verticale, orientée vers le centre de la Terre), les radars imageurs fonctionnent eux en visée latérale afin d'éviter les ambiguïtés gauche-droite.

Cet angle de visée est appelé **angle d'incidence** (angle par rapport à la normale à la surface) ou, son complémentaire, angle de dépression. Un système radar imageur émet une onde électromagnétique (EM) à partir d'une antenne qui pointe donc vers le côté de la plateforme. L'antenne utilisée est de taille rectangulaire afin de produire un faisceau étroit dans la direction longitudinale (axe **azimut**) et

un faisceau large dans la direction transversale (axe **distance**). Des impulsions cohérentes, de courte durée (τ – de l'ordre des quelques microsecondes) et de forte énergie sont transmises radialement par l'antenne, elles se propagent en direction du sol qui en rétrodiffuse une partie pour être captée par le système en réception. La très grande majorité des systèmes d'observation de la Terre est composée d'un seul système qui opère alternativement en émission et réception, on parle alors de système monostatique. Lorsque émetteur et récepteur sont différents, il s'agit d'un système bi-statique. A un instant fixe, l'empreinte au sol du lobe d'antenne définit la zone imagée dans l'axe distance (fauchée), comprise entre la distance proche (Near Range) et la distance lointaine (Far Range). En générale, la fauchée est limitée par l'ouverture du lobe d'antenne à -3 dB (θ_{-3dB}), ce qui permet de limiter les effets de remontée de bruit en bords de lobe :

$$\theta_{-3dB} = \frac{\lambda}{L}\ [rad] \tag{1}$$

avec L la taille de l'antenne et λ la longueur d'onde du radar.

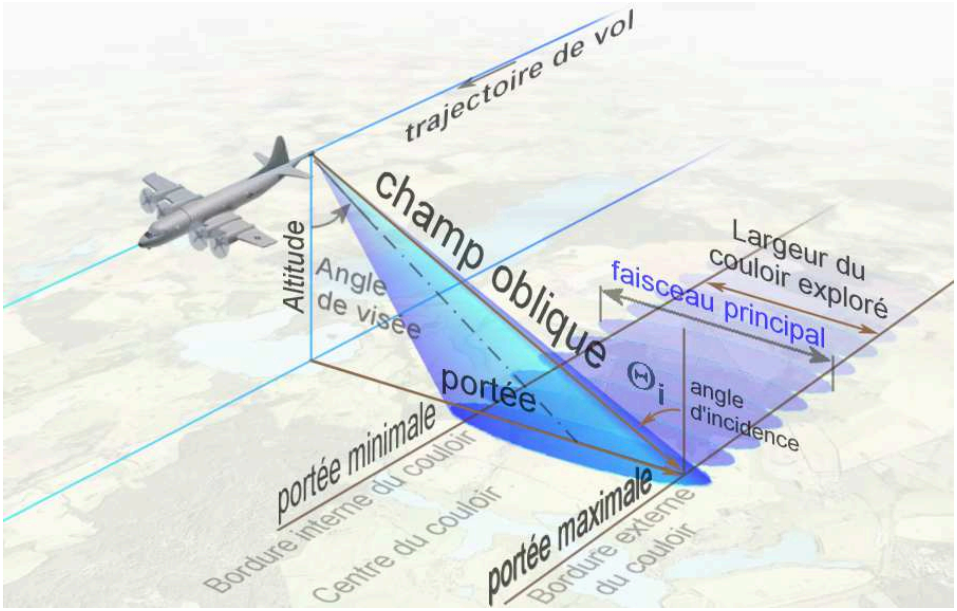

Fig. 2: Illustration de la géométrie d'acquisition des images SAR – source : https://www.wikiwand.com/fr/Radar_imageur

On observe alors que ce mode de fonctionnement induit la coexistence de deux géométries, l'une correspondant à la géométrie des ondes radar (dite *Slant Range*) et l'autre correspondant à la projection de la précédente sur la surface Terrestre (dite *Ground Range*). Le passage d'un paramètre A de la géométrie slant range (A_{SR}) à la géométrie ground range (A_{GR}) s'effectue de la façon suivante :

$$A_{GR} = \frac{A_{SR}}{\sin\theta} \tag{2}$$

avec θ l'angle d'incidence. Pour une prise de vue aéroportée, l'approximation de la Terre plate est valide et l'angle d'incidence correspond à l'angle d'émission des ondes radar. Ce n'est plus le cas en configuration satellitaire et il convient de considérer l'angle normal à la surface pour l'angle d'incidence.

Les ondes EM émises par le radar se propageant à la célérité de la lumière ($c=3.10^8 m.s^{-1}$), la mesure du temps entre l'émission de l'impulsion et la réception du signal donne la distance entre un point de la surface imagée et l'instrument radar (distance en aller-retour). L'intensité rétrodiffusée dépend de la nature du terrain observé ainsi que des paramètres du système radar. Les principaux éléments impactant sont : la résolution de l'instrument, les conditions géométriques de l'observation, la fréquence et la polarisation des ondes EM.

2.2.1. Notion de résolution

La notion de résolution est au cœur de la problématique de la télédétection radar : c'est la capacité d'un système d'observation à différencier deux cibles ponctuelles. Plus la résolution de l'instrument est importante (valeur faible), mieux il sera capable de différencier des cibles faiblement éloignées.

Dans l'axe distance, la résolution δr est donnée par la durée de l'impulsion τ :

$$\delta r = \frac{c\tau}{2} \; [m] \tag{3}$$

ce qui donne une résolution radiale de 6000 m pour une impulsion de 40 µs. Une amélioration de la résolution dans l'axe radiale nécessite la réduction de la durée d'impulsion, tout en conservant la puissance émise (nécessaire au rapport signal à bruit – RSB), ce qui implique des contraintes instrumentales majeures. Pour passer outre, la technique de la **compression d'impulsion** est habituellement utilisée en imagerie radar. Il s'agit d'émettre une impulsion d'amplitude constante pendant la durée d'émission (τ) mais **modulée linéairement en fréquence** au cours du temps *t*, telle que $f_i = kt_i$, avec k la pente de l'impulsion et $B = k\tau$ la bande passante émise. En réception, le signal est comprimé en utilisant la méthode du filtrage adapté. La résolution radiale ne dépend alors plus que de la bande passante du signal émis telle que [17] :

$$\delta_r^{SAR} = \frac{c}{2B} \; [m] \tag{4}$$

L'émission d'une impulsion avec une bande passante de 150 MHz autour d'une fréquence porteuse f_{EM} permet d'atteindre une résolution spatiale dans l'axe radial de 1 m (en géométrie *Slant Range*). La procédure d'émission d'une impulsion modulée linéairement en fréquence est répétée chaque PRI (*Pulse Repetition Interval*) secondes au cours du déplacement du radar le long de sa trajectoire de vol, ce qui correspond à la fréquence de répétition PRF (*Pulse Repetition Frequency*) telle que :

$$PRI = \frac{1}{PRF} \; [s] \tag{5}$$

Chaque contributeur de la surface imagée est ainsi illuminé par le faisceau de l'antenne pendant un intervalle de temps T tel que :

$$T = \frac{L}{v} \; [s] \tag{6}$$

avec v la vitesse du porteur et L la taille de l'antenne dans la direction azimutale.

Dans l'axe azimut, la résolution δa d'un système radar classique est fonction de l'ouverture du lobe d'antenne (θ_{-3dB}) et de la distance radiale entre le radar et la zone imagée (R) telle que :

$$\delta a = R\theta_{-3dB} = R\frac{\lambda}{L}\ [m] \tag{7}$$

Cette formulation donne une résolution de 75 m pour une antenne de 2 m de longueur, une distance R de 5 km et une longueur d'onde de 3 cm.

Une résolution fine en azimut nécessite donc une antenne de grande dimension. La solution pour obtenir une haute résolution azimutale avec une antenne de taille raisonnable est donnée par le concept d'antenne synthétique (d'où la dénomination d'image SAR « Synthetic Aperture Radar ») qui est basée sur la construction d'une antenne virtuelle de grande taille en utilisant le déplacement de l'antenne réelle du capteur le long de sa trajectoire. La longueur maximale de l'antenne synthétique est la longueur de la portion de trajectoire depuis laquelle un point de la scène imagée est illuminé, ce qui correspond à la taille de l'empreinte de l'antenne au sol. Lorsque la réponse d'un diffuseur, à une distance R, est intégrée de façon cohérente le long de la trajectoire, la résolution azimutale obtenue est égale à [18][19] :

$$\delta_a^{SAR} = \frac{L}{2}\ [m] \tag{8}$$

Il est intéressant de noter que la résolution en azimut est uniquement déterminée par la taille (dans la direction azimutale) de l'antenne physique de l'instrument et est indépendante de la longueur d'onde du signal émis et de la distance entre le radar et la zone observée.

La Fig. 3 ci-dessous illustre une image radar dont les paramètres de traitement ont été adaptés afin d'obtenir des images de résolutions spatiales en distance et azimut de 0.5, 3 et 10 m. On observe aisément l'impact de la résolution sur le rendu de l'image, en particulier le gain considérable de netteté obtenu entre les échelles de résolution décimétrique à métrique.

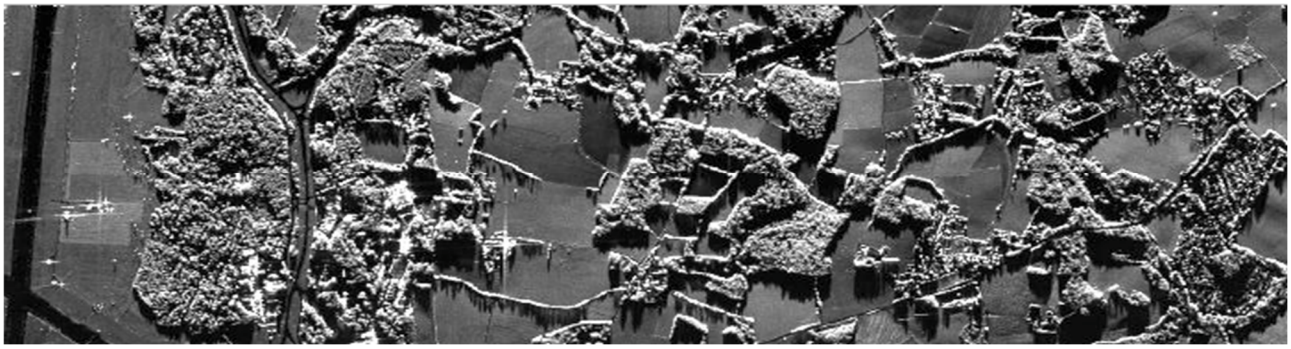

(a) : résolution 0.5 m

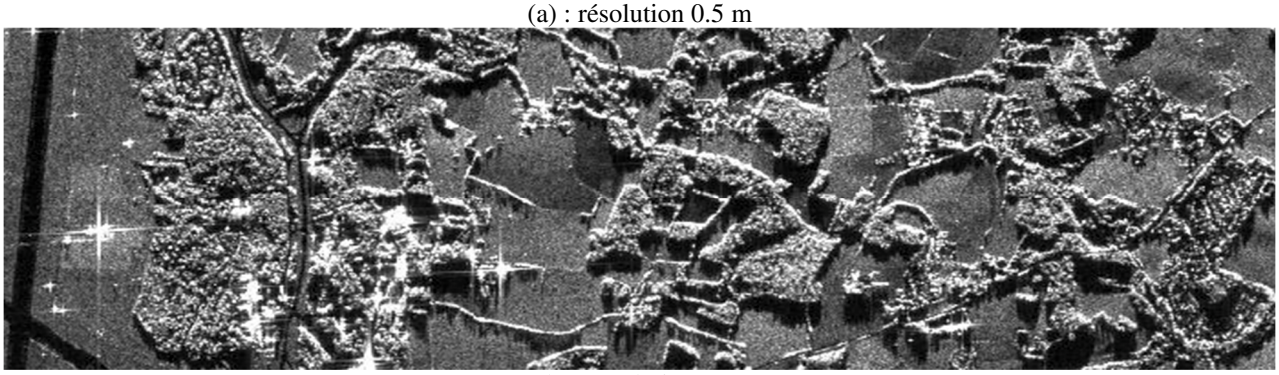

(b) : résolution 3 m

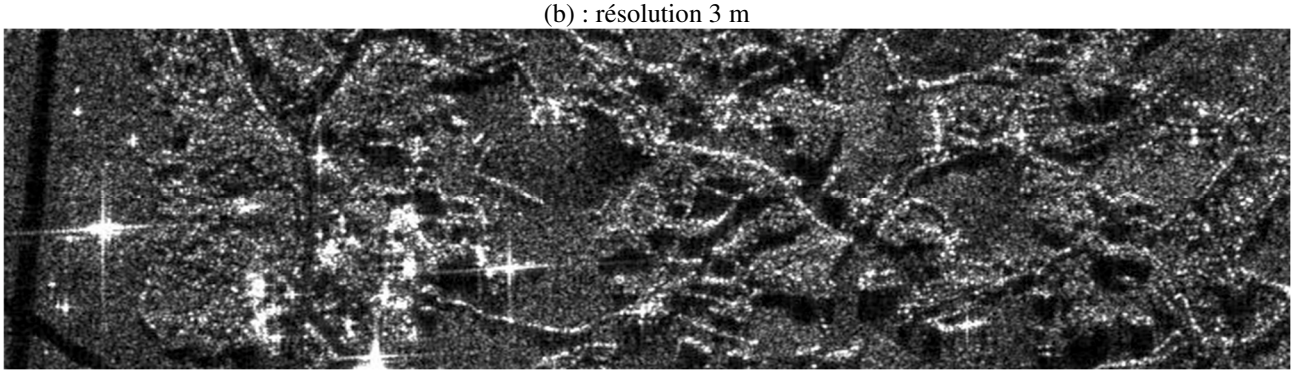

(c) : résolution 10 m

Fig. 3 : Illustration de l'impact de la résolution – image SAR traitée avec des résolutions spatiales en distance et azimut de (a) 0.5 m, (b) 3 m et (c) 10 m – Images SAR ONERA/SETHI

2.2.2. Echantillonnage et ambiguïté

Un élément important lors de la formation des images radar est la notion d'échantillonnage, et donc d'ambiguïté. Les ambiguïtés apparaissent dès lors que la fréquence d'échantillonnage n'est pas adaptée à la bande de fréquence du signal à échantillonner.

Dans l'axe distance, la fréquence d'échantillonnage (f_e) doit respecter le critère de Shannon ($f_e \geq B$ avec B la bande passante émise) ce qui ne pose pas de problème en général vue les cadences d'enregistrement disponibles. Cet échantillonnage en distance produit les cases distances de dimension Δ_R (en géométrie Slant Range) telle que :

$$\Delta_R = \frac{c}{2f_e}\ [m] \tag{9}$$

De même en azimut, il est nécessaire d'adapter correctement la fréquence d'émission des impulsions (PRF). Il y aura ambiguïté si la bande Doppler du signal reçu n'est pas correctement échantillonnée (cf. Fig. 4). On parle alors **d'ambiguïté Doppler**. Il convient de respecter le critère de Shannon dans cette dimension, c'est-à-dire adapter la PRF de telle sorte que :

$$PRF \geq B_D = \frac{2v}{L}\ [Hz] \tag{10}$$

L'ambigüité Doppler (A_D) est donnée par la formule ci-dessous. Il convient alors d'augmenter la valeur de la PRF pour augmenter l'ambigüité Doppler.

$$A_D = \frac{\lambda R}{2v} PRF\ [m] \tag{11}$$

avec R la distance radiale.

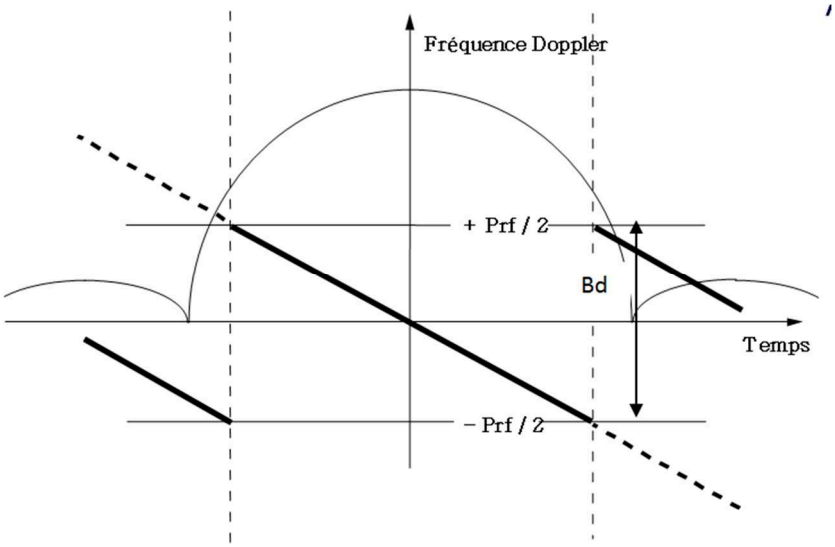

Fig. 4 : Illustration de la formation des ambigüités Doppler (repliements Doppler)

Il y aura également ambiguïté dans la réponse si le délai entre deux impulsions est inférieur au temps mis par l'écho le plus lointain pour être enregistré par le radar (Fig. 5). On parle alors **d'ambiguïté distance** [19]. Afin d'éviter la situation dans laquelle l'écho du Far Range de l'impulsion N arrive en même temps que l'écho du Near Range de l'impulsion N+1, il convient d'adapter la PRF de sorte que :

$$PRF \leq \frac{1}{2\tau + 2\frac{(R_{FR} - R_{NR})}{c} PRF}\ [Hz] \tag{12}$$

avec τ la durée de l'impulsion et R_{FR}, R_{NR} la distance radiale respectivement la plus éloignée (Far Range) et la plus proche (Near Range). L'ambigüité distance (A_R) est donnée par la formule ci-dessous. Il convient dans ce cas de diminuer la valeur de la PRF pour augmenter l'ambigüité distance.

$$A_R = \frac{c}{2PRF}\ [m] \tag{13}$$

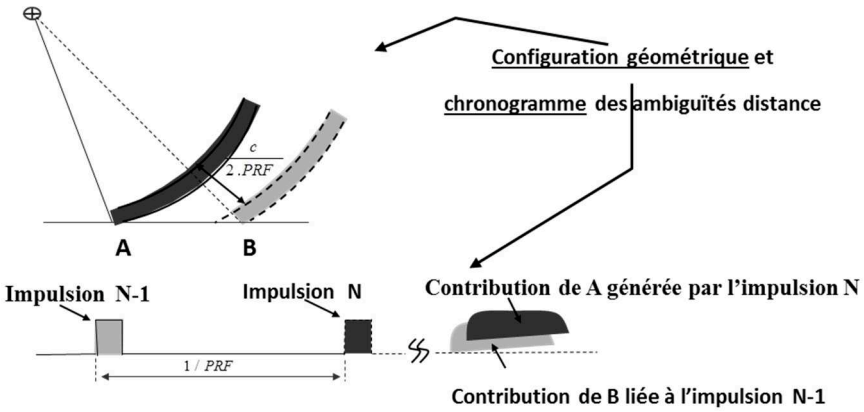

Fig. 5 : Illustration de la formation des ambigüités distance

Ces contraintes viennent imposer des bornes supérieure et inférieure à la PRF et mettent en évidence une contradiction sur celle-ci afin de limiter les ambigüités distance et azimut. De plus, alors qu'une résolution fine en azimut nécessite l'acquisition de données avec une bande Doppler importante et donc une PRF élevée pour respecter le critère de Shannon, l'obtention d'images radar avec une large fauchée requiert une réduction de la PRF pour limiter les ambigüités distance. Il existe donc à nouveau une contradiction, entre imagerie SAR haute résolution spatiale et large fauchée, qu'il n'est pas possible de lever avec un mode d'acquisition classique. La Fig. 6 ci-dessous présente une image SAR acquise avec une PRF adaptée (5000 Hz) et une illustration de l'impact des ambigüités azimutes (sous-échantillonnage des données brutes radar à la PRF de 417 Hz). On voit parfaitement l'impact des repliements en azimut qui interdisent toute interprétation.

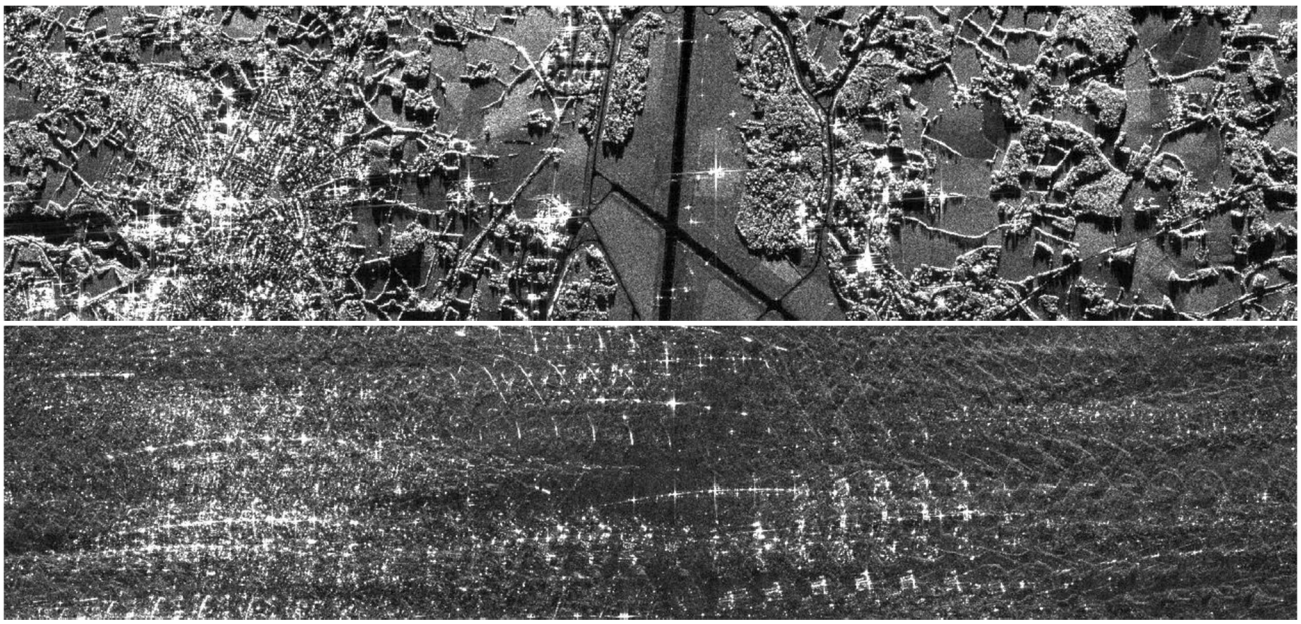

Fig. 6 : Image SAR traitée avec (haut) une PRF adaptée (5000 Hz) et (bas) une PRF non-adaptée (471 Hz) – Images SAR ONERA/SETHI

2.2.3. *Bande des micro-ondes*

En télédétection (ou observation de la Terre), les ondes radar utilisées sont globalement comprises entre des fréquences (f_{EM}) de 0.25 à 40 GHz, ce qui correspond à des longueurs d'onde (λ) comprises entre 120 et 0.75 cm telles que :

$$\lambda = \frac{c}{f_{EM}} \ [m] \tag{14}$$

avec c=3.10^8 m.s^{-1} en espace libre

Bande de fréquence	Ka	Ku	X	C	S	L	P
Fréquence [GHz]	40 – 25	17.6 – 12	12 – 7.5	7.5 – 3.75	3.75 – 2	2 – 1	0.5 – 0.25
Longueur d'onde [cm]	0.75 – 1.2	1.7 – 2.5	2.5 – 4	4 – 8	8 – 15	15 – 30	60 – 120

Tableau 1 : Bandes de fréquence et longueurs d'onde usuelles en observation de la Terre [20]

Le choix de la fréquence d'émission des ondes EM est de toute première importance puisque le signal rétrodiffusé par la surface imagée est fortement dépendant de la longueur d'onde du signal émis, notamment au travers de la notion de rugosité et de la capacité de pénétration des ondes radar. La Fig. 7 ci-dessous illustre deux images radar acquises simultanément dans deux bandes de fréquences (bande X et bande L). On observe aisément l'impact de la longueur d'onde sur la réponse radar avec notamment la zone centrale (pistes de l'aéroport de Nîmes Garons) qui apparait rugueuse en haute fréquence et plutôt lisse en plus basse fréquence et des contrastes inter-parcelles plus importants en bande L qu'en bande X.

(a) : image SAR bande X

(b) : image SAR bande L

Fig. 7 : Images SAR acquises par l'instrument aéroporté ONERA/SETHI sur l'aéroport de Nîmes-Garons simultanément en bande X (a) et bande L (b) – Polarisation Hh – 04 juin 2015.

2.2.4. *Notion de rugosité*

La rugosité se définit comme la variation moyenne des aspérités de la surface par rapport à une surface plane et contrôle la manière dont les ondes hyperfréquences interagissent avec celle-ci. L'apparence rugueuse ou lisse d'une surface dépend de la longueur d'onde et de l'angle d'incidence.

De façon qualitative (Fig. 8), une surface sera « vue » comme lisse par le radar si les variations verticales des éléments la constituant sont plus faibles que la longueur d'onde du radar. Dans ce cas, la surface produira une réponse spéculaire, la quasi-totalité de l'énergie sera diffusée dans la direction opposée à la direction incidente et peu ou pas d'énergie sera rétrodiffusée en direction du radar (cas mono-statique). Lorsque les variations verticales des aspérités sont de l'ordre de grandeur de la longueur d'onde (et au-delà), la surface devient « rugueuse » et réfléchira l'énergie dans toutes les directions (il y aura **diffusion**), et une partie de l'énergie sera rétrodiffusée vers le radar.

(a) : surface lisse (b) : surface rugueuse

Fig. 8 : Illustrations d'une surface lisse (a) et d'une surface rugueuse (b)

Le critère de Rayleigh [21] permet d'exprimer quantitativement la notion de rugosité tel que :

$$H_{RMS} \leq \frac{\lambda}{8\cos\theta}\ [m] \qquad \text{: surface lisse} \qquad (15)$$

$$H_{RMS} \geq \frac{\lambda}{8\cos\theta}\ [m] \qquad \text{: surface rugueuse} \qquad (16)$$

avec θ l'angle d'incidence des ondes radar de longueur d'onde λ et H_{RMS} la racine carrée de la hauteur quadratique moyenne (Root Mean Square) des aspérités de la surface. Ce critère conduit à une hauteur H_{RMS} d'environ deux dixièmes de λ à 45° d'incidence. La plupart des surfaces naturelles sont ainsi considérées comme rugueuses en bandes C et X.

2.2.5. Capacité de pénétration des ondes EM

Les ondes radar ont une capacité de pénétration à travers le milieu observé, fonction de la fréquence EM et des propriétés radioélectriques de ce milieu. On peut distinguer deux cas différents : la pénétration à travers le volume présent au-dessous de la surface et la pénétration à travers celle-ci.
De façon générale, les ondes radar sont sensibles aux éléments géométriques dont la dimension caractéristique est du même ordre de grandeur que la longueur d'onde (comme pour la notion de rugosité). Ce qui signifie que dans le cas d'une acquisition radar sur une zone forestière, en longueur d'onde décimétrique ou métrique le radar sera peu sensible aux couches supérieures de la végétation et le signal interagira avec le sol sous la forêt. A l'inverse, en longueur d'onde centimétrique, le radar sera sensible à la canopée.

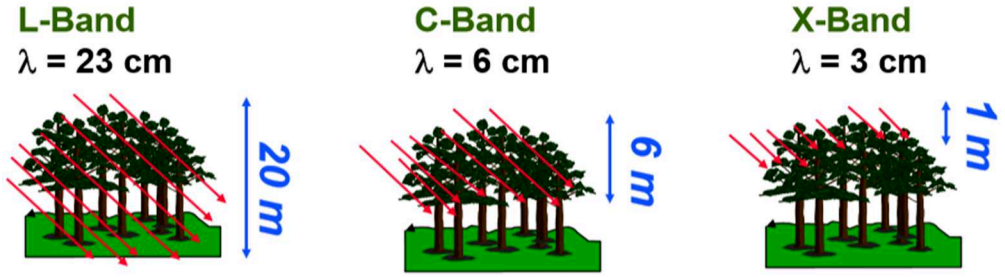

Fig. 9 : Illustration du pouvoir de pénétration des ondes radar à travers une forêt selon la fréquence

Lorsque le signal EM atteint la surface, il s'y propage en fonction des paramètres radioélectriques du milieu hôte et en particulier au travers de sa constante diélectrique relative, ε_r, qui caractérise le caractère isolant ou conducteur du milieu. La constante diélectrique relative est définie comme le rapport entre la constante diélectrique du milieu et celle du vide. Elle dépend du milieu ainsi que de la fréquence des ondes EM. C'est un nombre complexe dont la partie imaginaire caractérise la profondeur de pénétration, δ_p, qui correspond à la profondeur à laquelle la puissance transmise est atténuée d'un facteur à $1/e \approx 0.37$.

$$\varepsilon_r = \varepsilon' - j\varepsilon'' \tag{17}$$

$$\delta_p = \frac{1}{2k_{EM} Im(\sqrt{\varepsilon_r})} \ [m] \tag{18}$$

avec ε' le terme de permittivité relative, ε'' le terme de perte et $k_{EM} = 2\pi/\lambda$ le nombre d'onde EM. On trouve également dans la littérature la notion d'épaisseur de peau, δ_s, définie par :

$$\delta_s = 2\delta_p \ [m] \tag{19}$$

En télédétection micro-ondes des surfaces océaniques, le modèle empirique de Messner et Wentz [22] fait référence pour caractériser la constante diélectrique de l'eau de mer. Il est paramétré par la fréquence EM ainsi que par la température (en degrés Celsius – C°) et la salinité (en Practical Salinity Unit – PSU) de la mer. Le Tableau 2 résume quelques valeurs de constante diélectrique de l'eau de mer ε_w calculées à partir du modèle de Meissner and Wentz pour une température de surface de l'eau de mer de 15°C et une salinité de 35 PSU. Pour chaque fréquence est également calculée la profondeur de pénétration, qui est de l'ordre millimétrique pour la gamme des micro-ondes. L'air, quant à lui, est classiquement assimilé à l'espace libre. Pour les sols nus, des valeurs de constantes diélectriques en fonction du taux d'humidité sont fournies dans [23] et [24].

Bande de fréquence [fréquence GHz]	**Bande X [10 GHz]**	**Bande C [5.0 GHz]**	**Bande L [1.3 GHz]**
Constante diélectrique	52.9+39.0j	66.8+35.7j	73.0+65.1j
Profondeur de pénétration [mm]	0.9	2.3	5.2

Tableau 2 : Valeurs de constantes diélectriques [22] et de profondeurs de pénétration pour l'eau de mer à différentes fréquences électromagnétiques – température de 15°C et salinité de 35 PSU

2.2.6. Notion de bruit

Si on néglige le bruit de quantification, deux sources de bruit principal viennent impacter le signal EM du capteur SAR : le bruit thermique de l'instrument et le bruit de speckle.

2.2.6.1. Le bruit thermique

Le bruit thermique est un bruit **additif**, causé par la température de bruit en entrée du récepteur. Il quantifie le niveau minimal de signal pouvant être enregistré par l'instrument. Le rapport signal à bruit peut être amélioré en augmentant la puissance du signal émis.
Le niveau de bruit thermique (ou bruit instrumental) est un paramètre intrinsèque d'un capteur et doit être pris en compte lors de l'acquisition ou la sélection de données. La Fig. 10 ci-dessous donne quelques valeurs de bruit instrumental pour le capteur aéroporté UAVSAR du JPL/NASA [25] ainsi que pour les instruments spatiaux RADARSAT-2 et TERRASAR-X. On peut observer que, pour

chaque capteur, le niveau de bruit varie dans la fauchée en fonction de l'incidence. On peut également noter des différences très importantes entre les niveaux de bruit de ces trois instruments : UAVSAR avec un bruit extrêmement faible (minimum à -51 dBm^2/m^2), RADARSAT-2 possédant le niveau de bruit le plus faible pour un capteur spatial et TERRASAR-X avec un plancher de bruit relativement haut.
Le niveau de bruit thermique dépend de l'instrument mais également de la forme d'onde radar mise en œuvre (au travers de la bande passante émise et de la distance radar cible). C'est pour cela qu'il ne peut y avoir une seule valeur de niveau de bruit pour un instrument, mais (pour chaque instrument) des valeurs en fonction de la configuration de mesure.

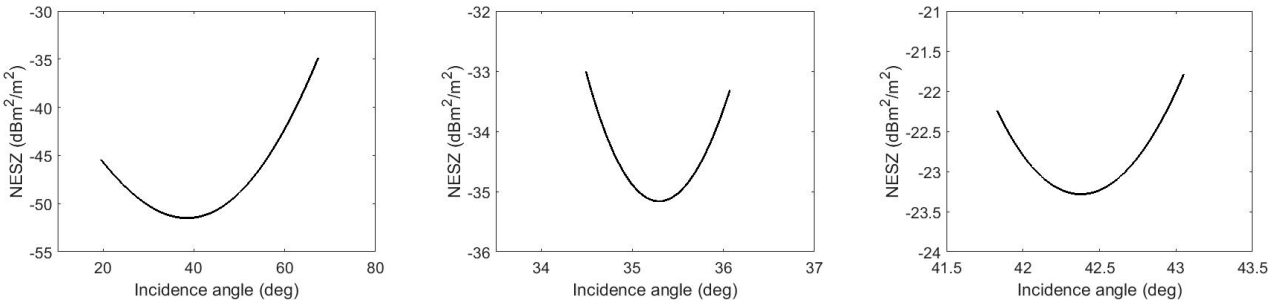

(a) UAVSAR (b) RADARSAT-2 (c) TERRASAR-X

Fig. 10 : Niveau de bruit instrumental pour les capteurs (a) UAVSAR, (b) RADATSAT-2 et (c) TERRASAR-X

2.2.6.2. Le bruit de speckle

Le bruit de speckle (« chatoiement » en français) est un bruit **multiplicatif** (sur chaque pixel), induit par le caractère cohérent de la formation des images SAR. Le bruit de speckle est proportionnel à la puissance du signal rétrodiffusé, son effet sur les images peut être réduit en moyennant des réalisations indépendantes. De façon générale en imagerie radar micro-ondes, la taille de la cellule de résolution est de dimension supérieure à la longueur d'onde EM. Elle est alors constituée d'un certain nombre de diffuseurs élémentaires, aléatoirement répartis au sein de cette cellule de résolution. Chaque réflecteur élémentaire rétrodiffuse de façon propre l'onde incidente et le signal EM rétrodiffusé est la sommation cohérente des contributions élémentaires de chaque diffuseur présent dans la cellule. Selon « l'alignement » de ces réponses, la sommation cohérente peut être constructive ou destructive. La conséquence importante est qu'une surface homogène sera « vue » par le radar comme hétérogène sous l'effet du bruit de speckle. Lorsque le nombre de diffuseurs au sein de la cellule de résolution est suffisamment grand, on dit alors que le speckle est « pleinement développé », et dans ce cas il est caractérisé par les critères statistiques suivants [26] :

1. La phase suit une variable aléatoire uniformément distribuée sur [0 ; 2π [
2. L'amplitude suit une loi de Rayleigh telle que :

$$p_A(A) = \frac{2A}{\mu_A^2} e^{-\frac{A^2}{\mu_A^2}} \quad \text{avec } \mu_A = \sqrt{2}\sigma \tag{20}$$

L'intensité suit une loi exponentielle telle que

$$p_I(I) = \frac{1}{\mu_I} e^{-\frac{I}{\mu_I}} \quad \text{avec } \mu_I = 2\sigma^2 \tag{21}$$

avec σ la variance de l'amplitude des N diffuseurs constituants la cellule.

Lorsque le paramètre $\mu = 2\sigma^2$ est lui-même une valeur aléatoire qui suit une loi $p_\mu(\mu)$, on parle alors de modèle composite, dont la loi en intensité est donnée par la formule de Bayes telle que :

$$p(x) = \int_{\mu=0}^{\infty} p_\mu(\mu) p_I(x) d\mu \tag{22}$$

$$= \int_{\mu=0}^{\infty} p_\mu(\mu) \frac{1}{\mu} e^{-\frac{x}{\mu}} d\mu \tag{23}$$

2.3. La polarisation des ondes électromagnétiques

2.3.1. Principes physiques

En espace libre, les champs électrique ($\vec{E}$) et magnétique ($\vec{H}$) d'une onde électromagnétique se propagent selon la direction du vecteur de propagation ($\vec{k}$) et forment une base orthogonale. La polarisation d'une onde plane est la figure décrite par l'extrémité du champ électrique dans le plan perpendiculaire à la direction de propagation. Si cette figure est bien définie l'onde est parfaitement polarisée ; si l'extrémité du champ électrique se comporte de façon aléatoire au cours du temps de propagation alors l'onde est partiellement polarisée. Dans le cas d'une onde parfaitement polarisée, la figure décrite par le champ électrique est, en toute généralité, une ellipse, appelée ellipse de polarisation. Celle-ci est caractérisée par son demi-grand axe (a) et demi-petit axe (b), ou bien de façon équivalente par ses angles d'ellipticité (χ) et d'orientation (ψ).

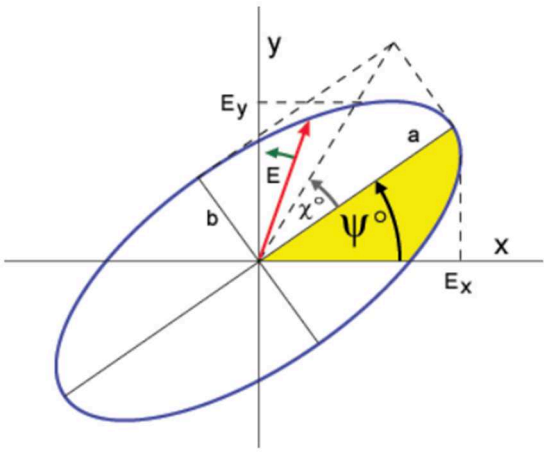

Fig. 11 : Ellipse de polarisation – source : Ressources naturelles Canada

Une onde électromagnétique parfaitement polarisée est définie dans la base $\{x, y\}$ par le vecteur de Jones [27] :

$$\overrightarrow{E_{xy}} = \begin{bmatrix} E_x \\ E_y \end{bmatrix} = \begin{bmatrix} |E_x| e^{j\varphi_x} \\ |E_y| e^{j\varphi_y} \end{bmatrix} = |E| e^{j\varphi_x} \begin{bmatrix} \cos\alpha \\ \sin\alpha e^{j\varphi} \end{bmatrix} \tag{24}$$

avec

$$\tan\alpha = \left|\frac{E_y}{E_x}\right| \; et \; \varphi = \varphi_y - \varphi_x \tag{25}$$

Dans le cas d'une onde parfaitement polarisée, $|E_x|$, $|E_y|$ et φ sont constants dans le temps. Lorsque l'onde EM est partiellement polarisée, un unique vecteur de Jones n'est pas suffisant pour décrire la polarisation de l'onde et il convient alors d'utiliser le formalisme de Stokes dont les paramètres s'écrivent dans la base $\{x, y\}$:

$$\begin{aligned} q_0 &= \langle |E_x|^2 + |E_y|^2 \rangle \\ q_1 &= \langle |E_x|^2 - |E_y|^2 \rangle \\ q_2 &= \langle 2|E_x||E_y| \cos\varphi \rangle \\ q_3 &= \langle 2|E_x||E_y| \sin\varphi \rangle \end{aligned} \tag{26}$$

Les paramètres de Stokes permettent de décrire la polarisation d'une onde à 2 dimensions : q_0 est égale à la puissance totale, q_1 est égal à la puissance de la composante linéaire horizontale ou verticale, q_2 à la puissance de la composante linéaire orientée à 45 ou 135° et q_3 à la puissance de la composante circulaire gauche ou droite. Lorsque l'onde est parfaitement polarisée, seuls 3 paramètres sont linéairement indépendants et liés par la relation : ${q_0}^2 = {q_1}^2 + {q_2}^2 + {q_3}^2$.

Le formalisme de Stokes permet de représenter une onde totalement ou partiellement polarisée au travers de la matrice de cohérence $[J]$ de taille 2x2 qui est semi-défini positive hermitienne complexe :

$$[J] = \begin{bmatrix} \langle E_x E_x^* \rangle & \langle E_x E_y^* \rangle \\ \langle E_y E_x^* \rangle & \langle E_y E_y^* \rangle \end{bmatrix} = \begin{bmatrix} J_{xx} & J_{xy} \\ J_{yx} & J_{yy} \end{bmatrix} \tag{27}$$

avec $\langle . \rangle$ l'opérateur de moyenne spatiale ou temporelle. On peut alors réécrire les paramètres de Stokes tels que :

$$\begin{aligned} q_0 &= J_{xx} + J_{yy} \\ q_1 &= J_{xx} - J_{yy} \\ q_2 &= J_{xy} + J_{yx} \\ q_3 &= jJ_{xy} - jJ_{yx} \end{aligned} \tag{28}$$

Finalement, on définit le degré de polarisation DoP tel que $DoP = 1$ pour une onde totalement polarisée et $DoP = 0$ pour une onde totalement dépolarisée :

$$DoP = \frac{\sqrt{q_1^2 + q_2^2 + q_3^2}}{q_0} \tag{29}$$

Le Tableau 3 ci-dessous donne les valeurs des vecteurs de Jones, paramètres de Stokes et matrice de cohérence pour quelques états de polarisation canoniques :

POLARISATION	E	q	[J]
Linéaire horizontale	$\begin{bmatrix}1\\0\end{bmatrix}$	$\begin{bmatrix}1\\1\\0\\0\end{bmatrix}$	$\begin{bmatrix}1&0\\0&0\end{bmatrix}$
Linéaire verticale	$\begin{bmatrix}0\\1\end{bmatrix}$	$\begin{bmatrix}1\\-1\\0\\0\end{bmatrix}$	$\begin{bmatrix}0&0\\0&1\end{bmatrix}$
Linéaire à 45°	$\frac{1}{\sqrt{2}}\begin{bmatrix}1\\1\end{bmatrix}$	$\begin{bmatrix}1\\0\\1\\0\end{bmatrix}$	$\frac{1}{2}\begin{bmatrix}1&1\\1&1\end{bmatrix}$
Linéaire à 135°	$\frac{1}{\sqrt{2}}\begin{bmatrix}-1\\1\end{bmatrix}$	$\begin{bmatrix}1\\0\\-1\\0\end{bmatrix}$	$\frac{1}{2}\begin{bmatrix}1&-1\\-1&1\end{bmatrix}$
Circulaire gauche	$\frac{1}{\sqrt{2}}\begin{bmatrix}1\\j\end{bmatrix}$	$\begin{bmatrix}1\\0\\0\\1\end{bmatrix}$	$\frac{1}{2}\begin{bmatrix}1&-j\\j&1\end{bmatrix}$
Circulaire droite	$\frac{1}{\sqrt{2}}\begin{bmatrix}1\\-j\end{bmatrix}$	$\begin{bmatrix}1\\0\\0\\-1\end{bmatrix}$	$\frac{1}{2}\begin{bmatrix}1&j\\-j&1\end{bmatrix}$

*Tableau 3 : Vecteur de Jones **E**, paramètres de Stokes **q** et matrice de cohérence **[J]** pour quelques états de polarisation canoniques*

2.3.2. Mise en œuvre instrumentale

La polarimétrie radar concerne l'acquisition et l'analyse de données acquises dans différents états de polarisation. C'est une technique largement utilisée en télédétection micro-ondes puisqu'elle permet de collecter des informations physiques sur la nature, la structure et la composition de la zone imagée, pour des applications sur les surfaces terrestres ou océaniques. Elle est basée sur la mesure et l'analyse des propriétés polarimétriques des diffuseurs présents au sein de la cellule de résolution. La polarimétrie SAR (POLSAR) permet de mesurer des paramètres géophysiques des surfaces imagées (humidité, rugosité …) et apporte des informations sur les mécanismes de rétrodiffusion présents. En télédétection radar, les polarisations les plus couramment utilisées sont les polarisations linéaires horizontale (Fig. 12 – (a)) et verticale (Fig. 12 – (b)), telles que :

- Polarisation linéaire **horizontale (H)** : $\chi = 0° \; ; \; \psi = 0/180°$
- Polarisation linéaire **verticale (V)** : $\chi = 0° \; ; \; \psi = 90°$

où χ et ψ sont les angles d'ellipticité et d'orientation de l'ellipse de polarisation (cf. 2.3.1).

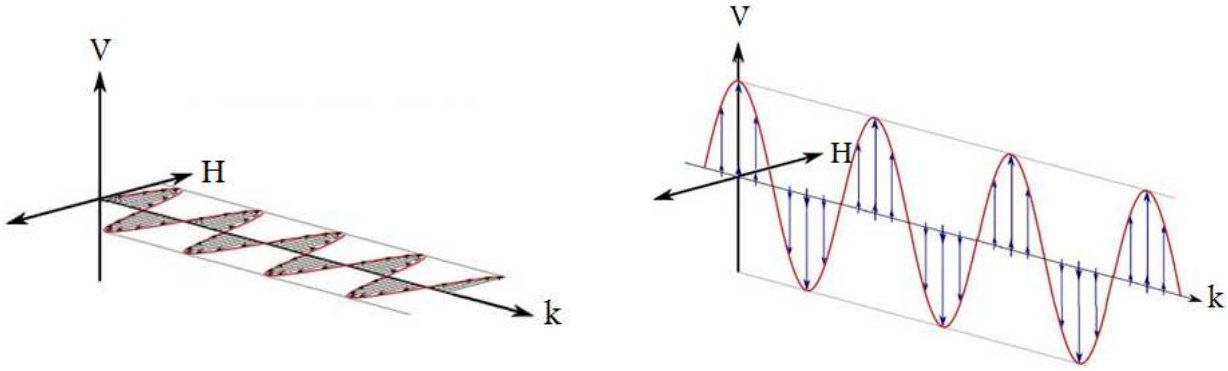

(a) : polarisation linéaire horizontale (H) (b) : polarisation linéaire verticale (V)

Fig. 12 : Illustration des polarisations linéaires (a) horizontale et (b) verticale – les axes k, H et V correspondent respectivement à la direction de propagation et aux composantes horizontale et verticale du champ électrique

D'un point de vue instrumental, différents modes d'acquisition polarimétriques sont envisageables. Dans tous les cas, l'instrument radar sera caractérisé par le(s) état(s) de polarisation disponible(s) en émission et réception, identifié tel que : XY avec $X \epsilon \{H, V\}$ la polarisation en émission et $Y \epsilon \{H, V\}$ la polarisation en réception. Il s'en suit les différentes combinaisons possibles suivantes :

- HH : polarisation horizontale en émission et en réception
- VV : polarisation verticale en émission et en réception
- HV : polarisation horizontale en émission et verticale en réception
- VH : polarisation verticale en émission et horizontale en réception

Les états de polarisations HH et VV sont habituellement dénommés *polarisation directe* ou *co-polar* et les états HV et VH sont dénommés *polarisation croisée* ou *cross-polar*. D'après le principe de réciprocité, les deux canaux en polarisation croisée sont identiques (même valeur d'amplitude et de phase) [28] dans le cas monostatique.

La mise en œuvre d'un mode polarimétrique sur un instrument SAR est en général contraint par le nombre de voies de polarisation en émission ; disposer de deux voies de réception n'étant pas contraignant (sauf pour le volume de données à enregistrer). Les modes envisageables sont :

- Mono-polarisation : émission et réception d'un seul état polarimétrique (HH ou VV).
- Polarisation duale : émission d'un état de polarisation et réception des deux états simultanément, soit HH+HV ou VV+VH.
- Polarisation complète : émission alternée (entre PRF) des deux états de polarisation et réception simultanée des états H et V, soit HH+HV+VH+VV. Le chronogramme est à 2 PRF pour ce mode d'acquisition.

Il existe un autre mode, plus marginal mais néanmoins mis en œuvre sur l'instrument spatial COSMO-Skymed, qui consiste à émettre de façon alternée les états H et V et également de recevoir de façon alternée les états H et V. Ce mode présente le désavantage de considérablement augmenter l'écart temporel entre l'acquisition des composantes HH et VV puisque nous avons dans ce cas un chronogramme à 4 PRF, ce qui peut être contraignant pour des applications nécessitant une parfaite corrélation entre les canaux en polarisation directe ou lorsque l'acquisition est réalisée sur une surface en mouvement, comme sur les océans.

Un radar polarimétrique permet de collecter les signaux émis et rétrodiffusés dans différents états de polarisation au sein d'une même cellule de résolution que l'on peut écrire pour chaque pixel (i,j) sous la forme du vecteur de rétrodiffusion $\vec{k}$ dans les bases lexicographique et de Pauli :

$$\vec{k}_{H,V} = \begin{bmatrix} S_{HH} \\ S_{HV} \\ S_{VH} \\ S_{VV} \end{bmatrix} \quad \text{: base lexicographique} \tag{30}$$

$$\vec{k}_{Pauli} = \frac{1}{\sqrt{2}} \begin{bmatrix} S_{HH} + S_{VV} \\ S_{HH} - S_{VV} \\ S_{HV} + S_{VH} \\ j(S_{HV} - S_{VH}) \end{bmatrix} \quad \text{: base de Pauli} \tag{31}$$

Dans le cas monostatique, on peut simplifier le vecteur de rétrodiffusion en vertu du principe de réciprocité ($S_{HV} \Leftrightarrow S_{VH}$) et définir les matrices de covariance ([C] – base lexicographique) et de cohérence ([T] – base de Pauli) de taille 3x3 :

$$\vec{k}_{H,V} = \begin{bmatrix} S_{HH} \\ \sqrt{2}S_{HV} \\ S_{VV} \end{bmatrix} \tag{32}$$

$$[C] = \langle \vec{k}_{H,V} . \vec{k}_{H,V}^{\dagger} \rangle = \begin{bmatrix} \langle |S_{HH}|^2 \rangle & \sqrt{2}\langle S_{HH} . S_{HV}^{*} \rangle & \langle S_{HH} . S_{VV}^{*} \rangle \\ \sqrt{2}\langle S_{HV} . S_{HH}^{*} \rangle & 2\langle |S_{HV}|^2 \rangle & \sqrt{2}\langle S_{HV} . S_{VV}^{*} \rangle \\ \langle S_{VV} . S_{HH}^{*} \rangle & \sqrt{2}\langle S_{VV} . S_{HV}^{*} \rangle & \langle |S_{VV}|^2 \rangle \end{bmatrix} \tag{33}$$

$$\vec{k}_{Pauli} = \frac{1}{\sqrt{2}} \begin{bmatrix} S_{HH} + S_{VV} \\ S_{HH} - S_{VV} \\ 2S_{HV} \end{bmatrix} \tag{34}$$

$$\begin{aligned} [T] &= \langle \vec{k}_{Pauli} . \vec{k}_{Pauli}^{\dagger} \rangle \\ &= \frac{1}{2} \begin{bmatrix} \langle |S_{HH} + S_{VV}|^2 \rangle & \langle (S_{HH} + S_{VV})(S_{HH} - S_{VV})^{*} \rangle & 2\langle (S_{HH} + S_{VV}) S_{HV}^{*} \rangle \\ \langle (S_{HH} - S_{VV})(S_{HH} + S_{VV})^{*} \rangle & \langle |S_{HH} - S_{VV}|^2 \rangle & 2\langle (S_{HH} - S_{VV}) S_{HV}^{*} \rangle \\ 2\langle S_{HV}(S_{HH} + S_{VV})^{*} \rangle & 2\langle S_{HV}(S_{HH} - S_{VV})^{*} \rangle & 4\langle |S_{HV}|^2 \rangle \end{bmatrix} \end{aligned} \tag{35}$$

avec $.^{\dagger}$ l'opérateur transposé conjugué.

Les matrices de cohérence [T] et de covariance [C] définies ci-dessus contiennent les mêmes informations, elles sont seulement représentées différemment.

L'apport de la polarisation des ondes EM est un atout considérable pour estimer les propriétés géophysiques des surfaces continentales et océaniques [29]-[32]. La Fig. 13 ci-dessous illustre l'apport de la polarisation avec une image en polarisation unique et une image en polarisation complète représentée en fausses couleurs telles que :

- Base lexicographique : Rouge = canal HH, Vert = canal HV, Bleu = canal VV.
- Base de Pauli : Rouge = canal HH-VV, Vert = canal 2HV, Bleu = canal HH+VV.

Sur ces images, les différences de réponses dans les trois canaux polarimétriques signent les propriétés géométriques et radioélectriques au sein du pixel. Elles permettent également de fournir des informations sur les mécanismes de rétrodiffusion dominants, tels que [29] :

- **La diffusion de Bragg :** correspond à une surface rugueuse pour laquelle l'intensité en polarisation VV est supérieure à celle en HH
- **La diffusion de Fresnel :** correspond à une surface lisse pour laquelle l'intensité en polarisation HH est supérieure à celle en VV
- **La diffusion de volume :** l'intensité de la polarisation HV est particulièrement élevée, la diffusion de volume ayant tendance à très largement modifier la polarisation.

En générale, lorsqu'il s'agit d'afficher les données polarimétriques, on préfère substituer la représentation dans la base lexicographique à celle dans la base de Pauli qui permet une interprétation encore plus aisée des images polarimétriques selon les principes suivants :

- Bleu dominant : le canal polarimétrique HH + VV est de forte amplitude par rapport aux autres, c'est-à-dire que l'amplitude de HV est faible et la phase entre HH et VV est proche de zéro. Ceci est caractéristique de la rétrodiffusion par une surface.
- Rouge dominant : la phase entre HH et VV est proche de π, et dénote une réflexion de type double rebond, par un bâtiment par exemple.
- Vert dominant : contribution majoritaire en polarisation croisée, caractéristique d'une zone de forêt.

Néanmoins, il est important de noter que les représentations en fausses couleurs ne fournissent que des indications sur les propriétés polarimétriques de la scène observée et que leur interprétation doit être faite avec précaution. En particulier, les différents canaux sont mis à l'échelle en fonction de leur propre dynamique, les informations affichées ne concernent que les intensités rétrodiffusées et ne prennent pas en compte les informations de corrélation polarimétrique (sauf dans la base de Pauli) et surtout l'interprétation des mélanges de couleur reste très subjective.

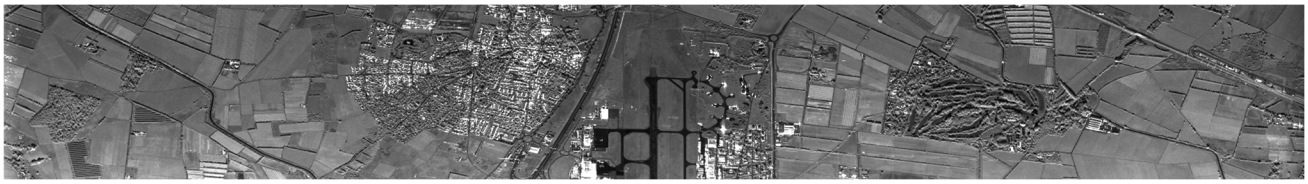

(a) : image radar en polarisation unique

(b) : image radar en polarisation complète – base lexicographique (R,G,B)=(HH,HV,VV)

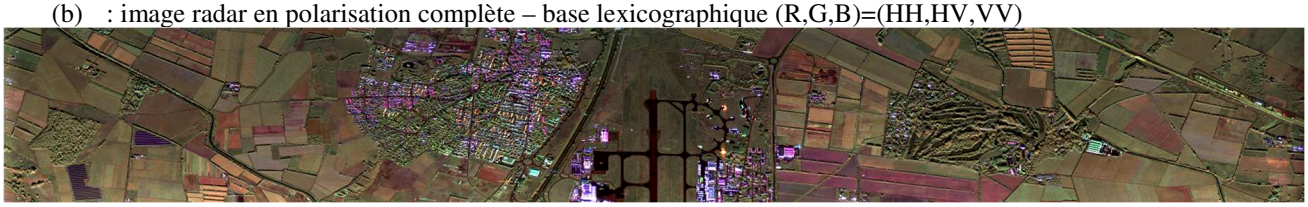

(c) : image radar en polarisation complète – base de Pauli (R,G,B)=(HH-VV,2HV,HH+VV)

Fig. 13 : Image radar en (a) polarisation unique et en polarisation complète avec représentation en fausses couleurs dans la base (b) lexicographique et (c) de Pauli – Images SAR ONERA/SETHI

2.3.3. Synthèse de polarisation

La base $\{H, V\}$ étant une base orthonormée des états de polarisation, il est possible de transformer toute acquisition dans cette base dans une autre base quelconque, par l'utilisation d'une matrice de passage. En particulier, il est possible de transformer des acquisitions SAR en polarisation complète (HH,HV,VH,VV) dans la base des ondes polarisées circulairement L (Left) et R (Right) par exemple. C'est ce qu'on appelle la synthèse de polarisation.
Dans la base linéaire $\{H, V\}$, la matrice de covariance est explicitement donnée par :

$$[C]_{H,V} = \langle \vec{k}_{H,V} . \vec{k}_{H,V}{}^{\dagger} \rangle = \begin{bmatrix} \langle |S_{HH}|^2 \rangle & \sqrt{2}\langle S_{HH} . S_{HV}{}^{*} \rangle & \langle S_{HH} . S_{VV}{}^{*} \rangle \\ \sqrt{2}\langle S_{HV} . S_{HH}{}^{*} \rangle & 2\langle |S_{HV}|^2 \rangle & \sqrt{2}\langle S_{HV} . S_{VV}{}^{*} \rangle \\ \langle S_{VV} . S_{HH}{}^{*} \rangle & \sqrt{2}\langle S_{VV} . S_{HV}{}^{*} \rangle & \langle |S_{VV}|^2 \rangle \end{bmatrix} \tag{36}$$

Elle est composée de neuf paramètres indépendants : les trois termes diagonaux réels et les trois termes de corrélation complexes entre les canaux polarimétriques.
Sous un changement de base de polarisation quelconque $\{A, B\}$ définit par ses angles d'ellipticité (χ) et d'orientation (ψ), la matrice de covariance se transforme en [33] :

$$[C]_{A,B} = [U]_{A,B} [C]_{H,V} \left[\widetilde{U}^{*}\right]_{A,B} \tag{37}$$

Avec $[U]_{A,B}$ la matrice de passage unitaire définit telle que :

$$[U]_{A,B} = \frac{1}{1 + \rho\rho^{*}} \begin{bmatrix} 1 & \sqrt{2}\rho & \rho^2 \\ -\sqrt{2\rho^{*}} & (1 - \rho\rho^{*}) & \sqrt{2}\rho \\ \rho^{*2} & -\sqrt{2}\rho^{*} & 1 \end{bmatrix} \tag{38}$$

avec ρ le ratio de polarisation :

$$\rho = \frac{\cos 2\chi \sin 2\psi + i \sin 2\chi}{1 + \cos 2\chi \cos 2\psi} \tag{39}$$

Une application importante de cette technique est l'identification analytique d'un état de polarisation qui permet de maximiser le contraste entre une cible et son environnement. Cette technique est appelée *l'optimisation de contraste* [34].

2.4. Paramètres de qualité et calibration des données SAR

2.4.1. Paramètres de Qualité Image

La qualité d'une image radar s'apprécie à travers un ensemble de paramètres, dits Paramètres de Qualité Image (PQI). Ils permettent une mesure quantitative de l'ensemble de la chaîne radar (émission, réception et formation de l'image) à partir de cibles étalons dont la réponse est parfaitement connue. Les cibles étalons les plus couramment utilisées sont des trièdres et des dièdres (cf. Fig. 14). Ce sont des installations mécaniques passives dont la Surface Equivalente Radar (SER) ne dépend que de la géométrie (pour une longueur d'onde radar λ donnée) et sont assimilables à des cibles ponctuelles dont la réponse radar est une réponse impulsionnelle connue.

$$\sigma = \frac{4\pi a^4}{3\lambda^2}\ [m^2] \quad : \text{SER d'un trièdre d'arête « a »} \qquad (40)$$

$$\sigma = \frac{8\pi a^2 b^2}{\lambda^2}\ [m^2] \quad : \text{SER d'un dièdre de côtés « a » et « b »} \qquad (41)$$

Par exemple, un trièdre de 56 cm d'arête (cf. Fig. 14(a)) produit à 10 GHz une SER de 457.7 m^2 (soit 26.6 dBm^2). Cet étalonnage de la radiométrie (énergie rétrodiffusée) permet de rendre la réponse radar d'un objet et/ou d'une surface indépendante de l'instrument de mesure radar.
Les équations ci-dessus sont des formulations générales qu'il convient de préciser en fonction de l'état de polarisation de l'onde EM, en particulier :

- **Réponse polarimétrique d'un trièdre** : les réponses dans les voies cross-polaires sont nulles et celles dans les voies co-polaires sont de même amplitude et en phase (il s'agit d'un nombre de réflexion impair), soit :

$$\begin{aligned} &|S_{HV}| = |S_{VH}| = 0 \\ &|S_{HH}| = |S_{HV}|\ et\ arg(S_{HH}.S_{VV}^*) = 0° \end{aligned} \qquad (42)$$

- **Réponse polarimétrique d'un dièdre** : lorsque le dièdre est orienté à 22.5°, les réponses sont de mêmes amplitude dans les 4 canaux polarimétriques et les voies co-polaires sont en opposition de phase (il s'agit d'un nombre de réflexion pair), soit :

$$\begin{aligned} &|S_{HH}| = |S_{HV}| = |S_{VV}| \\ &arg(S_{HH}.S_{VV}^*) = 180° \end{aligned} \qquad (43)$$

(a) : trièdre

(b) : dièdre

Fig. 14 : Cibles étalons de type (a) trièdre et (b) dièdre

La mesure de la Réponse Impulsionnelle (RI) de ces cibles étalons permet de « qualifier » les images radar acquises par l'instrument et produites par la chaîne de traitement radar. La RI d'une cible ponctuelle sur une image radar est une courbe en 2 dimensions, correspondant aux réponses impulsionnelles dans les axes distance et azimut.

Les PQI habituellement utilisés sont :

- La résolution (δ) : qui correspond à la largeur à -3 dB du lobe principal de la réponse.

- Le PSLR (Peak Side Lobe Ratio) : c'est le rapport entre le niveau du lobe secondaire le plus élevé (sur une étendue de 10 résolutions) et le niveau du lobe principal. Le PSLR mesure l'habilité du radar à identifier une cible de faible réponse par rapport à une cible adjacente de forte réponse. Un PSLR de niveau inférieur ou égale à -13 dB signe une bonne formation des images.

- Le ISLR (Integrated Side Lobe Ratio) : c'est le rapport entre l'énergie contenue dans les lobes secondaires (sur une étendue de 10 résolutions) et l'énergie contenue dans le lobe principal. L'ISLR mesure l'aptitude du radar à identifier une cible de faible réponse dans un environnement de réponse élevée. Un ISLR de -7 à -10 dB est communément admis.

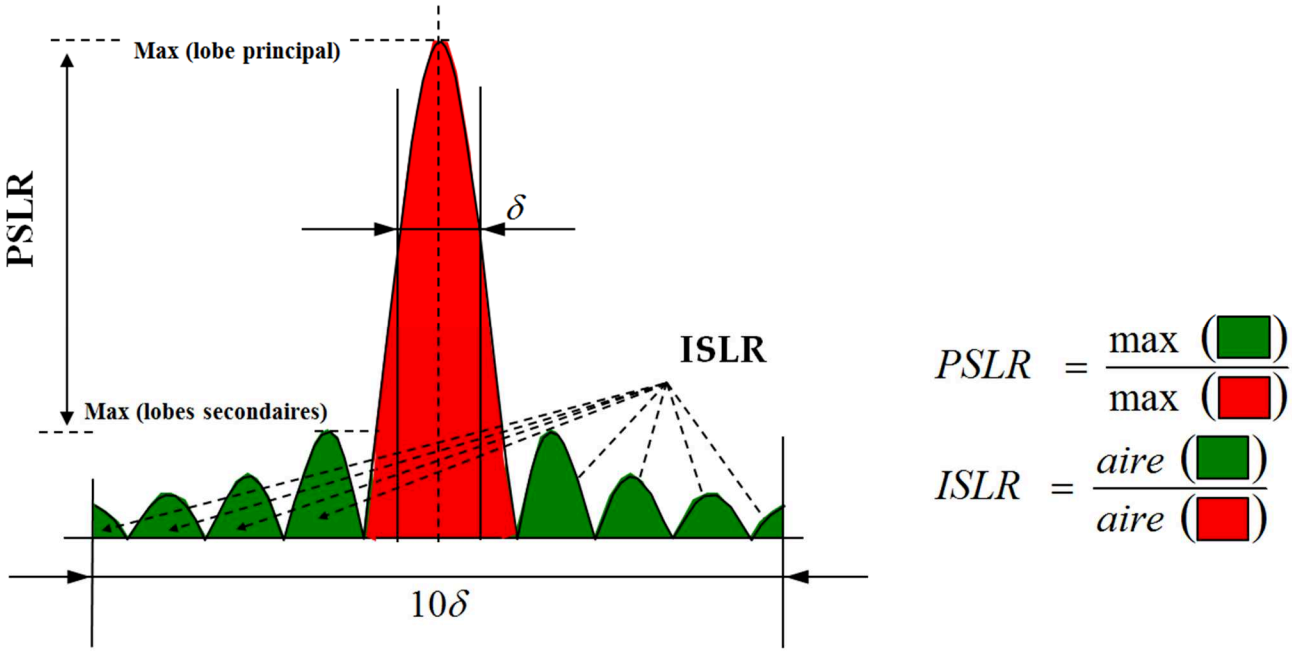

Fig. 15 : Réponses impulsionnelles et mesures de Paramètres Qualité Image (PQI).

Dans le cas de données polarimétriques, un paramètre important à mesurer est la diaphonie entre les voies H et V (ou « cross-talk » en anglais). Il s'agit de mesurer l'imperfection de l'orthogonalité de la base de polarisation $\{H, V\}$. Une méthode efficace pour cela est de mesurer la réponse radar d'une cible de type trièdre dans un canal HV ou VH, cette dernière étant théoriquement nulle. Une valeur de cross-talk inférieure ou égale à -35 dBm^2 est en générale jugée suffisante.

2.4.2. Calibration des images SAR

La calibration des images SAR consiste à étalonner les valeurs d'amplitude et de phase du signal radar. Cette opération est effectuée à partir d'acquisitions sur des cibles étalons, de type trièdre et dièdre. L'utilisation de trièdres est relativement aisée. Une fois le dispositif orienté correctement (en site et gisement), ces cibles produisent des réponses facilement exploitables pour la calibration. L'utilisation d'un dièdre est par contre beaucoup plus délicate car son orientation doit être réglée de façon très précise à 22.5°, ce qui se révèle parfois délicat.

Lorsque l'instrument radar opère en mono-polarisation, la calibration consiste à étalonner le niveau de SER de la cible mesuré sur l'image radar.

Lorsque que le radar fonctionne en polarisation duale (HH+HV ou VV+VH), la calibration consiste là aussi à étalonner le niveau de SER, mais cette fois dans les deux canaux (les voies co- et cross-polaire étant décorrélées, la différence de phase est un nombre aléatoire uniformément distribuée entre 0 et 2π).

Pour la calibration de données acquises en polarisation complète, la méthode de calibration utilisée habituellement est la méthode de Sarabandi [35]. Elle consiste à calculer un ensemble de paramètres complexes de calibration, $A_{XY} = |A_{XY}|e^{j\varphi_{XY}}$, avec $X, Y \epsilon \{H, V\}$. Les étapes sont les suivantes :

- Etape 1 : calibrer la voie HH en multipliant chaque pixel de la matrice HH par le paramètre de calibration en amplitude $|A_{HH}|$ afin que la SER mesurée sur la cible étalon (trièdre) coïncide avec sa valeur théorique :

$$S_{HH} \rightarrow S_{HH} \times |A_{HH}| \tag{44}$$

- Etape 2 : calibrer la voie VV en multipliant chaque pixel de la matrice VV par le paramètre de calibration complexe A_{VV} afin que la SER mesurée sur la cible étalon (trièdre) coïncide avec sa valeur théorique ($|A_{VV}|$) et afin que la différence de phase entre les voies HH et VV soit nulle sur le trièdre (φ_{VV}).

$$S_{VV} \rightarrow S_{VV} \times |A_{VV}|e^{j\varphi_{VV}} \tag{45}$$

- Etape 3 : calibrer les voies HV et VH en mesurant sur une surface homogène dépolarisante (forêt …) les différences entre les réponses en amplitude ($|A_{HV}|$) et en phase (φ_{HV}) des canaux en polarisation croisée et appliquer les paramètres de calibration tels que :

$$S_{HV} \rightarrow S_{HV} * \sqrt{|A_{HH}| \times |A_{VV}| \times |A_{HV}|}e^{j^{(\varphi_{VV}+\varphi_{HV})}/_2} \tag{46}$$

$$S_{VH} \rightarrow S_{VH} * \sqrt{|A_{HH}| \times |A_{VV}| / |A_{HV}|}\, e^{j^{(\varphi_{VV}-\varphi_{HV})}/_2} \tag{47}$$

Une fois les canaux polarimétriques calibrées en amplitude et phase, les données de télédétection peuvent être exploitées pour l'application visée (estimation des propriétés géo-physiques sur la surface imagée, production des signaux de référence,…).

2.4.3. Estimation du bruit thermique

La résolution radiométrique d'un instrument radar est souvent spécifiée en termes de NESZ (Noise Equivalent Sigma Zero). Le NESZ est définie comme la valeur de rétrodiffusion, σ^0, qui produit en un pixel un Rapport Signal à Bruit de 1 (soit 0 dB). Les cibles et/ou surfaces dont la valeur du coefficient de rétrodiffusion est inférieure au NESZ du radar ne peuvent pas être imagées de manière fiable car le niveau de l'intensité mesurée est alors dominé par le plancher de bruit de l'instrument. Les niveaux de NESZ pour les systèmes spatiaux sont généralement compris entre -25 et -35 dBm^2/m^2.

Le NESZ peut être estimé par des mesures en laboratoire mais une mesure tout au long du cycle de vie de l'instrument est en générale nécessaire. Pour ce faire, trois méthodes sont utilisées à l'ONERA :

- Méthode n°1 – coupure de l'émission radar : cette méthode consiste à effectuer une acquisition radar sans émettre de signal. Le niveau de signal mesuré est donc une estimation du bruit enregistré (chaîne de réception) prenant en compte les gains et imperfections de la chaîne de traitement radar. Bien qu'un amplificateur faible bruit soit en général positionné au niveau de la chaîne d'émission, cette méthode a le désavantage de sous-estimer le bruit de cette dernière.
- Méthode n°2 – corrélation polarisation croisée : une fois les deux images SAR en polarisation croisée (HV et VH) produites par la chaîne de traitement radar, on peut supposer que, si les données sont acquises avec un très faible écart temporel et si les deux images sont « parfaitement » superposées, alors la seule source de décorrélation est celle liée au bruit instrumental. On peut ainsi estimer le niveau de bruit instrumental par le biais de la corrélation entre les canaux en polarisation croisée en utilisant la formule ci-dessous ; cette méthode nécessite cependant de disposer des données en polarisation croisée :

$$\rho_{HVVH^*} = \frac{\langle S_{HV}.S_{VH}^* \rangle}{\sqrt{\langle |S_{HV}|^2 \rangle \langle |S_{VH}|^2 \rangle}} = \frac{1}{1 + SNR^{-1}} \tag{48}$$

avec SNR (Signal to Noise Ratio) le rapport signal à bruit.

- Méthode n°3 – matrice de covariance polarimétrique [36] : la matrice de covariance polarimétrique [C] de taille 4x4 est une matrice hermitienne, semi-défini et positive. Elle peut donc être décomposée en valeurs et vecteurs propres de telle sorte que les valeurs propres, $\lambda_i \; i \; \epsilon \; \{1,2,3,4\}$, vérifient :

$$\lambda_1 > \lambda_2 > \lambda_3 > \lambda_4 \geq 0 \tag{49}$$

Cependant, d'après le principe de réciprocité les deux canaux polarimétriques HV et VH sont égaux, la matrice de covariance n'a donc que 3 vecteurs propres linéairement indépendants, elle est donc de rang 3. Ce qui signifie qu'en absence de bruit, $\lambda_4 = 0$.
Dans un système réel, bruité, la quatrième valeur propre $\boldsymbol{\lambda_4}$ **est une estimation de la puissance de bruit**. Cette méthode d'estimation du niveau de bruit instrumental est robuste, elle nécessite cependant de disposer des 4 canaux polarimétriques, calibrées. Elle est également lourde d'un point de vue calculatoire puisqu'il est nécessaire de calculer, en chaque pixel de l'image, les valeurs et vecteurs propres de la matrice de covariance.

Une simplification peut être appliquée en utilisant la matrice de covariance de taille 2x2 suivante (dans ce cas, la seconde valeur propre donnera l'estimation du niveau de bruit) :

$$[C] = \langle \vec{k}_{H,V} . \vec{k}_{H,V}{}^{\dagger} \rangle = \begin{bmatrix} \langle |S_{HV}|^2 \rangle & \langle S_{HV} . S_{VH}{}^{*} \rangle \\ \langle S_{VH} . S_{HV}{}^{*} \rangle & \langle |S_{VH}|^2 \rangle \end{bmatrix} \quad (50)$$

Nous avons mis en œuvre ces trois méthodes d'estimation sur une acquisition SAR aéroportée (cf. Fig. 16). Pour les 3, on observe une forme en cloche de la courbe du niveau de bruit instrumental en fonction de la variation d'angle d'incidence de la fauchée, induite par le lobe d'antenne. Les deux dernières méthodes (cohérence cross-polaire, courbe bleue et inversion de la matrice de covariance, courbe rouge) produisent des courbes dont les tendances sont similaires. On observe cependant un léger écart de moins de 1 dB environ entre ces deux méthodes. On peut supposer que l'estimation par la mesure de la cohérence cross-polaire est plus sensible aux variations d'intensité et produit une légère surestimation du niveau de bruit. Elle est également assez sensible au seuil sur la valeur de la cohérence sélectionnée pour le calcul (0.8 ici). La méthode d'estimation par la coupure de l'émission radar (courbe noire) produit une courbe avec une tendance légèrement différente des autres, ce qui suggère qu'elle ne restitue que partiellement la figure de bruit et fournit une sous-estimation (environ 1.5 dBm^2/m^2 ici) du NESZ.

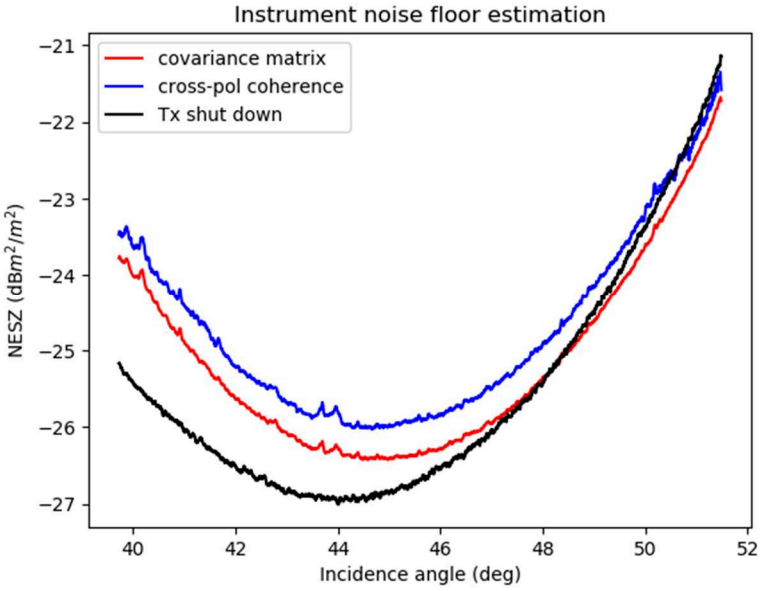

Fig. 16 : Estimation du niveau de bruit instrumental par les 3 méthodes proposées

3. ETAT DE L'ART SUR L'INTERACTION DE L'ONDE ELECTROMAGNETIQUE AVEC LA SURFACE OCEANIQUE

3.1. Description de la surface de mer

La surface de la mer est constituée d'un ensemble de vagues chacune caractérisée par une longueur d'onde, une amplitude et une direction de propagation. Cette surface est le siège d'interactions non linéaires entre les différentes échelles spatiales et temporelles des processus la constituant, ce qui rend difficile sa description exacte. Elle présente également un caractère dispersif puisque la vitesse de propagation des différentes échelles de vagues est fonction de leur longueur d'onde respective (les grandes vagues se propagent plus rapidement que les plus courtes), exprimée par la relation dite « relation de dispersion » suivante :

$$\omega^2 = \left(gk + \frac{\gamma k^3}{\rho}\right) tanh(kP) \tag{51}$$

avec ω la pulsation des vagues, $g = 9.81\, m.s^{-2}$ l'accélération de la pesanteur, γ la tension superficielle de l'eau de mer ($\gamma = 0.07497\, N.m^{-1}$ à une température de 10°C) et ρ la masse volumique de l'eau de mer ($\rho = 1027\, kg.m^{-3}$ à une température de 10°C). $k = \frac{2\pi}{\lambda}$ est le nombre d'onde pour une vague de longueur d'onde λ et P est la profondeur de l'eau (bathymétrie - exprimée en mètre).

La complexité des processus mis en œuvre ainsi que leurs interactions respectives rend illusoire toute description déterministe et il est d'usage de décrire la surface de la mer de façon statistique. Sous l'effet du vent, la force de friction qu'exerce celui-ci sur l'océan amène la surface de l'eau à prendre une forme complexe composée de vagues dites de capillarités (de longueur d'onde centimétrique ou inférieure). Elles entrainent alors, par interactions non linéaires, la formation de vagues de plus grandes longueurs d'onde (cf. profil Fig. 17). Le profil des vagues est asymétrique avec une pente face au vent supérieure à celle dos au vent. Les vagues de capillarité interagissent entre-elles de façon non linéaire et produisent des vagues de taille supérieure appelées vagues de capillarité-gravité (longueur d'onde centimétrique) et de gravités (échelle décimétrique à métrique). Les vagues longues peuvent se propager sur de très longues distances. On définit parmi celles-ci « la houle » qui est caractérisée par une vitesse de phase plus grande que la vitesse du vent projetée dans la direction de propagation.

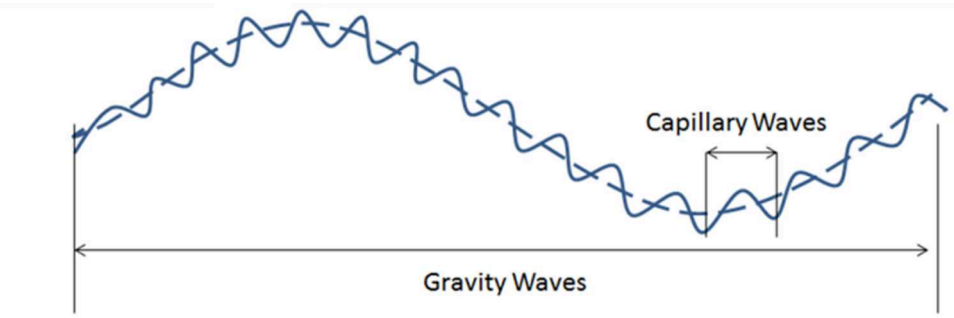

Fig. 17 : Profil de la surface océanique

La surface océanique est le lieu de transfert d'énergie entre les différentes échelles de vagues : des grandes échelles vers les petites échelles et vice versa (les interactions non-linéaires entre les vagues de gravité courtes conduisent à des transferts d'énergie vers les vagues de gravité longues). La viscosité de l'eau provoque une dissipation d'énergie au niveau des plus petites vagues. Et inversement, il existe une « cascade d'énergie » des vagues courtes vers les vagues longues sous l'effet des interactions non linéaires entre vagues de gravité. De l'énergie est également perdue lors du déferlement des plus grandes vagues. Lorsque le vent est constant, un équilibre se produit et on parle de mer pleinement développée (*fully developed sea*). La surface est alors décrite par son spectre de longueur d'onde de vagues. Le plus couramment utilisé en télédétection micro-ondes est le spectre d'Elfouhaily [37] dont une illustration tirée de [38] est donnée Fig. 18 ci-dessous.

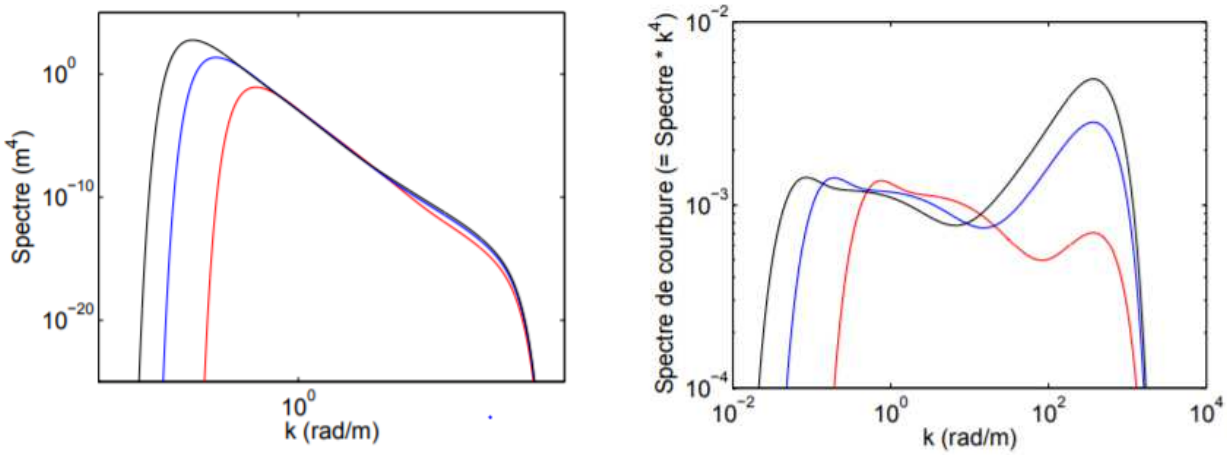

Fig. 18 : Illustrations d'un spectre océanique d'Elfouhaily – Amplitude du spectre de hauteur (gauche) et de courbure (droite) pour des vitesses de vent de 5 m.s^{-1} (rouge), 10 m.s^{-1} (bleu) et 15 m.s^{-1} (noir) – conditions de visée face au vent figures tirées de [38].

Il est d'usage d'exprimer les conditions de vent en fonction de :

La direction de propagation (convention « to ») : avec ψ l'angle entre la visée radar et la direction du vent. Les conventions sont : ψ=0° (upwind) pour une visée radar face au vent, ψ=90° (crosswind) pour une visée travers au vent et ψ=180° (downwind) pour une visée dos au vent

La vitesse moyenne à 10 m de la surface (U_{10}) : la vitesse $U(z)$ exprimée en m.s^{-1} à une altitude z au-dessus de la surface est liée à la vitesse de friction en surface (u^*) par la relation suivante, aussi appelée profil von Karmann :

$$U(z) = \frac{u^*}{0.4} ln\left(\frac{z}{z_0}\right) \quad ; \quad z_0 = \frac{0.684}{u^*} + 4{,}28.10^{-5}(u^*)^2 - 4{,}43.10^{-2} \tag{52}$$

où z et z_0 sont exprimés en cm. La variation de la vitesse avec l'altitude est non négligeable (cf. Fig. 19) et il est nécessaire de connaitre avec précision l'altitude à laquelle sont effectuées les mesures de vitesse du vent. Il est d'usage, en télédétection des surfaces océaniques, d'utiliser une vitesse de vent mesurée à 10 m de la surface (U_{10}).

En conditions océanographies et atmosphériques stables, un vent mesuré à une altitude z peut être converti en U_{10} par la relation suivante :

$$U_{10} = U(z)\frac{8.7403}{ln\left({}^{z}/_{0.0016}\right)} \tag{53}$$

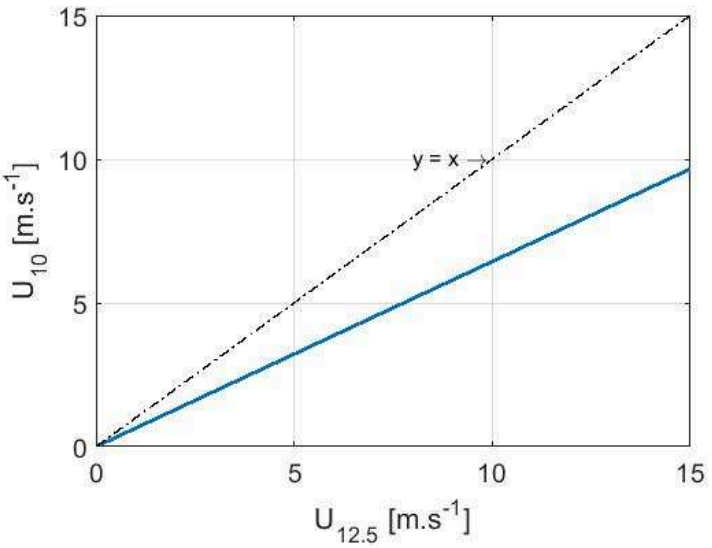

Fig. 19 : Vitesse de vent au-dessus de la surface : évolution entre un vent mesuré à 10 m et un vent mesuré à 12.5 m

Le vent est le paramètre principal pour décrire la surface de mer mais d'autres facteurs doivent également être pris en compte, parmi ceux-ci on peut citer :

- Le « fetch », qui est la durée ou la distance sur laquelle le vent souffle de façon constante et qui permet de distinguer les mers jeunes des conditions de mer pleinement développée. Les conditions de fetch limitées correspondent à une période de croissance des vagues sous l'action du vent, jusqu'au régime d'équilibre (fetch infini). A vent équivalent, les vagues observées en conditions de fetch limitées (près des côtes ou lorsque la vitesse du vent n'est pas établi) sont de moindre hauteur par rapport à celles observées en conditions de fetch infini (mer pleinement développée), mais de plus forte pente.

- La houle qui correspond aux vagues de grandes échelles qui ne peuvent plus croître sous l'effet du vent en raison de leur vitesse de phase qui dépasse celle du vent et qui peuvent venir modifier localement la surface de la mer. On considère habituellement que la houle correspond à des vagues générées dans des zones différentes de la zone d'intérêt (à des distances pouvant aller jusqu'à plusieurs milliers de km). La surface de la mer est alors une superposition de vagues, celles issues de la houle et celles générées par le vent localement, appelée « mer du vent ».

3.2. Modèles de diffusion électromagnétiques

Dans le domaine des micro-ondes, la surface océanique est considérée comme une surface rugueuse, pour laquelle le mécanisme de rétrodiffusion dominant est de type « rétrodiffusion surfacique ». Depuis les années 1950, de nombreux auteurs se sont intéressés à développer des modèles mathématiques pour décrire l'interaction de l'onde EM avec une surface rugueuse.

La plupart des modèles reposent sur deux approches asymptotiques qui sont les modèles de référence :

1) Le premier d'entre eux, proposé en 1951 [39], a été développé pour les surfaces faiblement rugueuses (c'est-à-dire dont les échelles de rugosité sont petites par rapport à la longueur d'onde EM) est appelé Modèle des Petites Perturbations ou *Small-Perturbation Model (SPM)*. Il est également connu sous le nom de diffusion de ***Bragg*** en contexte océanique.

2) Le second modèle approché est le modèle dit de ***Kirchhoff*** ou de *l'Optique Physique* qui permet de décrire l'interaction d'une onde EM avec une surface dont les échelles de rugosité sont grandes devant la longueur d'onde [40]. Pour résoudre le calcul intégral qui représente le champ total diffusé par la surface illuminée, deux types d'approximations ont été utilisées selon les échelles de rugosité :

    - Le modèle de l'optique géométrique pour $ks \geq 3$
    - Le modèle de l'optique physique pour $ks < 3$

avec s la hauteur quadratique moyenne (ou rms pour « Root Mean Square » en anglais) de la surface et $k = 2\pi/\lambda$ le nombre d'onde EM.

Dans le cadre de la théorie de Bragg, l'énergie rétrodiffusée par la surface océanique en direction du radar est essentiellement produite par un mécanisme de résonance entre l'onde radar (de longueur d'onde λ_{EM}) et les vagues dont la longueur d'onde (λ_B) satisfait la relation suivante :

$$\lambda_B = \frac{\lambda_{EM}}{2sin\theta} \tag{54}$$

avec θ l'angle d'incidence de l'onde radar sur la surface de mer.
Selon la théorie de Bragg du première ordre, l'énergie rétrodiffusée en polarisation croisée est nulle et la surface équivalente radar normalisée (σ^0) en polarisation directe est directement liée au spectre des hauteurs de la surface et aux coefficients de réflexion telle que [41] :

$$\sigma^0(\theta)_{pp} = 4\pi k^4 \cos^4\theta \left|\mathcal{B}_{pp}\right|^2 W(k_B) \tag{55}$$

avec $p \in \{H, V\}$ l'état de polarisation de l'onde radar, θ l'angle d'incidence de l'onde radar, W le spectre des hauteurs de la surface évalué au nombre d'onde de Bragg $k_B = {}^{2\pi}/_{\lambda_B}$ et $\mathcal{B}_{pp}$ les coefficients de réflexion au premier ordre tels que :

$$\begin{cases} \mathcal{B}(\theta)_{HH} = \dfrac{\varepsilon_r - 1}{\left[\cos\theta + \sqrt{(\varepsilon_r - \sin^2\theta)}\right]^2} \\ \mathcal{B}(\theta)_{VV} = \dfrac{(\varepsilon_r - 1)[\varepsilon_r(1 + \sin^2\theta) - \sin^2\theta]}{\left[\varepsilon_r\cos\theta + \sqrt{(\varepsilon_r - \sin^2\theta)}\right]^2} \end{cases} \tag{56}$$

avec ε_r la constante diélectrique relative (cf. 2.2.4).

Les modèles de *Bragg* (petites perturbations) et de *Kirchhoff* (Optique Physique) ont des domaines de validité distincts en général :

- Kirchhoff : valide aux incidences normales [0 - 60° environ] – rugosité grande devant λ_{EM}
- Bragg : valide aux incidences modérées [30 - 60° environ] – rugosité faible devant λ_{EM}

La surface de mer présentant un continuum d'échelles de rugosité, les modèles dits « unifiés » ou « deux échelles » ont été proposés afin de réaliser la transition entre les théories de Bragg et de Kirchhoff. Selon le modèle deux échelles, la surface de mer est vue comme la superposition de deux échelles (comme illustrée Fig. 17) : les petites échelles (dont la longueur caractéristique est proche de la longueur d'onde radar) correspondent aux vagues de gravités-capillarités produites par l'effet du vent sur la surface de mer. Elles sont le principal mécanisme de rétrodiffusion à l'origine de l'énergie renvoyée en direction du radar. Ces petites échelles sont « portées » par les grandes qui modifient localement leur orientation dans les deux directions. Le modèle deux-échelles le plus populaire et le plus ancien [41] est le modèle de **Bragg composite**. Il permet de prendre en compte les variations locales de l'angle d'incidence induites par les grandes vagues, on parle alors de modulation de pente des vagues et du modèle de « Bragg tilté » (*tilted Bragg scattering model*). Dans cette théorie, la surface de la mer est modélisée comme un ensemble de facettes, inclinées et rugueuses, dont chacune contribue à la rétrodiffusion du rayonnement incident par un mécanisme de type Bragg. Ces facettes constituent les petites échelles de la surface (vagues de longueur d'onde centimétrique à décimétrique et de période inférieure à la seconde [42]), elles dépendent directement de la vitesse du vent local et sont réparties aléatoirement sur la surface de diffusion. L'inclinaison de chaque facette est causée par des ondes de gravité de plus grande échelle à la surface de l'océan qui modifient l'orientation locale, ou inclinaison, des ondes courtes [43]. L'orientation de la facette de la surface de la mer est définie par deux angles: ψ l'inclinaison dans le plan d'incidence et ξ l'inclinaison dans le plan perpendiculaire au plan d'incidence (cf. [44] Fig. 1).

D'après la théorie de Bragg composite, la rétrodiffusion de chaque facette s'écrit comme [44] :

$$\sigma^0(\theta_i,\psi,\xi)_{HH} = 4\pi k^4 \cos^4\theta \left| \left(\frac{\sin(\theta-\psi)\cos\xi}{\sin\theta_i}\right)^2 \mathcal{B}_{HH}(\theta_i) + \left(\frac{\sin\xi}{\sin\theta_i}\right)^2 \mathcal{B}_{VV}(\theta_i) \right|^2 W(k_B) \quad (57)$$

$$\sigma^0(\theta_i,\psi,\xi)_{VV} = 4\pi k^4 \cos^4\theta \left| \left(\frac{\sin(\theta-\psi)\cos\xi}{\sin\theta_i}\right)^2 \mathcal{B}_{VV}(\theta_i) + \left(\frac{\sin\xi}{\sin\theta_i}\right)^2 \mathcal{B}_{HH}(\theta_i) \right|^2 W(k_B) \quad (58)$$

avec $\theta_i = cos^{-1}[cos(\theta-\psi)cos\xi]$ l'angle d'incidence au niveau de chaque facette, modulée localement par les grandes échelles. L'effet de la modulation permet également d'introduire un terme de polarisation croisée non nul (contrairement au modèle SPM), sa formulation analytique n'est cependant pas triviale et nécessite un développement au second ordre.

Dans un raisonnement deux échelles, le coefficient de rétrodiffusion totale provenant de l'ensemble de la surface s'obtient en intégrant les contributions de chacune des facettes, pondérées par la probabilité d'occurrence des pentes des grandes échelles.

$$\sigma^0(\theta_i)_{pp} = \sigma^0(\theta_i,\psi,\xi)_{pp} * P(\psi,\xi) \quad (59)$$

où * est l'opérateur de convolution.

Le problème majeur de ce type de méthode est l'existence d'une fréquence de coupure séparant les deux échelles de vagues (vagues courtes et vagues longues). Le coefficient de rétrodiffusion radar estimé étant largement dépendant du choix de cette fréquence de coupure (une illustration est fournie Fig. 20 – la fréquence de coupure entre les parties haute fréquence et basse fréquence a été choisie arbitrairement).

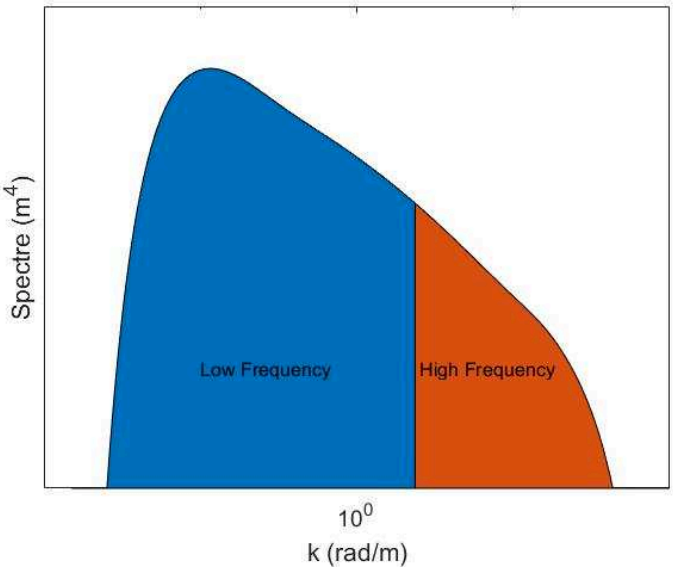

Fig. 20 : Illustration d'une séparation entre les parties basse fréquence (zone bleue) et haute fréquence (zone rouge) d'un spectre océanique – La fréquence de coupure est choisie arbitrairement

Un second modèle asymptotique deux-échelles largement utilisé dans la littérature est le modèle dit de **l'approximation des petites pentes** (SSA pour Small Slope Approximation) [45]-[47]. C'est un modèle unifié qui peut donc être appliqué à une surface constituée de différentes échelles de rugosité telle la surface de mer. Il dispose d'un large domaine de validité angulaire (incidence comprise entre 0 et 60° environ). Le modèle SSA consiste en un développement en série sur les pentes de la surface. Cette approximation est valide si l'écart type des pentes de la surface n'excède ni la tangente de l'angle d'incidence ni celle de l'angle de diffusion [48].

Comme dit précédemment, une limitation importante des modèles deux échelles est le choix de la fréquence de coupure (entre les deux domaines de rugosité). Cette limitation a été levée en 2008 avec l'introduction du modèle **GO-SSA** [49]. Alors que les modèles deux échelles classiques considèrent l'hybridation entre les deux modèles asymptotiques de référence, Kirchhoff (GO) et Bragg (SPM), le modèle GO-SSA combine lui les méthodes de Kirchhoff (GO) et l'approximation des petites pentes (SSA). De plus, la combinaison des deux modèles (GO et SSA) n'est pas effectuée brutalement à l'aide d'une fréquence de coupure entre les deux échelles mais en utilisant une fonction assurant une transition « douce » entre les deux domaines. La réflectivité radar estimée par le modèle GO-SSA est globalement similaire à celle fournie par les autres modèles deux échelles, sont apport se situe principalement au niveau de la zone de transition (angle d'incidence autour de 30°).

La Fig. 21 ci-dessous donne des illustrations de la réflectivité radar moyenne obtenue par le modèle deux échelles GO-SSA pour deux fréquences EM (1 et 10 GHz) et pour deux vitesses de vent mesurées à 10 m de la surface (U_{10}=5 et 10 m.s^{-1}). On observe les tendances générales suivantes :

- Electromagnétique : réflectivité maximale en polarisation VV au-delà de 20° d'incidence
- Géométrie : décroissance de la puissance rétrodiffusée lorsque l'angle d'incidence augmente
- Fréquentielle : augmentation de la puissance rétrodiffusée avec la fréquence
- Environnementale : augmentation de la puissance rétrodiffusée avec la vitesse du vent au-delà de 10-15° d'incidence

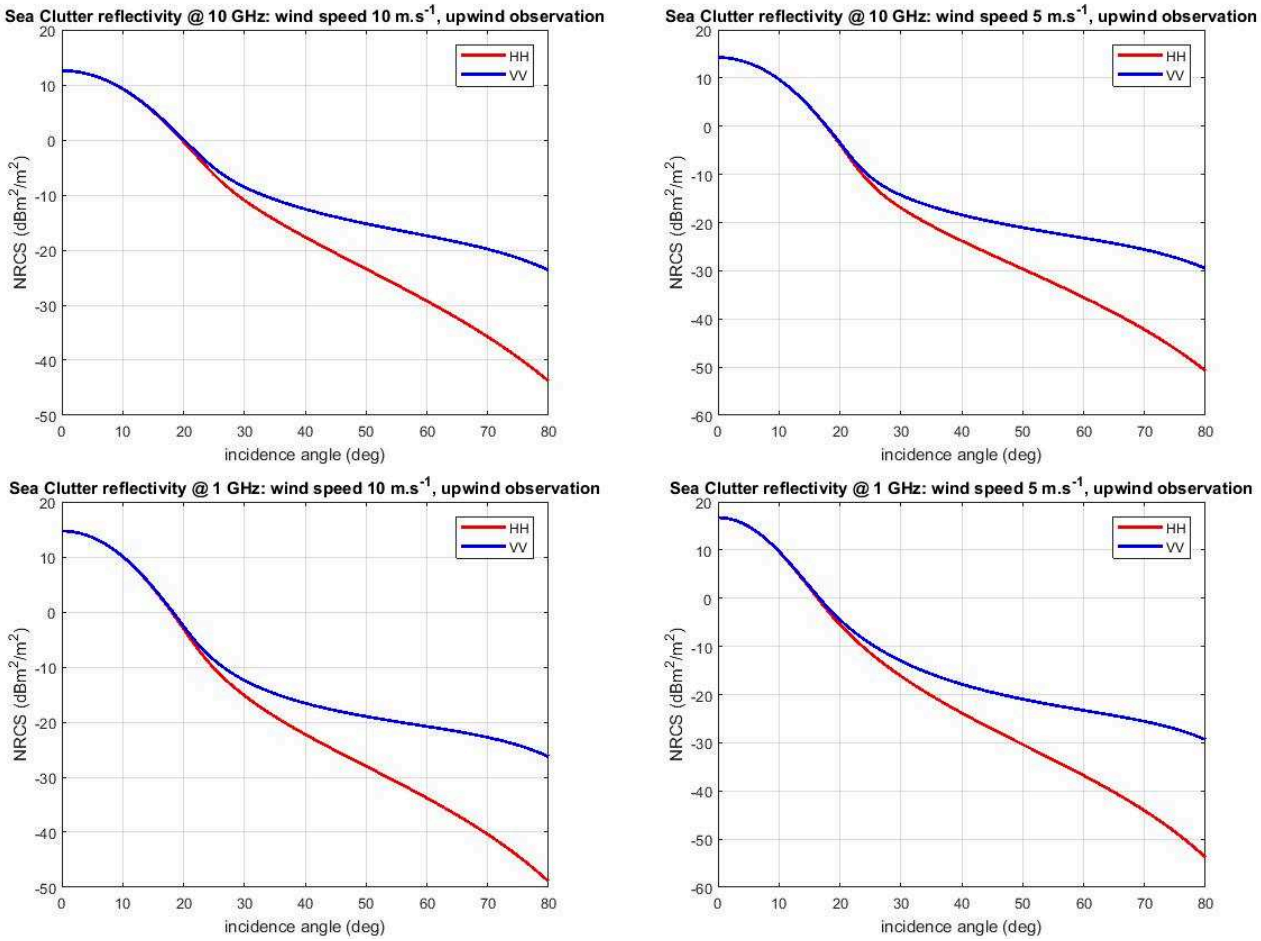

Fig. 21 : Courbes de réflectivité de la surface de mer estimée par le modèle GO-SSA en polarisation HH (rouge) et VV (bleue) pour une fréquence radar de 10 GHz (haut) et de 1 GHz (bas), un vent de 10 m/s (gauche) et de 5 m/s (droite)

Les systèmes radar micro-onde sont utilisés depuis des décennies en contexte opérationnel pour la détection et le suivi de navires. Ils opèrent en général à une fréquence porteuse comprise entre 1 et 15 GHz, en polarisation HH et en configuration d'observation rasante pour accroître le niveau du rapport cible à clutter (contraste entre la réflectivité de la cible et celle de la mer).
Cet aspect particulier de la mesure radar en configuration rasante sera abordé plus en détails dans la suite de ce manuscrit. On peut néanmoins dès à présent préciser que ces configurations sont propices à l'apparition de phénomènes dits « sea spike » qui correspondent à des échos radar de forte énergie.
On peut distinguer deux types de spike [50] :

- « Bursts » : ce sont des échos radar brefs (typiquement d'une durée de vie de 200 ms [50]) qui ne fluctuent que très peu avec le temps (phénomène stationnaire). Il n'y a pas de consensus dans la littérature sur leur l'origine mais pour nombreux auteurs ils proviendraient principalement des crêtes des vagues, juste avant leur déferlement. Ces événements induisent une réflexion spéculaire, pour lesquelles la rétrodiffusion est supérieure en polarisation HH qu'en VV.

- « Whitecaps » (« moutons ») : ce sont des évènements d'une durée de l'ordre de la seconde et qui ont une fluctuation similaire à celle du bruit, c'est-à-dire qui décorrèlent en quelques millisecondes. Ils proviennent d'une rétrodiffusion par une partie très rugueuse des vagues lorsqu'elles déferlent. Dans ce cas, il se produit un mécanisme de rétrodiffusion de type volumique, ce qui implique une énergie similaire dans les canaux HH et VV et une énergie en polarisation croisée non nulle (mais environ 10 dB plus faible qu'en co-polarisation [50]).

Les « spikes » (échos brefs et très énergétiques) de mer sont des événements qui induisent de forts échos et peuvent avoir une contribution non négligeable à la rétrodiffusion totale de la surface captée par le radar. A ces mécanismes, viennent également s'ajouter des contributions géométriques induites par les vagues de forte pente. Comme explicité précédemment, la surface de la mer est habituellement représentée comme une surface découpée en facettes, chacune de ces facettes étant caractérisée par une pente qui vient modifier localement l'angle d'incidence des ondes EM au niveau de la facette. Certaines vagues (ou facettes) ont une pente importante (orientée vers le radar) et vont donc produire une forte réponse, par simple effet géométrique (réduction de l'angle d'incidence local).

4. CARACTERISATION DE LA REPONSE RADAR D'UNE SURFACE OCEANIQUE

Les systèmes radar permettent des observations de jour comme de nuit et de façon quasi indépendante des conditions météorologiques. Ils sont donc des outils privilégiés pour la surveillance des territoires, en particulier dans le domaine maritime. Il en résulte de très nombreuses études et publications scientifiques sur la caractérisation de la rétrodiffusion des surfaces océaniques dans le domaine des micro-ondes. Cependant, certains verrous scientifiques demeurent à ce jour et ce paragraphe est dédié aux travaux que nous avons réalisés dans ce domaine.

4.1. Extension des modèles analytiques du coefficient de rétrodiffusion moyen

L'intensité moyenne du signal EM rétrodiffusée par une surface de mer est plutôt bien maîtrisée et on trouve dans la littérature de nombreux modèles qui permettent d'estimer la puissance moyenne du signal en fonction des paramètres du radar (angles de prises de vue, longueur d'onde et polarisation) et des conditions de mer (vitesse et direction du vent). Le modèle deux échelles GO-SSA [49] est un modèle analytique qui permet d'estimer le coefficient de rétrodiffusion moyen d'une surface de mer en polarisation directe (HH et VV). Les principales limites du domaine de validité de ce modèle analytique sont les suivantes :

- Domaine fréquentiel : fréquence radar [1 – 15 GHz]
- Domaine angulaire : angle d'incidence [0 – 60 °] ; angle d'azimut [0 – 360°]
- Domaine environnemental : vent U_{10} [3 – 15 m.s^{-1}]

Nous présentons dans les sous-sections suivantes les travaux que nous avons menés pour étendre les différents domaines de validité du modèle GO-SSA.

4.1.1. Extension du domaine angulaire – angle d'incidence

La principale limitation du modèle GO-SSA est sa limitation pour les angles d'incidences élevés (valide uniquement pour une incidence inférieure à 75-80°). Deux ajouts successifs ont été apportés au modèle GO-SSA initial pour étendre son domaine de validité en incidence.

Afin de prendre en compte les contributions non polarisées (ou non-Bragg) provenant, par exemple, du déferlement des vagues et dont l'impact sur la réflectivité totale augmente avec l'angle d'incidence, un terme correctif isotrope est ajouté à la section efficace radar estimée par GO-SSA [51]. Ce terme empirique, Q, proposé dans [52][53] permet de corriger le modèle GO-SSA aux forts angles d'incidence. Le modèle corrigé s'exprime tel que :

$$\sigma^0_{GO-SSA\,+\,Breaking\,wave} = \sigma^0_{GO-SSA}(1-Q) + Q \times \sigma^0_{wb} \tag{60}$$

avec $0 \leq Q \leq 1$ le paramètre correctif qui représente la fraction de surface de mer couverte par les vagues déferlantes et σ^0_{wb} la réflectivité d'une vague déferlante.

Des valeurs de σ^0_{wb} sont fournies dans [51] et le terme Q, adapté uniquement à la bande X, peut être approximé par la fonction suivante [51] :

$$\tilde{Q}_{X-band} \cong 1.35 \times 10^{-5} U_{10}^{3.4} \tag{61}$$

La correction apportée est significative en polarisation HH (supérieure à 10 dB en bande X, 80° d'incidence et pour un vent de 10 m/s), cf. Fig. 22. En polarisation VV la réflectivité estimée par le modèle deux échelles est toujours bien supérieure à ce terme correctif qui est alors négligeable.

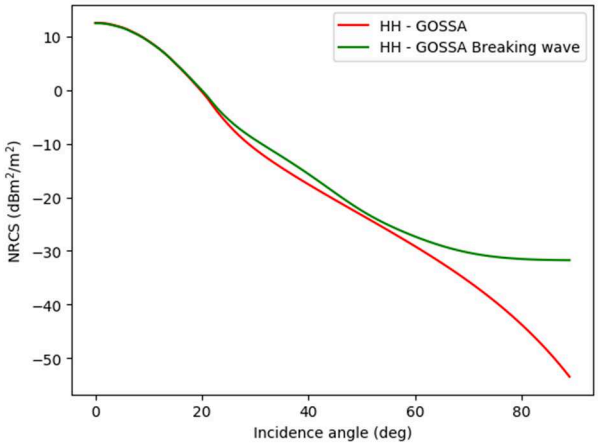

Fig. 22 : Courbes de réflectivité de la surface de mer en bande X polarisation HH estimées pour ce manuscrit par les modèles GO-SSA et GO-SSA corrigé du déferlement – vent U_{10}=10m/s.

Le modèle GO-SSA corrigé des contributions non polarisées « GO-SSA Breaking wave » proposé dans [51] et présenté ci-dessus a, d'après les conclusions fournies dans [51], un domaine de validité en angle d'incidence au-delà de 80°. Néanmoins, il ne restitue pas la variation attendue [54][55] en θ^4 aux incidences très rasantes ($\theta > 89°$ avec θ l'angle d'incidence). Il n'existe actuellement aucun modèle analytique qui permet d'estimer la réflectivité radar pour ces angles d'incidences extrêmes. Pour cette configuration de mesure particulière, le modèle qui fait référence est le modèle empirique GIT (*Georgia Institute of Technology empirical sea clutter model*) [56] dont la validité en incidence est limité aux angles supérieurs à 80°. Ce modèle fait consensus dans la communauté scientifique, il permet de prédire la réflectivité radar (en incidence rasante seulement) dans des configurations « normales » de propagation de l'onde radio au-dessus de la surface.

Selon le modèle GIT, la réflectivité radar moyenne en polarisation HH est donnée par [56] :

$$\sigma^0_{HH} = 3.9 \times 10^{-6} \lambda \psi^{0.4} A_i A_u A_w \tag{62}$$

De laquelle est déduite la réflectivité moyenne en polarisation VV :

$$\sigma^0_{VV} = \begin{cases} 9.33(h_{av} + 0.015)^{-0.24} \lambda^{0.25} (\psi + 0.0001)^{0.29} \times \sigma^0_{HH} & - \quad si\ f_{EM} \geq 3\ GHz \\ 166.0(h_{av} + 0.015)^{-0.4} \lambda^{0.87} (\psi + 0.0001)^{0.57} \times \sigma^0_{HH} & - \quad si\ f_{EM} < 3\ GHz \end{cases} \tag{63}$$

avec h_{av} la hauteur moyenne des vagues, ψ l'angle de rasance (complémentaire de l'angle d'incidence) et λ la longueur d'onde de radar.
On observe que la réflectivité radar en polarisation HH s'écrit comme la combinaison de trois termes : A_w lié à l'état de mer, A_u lié à la direction du vent et A_i un terme de multi-trajet permettent de prendre en compte les réflexions multiples sur la surface. La dépendance en $\psi^{0.4}$ permet quant à elle de prendre en compte les effets d'ombrage en incidence rasante.

Le terme d'état de mer A_w du modèle GIT s'exprime tel que [56] :

$$A_w = \left[\frac{1.94 \times V}{1 + {V}/{15.4}}\right]^{1.1(\lambda+0.015)^{-0.4}} \tag{64}$$

avec V la vitesse moyenne du vent liée, en condition de mer pleinement développée, à la hauteur moyenne des vagues h_{av} par la relation :

$$V = 8.67 \times h_{av}^{0.4} \quad \text{ou inversement} \quad h_{av} = 0.004525 \times V^{2.5} \tag{65}$$

Habituellement, la hauteur des vagues est décrite à partir de la hauteur significative, $h_{1/3}$, définie comme la hauteur moyenne du pic au creux du tiers des vagues les plus élevées. La relation avec la hauteur moyenne est telle que [57] :

$$h_{1/3} = 1.6\, h_{av} \tag{66}$$

La dépendance à la direction du vent est prise en compte par le terme A_u tel que :

$$A_u = exp[0.2cos(\phi)(1 - 2.8\psi)(\lambda + 0.015)^{-0.4}] \tag{67}$$

Le terme de multi-trajet A_i s'exprime tel que :

$$A_i = \frac{\sigma_\psi^4}{1 + \sigma_\psi^4} \tag{68}$$

avec σ_ψ un terme de rugosité tel que :

$$\sigma_\psi = \frac{(14.4\lambda + 5.5)\psi h_{av}}{\lambda} \tag{69}$$

Le terme de multi-trajet (ou d'interférence) A_i est un terme qui permet de restituer, aux angles d'incidences extrêmes, la variation de la réflectivité en ψ^4 comme indiqué dans [54][55]. Il dépend également de la longueur d'onde radar mais pas de la polarisation HH ou VV [56]. Nous en proposons une illustration en Fig. 23.
Nous avons ajouté ce terme d'atténuation global du modèle GIT au modèle de réflectivité « GO-SSA Breaking wave », ce qui conduit à une nouvelle correction du modèle analytique GO-SSA et un modèle semi-empirique intitulé « GO-SSA-Extended », valide pour l'ensemble de la plage angulaire en incidence [0 90°] [58]. Le modèle que nous avons proposé dans [58] s'exprime tel que :

$$\sigma^0_{GO-SSA-Extended} = [\sigma^0_{GO-SSA}(1 - Q) + Q \times \sigma^0_{wb}] \times A_i \tag{70}$$

Ce nouveau modèle a également été confronté à des données radar expérimentales acquises selon une large plage angulaire en incidence [58]. Une illustration est fournie Fig. 24 dans le cas des bandes X et L et une comparaison avec des données expérimentales réalisée dans le cadre du groupe OTAN SET-185 [59] est donnée Fig. 25. L'impact du terme de multi-trajet n'est visible sur la Fig. 24 que pour un angle d'incidence supérieur à 89°.

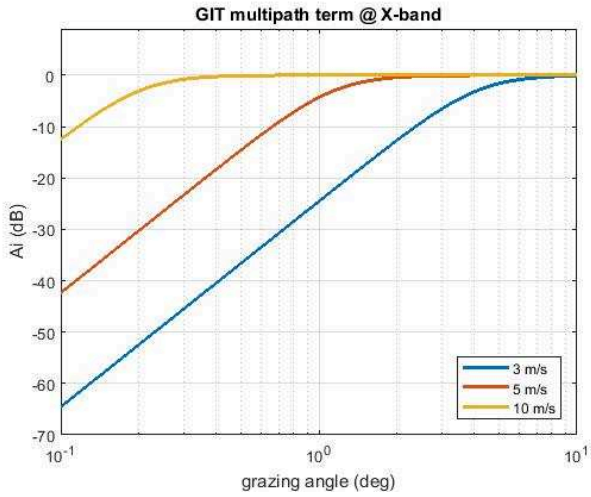

Fig. 23 : Terme de multi-trajet A_i du modèle GIT en fonction de l'angle de rasance (complémentaire à l'angle d'incidence) en bande X et pour 3 vitesses de vent : 3 m/s (bleu), 5 m/s (rouge) et 10 m/s (jaune)

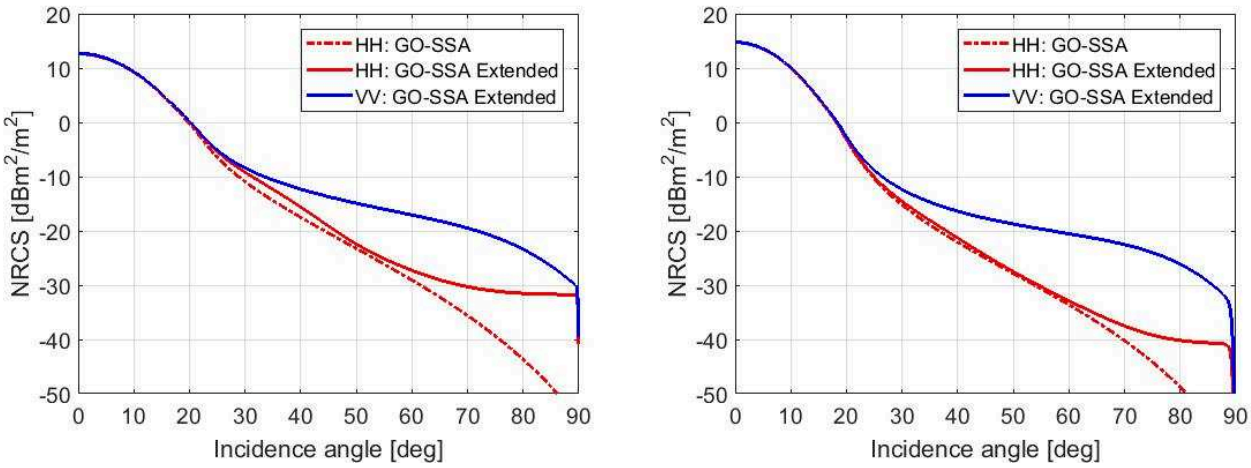

Fig. 24 : Courbes de réflectivité de la surface de mer en bande X (gauche) et en bande L (droite) estimées par les modèles GO-SSA (courbe pointillé) et GO-SSA-Extended (courbes pleines) – vent U_{10}=10m/s.

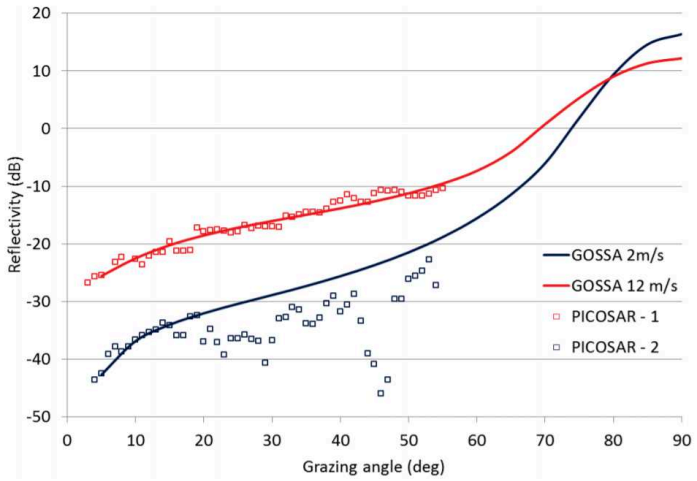

Fig. 25 : Courbes de réflectivité en bande X polarisation VV estimée par le modèle GO-SSA-Extended et comparaison avec des mesures expérimentales acquises par l'instrument PicoSAR – collaboration NOTA SET-185, [59]

4.1.2. Extension du domaine angulaire – angle d'azimut

La direction d'émission des ondes radar par rapport à la direction de propagation du vent est un paramètre clef qui doit être pris en compte pour une estimation fiable de la réflectivité radar.
Dans une approche de type deux échelles, comme le modèle GO-SSA, l'information d'état de mer est contenu dans le spectre de mer (celui d'Elfouhaily étant le plus répandu en télédétection micro-ondes). La prise en compte de la dépendance à l'angle d'azimut par rapport à la direction du vent peut alors être obtenue via :

- L'utilisation dans le modèle analytique d'un spectre de mer directionnel en ajoutant une fonction d'étalement au spectre de mer omnidirectionnel. Cette approche permet de restituer les asymétries upwind/crosswind (UCA) mais elle ne permet pas de restituer les asymétries upwind/downwind (UDA) à cause de la symétrie de la fonction d'étalement.
- Le calcul de la réflectivité en direction upwind (avec par exemple un modèle analytique tel que GO-SSA) et l'utilisation d'une fonction de pondération pour le calcul de la dépendance azimutal, dont l'expression générale est [60] :

$$\sigma^0(\lambda,\theta,U_{10},\phi) = \sigma_1^0(\lambda,\theta,U_{10}) + \sigma_2^0(\lambda,\theta,U_{10}) \times cos(\phi) + \sigma_3^0(\lambda,\theta,U_{10}) \times cos(2\phi) \qquad (71)$$

avec ϕ l'angle d'azimut relatif à la direction du vent (upwind $\Leftrightarrow \phi = 0°$ / downwind $\Leftrightarrow \phi = 180°$). Le terme σ_1^0 est la composante isotrope de la rétrodiffusion, σ_2^0 est lié à l'asymétrie upwind /downwind de la surface et σ_3^0 est lié à l'asymétrie upwind /crosswind.

La surface de mer étant en général considérée comme un processus Gaussien (caractérisé par une distribution de pentes Gaussienne et donc symétrique), l'asymétrie upwind/downwind n'est pas prise en compte dans les modèles analytiques de rétrodiffusion. Cependant, certains modèles empiriques (notamment ceux utilisés pour inverser les signaux des diffusiomètres en vecteur vent) prennent eux en compte cette propriété d'anisotropie entre les visées upwind et downwind pour lever l'ambiguïté entre ces deux directions cardinales. Pour des configurations de mesure classiques, comme les observations satellitaires, les écarts entre les niveaux de réflectivité mesurés en visée upwind et downwind sont limités à quelques dB tout au plus (et bien inférieurs aux écarts qu'on observe expérimentalement en visée rasante). La Fig. 26 ci-dessous illustre la dépendance azimutale du modèle empirique CMOD-5 [61], estimée à partir d'observations spatiales.

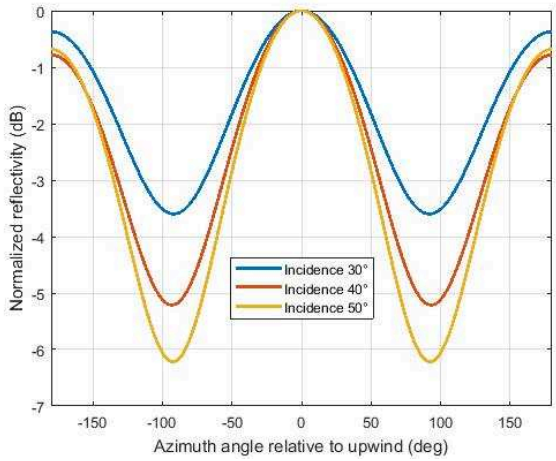

Fig. 26 : Dépendance azimutale du modèle empirique CMOD-5[61]

La dépendance azimutale de la réflectivité radar est aujourd'hui bien référencée dans la littérature aux incidences et fréquences correspondants aux configurations spatiales. Cette dépendance est moins maîtrisée aux incidences plus rasantes. A partir d'observations aéroportées, nous avons mis en évidence dans [62] et conformément à [63] Fig.3, que la variation azimutale de la réflectivité passe d'un comportement bi-modal à un comportement uni-modal lorsque l'angle d'incidence augmente, en polarisation HH uniquement. La variation en polarisation VV demeure quant à elle toujours bi-modale jusqu'à des incidences de 75° environ (cf. Fig. 27 ci-dessous reproduite de [62]).

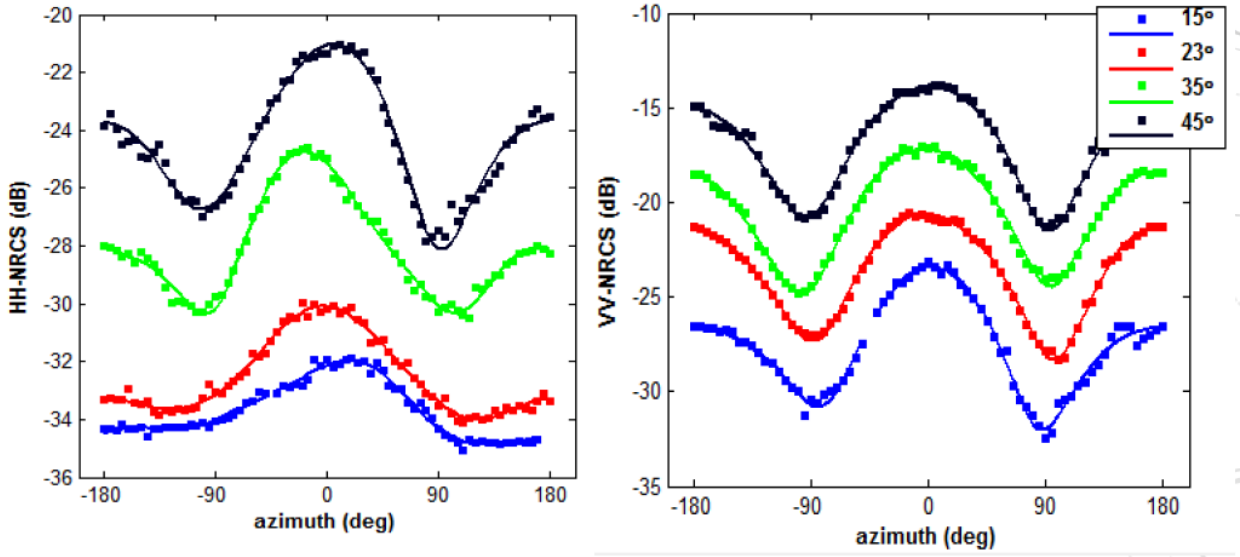

Fig. 27 : Variations azimutales de la réflectivité radar en bande X polarisation HH (gauche) et VV (droite), angle de rasance de 15° (incidence 75° - bleu), 23° (incidence 67° - rouge), 35° (incidence 55°- vert) et 45° (incidence 45° - noir) – données RAR INGARA – vent de 8.5 m.s^{-1} [62]

Des travaux théoriques ont été entrepris pour expliquer cette variation avec l'angle d'incidence et son caractère polarisé. Nous avons montré dans [64][65] que la prise en compte d'une géométrie des vagues adaptée permet de restituer les tendances observées (mais pas à ce stade les valeurs absolues d'asymétries). En effet, une distribution gaussienne des vagues est par définition symétrique. La prise en compte de l'asymétrie des vagues (front face au vent plus pentu que dos au vent) semble nécessaire et pourra s'appuyer sur des travaux publiés sur ce sujet tels que [66][67].

Des mesures unidirectionnelles de distribution de pentes ont été effectuées en soufflerie [68]. Dans le travail de thèse que j'ai co-encadré [64], elles ont été utilisées dans le modèle deux échelles GO-SSA au lieu d'une distribution Gaussienne classique (dans la direction de visée du radar uniquement). La distribution des pentes est fournies en Fig. 28 , elle correspond au « régime 4 » dont les conditions de mesures sont décrites en détails dans [68]. Sur cette Fig. 28, les faces orientées vers le radar correspondent aux valeurs de pentes négatives. On observe effectivement une probabilité d'occurrence des fortes pentes plus importante pour celles orientées vers le radar, ce qui restitue effectivement le caractère asymétrique des vagues. On remarque également que les probabilités d'occurrence des fortes pentes mesurées en soufflerie sont plus importantes que celles restituées par les modèles de distribution fournies par la littérature, et notamment la distribution de Gram-Charlier issue des observations optiques de Cox et Munk en 1954 [69].

Dans le cadre des travaux de thèse de Z. Guerraou que j'ai co-encadrés [64], nous avons calculé les asymétries upwind-downwind obtenues avec le modèle GO-SSA, un spectre de mer d'Elfouhaily et cette distribution des pentes mesurées en soufflerie [68] pour les bandes de fréquence X et L (cf. Fig. 29). L'asymétrie upwind/downwind observée a un comportement non monotone (et non trivial) avec l'angle d'incidence : on obtient en bande X un maximum d'asymétrie pour un angle d'incidence de 20-30° et pour les deux états de polarisation HH et VV, ainsi qu'une augmentation de l'asymétrie, en polarisation HH uniquement, au-delà de 70° d'incidence environ [64], ce qui est cohérent avec les observations radar. On observe également des valeurs d'asymétrie upwind-downwind globalement supérieures en haute fréquence radar (10 GHz) qu'en basse fréquence (1.25 GHz), ce qui est conforme avec les mesures aéroportées acquises simultanément en bandes X et L (Fig. 30). Le modèle reproduit de plus une asymétrie upwind-downwind à 45° d'incidence supérieure en polarisation HH qu'en VV, ce qui est à nouveau conforme avec les observations expérimentales. L'inversion de signe en configuration plongeante (incidence inférieure à 10-15°) observée sur la Fig. 30 est également cohérente avec les mesures spatiales ou aéroportées, notamment [70] et indirectement [71].

L'asymétrie upwind-crosswind est quant à elle restituée par l'utilisation d'une fonction d'étalement du spectre de mer. Il a été démontré dans [64] que les spectres de mer récemment proposés dans la littérature (Yurovskaya [72] et Bringer [73]) permettent d'estimer cette asymétrie avec plus de représentativité que le spectre d'Elfouhaily classique. L'utilisation d'une distribution des pentes non Gaussienne dans la direction transverse à la visée radar ne semble pas nécessaire.

Les travaux exposés dans [64][65] permettent de restituer les tendances observées expérimentalement de l'asymétrie upwind-downwind. Par contre ces travaux demeurent insuffisants pour expliquer les niveaux absolus d'asymétrie upwind/downwind du coefficient de rétrodiffusion. En particulier, le déferlement joue un rôle majeur dans ces asymétries mais celui-ci n'est pas complétement maîtrisé à ce jour. En outre, ces travaux se sont basés sur des mesures unidirectionnelles de distribution de pentes totales des vagues. Une recommandation pour progresser dans ces travaux serait d'utiliser les pentes des facettes (a priori plus faibles que les pentes totales).

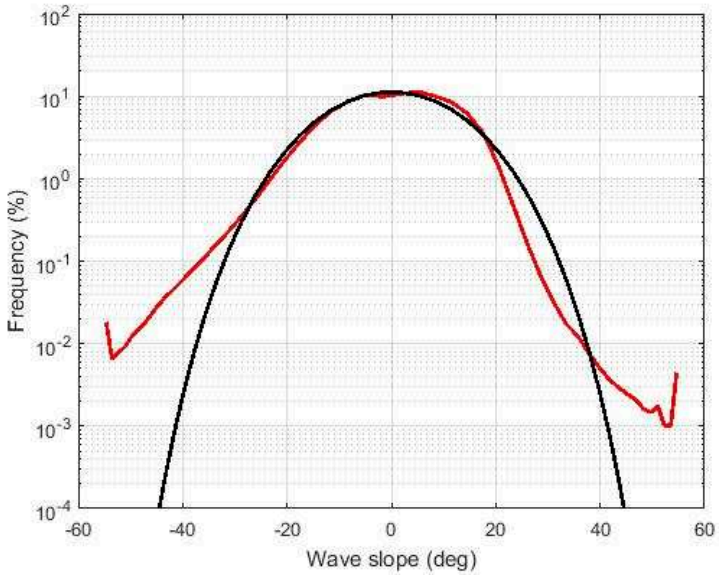

Fig. 28 : Distributions des pentes pour un cas Gaussien de référence (courbe noire) et pour les mesures en souffleries [68] (courbe rouge)

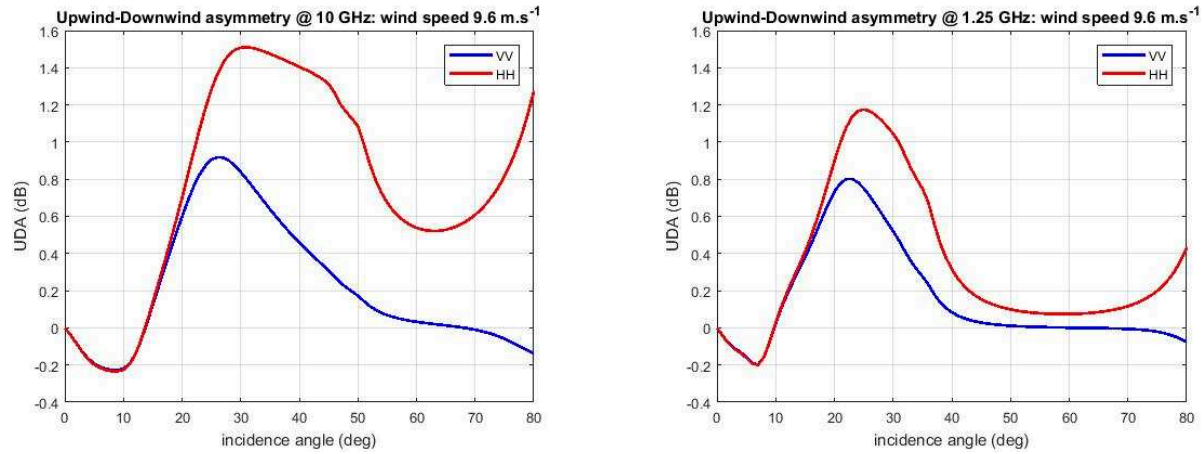

Fig. 29 : Asymétrie Upwind-Downwind (UDA) du coefficient de rétrodiffusion radar en fonction de l'angle d'incidence en polarisation HH (rouge) et VV (bleue) obtenue avec le modèle GO-SSA et la distribution des pentes mesurées en soufflerie (U_{10}=9.6 m.s^{-1} converti d'après la relation 5.6.23 de [64]) – bande X à gauche et bande L à droite

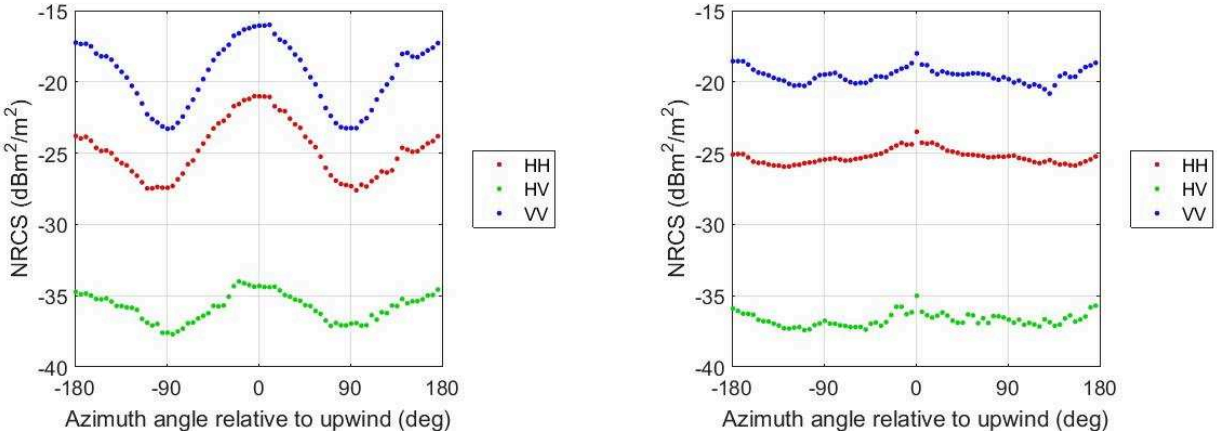

Fig. 30 : Réflectivité radar en fonction de l'angle d'observation en azimut, incidence 45°, U_{10}=8.5 m.s^{-1} bande X (gauche) et bande L (droite) – campagne aéroportée ONERA/SETHI ANR-POLLUPROOF 2015.

4.1.3. Rapport de polarisation

Le rapport de polarisation (noté PR dans la suite du manuscrit pour *Polarization Ratio*), défini comme le rapport des réflectivités en polarisation HH et VV $PR = \sigma^0_{HH}/\sigma^0_{VV}$, est un paramètre important pour décrire la surface océanique [42][52][53][74][75]. Une étude spécifique lui sera consacrée dans le paragraphe 5 suivant dédié à la télédétection des pollutions marines. Néanmoins les modèles analytiques classiques ne permettent pas de décrire avec suffisamment de fiabilité le rapport de polarisation mesuré expérimentalement sur l'océan dans la partie supérieure de la gamme des micro-ondes (bande X notamment), ni de restituer les tendances observées avec l'état de mer. C'est pourquoi on préfère souvent utiliser des modèles empiriques du rapport de polarisation. L'un des plus répandu est le modèle de Thompson [76] :

$$PR_{Th} = \frac{(1 + \alpha \tan^2\theta)^2}{(1 + 2\tan^2\theta)^2} \tag{72}$$

avec θ l'angle d'incidence et $0 \leq \alpha \leq 1$ le paramètre du modèle qui fait la transition entre les modèles de Bragg et de Kirchhoff ($\alpha = 0 \Leftrightarrow$ Bragg ; $\alpha = 1 \Leftrightarrow$ Kirchhoff – plus α augmente, plus le modèle s'écarte du modèle de Bragg).

Dans [76], les auteurs suggèrent d'après les observations radar des valeurs $\alpha = 0.6$ en bande C et $\alpha = 0.95$ en bande Ku. Dans ce modèle, le paramètre α est omnidirectionnel et ne permet donc pas de restituer les asymétries directionnelles observées sur le rapport de polarisation.
Sur la Fig. 31 ci-dessous, on observe que le modèle de Thompson encadre effectivement les valeurs du rapport de polarisation mesurées expérimentalement en bandes X et L, mais faute de paramètre α disponible à ces bandes de fréquence il n'est pas possible à ce stade de prédire le rapport de polarisation pour des acquisitions en bandes X et L. Pour référence, les valeurs de PR prédites par le modèle de Bragg en bande X et en bande L sont données Fig. 31, on observe un écart très important entre le modèle de Bragg et les valeurs expérimentales.

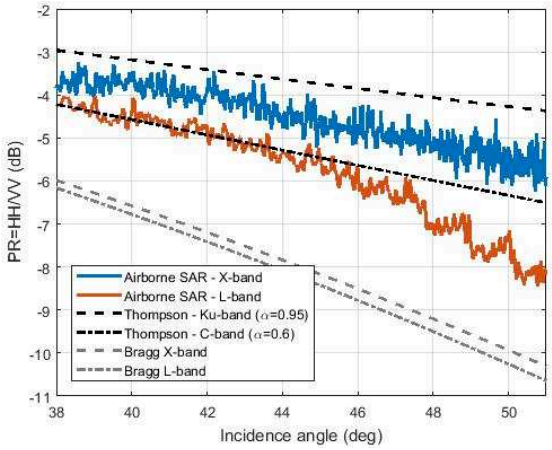

Fig. 31 : Rapport de polarisation (PR) prédit par le modèle de Bragg en bandes X et L, par le modèle de Thompson en bandes Ku et C et mesuré expérimentalement par l'instrument SETHI/ONERA en bandes X et L – U_{10}=8 m.s^{-1}, observation crosswind

Il existe d'autres modèles du rapport de polarisation, calculés en parallèle des *Geophysical Model Function* (GMF) qui relient de façon empirique la réflectivité radar à l'état de mer. Ces modèles ont été estimés à partir des données SAR satellitaires, tels que les modèles LMOD [77], CMOD-5 [61][78] et XMOD2 [79] adaptés aux bandes L, C et X respectivement. Cependant, les rapports de polarisations estimés par certains de ces modèles ne semblent pas toujours en adéquation avec les mesures expérimentales (cf. comparaison entre données SAR bande X et XMOD-2 Fig. 32) et il est nécessaire de disposer d'un modèle physique de prédiction du rapport de polarisation pour étendre le domaine de validité du modèle de Thompson, notamment à d'autres fréquences radar et pour mieux comprendre les mécanismes qui en sont à l'origine.

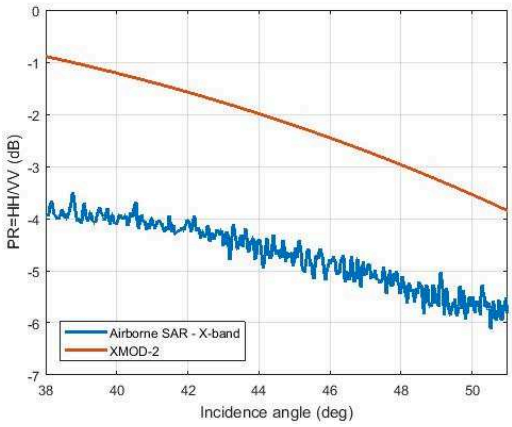

Fig. 32 : Rapport de polarisation (PR) prédit par le modèle XMOD-2 et mesuré expérimentalement par l'instrument SETHI/ONERA en bande X.

Deux approches ont été proposées dans la littérature pour tenter d'expliquer les écarts entre les valeurs de PR mesurées et modélisées, notamment en haute fréquence EM.
Le premier repose sur l'existence de contributions non-polarisées (ou « non-Bragg » ou « non-résonnantes ») [52][53] [74][75], produites par exemple par le déferlement des vagues, et dont l'impact relatif est plus important en polarisation HH qu'en VV. La difficulté est dans ce cas de décrire de façon suffisamment représentative la NRCS décrite par ces mécanismes et leur occurrence sur la surface de mer. La seconde approche consiste à traiter de façon plus exacte l'impact des grandes échelles sur le signal rétrodiffusé comme suggéré dans [76]. C'est cette approche qui a été suivi dans les travaux auxquels j'ai contribués et qui sont décrits ci-dessous [80].

Le paramètre α du rapport de polarisation du modèle de Thompson [76] permet de piloter le poids respectif des contributions de Bragg et de Kirchhoff. Le modèle analytique de rétrodiffusion U-WCA (Universal *Weighted Curvature Approximation*) [81] a été formulé en suivant le même principe puisque la réflectivité totale est construite comme la somme pondérée d'une contribution de type Bragg et d'une contribution de type Kirchhoff (cf. paragraphe 5.2.2 pour plus de détails). Selon ce principe, la réflectivité radar peut s'écrire comme :

$$\sigma_{pp}^{0}(\theta) = 16\pi k_{EM}^{4} cos^{4}(\theta) \left(\mathcal{B}_{pp} + \beta\left(K - \mathcal{B}_{pp}\right)\right) W(k_B) \tag{73}$$

avec $p \in \{H, V\}$ l'état de polarisation, θ l'angle d'incidence, $\mathcal{B}_{pp}$ et K les noyaux de Bragg et de Kirchhoff respectivement, W le spectre de mer, k_B le nombre de Bragg et β le paramètre du modèle. Ce modèle est supposé valide uniquement aux angles d'incidences faibles à modérés car le terme correctif $\beta(K - \mathcal{B})$ doit rester faible (les noyaux de Bragg et de Kirchhoff divergent rapidement avec l'incidence, surtout en polarisation VV).
Partant de l'observation que $(K - \mathcal{B}) \sim sin^{2}\theta$, nous avons proposé dans [80] une reformulation originale de l'expression du coefficient de rétrodiffusion radar telle que :

$$\sigma_{HH}^{0}(\theta) = 16\pi k_{EM}^{4} cos^{4}(\theta) \mathcal{B}_{HH}(1 + \alpha sin^{2}\theta) W(k_B) \tag{74}$$

$$\sigma_{VV}^{0}(\theta) = 16\pi k_{EM}^{4} cos^{4}(\theta) \mathcal{B}_{VV}(1 - \alpha sin^{2}\theta) W(k_B) \tag{75}$$

La correction appliquée est cette fois répartie de façon pondérée (par le coefficient α) entre les polarisation HH et VV. Ce modèle est appelé modèle « hybride » puisqu'il combine les contributions des noyaux de Bragg et Kirchhoff tout en conservant une formulation similaire à celle de la théorie de Bragg. Suivant le formalisme offert par ce modèle hybride, le rapport de polarisation s'écrit de la façon suivante :

$$PR = \frac{\sigma_{HH}^{0}}{\sigma_{VV}^{0}} = \frac{\mathcal{B}_{HH}(1 + \alpha sin^{2}\theta)}{\mathcal{B}_{VV}(1 - \alpha sin^{2}\theta)} = PR_{Bragg}(\theta) \frac{(1 + \alpha sin^{2}\theta)}{(1 - \alpha sin^{2}\theta)} \tag{76}$$

avec $PR_{Bragg} = \mathcal{B}_{HH}/\mathcal{B}_{VV}$ le rapport des noyaux de Bragg en polarisation HH et VV. Le paramètre α est le paramètre du modèle qu'il convient à nouveau d'ajuster en fonction de la fréquence radar. Ce modèle se réduit donc à une correction du rapport de polarisation obtenu avec un modèle de type Bragg.
La dernière étape des travaux conduits dans [80] a consisté à remplacer l'utilisation d'un modèle de type Bragg par un modèle deux échelles et à appliquer la même correction sur les niveaux de réflectivités estimés par le modèle analytique. Dans ce cas, il est montré dans [80] que le paramètre α prend une valeur identique ($\alpha = 0.6$) pour les bandes de fréquences C, X et Ku investiguées dans ces travaux.

Cela implique que la dépendance à la fréquence EM et à la vitesse du vent du paramètre α dans un modèle de type Bragg est prise en compte par la modulation des vagues du modèle deux échelles et que l'expression du rapport de polarisation du modèle hybride devient simplement :

$$PR_{Hybrid} = \frac{1}{N}\sum_{i=1}^{N} PR_{Bragg}(\theta_i)\frac{(1+0.6sin^2\theta_i)}{(1-0.6sin^2\theta_i)} \quad (77)$$

Il s'agit donc de la valeur moyenne obtenue en parcourant les différentes valeurs des pentes des vagues (et donc pour la gamme de variation de l'angle d'incidence local, θ_i).

Les valeurs du rapport de polarisation calculées par le modèle de Bragg (PR_{Bragg}), le modèle deux échelles GOSSA (PR_{TSM}) et le modèle deux échelles hybrides (PR_{Hybrid}) sont comparées en Fig. 33 avec des données SAR expérimentales acquises en bande X pour un vent U_{10}=8 m.s^{-1} en observation crosswind. On observe alors la pertinence du modèle « hybride » et la très bonne correspondance avec les données expérimentales.

Notons finalement que ce modèle hybride est adapté aux hautes fréquences EM (bandes C, X et Ku). En plus basse fréquence (bande L typiquement) les modèles deux échelles permettent déjà une bonne approximation du rapport de polarisation (cf. par exemple nos publications [82][83] pour l'utilisation du modèle U-WCA pour approximer le PR en bande L).

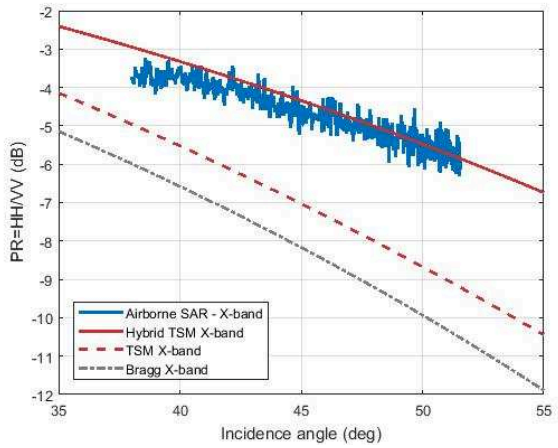

Fig. 33 : Rapport de polarisation (PR) en bande X prédit par le modèle de Bragg, par le modèle deux échelles GO-SSA et par le modèle hybride et mesuré expérimentalement par l'instrument SETHI/ONERA – U_{10}=8 m.s^{-1}, crosswind.

4.2. Caractérisation de la statistique du fouillis de mer

Les systèmes d'observation micro-ondes sont très largement utilisés pour la détection et le suivi de cibles marines, notamment en raison de leur capacité à surveiller de vastes zones et à être opérés dans presque toutes les conditions météorologiques, de jour comme de nuit.
La détection de cible est généralement abordée selon un schéma de type « taux de fausses alarmes constant » (ou CFAR pour « Constant False Alarm Rate » en anglais) [84]. Cette approche consiste à sélectionner un seuil de détection qui limite le nombre de fausses alarmes, tout en maintenant une probabilité de détection souhaitée. Ceci est généralement réalisé en comparant une distribution théorique à la distribution des échos radar d'une surface d'intérêt. Plus précisément, la présence d'une cible marine se manifeste généralement dans la queue de la distribution des échos radar en raison de son fort niveau d'énergie renvoyée.

La CCDF (« Complementary Cumulative Distribution Function » en anglais, soit le complémentaire de la fonction de distribution cumulative) est alors particulièrement bien adaptée puisqu'elle permet de mettre en évidence les échos de forte énergie qui se manifestent en queue de PDF (cf. par exemple les figures 1 et 2 que nous avons proposées dans [85]). La CCDF est importante en raison de sa relation avec le seuil utilisé dans un schéma de détection de cibles de type CFAR. Dans ce contexte, elle est communément appelé la probabilité de fausse alarme (P_{fa}). Cette fonction sera explicitement utilisée dans la suite des travaux que nous exposons dans ce manuscrit.

Cette méthodologie nécessite donc de disposer d'un modèle précis de distribution des échos rétrodiffusés par la surface de l'océan. Dans le cas d'un système radar qui collecte des données avec une faible résolution spatiale (métrique ou au-delà), la cellule de résolution est constituée d'un très grand nombre de contributeurs. L'intensité du signal EM rétrodiffusé par la surface océanique suit une distribution Exponentielle [86] (l'amplitude du signal suit elle une loi de Rayleigh) paramétrée par la valeur moyenne de l'intensité de la réponse radar x :

$$P(z) = \frac{1}{x} exp\left(-\frac{z}{x}\right) ; x = \langle z \rangle \tag{78}$$

Lorsque la résolution spatiale de l'instrument s'améliore (i.e. diminue) et que la taille de la cellule de résolution devient de l'ordre de quelques longueur d'onde radar, on entre dans le cadre de la haute résolution spatiale. Dans ce cas, la statistique du signal radar s'écarte significativement d'une loi Exponentielle [50][86][87].
Un cadre naturel mais peu utilisé dans la littérature pour développer des modèles de distribution adaptée au fouillis de mer en haute résolution spatiale est le modèle de Bragg composite dit « Compound Model ». La surface de mer est vue comme un ensemble de facettes qui correspondent aux « petites échelles » et dont la taille est similaire à la cellule de résolution. Le signal rétrodiffusé par chacune de ces facettes est résolu statistiquement (composante dite du « speckle ») et suit une distribution Exponentielle autour d'une valeur moyenne (composante dite de la « texture ») qui correspond à la NRCS localement modulée par les grandes échelles et qui peut par exemple être fourni par un modèle de type Bragg composite. L'impact de la modulation des petites échelles (speckle) par les grandes échelles (texture) est inclus en intégrant sur la moyenne du speckle :

$$P(z) = \int_0^\infty P(z|x)P(x)dx \ ; x = \langle z \rangle \tag{79}$$

avec $P(z|x)$ la distribution du speckle et $P(x)$ la distribution de la texture.

Deux approches peuvent être suivies pour proposer des distributions du signal radar $P(z)$ en haute résolution spatiale et nous décrivons dans les deux sous-sections suivantes les travaux que nous avons réalisés selon ces deux méthodes :

- Une approche statistique qui permet de s'adapter à la plupart des distributions statistiques suivies par le fouillis radar et notamment dans des configurations de mesure ou d'états de mer peu usuels comme en incidence rasante.

- Une approche physique qui permet de restituer les échos radar rétrodiffusés par une surface de mer à partir d'une formulation analytique qui ne requiert qu'un seul paramètre, mais uniquement pour des angles d'incidence modérés.

4.2.1. Approche statistique

Le modèle composite le plus populaire pour décrire la statistique du fouillis de mer en haute résolution spatiale est le modèle de la loi K [50][86] et sa version étendue pour prendre en compte le bruit de l'instrument, K+Noise (K+N) [50]. La distribution de Pareto et sa version étendue Pareto+Noise (P+N) ont également démontré leur habileté à reproduire la statistique du fouillis de mer [88]-[90]. Plus récemment, la distribution K+Rayleigh (K+R) a été proposée [91].
C'est une extension de la loi K+Noise qui permet de modéliser une contribution supplémentaire dans les données produites par des mécanismes de rétrodiffusions non polarisés et modélisés par une distribution de type Rayleigh. D'autres distributions théoriques ont été proposées dans la littérature pour représenter le fouillis de mer. Parmi les plus populaires on peut citer les lois log-normal [92] ou Weibull [93]. Mais de façon générale ces distributions sont moins adaptées pour représenter la distribution statistique des échos radar effectivement rétrodiffusés par la surface de mer que celles proposées plus récemment dans la littérature et introduites en début de cette sous-section [50][94].

La formulation du modèle composite définie par l'équation (79) implique une probabilité faible mais non nulle d'occurrence de valeurs de texture proches de l'infini. Une approche plus réaliste a récemment été proposée dans [95]. Le modèle « 3MD » proposé consiste à utiliser un modèle de texture discret constitué d'un nombre fini de types de diffuseurs. Cela implique que les diffuseurs présents dans la scène imagée sont des réalisations de variables aléatoires avec des valeurs de texture différentes.

Nous décrivons ci-dessous les formulations mathématiques de ces distributions. Lorsque la puissance du bruit est non nulle, les distributions des lois K+Noise et P+Noise n'ont pas de formulation analytique explicite [50] et $P(z)$ doit être résolue numériquement.

- Loi K+Noise (K+N) :

La distribution K+N est une loi très populaire pour représenter le fouillis de mer. La composante du speckle est modélisée par une loi Exponentielle et la texture par une loi Gamma telle que :

$$P(z|x) = \frac{1}{x + p_n} exp\left(-\frac{z}{x + p_n}\right) \tag{80}$$

$$P(x) = \frac{b^{\nu}}{\Gamma(\nu)} x^{\nu-1} exp(-bx) \tag{81}$$

avec $\nu > 0$ et $b = \nu/p_c$ les paramètres de forme et d'échelle respectivement, p_c la puissance moyenne du clutter et p_n la puissance moyenne du bruit.

- Loi P+Noise (P+N) :

La distribution P+N est formée par une loi Exponentielle pour le speckle (de façon identique à K+N) et une distribution inverse Gamma pour la texture telle que :

$$P(x) = \frac{d^{\nu}}{\Gamma(\nu)} x^{-\nu-1} exp(-d/x) \tag{82}$$

avec $\nu > 0$ et $d = p_c(\nu - 1)$ les paramètres de forme et d'échelle respectivement.

- Loi K+Rayleigh (K+R) :

La distribution K+R est une extension de la loi K+N, formée pour prendre en compte les contributions de type non-Bragg présentes dans les données. Elle est écrite en séparant de façon explicite la puissance moyenne de la composante du speckle en deux termes ($x \stackrel{\text{def}}{=} x_r + p_r$) avec x_r la puissance moyenne du speckle et p_r la puissance moyenne de la composante de Rayleigh.

$$P(z|x_r) = \frac{1}{x_r + p_r + p_n} exp\left(-\frac{z}{x_r + p_r + p_n}\right) \tag{83}$$

$$P(x) = \frac{b_r^{\nu_r}}{\Gamma(\nu_r)} x_r^{\nu_r - 1} exp(-b_r x_r) \tag{84}$$

avec ν_r et $b_r = \nu_r / p_c$ les paramètres de forme et d'échelle respectivement. L'intégral $P(z)$ du modèle composite est alors calculée en intégrant sur la puissance moyenne du speckle x_r et non plus sur la puissance totale x.
L'influence de la composante Rayleigh additionnelle peut être mesurée par le ratio entre la moyenne de la distribution de Rayleigh et la moyenne de la distribution Gamma du speckle tel que :

$$k_r = \frac{p_r}{p_c} \tag{85}$$

- Modèle discret 3MD :

Dans le modèle 3MD, la texture est supposée suivre un modèle discret de distribution telle que :

$$P(x) = \sum_{n=1}^{I} c_n \delta(x - a_n) \quad ; \quad avec \sum_{n=1}^{I} c_n = 1 \; et \; a_n, c_n > 0 \tag{86}$$

$$\delta(A) \stackrel{\text{def}}{=} \begin{cases} 1 \; si \; A = 0 \\ 0 \; sinon \end{cases} \tag{87}$$

avec $a = [a_1, \ldots\ldots, a_I]$ les valeurs d'intensité de texture et $c = [c_1, \ldots\ldots, c_I]$ leur poids respectif. Dans le cas où la composante du speckle suit à nouveau une distribution de type Exponentielle, la distribution résultante du modèle composite 3MD dans le cas mono-vue (i.e. sans moyenne spatial) est telle :

$$P(z) = \sum_{n=1}^{I} c_n \frac{exp\left(-\frac{z}{\rho_c a_n^2 + \rho_n}\right)}{\rho_c a_n^2 + \rho_n} \tag{88}$$

avec

$$\rho_c + \rho_n = \frac{p_c}{p_c + p_n} + \frac{p_n}{p_c + p_n} = 1 \tag{89}$$

Dans leur publication originale [95], les auteurs ont rapporté que 3 modes sont suffisants pour modéliser avec précision les données de résolution spatiale métriques recueillies par des capteurs SAR spatiaux. Ce que nous avons confirmé sur des données SAR et RAR aéroportées dans [96]. L'une des conséquences de cette discrétisation est que la distribution 3MD nécessite une estimation non triviale de 2I paramètres. Ceci peut être réalisé avec une minimisation par moindres carrés entre le modèle 3MD et la CCDF des données [85].
Nous avons réalisé une évaluation de ces distributions dans [85]. Le travail a consisté à mesurer de façon quantitative la capacité des lois K+N, P+N, K+R et 3MD à représenter la statistique du signal enregistré par trois instruments radar différents : des données SAR aéroportées polarimétriques acquises en bande X et/ou L en mer Méditerranée et en Atlantique, des données RAR aéroportées polarimétriques acquises en bande X dans le Pacifique et des données acquises en Afrique du Sud par un radar côtier fonctionnant en bande S en modes mono- et bi-statique.

Une description complète de ces jeux de données est fournie dans [85], nous en synthétisons ici les principales caractéristiques :

- Bandes de fréquence : S, L et X
- Types de radar / configuration : SAR et RAR aéroporté monostatique et radar sol côtier mono et bistatique, polarimétrique
- Géométries de mesure : incidence ~89° pour le radar sol ; [45-80°] pour les radar aéroportés
- Etats de mer : modérée, agitée et forte

L'évaluation des distributions statistiques étudiées a été effectuée à partir de deux mesures : la distance de Bhattacharyya [97] et l'erreur de seuillage ou *Threshold error*. :

- Distance de Bhattacharyya (BD) [97] : c'est une mesure qui varie entre 0 et l'infini. Elle mesure la similarité entre la PDF du modèle $P(.)$ et la distribution réelle des données $Q(.)$. On notera que contrairement à sa dénomination, la Distance de Bhattacharyya n'est pas une distance au sens mathématique du terme puisqu'elle ne respecte pas l'inégalité triangulaire. Un intérêt majeur de cette mesure est qu'elle fournit une borne supérieure de la probabilité d'erreur de détection. Nous l'avons appliquée dans [85] sur l'ensemble de l'intervalle de définition des distributions :

$$BD = -ln\left(\sum_{x}\sqrt{P(x).Q(x)}\right) \quad ; \quad 0 \leq BD \leq \infty \tag{90}$$

  avec x les valeurs d'intensité.

- Threshold error : l'erreur de seuillage ou *Threshold error* est une mesure de l'écart entre le modèle et les données calculé spécifiquement en queue de distribution. Cet écart est mesuré sur la CCDF, à une valeur de seuillage donnée (10^{-4} sur l'exemple de la Fig. 34). L'erreur de seuillage est calculée sur l'axe des ordonnées en mesurant la différence entre le CCDF des données (Fig. 34 – courbe bleue) et le CCDF du modèle (Fig. 34 – ligne verte). Plus cet écart est faible, meilleure est l'adéquation entre les données et le modèle. Il s'agit d'une mesure pratique qui définit dans quelle mesure une détection de type CFAR sur-estimera ou sous-estimera la probabilité de détection d'une cible au sein du fouillis de mer.

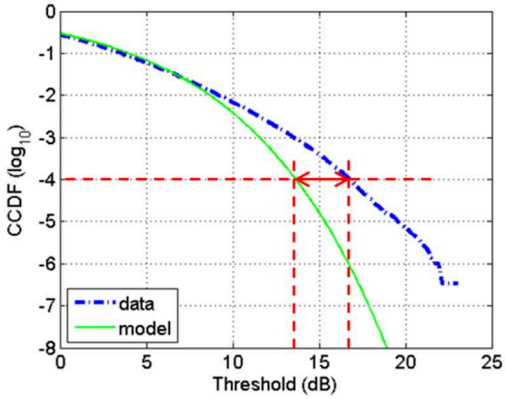

Fig. 34 : Mesure de l'erreur de seuillage (Threshold error) à 10^{-4} entre la CCDF des données (pointillée bleu) et la CCDF du modèle (vert)

Les résultats obtenus sur l'analyse des données RAR aéroportées acquises en bande X sur l'océan Pacifique (base de données INGARA – large gamme de géométries et de conditions de mer) montrent que la distribution 3MD est la plus proche des données [85], avec au plus 3 modes requis. La distribution K+R fournit une bonne correspondance avec l'ensemble du corps de la distribution, mais produit une erreur de seuillage légèrement plus élevée et donc un décalage en queue de distribution. Les distributions P+N et K+N produisent les plus mauvaises correspondances avec les données, en particulier en polarisation HH.
L'analyse des données SAR aéroporté SETHI montre que la distance de Bhattacharyya est systématiquement faible (de l'ordre de -30 dB ou inférieur) avec les quatre modèles étudiés, ce qui indique qu'ils peuvent tous modéliser avec précision l'ensemble de la distribution des données. Cependant, lorsqu'on se focalise sur la queue de la distribution, les modèles K+R et 3MD (avec à nouveau 3 modes) produisent les meilleurs correspondances avec les données expérimentales, en particulier en polarisation HH [85]. De plus, aucune variation significative de l'erreur de seuillage avec la vitesse du vent et les angles d'observation (incidence et azimut) n'est observée sur ces données.
L'analyse du jeu de données acquis par le capteur NetRAD en bande S en modes mono- et bi-statique montre que les distributions K+N et P+N ne permettent pas de représenter correctement les données et fourniraient des performances de détection dégradées si elles étaient utilisées dans un schéma de détection [85]. Seules, les distributions K+R et 3MD montrent une bonne correspondance avec les données en queue de distribution (Fig. 35). Lorsque l'on considère l'ajustement total à la fois au corps et à la queue de distribution, seul le modèle 3MD est capable de fournir de bons fits avec les données, mais au prix d'un plus grand nombre de paramètres à estimer (2I avec I pouvant aller jusqu'à 5 – cf. illustration Fig. 36).

En conclusion, les résultats que nous avons présentés dans [85] démontrent que les modèles K+R et 3MD permettent de correctement représenter l'ensemble de la statistique des différents jeux de données analysées, tandis que les modèles K+N et P+N sont souvent trop éloignés des données expérimentales. Lorsqu'on se focalise sur la queue de distribution, c'est le modèle 3MD qui propose la meilleure correspondance avec les données, l'erreur de seuillage avec le modèle K+R étant légèrement plus élevée. La contrepartie dans l'utilisation du modèle 3MD est un plus grand nombre de paramètre à estimer (jusqu'à 10 paramètres pour le modèle 3MD, contre 3 pour la loi K+R).

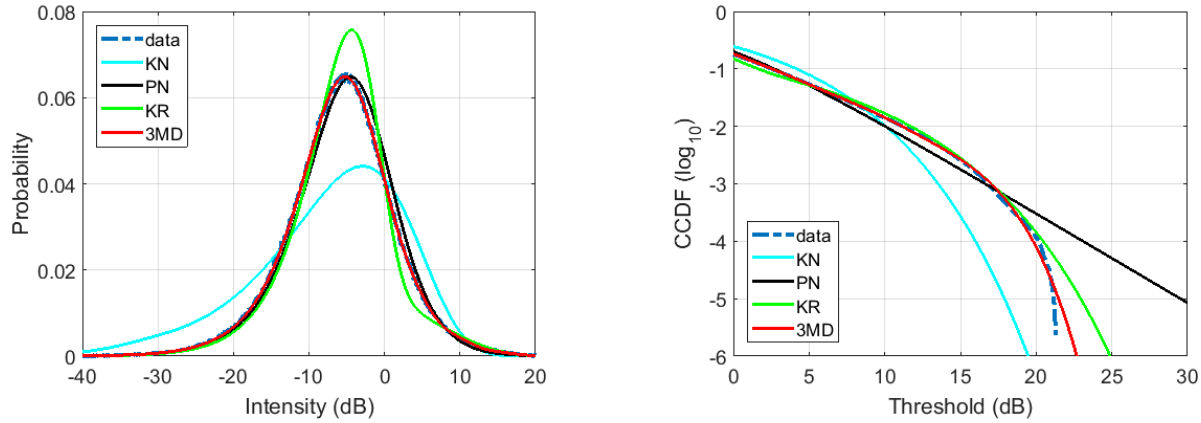

Fig. 35 : Ajustement des modèles de distributions KN, PN, KR et 3MD avec des données NetRAD polarisation HH mode bistatic ($\beta = 60°$) – PDF à gauche et CCDF à droite

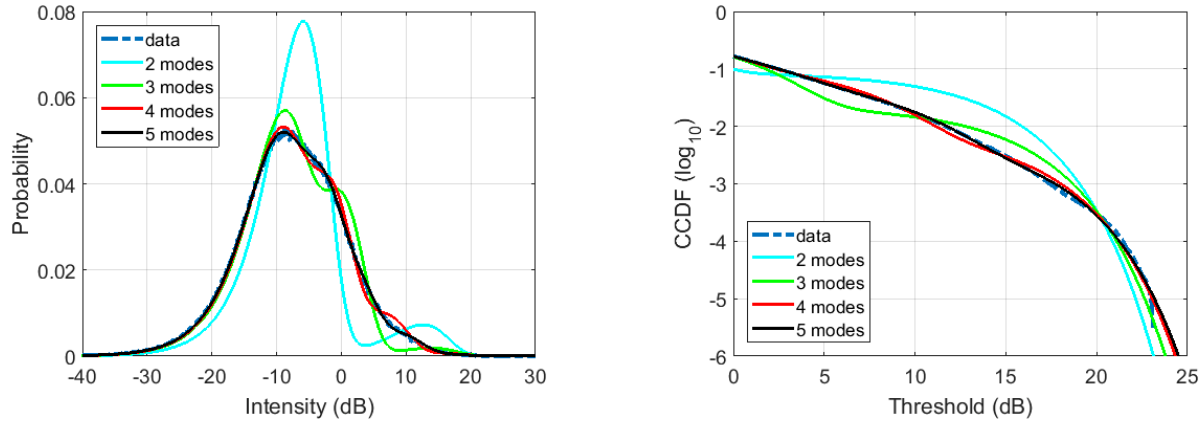

Fig. 36 : Ajustement du modèle 3MD avec des données NetRAD polarisation VV mode bistatic ($\beta = 60°$) – ajustement du modèle 3MD avec I=2,3,4,5 modes – PDF à gauche et CCDF à droite

4.2.2. Approche analytique

Les modèles de distribution statistique présentés au paragraphe 4.2.1 précédent permettent de décrire les statistiques du fouillis de mer en bande micro-ondes. Ces lois sont paramétrées par différentes variables, dont les paramètres de forme et d'échelle pour la plupart d'entre elles. Ils permettent d'ajuster correctement les lois aux données expérimentales. Cependant, il n'existe pas à ce jour de modèle analytique capable de prédire a priori les valeurs de ces paramètres, ils nécessitent alors d'être estimés au préalable sur une surface de mer de référence. Il existe néanmoins des évidences expérimentales qui montrent que le paramétrage des distributions est fonction des conditions de mer ainsi que des configurations de mesure, comme la résolution, la fréquence EM etc… L'utilisation d'un modèle deux échelles pour décrire la statistique du fouillis de mer a été précédemment envisagée dans [98]-[100] mais sans fournir de résultat abouti. Nous avons repris cette idée dans un travail qui a été publié dans [80] et c'est lors de cette analyse qu'est apparue la nécessité d'évaluer correctement le rapport de polarisation afin de pouvoir proposer un modèle physique de caractérisation du fouillis de mer en haute fréquence EM.

Les travaux sur l'amélioration du modèle analytique deux échelles ont été présentés dans le paragraphe 4.1.3. et ont abouti au modèle « hybride » que nous avons publié dans [80] et dont les expressions du coefficient de rétrodiffusion radar en polarisation HH et VV sont fournies aux équations (74) et (75).
Dans l'approche deux échelles, la distribution du fouillis de mer en intensité $P(I)$ est obtenue en intégrant sur la distribution en 2 dimensions des pentes des facettes $P(s)$ de la surface :

$$P(I) = \int P(I|s)P(s)ds \tag{91}$$

avec $P(I|s)$ la probabilité conditionnelle de l'intensité d'une facette de taille L pour une pente (s) donnée telle que :

$$P(I|s) = \frac{1}{\sigma_L^0(\theta;s)} exp\left(-\frac{I}{\sigma_L^0(\theta;s)}\right) \tag{92}$$

Les valeurs de réflectivités en polarisation HH ou VV sont données par le modèle « hybride » à partir d'un spectre de mer d'Elfouhaily et d'une distribution Gaussienne des pentes, uniquement paramétrée par la mss (mean square slope) des vagues (en supposant la composante transverse (mss_y) identique à la composante parallèle (mss_x) à la visée radar).

Il est d'usage de représenter les distributions en dB, ce qui se fait via le changement de variable :

$$P(I_{dB}) = \frac{log(10)}{10} \times I \times P(I) \tag{93}$$

Il est important de noter que ce modèle n'est valide qu'en haute résolution spatiale (métrique ou inférieure), condition nécessaire pour l'utilisation du modèle composite : en effet, la résolution spatiale doit être de l'ordre de grandeur de la taille des facettes (~8λ soit ~24 cm en bande X) composant la surface.

Le modèle composite de distribution ainsi obtenu a été comparé avec le fouillis de mer en bande X obtenu lors de la campagne SAR POLLUPROOF (cf. 5.1.2.1), Fig. 37. L'incidence est de 45°, la résolution de 0.5 m dans les deux directions, le vent U_{10}=8 m.s^{-1} et en observation crosswind.

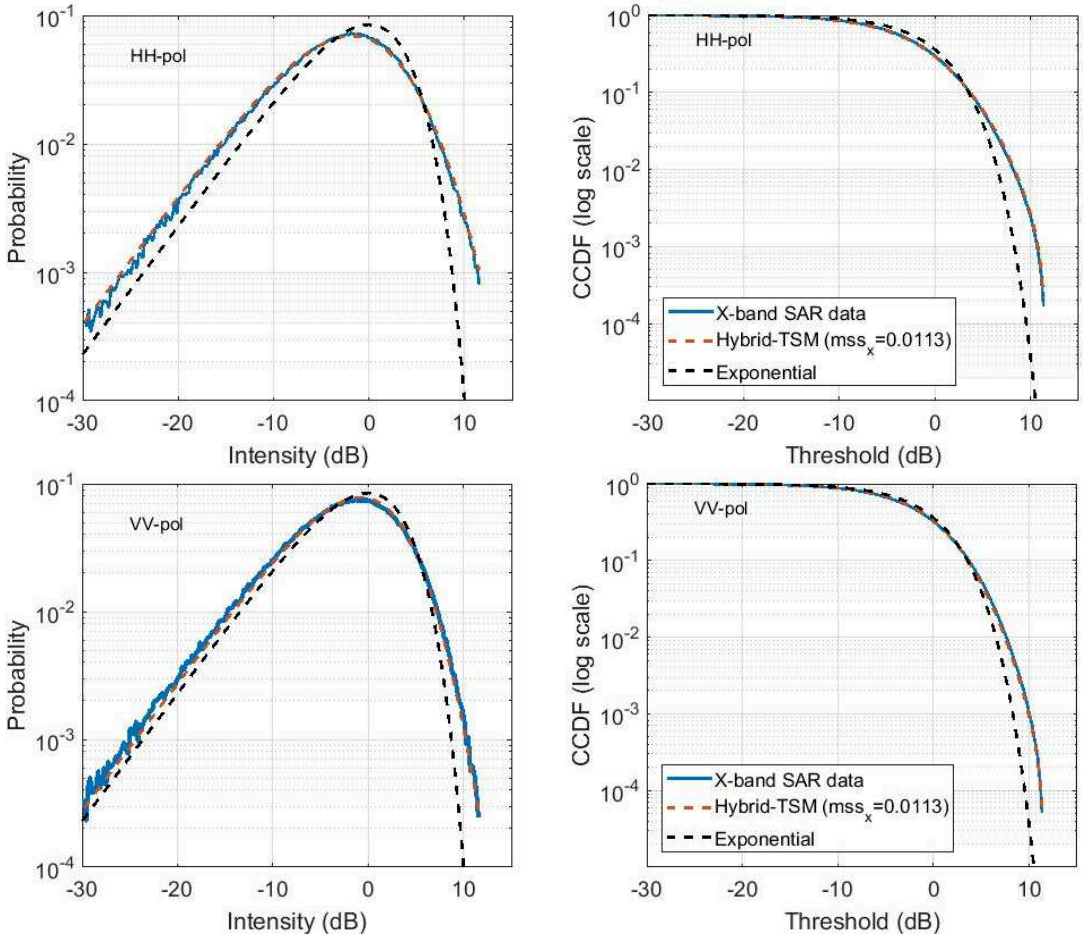

Fig. 37 : PDF (gauche) et CCDF (droite) des intensités normalisées obtenues avec des données SAR expérimentales (bleu), le modèle deux échelles hybride (pointillé rouge) et la loi exponentielle en référence (pointillé noir) – SAR bande X, résolution 0.5x0.5m, incidence 45°, polarisation HH (haut) et VV (bas)- Méditerranée U_{10}=8m.s^{-1}, crosswind

Le modèle proposé est uniquement paramétré par la valeur de mss_x et on suppose que $mss_x = mss_y$. Il a été calculé pour un ensemble de valeurs de mss_x et la valeur produisant la plus petite distance de Bhattacharyya (cf. 4.2.1) est retenue comme paramètre du modèle (ici $mss_x = 0.0113$). Le paramétrage du modèle par la valeur de la mss_x rend celui-ci indépendant de la polarisation. Nous obtenons effectivement une distance de Bhattacharyya minimale pour la même valeur de mss_x en polarisation HH et VV grâce à la correction apportée par le modèle deux échelles hybride. On obtient alors une excellente correspondance entre le modèle et les données, pour les deux polarisations HH et VV, sur l'ensemble de la distribution mais également en queue de distribution.

Inversement des valeurs de $mss_x = mss_y = 0.0113$ correspondent à une mss totale $mss_x + mss_y = 0.0226$. D'après la formule de Cox and Munk « slick » [69] et en négligeant l'impact de la direction du vent, cette valeur de mss totale correspond à un vent à 12.5 m de la surface de $U_{12.5}$=9.36 m.s^{-1}, soit $u^* = 1.1865$ m.s^{-1} (eq. (52)), soit finalement un vent à 10 m de la surface U_{10}=8.7 m.s^{-1}, ce qui est très proche des informations terrains (U_{10}=8 m.s^{-1}).

4.3. Synthèse sur la caractérisation de la réponse radar d'une surface océanique

Les travaux auxquels j'ai contribué ont permis de faire progresser les connaissances sur la caractérisation de la réponse radar d'une surface de mer. J'ai participé à l'extension du domaine de validité du modèle analytique de rétrodiffusion GO-SSA. Il en résulte un modèle semi-empirique, « GO-SSA Extended », valide sur l'ensemble du domaine angulaire en incidence. Nous avons ensuite montré dans le cadre des travaux de thèse de Z. Guerraou que j'ai co-encadrés que la prise en compte d'une distribution des pentes des vagues adaptée (notamment asymétrique) permet de restituer qualitativement les asymétries directionnelles et notamment leurs variations polarimétrique, fréquentielle et angulaire. Nous avons ensuite proposé une correction du rapport de polarisation, celle-ci est basée sur des considérations physiques et concorde avec le modèle empirique de Thompson, largement reconnu et utilisé.

J'ai également mené une analyse quantitative des performances des lois de distributions théoriques récemment proposées dans la littérature pour représenter le fouillis de mer. Cette analyse a été conduite sur un jeu de données particulièrement original, en termes de configurations de mesure et d'états de mer. L'inconvénient majeur des distributions théoriques habituellement utilisées et l'absence de lien explicite entre leurs paramètres (classiquement d'échelle et de forme) et les conditions océanographiques. Dans le cadre des travaux de thèse de F. Schreiber que j'ai co-encadrés, nous avons proposé et validé un modèle permettant de restituer l'ensemble de la statistique des échos radar rétrodiffusés par la surface océanique, uniquement paramétré par la pente quadratique moyennes des vagues, qui est directement relié à l'état de la surface de mer (les modèles météorologiques actuels en proposent une estimation sur l'ensemble de globe). Il est basé sur un modèle physique de type « deux-échelles » et fournit l'ensemble de la distribution statistique du fouillis de mer dans la partie supérieure du spectre des micro-ondes, en polarisation HH et VV, pour des angles d'incidence modérés et en haute résolution spatiale uniquement. Ce modèle permet également de résoudre un problème inverse, c'est-à-dire qu'il permet d'estimer l'état de mer tout en étant robuste aux erreurs de calibration des données SAR utilisées.

5. TELEDETECTION DES POLLUTIONS MARINES

La télédétection est un moyen privilégié pour la surveillance des océans et en particulier pour le suivi des pollutions marines [101][102]. Les systèmes imageurs actuellement disponibles depuis l'espace permettent de couvrir de larges étendues spatiales avec un temps de revisite parfois réduit à quelques heures en combinant différents instruments et selon la position géographique de la zone d'intérêt. Les données de télédétection radar sont communément utilisées par les autorités (Douanes [103], Agence de Surveillance Maritime Européenne [104] …) et les compagnies pétrolières [105] pour détecter et suivre les pollutions sur la surface océanique. Historiquement, les performances des capteurs embarqués sur les moyens opérationnels de surveillance maritime restreignent l'utilisation des données acquises dans la gamme des micro-ondes à la seule détection des nappes en surface ; l'imagerie optique vient ensuite caractériser et quantifier le produit préalablement détecté [101][106].

Les travaux de recherche réalisés dans le cadre de mes activités à l'ONERA ont eu pour principal objectif de développer des méthodologies de télédétection innovantes pour étendre le domaine d'utilisation des données micro-ondes à la caractérisation et à la quantification des pollutions marines. Ces développements méthodologiques s'appuient pour la plupart sur un jeu de données radar expérimentales particulièrement riche et original (au regard des substances polluantes investiguées) acquis lors de deux campagnes de mesures aéroportées.

5.1. Campagnes de mesures radar expérimentales

Deux campagnes de mesures expérimentales ont été réalisées en 2015 à partir du système de télédétection radar aéroporté SETHI de l'ONERA. Elles ont été effectuées lors de deux exercices de déversements contrôlés en mer : POLLUPROOF-2015 et NOFO-2015 [107].

5.1.1. Le système de télédétection aéroporté SETHI de l'ONERA

SETHI est le principal système de télédétection aéroporté développé par l'ONERA [107]. Il embarque des instruments à bord d'un Falcon 20 de Dassault Aviation, qui peut voler jusqu'à 30 000 ft (environ 9.1 km) d'altitude et avec une autonomie de 2.5 heures. Le système est composé de baies électroniques installées dans le fuselage de l'avion qui permettent le positionnement, le contrôle et le réglage des instruments de télédétection embarqués eux dans 2 pods fixés sous les ailes (Fig. 38). Ils font 2.3 m de long et 0.53 m de diamètre et ont la capacité de transporter des charges utiles lourdes et encombrantes (jusqu'à 120 kg de charge utile par pod).

Fig. 38 : Illustrations du système de télédétection aéroporté SETHI de l'ONERA

SETHI dispose de deux spécificités principales qui justifient son intérêt en tant que plateforme de recherche de télédétection aéroportée. Tout d'abord c'est un instrument multi-spectral qui embarque des instruments dans les domaines optiques et micro-ondes :

- Domaine optique : une caméra panchromatique longueur d'onde visible (0.4 – 0.8 µm) haute résolution spatiale ; deux caméras hyperspectrales dans les bandes VNIR (0.4 – 1.0 µm) et SWIR (1.0 – 2.5 µm) haute résolution spectrale (nanométrique).

- Domaine micro-ondes : 4 radars en polarisation complète dans les bandes UHF, L, X et Ku en haute résolution spatiale et avec la capacité de numériser 4 voies en parallèle.

Sa flexibilité est également démontrée en ce qui concerne la géométrie du capteur et les possibilités de configuration. Tout d'abord il est possible d'acquérir des données en trajectoire circulaire et linéaire, ainsi que de faire varier l'angle d'incidence entre 2 passes de mesures successives, ce qui peut être de grand intérêt pour estimer les paramètres géophysiques d'une surface.

5.1.2. Campagnes de mesures expérimentales sur déversements contrôlés en mer

Des données de télédétection ont été acquises par l'instrument aéroporté SETHI lors de deux exercices de déversements contrôlés de polluants en mer. Pour ces deux campagnes, une même forme d'onde radar a été utilisée et consiste en l'acquisition de signaux radar polarimétriques simultanément dans les bandes de fréquences X et L, en résolution décimétrique et métrique (Tableau 4).

<table>
<tr><th>Bande de fréquence</th><th>Polarisation</th><th>Résolution spatiale</th><th>Incidence au centre de fauchée et variation</th><th>Altitude de vol</th><th>Surface imagée</th></tr>
<tr><td>Bande X
[9.60 – 9.90 GHz]</td><td rowspan="2">HH, HV, VH, VV</td><td>0.5 x 0.5 m</td><td rowspan="2">45°
[34° – 52°]</td><td rowspan="2">9000 ft</td><td rowspan="2">1.5 x 9.5 km</td></tr>
<tr><td>Bande L
[1.25 – 1.40 GHz]</td><td>1.0 x 1.0 m</td></tr>
</table>

Tableau 4 : Paramètres capteurs radar campagnes POLLUPROOF-2015 et SETHI-2015

Un paramètre important lors de l'étude de la pollution marine par télédétection radar est le Rapport Signal à Bruit (RSB ou Signal to Noise Ratio (SNR) en anglais) disponible car la puissance rétrodiffusée par une surface marine polluée est généralement très faible. Pour chacun des deux radar utilisés ici et pour la forme d'onde mise en œuvre pour les campagnes expérimentales, le bruit de l'instrument a été estimé en utilisant la méthode d'inversion de la matrice de covariance polarimétrique (cf. 2.4.3). Le NESZ estimé (Fig. 39) varie entre -33 et -45 dBm^2/m^2 en bande X et entre -54 et -56 dBm^2/m^2 en bande L. Ces valeurs sont très faibles, et même inférieures à celles des instruments actuellement disponibles dans l'espace, et assurent un SNR suffisamment élevé sur les zones polluées pour une analyse des propriétés de la surface.

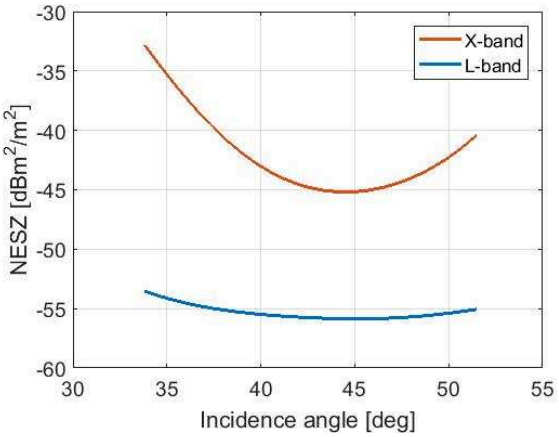

Fig. 39 : Niveaux de bruit (NESZ) des données radar en bande X (courbe rouge) et en bande L (courbe bleue) campagnes POLLUPROOF-2015 et NOFO-2015

5.1.2.1. Déversements contrôlés de produits chimiques : POLLUPROOF-2015

POLLUPROOF-2015 est une campagne de mesure réalisée par l'ONERA dans le cadre du projet ANR-POLLUPROOF [103], au profit des douanes françaises (DGDDI). L'objectif principal de cet exercice est d'établir une procédure permettant de recueillir des preuves de pollution par rejet de substances liquides dangereuses et nocives (SNPD) en mer à l'aide de capteurs aéroportés. Cette campagne a eu lieu du 18 au 22 mai 2015 en mer Méditerranée au large des côtes Françaises (latitude 42° 45' N, longitude 5° 45' E). Lors de cet exercice, des SNPD représentatifs des produits chimiques les plus couramment transportés par voie maritime ont été déversés par le BSAD (Bâtiment de Soutien, d'Assistance et de Dépollution) Ailette de La Marine Française.
L'efficacité des instruments radar pour la télédétection des SNPD dépend du produit imagé, ce dernier impactant différemment la surface de la mer en fonction de ses propriétés physico-chimiques. Afin d'évaluer rapidement le comportement des substances lors de leur rejet en mer, une classification a été créée dans le cadre de l'Accord de Bonn en 1994, il s'agit de la classification SEBC (Standard European Behavior Classification). Basée sur des propriétés physico-chimiques des produits (gravité spécifique, solubilité dans l'eau et pression de vapeur), cette classification permet une première estimation des comportements à court terme des substances chimiques une fois déversées en mer : Gazeux (« G » – Gas), Flottant (« F » – Floater), Coulant (« S » – Sinker), Evaporant (« E » – Evaporator) et Soluble (« D » – Dissolver) ; avec des combinaisons possibles comme FD, ED, FED etc …

Les substances liquides suivantes ont été testées lors de l'expérimentation POLLUPROOF-2015 :

Huile de colza : l'huile de colza est une huile végétale obtenue à partir de graines de colza broyées. A pression et température ambiantes, l'huile de colza est un liquide visqueux d'une densité de 0,910. Elle est insoluble dans l'eau et ne s'évapore pas (pression de vapeur inférieure à 0,01 kPa à 25 ° C), ces caractéristiques classent l'huile de colza comme Flottant « F » dans la classification SEBC.

FAME : les esters méthyliques d'acides gras sont des biocarburants ajoutés directement dans les carburants conventionnels tels que le diesel. A pression et température ambiantes, il s'agit d'un liquide de densité 0,888. Ce produit est pratiquement insoluble dans l'eau (solubilité de 0,023 mg.L-1 à 20 ° C) et a un potentiel d'évaporation relativement faible (pression de vapeur de 0,42 kPa à 25 ° C), ce qui en fait un produit classifié comme Flottant « F ».

Toluène : le toluène, également appelé méthylbenzène ou phénylméthane, est un hydrocarbure aromatique couramment utilisé comme réactif ou solvant chimique, en particulier dans le secteur industriel. Le toluène est un liquide à pression et température ambiantes et a une densité de 0,867. Le toluène est presque insoluble dans l'eau (535 mg.L-1 à 25 ° C) et a tendance à s'évaporer relativement facilement (pression de vapeur de 2,91 kPa à 20 ° C). Le toluène est une substance classifiée comme Flottant et Evaporant « FE » dans la nomenclature SEBC.

Heptane : l'heptane est le terme générique pour identifier l'un des 9 isomères de C_7H_{16} et est un hydrocarbure saturé de la famille des alcanes linéaires. C'est un constituant du carburant et est utilisé comme solvant dans l'industrie chimique. A pression et température ambiantes, l'heptane est un liquide volatil (6 à 7,7 kPa à 20 ° C) et presque insoluble dans l'eau (<2 mg.L-1 à 20 ° C). Avec une densité de 0,710, l'heptane est plus léger que l'eau et flotte. Selon la classification SEBC, l'heptane est considéré comme Evaporant « E ».

Xylène : le xylène, ou diméthylbenzène, est un groupe d'hydrocarbures aromatiques. Il est produit à partir de pétrole dans l'industrie pétrochimique et est l'un des 30 produits chimiques les plus produits aux États-Unis. Il est utilisé dans l'industrie de l'impression, du caoutchouc et du cuir principalement comme solvant. Le xylène est un liquide inflammable au parfum agréable. Les propriétés chimiques sont similaires d'un isomère à l'autre. Sa gravité spécifique de 0,87 le fait flotter sur l'eau. Le xylène est légèrement soluble dans l'eau (146 mg.L-1 à 25 ° C) et ne s'évapore pas (pression de vapeur de 0,89 kPa à 20 ° C). En raison de ces caractéristiques, le xylène est considéré comme Flottant et Evaporant « FE » dans la classification SEBC.

Méthanol : l'alcool méthylique ou le méthanol est l'alcool le plus simple de formule chimique CH_3OH. A pression et température ambiantes, ce liquide est utilisé comme antigel, solvant ou carburant (par exemple dans l'aéromodélisme). Le méthanol n'est pas présent en grande quantité dans la nature et est produit industriellement. Il est principalement utilisé comme matériau de base pour la synthèse de produits chimiques plus complexes. Près de 40% du méthanol est transformé en formaldéhyde pour être ensuite transformé en matières plastiques, résines synthétiques, peintures, explosifs ou tissus. Le méthanol est un liquide léger (densité de 0,791), volatil (pression de vapeur de 12,3 kPa à 20 ° C), miscible dans l'eau, inflammable et toxique avec une odeur caractéristique. Ces propriétés permettent de classer le méthanol en substance Soluble et Evaporant « DE ».

Les huiles végétales (comme l'huile de palme ou de colza) ont déjà été imagées par des capteurs SAR (l'huile végétale est souvent utilisée pour simuler une nappe biogénique monomoléculaire naturelle) et sont détectables par imagerie radar [108]. La télédétection micro-ondes des substances chimiques, en général, n'a quant à elle été que très peu étudiée par rapport aux rejets d'huiles minérales ou végétales.

Si l'on considère uniquement la classification SEBC, on peut s'attendre à détecter par imagerie radar uniquement le produit visqueux flottant à la surface soit : l'huile de colza « F », le FAME « F », le toluène « FE » et le xylène « FE ». Pour les deux derniers, la vitesse d'évaporation est cruciale. Ainsi, le délai entre le déversement de la SNPD et l'acquisition des images doit être suffisamment faible pour permettre une détection et une analyse efficace du produit. Pour le méthanol et l'heptane, on peut s'attendre à ne voir aucun effet sur l'image SAR et d'autres systèmes de télédétection comme les capteurs infrarouges ou ultraviolets doivent être privilégiés pour les détecter en mer [109].

Au cours de l'expérience POLLUPROOF, 1 m^3 de chacun de ces six produits a été déversé en mer et imagé par le système aéroporté SETHI. Le Tableau 5 ci-dessous résume les conditions de mer et créneaux horaires lors des déversements. Une description détaillée de la campagne de mesure est donnée dans [110].

Date	Vent (U_{10})		Vagues		Substance imagée ($1m^3$)
	Vitesse	Direction	Hauteur	Direction (provenance)	
18 mai 2015	8 $m.s^{-1}$	255°	0.5 m	240°	Heptane : 16:27 UTC
					Toluène : 16:34 UTC
22 mai 2015	7 $m.s^{-1}$	315°	2 m	270°	Méthanol : 12:35 – 12:46 UTC
					Xylène : 12:53 – 13:25 UTC
					Colza : 15:01 – 15:28 UTC
					FAME : 15:24 – 15:40 UTC

Tableau 5 : Conditions environnementales et horaires des déversements – campagne POLLUPROOF-2015

5.1.2.2. Déversements contrôlés d'hydrocarbures : NOFO-2015

NOFO-2015 est une campagne de mesure réalisée dans le cadre du programme de recherche NAOMI conclu entre l'ONERA et TOTAL. L'expérimentation en mer NOFO-2015 a eu lieu du 08 au 14 juin 2015 au cours de l'exercice annuel organisé par le NOFO (Norwegian Clean Seas Association for Operating Companies). L'objectif principal était de tester, en mer, des systèmes de récupération de pollution par hydrocarbures. Elle a eu lieu en mer du Nord au large des côtes Norvégiennes (latitude 59° 59' N, longitude 2° 27' E).
Les travaux menés concernent principalement les données de télédétection acquises lors de deux exercices de déversements réalisés le 09 juin 2015, au cours desquels les systèmes de récupération MOS Sweeper et DESMI Boom ont été testés en mer. Pour les deux expériences, des hydrocarbures ont été rejetés par une pompe flottante à la surface de la mer tractée par un navire de tête (Stril Mariner) et récupérés par un deuxième navire (Stril Luna), à une distance de quelques centaines de mètres seulement.
Lors des essais en mer, une quantité importante d'hydrocarbure a été déversée puis récupérée par les systèmes mis en œuvre : 45 m^3 pour l'essai avec MOS Sweeper et 35 m^3 pour l'essai avec DESMI Boom. Dans chaque cas, le produit déversé était une émulsion d'huile minérale dans de l'eau de mer, avec une teneur en eau de 60%. Il se compose d'un mélange d'eau de mer, de pétrole brut d'Oseberg et d'un petit ajout d'IFO 380 (fuel-oil intermédiaire ou diesel marin, avec une viscosité de 380 $mm^2.s^{-1}$). L'émulsion a été préparée, à terre, par le NOFO plusieurs semaines avant les exercices en mer. La stabilité et la constitution exacte du produit déversé au moment de l'exercice n'est donc pas connue avec précision.

Au cours de la campagne NOFO-2015, quatre vols de mesure ont été réalisés. Une description détaillée de la campagne a été publiée dans [107] et résumée dans le Tableau 6 ci-dessous.

On notera que SETHI a également collecté des données SAR le 04 juin 2015 en Méditerranée (latitude 43 ° 13,5 'N, longitude 4 ° 38,5' E) sur une large zone de film biogénique naturel. Ce dernier vol de mesure complète avantageusement un ensemble de données très original, composé d'images SAR acquises sur une grande variété de substances liquides en mer. Toutes ces données ont été obtenues avec le même capteur, avec la même forme d'onde et dans les mêmes conditions géométriques, ce qui permet de se concentrer uniquement sur l'impact du produit sur le signal rétrodiffusé et limite tout artefact lié à l'instrument.

Date	Vent (U_{10})		Vagues		Substance imagée
	Vitesse	Direction	Hauteur	Direction (provenance)	
04 juin 2015	1 $m.s^{-1}$	330°	0.1 m	180°	Huile naturelle (biogénique)
09 juin 2015	5 $m.s^{-1}$	250°	1 m	0°	Huile minérale (45 m^3) – MOS Sweeper (05:00 – 11:00 UTC)
09 juin 2015	7 $m.s^{-1}$	250°	1 m	0°	Huile minérale (35 m^3) – DESMI Boom (12:20 – 14:50 UTC)

Tableau 6 : Conditions environnementales et horaires des déversements – campagne NOFO-2015

5.2. Détection des pollutions marines par imagerie radar

5.2.1. Détectabilité de substances liquides nocives par télédétection micro-ondes

Alors que la détectabilité des hydrocarbures en mer par imagerie radar est avérée depuis des décennies, la question reste posée pour de nombreuses substances liquides transportées par fret maritime. Cette problématique est au cœur du programme de recherche POLLUPROOF. La détectabilité des substances chimiques dépend fortement de leur comportement une fois déversées sur la surface océanique (cf. 5.1.2.1). Les données SAR acquises lors de l'exercice de déversement en mer POLLUPROOF-2015 ont permis d'aboutir aux observations suivantes :

Méthanol : le méthanol déversé en mer n'a pas été observé sur les acquisitions micro-ondes. Vues la grande volatilité et solubilité de produit, l'écart temporel de 40 minutes entre le déversement et la prise de mesure SAR rend délicat toute conclusion quant à la détectabilité de cette substance.

Toluène, heptane : malgré un écart temporel de seulement 5 à 10 minutes entre le déversement des produits et l'acquisition des données, aucune des deux substances n'a été observées sur les images SAR en bande X et L. L'absence de détection radar est probablement due à l'extrême volatilité de ces deux substances.

Xylène : les données collectées sur le déversement de xylène montrent que ce produit chimique est observable comme une zone d'amplitude réduite sur les images SAR [110]. La nappe de xylène est observée sur toutes les images acquises pendant le vol de mesure (la dernière ayant eu lieu 30 minutes après la fin du déversement). L'étendue approximative de la nappe observée est de 0,26 km^2, ce qui correspond à une épaisseur moyenne de 0.26 µm si on suppose que la totalité du produit reste en surface (ni évaporation, ni dissolution). On peut observer un fort impact du xylène sur la surface de mer en bande X. En bande L, la nappe est difficilement observable, probablement en raison d'un faible effet de cette SNPD sur la surface de la mer et n'amortissant que les vagues de capillarités / gravités de courtes longueur d'onde (correspondant principalement à la longueur d'onde de Bragg en bande X).

Huile de colza et FAME : les deux substances classifiées comme Flottant « F » dans la classification SEBC sont a priori les plus persistantes en surface et sont aisément observables sur les images SAR en bandes X et L. La Fig. 40 montre les données acquises à 16:07 UTC, soit 40 minutes après la fin du déversement de l'huile de colza et 30 minutes après celui du FAME. L'huile de colza, ayant été déversée en premier, se situe sur la partie droite de la nappe, le FAME sur la partie gauche. D'après les informations in situ, nous savons que la FAME se trouve entre les positions en azimut de 4100 m à 5500 m (Fig. 40, cadre rouge – couvrant une surface de 0,29 km^2), et que l'huile de colza est entre les azimuts 6000 m à 8500 m (Fig. 40, cadre vert – couvrant une surface de 1,26 km^2). Entre les deux, nous avons un mélange des deux produits (Fig. 40, cadre bleu – couvrant une surface de 0,195 km^2).

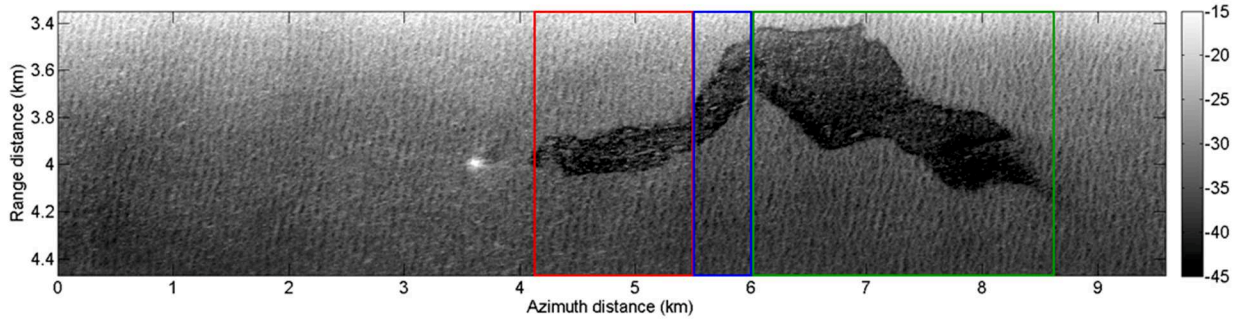

(a) : image SAR bande X acquise à 16 :07 – déversement d'huile de colza et de FAME

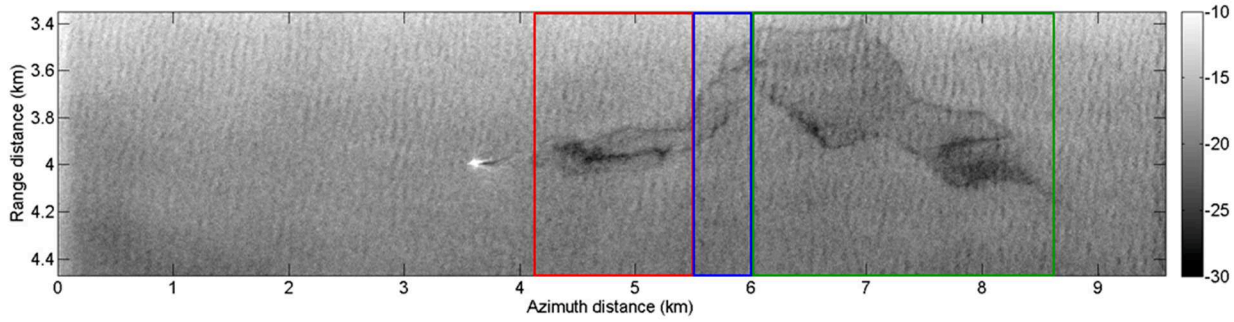

(b) : image SAR bande L acquise à 16 :07 – déversement d'huile de colza et de FAME

Fig. 40 : Images SAR SETHI acquise à 16:07 UTC sur les déversements de FAME et d'huile de colza en bande X (a) et bande L (b)

Le toluène et le xylène sont tous deux classés comme Flottant et Evaporant « FE » selon la classification SEBC. Cependant, le toluène (dont la pression de vapeur à 20 ° C est de 2,91 kPa) n'a pas été observé sur les images (les acquisitions SAR ont commencé 40 minutes après la fin du déversement), tandis que le xylène (dont la pression de vapeur à 20 ° C est de 0,89 kPa) est détectable sur toutes les images SAR (acquises jusqu'à 30 minutes après la fin du déversement). La classification SEBC ne permet donc qu'une première estimation des comportements des produits chimiques sur la surface, sans présager de leur détectabilité par télédétection micro-ondes [110].

De plus, sur ces images d'amplitude il n'est pas possible d'identifier une différence entre les produits déversés, notamment entre la nappe de FAME et d'huile de colza sur l'acquisition de 16:07 UTC. Des stratégies de caractérisation seront exposées dans la suite du manuscrit (paragraphe 5.3).

5.2.2. Paramètres polarimétriques optimaux pour la détection de pollutions marines

L'imagerie radar est utilisée depuis de nombreuses années pour la détection de pollutions en mer. Aujourd'hui, différents systèmes de télédétection (aéroportés et satellitaires) sont disponibles, chacun ayant des propriétés instrumentales et géométriques propres. Les modes d'acquisitions (polarimétriques en particulier) peuvent également varier d'un capteur à un autre. Il est donc primordial d'identifier les configurations de mesures optimales pour la détection des hydrocarbures en domaine offshore. Pour cela, il convient de disposer d'une méthodologie pouvant s'appliquer sur des paramètres de différente nature : réflectivité (nombre naturel ou dB), entropie polarimétrique (sans dimension)... Quelques études ont été proposées dans la littérature [111]-[114] mais sont toutes basées sur les premier (moyenne) et second (variance) moments des distributions statistiques des échos radar rétrodiffusées par la surface de mer. La méthodologie habituellement utilisée pour caractériser les performances d'un détecteur est basée sur l'exploitation des courbes ROC (Receiving Operating Characteristic). Elles sont obtenues en traçant la probabilité de détection par rapport à la probabilité de fausse alarme (estimées à partir des statistiques de l'image) et quantifient les performances d'un détecteur lorsque son seuil de détection varie. En d'autres termes, elles illustrent le compromis entre taux de détection et taux de fausses alarmes du détecteur [116].

De nombreuses études ont analysé l'apport de la polarisation pour la détection de nappes de pollution en mer et des paramètres ont été proposés dans la littérature à cet effet. Pour un état de l'art complet il convient de se référer aux références [117] et [118]. Un ensemble de paramètres a été sélectionné parmi ceux-ci et nous avons évalué leurs performances de détection dans [115] à partir de l'exploitation des courbes ROC obtenues pour chacun des paramètres.

Il a été observé des écarts importants entre les performances de détection des différents paramètres polarimétriques investigués et nous avons démontré dans [115] que le facteur prépondérant pour expliquer ces écarts de performance est le rapport signal à bruit mesuré sur les surfaces polluées, directement lié au niveau de bruit de l'instrument. Dans le passé, de nombreuses études ont été réalisées à partir de données SAR acquises depuis des instruments satellitaires disposant d'un niveau de bruit instrumental assez élevé. Ceci conduit à des erreurs d'interprétation, notamment la présence de mécanisme de rétrodiffusion autre que Bragg sur les surfaces de mer polluées. Pour une analyse critique complète, on pourra de se référer à [119].

Au fur et à mesure que le SNR diminue, le signal reçu devient aléatoirement polarisé. Au contraire, lorsque les données SAR sont collectées avec un faible niveau de bruit instrumental, le signal rétrodiffusé n'est pas corrompu par le bruit, l'onde EM est bien polarisée et un mécanisme de rétrodiffusion dominant se produit sur la surface de mer, que celle-ci soit propre et contaminée, un mécanisme de type Bragg (pour des angles d'incidence modérés). Lorsque le SNR sur une zone couverte de nappe n'est pas suffisamment élevé, comme pour les SAR spatiaux disponibles aujourd'hui, le bruit de l'instrument doit être pris en compte lors de l'évaluation des performances de détection des paramètres polarimétriques.
Nous concluons également dans [115] que pour la détection de pollution marine, le signal radar en polarisation VV offre le meilleur compromis entre performances de détection et exigences instrumentales (temps de revisite doublé pour un instrument collectant des données en polarisation complète par rapport au même instrument opérant en mono-polarisation). VV est suivi de près par les paramètres co-polarisés étudiés (différence de polarisation, HH, HV et produit hermitien entre les canaux co-polaires), tout en étant plus robuste au SNR que le canal en polarisé croisé.

5.3. Caractérisation des pollutions marines par imagerie radar

5.3.1. Caractérisation du comportement en surface du produit déversé

Lorsqu'un produit visqueux est déversé dans le milieu marin, le choix de la technique d'intervention nécessite une connaissance approfondie des propriétés de la substance impliquée. Il a été démontré dans [120] et [121] que, dans le cas d'une pollution par hydrocarbures, les images SAR peuvent indiquer si le produit déversé se comporte comme un film viscoélastique plus ou moins homogène et flottant à la surface ou s'il est mélangé avec l'eau de mer dans les quelques premiers centimètres de la colonne d'eau. Le principe de base de cette méthode, qui donne l'indice de mélange huile-eau (M – Mixing Index), consiste à différencier l'origine de la réduction de la puissance rétrodiffusée par la surface : soit l'amortissement mécanique des vagues de gravités-capillarités à la longueur d'onde de Bragg, soit la réduction de la constante diélectrique relative de la couche supérieure de la surface de la mer imagée [120][121]. En découplant la contribution relative à l'atténuation du signal provenant de l'amortissement mécanique de la rugosité de surface et de la modification de la constante diélectrique, il est possible de définir les caractéristiques de la nappe le long d'un spectre allant d'un film fin en surface à un produit mélangé à l'eau de mer.
Les étapes importantes du processus de découplage des mécanismes d'atténuation mécanique et électromagnétique sont décrites en détails dans [121] et peuvent être résumées comme suit:

1. Utiliser le rapport de co-polarisation sur l'eau de mer non contaminée et une valeur connue pour la constante diélectrique de l'eau de mer pure (cf. Tableau 2) afin de déduire l'angle d'incidence local θ_i.
2. Calculer le spectre de rugosité sur une surface de mer propre, W_{eau}, en appliquant les angles d'inclinaison (« tilt ») estimés à l'étape 1.
3. Pour chaque pixel d'eau polluée, déduire la constante diélectrique relative locale (effective), ε_r^{nappe}, à partir du rapport de polarisation et des angles d'inclinaison estimés à l'étape 1.
4. Calculer le spectre de rugosité des ondes courtes sur de l'eau contaminée, W_{nappe}, en utilisant la constante diélectrique déduite à l'étape 3 et les angles d'inclinaison obtenus à l'étape 1.

Une fois les étapes 1 à 4 terminées, le Mixing Index, M, se calcule tel que :

$$M = M_w - M_\alpha \tag{94}$$

où:

$$M_w = \frac{W_{eau} - W_{nappe}}{W_{eau}} \tag{95}$$

$$M_\alpha = \frac{|\mathcal{B}_{VV}^{eau}|^2 - |\mathcal{B}_{VV}^{nappe}|^2}{|\mathcal{B}_{VV}^{eau}|^2} \tag{96}$$

où les indices eau et $nappe$ correspondent à des régions d'eau non contaminée et contaminée, respectivement et $\mathcal{B}_{VV}$ le noyau de Bragg en polarisation VV définit à l'équation (56). La polarisation VV est favorisée ici à cause de son rapport signal à bruit supérieur à celui en polarisation HH..
M_w ($0 \leq M_w \leq 1$) est le facteur d'amortissement normalisé et est une mesure de l'amortissement de la rugosité de la surface de la mer par le produit (0 signifie aucun amortissement et 1 indique un amortissement total). M_α ($0 \leq M_\alpha \leq 1$) est le facteur d'atténuation de la puissance normalisé, c'est une mesure de l'atténuation du signal rétrodiffusé en raison d'une constante diélectrique relative plus faible.

M varie alors entre -1 et 1. Des valeurs négatives indiquent que la réduction de la puissance du signal EM est principalement due à une réduction de la constante diélectrique relative, ce qui signifie que le produit est largement mélangé à l'eau de mer. Des valeurs positives indiquent que la réduction de la puissance du signal EM est principalement due à un lissage de la surface de l'océan (amortissement des vagues de capillarités) et que, par conséquent, le produit est principalement présent sous forme de film à la surface de la mer.

Cette méthodologie a été mise en œuvre sur les données acquises en bande L lors de la campagne POLLUPROOF-2015 et nous avons pu mettre en évidence dans [110] une différence de signature sur le « Mixing Index » traduisant la différence du comportement entre les 2 substances chimiques une fois déversées en surface :

- Mixing Index négatif (couleur bleue sur la Fig. 41) : indique un produit qui se mélange dans la colonne d'eau (FAME) et signe une modification de la constante diélectrique.
- Mixing Index positif (couleur rouge sur la Fig. 41) : indique un produit qui forme un film fin en surface (huile de colza) ce qui se traduit par une atténuation de la rugosité de surface.

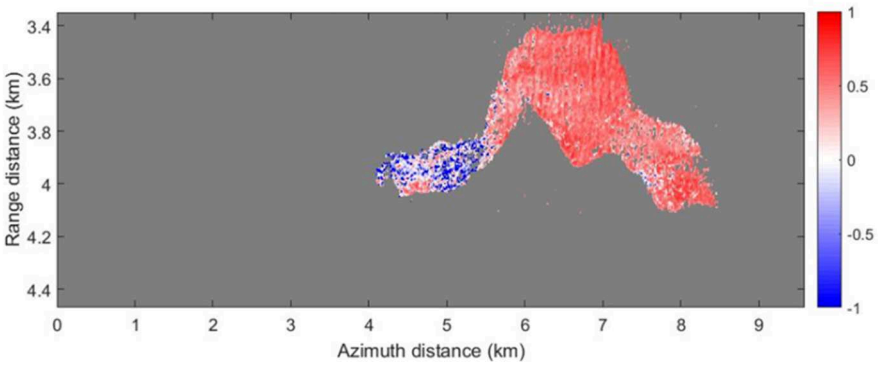

Fig. 41 : Image du paramètre M (Mixing Index) estimé sur les données SAR acquises en bande L par SETHI lors de l'exercice POLLUPROOF-2015 – déversement de FAME et d'huile de colza – 22 mai 2015 16:07 UTC.

Le Mixing Index a ensuite été appliqué sur les données acquises en bande L par SETHI lors de l'exercice de déversement contrôlés d'hydrocarbures en mer de Norvège (NOFO-2015). On observe (Fig. 42) un gradient des valeurs dans la direction de propagation du vent, le paramètre calculé passant de valeurs négatives à positives, ce qui signe le passage d'un produit en mélange à un produit sous la forme d'un film. Ceci s'explique par l'effet du vent sur la nappe qui déplace plus rapidement les huiles lourdes (formant un film épais en surface). Les huiles légères sont quant à elles moins déplacées par le vent et se mélangent plus facilement avec l'eau de mer [122].

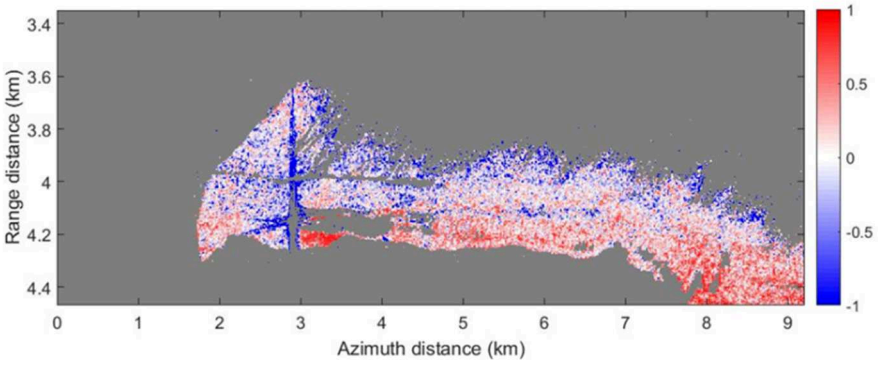

Fig. 42 : Image du paramètre M (Mixing Index) estimé sur les données SAR acquises en bande L par SETHI lors de l'exercice NOFO-2015 – déversement d'hydrocarbures – 09 juin 2015 10:02 UTC.

5.3.2. Tentative de différenciation entre pollution marine et film biogénique

Un problème majeur qui persiste encore aujourd'hui concerne la fiabilité des détections par télédétection micro-ondes. De nombreux phénomènes océaniques et atmosphériques peuvent se produire à la surface de la mer et se manifester sur les images radar de la même manière que les zones couvertes de produits chimiques ou d'hydrocarbures. Celles-ci sont appelées sosies et peuvent provenir de plusieurs sources [119] : films de surface biogéniques naturels produits par le poisson ou le plancton, glace de mer jeune et mince, zones de vent faible et remontée d'eau froide, entre autres. Pendant des décennies, de nombreux chercheurs ont tenté de développer des méthodologies pour différencier les zones océaniques couvertes d'hydrocarbures des sosies. Dans [75] et [123] les auteurs ont rapporté que l'utilisation du rapport de polarisation, qui est le rapport entre le signal collecté dans les canaux de polarisation horizontale et verticale, est un paramètre approprié pour distinguer les surfaces de faible réflectivité causée par un vent faible des zones de films marins. Aujourd'hui, la discrimination entre les films biogéniques, également appelés tensioactifs, et les nappes d'huiles minérales reste un domaine de recherche actif. Des méthodologies empiriques pour différencier les deux substances ont été rapportées dans la littérature (voir par exemple [108] et [124]) mais elles ont été remises en cause dans [119] car les données expérimentales utilisées sont fortement corrompues par le bruit instrumental et le rapport signal à bruit obtenu ne permet pas une estimation des propriétés physiques de la surface observée.

Une alternative intéressante a été proposée il y a plus de 20 ans [125]. Elle est basée sur l'utilisation conjointe d'images SAR multifréquences (bandes X, C et L) acquises par la charge utile radar SIR-C/X-SAR embarqué en 1994 à bord de la navette spatiale Endeavour. Depuis cette expérience inédite, les travaux sur l'utilisation des données SAR multifréquences pour la télédétection de la pollution marine n'ont pas été poursuivis puisqu'aucun instrument opérant depuis l'espace n'a embarqué de radar imageur collectant des données à différentes longueurs d'onde.

L'amortissement des vagues de gravités-capillarités par la présence d'un film fin en surface est causé par l'effet de Marangoni [126][127]. Selon cette théorie, le coefficient d'amortissement visqueux s'écrit tel que [125] :

$$y(k) = \frac{1 + X(\cos\alpha - \sin\alpha) + XY - Y\sin\alpha}{1 + 2X(\cos\alpha - \sin\alpha) + 2X^2} \tag{97}$$

avec

$$X = \frac{|E|k^2}{\sqrt{2\omega^3\eta\rho}} \quad ; \quad Y = \frac{|E|k}{4\omega\eta} \quad ; \quad \omega = \sqrt{gk + \tau k^3} \tag{98}$$

k est le nombre d'onde des vagues, ω est la pulsation (ou fréquence angulaire) des vagues donnée par la relation de dispersion, ρ est la masse volumique de l'eau de mer, η est la viscosité dynamique de l'eau de mer, g est l'accélération de la pesanteur et τ est le ratio entre la tension de surface et la masse volumique de l'eau de mer. Dans la suite, nous prenons les valeurs suivantes pour ces paramètres : η =0.001 Pas, ρ =1000 kg.m^{-3}, g=9.81 m.s^{-2}, τ =7.3.10^{-5} m^3.s^{-2}. Les paramètres $|E|$ et α sont respectivement le module et la phase du module dilatationnel élastique complexe et caractérisent l'élasticité d'une substance.

La relation entre ce coefficient d'amortissement visqueux $y(k)$ et le facteur d'amortissement $D(k)$ du spectre de rugosité de la surface océanique est donnée dans [128] par :

$$D(k) = \frac{1}{1 - f + \frac{f}{y(k)}} \tag{99}$$

f est la proportion de la surface de la mer couverte par le film (0 indique qu'il n'y a pas de film et 1 indique une couverture complète). Le facteur d'amortissement, $D(k)$, dépend de la substance visqueuse à la surface de la mer (via les valeurs de $|E|$ et α) et du nombre d'onde des vagues, ce qui suggère que les échelles de rugosité sont affectées différemment selon les propriétés de la substance. Les valeurs du module $|E|$ et de la phase α du module de dilatation complexe sont mal connues dans la littérature. On trouve dans [129] des valeurs pour certains hydrocarbures et dans [125] pour l'alcool oléylique (OLA) qui est une substance visqueuse habituellement utilisée pour simuler un film d'huile biogénique. Le comportement du facteur d'amortissement $D(k)$ est donné Fig. 43 (pour une fraction surfacique, f, fixée à 1). Pour le film biogénique, les valeurs du module de dilatation complexe sont celles de l'OLA [125] et pour l'huile minérale, on utilise les valeurs moyennes de celles données pour les hydrocarbures dans [129], cf. Tableau 7.

Cela permet d'établir la tendance suivante sur la dépendance en fréquence du facteur d'amortissement : on peut trouver deux domaines spectraux, appelés basse et haute fréquence sur la Fig. 43, pour lesquels le facteur d'amortissement d'un film biogénique (courbe verte) est plus élevé en basse fréquence qu'en haute fréquence et pour lesquels le comportement est inversé sur l'huile minérale (courbe rouge), à savoir que l'amortissement est plus important en haute fréquence qu'en basse fréquence (qui est le comportement généralement observé pour les déversements d'huile minérale [130]). Les domaines de fréquence indiqués sur la Fig. 43 correspondent globalement aux bandes X et L avec une incidence de 45°. Sur cette figure, l'axe des abscisses correspond au nombre d'onde de Bragg, $k_B = \frac{2\pi}{\lambda_B}$ avec λ_B la longueur d'onde de Bragg définie par l'équation (54).

Substance	**|E| [N.m^{-1}]**	**α [deg]**
Film biogénique (OLA – [125])	2.55x10^{-2}	-175
Huile minérale (hydrocarbures – [129])	1.83x10^{-2}	-165

Tableau 7 : Valeurs du module dilatationnel élastique complexe pour deux substances types.

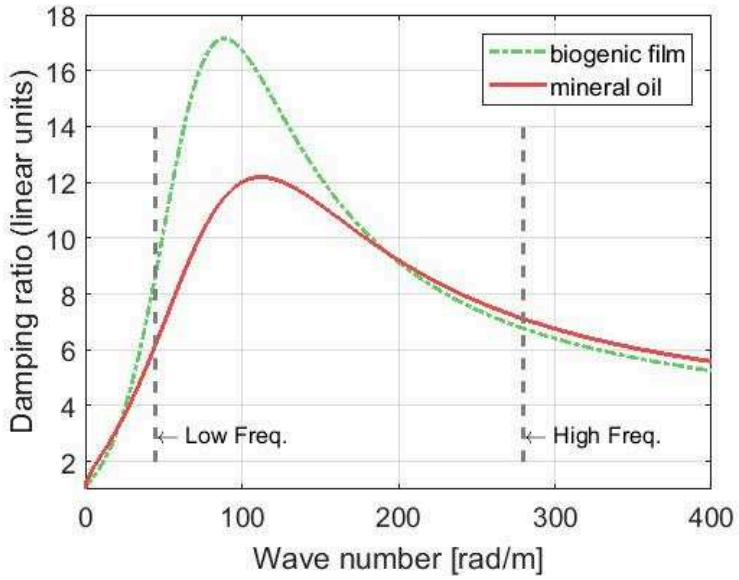

Fig. 43 : Coefficient d'amortissement théorique pour deux nappes typiques : film biogénique (OLA) en vert pointillé et huile minérale (hydrocarbures) en rouge. Les valeurs du module de dilatation sont données dans le Tableau 7 et la fraction surfacique, f, est égale à 1.

Nous avons développé, à partir de ce résultat, une méthodologie applicable à l'imagerie SAR bi-fréquence. Elle est basée sur l'analyse du Damping Ratio (DR – contraste entre les valeurs de réflectivité radar obtenues sur mer non couverte et mer couverte) mesuré sur des données acquises en bande X et en bande L sur la même zone. Le Damping Ratio permet de mesurer l'atténuation de la rugosité de surface induite par la présence d'une substance visqueuse, ce qui est sensiblement équivalent au facteur d'atténuation du spectre de mer, $D(k)$. Le SNR étant de façon générale plus élevé en polarisation VV qu'en polarisation HH, nous n'utilisons dans la suite que des données acquises en polarisation VV (ainsi la méthode proposée ne requiert pas de données polarimétriques).

$$\mathrm{DR} = \frac{\sigma^0_{unslicked}}{\sigma^0_{slicked}} \tag{100}$$

Nous avons alors calculé les valeurs de Damping Ratio sur les données SAR acquises lors des exercices de déversements contrôlés POLLUPROOF-2015 et NOFO-2015, ainsi que sur l'acquisition du 04 juin 2015 en mer Méditerranée sur une nappe d'huile biogénique (Fig. 44).

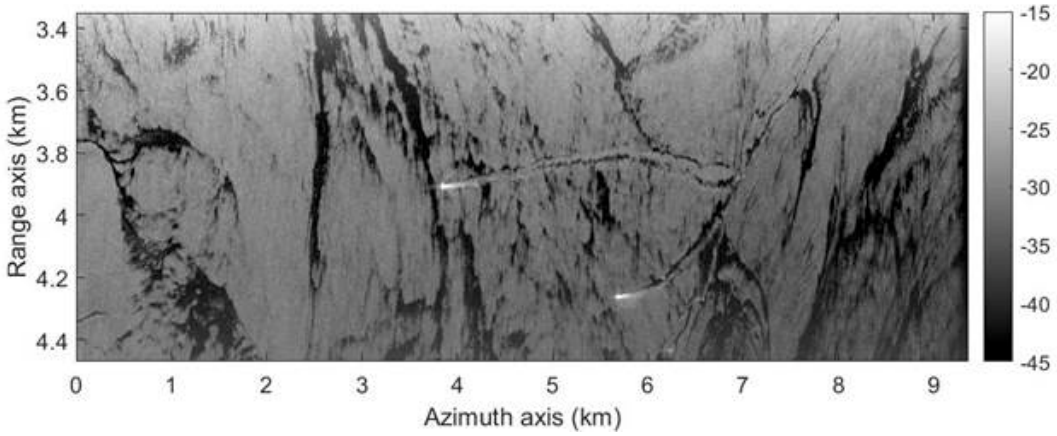

(a) : image SAR bande X acquise sur une nappe d'huile biogénique – SETHI 04 juin 2015

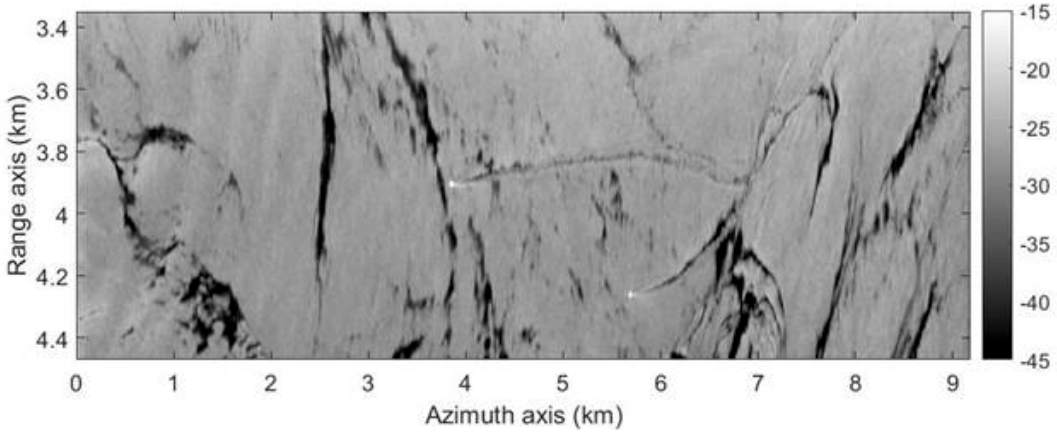

(b) : image SAR bande L acquise sur une nappe d'huile biogénique – SETHI 04 juin 2015

Fig. 44 : Images SAR SETHI acquise le 04 juin 2015 en mer Méditerranée sur une nappe d'huile biogénique en bande X (a) et bande L (b)

Les histogrammes des valeurs de Damping Ratio mesurées aux deux fréquences et pour chaque substance étudiée (xylène, FAME, huile de colza, hydrocarbures et huile biogénique) ont été calculés et sont donnés Fig. 45. La partie gauche des histogrammes correspond aux valeurs les plus faibles du coefficient d'amortissement qui dépendent sensiblement de la valeur de seuil utilisée lors du processus de détection des nappes. La partie droite correspond aux valeurs les plus fortes du coefficient d'amortissement, elles dépendent moins des traitements mis en œuvre mais sont davantage liées à l'impact effectif de la nappe sur la rugosité de la surface de la mer. Elles dépendent également de l'instrument et un niveau de bruit suffisamment faible est nécessaire pour mesurer des valeurs élevées de DR.

On constate que pour toutes les substances polluantes étudiées ici, le coefficient d'amortissement est plus élevé en haute fréquence radar qu'en basse fréquence. Il n'y a que sur la nappe d'huile biogénique que l'on observe des valeurs plus fortes en bande L qu'en bande X. Ces valeurs élevées de DR en bande L apparaissent au centre de la nappe, tandis qu'aux bords nous observons peu de différence entre les valeurs de DR mesurées aux deux fréquences. Ainsi, un schéma de caractérisation basé sur les valeurs de DR les plus élevées, plutôt que sur la valeur moyenne sur toute la nappe, est plus efficace pour différencier le surfactant des autres nappes marines. Pour mesurer ces variations au sein de la nappe, les données SAR doivent être acquises par un instrument à haute résolution spatiale, disposant d'un très faible niveau de bruit instrumental.

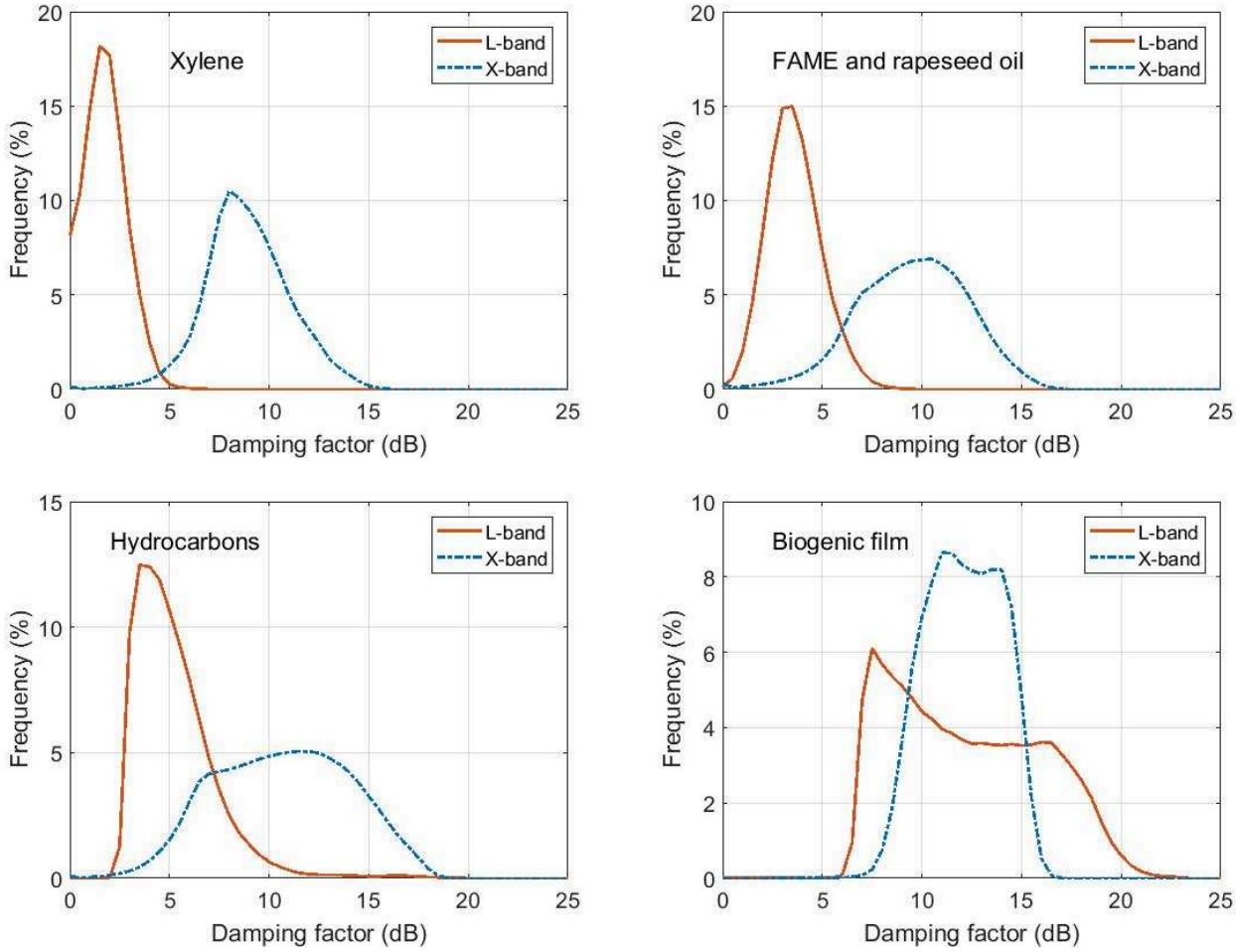

Fig. 45 : Histogrammes des valeurs de Damping Ratio mesurées en bande X (trait pointillé bleu) et en bande L (trait rouge) sur des nappes de xylène, de FAME, d'huile de colza, d'hydrocarbones et d'huile biogénique

En conclusion, l'analyse de ce jeu de données particulièrement riche montre que le facteur d'amortissement de la rugosité de la surface de mer mesuré à deux fréquences radar varie différemment pour le film biogénique et pour les autres nappes d'huiles minérales ou végétales étudiées ici. Pour le premier, on constate une diminution du coefficient d'amortissement de la bande L à la bande X, contrairement à toutes les autres nappes analysées. Ces comportements sont cohérents avec ceux prédits par le modèle théorique exposé à l'équation (96) et les observations rapportées dans [125]. D'un point de vue instrumental, le principal avantage de cette méthode est qu'elle ne nécessite pas de données polarimétriques (les données en polarisation VV sont préférables à celles en HH en raison du rapport signal à bruit). De plus, bien que les données utilisées ici aient été collectées par deux radars fonctionnant simultanément en bandes X et L, la stricte simultanéité entre les acquisitions n'est pas nécessaire. Cependant, pour garantir que le coefficient d'amortissement mesuré a effectivement atteint son maximum sans être limité par le rapport signal à bruit, le niveau de bruit de l'instrument doit être extrêmement faible. La résolution spatiale de l'instrument est également primordiale pour caractériser les nappes qui peuvent se manifester sous forme de filaments fins et étalés à la surface de la mer.

5.4. Quantification des pollutions marines par imagerie radar

Une fois la pollution marine détectée et identifiée, il est de première importance de pouvoir estimer au plus vite la quantité de polluant présente sur la surface océanique. Les capteurs optroniques peuvent apporter une telle information mais nécessitent des conditions d'emploi spécifiques (ciel clair …) ou une bonne connaissance de toute la colonne atmosphérique. La mesure de la quantité de polluant par télédétection micro-ondes serait donc une avancée majeure pour la lutte contre les pollutions marines. Je reprends ci-dessous les travaux que nous avons réalisés dans ce contexte.

5.4.1. Méthodologie de quantification relative

D'après la théorie de Bragg, la rétrodiffusion en polarisation directe du signal EM par la surface océanique (couverte ou non de pollution marine) s'écrit de la façon suivante [75] :

$$\sigma^0(\theta)_{pp} = 4\pi k^4 cos^4\theta \left|\mathcal{B}_{pp}\right|^2 W(k_B) + \sigma^0_{NB} \tag{101}$$

avec $p \in \{H, V\}$ l'état de polarisation de l'onde radar .

Le terme de gauche correspond au modèle de Bragg comme exprimée précédemment avec l'équation (55). σ^0_{NB} est un terme additionnel qui correspond aux contributions non polarisées [52][53][74][75]. Cette dernière est induite par différents mécanismes sur la surface de mer tels que les déferlements, les moutonnements … Il n'existe pas d'expression analytique de ce terme mais il a été démontré dans [53] que son impact sur la réflectivité totale dépend de la fréquence radar et est négligeable en basse fréquence radar mais devient non négligeable en bande X.

Indépendamment de la bande de fréquence radar, le paramètre de différence de polarisation (en unités linéaires) permet de supprimer l'effet de cette contribution non résonnante [75] :

$$PD = \sigma^0_{VV} - \sigma^0_{HH} \tag{102}$$

L'intérêt de ce paramètre pour la télédétection des pollutions marines est qu'il est directement proportionnel à la rugosité de la surface océanique, à travers le terme $W(k_B)$. En effet, la partie non polarisée du signal rétrodiffusée est supprimée en utilisant la différence de polarisation, elle contient donc principalement la contribution due aux vagues de courtes longueurs d'onde autour du nombre d'onde de Bragg. C'est précisément cette échelle de rugosité qui est principalement affectée par la présence d'une substance liquide à la surface de la mer, ce qui fait de PD un paramètre très efficace pour la détection des pollutions marines [75][115].

Pour étendre son utilisation, nous avons proposé dans [110] une variante normalisée de PD. En effet, on peut observer que PD varie entre une valeur maximale qui se produit dans le cas d'une surface de mer propre et diminue au fur et à mesure que l'impact de la substance sur la surface augmente, puisque les réflectivités en polarisation VV et HH tendent toutes les deux vers 0 sur une surface parfaitement lisse. Par conséquent, on peut définir la différence de polarisation normalisée NPD :

$$NPD = 1 - \frac{PD}{PD^{eau}} \quad 1 \leq NPD \leq 0 \tag{103}$$

avec PD^{eau} la valeur de la différence de polarisation sur une surface de mer propre (soit estimée directement sur les données si on dispose d'une telle surface dans toute la fauchée, soit à partir d'un modèle de rétrodiffusion mais dans ce cas les informations sur l'état de mer seront nécessaires).

Cette expression permet de formuler la différence de polarisation normalisée comme le rapport de deux contributions, liées à l'atténuation de la rugosité et de la réflectivité (directement reliée à une modification de la constante diélectrique) :

$$NPD = 1 - \frac{W^{nappe}}{W^{eau}} \frac{\Gamma_{VV}^{nappe} - \Gamma_{HH}^{nappe}}{\Gamma_{VV}^{eau} - \Gamma_{HH}^{eau}} \tag{104}$$

où les indices eau et $nappe$ correspondent à des régions d'eau non contaminée et contaminée, respectivement et Γ_{pp} est le noyau du modèle de Bragg composite introduit équation (58). NPD dépend de deux contrastes entre l'eau contaminée (indice $nappe$) et non contaminée (indice eau) : un premier contraste sur la rugosité de la surface (W), et un second contraste sur la différence de réflectivité polarimétrique (Γ_{pp}). Le premier contraste signe la décroissance de la rugosité de surface causée par l'impact du polluant à la surface. En supposant que les angles d'inclinaison sont constants quelle que soit la présence d'une nappe ou non comme supposé dans [121], le second contraste dépend de la différence de constante diélectrique entre la surface de la mer propre et l'eau polluée. Ces deux contrastes dépendent donc de la présence ou non d'un produit polluant et décroissent tous les deux avec l'impact (ou la concentration) de ce polluant. Ce paramètre NPD est égal à 0 sur la zone de mer propre et tend vers 1 lorsque la concentration ou l'impact du produit sur l'océan augmente. Par conséquent, NPD peut être interprété comme une indication de l'impact relatif d'une substance à la surface de la mer. Il peut également être utilisé directement ou avec un seuil pour produire une carte de détection binaire. Ces informations sont utiles à la fois pour identifier les surfaces marines polluées et pour localiser les zones les plus contaminées, et ainsi guider les opérations de nettoyage.

Une image du paramètre NPD a été calculée (Fig. 46) sur les données acquises en bande X et en bande L par SETHI lors de l'exercice NOFO-2015 (vol du 09 juin 2015, acquisition de 10:02 UTC). Sur la surface de mer « propre », le paramètre NPD prend des valeurs proches de 0, conformément à sa définition. Sur la zone couverte d'huile minérale, on observe que le paramètre NPD en bande X (Fig. 46 – haut) prend des valeurs comprises principalement entre 0.9 et 1. Sur la donnée en bande L (Fig. 46 – bas), NPD prend des valeurs comprises entre 0.5 et 1. Nous pouvons supposer que les vagues de capillarités, correspondant à la longueur d'onde de Bragg en bande X, sont fortement amorties partout dans la nappe, et le SNR disponible sur les mesures en bande X ne permet pas d'en mesurer les variations. On observe par contre que sur l'image du paramètre NPD en bande L, celui-ci prend des valeurs hétérogènes au sein de la nappe et un SNR élevé nous permet d'identifier les zones du déversement où les polluants ont un impact plus fort qu'ailleurs, probablement en raison d'une concentration localement plus élevée.

En outre, le paramètre NPD permet de contrôler l'efficacité du système de dépollution MOS Sweeper testé par le NOFO lors du survol par le système de télédétection SETHI [107][110]. En effet, on peut observer que juste derrière le passage de MOS Sweeper (Range [4.1-4.2 km] et Azimut [3.0-4.1 km]), NPD prend des valeurs proche de 0, ce qui correspond à la rugosité de l'eau de mer propre alentour.

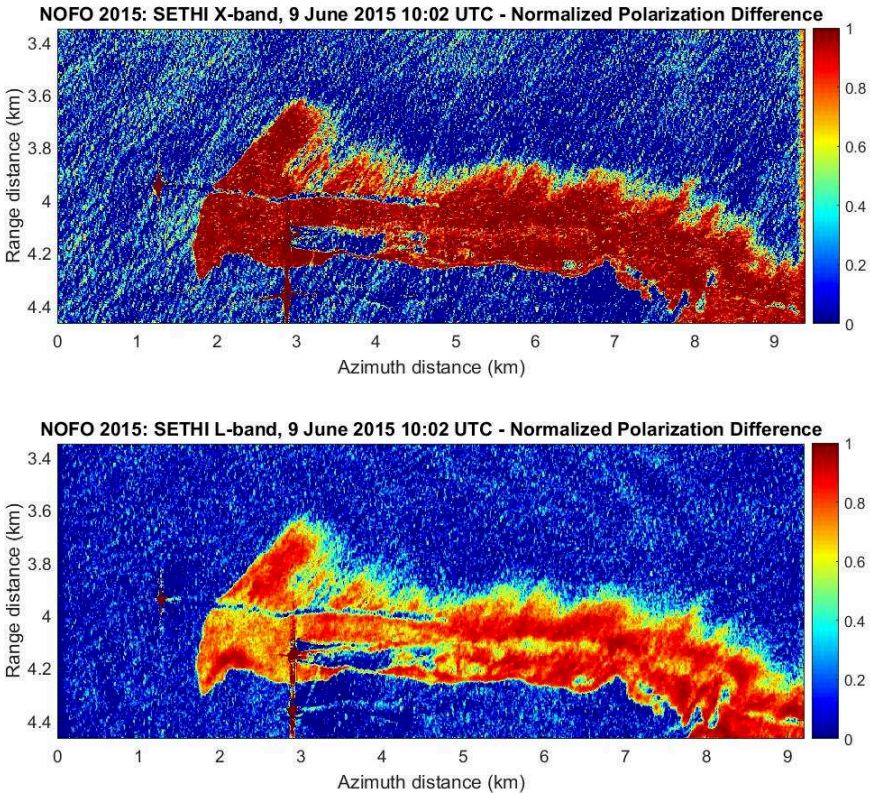

Fig. 46 : Paramètre NPD obtenus sur des données SAR acquises par SETHI le 09 juin 2015 à 10 :02 UTC (haut) en bande X et (bas) en bande L.

5.4.2. Méthodologie de quantification absolue

Lorsqu'un polluant est libéré dans le milieu marin, il peut se comporter de deux manières différentes : soit sous la forme d'un film en surface, soit comme un mélange dans la colonne d'eau de mer. Dans le premier cas, le film produit un amortissement des vagues de gravités-capillarités, qui sont les principaux contributeurs au signal EM rétrodiffusé, atténuant ainsi la puissance radar rétrodiffusée. L'épaisseur des films habituellement rencontrés en mer (micrométrique à millimétrique [102]) étant faible par rapport à la profondeur de pénétration, l'onde EM n'est pas atténuée et pénètre le film pour interagir avec l'eau de mer en dessous. Par conséquent, la constante diélectrique effective reste celle de l'eau de mer et n'est pas modifiée par la présence du polluant. Dans le second cas, le mélange du polluant et de l'eau de mer modifie les propriétés diélectriques de la surface imagée, impactant ainsi les coefficients de réflexion polarisés $\mathcal{B}_{pp}$ des équations (55) et (98). Une fois rejeté en mer, le polluant va rapidement se mélanger à l'eau sous l'action du vent et des vagues et produira un mélange avec une teneur en eau comprise entre 50 et 75% [131].

Les valeurs de constante diélectrique sont très différentes entre l'eau de mer et les substances polluantes. Dans le premier cas, le modèle empirique de Messner et Wentz [22] fait référence (cf. Tableau 2 – ε_{eau}). Dans le cas des huiles minérales [132][133] ou végétales [134][135], la constante diélectrique est constante dans la gamme 1 – 10 GHz ($\varepsilon_{huile} = 2.3 + 0.01i$) avec un facteur de perte (composante imaginaire) proche de zéro, suggérant une pénétration non négligeable de l'onde EM à travers ce milieu.

Un modèle de mélange linéaire entre huile minérale et eau de mer est souvent utilisé dans la littérature [120][121] pour estimer la constante diélectrique effective du mélange ($\varepsilon_{mélange}$) :

$$\varepsilon_{mélange} = \upsilon\varepsilon_{huile} + (1-\upsilon)\varepsilon_{eau} \tag{105}$$

avec $0 \leq \upsilon \leq 1$ la concentration volumique dans le mélange polluant – eau de mer.

Cependant, une approche plus pertinente, celle de la théorie des milieux effectifs [136], préconise d'utiliser la formule dite de Bruggeman pour estimer la constante diélectrique effective d'un tel mélange :

$$\varepsilon_{mélange} = \frac{1}{4}\left\{\varepsilon_{eau} - (1-3\upsilon)(\varepsilon_{huile} - \varepsilon_{eau}) + \sqrt{[\varepsilon_{eau} - (1-3\upsilon)(\varepsilon_{huile} - \varepsilon_{eau})]^2 + 8\varepsilon_{eau}\varepsilon_{huile}}\right\} \tag{106}$$

Les parties réelles et imaginaires de la constante diélectrique effective d'un mélange d'hydrocarbures dans de l'eau de mer estimées par les deux modèles (fonction de la concentration volumique du polluant en %) sont données ci-dessous (Fig. 47). On peut observer une forte surestimation des parties réelles et imaginaires avec le modèle linéaire par rapport à la formule de Bruggeman. Cette surestimation est d'autant plus prononcée à forte concentration de polluant (teneur en huile ~ 60–80%). Dans ce qui suit, la formule de Bruggeman sera adoptée.

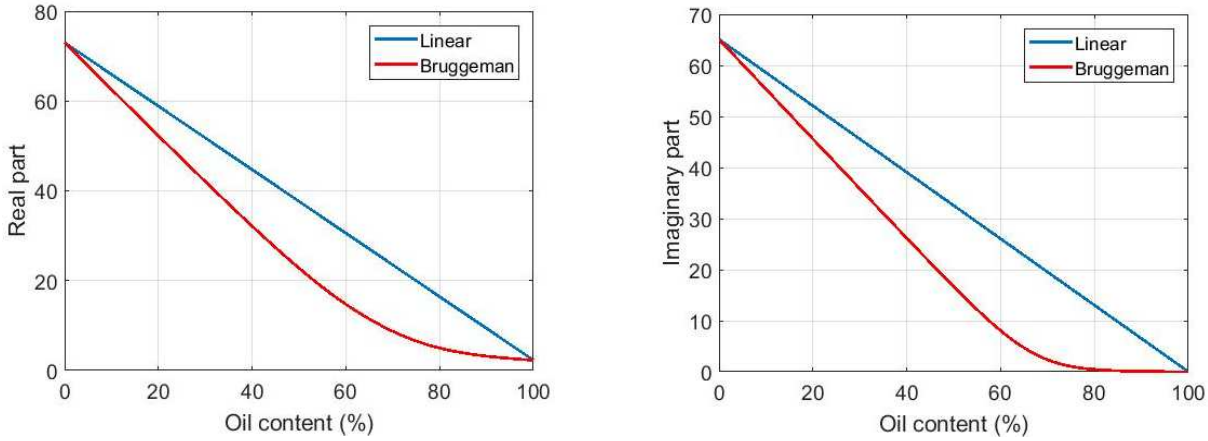

Fig. 47 : Parties réelle et imaginaire de la constante diélectrique effective d'un mélange d'huile minérale et d'eau de mer estimées par un modèle linéaire (bleu) et par la formule de Bruggeman (rouge).

En basse fréquence EM, la contribution de la composante non-polarisée σ_{NB}^0 (cf. équation (98)) au signal total est négligeable (cf. 5.4.1), le rapport de polarisation (défini comme le ratio entre les réflectivités mesurées en polarisation HH et VV) est alors une quantité pertinente pour mesurer la constante diélectrique d'un mélange et ainsi estimer la concentration volumique de polluant. Nous avons proposé une approche originale dans [82] et [83]. Il s'agit de comparer les signaux radar mesurés en bande L au modèle de rétrodiffusion analytique U-WCA (*Universal Weighted Curvature Approximation* – [81]). Ce modèle appartient à la famille des modèles dit « unifiés » [137], tels que les modèles à deux échelles [49] ou l'approximation des petites pentes [46], qui sont des modèles capables de traiter à la fois les grandes et les petites échelles présentes sur la surface de mer (cf. paragraphe 3.2).

Le modèle U-WCA conduit à une expression non triviale du rapport de polarisation qui dépend de la rugosité de la surface et présente l'avantage considérable de ne dépendre que de l'angle d'incidence nominal des ondes radar (et non pas de l'angle d'incidence localement modulé par la surface, comme dans un modèle de type Bragg composite, cf. paragraphe 3.2 équations (57) et (58)).

L'expression de la réflectivité radar copolarisée donnée par le modèle U-WCA est la suivante :

$$\sigma_{pp} = 4\pi\left|B_{pp}\right|^2 W(k_B) + |K|^2[I_s - 4\pi W(k_B)] \tag{107}$$

où $p \in \{H, V\}$ l'état de polarisation de l'onde radar, I_s est proportionnel à l'intégrale de Kirchhoff classique et B_{pp} et K sont les noyaux de Bragg et de Kirchhoff [137], respectivement. Les valeurs de $PR = \sigma_{HH}/\sigma_{VV}$ estimées avec le modèle U-WCA à 1.325 GHz sont illustrées Fig. 48. La simulation a été réalisée dans le sens au vent (upwind) avec le modèle U-WCA en utilisant le spectre de mer d'Elfouhaily [37].

Comme attendu, on observe de fortes variations du rapport de polarisation avec l'angle d'incidence mais peu de dépendance à la rugosité de la surface. On trouve également que PR varie fortement (mais non linéairement) avec la concentration volumique en huile dans le mélange huile – eau de mer, en particulier on observe une importante variabilité pour les concentrations élevées. On peut également noter la différence importante entre les théories de Bragg ou Bragg composite et le modèle U-WCA. Par construction, le modèle U-WCA, qui est une somme pondérée des noyaux de Bragg et Kirchhoff, produit un PR plus élevé que le modèle de Bragg pur. Le modèle de Bragg composite nécessite la connaissance de l'angle d'incidence local ce qui le rend difficilement exploitable pour un processus d'inversion.

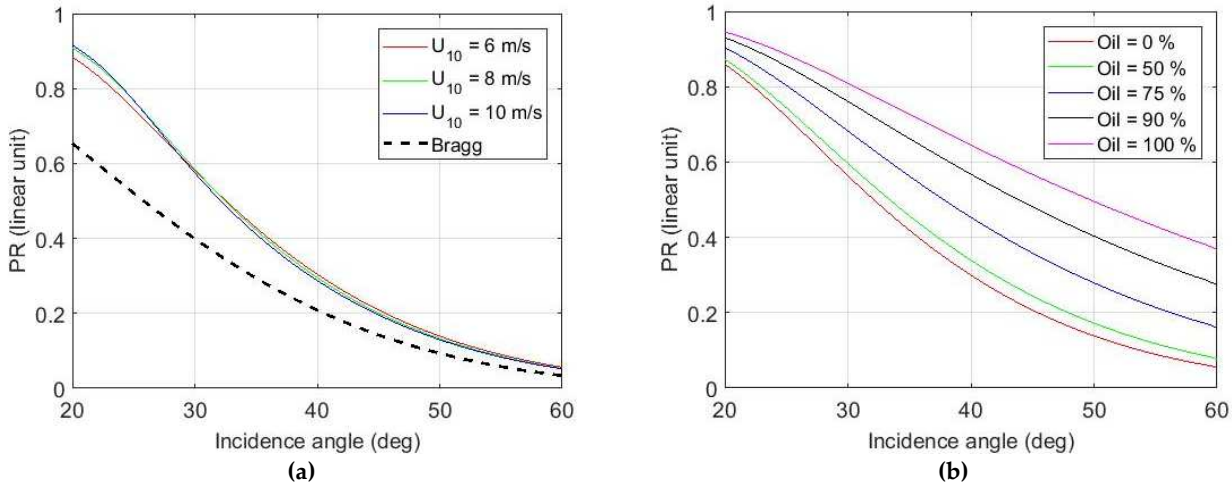

Fig. 48 : Rapport de polarisation en fonction de l'angle d'incidence pour différentes vitesses de vent (a) et différentes concentration d'huile minérale dans un mélange huile – eau de mer (b)

Nous avons proposé deux approches dans [82][83] pour permettre l'estimation de la concentration volumique de polluant à partir de données SAR acquises en bande L. La première [83], consiste à inverser analytiquement le rapport de polarisation fourni par le modèle U-WCA en chaque pixel de l'image radar pour estimer la constante diélectrique effective du mélange et en déduire la concentration volumique par la formule de Bruggeman. Selon le modèle de Bragg composite, le rapport de polarisation dépend de la constante diélectrique et de l'angle d'incidence local (cf. paragraphe 3.2 équations (57) et (58)).

En général, une connaissance précise de l'angle d'incidence local n'est pas disponible; une approximation à partir des données SAR peut être obtenue à partir d'une zone de mer propre proche de la nappe d'hydrocarbures en supposant des phénomènes homogènes à grande échelle sur toute la zone imagée (comme pour la méthode du « Mixing Index » publiée dans [121] et décrite au paragraphe 5.3.1 précédent).

Pour pallier cette forte limitation, l'utilisation du modèle de diffusion U-WCA permet d'estimer le rapport de polarisation sans nécessiter la connaissance de l'angle d'incidence locale [81], résultant de l'inclinaison locale des facettes composant la surface de la mer. La méthode que nous avons proposée dans [83] permet une estimation quantitative de la concentration d'hydrocarbures au sein d'une nappe. Elle a comme principaux inconvénients une importante complexité calculatoire et la sélection sur les images SAR d'une surface de mer non couverte par les hydrocarbures tout au long de la fauchée de la zone imagée.

Pour passer outre ces inconvénients, nous avons proposé dans [82] une seconde méthode par inversion d'un abaque. Elle consiste à comparer les valeurs du rapport de polarisation mesurées sur les images avec un abaque pré-calculé. Elle offre des résultats proches de ceux obtenus avec la méthode rigoureuse (Fig. 49), en particulier pour les zones de fortes concentrations d'huiles. Elle est très efficace en temps de calcul (les abaques pouvant être calculées au préalable) et ne nécessite pas la sélection d'une surface de mer non couverte mais uniquement les informations de vitesse et direction du vent. Afin de lever partiellement cette contrainte pouvant être forte sur la nécessité de connaitre les conditions de mer, nous avons démontré dans [82] que la méthodologie que nous avons proposée est robuste aux informations météorologiques.

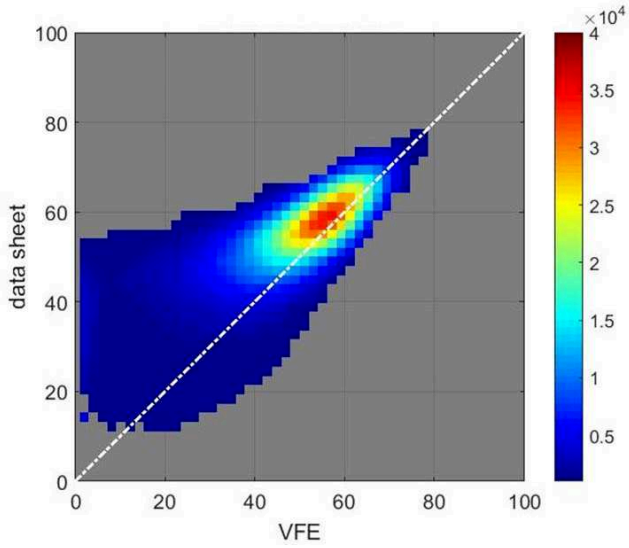

Fig. 49 : Comparaison entre les valeurs de fraction volumique d'huile dans l'eau résultant de l'application des méthodes d'inversion par abaque (data sheet) et par la méthode rigoureuse (VFE) sur les données ONERA/SETHI bande L de la campagne NOFO-2015 du 09 Juin 2015 à 10 :01 UTC.

La méthodologie d'estimation de la fraction volumique par inversion d'un abaque a été appliquée sur 4 images SAR acquises lors de l'exercice NOFO-2015, à 09:37, 10:02, 10:27 et 13:30 (soit jusqu'à 4 heures d'intervalle entre la première et la dernière). Ces 4 acquisitions successives se prêtent bien au suivi temporel de l'évolution de cette nappe entre 09:37 et 13:30.

Les cartes de concentration d'huile ont été calculées et les histogrammes normalisés associés (Fig. 50) mettent en évidence la diminution du taux de concentration volumique d'huile avec le temps. On note peu d'évolution de la concentration entre les 3 premières acquisitions (écart temporel de 50 mn) mais une diminution importante sur la dernière (écart temporel maximum de 4 heures).

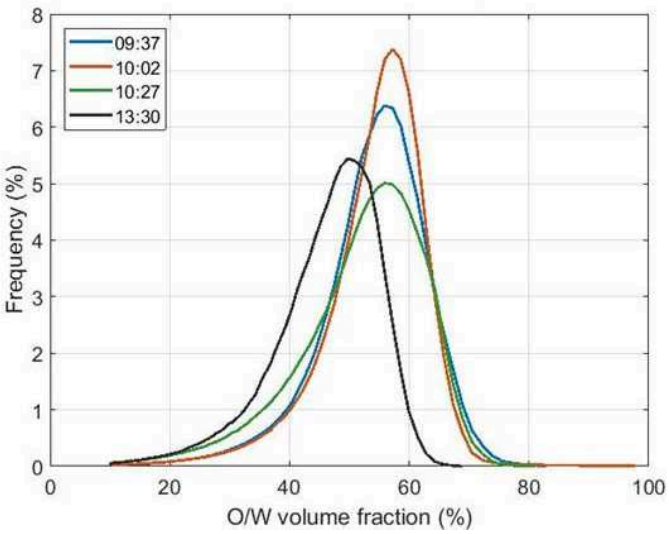

Fig. 50 : histogrammes des concentrations (volumique) d'huile dans l'eau, approche par abaques. Acquisitions du 09 juin 2015 à 09 :37 (bleu), 10 :02 (rouge), 10 :27 (vert) et 13 :30 (noir) UTC.

5.5. Synthèse sur la télédétection des pollutions marines

Les travaux que j'ai réalisés ont permis de fiabiliser les outils de détection des pollutions marines et d'étendre l'utilisation classique de l'imagerie radar en proposant des méthodologies innovantes de caractérisation et de quantification des pollutions dans le domaine offshore.

En termes de détection, j'ai tout d'abord démontré que l'utilisation de l'imagerie radar était tout autant pertinente pour la détection des substances liquides dangereuses et nocives en mer que pour la détection des hydrocarbures. J'ai également proposé une hiérarchisation des paramètres radar en fonction de leur performance de détection et j'ai quantitativement démontré l'impact du niveau de bruit de l'instrument sur ces performances.

L'imagerie radar peut également être utilisée à des fins de caractérisation. Tout d'abord pour lever les ambiguïtés entre zones de faible réflectivité : pollutions ou zones de faible vent local, de conjonction de courants … J'ai ensuite repris une idée initialement proposée à la fin des années 2000 pour permettre une différenciation entre une surface couverte d'hydrocarbure et couverte d'un film fin d'origine biologique. J'ai appliqué cette méthode sur un jeu de données SAR acquises par l'ONERA en bande X et L et j'ai démontré qu'il était effectivement possible de différencier les deux substances, à conditions de disposer de données acquises avec un rapport signal à bruit suffisant. J'ai de même appliqué un processus de caractérisation du comportement du produit polluant sur des données acquises en bande L, sur un déversement d'hydrocarbures et sur une nappe constituée de deux substances différentes.

Finalement j'ai participé au développement théorique et à la validation expérimentale de deux différentes méthodes de quantification (relative et absolue) des pollutions marines. La méthode de quantification relative proposée exploite la différence des signaux acquis en polarisation HH et VV, qui signe principalement une modification de la rugosité de surface. Deux méthodes de quantification absolues ont également été développées, l'une basée sur l'inversion

pixel à pixel d'un modèle analytique de rétrodiffusion et l'autre sur la comparaison entre les signaux radar mesurés et un abaque. Alors que la méthode de quantification relative exploite la différence de polarisation, les méthodes absolues utilisent le rapport de polarisation pour accéder à la constante diélectrique de la surface imagée et estiment la concentration volumique par inversion de la formule de Bruggeman.

Les méthodes développées dans le cadre des travaux que j'ai réalisés ont toutes été testées et validées sur des données expérimentales, pour la plupart lors de campagne de mesures SETHI sur des déversements contrôlés que j'ai moi-même coordonnés. Il ressort de mes travaux que, dans le domaine micro-ondes, les nappes d'hydrocarbures ou tout autre produit visqueux sont par nature des régions de faible réflectivité pour lesquelles l'acquisition de signaux radar doit être réalisée à partir d'un instrument disposant d'un niveau de bruit suffisamment faible pour garantir un rapport signal à bruit permettant une estimation fiable des paramètres d'intérêt. Cette contrainte forte, mais régulièrement omise dans la littérature, a été systématiquement prise en considération tout au long de mes travaux. Bien que particulièrement riches et originales, les données expérimentales que j'ai exploitées correspondent à des cas de vent faible ou modéré, plutôt propices pour les thématiques investiguées. En cas de vent plus fort, on peut s'attendre à une disparition de la signature des produits polluants, alors mélangés au sein de la colonne d'eau et l'énergie apportée par le vent venant contrebalancer l'atténuation de la rugosité de la surface par le produit visqueux. Cette disparation de la signature peut être partielle ou totale en fonction de la vitesse du vent, de la concentration du produit, de la fréquence radar, … et l'impact de chacun de ces facteurs semblent à ce jour difficile à quantifier tant que nous ne disposons pas d'un modèle analytique de diffusion valable pour une surface de mer polluée et pour les bandes de fréquences que j'ai utilisées.

6. CONCLUSION

Les systèmes d'observation micro-ondes offrent des opportunités majeures pour la télédétection des surfaces océaniques. Ils peuvent être opérés de jour comme de nuit et sont quasiment insensibles aux conditions atmosphériques et/ou météorologiques. Ils sont ainsi utilisés dans de nombreux contextes applicatifs, parmi lesquels la surveillance du trafic maritime et des pollutions inhérentes, l'estimation de paramètres géophysiques (caractérisation de l'état de mer, de la salinité, des courants …) ou la prospection et l'exploration des ressources naturelles.

Sur la caractérisation de l'état de mer, les travaux que j'ai réalisés ont tout d'abord consisté à étendre le domaine de validité du modèle de rétrodiffusion analytique GO-SSA. Tout d'abord en s'appuyant sur les derniers développements de la littérature j'ai participé à la validation du modèle GO-SSA étendu et à l'ajout d'un terme correctif supplémentaire pour restituer les tendances aux angles extrêmes de rasance. Il en résulte le modèle semi-empirique GO-SSA-Extended.
La dépendance de la réponse radar à l'angle de visée par rapport à la direction du vent a été abordée au travers des travaux de thèse de Z. Guerraou que j'ai co-encadrés. Ils ont permis de nous faire progresser sur la compréhension des mécanismes qui gouvernent les asymétries directionnelles et en particulier leur caractère polarisé. Il en résulte que la prise en compte de l'asymétrie des vagues (via l'utilisation d'une distribution des pentes des vagues adaptée) permet de restituer qualitativement les tendances observées, mais pas les valeurs absolues de l'asymétrie upwind-downwind mesurées expérimentalement.

Les modèles analytiques de rétrodiffusion, de type deux échelles, permettent de restituer les tendances observées sur les niveaux de réflectivités radar en polarisation directe et croisée mais leur précision est mise à défaut en haute fréquence EM lorsqu'on s'intéresse au rapport de polarisation entre les niveaux de réflectivités dans les canaux co-polaires (PR=HH/VV). Les travaux de thèse de F. Schreiber que j'ai co-encadrés ont permis de proposer un modèle analytique dit « hybride », dans lequel un terme correctif est appliqué de façon symétrique aux niveaux de rétrodiffusion modélisés dans les voies HH et VV. Ce modèle permet de restituer avec une très bonne fidélité les niveaux de réflectivités, différences et rapports de polarisation mesurés expérimentalement en bande C, X et Ku. Ce qui constitue une avancée très importante dans ce domaine.

Au-delà de la caractérisation du niveau moyen de l'intensité, la description de la statistique complète du signal radar rétrodiffusé par une surface de mer est de toute première importance, notamment pour des applications de surveillance de l'espace maritime. Les lois de distribution les plus récemment proposées dans la littérature ont été quantitativement évaluées en appliquant des métriques sur un jeu de données expérimentales particulièrement riche et varié. Il résulte de cette évaluation une préconisation quant au choix du modèle de distribution : K+Rayleigh et 3MD. De plus, même si elles permettent de restituer la statistique du signal mesurée expérimentalement, les lois de distribution proposées ne peuvent être paramétrées a priori par les conditions de mer en surface, ce qui d'un point de vue opérationnel est particulièrement préjudiciable. A nouveau les travaux de thèse de F. Schreiber que j'ai co-encadrés ont permis de progresser dans cette direction puisque le modèle « hybride » proposé permet une formulation analytique de la statistique du signal fidèle aux données expérimentales haute résolution spatiale (acquises en bande C, X ou Ku) et dont l'unique paramètre, la pente quadratique moyenne des vagues, est directement relié à l'état de mer. Utilisé dans un schéma de détection, ce modèle permet de paramétrer a priori les seuils de détection en fonction de l'état de mer en surface. Il permet également d'estimer l'état de mer, tout en étant robuste aux erreurs de calibration des données SAR utilisées. Une perspective importante de ces travaux serait l'extension du domaine de validité du modèle « hybride » aux angles de visée rasant et au cas spécifique du côtier.

Les pollutions marines par hydrocarbures sont suivies de façon opérationnelle par des systèmes d'observation radar, aéroportés ou satellitaires. L'acquisition et l'exploitation de données SAR expérimentales acquises lors de deux exercices de déversements contrôlés en mer m'a permis d'étendre l'utilisation classique de l'imagerie radar dans le contexte de la lutte contre les pollutions marines.

L'ensemble des acteurs du domaine maritime connait les performances (et les limitations) de l'imagerie radar pour la détection des pollutions par hydrocarbures. Les tribunaux reconnaissent l'image radar comme outil de preuve juridique et s'en servent pour poursuivre et sanctionner les contrevenants. Ce n'est pas le cas lorsqu'il s'agit d'une pollution par déversements de produits chimiques. Les travaux réalisés sur l'imagerie radar lors du projet ANR-POLLUPROOF ont dans un premier temps permis d'identifier, parmi celles testées, les substances chimiques détectables par imagerie radar. Les résultats montrent que 3 produits sur 6 sont détectés et que l'absence de détection pour les autres substances est probablement due à leur extrême volatilité. Il existe également d'autres limitation à la détection des produits polluants en mer, une des plus importantes étant les conditions de vent fort pour lesquelles le produit sera rapidement brassé et mélangé dans la colonne d'eau. Les acquisitions bi-fréquences (X et L) réalisées par le système radar imageur SETHI de l'ONERA ont également permis de confirmer l'intérêt de l'imagerie radar haute fréquence (bande X ici) par rapport à l'imagerie basse fréquence (bande L ici) pour la détection de pollutions marines.

Au-delà de ces travaux qui constituaient le cœur de la problématique POLLUPROOF, nous avons tout d'abord tenté d'identifier le mode d'imagerie radar (aéroportée ou satellitaire) qui offre les meilleures capacités de détection. Nous avons également exploré dans quelle mesure l'imagerie radar peut apporter des informations pour la caractérisation et la quantification de polluants présents sur la surface de mer. Notons que ces travaux s'appliquent tout autant au cas des substances chimiques qu'au cas de pollution par huile minérale (hydrocarbures).

Lorsqu'un produit visqueux est déversé en mer, le choix de la technique d'intervention nécessite une connaissance approfondie des propriétés de la substance polluante. Il a été préalablement démontré lors de l'accident de la plateforme *DeepWater Horizon* dans le golfe du Mexique que, dans le cas d'une pollution par hydrocarbures, les images SAR acquises en bande L peuvent indiquer si le produit déversé se comporte comme un film flottant à la surface ou s'il est mélangé dans les quelques premiers centimètres de la colonne d'eau. Cette méthodologie a été appliquée sur les données SAR acquises en bande L lors de l'exercice POLLUPROOF-2015 et nous avons pu mettre en évidence un écart de signature traduisant un comportement différent entre deux substances chimique déversées en mer.

Le jeu de données acquis lors des exercices POLLUPROOF-2015 et NOFO-2015 a également permis de proposer une méthodologie pour différencier les nappes de pollution par huiles minérales ou végétales de substances visqueuses (*film biogenic*) naturellement présentes en surface. Elle est basée sur l'analyse du Damping Ratio (contraste entre niveaux mesurés sur mer non couverte et sur mer couverte) mesuré sur des données SAR bi-fréquence acquises en bande X et en bande L. Nous avons démontré que le facteur d'amortissement de la rugosité de la surface de mer mesuré à deux fréquences radar varie différemment pour le film naturel que pour les autres nappes d'origine anthropique étudiées. Ces comportements sont cohérents avec ceux prédits par un modèle analytique et confirment des observations expérimentales précédemment réalisées depuis la navette spatiale Endeavour.

Finalement j'ai démontré que l'imagerie radar peut apporter des informations cruciales sur la quantité de polluant présente sur la surface de mer. Une méthodologie de quantification relative a tout d'abord été proposée. Facile d'utilisation elle permet de guider rapidement les opérations de dépollution vers les zones les plus impactées. Elle peut également permettre de vérifier l'efficacité des moyens de lutte mis en œuvre. Deux méthodes de quantification absolue du volume de polluant dans la colonne d'eau ont également été proposées. L'une est basée sur l'inversion d'un modèle analytique de rétrodiffusion et l'autre utilise un abaque pré-calculé. Au-delà de la quantité de polluant effectivement présente, ces méthodes permettent surtout de suivre l'évolution du volume au cours du temps ce qui est crucial dans le suivi d'une pollution.

Le point commun entre ces différents développements méthodologiques sur la caractérisation et la quantification des pollutions marines est qu'ils nécessitent tous l'utilisation de données SAR acquises avec un niveau de bruit instrumental suffisamment faible pour permettre une estimation fiable des propriétés de la surface observée. Ce qui n'est pas le cas avec les instruments radar actuellement disponibles depuis l'espace.

De plus, les méthodes de caractérisation du comportement du produit en surface (*Mixing Index*) et de quantification absolue du volume de polluant présent dans la colonne d'eau sont basées sur l'utilisation du rapport de polarisation. L'avancée des connaissances lors de ces travaux les restreignaient à l'utilisation de données SAR acquises en basse fréquence EM (bande L ici). Une perspective particulièrement intéressante serait alors de bénéficier des avancées apportées par les travaux de thèse de F. Schreiber et le modèle deux échelles « hybride » pour étendre ces méthodologies à des données expérimentales acquises en plus haute fréquence radar (bande X par exemple). Cependant, le point crucial pour aboutir dans cette direction sera de disposer des données acquises avec un rapport signal à bruit suffisant (supérieur à 3-5 dB) sur les zones polluées.

7. DEFINITIONS ET ABREVIATIONS

ASI	Agenzia Spatiale Italiana
CCDF	Complementary Cumulative Distribution Function
CDF	Cumulative Distribution Function
CFAR	Constant False Alarm Rate
DGDDI	Direction Générale des Douanes et Droits Indirects
DLR	Deutsche Luft und Raumfahrt
EM	ElectroMagnétique
ESA	European Space Agency
ISLR	Integrated Side Lobe Ratio
JAXA	Japan Aerospace Exploration Agency
JPL	Jet Propulsion Laboratory
NASA	National Aeronautics and Space Administration
NESZ	Noise Equivalent Sigma Zero
NOFO	Norwegian Clean Seas Association for Operating Companies
MNT	Modèle Numérique de Terrain
PDF	Probability Distribution Function
POLSAR	Polarimétrie SAR
PQI	Paramètres de Qualité Image
PRF	Pulse Repetition Frequency
PRI	Pulse Repetition Interval
PSLR	Peak Side Lobe Ratio
RADAR	Radio Detection And Ranging
RAR	Real Aperture Radar
SAR	Synthetic Aperture Radar
SEBC	Standard European Behavior Classification
SER	Surface Equivalente Radar
SLAR	Side-Looking Airborne Radar – Radar à visée latérale en français
SNPD	Substances Nocives et Potentiellement Dangereuses
SNR	Signal to Noise Ratio
U_{10}	Vitesse du vent à 10 m de la surface
U-WCA	Universal Weighted Curvature Approximation

8. REFERENCES BIBLIOGRAPHIQUES

[1] P. C. Dubois-Fernandez, J. Souyris, S. Angelliaume and F. Garestier, "The Compact Polarimetry Alternative for Spaceborne SAR at Low Frequency," in *IEEE Transactions on Geoscience and Remote Sensing*, vol. 46, no. 10, pp. 3208-3222, Oct. 2008.

[2] C. Albinet, P. Borderies, A. Hamadi, P. Dubois-Fernandez, T. Koleck and S. Angelliaume, "High-resolution vertical polarimetric imaging of pine forests," in *Radio Science*, vol. 49, no. 3, pp. 231-241, March 2014.

[3] https://www.jpl.nasa.gov/missions/seasat/

[4] https://www.esa.int/Applications/Observing_the_Earth/ERS_1_and_2

[5] https://global.jaxa.jp/projects/sat/jers1/index.html

[6] https://www.jpl.nasa.gov/missions/spaceborne-imaging-radar-c-x-band-synthetic-aperture-radar-sir-c-x-sar/

[7] https://www.asc-csa.gc.ca/fra/satellites/radarsat1/default.asp

[8] https://www2.jpl.nasa.gov/srtm/

[9] https://www.asc-csa.gc.ca/fra/satellites/radarsat2/default.asp

[10] https://www.dlr.de/content/en/articles/missions-projects/terrasar-x/terrasar-x-earth-observation-satellite.html

[11] https://www.esa.int/Applications/Observing_the_Earth/The_Living_Planet_Programme/Earth_Explorers/Biomass

[12] https://nisar.jpl.nasa.gov/

[13] A. Reigber *et al.*, "Very-High-Resolution Airborne Synthetic Aperture Radar Imaging: Signal Processing and Applications," in *Proceedings of the IEEE*, vol. 101, no. 3, pp. 759-783, March 2013.

[14] https://uavsar.jpl.nasa.gov/

[15] R. Horn, A. Nottensteiner, A. Reigber, J. Fischer and R. Scheiber, "F-SAR — DLR's new multifrequency polarimetric airborne SAR," *2009 IEEE International Geoscience and Remote Sensing Symposium*, Cape Town, 2009, pp. II-902-II-905.

[16] R. Baqué *et al.*, "SETHI/RAMSES-NG new performances of the flexible multi-spectral airborne remote sensing research platform," *International Conference on Radar Systems (Radar 2017)*, Belfast, 2017, pp. 1-4.

[17] S. Hovanessian, "*Introduction to synthetic array and imaging radar*", Artech House, 1980.

[18] W. M. Brown, "Synthetic Aperture Radar," in *IEEE Transactions on Aerospace and Electronic Systems*, vol. AES-3, no. 2, pp. 217-229, March 1967.

[19] D. Massonnet and J. Souryis, Imaging with Synthetic Aperture Radar. EPFL Press, 2008.

[20] A. Moreira, P. Prats-Iraola, M. Younis, G. Krieger, I. Hajnsek and K. P. Papathanassiou, "A tutorial on synthetic aperture radar," in IEEE Geoscience and Remote Sensing Magazine, vol. 1, no. 1, pp. 6-43, March 2013.

[21] L. Rayleigh,The Theory of Sound, Dover, New York, 1945,(originally published in 1877).

[22] T. Meissner et W. J. Wentz, «The complex dielectric constant of pure and sea water from microwave satellite observations,» *IEEE Transactions on Geoscience and Remote Sensing,* vol. 42, n°9, pp. 1836-1849, 2004.

[23] M. T. Hallikainen, F. T. Ulaby, M. C. Dobson, M. A. El-rayes and L. Wu, "Microwave Dielectric Behavior of Wet Soil-Part 1: Empirical Models and Experimental Observations," in *IEEE Transactions on Geoscience and Remote Sensing*, vol. GE-23, no. 1, pp. 25-34, Jan. 1985.

[24] M. C. Dobson, F. T. Ulaby, M. T. Hallikainen and M. A. El-rayes, "Microwave Dielectric Behavior of Wet Soil-Part II: Dielectric Mixing Models," in *IEEE Transactions on Geoscience and Remote Sensing*, vol. GE-23, no. 1, pp. 35-46, Jan. 1985.
[25] A. G. Fore *et al*., "UAVSAR Polarimetric Calibration," in *IEEE Transactions on Geoscience and Remote Sensing*, vol. 53, no. 6, pp. 3481-3491, June 2015.
[26] J. W. Goodman, "Some fundamental properties of speckle", *J. Opt. Soc. Amer.*, vol. 66, no. 11, pp. 1145-1150, Nov. 1976.
[27] P. Beckmann, The Depolarization of Electromagnetic Waves. The Golem Press, Boulder, CO, 1968.
[28] M. Born and E. Wolf, "Principles of Optics", 3rd ed. Pergamon Press, New York: 808 p., 1965.
[29] J.S. Lee, E. Pottier. Polarimetric Radar Imaging : From basics to applications.. Brian J. Thompson, University of Rochester, NY, USA. CRC Press, Taylor & Francis Editor,, pp.397, 2009, Optical Science and Engineering.
[30] S. R. Cloude and E. Pottier, "An entropy based classification scheme for land applications of polarimetric SAR," in *IEEE Transactions on Geoscience and Remote Sensing*, vol. 35, no. 1, pp. 68-78, Jan. 1997, doi: 10.1109/36.551935.
[31] I. Hajnsek *et al*., "PolSAR-Ap: Exploitation of fully polarimetric SAR data for application demonstration," *2015 IEEE International Geoscience and Remote Sensing Symposium (IGARSS)*, Milan, 2015, pp. 1559-1561, doi: 10.1109/IGARSS.2015.7326079.
[32] R. Touzi, "Polarimetric target scattering decomposition: A review," *2016 IEEE International Geoscience and Remote Sensing Symposium (IGARSS)*, Beijing, 2016, pp. 5658-5661, doi: 10.1109/IGARSS.2016.7730478.
[33] K. Tragl, "Polarimetric radar backscattering from reciprocal random targets," in *IEEE Transactions on Geoscience and Remote Sensing*, vol. 28, no. 5, pp. 856-864, Sept. 1990.
[34] J. Yang, Y. Yamaguchi, W. Boerner and S. Lin, "Numerical methods for solving the optimal problem of contrast enhancement," in *IEEE Transactions on Geoscience and Remote Sensing*, vol. 38, no. 2, pp. 965-971, March 2000.
[35] K. Sarabandi, L. E. Pierce and F. T. Ulaby, "Calibration of a polarimetric imaging SAR," in *IEEE Transactions on Geoscience and Remote Sensing*, vol. 30, no. 3, pp. 540-549, May 1992.
[36] I. Hajnsek, E. Pottier and S. R. Cloude, "Inversion of surface parameters from polarimetric SAR," in *IEEE Transactions on Geoscience and Remote Sensing*, vol. 41, no. 4, pp. 727-744, April 2003.
[37] T. M. Elfouhaily, B. Chapron, K. Katsaros, and D. Vandemark, “A unified directional spectrum for long and short wind-driven waves,” J. Geophys. Res. Ocean., vol. 102, no. C7, pp. 15781–15796, 1997.
[38] Philippe Spiga. Diffraction des ondes électromagnétiques par des surfaces rugueuses en incidence rasante. Université du Sud Toulon Var, 2008.
[39] S. O. Rice, “Reflection of electromagnetic waves from slightly rough surfaces,” Commun. Pure Appl. Math., vol. 4, no. 2-3, pp. 351–378, 1951.
[40] P. Beckmann and A. Spizzichino, “The Scattering of Electromagnetic Waves from Rough Surfaces,” Artech House Radar Library, USA, 1963.
[41] J. Wright, "A new model for sea clutter," in *IEEE Transactions on Antennas and Propagation*, vol. 16, no. 2, pp. 217-223, March 1968, doi: 10.1109/TAP.1968.1139147.
[42] B. Holt, "SAR imaging of the ocean surface," in *Synthetic Aperture Radar (SAR) Marine User’s Manual*, C. R. Jackson and J. R. Apel, Eds. Silver Spring, MD:NOAA, 2004, pp.263-275.
[43] K. Hasselmann, R. K. Raney, W. J. Plant, W. Alpers, R. A. Shuchman, D. R. Lyzenga, C. L. Rufenach, and M. J. Tucker, "Theory of synthetic aperture radar ocean imaging: A MARSEN view," in *J. Geophys. Res.*, 90 (C3) 4659–4686, 1985.

[44] G. R. Valenzuela, "Scattering of electromagnetic waves from a tilted slightly rough surface," in *Radio Science*, vol. 3, no. 11, pp. 1057-1066, Nov. 1968.

[45] A. G. Voronovich. Small-slope approximation in wave scattering from rough surfaces. *Journal of Experimental and Theoretical Physics*, 62(1): 65–70, 1985.

[46] A. G. Voronovich. Small-slope approximation for electromagnetic wave scattering at a rough interface of two dielectric half-spaces. *Waves in Random and Complex Media*, 4(3): 337–367, 1994.

[47] A. G. Voronovich. *Wave scattering from rough surfaces*. Springer Berlin Heidelberg, 1994.

[48] A. Mainvis, "Modélisation et mesure de l'interaction d'une onde électromagnétique avec une surface océanique. Application à la détection et à la caractérisation radar de films d'hydrocarbures," 2018.

[49] G. Soriano and C. Guerin, "A Cutoff Invariant Two-Scale Model in Electromagnetic Scattering From Sea Surfaces," in IEEE Geoscience and Remote Sensing Letters, vol. 5, no. 2, pp. 199-203, April 2008, doi: 10.1109/LGRS.2008.915746.

[50] K.D. Ward, R.J.A. Tough and S. Watts. *"Sea Clutter: Scattering, the K-Distribution and Radar Performance"*, 2nd ed.; The Institute of Engineering Technology UK: London, 2013.

[51] Ph. Spiga. Diffraction des ondes électromagnétiques par des surfaces rugueuses en incidence rasante. Université du Sud Toulon Var, 2008.

[52] V. Kudryavtsev, D. Hauser, G. Caudal and B. Chapron, "A semiempirical model of the normalized radar cross section of the sea surface, 1, The background model," in *J. Geophys. Res.,* 108*(*C3*)*, 2156-2202, 2003.

[53] V. Kudryavtsev, D. Hauser, G. Caudal and B. Chapron, "A semiempirical model of the normalized radar cross section of the sea surface, 2, Radar modulation transfer function," in *J. Geophys. Res.,* 108*(*C3*)*, 2156-2202, 2003.

[54] D. E. Barrick, "Grazing behavior of scatter and propagation above any rough surface," in *IEEE Transactions on Antennas and Propagation*, vol. 46, no. 1, pp. 73-83, Jan. 1998.

[55] V. I. Tatarskii and M. I. Charnotskii, "On the universal behavior of scattering from a rough surface for small grazing angles," in *IEEE Transactions on Antennas and Propagation*, vol. 46, no. 1, pp. 67-72, Jan. 1998.

[56] M.M. Horst, F.B. Dyer and M.T. Tuley, "Radar sea clutter model", International IEEE AP/S URSI Symposium, Maryland, 1978, pp 6-10.

[57] V. Gregers-Hansen and R. Mital, "An Improved Empirical Model for Radar Sea Clutter Reflectivity," in *IEEE Transactions on Aerospace and Electronic Systems*, vol. 48, no. 4, pp. 3512-3524, October 2012.

[58] S. Angelliaume, V. Fabbro, G. Soriano and C. A. Guerin, "The GO-SSA Extended model for all-incidence sea clutter modeling," *2014 IEEE Geoscience and Remote Sensing Symposium*, Quebec City, QC, 2014, pp. 5017-5020, doi: 10.1109/IGARSS.2014.6947623.

[59] T. Johnsen, "Characterisation of X-band radar sea-clutter in a limited fetch condition from low to high grazing angles", submitted to RadarConf 2015, Johannesburg.

[60] C. Bourlier, "Azimuthal harmonic coefficients of the microwave backscattering from a non-Gaussian ocean surface with the first-order SSA model," in IEEE Transactions on Geoscience and Remote Sensing, vol. 42, no. 11, pp. 2600-2611, Nov. 2004, doi: 10.1109/TGRS.2004.836874.

[61] H. Hersbach, A. Stoffelen, and S. de Haan, ''An improved C-band scatterometer ocean geophysical model function: CMOD5,'' J. Geophys. Res., vol. 112, no. C3, pp. 1–18, Mar. 2007.

[62] Z. Guerraou, S. Angelliaume and C. Guérin, "Angular variations of radar sea clutter: Airborne experiment and model comparison," 2015 IEEE International Geoscience and Remote Sensing Symposium (IGARSS), Milan, 2015, pp. 2755-2758, doi: 10.1109/IGARSS.2015.7326384.
[63] D. J. Crisp, R. Kyprianou, L. Rosenberg and N. J. S. Stacy, "Modelling X-band sea clutter at moderate grazing angles.," *2008 International Conference on Radar*, Adelaide, SA, 2008, pp. 569-574.
[64] Z. Guerraou, "Rétrodiffusion micro-onde par la surface océanique en incidence élevée: Approche conjointe expérimentale et théorique," (in French), Ph.D. dissertation, Univ. Toulon, Toulon France, Sep. 2017.
[65] Z. Guerraou, S. Angelliaume, L. Rosenberg and C. Guérin, "Investigation of Azimuthal Variations From X-Band Medium-Grazing-Angle Sea Clutter," in *IEEE Transactions on Geoscience and Remote Sensing*, vol. 54, no. 10, pp. 6110-6118, Oct. 2016, doi: 10.1109/TGRS.2016.2581181.
[66] A.G. Voronovich and V. U. Zavorotny, "Theoretical model for scattering of radar signals in Ku and C bands from a rough sea surface with breaking waves, " in Waves in Random Media, 11(3), 247 – 269.
[67] M. Joelson, M.-C. Néel, G. Soriano and M. Saillard, "Sur la distribution alpha stable de la pente des vagues du vent, " in 19ème Congrès Français de Mécanique, 2009.
[68] G. Caulliez, C.-A. Guérin, "Higher-order statistical analysis of short wind wave fields, " in *Journal of Geophysical Research. Oceans*, Wiley-Blackwell, 2012, 117, pp.C06002.
[69] C. Cox and W. Munk, "Measurement of the roughness of the sea surface from photographs of the sun's glitter," J. Opt. Soc. Amer., vol. 44, no. 11, pp. 838–850, 1954.
[70] X. Chu, Y. He and G. Chen, "Asymmetry and Anisotropy of Microwave Backscatter at Low Incidence Angles," in *IEEE Transactions on Geoscience and Remote Sensing*, vol. 50, no. 10, pp. 4014-4024, Oct. 2012.
[71] Ping et al, "Quasi-Gaussian probability density function of sea wave slopes from near nadir Ku-band radar observations", Remote Sensing of environment, 217 (2018).
[72] M. V. Yurovskaya, V. A. Dulov, B. Chapron, and V. N. Kudryavtsev, "Directional short wind wave spectra derived from the sea surface photography," J. Geophys. Res., Oceans, vol. 118, no. 9, pp. 4380–4394, Sep. 2013.
[73] A. Bringer, B. Chapron, A. Mouche and C. Guérin, "Revisiting the Short-Wave Spectrum of the Sea Surface in the Light of the Weighted Curvature Approximation," in *IEEE Transactions on Geoscience and Remote Sensing*, vol. 52, no. 1, pp. 679-689, Jan. 2014.
[74] A.A. Mouche, D. Hauser and V. Kudryavtsev, "Radar scattering of the ocean surface and sea-roughness properties: A combined analysis from dual-polarizations airborne radar observations and models in C band, " in *J. Geophys. Res.*, 111, C09004, 2006.
[75] V. Kudryavtsev, B. Chapron, A. G. Myasoedov, F. Collard and J. A. Johannessen, "On Dual Co-Polarized SAR Measurements of the Ocean Surface," in *IEEE Geoscience and Remote Sensing Letters*, vol. 10, no. 4, pp. 761-765, July 2013.
[76] D. R. Thompson, T. M. Elfouhaily and B. Chapron, "Polarization ratio for microwave backscattering from the ocean surface at low to moderate incidence angles," *IGARSS '98. Sensing and Managing the Environment. 1998 IEEE International Geoscience and Remote Sensing. Symposium Proceedings. (Cat. No.98CH36174)*, Seattle, WA, USA, 1998, pp. 1671-1673 vol.3.
[77] O. Isoguchi and M. Shimada, "An L-Band Ocean Geophysical Model Function Derived From PALSAR," in *IEEE Transactions on Geoscience and Remote Sensing*, vol. 47, no. 7, pp. 1925-1936, July 2009, doi: 10.1109/TGRS.2008.2010864.

[78] A. A. Mouche, D. Hauser, J. -. Daloze and C. Guerin, "Dual-polarization measurements at C-band over the ocean: results from airborne radar observations and comparison with ENVISAT ASAR data," in *IEEE Transactions on Geoscience and Remote Sensing*, vol. 43, no. 4, pp. 753-769, April 2005, doi: 10.1109/TGRS.2005.843951.
[79] X. Li and S. Lehner, "Algorithm for Sea Surface Wind Retrieval From TerraSAR-X and TanDEM-X Data," in IEEE Transactions on Geoscience and Remote Sensing, vol. 52, no. 5, pp. 2928-2939, May 2014, doi: 10.1109/TGRS.2013.2267780.
[80] F.M. Schreiber, S. Angelliaume and C.-A. Guérin, "Modeling the Polarization Ratio in the ujpper microwave band for Sea Clutter Analysis", in *IEEE Transactions on Geoscience and Remote Sensing*, submitted.
[81] C.-A. Guérin, G. Soriano, and T. Elfouhaily, "Weighted curvature approximation: numerical tests for 2d dielectric surfaces," Waves in Random Media, vol. 14, no. 3, pp. 349–363, 2004.
[82] S. Angelliaume, O. Boisot and C.-A. Guerin, "Dual-polarized L-band SAR Imagery for Temporal Monitoring of Marine Oil Slick Concentration," in *Remote Sensing*, 10(7), 1012, June 2018.
[83] O. Boisot, S. Angelliaume and C.-A. Guerin, "Marine Oil Slicks Quantification from L-band dual-polarimetric SAR imagery," in *IEEE Transactions on Geoscience and Remote Sensing*, vol. 57, no. 4, pp. 2187-2197, April 2019.
[84] D.J. Crisp, "The State-of-the-Art in Ship Detection in Synthetic Aperture Radar Imagery"; Defence Science and Technology Organisation, Information Sciences Laboratory: Edinburgh, South Australia, 2004.
[85] S. Angelliaume, L. Rosenberg and M. Ritchie, "Modeling the Amplitude Distribution of Radar Sea Clutter," in *Remote Sensing*, 11(3), 319, Feb. 2019.
[86] E. Jakeman and P. Pusey, "A model for non-Rayleigh sea echo," in IEEE Transactions on Antennas and Propagation, vol. 24, no. 6, pp. 806-814, November 1976, doi: 10.1109/TAP.1976.1141451.
[87] F. L. Posner, "Spiky sea clutter at high range resolutions and very low grazing angles," in *IEEE Transactions on Aerospace and Electronic Systems*, vol. 38, no. 1, pp. 58-73, Jan. 2002.
[88] A. Balleri, A. Nehorai and J. Wang, "Maximum likelihood estimation for compound-gaussian clutter with inverse gamma texture," in IEEE Transactions on Aerospace and Electronic Systems, vol. 43, no. 2, pp. 775-779, April 2007, doi: 10.1109/TAES.2007.4285370.
[89] G. V. Weinberg, "Assessing Pareto fit to high-resolution high-grazing-angle sea clutter," in Electronics Letters, vol. 47, no. 8, pp. 516 -517, 14 April 2011, doi: 10.1049/el.2011.0518.
[90] L. Rosenberg and S. Bocquet, "Application of the Pareto Plus Noise Distribution to Medium Grazing Angle Sea-Clutter," in IEEE Journal of Selected Topics in Applied Earth Observations and Remote Sensing, vol. 8, no. 1, pp. 255-261, Jan. 2015, doi: 10.1109/JSTARS.2014.2347957.
[91] L. Rosenberg, S. Watts and S. Bocquet, "Application of the K+Rayleigh distribution to high grazing angle sea-clutter," 2014 International Radar Conference, Lille, 2014, pp. 1-6, doi: 10.1109/RADAR.2014.7060344.
[92] G. V. Trunk and S. F. George, "Detection of Targets in Non-Gaussian Sea Clutter," in *IEEE Transactions on Aerospace and Electronic Systems*, vol. AES-6, no. 5, pp. 620-628, Sept. 1970.
[93] D. C. Schleher, "Radar Detection in Weibull Clutter," in *IEEE Transactions on Aerospace and Electronic Systems*, vol. AES-12, no. 6, pp. 736-743, Nov. 1976.
[94] W. A. Al-Ashwal, K. Woodbridge and H. D. Griffiths, "Analysis of bistatic sea clutter - Part II: Amplitude statistics," in IEEE Transactions on Aerospace and Electronic Systems, vol. 50, no. 2, pp. 1293-1303, April 2014.

[95] C. H. Gierull and I. Sikaneta, "A Compound-Plus-Noise Model for Improved Vessel Detection in Non-Gaussian SAR Imagery," in *IEEE Transactions on Geoscience and Remote Sensing*, vol. 56, no. 3, pp. 1444-1453, March 2018, doi: 10.1109/TGRS.2017.2763089.
[96] L. Rosenberg and S. Angelliaume, "Characterisation of the Tri-Modal Discrete Sea Clutter Model," 2018 International Conference on Radar (RADAR), Brisbane, QLD, 2018, pp. 1-6, doi: 10.1109/RADAR.2018.8557239.
[97] Kil, D.H.; Shin, F.B. Pattern Recognition and Prediction with Applications to Signal Processing; Springer: New York, NY, USA, 1998.
[98] G.R. Valenzuela and M. B. Laing, "On the statistics of sea clutter", Naval Research Lab., Rept. 7349, 1971.
[99] B.L. Gotwols and D.R. Thompson, "Ocean microwave backscatter distributions," in *J. Geophys. Res.*, 99(C5), 9741– 9750, 1994.
[100] H. Li and J. T. Johnson, "On the Amplitude Distributions of Bistatic Scattered Fields From Rough Surfaces," in IEEE Transactions on Geoscience and Remote Sensing, vol. 55, no. 12, pp. 6883-6892, Dec. 2017.
[101] C. Brekke, A. Solberg, "Oil spill detection by satellite remote sensing," *Remote Sensing of Environment.* ISSN 0034-4257. *95*(1), s 1- 13, 2005.
[102] I. Leifer, W. J. Lehr, D. Simecek-Beatty, E. Bradley, R. Clark, P. Dennison, Y. Hu, S. Matheson, C. E. Jones, B. Holt, M. Reif, D. A. Roberts, J. Svejkovsky, G. Swayze and J. Wozencraft, "State of the art satellite and airborne marine oil spill remote sensing: Application to the BP oil spill," in *Remote Sensing of Environment*, Volume 124, 2012, Pages 185-209, ISSN 0034-4257.
[103] https://anr.fr/Projet-ANR-13-ECOT-0007
[104] https://portal.emsa.europa.eu/web/csn
[105] https://www.ep.total.com/sites/shared/totalep/files/atoms/files/1704180101_use_remote_sensing_radar_techniques_og_facilities.pdf
[106] M. Fingas and C. Brown, "Review of oil spill remote sensing," in *Marine Pollut. Bull.* 83, p. 9-23, 2014.
[107] S. Angelliaume, X. Ceamanos, F. Viallefont-Robinet, R. Baqué, Ph. Déliot and Miegebielle, "Hyperspectral and Radar Airborne Imagery over Controlled Release of Oil at Sea", in *Sensors*, 17(8), 1772, Aug. 2017.
[108] S. Skrunes, C. Brekke and T. Eltoft, "Characterization of Marine Surface Slicks by Radarsat-2 Multipolarization Features," in *IEEE Transactions on Geoscience and Remote Sensing*, vol. 52, no. 9, pp. 5302-5319, Sept. 2014.
[109] J. Harrison, N.D.C. Allen, P. F. Bernath, "Infrared absorption cross sections for methanol," *Journal of Quantitative Spectroscopy and Radiative Transfer*, Volume 113, Issue 17, November 2012, Pages 2189-2196, ISSN 0022-4073.
[110] S. Angelliaume, B. Minchew, S. Chataing, P. Martineau and V. Miegebielle, "Multifrequency Radar Imagery and Characterization of Hazardous and Noxious Substances at Sea," in *IEEE Transactions on Geoscience and Remote Sensing*, vol. 55, no. 5, pp. 3051-3066, May 2017.
[111] S. Skrunes, C. Brekke, C. E. Jones and B. Holt, "A Multisensor Comparison of Experimental Oil Spills in Polarimetric SAR for High Wind Conditions," in *IEEE Journal of Selected Topics in Applied Earth Observations and Remote Sensing*, vol. 9, no. 11, pp. 4948-4961, Nov. 2016.
[112] S. Angelliaume, P. Dubois-Fernandez, V. Miegebielle and D. Dubucq, "Polarimetric parameters for oil slicks detection using SAR data remote sensing — An evaluation," *Geoscience and Remote Sensing Symposium (IGARSS), 2015 IEEE International*, Milan, 2015, pp. 3794-3797.

[113] S. Skrunes, C. Brekke, T. Eltoft and V. Kudryavtsev, "Comparing Near-Coincident C- and X-Band SAR Acquisitions of Marine Oil Spills," in *IEEE Transactions on Geoscience and Remote Sensing*, vol. 53, no. 4, pp. 1958-1975, April 2015.

[114] A. B. Salberg, Ø. Rudjord and A. H. S. Solberg, "Oil Spill Detection in Hybrid-Polarimetric SAR Images," in *IEEE Transactions on Geoscience and Remote Sensing*, vol. 52, no. 10, pp. 6521-6533, Oct. 2014.

[115] S. Angelliaume *et al.*, "SAR Imagery for Detecting Sea Surface Slicks: Performance Assessment of Polarization-Dependent Parameters," in *IEEE Transactions on Geoscience and Remote Sensing*, vol. 56, no. 8, pp. 4237-4257, Aug. 2018.

[116] J.P. Egan, "Signal detection theory and ROC analysis, Series in Cognition and Perception", *Academic Press, New York*, 1975.

[117] A. H. S. Solberg, "Remote Sensing of Ocean Oil-Spill Pollution," in *Proceedings of the IEEE*, vol. 100, no. 10, pp. 2931-2945, Oct. 2012.

[118] M. Migliaccio, F. Nunziata and A. Buono, "SAR polarimetry for sea oil slick observation", in *International Journal of Remote Sensing*, 36, 3243-3273, 2015.

[119] W. Alpers, B. Holt and K. Zeng, "Oil spill detection by imaging radars: Challenges and pitfalls," in *Remote Sensing of Environment*, Volume 201, Pages 133-147, 2017.

[120] B. Minchew, C. E. Jones and B. Holt, "Polarimetric Analysis of Backscatter From the Deepwater Horizon Oil Spill Using L-Band Synthetic Aperture Radar," in *IEEE Transactions on Geoscience and Remote Sensing*, vol. 50, no. 10, pp. 3812-3830, Oct. 2012.

[121] B. Minchew, "Determining the mixing of oil and seawater using polarimetric synthetic aperture radar," *Geophys. Res. Lett.,* 39, L16607, 2012.

[122] https://earth.esa.int/web/guest/events/-/asset_publisher/5YrWLNknVkVH/content/oil-pollution/maximized;jsessionid=61F6D9E52FE3E72AA4A6D24545220465?redirect=https%3A%2F%2Fearth.esa.int%2Fweb%2Fguest%2Fevents%3Bjsessionid%3D61F6D9E52FE3E72AA4A6D24545220465%3Fp_p_id%3D101_INSTANCE_5YrWLNknVkVH%26p_p_lifecycle%3D0%26p_p_state%3Dmaximized%26p_p_mode%3Dview%26_101_INSTANCE_5YrWLNknVkVH_struts_action%3D%252Fasset_publisher%252Fview.

[123] M. W. Hansen, V. Kudryavtsev, B. Chapron, C. Brekke and J. A. Johannessen, "Wave Breaking in Slicks: Impacts on C-Band Quad-Polarized SAR Measurements," in *IEEE Journal of Selected Topics in Applied Earth Observations and Remote Sensing*, vol. 9, no. 11, pp. 4929-4940, Nov. 2016.

[124] M. Migliaccio, F. Nunziata, A. Gambardella, "On The Copolarised Phase Difference for Oil Spill Observation", *Int. Journal of Remote Sensing*, vol. 30, n. 6, pp. 1587-1602, 2009.

[125] M. Gade, W. Alpers, H. Hühnerfuss, H. Masuko, and T. Kobayashi, "Imaging of biogenic and anthropogenic ocean surface films by the multifrequency/multipolarization SIR-C/X-SAR," in *J. Geophys. Res.*, vol. 103, no. C9, pp. 18 851–18 866, 1998.

[126] R. Cini and P. P. Lombardini, "Damping effect of monolayers on surface wave motion in a liquid," *Journal of Colloid and Interface Science*, vol. 65, no. 2, pp. 387-389, 1978.

[127] W. Alpers and H. Hühnerfuss, "The damping of ocean waves by surface films: A new look at an old problem," *Journal of Geophysical Research: Oceans*, vol. 94, no. C5, pp. 6251-6265, 1989.

[128] L. Lombardini P., B. Fiscella, P. Trivero, C. Cappa, and W. Garrett "Modulation of the Spectra of Short Gravity Waves by Sea Surface Films : Slick Detection and Characterization with a Microwave Probe" Journal of Atmospheric and Oceanic Technology, 6 :882–890 (1989).

[129] N. Aske, R. Orr et j. Sjøblom, «Dilatational Elasticity Moduli of Water–Crude Oil Interfaces Using the Oscillating Pendant Drop,» *Journal of Dispersion Science and Technology,* vol. 23, n°6, pp. 809-825, 2002.

[130] V. Wismann, M. Gade, W. Alpers and H. Huhnerfuss, "Radar sigatures of marine mineral oil spills measured by an airborne multi-frequency radar," in *Int. J. Remote. Sens.* 19, 3607-3623(1998).
[131] M. Fingas and B. Fieldhouse, "Studies on water-in-oil products from crude oils and petroleum products," in *Marine Pollution Bulletin*, Volume 64, Issue 2, 2012, Pages 272-283, ISSN 0025-326x.
[132] K. Folgerø, "Bilinear calibration of coaxial transmission/reflection cells for permittivity measurement of low-loss liquids," in *Measurement Science and Technology,* vol. 7, n°9, pp. 1260-1269, 1996.
[133] T. Friisø, Y. Schildberg, O. Rambeau, T. Tjomsland, H. Førdedal et J. Sjøblom, "Complex premittivity of crude oils and solutions of heavy crude oil fractions," in *Journal of Dispersion Science and Technology,* vol. 19, n°1, pp. 93-126, 1998.
[134] Z. H. Shah and Q. A. Tahir, "Dielectric Properties of Vegetable Oils," in *Journal of Scientific Research*, vol. 3, n0. 3, pp. 481-492, aug. 2011. ISSN 2070-0245.
[135] U. Erle, M. Regier, C. Persch, and H. Schubert, "Dielectric properties of emulsions and suspensions: Mixture equations and measurement comparisons," in *Journal of Microwave Power and Electromagnetic Energy*, 35(3) :185–190, 2000.
[136] A. Sihvola, Electromagnetic Mixing Formulas and Applications. Electromagnetic Waves, Institution of Engineering and Technology, 1999.
[137] T. Elfouhaily and C.-A. Guérin, “A critical survey of approximate scattering wave theories from random rough surfaces,” Waves in Random Media, vol. 14, no. 4, pp. R1–R40, 2004.

9. PUBLICATIONS DANS REVUES SCIENTIFIQUES

- P. C. Dubois-Fernandez, J-C. Souyris, S. Angelliaume and F. Garestier, "*The Compact Polarimetry Alternative for Spaceborne SAR at Low Frequency*, " in IEEE Transactions on Geoscience and Remote Sensing, vol. 46, no. 10, October 2008.
- C. Albinet, P. Borderies, A. Hamadi, P. Dubois-Fernandez, T. Koleck and S. Angelliaume, "High-resolution vertical polarimetric imaging of pine forests," in *Radio Science*, vol. 49, no. 3, pp. 231-241, March 2014.
- Fiche, S. Angelliaume, L. Rosenberg and A. Khenchaf, "Analysis of X-band SAR sea-clutter distributions at different grazing angles," IEEE Transactions of Geoscience and Remote Sensing, vol. 53, pp. 4650-4660, August 2015.
- El Hajj, M.; Baghdadi, N.; Zribi, M.; Angelliaume, S. Analysis of Sentinel-1 Radiometric Stability and Quality for Land Surface Applications. *Remote Sens.* 2016, *8*, 406.
- Z. Guerraou, S. Angelliaume, L. Rosenberg and C. A. Guérin, "Investigation of Azimuthal Variations From X-Band Medium-Grazing-Angle Sea Clutter," in *IEEE Transactions on Geoscience and Remote Sensing*, vol. 54, no. 10, pp. 6110-6118, Oct. 2016.
- S. Angelliaume, B. Minchew, S. Chataing, P. Martineau and V. Miegebielle, "Multifrequency Radar Imagery and Characterization of Hazardous and Noxious Substances at Sea," in *IEEE Transactions on Geoscience and Remote Sensing*," vol. 55, no. 5, pp. 3051-3066, May 2017.
- S. Angelliaume, X. Ceamanos, F. Viallefont-Robinet, R. Baqué, Ph. Déliot and Miegebielle, "Hyperspectral and Radar Airborne Imagery over Controlled Release of Oil at Sea", in *Sensors*, 17(8), 1772, Aug. 2017.
- S. Angelliaume, O. Boisot and C.-A. Guerin, "Dual-polarized L-band SAR Imagery for Temporal Monitoring of Marine Oil Slick Concentration," in *Remote Sensing*, 10(7), 1012, June 2018.
- S. Angelliaume, P. Dubois-Fernandez, C. E. Jones, B. Holt, B. Minchew, E. Amri and V. Miegebielle, " SAR Imagery for Detecting Sea Surface Slicks: Performance Assessment of Polarization-Dependent Parameters," in *IEEE Transactions on Geoscience and Remote Sensing*," vol. 56, no. 8, pp. 4237-4257, Aug. 2018.
- S. Angelliaume, L. Rosenberg and M. Ritchie, "Modeling the Amplitude Distribution of Radar Sea Clutter," in *Remote Sensing*, 11(3), 319, Feb. 2019.
- O. Boisot, S. Angelliaume and C.-A. Guerin, "Marine Oil Slicks Quantification from L-band dual-polarimetric SAR imagery," in *IEEE Transactions on Geoscience and Remote Sensing*, vol. 57, no. 4, pp. 2187-2197, April 2019.
- F.M. Schreiber, S. Angelliaume and C.-A. Guerin, "Modeling the Polarization Ratio in the upper microwave band for Sea Clutter Analysis," in *IEEE Transactions on Geoscience and Remote Sensing*, accepted for publication, September 2020.

Suivent ci-après une sélection de mes publications scientifiques les plus marquantes

The Compact Polarimetry Alternative for Spaceborne SAR at Low Frequency

Pascale C. Dubois-Fernandez, *Senior Member, IEEE*, Jean-Claude Souyris, Sébastien Angelliaume, and Franck Garestier

***Abstract*—In spaceborne synthetic aperture radar (SAR), a single-polarization on-transmit offers twice the swath width compared to full polarization. This is linked to SAR system design issues, and, without getting into the technical details deserving by themselves a full paper, we can just mention the swath characteristics of ALOS PALSAR (the Advanced Land Observing Satellite, Phased Array L-Band Synthetic Aperture Radar), reducing from 70 km for the dual-pol mode to 30 km for the full polarization mode. The reduced coverage in the full polarization mode has a harmful impact on the revisit time, which is always a major drive for the Earth-observing community. The options chosen up to now for dual-pol system designs (or single-polarization on-transmit) rely on a linear polarization on-transmit [either horizontal (H) or vertical (V)], with two orthogonal polarizations on-receive. Souyris and Raney in earlier papers proposed more pertinent alternatives for the selection of the transmit polarization leading to a better characterization of the scattering mechanisms. In this paper, the analysis is pursued in more depth by including the effect of the ionosphere on the wave propagation and extending the applications to polarimetric interferometry SAR (PolInSAR). A compact mode is developed where the transmit polarization is circular, whereas the only constraint on the two receiving polarizations is independence. Indeed, the choice of the polarizations of the two receive channels does not matter, as any polarization on-receive can be synthesized from these two measurements. This is, however, not the case for the unique transmit polarization. At a low frequency, where the ionosphere has a significant effect, the circular transmit polarization is the only sensible option, as it provides an effective constant polarization as seen by the scattering surface. This is an essential condition for a meaningful multitemporal analysis. Both the polarimetric SAR applications and the PolInSAR applications in the context of this compact polarimetry (CP) mode are explored. A pseudocovariance matrix can be reconstructed following Souyris' proposed approach for distributed targets and is shown to be very similar to the full polarimetric (FP) covariance matrix. The reconstruction of the cross-polarized Sigma0 is shown to be reliable and to have very low sensitivity to Faraday rotation. A PolInSAR vegetation height inversion for P-band is presented and applied to the CP data with a level of performance that is similar to the one derived from FP (a 1.2-m root-mean-square height error on the ONERA Airborne radar (RAMSES) data over the Landes Forest). A procedure is developed to correct for the ionospheric effects for the PolInSAR acquisition in the FP or CP mode and is assessed on the data simulated from an airborne acquisition. The results demonstrate that the technique is efficient and robust. The calibration of CP data is identified as an important challenge to be solved, and some clues are provided to address the problem.**

***Index Terms*—Compact polarimetry (CP), forest height inversion, low frequency, polarimetric interferometry, polarimetry, synthetic aperture radar (SAR).**

I. Introduction

THE USUAL full polarimetric (FP) synthetic aperture radar (SAR) design architectures are built around the standard linear basis, i.e., horizontal (H) and vertical (V). On transmission, the radar interleaves pulses with H and V polarizations. On-receive, both polarizations are simultaneously and coherently recorded. This acquisition scheme guarantees phase coherence between channels, resulting in an FP data set, for which polarization synthesis is possible and has proven its increased potential compared to a single channel acquisition. Several spaceborne SAR systems in the near future will have this capability, but will operate in the polarimetric mode only punctually. This is linked to the added complexity and timing constraints in the transmit chain when two orthogonal polarizations have to be transmitted on interleaved pulses. To maintain the performance with respect to range ambiguities, the imaged swath is usually halved, resulting in reduced coverage and a degraded revisiting time. A possible tradeoff, proposed by several existing systems like ENVISAT ASAR and ALOS PALSAR, is to offer a dual-polarized (DP) mode, where one polarization (H or V) is transmitted, whereas two are received. The acquired data set has the same coverage as for the single transmit polarization, but provides added information due to the two independent channels on-receive. This solution has proven to be very attractive but can still be improved. Souyris *et al.* [1], [2] proposed an elegant alternative to the DP mode, where, instead of transmitting one of the two linear orthogonal polarized waves, the system transmits only one polarization, either H + V or circular (right or left circular, RC or LC). They called this mode compact polarimetry (CP), which is also referred to as the $\pi/4$ mode when the H + V option is selected on transmission. They showed that the polarimetric information is well preserved for natural targets for which some symmetry properties can generally be assumed. For these targets, an equivalent covariance or coherency matrix may be reconstructed and has proven to be very similar to the

Manuscript received July 11, 2007; revised January 16, 2008. Current version published October 1, 2008. This work was carried out at the Office National d'Études et de Recherches Aérospatiales (ONERA) and was supported in part by the European Space Agency, in part by Centre National d'Etudes Spatiales, and in part by ONERA.

P. C. Dubois-Fernandez and S. Angelliaume are with the Département Electromagnétisme et Radar, Office National d'Études et de Recherches Aérospatiales, 13661 Salon Air Cedex, France (e-mail: pdubois@onera.fr).

J.-C. Souyris is with Centre National d'Études Spatiales, 31401 Toulouse Cedex, France.

F. Garestier is with Centre d'Etudes Spatiales de la Biosphère, Centre National d'Études Spatiales, Centre National de la Recherche Scientifique, Université Paul Sabatier, 31401 Toulouse Cedex 9, France.

Color versions of one or more of the figures in this paper are available online at http://ieeexplore.ieee.org.

Digital Object Identifier 10.1109/TGRS.2008.919143

ones issued from FP data. Raney [3], [4] followed a parallel path of research and suggested a mode of operation with a circular polarization transmitted and two linear polarizations on-receive. He called this mode the hybrid mode, referring to the difference in the polarization on the transmit and receive paths, and showed how the associated CP Stokes parameters can provide a level of information that is almost equivalent to that of FP. More recently, other papers have also assessed the same concepts [5], [6].

In this paper, we start by describing the theoretical background associated with the polarization synthesis and summarize the results of the previous papers on CP. We then review the ionospheric effects on propagation for low frequencies, explore the consequences on a CP mode, and identify the implications on the choice of the transmit polarization. The resulting CP mode adapted to the ionosphere is a mode where the transmit polarization is circularly polarized. This is indeed essential at low frequencies where the Faraday angle can significantly rotate any linear polarization. A circular polarization on-transmit guarantees that the scattering surface will always be illuminated by wave of a constant polarization. We refer to this mode as the $\pi/2$ CP mode. The two receiving polarizations are arbitrary as long as they are independent. For clarity's sake, we choose among all the different equivalent realizations the mode for which the receiving polarizations are linear H and V. The polarimetric analysis and the pseudocovariance matrix reconstruction as described by Souyris *et al.* [1] are explored specifically for this CP mode, and the study is completed by an analysis of the ionospheric effect on the HV Sigma0 estimation from the CP data. In the following sections, we address the polarimetric interferometry SAR (PolInSAR) applications and the vegetation height inversion at P-band. The random-volume-over-ground (RVoG) model [7] can be directly applied with a necessary minor modification due to the high penetration of the P-band inside the vegetation canopy. This adapted algorithm can be readily applied to CP by exploring the accessible polarization synthesis space, and the performance is shown to be identical to the FP case over the Landes forest. The ionospheric effects on the inversion are then analyzed, and a procedure to be applied on multitemporal data sets is proposed and assessed.

II. Theoretical Background

In this section, the theoretical background and the associated notation are presented.

In case of FP, the backscattering properties of a surface at one frequency, one incidence angle and under the reciprocity principle are usually described through a backscattering matrix S, noted in the lexicographic basis as:

$$S = \begin{pmatrix} S_{HH} & S_{HV} \\ S_{HV} & S_{VV} \end{pmatrix}.$$

The measured field E associated with any given polarization on-transmit and on-receive can then be written through the relation [8]

$$E = \vec{J}_r^{\,T} S \vec{J}_t \tag{1}$$

TABLE I
Jones Vectors

	H	V	Right circ.	Left circ.
$\vec{J}$	$\begin{pmatrix}1\\0\end{pmatrix}$	$\begin{pmatrix}0\\1\end{pmatrix}$	$\frac{1}{\sqrt{2}}\begin{pmatrix}1\\-j\end{pmatrix}$	$\frac{1}{\sqrt{2}}\begin{pmatrix}1\\j\end{pmatrix}$
(ψ, χ)	(0°,0°)	(90°,0°)	(undefined,45°)	(undefined,-45°)

TABLE II
CP Modes

Name	Transmit/ receive	$\vec{K}$
Dual-Pol 1	H/(H,V)	$\begin{pmatrix}HH\\HV\end{pmatrix}$
Dual-Pol 2	V/(H,V)	$\begin{pmatrix}VV\\HV\end{pmatrix}$
CP1(π/4)	45°/ (H,V)	$\frac{1}{\sqrt{2}}\begin{pmatrix}HH+HV\\VV+HV\end{pmatrix}$
CP2(π/2)	RC/(H,V)	$\frac{1}{\sqrt{2}}\begin{pmatrix}HH-jHV\\HV-jVV\end{pmatrix}$

In this table, RC stands for right circular polarization, and 45° stands for linear polarization with a 45° inclination.

where T denotes the transpose operator, and $\vec{J}_t$ and $\vec{J}_r$ represent the electric field vectors [8] or Jones vectors associated with the transmit and receive polarization states, respectively. Table I provides examples of Jones vectors for four canonical polarization cases.

Equation (1) is central to all polarimetric analysis: given the full backscattering matrix, the backscattered electric field can be synthesized for all possible polarization states of the receiving or transmitting antennas.

If a single polarization is transmitted, whereas the two canonical orthogonal linear polarizations (H and V) are received, the 2-D measurement vector (or observable) $\vec{K}$ is the projection of the full backscattering matrix on the transmit polarization state. The relation between $\vec{K}$ and S is given by

$$\vec{K} = S\vec{J}_t. \tag{2}$$

In the CP case, polarimetric synthesis on-receive can still be performed using the relation

$$E = \vec{J}_r^{\,T}\vec{K}. \tag{3}$$

Any polarization state of the receiving antenna can be synthesized. This is a basic yet important statement for the rest of this paper. This implies that the receiving antenna polarizations are not important as long as they are independent. From a theoretical point of view, a CP mode is fully characterized by the transmit polarization; all implementations of the receiving channels are completely equivalent. The choice of the receiving polarizations does, however, significantly impact the design and the performance of the radar system, and a system-oriented study evaluating the different options is a required step.

In Table II, several CP modes are proposed and described via the associated measurement vectors. These various modes can be compared with respect to a wide range of criteria associated with the performance of the different CP and FP data sets

given a particular application. For example, if classification or segmentation is the goal of the data acquisition, the evaluation of the different modes should be made by comparing the different output partitions to a reference partition, either obtained from ground truth or from the full polarimetry data set.

In this study, two applications will be explored, polarimetric synthesis and PolInSAR analysis. However, first and most importantly, a discussion on the effect of the ionosphere on the CP acquisition technique at a low frequency is presented to justify the choice of a specific transmission polarization.

III. Effect of the Ionosphere

The ionosphere is a region of free electrons ranging from an altitude of 100 km and extending to the magnetosphere with a peak value in the electron density at around 250–400 km. When an electromagnetic (EM) wave travels through the ionosphere, it undergoes a transformation depending on the polarization state of the EM wave. It is a simple phase shift when the wave is circularly polarized, and this shift has an opposite sign for clockwise and counterclockwise circular polarizations. The effect on a linearly polarized wave is a rotation of the polarization plane about the radar line of sight. The angle associated with the phase shift or the rotation is called the Faraday angle and depends on the total electron density (TEC) and the EM wave frequency f [9], i.e.,

$$\Omega = \frac{A}{f^2} B_0 G \,\mathrm{TEC} \tag{4}$$

where A is a constant, B_0 is the magnetic flux density, and G is a geometrical factor depending on the angles between the wave propagation and the Earth's magnetic field. For the given ionosphere, the Faraday angle that is associated with P-band is ten times the one that is associated with L-band, with typical P-band and L-band wavelengths of 70 and 22 cm, respectively.

Whereas we can expect the median value of Faraday angles at the solar maximum to be of the order of 10° for L-band, this one-way Faraday rotation reaches 100° at P-band due to the frequency square dependence.

Apart from a Faraday rotation, the effect of the ionosphere on imaging SAR at a low frequency will include an ionospheric delay depending on the TEC and defocusing.

The ionospheric delay has been extensively studied in the context of the GPS. It can be approximated to a first order by the following formula [10]:

$$d_{\mathrm{iono}} \approx 40.48 \frac{\mathrm{TEC}}{f^2}. \tag{5}$$

The ionospheric delay can, therefore, spatially and temporally vary, but is identical for all polarizations. As a result, the polarization signature stays unchanged. However, in a repeat path interferometric configuration, where the interferometric pair is not simultaneously acquired, the ionospheric variations between the two scenes will create an interferometric phase, which can spatially vary. This will create artifacts in the digital terrain model issued from the interferometry at a low frequency. However, this phase delay is constant with the polarization, and the PolInSAR application associated with the vegetation height estimation is relying only on the relative differences between the interferometric phases associated with different polarizations. As a consequence, the ionospheric delay has no influence on this specific application.

The defocusing in SAR images results from a poor compression in either the range or the azimuth directions. In the azimuth direction, the defocusing is linked to the variations of the TEC content in the ionosphere across the synthetic aperture (either temporal or spatial). In the range direction, the defocusing is the result of the dispersivity of the medium across the transmitted bandwidth to provide the resolution. This effect is small when the relative transmitted bandwidth is narrow, which is the case at P-band, given the restricted frequency allocation of 6 MHz.

In this paper, we will concentrate on the Faraday rotation, ignoring the defocusing effects. The ionospheric delays have no effect on the applications presented in this paper for the reasons developed in the previous paragraphs. Under this assumption, and assuming the reciprocity principle on the true backscattering matrix, the effect of this ideal ionosphere can then be modeled as follows:

$$\begin{aligned} M &= \begin{pmatrix} \cos\Omega & \sin\Omega \\ -\sin\Omega & \cos\Omega \end{pmatrix} \begin{pmatrix} S_{HH} & S_{HV} \\ S_{HV} & S_{VV} \end{pmatrix} \begin{pmatrix} \cos\Omega & \sin\Omega \\ -\sin\Omega & \cos\Omega \end{pmatrix} \\ &= R_\Omega S R_\Omega \end{aligned} \tag{6}$$

where S is the symmetrical surface backscattering matrix, M is the measured backscattering matrix (notice that it is not symmetrical, i.e., $M^T = (R_\Omega S R_\Omega)^T = R_\Omega^T S R_\Omega^T = R_{-\Omega} S R_{-\Omega} \neq M$), and Ω is the one-way Faraday rotation angle. The two matrices associated with the Faraday angle are canonical real rotation matrices and will be noted R_Ω in the following developments. The true backscattering matrix can be retrieved if the Faraday angle is known, i.e.,

$$S = R_{-\Omega} M R_{-\Omega}. \tag{7}$$

The Faraday angle could also be determined through (4) based on a TEC estimate obtained through the following:

- using TEC maps computed from GPS measurements [11];
- by comparing the returns at two widely separated frequencies in a similar fashion to the GPS technique.

This angle could also be evaluated from the FP data themselves based on the physical properties of specific targets [12], [13].

In the case of CP where only one polarization is transmitted, the issue of ionospheric corrections becomes more critical. The knowledge of the full backscattering matrix is not available when a single polarization is transmitted. The surface is illuminated by an EM wave that is characterized by the Jones vector $\vec{J}_s$, i.e.,

$$\vec{J}_s = \begin{pmatrix} \cos\Omega & \sin\Omega \\ -\sin\Omega & \cos\Omega \end{pmatrix} \vec{J}_t = R_\Omega \vec{J}_t \tag{8}$$

where $\vec{J}_t$ is the Jones vector of the transmit wave. If the transmit wave is linearly polarized (horizontal for example), the surface is illuminated by a linearly polarized wave rotated by an orientation angle Ω about the radar line of sight.

At P-band, where a Faraday rotation is easily larger than 90°, the impinging wave associated with a linearly polarized transmitted wave can, therefore, have any orientation depending on the TEC content of the ionosphere. Over the same area, the scattering at two different times characterized by two ionospheric states will, therefore, trigger different scattering mechanisms, depending on the polarization of the impinging wave, which may be H, V, or any other intermediate linear polarization.

On the other hand, if a circularly polarized wave is transmitted, the EM wave impinging on the scattering element will have the same polarization independently of the Faraday rotation, i.e.,

$$\vec{J}_s = \begin{pmatrix} \cos\Omega & \sin\Omega \\ -\sin\Omega & \cos\Omega \end{pmatrix} \vec{J}_{RC} = e^{-j\Omega}\vec{J}_{RC} \tag{9}$$

where $\vec{J}_{RC}$ is the Jones vector associated with the right circular wave polarization. The ionospheric effect on a circular polarization is limited to an absolute phase delay (Ω) with no impact on the polarization. As a direct consequence, the scattering response of the surface will remain unchanged whatever the TEC content of the ionosphere.

On the way back through the ionosphere, the scattered wave will also be affected by the Faraday rotation. However, the reception is performed on two orthogonal polarizations, allowing polarization synthesis on-receive. One can, therefore, readily correct the return path rotation if the Faraday rotation is known, i.e.,

$$\vec{K}_\Omega = R_\Omega S R_\Omega \vec{J}_{RC} = e^{-j\Omega} R_\Omega S \vec{J}_{RC} = e^{-j\Omega} R_\Omega \vec{K}_0 \tag{10}$$

where $\vec{K}_0$ and $\vec{K}_\Omega$ are the measurement vectors associated with 0° and Ω Faraday angles, respectively, R_Ω is the unitary rotation matrix of angle Ω, S is the scattering matrix, and $\vec{J}_{RC}^{\,T} = (1, -j)/\sqrt{2}$ as defined in Table II.

In this special CP mode, called the $\boldsymbol{\pi}/2$ CP mode, the Faraday rotation if known can be corrected for

$$\vec{K}_0 = e^{+j\Omega} R_{-\Omega} \vec{K}_\Omega. \tag{11}$$

It is important to realize that this is not the case for any linear transmit polarization. As an example, if a vertically polarized wave is transmitted and rotated by 90° through the ionosphere, the surface will be illuminated by a horizontal wave and, therefore, will scatter HH and HV; in this case, the VV signal will never be generated and could not be recovered.

Another perspective to this problem is provided by the analysis of the degrees of freedom in terms of polarization features. An FP system has four degrees of freedom, which are the orientation and ellipticity angles that are associated with the polarization state of the incidence EM wave and the receiving antenna. A CP system is restricted to two degrees of freedom related to the polarization (orientation and ellipticity) of the receiving antenna, as the transmit polarization wave is fixed. It is, therefore, a subspace of the FP case. This subspace may vary with the incident polarization or the Faraday angle. For this subspace to be invariant with the ionosphere, it is necessary to transmit a circular polarization.

This is why the transmission of a circularly polarized wave is the only sensible option for spaceborne CP at a low frequency providing exploitable multitemporal observations. Note that the transmission can be either right circular or left circular. In the rest of this paper, we will concentrate on the right circular case, relying on the fact that the equations can be easily modified to account for a left circular polarization.

Because wave synthesis can be applied on-receive, any pairs of receiving polarizations, as long as they are independent, are appropriate. For clarity's sake, we choose the $\boldsymbol{\pi}/2$ CP mode along Souyris' notation and strongly refer to the required circularity of the transmit polarization. Raney [3] called this mode the hybrid mode, stressing the difference in the polarization states between the transmit and receive channels. Note, however, that any two polarizations on-receive are suitable because of the potential wave synthesis on-receive.

IV. CP and Polarimetric Analysis

The polarimetric behavior of point targets and natural targets has been extensively explored in the last three decades. In the case of natural surfaces, several parameters have been proposed as carrying useful information. They are usually derived from the covariance matrix (the related coherency matrix or the Mueller matrix), which is derived from the scattering matrix by forming cross-products between elements, i.e.,

$$C = \begin{pmatrix} \langle S_{\rm HH} S_{\rm HH}^* \rangle & \sqrt{2}\langle S_{\rm HH} S_{\rm HV}^* \rangle & \langle S_{\rm HH} S_{\rm VV}^* \rangle \\ \sqrt{2}\langle S_{\rm HV} S_{\rm HH}^* \rangle & 2\langle S_{\rm HV} S_{\rm HV}^* \rangle & \sqrt{2}\langle S_{\rm HV} S_{\rm VV}^* \rangle \\ \langle S_{\rm VV} S_{\rm HH}^* \rangle & \sqrt{2}\langle S_{\rm VV} S_{\rm HV}^* \rangle & \langle S_{\rm VV} S_{\rm VV}^* \rangle \end{pmatrix} \tag{12}$$

where $\langle A \rangle$ denotes the spatial average of A over a window size chosen to be at least 5×5 in this paper. This equation holds in the case of monostatic radar, where reciprocity can be assumed (HV = VH). The factors 2 and $\sqrt{2}$ ensure the invariance of the span of the covariance matrix (in this case, the total power) through a polarization basis change [8].

The C matrix is Hermitian and has nine unknowns—three real diagonal elements, and the real and imaginary parts of the three off-diagonal terms.

In the case of the $\boldsymbol{\pi}/2$ CP mode with a right circular polarization on-transmit, and two linear polarizations on-receive (H and V), the measurement vector and its corresponding covariance matrix are given by

$$\vec{K}_{\rm CP} = \frac{1}{\sqrt{2}} \begin{pmatrix} S_{\rm HH} - jS_{\rm HV} \\ S_{\rm HV} - jS_{\rm VV} \end{pmatrix}$$
$$C_{\rm CP} = 2\left\langle \vec{K}_{\rm CP} \vec{K}_{\rm CP}^{+} \right\rangle = \begin{pmatrix} C_{\rm CP11} & C_{\rm CP12} \\ C_{\rm CP21} & C_{\rm CP22} \end{pmatrix} \tag{13}$$

where the superscript "+" denotes the transpose conjugate. $C_{\rm CP}$, shown at the bottom of the next page, is Hermitian and, therefore, provides four measurements—two real diagonal terms and the real and imaginary parts of one of the off-diagonal terms. Hence, the FP covariance matrix C characterized by nine unknowns cannot be reconstructed using the $C_{\rm CP}$ matrix only.

In the following development, we will revisit the technique proposed by Souyris *et al.* [1]. Note that in the referenced paper,

the reconstruction technique was explicitly described for a linear transmitted polarization with a 45° inclination ($\pi/4$ mode), although the authors identified the circular transmit mode as having the same properties in terms of the FP reconstruction. In this paper, we complete the initial paper by providing the step-by-step reconstruction associated with a right circular polarization on-transmit.

In the case of the target characterized by reflection symmetry [14], the following relations hold:

$$\langle S_{\mathrm{HH}} S_{\mathrm{HV}}^{*} \rangle = \langle S_{\mathrm{VV}} S_{\mathrm{HV}}^{*} \rangle = 0. \tag{14}$$

Equations (12) and (13) can then be written as

$$C = \begin{pmatrix} \langle S_{\mathrm{HH}} S_{\mathrm{HH}}^{*} \rangle & 0 & \langle S_{\mathrm{HH}} S_{\mathrm{VV}}^{*} \rangle \\ 0 & 2\langle S_{\mathrm{HV}} S_{\mathrm{HV}}^{*} \rangle & 0 \\ \langle S_{\mathrm{VV}} S_{\mathrm{HH}}^{*} \rangle & 0 & \langle S_{\mathrm{VV}} S_{\mathrm{VV}}^{*} \rangle \end{pmatrix} \tag{15}$$

and (16), shown at the bottom of the page, respectively.

There are five unknowns in (15)—the three real diagonal terms and the real and imaginary parts of one of the nonzero off-diagonal terms. The C_{CP} matrix provides four relations.

To remove this underdetermination, Souyris *et al.* proposed an additional equation to allow for the reconstruction, i.e.,

$$\frac{4\langle S_{\mathrm{HV}} S_{\mathrm{HV}}^{*} \rangle}{\langle S_{\mathrm{HH}} S_{\mathrm{HH}}^{*} \rangle + \langle S_{\mathrm{VV}} S_{\mathrm{VV}}^{*} \rangle} \approx 1 - \frac{|\langle S_{\mathrm{HH}} S_{\mathrm{VV}}^{*} \rangle|}{\sqrt{\langle S_{\mathrm{HH}} S_{\mathrm{HH}}^{*} \rangle \langle S_{\mathrm{VV}} S_{\mathrm{VV}}^{*} \rangle}}. \tag{17}$$

Through this equation, on one hand, the ratio of a cross-polarized signal to a copolarized signal is linked to the loss of coherence between the two copolarized signals. This ratio is, therefore, associated to the diffuse component of the scattering. Going to the limit, when the copolarized signals are independent, the C matrix reduces to the identity matrix, and (17) holds. On the other hand, when the copolarized signals are fully correlated indicating no depolarization, the cross-polarized signal is zero. Note that, in both cases, this empirical relationship obeys the assumptions made by Freeman and Durden's [15] decomposition model.

The nonlinear system of equations can be solved by iteration. In the initial step, the cross-polarized term is set to 0.

$$X = \langle S_{\mathrm{HV}} S_{\mathrm{HV}}^{*} \rangle$$

$$\gamma_{\mathrm{HHVV}} = \frac{\langle S_{\mathrm{HH}} S_{\mathrm{VV}}^{*} \rangle}{\sqrt{\langle S_{\mathrm{HH}} S_{\mathrm{HH}}^{*} \rangle \langle S_{\mathrm{VV}} S_{\mathrm{VV}}^{*} \rangle}}.$$

Step 0: initialization

$$X = 0$$

$$\gamma_{\mathrm{HHVV}} = \frac{-jC_{\mathrm{CP12}}}{\sqrt{C_{\mathrm{CP11}} * C_{\mathrm{CP22}}}}.$$

Step 1: iteration

$$X = \frac{1}{2}\left(C_{\mathrm{CP11}} + C_{\mathrm{CP22}}\right)\frac{1 - |\gamma_{\mathrm{HHVV}}|}{3 - |\gamma_{\mathrm{HHVV}}|} \tag{18}$$

$$\gamma_{\mathrm{HHVV}} = \frac{X - jC_{\mathrm{CP12}}}{\sqrt{(C_{\mathrm{CP11}} - X) * (C_{\mathrm{CP22}} - X)}}. \tag{19}$$

This value of coherence is injected back into the cross-polarized term (18).

Step 2: final

$$\begin{aligned} \langle S_{\mathrm{HH}} S_{\mathrm{HH}}^{*} \rangle &= C_{\mathrm{CP11}} - X \\ \langle S_{\mathrm{VV}} S_{\mathrm{VV}}^{*} \rangle &= C_{\mathrm{CP22}} - X \\ \langle S_{\mathrm{HH}} S_{\mathrm{VV}}^{*} \rangle &= X - jC_{\mathrm{CP12}}. \end{aligned} \tag{20}$$

This loop is executed a few times, and the process converges rather quickly (in about five iterations). Whenever the cross-polarized term becomes negative, it is set back to zero.

Figs. 1 and 2 are representing the quality of the reconstruction. In Fig. 1, the standard polarimetric color composite image of a forested zone observed at P-band with HH, HV, and VV in red, green, and blue, respectively, is compared to the equivalent composite image associated to the CP acquisition followed by the reconstruction.

Fig. 2 can be read as a histogram over a large area of the previous image, where on the x- and y-axes are the Sigma0 values associated with the initial image and the reconstructed image for HH, VV, and HV terms, respectively.

Most of the points of this scatter plot fall close to the one-to-one line with a small spread. A small systematic overestimation of the HV Sigma0 can be observed over this data set, which, if this behavior is confirmed on other data sets, could then be corrected for.

These results are similar to the one published in [1].

Once an adequate reconstruction of the HV backscatter has been achieved, several authors have shown a correspondence between the radiometric value of the HV backscatter (or the HV Sigma0) and the forest biomass over a variety of forest types [15], [17], [18]. This correspondence tends to saturate (and, thus, have lower sensitivity) at higher biomass levels; however, there is a general agreement that a radiometric uncertainty of

$$C_{\mathrm{CP}} = \begin{pmatrix} \langle S_{\mathrm{HH}} S_{\mathrm{HH}}^{*} \rangle + \langle S_{\mathrm{HV}} S_{\mathrm{HV}}^{*} \rangle + j\left(\langle S_{\mathrm{HH}} S_{\mathrm{HV}}^{*} \rangle - \langle S_{\mathrm{HV}} S_{\mathrm{HH}}^{*} \rangle\right) & \langle S_{\mathrm{HH}} S_{\mathrm{HV}}^{*} \rangle + \langle S_{\mathrm{HV}} S_{\mathrm{VV}}^{*} \rangle + j\left(\langle S_{\mathrm{HH}} S_{\mathrm{VV}}^{*} \rangle - \langle S_{\mathrm{HV}} S_{\mathrm{HV}}^{*} \rangle\right) \\ \langle S_{\mathrm{HV}} S_{\mathrm{HH}}^{*} \rangle + \langle S_{\mathrm{VV}} S_{\mathrm{HV}}^{*} \rangle + j\left(\langle S_{\mathrm{HV}} S_{\mathrm{HV}}^{*} \rangle - \langle S_{\mathrm{VV}} S_{\mathrm{HH}}^{*} \rangle\right) & \langle S_{\mathrm{HV}} S_{\mathrm{HV}}^{*} \rangle + \langle S_{\mathrm{VV}} S_{\mathrm{VV}}^{*} \rangle + j\left(\langle S_{\mathrm{HV}} S_{\mathrm{VV}}^{*} \rangle - \langle S_{\mathrm{VV}} S_{\mathrm{HV}}^{*} \rangle\right) \end{pmatrix} \tag{13b}$$

$$C_{\mathrm{CP}} = \begin{pmatrix} \langle S_{\mathrm{HH}} S_{\mathrm{HH}}^{*} \rangle + \langle S_{\mathrm{HV}} S_{\mathrm{HV}}^{*} \rangle & j\left(\langle S_{\mathrm{HH}} S_{\mathrm{VV}}^{*} \rangle - \langle S_{\mathrm{HV}} S_{\mathrm{HV}}^{*} \rangle\right) \\ j\left(\langle S_{\mathrm{HV}} S_{\mathrm{HV}}^{*} \rangle - \langle S_{\mathrm{VV}} S_{\mathrm{HH}}^{*} \rangle\right) & \langle S_{\mathrm{HV}} S_{\mathrm{HV}}^{*} \rangle + \langle S_{\mathrm{VV}} S_{\mathrm{VV}}^{*} \rangle \end{pmatrix} \tag{16}$$

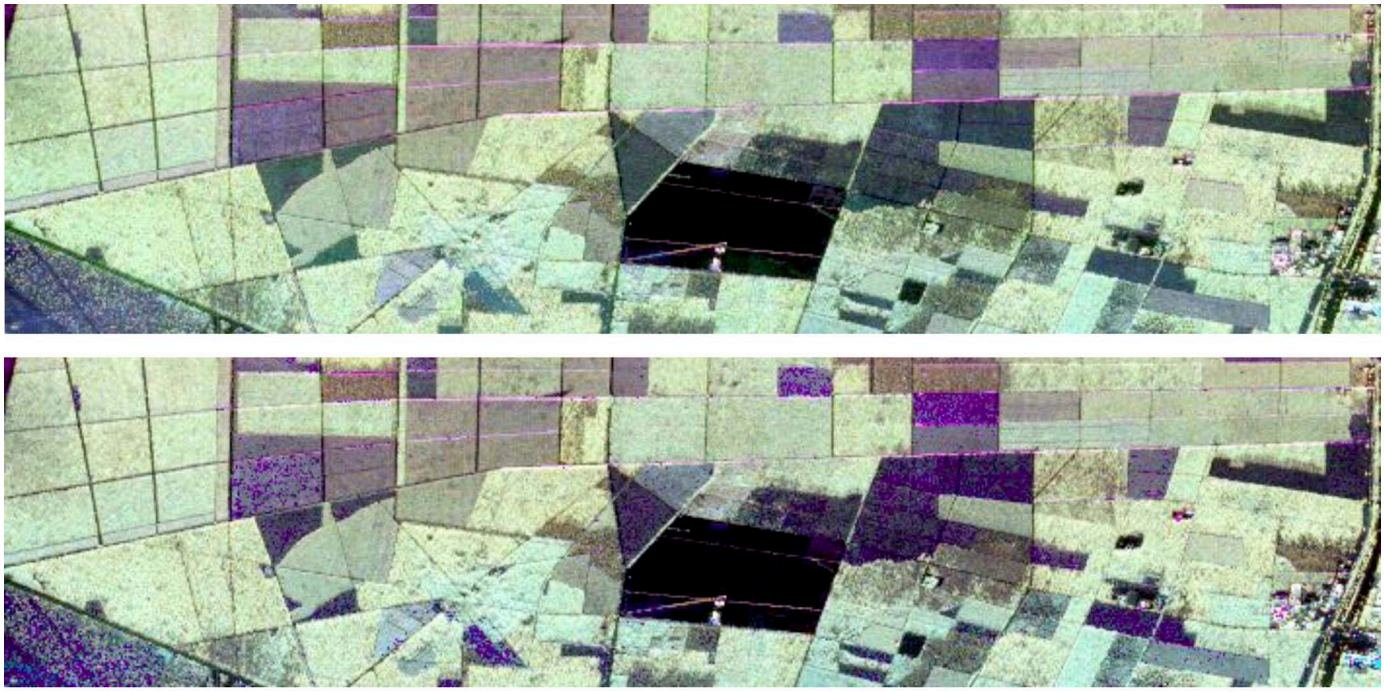

Fig. 1. P-band polarimetric image over the Nezer forest. The top image is a false color composition between HH (red), HV (green), and VV (blue) Sigma0. The bottom image was computed from the CP mode.

± 0.5 dB in the HV backscatter is required to estimate the biomass with the desired degree of precision, which is typically on the order of 10 tons/ha. In Section V, we show that for the $\boldsymbol{\pi}/2$ CP mode, the degradation on the reconstructed values of the HV backscatter due to the presence of a Faraday rotation is well within this requirement.

V. Compact POLSAR and the Faraday Rotation

We have seen in the previous section that the HV term can be reconstructed with good accuracy from the CP data, with the $\boldsymbol{\pi}/2$ CP mode characterized by a circular polarization on-transmit and two linear polarizations on-receive.

The question that will be addressed in this section is the sensitivity of the reconstruction to a Faraday rotation. The theoretical model is described below.

The measurement vector $\vec{K}$ in the presence of a Faraday rotation can be written as a function of the scattering matrix and the Faraday angle Ω [see (10)], i.e.,

$$\vec{K}_\Omega = e^{-j\Omega} R_\Omega S \vec{J}_{RC} = \begin{pmatrix} K_{\Omega 1} \\ K_{\Omega 2} \end{pmatrix}. \tag{21}$$

The study is conducted via a simulation on the P-band RAMSES airborne data set over the Landes forest. The CP measurement vector is computed from the FP data, on which a Faraday rotation is applied following (21).

The CP polarimetric SAR (POLSAR) reconstruction, as described in the previous section, is then performed for several values of this Ω angle. The plots presented in Fig. 3 represent the difference between two estimations of the HV backscatter coefficient—one from the acquisition with a Faraday rotation and the other from the acquisition with no Faraday rotation. This difference, by definition, is zero for no Faraday rotation. The evolution of the reconstruction performance as a function of the Faraday rotation is shown for two areas—low and high biomass areas. The algorithm shows very low sensitivity to the Faraday angle (less than 0.5-dB variation in the estimation of the HV backscatter for any Faraday rotation).

This robustness can be explained by observing the very low sensitivity to the Faraday rotation of the driving factors of the iteration. The inversion is based on three terms, i.e., $C_{\mathrm{CP}12}/\sqrt{C_{\mathrm{CP}11}C_{\mathrm{CP}22}}$, $C_{\mathrm{CP}11}C_{\mathrm{CP}22}$, and $C_{\mathrm{CP}11}+C_{\mathrm{CP}22}$. The variation of the first term is shown in Fig. 4 as a function of the Faraday rotation for the two areas identified above. The variation of the second term is also very small.

The last term is a constant with respect to Faraday rotation angle as derived in the following paragraph. The covariance matrix associated with the measurement vector $\vec{K}$ can be obtained via the following formula: $C_{\mathrm{CP}} = 2\langle \vec{K} \cdot \vec{K}^{+} \rangle$.

In the presence of the ionosphere, the measured covariance matrix can be expressed as a function of the unperturbed one via the relationship

$$\begin{aligned} C_{\mathrm{CP}}(\Omega) &= 2\left\langle \vec{K}_\Omega . \vec{K}_\Omega^{+} \right\rangle \\ &= 2e^{+j\Omega} e^{-j\Omega} \left\langle R_\Omega \vec{K} . (R_\Omega \vec{K})^{+} \right\rangle \\ &= 2R_\Omega \left\langle \vec{K} . \vec{K}^{+} \right\rangle R_{-\Omega} = R_\Omega C_{\mathrm{CP}} R_{-\Omega}. \end{aligned}$$

The ionospheric rotation matrix is unitary; therefore, the span of the covariance matrix, i.e., $C_{\mathrm{CP}11}+C_{\mathrm{CP}22}$, is invariant with the Faraday rotation.

The reconstruction of the HV backscattering coefficient from the $\boldsymbol{\pi}/2$ CP mode is robust with the Faraday rotation for vegetated areas. This is an important result, as the ionospheric effect will always be present for a low frequency. It has to be

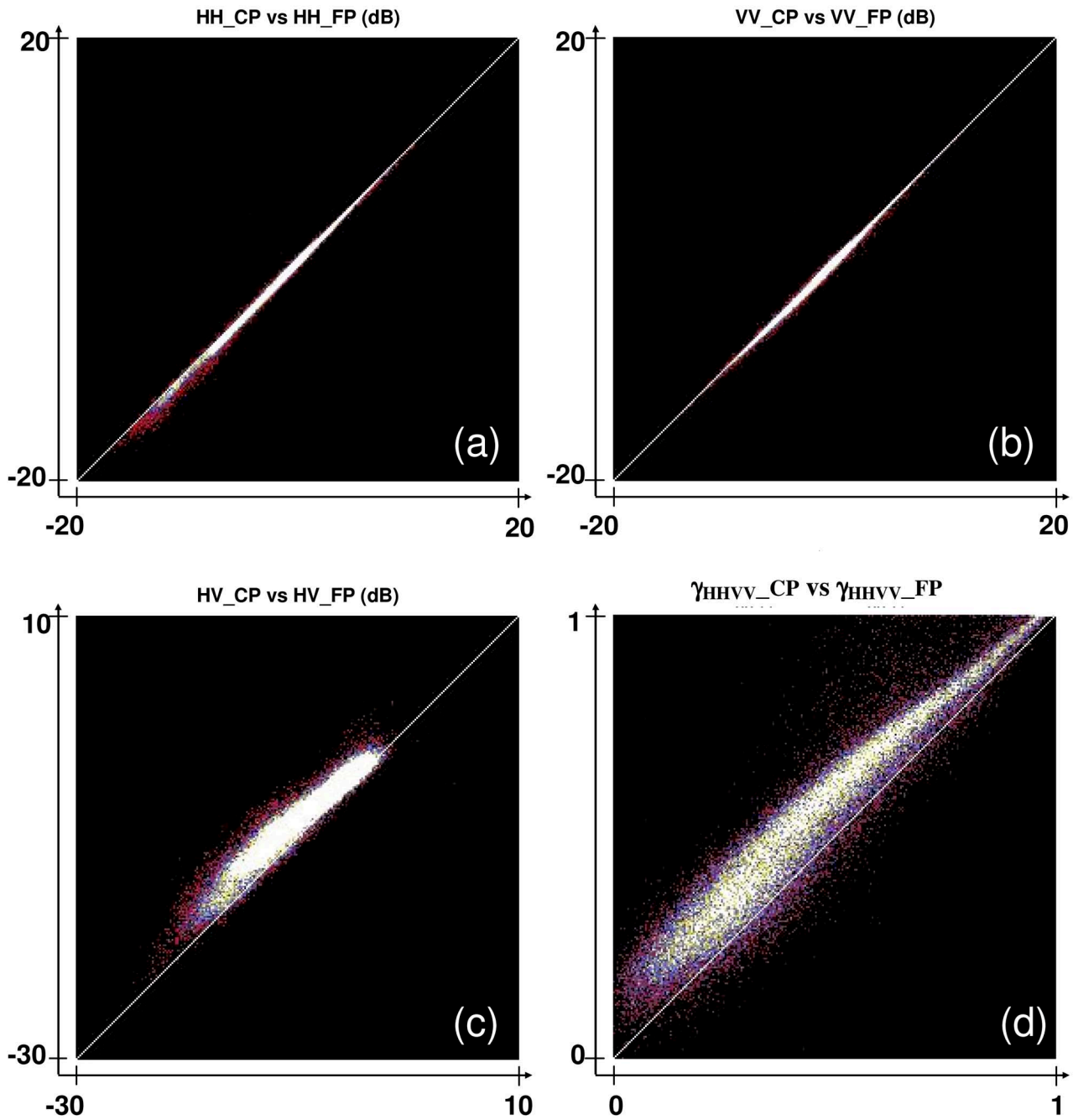

Fig. 2. Two-dimensional histograms presenting the reconstruction performance for HH, VV, and HV and the polarimetric coherence between HH and VV. The color scale is indicative of the population of the bin. White are the most populated bins.

noted, however, that the reconstruction of the copolarized term (HH and VV) does not have this robustness.

VI. Compact PolInSAR

The PolInSAR analysis relies on the joint exploration of two polarimetric data sets acquired over the same area under interferometric conditions, i.e., from slightly different geometry. These two data sets could, in theory, be simultaneously acquired if the radar system included two receiving antennas sufficiently far apart to provide an adequate baseline. For low frequencies, this is rarely the case. In airborne systems, the required spacing between the two antennas often exceeds the size of the plane. In spaceborne systems, a space instrument with two bulky receiving antennas required for P-band operation from the space is currently beyond the reach of a standard mission in terms of cost and weight. As a cheaper alternative to the single pass acquisition, the PolInSAR data sets or the interferometric data sets for a low frequency are usually acquired at different times with the same instrument.

The breakthrough with the PolInSAR application was the development and the validation of the vegetation height inversion technique associated to the RVoG model [7]. This algorithm has been extensively tested at L-band.

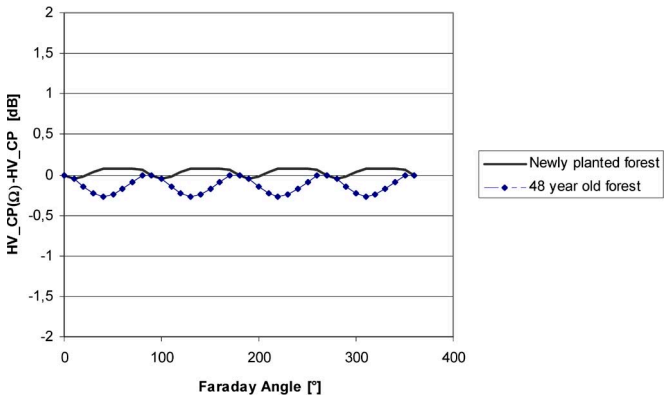

Fig. 3. Difference in the estimation of the HV backscattering coefficient from the CP mode in the presence of a Faraday rotation ranging from 0° to 360°. With this definition, the difference is null when there is no Faraday rotation.

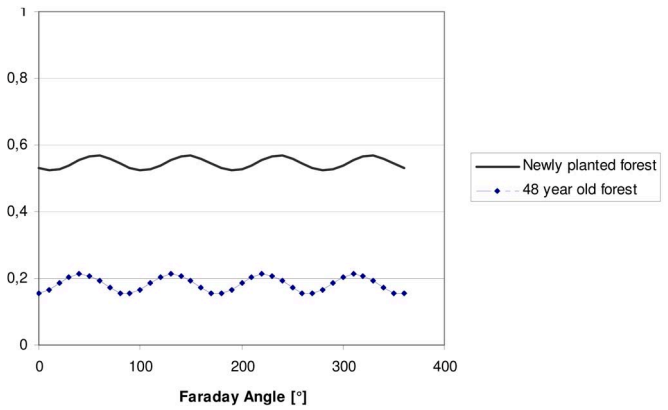

Fig. 4. Variation of the term $C_{\mathrm{CP12}}/\sqrt{C_{\mathrm{CP11}}C_{\mathrm{CP22}}}$ as a function of the Faraday rotation.

In the RVoG model [7], the signal backscattered from the forest is modeled as the combination of a ground contribution and a volume-only contribution. The ground contribution can be the surface scattering or the double-bounce effect (surface-tree trunks). The associated interferometric coherence is assumed to be of unit magnitude (no decorrelation) with an interferometric phase signing the height of the ground surface. In [19], the interferometric coherence associated with the volume contribution was shown to be polarization independent (under the hypothesis that the attenuation is polarization independent), with the corresponding backscattering depending on polarization. When both contributions are present (they are assumed independent), the resulting interferometric coherence γ_T can be written as follows:

$$\gamma_T = f(\gamma_g, \gamma_v) = \frac{\sigma_{0g}}{\sigma_{0g}+\sigma_{0v}}\gamma_g + \frac{\sigma_{0v}}{\sigma_{0g}+\sigma_{0v}}\gamma_v \qquad (22)$$

where γ_v is the volume-only coherence, γ_g is the ground coherence, and σ_{0g} and σ_{0v} are the normalized backscatter coefficient respectively associated to the ground scattering (including the attenuation through the canopy) and to the volume return. Both are varying with a polarization, and the total coherence is simply the weighted average of the two coherence values. As a direct consequence, the locus of the interferometric coherence

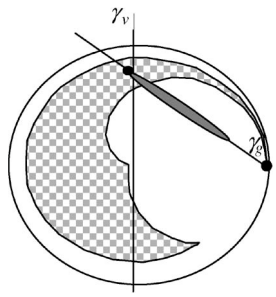

Fig. 5. RVoG behavior. The gray ellipse is the one corresponding to the position of the interferometric coherence values as the polarization varies. The checkered pattern represents the LUT.

when the polarization varies is a line segment between points B (ground) and A (volume-only).

The inversion scheme, as described by Cloude and Papathanassiou [7], can be summarized in four steps and is illustrated in Fig. 5.

1) Synthesize many interferometric coherence values by varying the polarization of the transmit and receive antennas and identify the line AB.
2) Identify the two intersection points between the line AB and the circle. Choose between the two the one that is associated with the ground $e^{i\varphi_0}$ as being the one closer to the HH coherence and furthest to the HV coherence.
3) Select the interferometric coherence that is furthest from the ground coherence as $e^{i\varphi_0}\gamma_v$. This assumes that there is a polarization state of the transmit and receive antennas such that there is no contribution from the ground.
4) From γ_v, invert the vegetation height and the attenuation from the following equation [19]:

$$\gamma_v = \frac{\int_{h_v}^{0}\sigma_{0l}e^{uz}dz}{\int_{h_v}^{0}\sigma_{0l}e^{vz}dz} = \frac{\int_{h_v}^{0}e^{uz}dz}{\int_{h_v}^{0}e^{vz}dz} = \frac{v[e^{uz}]_0^{h_v}}{v[e^{vz}]_0^{h_v}}$$
$$\text{with } u = 2\frac{\sigma_x}{\cos\theta} + ik_z \text{ and } v = 2\frac{\sigma_x}{\cos\theta}. \qquad (23)$$

This equation reflects the fact that the volume can be modeled as a succession of identical layers, each one characterized by a backscatter coefficient σ_{0l}. θ is the incidence angle. In the denominator, the scattered power is just the sum of the contribution of each layer weighted by the attenuation resulting from the roundtrip through the layers sitting on top with the attenuation coefficient being σ_x. In the numerator, the interferometric phase associated with each layer is also introduced via the vertical interferometric wavenumber, k_z. Because all layers are identical and independent, the σ_{0l} term vanishes.

The inversion process that consists of estimating the vegetation height and the attenuation from the volume-only interferometric coherence can be done using many mathematical techniques. The simplest one is the lookup table (LUT) technique. For a selected range of height and extinction coefficients, the interferometric coherence values are computed and stored in a LUT. This LUT is represented in Fig. 5 and is the locus of the possible interferometric coherence values. Inside this region

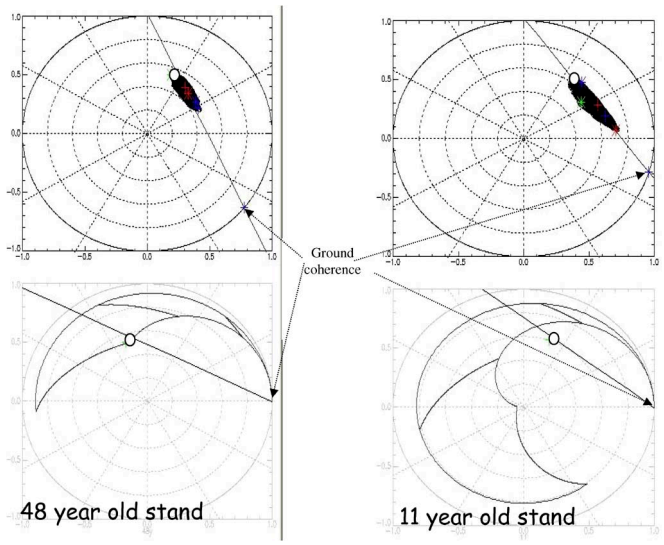

Fig. 6. Complex unitary circle for two forest plots (age 48 on the left and age 11 on the right). The top figures represent the locus of the interferometric coherence values, the fitted lines, and the highest phase center as a white dot. This dot is then represented on the rotated unitary circle such that the ground interferometric phase is zero. The valid LUT domain is also represented on the bottom figures. For the younger forest, the highest phase center is not inside the valid LUT domain. The height inversion algorithm had to be adapted to retrieve the height corresponding to the intersection of the line and the curve corresponding to a known attenuation.

(represented as a checker pattern), each point corresponds to a height and extinction coefficient belonging to the selected range. The inverted height and extinction coefficients are the ones associated with the LUT point that is closest to the measured interferometric coherence.

In order for this scheme to be successful, one must be certain that the volume-only coherence is observed for one polarization. This can be true at X- or C-band, but becomes more questionable as the frequency decreases. At P-band, this is certainly rarely the case. On the complex unitary circle, the pseudoellipse will shift toward the ground point as penetration increases. Fig. 6 is an illustration of what can happen at P-band when the ellipse does not contain the point that is associated with the volume-only contribution.

For the young forest (right plots), and if we assume that the RVoG model is valid, we can conclude that the volume-only contribution is not observed, as the extreme (or highest) phase center (white dot) in Fig. 6 is not inside the LUT area. In the following paragraphs, we describe how the initial procedure was slightly modified for a lower frequency acquisition.

Within the frame of the model, the volume-only coherence must lie on the fitted line to the left of the last observed coherence. Assuming a given attenuation coefficient (for P-band, we chose 0.3 dB/m from the analysis of a trihedral under canopy) reduces the LUT to a single curve. The volume-only contribution is determined as the intersection of the fitted line and this curve. This position is then inverted for height.

In Fig. 7, the inversion results are presented. The rms error of the height is 1.2 m. The lower vegetation plots are not correctly estimated by the PolInSAR technique. This can be expected if we consider that the interferometric phase centers associated with the different polarizations are extremely close

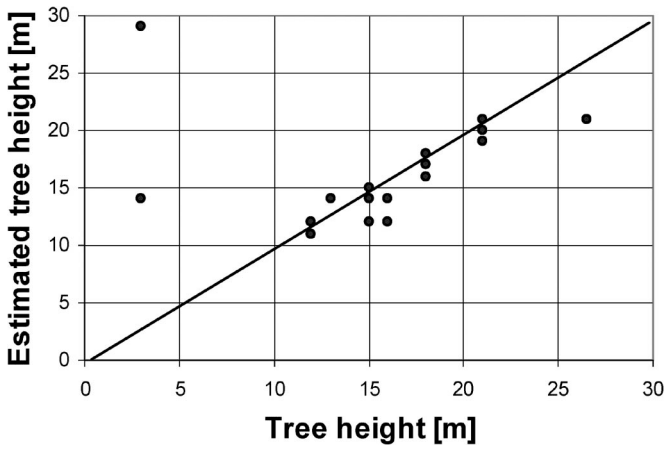

Fig. 7. Height inversion results from the analysis of the FP P-band PolInSAR RAMSES data acquired over the Nezer forest. For this data set, the resolution is 2 m in both range and azimuth directions. The incidence angle varies between 30° and 45°. The noise equivalent Sigma0 is around −35 dB. The height of the ambiguity ranges from 20 to 100 m.

to each other in elevation for low or sparse vegetation within a range of the order of the height accuracy associated with the geometry. We know, however, that the standard biomass estimation from the radiometric information of the cross-polarized signal (HV) performs well in that range, indicating interesting complementarity between the two techniques. The PolInSAR inversion becomes very efficient as soon as the vegetation gets higher.

The inverted height is extremely stable within a forest plot, as can be seen in Fig. 8. In this plot, four independent transects across the same forest area are presented, and the stability of the estimation from one transect to the other is within 1 m.

Central to this inversion is the quality of the line estimation as depicted in Fig. 5. In the FP PolInSAR inversion, the locus of all interferometric coherence values associated with the different polarization states of the receiving and transmitting antennas is available to describe the line. This is a four-parameter space, as the polarization of each antenna can be parameterized with two parameters each—the ellipticity and the orientation angles. In the CP mode, the transmit polarization is fixed resulting in a two-parameter space corresponding to the polarization state of the receiving antenna. Note that because the reception occurs on two independent polarizations, any receiving antenna polarization can be synthesized from the data following (3). In the compact PolInSAR inversion, we compute the locus associated with all the polarization states of the receiving antenna (a two-parameter space) described as follows:

$$\gamma(\psi,\eta)=\frac{\left\langle E^{\mathrm{ref}}(\psi,\eta)E^{\mathrm{int}}(\psi,\eta)^{*}\right\rangle}{\sqrt{\left\langle E^{\mathrm{ref}}(\psi,\eta)E^{\mathrm{ref}}(\psi,\eta)^{*}\right\rangle\left\langle E^{\mathrm{int}}(\psi,\eta)E^{\mathrm{int}}(\psi,\eta)^{*}\right\rangle}} \tag{24}$$

where ref and int refer to the reference and interferometric measurements and

$$E(\psi,\eta)=\begin{pmatrix}\cos\psi\cos\eta-j\sin\psi\sin\eta\\ \sin\psi\cos\eta+j\cos\psi\sin\eta\end{pmatrix}^{T}\vec{K}_{CP}$$

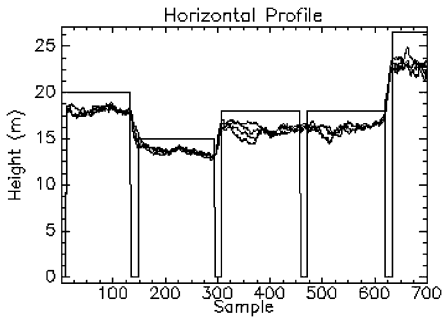

Fig. 8. Four independent parallel forest height transects crossing the same five forest plots. The transects were computed at different range distances, sufficiently apart to provide an independent height estimation. The thin line corresponds to the ground measurements. The four inverted profiles are showing very consistent results.

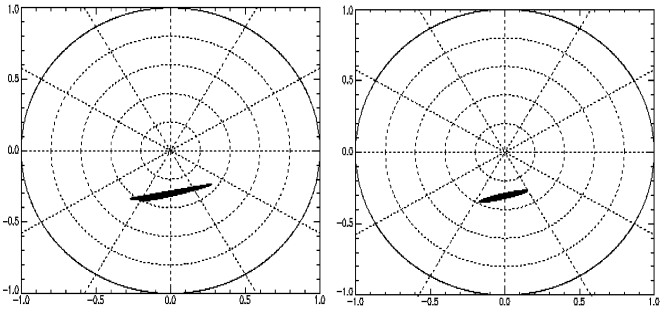

Fig. 9. Example of the interferometric coherence set obtained with the complete synthesis for (left) the FP and (right) CP modes over a forest plot of age 49 years. As expected, the CP set is included in the FP set, with a narrower angular extent.

where $\psi \in \lfloor -\pi/2, \pi/2 \rfloor$ and $\eta \in \lfloor -\pi/4, \pi/4 \rfloor$ and $\vec{K}_{CP}$ is the measurement vector (see Table II) associated with the $\boldsymbol{\pi}/2$ CP mode.

Note that the polarization states are identical between the two interferometric acquisitions. This ensures that the measured phase is truly an interferometric phase and not a polarimetric phase.

Ignoring the ionosphere for now, this two-parameter space is a subspace of the FP four-parameter space. The angular sector described by this subspace in the unitary circle is included (and, therefore, smaller) in the four-parameter space described by the FP locus of the interferometric coherence values in Figs. 9 and 10. The inversion procedure described in the previous sections can then be applied to the subspace of interferometric coherence values corresponding to the CP mode.

The inversion results associated with the CP mode are extremely similar to the FP ones. Both results are presented in Fig. 10.

On the Landes data set, in the case of well-calibrated data, the compact PolInSAR performs as well as the FP PolInSAR. The results obtained on CP are very encouraging, but need to be taken one step further. At P-band, propagation through the ionosphere introduces a Faraday rotation. The two necessary polarimetric acquisitions will not be acquired at the same time, and, as a consequence, the experienced Faraday rotation could be different between the two acquisitions. Even under perfect interferometric conditions, i.e., with no temporal decorrelation, the PolInSAR acquisitions will be decorrelated due to this differential rotation—the polarizations being not perfectly matched between the two. Section VII investigates this problem and proposes a solution.

VII. Compact PolInSAR and the Faraday Rotation

In this section, the PolInSAR sensitivity of the $\boldsymbol{\pi}/2$ CP mode to the ionospheric effect will be evaluated. Two issues will be investigated. The first one concerns the effect on the inversion of the polarization mismatch associated with a differential Faraday rotation between two acquisitions. The sensitivity of the height estimation to this angle will be assessed. This point is of importance as it will provide a guideline for the required ionospheric correction accuracy. The second issue concerns the estimation of the differential Faraday rotation angle from the data.

A. Sensitivity to the Differential Faraday Rotation Angle

What is the effect of an identical Faraday rotation on both $\boldsymbol{\pi}/2$ CP acquisitions? Both electric fields will be rotated by the same amount and delayed by the same angle, resulting in exactly the same interferometric coherence values as the ionosphere-free measurements (even if these coherence values do not correspond to the expected polarization states). The problems arise when the ionosphere states characterising the two acquisitions are different, introducing a differential effect. In Section III, we have identified the ionospheric delay as a strong effect of the ionosphere at a low frequency [see (5)]. However, this delay is identical for all polarizations and will, therefore, have no effect on the PolInSAR vegetation height estimation from the RVoG model as all complex coherence values are rotated by the same amount in the unit circle. The estimation of the ground level will, however, be biased, and a specific ionospheric correction will have to be developed and applied to the data if this information is sought. In this paper, we are exclusively concerned with the vegetation height estimation.

In this paragraph, the effect of a differential Faraday rotation on the two acquisitions forming the PolInSAR data sets is analyzed.

The study is conducted via a simulation on the RAMSES P-band airborne data set over the Landes forest. The CP measurement vectors are computed from the FP data, and the reference channel is processed without any ionospheric effect. On the "slave" channels, a uniform Faraday rotation is applied following (10).

The CP PolInSAR inversion, as described in the previous section, is then performed for several values of the Faraday angle.

In this exercise, we consider the $\boldsymbol{\pi}/2$ CP mode, where the transmit polarization is circularly polarized, and the receive channels are the two orthogonal linear polarizations H and V.

The result of this analysis is presented in Fig. 11. The inversion results are showing little sensitivity to the ionosphere for a Faraday rotation difference of less than 10°. Beyond 10°, the inversion results are significantly degraded.

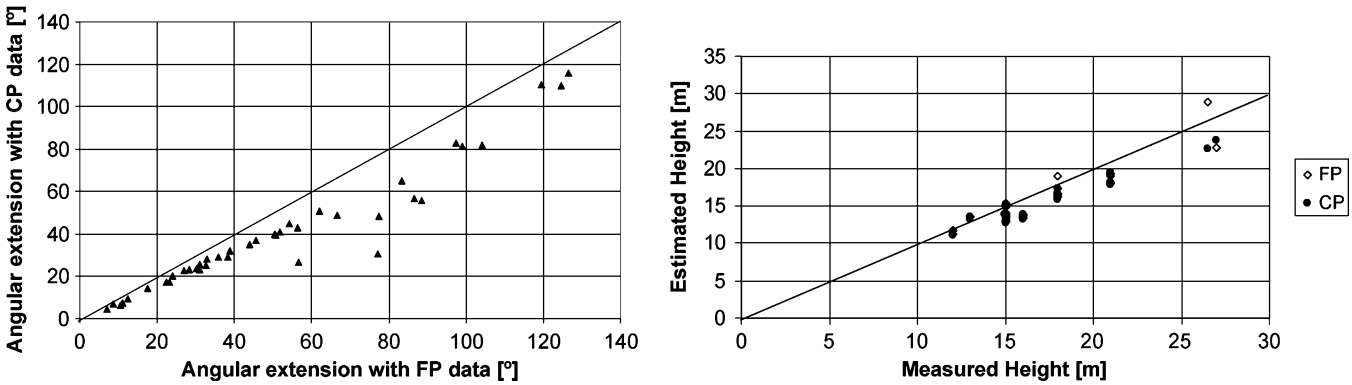

Fig. 10. (Left) Angular extent of the interferometric coherence values associated with CP as a function of the FP angular extent for all forest stands examined. (Right) RVoG inversion results for FP and CP modes. For most cases, the points are exactly overlapping, indicating that the estimation yields the same values for FP and CP modes.

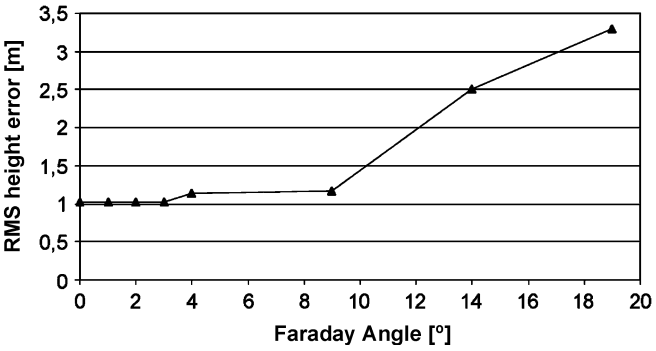

Fig. 11. Compact PolInSAR inversion results for the $\boldsymbol{\pi}/2$ CP mode compared to the FP case as a function of the residual Faraday rotation angle.

Considering that, under a sun-synchronous orbit, the two polarimetric data sets that are required to perform interferometry are acquired on different days but at the same local time, the expected ionospheric variations can be assumed smaller than the ones occurring along the day cycle. Using the $\boldsymbol{\pi}/2$ CP mode and for a differential Faraday rotation of less than 10°, no correction is needed, and the standard inversion procedure can be directly applied on the noncorrected data. This could prove to be a strong case for a sun-synchronous orbit.

However, in the case where the ionospheric variation is larger, another approach can be applied. This is the topic of Section VII-B.

B. Evaluation of the Differential Faraday Angle

Let us assume now that two $\boldsymbol{\pi}/2$ CP polarimetric measurements have been acquired on two different dates. The two measurement vectors $\vec{K}^i$ $(i = \text{int}, \text{ref})$ can be written as a function of the two scattering matrices and the Faraday angles Ω^i [see (10)], i.e.,

$$\vec{K}^i = e^{-j\Omega^i} R_{\Omega^i} S^i \vec{J}_{RC} = \begin{pmatrix} K_1^i \\ K_2^i \end{pmatrix}. \tag{25}$$

To estimate the differential Faraday rotation, we will maximize the interferometric coherence by rotating one of the received measurement vectors by the angle Ω, i.e.,

$$\begin{aligned} \vec{K}^{\text{int}}(\Omega) &= R_{-\Omega} \vec{K}^{\text{int}} \\ &= e^{-j\Omega^{\text{int}}} R_{-\Omega} R_{\Omega^{\text{int}}} S^{\text{int}} \vec{J}_{RC} \\ &= e^{-j\Omega^{\text{int}}} R_{\Omega^{\text{int}}-\Omega} S^{\text{int}} \vec{J}_{RC} \\ &= \begin{pmatrix} K_1^{\text{int}}(\Omega) \\ K_2^{\text{int}}(\Omega) \end{pmatrix}. \end{aligned}$$

Then, following (24), we can write the interferometric coherence associated with any synthesized on-return polarization state as a function of the corrected Faraday angle (see (26), shown at the bottom of the next page), with

$$E^{\text{ref}}(\psi, \eta) = \begin{pmatrix} \cos\psi\cos\eta - j\sin\psi\sin\eta \\ \sin\psi\cos\eta + j\cos\psi\sin\eta \end{pmatrix}^T \vec{K}_{CP}^{\text{ref}}$$

$$E^{\text{int}}(\psi, \eta, \Omega) = \begin{pmatrix} \cos\psi\cos\eta - j\sin\psi\sin\eta \\ \sin\psi\cos\eta + j\cos\psi\sin\eta \end{pmatrix}^T \vec{K}_{CP}^{\text{int}}(\Omega)$$

where $\psi \in \lfloor -\pi/2, \pi/2 \rfloor$ and $\eta \in \lfloor -\pi/4, \pi/4 \rfloor$.

The next step is to maximize the interferometric coherence values with respect to the Ω parameter. For any given polarization state characterized by the pair (ψ, η), the angle Ω for which the interferometric coherence amplitude is maximum is noted $\Omega_C(\psi, \eta)$, i.e.,

$$|\gamma(\Omega_C(\psi, \eta))| = \max\left(|\gamma(\psi, \eta, \Omega)|\right)_{\Omega \in [0,\pi]}. \tag{27}$$

If the only change between the two acquisitions is the ionosphere, i.e., $S^{\text{ref}} = S^{\text{int}}$, the maximization process is straightforward and $\Omega_C(\psi, \eta) = \Omega_{\text{int}} - \Omega_{\text{ref}}$ modulo π, with the two solutions aligning the vectors associated with the basis (either the same or of opposite direction).

In a more realistic case, allowing small changes in the backscattering mechanisms between the two acquisitions, but staying in interferometric conditions, it can be assumed that this relation will globally hold, and that the histogram associated with $\Omega_C(\psi, \eta)$ will be narrow and centered on the two solutions described above.

To illustrate the effect of this small natural variation in backscattering, the technique is investigated using the RAMSES airborne data over the Nezer forest. The ionospheric distortion corresponding to a uniform Faraday rotation angle

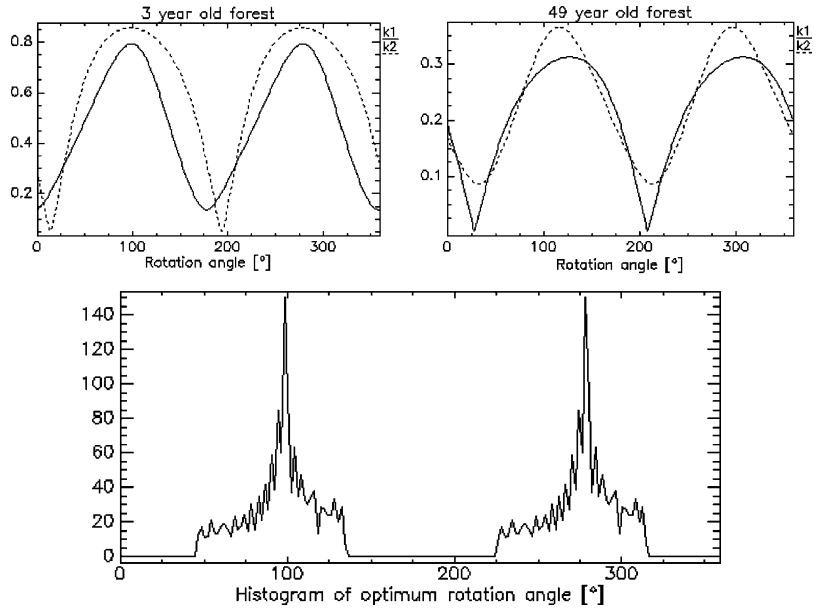

Fig. 12. Interferometric coherence as a function of the rotation angle Ω applied to the second measurement vector according to (26), where $k1$ corresponds to $(\Psi = 0°, \eta = 0°)$ and $k2$ to $(\Psi = 90°, \eta = 0°)$. The ionospheric differential Faraday angle is 100°. The figures correspond to two different areas. The maximum is reached for an Ω value around 100°, with, however, a slight shift between the two curves for the older forest. The estimation of the Faraday angle is better and more accurate over a zone for which the interferometric coherence is higher. On the younger forest, the bottom plot is the histogram of the optimum rotation angle over the full set of the synthesis space (for all Ψ and η).

$\Omega^{\text{int}} = 100°$ is introduced on one of the acquisitions. For all possible ψ and η, the interferometric coherence is maximized with respect to Ω. Fig. 12 presents the variation of the interferometric coherence [see (26)] for two polarization states, i.e., H receive $(\psi = 0°)$ and V receive $(\psi = 90°, \eta = 0°)$, over two surfaces, one composed of small trees and the other one composed of high trees. The histogram associated with $\Omega_C(\psi, \eta)$ is displayed for the short vegetation case. It is characterized by two obvious peaks, distant of 180° and centered at 100° for the first one. The technique can, indeed, provide an accurate estimate of the Faraday rotation. For best results, it should be performed on an area characterized by high coherence values. The broadening of the peak is linked to the variation in backscattering between the two acquisitions and is expected to increase with the time lag between acquisitions.

The bimodal form of the histogram results from the fact that the pair of fields (A, B) has the same correlation as the pair (A, -B).

The resulting ambiguity can be penalizing if one is interested in the absolute interferometric phase, as, for example, in digital elevation model mapping, where it can create a discontinuity of half a fringe. Special care has to be taken in the phase unwrapping problem to solve for it.

In the PolInSAR analysis, this ambiguity has no impact on the vegetation height estimation as long as the same correction is applied to all polarimetric channels, preserving the relative interferometric phases. The pseudoellipse formed by the interferometric coherence values and the fitted line as described earlier would only be globally rotated by 180°. However, if the sought parameter is the ground height, the indetermination has to be lifted by applying a propagation technique similar to phase unwrapping in interferometry.

The accuracy of the differential Faraday rotation estimation is better than 5°. We have seen in Section VII-A that with a 10° Faraday rotation on one acquisition, the inversion was still robust and provided reliable results.

This optimization procedure may look similar at first glance to the one first proposed by Papathanassiou [20]. However, it is rather different in philosophy and in implementation. In the previously published coherence optimization procedure, the authors were looking for a polarization state throughout the 8-D parameter space (four ellipticity angles and four orientation angles as the interferometric channels were independently considered), independently characterizing the receiving and transmitting antennas for two interferometric data sets. The result of this optimization was the maximum possible interferometric coherence.

In the optimization described in this paper, the goal is different. The estimation is not aimed at finding the maximum coherence; it is aimed at estimating the differential Faraday rotation occurring between the propagation of the EM wave through the ionosphere. There is a direct physical interpretation behind the optimization. The implementation is also different, as an infinite number of coherence values $\gamma(\psi, \eta)$ are

$$\gamma(\psi, \eta, \Omega) = \frac{\left\langle E^{\text{ref}}(\psi, \eta) E^{\text{int}}(\psi, \eta, \Omega)^* \right\rangle}{\sqrt{\left\langle E^{\text{ref}}(\psi, \eta) E^{\text{ref}}(\psi, \eta)^* \right\rangle \left\langle E^{\text{int}}(\psi, \eta, \Omega) E^{\text{int}}(\psi, \eta, \Omega)^* \right\rangle}} \tag{26}$$

simultaneously maximized with respect to a single parameter Ω, which is the differential Faraday rotation.

In this section, we have shown that compact PolInSAR analysis in the presence of the ionospheric effect can still be performed by following the step-by-step procedure, where the differential ionospheric angle is first estimated via interferometric coherence maximization, and then corrected for before applying the height inversion algorithm. The compact PolInSAR vegetation height estimation algorithm was shown to have similar performance to the FP data over one site—the Nezer forest.

VIII. Calibration Issues

One other main aspect that needs to be addressed is the calibration issue of CP data. Freeman [21] and Quegan [22] proposed a technique adapted to the FP case.

If the CP mode is considered as a complementary mode to FP, it can be assumed that the FP system can be calibrated prior to switching to the CP mode. If the CP mode is designed as a standalone system, the question on how to calibrate a CP system becomes critical. Raney [23] pointed at some very interesting properties of such a system, and this needs to be followed through.

In this paper, the intent is not to fully investigate the calibration of CP data; the analysis is on-going and not yet ready for a formal presentation. Nevertheless, some items that are specific to CP data can already be pointed out.

- The circular character of the transmit polarization is essential, as it is the required condition for a consistent illumination polarization at the surface level in the presence of the ionosphere. An elliptically polarized wave will have a major axis that will rotate with the TEC content. In general, to transmit a circular polarization, one uses an H and V linear antenna fed with a 90° delay. This requires a perfectly balanced system in amplitude and phase.
- On FP data, as long as the crosstalk level is low enough, the calibration procedure proposed by Freeman can be applied. The correction can be done after processing on the ground. The resulting corrected measurements are independent of the initial distortion levels. Contrary to the full polarization case where correction and calibration can be applied after the acquisition, the requirement on the circularity of the transmit polarization is a hardware requirement, as it cannot be corrected after the fact. The system needs to be designed to accommodate this constraint, including maybe a phase shifter and a variable attenuator. If the circularity condition is met, an *a posteriori* calibration procedure can be performed for the relative phase and amplitude unbalance on the receive channels and the absolute total gain. Even if not quite finalized yet, some interesting properties of single-bounce surfaces could be enforced, i.e.,

$$\begin{aligned}\operatorname{Arg}\langle M_{\mathrm{LL}} M_{\mathrm{LR}}^{*}\rangle &= 2\Omega \pm 180^{\circ}\\ \operatorname{Arg}\langle S_{\mathrm{LH}} S_{\mathrm{LV}}^{*}\rangle &= 90^{\circ} \pm 180^{\circ}.\end{aligned}$$

- The use of specular scattering from returns near nadir to calibrate polarimetric radar systems was proposed by Yueh *et al.* [24]. Raney [23] pointed out that this approach is also possible for the CP case. In his outlined procedure, the radar system is allowed to rotate to vertically transmit to the ground. If the incidence angle is zero, then the H and V polarizations are equivalent, the received signals on both channels can be balanced, and the relative phase can be adjusted.

The calibration issue needs to be addressed in a more detailed manner. The CP mode should be characterized by a calibration error model, and this is one of the challenges we are trying to solve. It is also important to address the behavior of the CP data over a wider range of forest, including tropical forests and areas where significant topography could impact the scattering behavior, modifying the relevance of the hypothesis made during the pseudocovariance matrix reconstruction.

IX. Conclusion

We have presented in this paper the implementation of the CP mode applied to low-frequency SAR. In such a mode, transmission occurs in a single polarization, whereas reception is conducted with two receiving channels. The only constraint on the two receiving polarization states is their independence (an orthogonal basis is assumed as it is more mathematically convenient). Based on these two measurements, polarization synthesis can be then applied to reconstruct any possible receiving polarization states. In the development in this paper, we selected the canonical basis (H and V) for the receiving polarization states for the sake of simplicity.

The choice of the transmit polarization is the only important option and can depend on the frequency. More specifically, the only sensible choice for the transmit polarization in the presence of ionospheric effects (low frequency) is found to be circularly polarized. This should not come as a surprise, as it has been known for decades by the radar astronomy community; however, surprisingly, it was never implemented on radar imaging satellites. This polarization setup will guarantee that the EM wave seen by the scattering element is always the same for all possible Faraday rotations, allowing meaningful analysis of a temporal series of measurements, as the scatterer always remains excited by the same polarization.

The CP measurements are then evaluated for polarimetric applications. In that area, we restricted our investigation to the reconstruction of a pseudo FP covariance matrix, revisiting the earlier paper by Souyris and illustrating the reconstruction algorithm for this $\boldsymbol{\pi}/2$ CP mode. In his paper, Souyris described the general strategy of reconstruction for the $\boldsymbol{\pi}/4$ mode (referring to an H + V linear polarization and indicating the similarity of the reconstruction algorithm when choosing the circular polarization on-transmit). In this paper, we specifically consider the $\boldsymbol{\pi}/2$ CP mode with a circular transmit polarization and demonstrated similar results. It should be noted, however, that the $\boldsymbol{\pi}/4$ mode is not adequate in the presence of the ionospheric effect, as the illumination at the surface level will vary with the TEC content, preventing multitemporal analysis and physical interpretation of the scattering. Furthermore, with the $\boldsymbol{\pi}/2$ CP mode, the reconstruction of the HV backscattering coefficient is robust with the Faraday rotation for the forest types analyzed

in this paper. This is particularly important in the context of Biomass, a low-frequency satellite mission project aimed at providing a global biomass map based on this HV parameter.

A very interesting approach to polarimetric analysis with the CP mode was proposed by Raney based on the Stokes parameters. The hybrid CP mode (transmitting circular and receiving two linear polarizations) was addressed and illustrated in his work, and it was chosen not to replicate this effort. However, we want to acknowledge the large unexplored potential of the parameters that he presented.

We have shown that FP PolInSAR data can be successfully inverted using the RVoG model and an inversion procedure adapted to the P-band data by assuming a known attenuation coefficient or a range of attenuation coefficients. The sensitivity to the attenuation parameter was observed to be weak given a proper baseline selection. The inversion proved to be performing very well at P-band with a measured rms height error of 1.2 m, which is below the assumed ground measurement accuracy.

The CP acquisitions were then evaluated for PolInSAR applications. The inversion could also be directly applied on the CP measurements taking advantage of the potential of polarization synthesis on-receive, and the results showed almost identical performance to the FP mode. This analysis is promising and should be pursued over a wide range of forest densities and forest types. Furthermore, the effect of the underlying topography should be explored.

One of the main difficulties with a CP or dual-polarization system was always thought to be the correction of the ionospheric effect, a correction that is possible on FP data. In the case of PolInSAR applications, we have proposed in this paper a two-step procedure producing accurate vegetation height inversion based on the RVoG model even in the presence of differential ionospheric effects on the two acquisitions forming the PolInSAR data sets. The first step is the estimation to within a few degrees of the differential Faraday rotation using an optimization procedure on the interferometric coherence. Once this effect is estimated, it is corrected, and the standard RVoG model can be applied to the resulting data set. It was shown in this paper that an estimate to within 10° of this Faraday differential angle is adequate to provide good inversion. The vegetation height inversion algorithm in the presence of the ionospheric effect is tested and is shown to maintain the same performance, of the order of 1.2 m rms height accuracy on the Landes data set.

CP from space at P-band was shown to have a good potential for forest monitoring, with its advantages over FP being a wider swath and a larger range of incidence angles over which it can operate. Given an adequate hardware design, which is not very far from the FP standard implementation, the system could accommodate both FP and CP modes.

ACKNOWLEDGMENT

The authors would like to thank K. Raney and A. Freeman for the constructive discussions that started in Frascati during PolInSAR 2007 and are still ongoing. They would also like to express their deep appreciation to the three reviewers for suggestions that markedly improved the manuscript. They would also like to thank the RAMSES team who acquired and processed the data, and I. Champion from the French agronomical research institute, INRA for sharing her great knowledge in the forest.

REFERENCES

[1] J. C. Souyris, P. Imbo, R. Fjortoft, S. Mingot, and J. S. Lee, "Compact polarimetry based on symmetry properties of geophysical media: The $\pi/4$ mode," *IEEE Trans. Geosci. Remote Sens.*, vol. 43, no. 3, pp. 634–646, Mar. 2005.

[2] J. C. Souyris, N. Stacy, T. Ainsworth, J. S. Lee, and P. Dubois-Fernandez, "SAR compact polarimetry for Earth observation and planetology: Concepts and challenges," in *Proc. POLINSAR*, Frascati, Italy, 2007, p. 90.

[3] K. Raney, "Hybrid polarimetric SAR architecture," *IEEE Trans. Geosci. Remote Sens.*, vol. 45, no. 11, pp. 3397–3404, Nov. 2007.

[4] K. Raney, "Dual-polarized SAR and stokes parameters," *IEEE Geosci. Remote Sens. Lett.*, vol. 3, no. 3, pp. 317–319, Jul. 2006.

[5] N. Stacy and M. Preiss, "Compact polarimetric analysis of X band SAR data," in *Proc. EUSAR*, Dresden, Germany, 2006.

[6] T. Ainsworth, M. Preiss, N. Stacy, M. Nord, and J. S. Lee, "Analysis of compact polarimetric SAR imaging modes," in *Proc. POLINSAR*, Frascati, Italy, 2007.

[7] S. R. Cloude and K. Papathanassiou, "A three stage inversion process for polarimetric SAR interferometry," *Proc. Inst. Electr. Eng.—Radar, Sonar Navig.*, vol. 150, no. 3, pp. 125–134, Jun. 2003.

[8] H. Zebker and J. J. van Zyl, "Imaging radar polarimetry: A review," *Proc. IEEE*, vol. 79, no. 11, pp. 1583–1606, Nov. 1991.

[9] P. A. Wright, S. Quegan, N. S. Wheadon, and C. D. Hall, "Faraday rotation effects on L-band spaceborne SAR data," *IEEE Trans. Geosci. Remote Sens.*, vol. 41, no. 12, pp. 2735–2744, Dec. 2003.

[10] G. Seeber, *Satellite Geodesy: Foundations, Methods & Applications*. New York: Walter de Gruyter, 1993.

[11] JPL-GPS networks and ionospheric systems development. [Online]. Available: http://iono.jpl.nasa.gov/

[12] A. Freeman and S. Saatchi, "On the detection of Faraday rotation in linearly polarized L-band SAR backscatter signatures," *IEEE Trans. Geosci. Remote Sens.*, vol. 42, no. 8, pp. 1607–1616, Aug. 2004.

[13] F. Meyer, R. Bamler, N. Jakowski, and T. Fritz, "The potential of low-frequency SAR systems for mapping ionospheric TEC distributions," *IEEE Geosci. Remote Sens. Lett.*, vol. 3, no. 4, pp. 560–564, Oct. 2006.

[14] S. V. Nghiem, S. H. Yueh, R. Kwok, and F. Li, "Symmetry properties in polarimetric remote sensing," *Radio Sci.*, vol. 27, no. 5, pp. 693–711, Sep./Oct. 1992.

[15] A. Freeman and S. L. Durden, "A three-component scattering model for polarimetric SAR data," *IEEE Trans. Geosci. Remote Sens.*, vol. 36, no. 3, pp. 963–973, May 1998.

[16] T. Le Toan, S. Quegan, I. Woodward, M. Lomas, N. Delbart, and G. Picard, "Relating radar remote sensing of biomass to modelling of forest carbon budgets," *J. Clim. Change*, vol. 67, no. 2, pp. 379–402, Dec. 2004.

[17] T. Le Toan, A. Beaudoin, J. Riom, and D. Guyon, "Relating forest biomass to SAR data," *IEEE Trans. Geosci. Remote Sens.*, vol. 30, no. 2, pp. 403–411, Mar. 1992.

[18] M. C. Dobson, F. Ulaby, T. Le Toan, A. Beaudoin, E. Kasischke, and N. Christensen, "Dependence of radar backscatter on coniferous forest biomass," *IEEE Trans. Geosci. Remote Sens.*, vol. 30, no. 2, pp. 412–415, Mar. 1992.

[19] R. N. Treuhaft, S. N. Madsen, M. Moghaddam, and J. J. van Zyl, "Vegetation characteristics and underlying topography from interferometric radar," *Radio Sci.*, vol. 31, no. 6, pp. 1449–1485, Nov./Dec. 1996.

[20] K. Papathanassiou, "Polarimetric SAR interferometry," Ph.D. dissertation, Univ. Graz, Graz, Austria, 1999.

[21] A. Freeman, "Calibration of linearly polarized polarimetric SAR data subject to Faraday rotation," *IEEE Trans. Geosci. Remote Sens.*, vol. 42, no. 8, pp. 1617–1624, Aug. 2004.

[22] S. Quegan, "A unified algorithm for phase and cross-talk calibration of polarimetric data—Theory and observations," *IEEE Trans. Geosci. Remote Sens.*, vol. 32, no. 1, pp. 89–99, Jan. 1994.

[23] K. Raney, "Comments on hybrid-polarity SAR architecture," in *Proc. IGARSS*, Barcelona, Spain, 2007, pp. 2229–2231.

[24] S. Yueh, R. West, F. K. Li, and W. Tsai, "Dual-polarized Ku-band backscatter signatures of hurricane ocean winds," *IEEE Trans. Geosci. Remote Sens.*, vol. 38, no. 1, pp. 73–88, Jan. 2000.

Pascale C. Dubois-Fernandez (A'04–M'04–SM'04) received the Diplôme d'Ingenieur degree from the Ecole Nationale Supérieure d'Ingénieur de Constructions Aéronautiques, Toulouse, France, in 1983, and the M.S. and Eng. degrees from the California Institute of Technology, Pasadena, in 1984 and 1986, respectively.

She was with the Radar Science and Technology Group at the Jet Propulsion Laboratory, Pasadena, where she stayed for ten years, participating in numerous programs like Magellan, AIRSAR, and SIR-C. She then moved back to France, where she worked on cartographic applications of satellite data. In 2000, she joined the Department of Electromagnetism and Radar, Office National d'Études et de Recherches Aérospatiales (ONERA), Salon de Provence, France, the French Aeronautics and Aerospace Research Institute, where she has been involved in the ONERA SAR airborne platform, RAMSES, developing science applications as the SAR civilian remote-sensing expert.

Jean-Claude Souyris received the Engineering degree in electronics from the Ecole Nationale Supérieure d'Electrotechnique, d'Electronique, d'Informatique, d'Hydraulique et des Télécommunications, Toulouse, France, in 1989 and the Ph.D. degree from the Université Paul Sabatier, Toulouse, in 1992.

In 1993, he was with the Remote Sensing Group, Centre d'Etudes Spatiales des Rayonnements, Toulouse. In 1994, he was a Visiting Scientist with the Center for Electromagnetic Theory and Applications, Massachusetts Institute of Technology, Cambridge. From 1995 to 1997, he was a Research Associate with the Centre d'Études Spatiales de la Biosphére, Toulouse. Since 1997, he has been with Centre National d'Études Spatiales, Toulouse, where he is currently the Head of the Altimetry and Radar Department. He coauthored with Dr. Didier Massonnet a book entitled *Imaging With Synthetic Aperture Radar* (EPFL Press, 2008). His research interests include theory and applications of SAR polarimetry and interferometry, radar image analysis, and radar altimetry.

Dr. Souyris served as the Technical Chairman of the 2003 International Geoscience and Remote Sensing Symposium, Toulouse. He is an Associate Editor of the IEEE GEOSCIENCE AND REMOTE SENSING LETTERS.

Sébastien Angelliaume received the Engineering degree from the Ecole Nationale Supérieure d'Ingénieur de Constructions Aéronautiques, Toulouse, France, and the M.S. degree from the Ecole Nationale Supérieure d'Electrotechnique, d'Electronique, d'Informatique, d'Hydraulique et des Télécommunications, Toulouse, both in 2003.

Since 2006, he has been with the Department of Electromagnetism and Radar, Office National d'Études et de Recherches Aérospatiales (ONERA), Salon de Provence, France. He has been involved in the ONERA SAR airborne platform RAMSES and SETHI, developing science applications.

Franck Garestier received the M.Sc. degree in geology–geophysics from the Université Paul Sabatier, Toulouse, France, in 2002 and the Ph.D. degree in SAR remote sensing from the Université de Bordeaux, Office National d'Études et de Recherches Aérospatiales, Bordeaux, France, in 2006.

He is currently with the Centre d'Etudes Spatiales de la Biosphére, Toulouse, to work on forestry applications using low-frequency SAR data. His research interests concern vegetation physical parameter estimation using advanced SAR techniques (polarimetry, interferometry, and PolInSAR), including data calibration, vegetation modeling, inversion algorithm development, and spaceborne condition investigation.

remote sensing

MDPI

Article

Modeling the Amplitude Distribution of Radar Sea Clutter

Sébastien Angelliaume [1,*], Luke Rosenberg [2] and Matthew Ritchie [3]

[1] DEMR, ONERA, F-13661 Salon CEDEX Air, France
[2] Defence Science and Technology Group, Edinburgh SA 5111, Australia; Luke.Rosenberg@dst.defence.gov.au
[3] Electrical and Electronic Engineering Department, University College, London WC1E 6EA, UK; m.ritchie@ucl.ac.uk
* Correspondence: Sebastien.Angelliaume@onera.fr; Tel.: +33-4-9017-6512

Received: 19 December 2018; Accepted: 31 January 2019; Published: 6 February 2019

Abstract: Ship detection in the maritime domain is best performed with radar due to its ability to surveil wide areas and operate in almost any weather condition or time of day. Many common detection schemes require an accurate model of the amplitude distribution of radar echoes backscattered by the ocean surface. This paper presents a review of select amplitude distributions from the literature and their ability to represent data from several different radar systems operating from 1 GHz to 10 GHz. These include the K distribution, arguably the most popular model from the literature as well as the Pareto, K+Rayleigh, and the trimodal discrete (3MD) distributions. The models are evaluated with radar data collected from a ground-based bistatic radar system and two experimental airborne radars. These data sets cover a wide range of frequencies (L-, S-, and X-band), and different collection geometries and sea conditions. To guide the selection of the most appropriate model, two goodness of fit metrics are used, the Bhattacharyya distance which measures the overall distribution error and the threshold error which quantifies mismatch in the distribution tail. Together, they allow a quantitative evaluation of each distribution to accurately model radar sea clutter for the purpose of radar ship detection.

Keywords: radar; sea clutter; statistical analysis; amplitude distribution; K; Pareto; Rayleigh; 3MD

1. Introduction

In an operational context, radar sensors are a powerful tool for detecting targets in the maritime environment as they can be used at any time of day and in almost any weather condition [1]. They typically operate with an electromagnetic frequency between 1 and 15 GHz by exploiting the fact that man-made targets scatter with a higher energy compared to the surrounding sea. Maritime surveillance radars typically operate at low grazing angles where the mean power of the sea clutter is smallest. However, sea clutter collected from this geometry also contains many "sea-spikes" which manifest as undesired strong returns and are often the cause of false detections [2]. This is due to the scattering caused by discrete returns and breaking waves/whitecaps, which are worse when a swell is present [3], or when the radar has a high range resolution and/or horizontal polarization [4].

Many detection methods have been published in the literature, for a review the reader is referred to [1] and [5]. They work by comparing the average value of the backscattered signal with a reference value estimated over a target-free area. Due to the randomness and the spatial variability of the sea clutter, a reasonable sized data region must be used to provide an accurate estimate of the amplitude statistics and enable the detection of targets with low reflectivity. Consider the synthetic aperture radar (SAR) image shown in Figure 1 which was collected by SETHI [6], the airborne remote sensing radar developed by ONERA (see Section 4.3). The statistics of the backscattered signal were computed over

a target-free sea surface (blue box) and over an area containing a ship (red box). By visualizing the complementary cumulative distribution function (CCDF), Figure 2 highlights the impact of the target on the signal statistics. A strong deviation is shown in the tail of the distribution, compared to that obtained when no target is present.

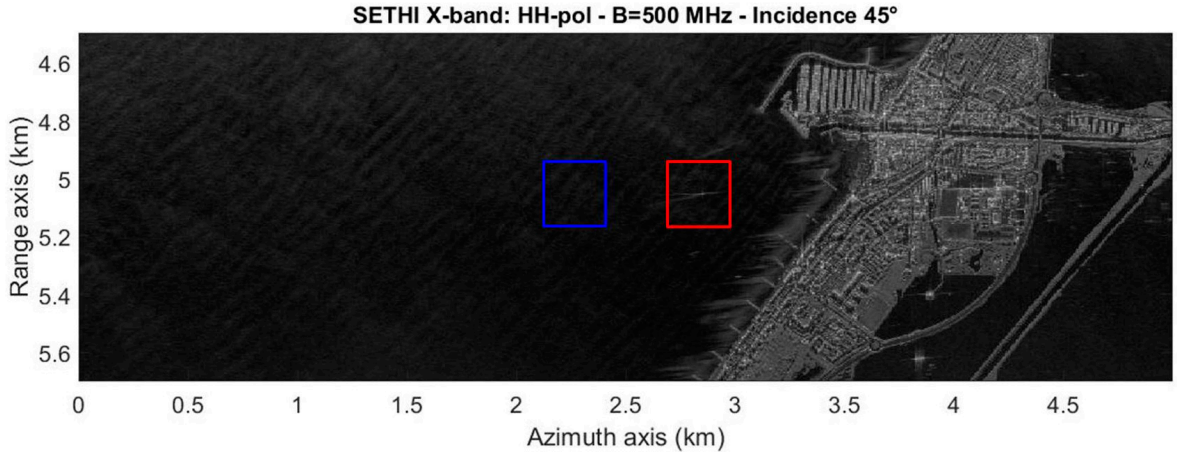

Figure 1. Illustration of an X-band SAR image in the Mediterranean Sea—blue box: target free area, red box: sea surface including a ship.

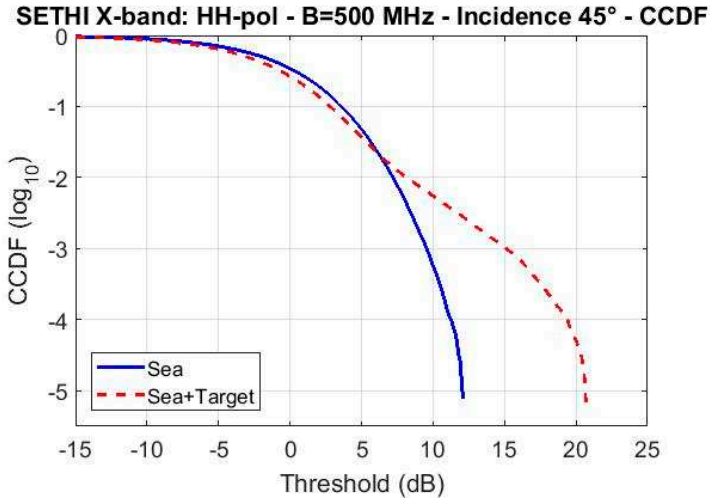

Figure 2. CCDF computed over the two areas shown in Figure 1—blue box: target free area, red box: sea surface including a ship.

Target detection is typically approached with a constant false alarm rate (CFAR) scheme [1,3] and the selection of a threshold which limits the number of false alarms, while maintaining a desired probability of detection. This can be achieved by fitting a theoretical amplitude distribution or probability density function (PDF) to the target-free radar backscatter. This also allows for much lower false alarm rates to be used when there is insufficient data. Also, the presence of a maritime target usually manifests itself in the tail of the radar distribution due to its higher amplitude return.

There has been a long development of PDF models used to fit both real aperture radar and SAR. With coarse range resolution, a reasonable model for the sea-clutter PDF is the Rayleigh distribution [7]. As the range resolution becomes finer, the variation of the sea swell is better resolved and the effect of sea-spikes becomes more pronounced. From a statistical point-of-view, sea-spikes produce a non-Gaussian 'long'-tailed, or 'spiky' distribution [4,7]. These radar returns have a larger magnitude which has led to the development of PDF models with longer tails such as the log-normal [8] and Weibull [9] distributions. A popular and widely used framework for developing PDF models is

the compound Gaussian model which was originally proposed for use in sea-clutter by Ward [3]. This model includes a temporal or fast varying component known as speckle which relates to the Bragg scattering (Bragg scattering occurs when the radar wavelength is resonant with the sea wave), and a slowly varying component which captures the underlying swell and models the texture. The most popular compound model in the literature is the K distribution [3,10,11] and its extended version which accounts for the radar instrument noise, namely the K+Noise [3]. Similarly, the Pareto distribution [12,13] and its extended version, the Pareto+Noise [14] has become popular due to its ability to model the extended tail of the amplitude distribution. In this paper, we consider these distributions as well as two others proposed in the literature, the K+Rayleigh [15,16] and the 3MD distributions [17]. The latter distribution has demonstrated great potential for modeling SAR sea-clutter and is unique in the way it models the sea clutter texture as a combination of discrete components.

While there are many studies in the literature looking at the suitability of PDF models to represent radar sea clutter, few contain a quantitative evaluation of the accuracy in fitting the amplitude distribution. The main contribution of this paper is an analysis of the most recent and effective theoretical models for modeling non-Gaussian distributed sea clutter. This is achieved using fine resolution datasets from a ground based bistatic radar and two airborne radars operating at different frequency bands (L-, S-, and X-band), and covering a wide range of sea states and geometries. This builds on the earlier study in [11] by expanding the range of measurement configurations and amplitude distribution models. To assess performance, two metrics are used to quantitatively evaluate the ability for each model to represent the sea clutter amplitude distribution.

The paper is organized as follows: Section 2 describes the goodness of fit metrics, Section 3 summarizes the theoretical distributions, and Section 4 describes the data sets. Section 5 then summarizes the results and concludes by identifying the most suitable distribution to model the sea clutter.

2. Measures of Goodness of Fit

The aim of this paper is to evaluate the accuracy of different PDF models for modeling radar sea clutter. To quantitatively measure how well a model fits actual observations, there are many statistical tests in the literature [11]. In this paper, we focus on two goodness of fit measures: the Bhattacharyya distance (BD) and the threshold error. These metrics will be measured for the three radar datasets covering a wide variety of wind speeds, collection geometries, frequencies, and polarizations.

2.1. The Bhattacharyya Distance

The Bhattacharyya distance is a metric which varies between 0 and infinity [18]. It measures the similarity between the theoretical PDF $P(.)$ and the actual data distribution $Q(.)$ computed over the same data samples, x_k. The Bhattacharyya distance is commonly used to evaluate the accuracy of statistical distributions to represent experimental data.

$$BD = -\ln\left(\sum_{x_k}\sqrt{P(x_k)Q(x_k)}\right) \quad 0 \leq BD \leq \infty \tag{1}$$

The smaller the Bhattacharyya distance, the better the goodness of fit and thus the accuracy of the model to represent the radar sea clutter.

2.2. Threshold Error

The second metric is the threshold error which is determined by first calculating the CCDF for both the empirical data and the proposed model. The threshold error is then the difference between the two results at a fixed CCDF value, often 10^{-4} or lower, depending on operational requirements [19]. The CCDF is important due to its relationship with the threshold in a detection scheme used for distinguishing between targets and interference. In this context, it is commonly

referred to as the probability of false alarm. This measure is illustrated in Figure 3 for a CCDF of 10^{-4} (see red arrows). The threshold error is computed on the x-axis by measuring the difference between the actual CCDF (blue line) and the modeled CCDF (green line). The smaller this gap, the better the goodness of fit between the data and the model. This is a useful practical metric as it defines how far over or under estimated a CFAR threshold would be set when the distribution of the sea clutter is incorrectly estimated.

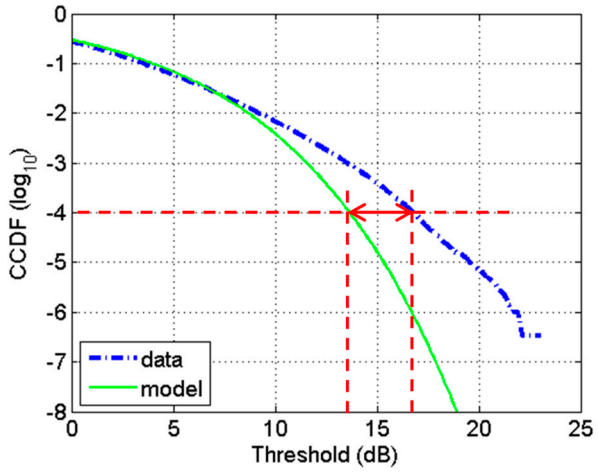

Figure 3. Measurement of the threshold error at 10^{-4} between the actual CCDF (blue thick dotted line) and the model CCDF (green line).

3. Amplitude Distribution Models

In this section, we outline the four distributions used for our analysis: K+noise, Pareto+Noise, K+Rayleigh and 3MD. As these are all compound distributions, we start by outlining the development of such models. Consider a radar receiving in-phase and quadrature data from an external clutter source with its amplitude defined by Gaussian statistics with zero mean and variance, x. In addition, instrument noise from the radar will add a component p_n which is included by offsetting the variance x.

In target detection analysis, the envelope of the received pulses is often converted to power (square law) and the clutter distribution becomes exponential. This component is known as speckle in the compound representation. For a frequency agile or scanning radar with sufficient time between looks, a common method to improve the detection performance is to sum a number of looks. If there are M independent exponential random variables, $z = \sum_{m=1}^{M} y_m$, then the received power is described by a gamma PDF,

$$P(z|x) = \frac{z^{M-1}}{(x+\sigma_n^2)^M \Gamma(M)} \exp\left[-\frac{z}{x+\sigma_n^2}\right] \tag{2}$$

where $0 \leq x \leq \infty$, $\Gamma(.)$ is the gamma function and σ_n^2 is the instrument noise power. In order to include the texture component which modulates the speckle, we integrate over the speckle mean,

$$P(z) = \int_0^\infty P(z|x)P(x)dx \tag{3}$$

where $P(x)$ is the distribution of the texture component. While there are analytic solutions in many cases, when instrument noise is included in the model, numerical integration must be used to evaluate the compound distribution. In the following, only single-look intensity data is considered with the data represented in decibels (dBs).

The parameters of the K+Noise, Pareto+Noise, and K+Rayleigh distributions are estimated using the zlogz method which has demonstrated the best tradeoff for accuracy and computational efficiency [20]. However, for the 3MD distribution, there is no suitable zlogz estimator and the model parameters are estimated using a least squares minimization between the CCDF of the data and the

model. This is a more computationally intensive parameter estimation approach. To quantify the difference in run time, 100 iterations were performed and the run times averaged. For the K+Noise, Pareto+Noise, and K+Rayleigh zlogz estimators, the mean run times were 0.13, 0.12, and 0.13 s respectively, while for the 3MD least squares minimization, the mean run time was 1.57 s, which is approximately 12 times longer than the zlogz estimators.

3.1. K+Noise Distribution

The K+Noise (KN) distribution is a well-established model for representing high-resolution radar sea clutter [3,7]. It is a continuous mixture of an exponential or gamma distribution for the uncorrelated speckle intensity (fast temporal variation) with a gamma distribution for the clutter mean power (slow spatial variation) [3,21],

$$P(x) = \frac{b^{\nu}}{\Gamma(\nu)} x^{\nu-1} \exp[-bx] \tag{4}$$

where $\nu > 0$ and $b = \nu / p_c$ are the shape and scale parameters respectively and p_c is the mean clutter power. In the absence of instrument noise, $p_n = 0$ and the solution to (3) is given by

$$P(z) = \frac{2(bz)^{\frac{\nu+M}{2}}}{z\Gamma(\nu)\Gamma(M)} K_{\nu-M}\left(2\sqrt{bz}\right) \tag{5}$$

where $K_{\nu-M}(.)$ is the modified Bessel function of the second kind with order $\nu - M$. The zlogz estimator for the shape is found by numerically solving the following equation for $\hat{\nu}$ [20],

$$\frac{E(z\log z)}{E(z)} - E(\log z) - \frac{1}{M} = \frac{1}{1+1/C} e^{\hat{\nu}/C} G_{\hat{\nu}+1}(\hat{\nu}/C) \tag{6}$$

where $E(.)$ is the statistical mean or expectation operator, C is the clutter to noise ratio (CNR) and $G(.)$ is the generalized exponential integral function [20].

3.2. Pareto+Noise Distribution

The Pareto+Noise (PN) distribution is another popular compound distribution used to model the sea-clutter backscatter [14]. It is formed with an inverse gamma distribution for the texture

$$P(x) = \frac{d^{a}}{\Gamma(a)} x^{-a-1} \exp[-d/x] \tag{7}$$

where a and $d = p_c(a-1)$ are the shape and scale parameters respectively. Similar to the K+Noise distribution, there is no closed form expression unless the mean instrument noise power, $p_n = 0$. In this case, the Pareto distribution is given by

$$P(z) = \frac{z^{M-1} d^{a} \Gamma(M+a)}{(d+z)^{M+a} \Gamma(\nu)\Gamma(M)} \tag{8}$$

For the Pareto+Noise distribution, the zlogz estimator for the shape is found by numerically solving the following equation for $\hat{a}$ [20],

$$\frac{E(z\log z)}{E(z)} - E(\log z) - \frac{1}{M} = \frac{1}{1+\frac{1}{C}} \left(\frac{1}{\hat{a}-1} - e^{(\hat{a}-1)C} G_{\hat{a}}((\hat{a}-1)C \right) \tag{9}$$

3.3. K+Rayleigh Distribution

The K+Rayleigh (KR) distribution is an extension to the KN model designed to capture any extra Rayleigh component in the data which arises from the non-Bragg scattering [16]. It explicitly separates

the speckle mean level into two components, $x = x_r + p_r$, where p_r is the power of the extra Rayleigh component. As with the KN model, the texture is given by a gamma distribution,

$$P(x_r) = \frac{b_r^{\nu_r}}{\Gamma(\nu_r)} x_r^{\nu_r - 1} \exp[-bx_r] \tag{10}$$

where $\nu_r > 0$ and $b_r = \nu_r / p_c$ are the shape and scale parameters respectively. The PDF of the KR distribution has no closed-form expression and is calculated by integrating (3) with respect to the modified speckle mean level, x_r instead of the total speckle x. The influence of the extra Rayleigh component can be measured by the ratio of the mean of the Rayleigh component, p_r, to the mean of the gamma distributed component, p_c, of the clutter and is defined by

$$k_r = \frac{p_r}{p_c} \tag{11}$$

To estimate the KR parameters, the sum of the instrument noise power and Rayleigh power needs to be estimated in addition to the shape. This is achieved by first substituting the CNR in (6) with the clutter to noise plus Rayleigh power, $\hat{C}$, using the following relationship for the distribution moments,

$$\hat{C} = \frac{p_c}{p_r + p_n} = \frac{1}{\frac{1}{\sqrt{\hat{\nu}_r r}} + 1} \tag{12}$$

where

$$r = \frac{M}{M+1} \frac{E(z^2)}{E^2(z)} - 1 \tag{13}$$

and then solving the numerical relation in (6). The Rayleigh mean power can then be found by rearranging (12),

$$p_r = \frac{p_c}{\hat{C}} - p_n \tag{14}$$

3.4. Tri-Modal Discrete Distribution

The compound models presented previously all assume a continuous texture distribution which suggests a small probability of infinite texture values. The motivation of the 3MD model is to instead use a discrete texture model that assumes the sea clutter consists of a finite number, I, of distinct modes or scatterer types [17]. This implies that the scatterers in the observed scene are realizations from homogeneous clutter random variables with different texture values. The PDF of the texture is given by

$$P(x) = \sum_{n=1}^{I} c_n \delta(x - a_n), \quad \sum_{n=1}^{I} c_n = 1, \quad a_n, c_n > 0 \tag{15}$$

$$\delta(A) := \begin{cases} 1 & \text{if } A = 0 \\ 0 & \text{otherwise} \end{cases} \tag{16}$$

where $a = [a_1, \ldots, a_I]$ are the discrete intensity texture levels and $c = [c_1, \ldots, c_I]$ are the corresponding weightings. The resulting PDF after solving (3) is then given by

$$P(z) = \frac{M^M}{\Gamma(M)} z^{M-1} \sum_{n=1}^{I} c_n \frac{\exp\left(-\frac{Mz}{\rho_c a_n^2 + \rho_n}\right)}{(\rho_c a_n^2 + \rho_n)^M} \tag{17}$$

with

$$\rho_c + \rho_n = \frac{p_c}{p_c + p_n} + \frac{p_n}{p_c + p_n} = 1 \tag{18}$$

In their original work [17], the authors have reported that $I = 3$ modes are sufficient to accurately model high spatial resolution sea clutter data collected by spaceborne SAR sensors. One of the consequences of this discretization is that spatial and long-time correlation cannot be modeled as part of the texture, and hence the model is less suitable for clutter simulation. The 3MD distribution also requires the non-trivial estimation of $2I$ unknown parameters. This can be achieved with a least squares minimization between the 3MD model and data CCDF in the log domain. The fitting process first assumes a single mode ($I = 1$). If the BD of that fit is greater than -30 dB, the parameters for a bi-modal fit ($I = 2$) are then estimated. This is repeated up to the maximum number of modes, which is set to $I = 5$ unless otherwise stated. The model components, a_n, are then ordered from largest to smallest and any modes where the weightings, $c_n < 10^{-3}$ are removed. Note that the threshold value of BD = -30 dB comes from experimental observation below which there is little change in the 3MD distribution.

4. Radar Sea Clutter Datasets

Three sea clutter datasets are used in this paper to evaluate the accuracy of the proposed PDF models. These have been collected by different radar sensors operating at different frequency bands (L-, S-, and X-band), different platforms (airborne and ground-based) and covering a wide range of sea state and geometries. Two of the data sets are from a real beam radar, while the third comprises images formed from a synthetic aperture radar.

4.1. NetRAD Dataset: Ground Based Radar Sensor

The Netted Radar (NetRAD) is a ground-based coherent bistatic radar system operating at S-band (carrier frequency of 2.45 GHz) [22,23]. The system was developed jointly by the University College London, UK and the University of Cape Town, South Africa. It works in both monostatic and bistatic configurations with the two nodes synchronized in time with GPS disciplined oscillators over a 5 GHz wireless link. The system configuration used for gathering the data analyzed included a peak transmit power of 57.7 dBm, pulse repetition frequency (PRF) of 1 kHz, antenna gain of 23.8 dBi, and a bandwidth of 45 MHz providing a range resolution of 3.3 m. The antennas work with either vertical (V) or horizontal polarizations (H).

The data assessed here is summarized in Table 1 and was generated during a 2010 series of trials in South Africa near the Cape Point area. The baselines between each of two radar nodes and the illuminated area were 1830 m and in order to vary the bistatic angle, the antennas were rotated to cover different regions of the sea. The grazing angles from the geometries varied from 0.6° to 1.5° [23], which will have a minor impact on the backscattered signal compared to changes with the polarization or the bistatic angle. In the following analysis, 10 s of data have been used for each run, resulting in more than 10^6 samples. Wind and wave information is given in Table 1 and was obtained from the Cape Point wave buoy, approximately 7 km from the trial location. In Figure 4, an example of the monostatic and bistatic radar data is displayed for a bistatic angle of 60°.

Table 1. Properties of the NetRAD radar sea clutter acquisitions investigated in this study.

Run	Frequency	Pol.	Bistatic Angle (°)	Wind Speed (m/s)	Wave Period (s)	Wave Direction (°)	Wave Height (m)
1	S-band	VV	60	10	7.1	289	3.3
2			90	10	7.7	279	3.5
3			120	11	8.3	270	3.7
4		HH	60	11	8.3	283	3.9
5			90	11	8.3	283	3.9
6			120	12	8.6	276	4.0

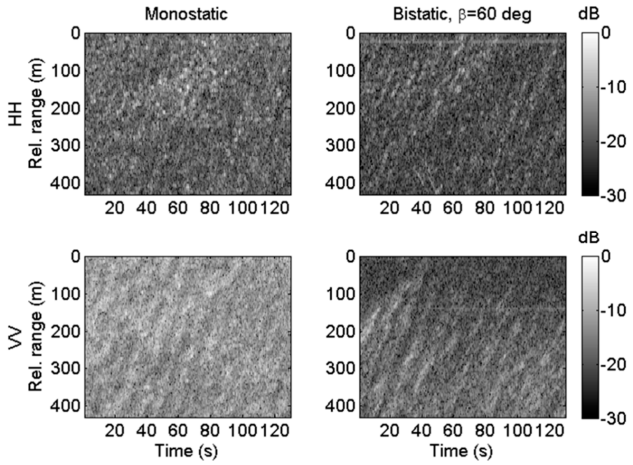

Figure 4. NetRAD: S-band time domain intensity images, monostatic (left), and bistatic 60° (right) for HH (top) and VV (bottom) polarizations.

4.2. INGARA Dataset: Airborne Radar Sensor

INGARA is a polarimetric radar system maintained and operated within the Defence Science and Technology Group in Australia [24]. During the ocean backscatter collections in 2004 and 2006, the sea clutter data was collected at X-band (10.1 GHz carrier frequency) with a 200 MHz bandwidth giving a 0.75 m range resolution. Alternate pulses transmitted horizontal and vertical polarizations resulting in a nominal PRF of 300 Hz. The radar was operated in a circular spotlight-mode covering 360° of azimuth angles and each day, the radar platform performed at least six full orbits around the same patch of ocean to cover a large portion of grazing angles between 15° and 45°.

During the trials at sea, the wind and wave information was collected using DST Group's wave buoy, which was located within 50 km of the imaging site. Wind data from several different sources were collected and compared during the trials. For the 2004 trial, the most reliable wind data were obtained from the Bureau of Meteorology automatic weather station located on a cliff top about 50 km northeast of the wave buoy deployment site. Hence, it will be subjected to some error and, possibly a time delay compared with the actual conditions at the wave buoy site. For the 2006 trial, the most reliable wind data were made with a handheld anemometer on a boat near the imaging area.

Table 2 shows the sea conditions over the two data collections, with Runs 1–8 from the 2004 collection and Runs 9–12 from 2006. The data analyzed in this paper has been pooled into blocks of 5° azimuth and 3° grazing with each block containing approximately 10^6 samples. An example of the data is shown in Figure 5 for the downwind direction and 30° grazing.

Table 2. Properties of the INGARA radar sea clutter acquisitions investigated in this study.

Run	Frequency	Pol.	Wind Direction (°)	Wind Speed (m/s)	Wave Period (s)	Wave Direction (°)	Wave Height (m)
1	X-band	Quad-pol	248	10.2	12.3	220	4.9
2			248	7.9	11.8	205	3.5
3			315	10.3	10.4	210	2.6
4			0	13.6	8.8	293	3.2
5			68	9.3	9.7	169	2.5
6			315	9.5	11.4	234	3.0
7			22	13.2	12.2	254	3.8
8			0	8.5	12.5	243	4.3
9			115	8.5	3.1	112	0.62
10			66	3.6	2.6	35	0.25
11			83	3.5	4.0	46	0.41
12			124	10.2	4.6	128	1.21

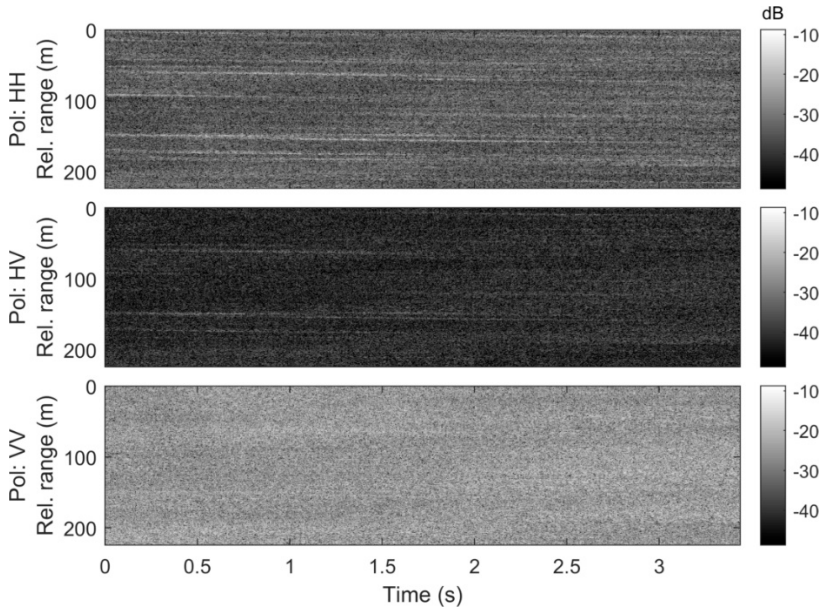

Figure 5. INGARA range/time example (Run 3), downwind, grazing angle 30°, wind speed 10.3 m/s.

4.3. SETHI Dataset: Airborne Imaging Radar Sensor

SETHI is the airborne remote sensing radar developed by ONERA [6]. It is a pod-based multi-frequency high resolution SAR system designed to explore the scientific applications of remote sensing. Both L- and X-band SAR data have been collected at two different geographical positions, the Atlantic ocean and the Mediteranean sea along the French coast. The bandwidths are 300 MHz at X-band (9.6–9.9 GHz) and 150 MHz at L-band (1.25–1.4 GHz). The data presented in this paper is described in Table 3 and covers grazing angles from 10° to 45°, different sea states (significant wave heights from 1.1 to 4.9 m), a range of azimuth angles and either dual-polarized (HH, VV) or quad-polarized (HH, HV, VH, VV) antenna combinations. The flying trajectory was either linear (stripmap mode) or circular (spotlight mode) and the wind and wave information given in Table 3 was obtained from Météo-France, the French national meteorological service. An illustration of the X-band dual-pol SAR data at 10° grazing is given in Figure 6 (Run 3) where the horizontal and vertical axes correspond to the along-track (azimuth) and across-track (range) directions. Strong differences in radar responses can be seen as a function of the polarization state: the HH backscattered signal (Figure 6a) is strongly affected by sea-spikes (e.g., breaking waves), while the VV signal (Figure 6b) is dominated by short scale waves [25].

Table 3. Properties of the SETHI data sets. Both the range and azimuth spatial resolutions are equal.

Run	Frequency	Pol.	Area	Spatial Res. (m)	Grazing Angle (°)	Wind Speed (m/s)	Wave Height (m/s)
1	X-band	Dual-pol	Atl.	0.5	10	17.65	4.9
2				0.5	20	17.65	4.9
3				0.5	10	7.2	3.3
4				0.5	20	7.2	3.3
5				0.5	30	7.2	3.3
6	X-band L-band	Dual-pol		0.5 1	20	10.2	3.6
7	X-band	Dual-pol		0.5	10	10.1	3.6
8	X-band L-band	Quad-pol	Med.	0.5 1	45	8.5	1.1

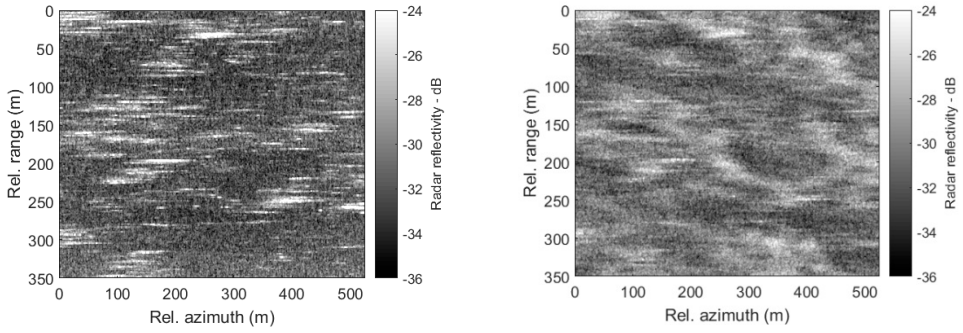

Figure 6. SETHI X-band SAR images (Run 3), grazing angle 10°, wind speed 7 m/s. (**a**) HH polarization, (**b**) VV polarization.

5. Results and Discussions

This section provides an analysis of the four amplitude PDF models applied to the NetRAD, INGARA, and SETHI datasets. For each result, the data is plotted in a thick blue dotted line, while the cyan, black, green, and red lines are for the K+Noise (KN), Pareto+Noise (PN), K+Rayleigh (KR), and 3MD models respectively. The PDF curves represent the probability of occurrence of radar intensity values (in dBs), while the CCDF curves show the probability that the radar intensity takes a value greather than the threshold (see Section 2.2). Both the Bhattacharyya distance and the threshold errors are provided for each example and reported in dBs.

5.1. NetRAD Analysis

In this section, we investigate the accuracy of the theoretical models to represent the NetRAD bi-static dataset. We first show an example of the model fits and report on the number of modes required by the 3MD model. We then study the model accuracy using the goodness of fit metrics, focusing firstly on the overall PDF fit and then the tail of the distribution.

The example in Figure 7 shows the results for Run 4 of the NetRAD bistatic data which has HH polarization and a bistatic angle of 60°. For this result, the 3MD model has been fitted to the data with $I = 5$ modes. The parameter estimates are given in Table 4, while the BD and threshold error results are given in Table 5. For the KN and KR distributions we observe a strong mismatch in the body of the distribution (Figure 7a) with high BD values (Table 5), while the PN and 3MD models fit the data closely over all intensity values. However, the CCDF fits in Figure 7b clearly shows that the KN and the PN distributions both have a mismatch in modeling the distribution by under and over estimating the tail respectively, while the 3MD and the KR both match closely. This is reflected in the threshold error values in Table 5.

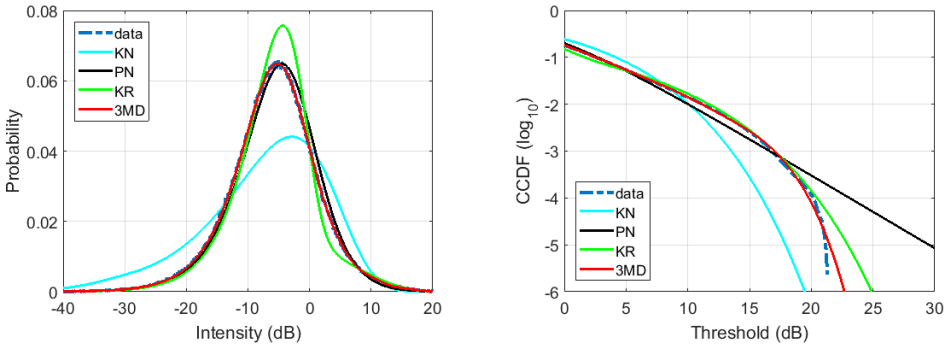

Figure 7. Amplitude distributions for the NetRAD data (Run 4): S-band, HH-polarization, bistatic acquisition, bistatic angle 60°. Illustrations show the (**a**) PDF, (**b**) CCDF.

Table 4. Parameter estimates for the models in Figure 7.

CNR (dB)	28.9
KN shape	0.58
PN shape	1.6
K+Rayleigh shape	0.04
K+Rayleigh k_r—value	0.41
3MD mode 1 (a, c)	(0.458, 0.379)
3MD mode 2 (a, c)	(0.682, 0.345)
3MD mode 3 (a, c)	(1.163, 0.220)
3MD mode 4 (a, c)	(2.334, 0.0488)
3MD mode 5 (a, c)	(5.463, 0.0064)

Table 5. Goodness of fit metrics for the models in Figure 7. Threshold error is measured at a CCDF of 10^{-4}.

	BD (dB)	Threshold Error (dB)
KN	−15.65	5.17
PN	−31.55	−1.73
KR	−22.75	−0.02
3MD	−37.31	0.11

5.1.1. Number of Modes Required for the 3MD Distribution

In previous work, it has been reported that three modes are sufficient to accurately model amplitude distributions from spaceborne SAR data [17], airborne SETHI SAR data, and airborne INGARA real aperture sea clutter data [26]. We now investigate how many modes of the 3MD distribution are required to accurately model the mono and bistatic sea clutter from the NetRAD dataset.

As discussed in Section 3.4, the minimum number of modes required for a good fit is determined when the BD goes below the desired value of −30 dB. Figure 8 shows an example model fit from the NetRAD bistatic data with 60° bistatic angle and VV polarization (Run 1) with different numbers of components, I. The BD for both polarizations is then shown in Figure 9 where we observe that four modes are required to satisfy the condition that the BD is less than −30 dB.

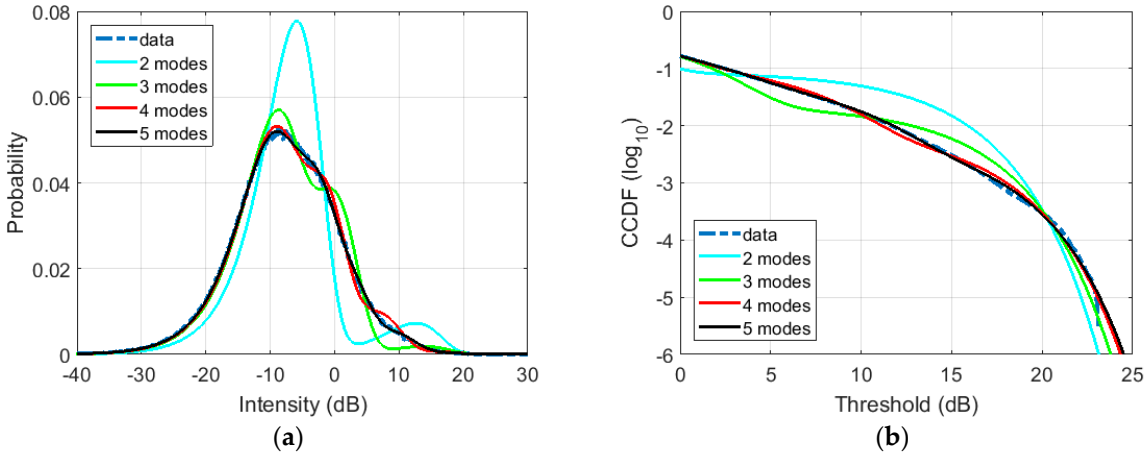

Figure 8. Model fits for the 3MD distribution with different numbers of modes using the NetRAD data S-band, VV-polarization, bistatic configuration, 60° bistatic angle (Run 1). Illustrations show the (**a**) PDF, (**b**) CCDF.

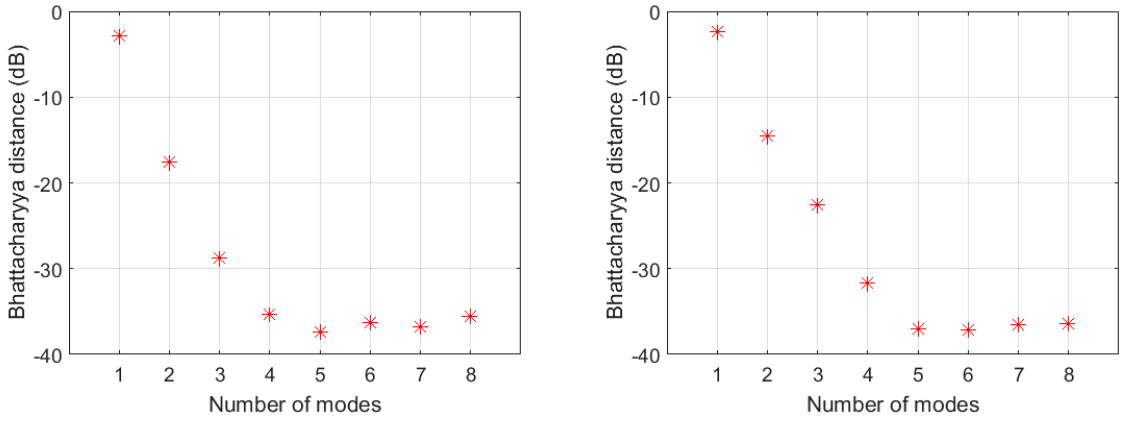

Figure 9. Bhattacharyya distance (dB scale) for the 3MD distribution using different numbers of modes with the NetRAD data, S-band, bistatic configuration, 60° bistatic angle. (**a**) HH polarization (Run 4), (**b**) VV polarization (Run 1).

Table 6 summarizes the minimum number of modes required by the NetRAD data. Among the 12 datasets (monostatic and bistatic), 7 need 2 or 3 modes (which is in agreement with [17,26]), but we find that 5 datasets need 4 or 5 modes. The link between the number of modes and the acquisition parameters are not obvious from the available data and further study is required to fully understand this relationship. Nevertheless, we have demonstrated that the 3MD distribution is able to accurately model the amplitude distribution of each of the NetRAD datasets, but at the cost of a greater number of parameters to estimate, 2*I*.

Table 6. 3MD distribution: minimum number of modes required to accurately match the NetRAD data.

Bistatic Angle	Polarization			
	HH		VV	
	Monostatic	Bistatic	Monostatic	Bistatic
60	4	4	3	4
90	4	3	2	5
120	3	3	2	3

5.1.2. Analysis of Model Accuracy

In this section we study the accuracy of the four models described in Section 3 when fitting amplitude distributions to the NetRAD dataset. Figure 10 first shows the BD for each bistatic angle and polarization. The only result that shows a good match for nearly every model (BD ≤ -30 dB) is the monostatic case with VV polarization (Figure 10c). However, it is only the 3MD distribution that has a consistently low BD over all the datasets. The other results are mixed with the PN and KR models both providing a good fit with some datasets, while mismatching with others (BD > -30 dB). The KN model nearly always fails to accurately fit the data.

Results of the threshold error for a CCDF of 10^{-4} are then displayed in Figure 11, where low errors are observed for both the KR and 3MD models ($<\pm 1$ dB), while the PN and KN distributions have a greater mismatch with errors up to ± 4 dB. If the PN distribution was used in a detection scheme with such a large mismatch, there will be a large number of missed detections. Conversely, if the KN distribution were used, there would be a higher probability of false alarm.

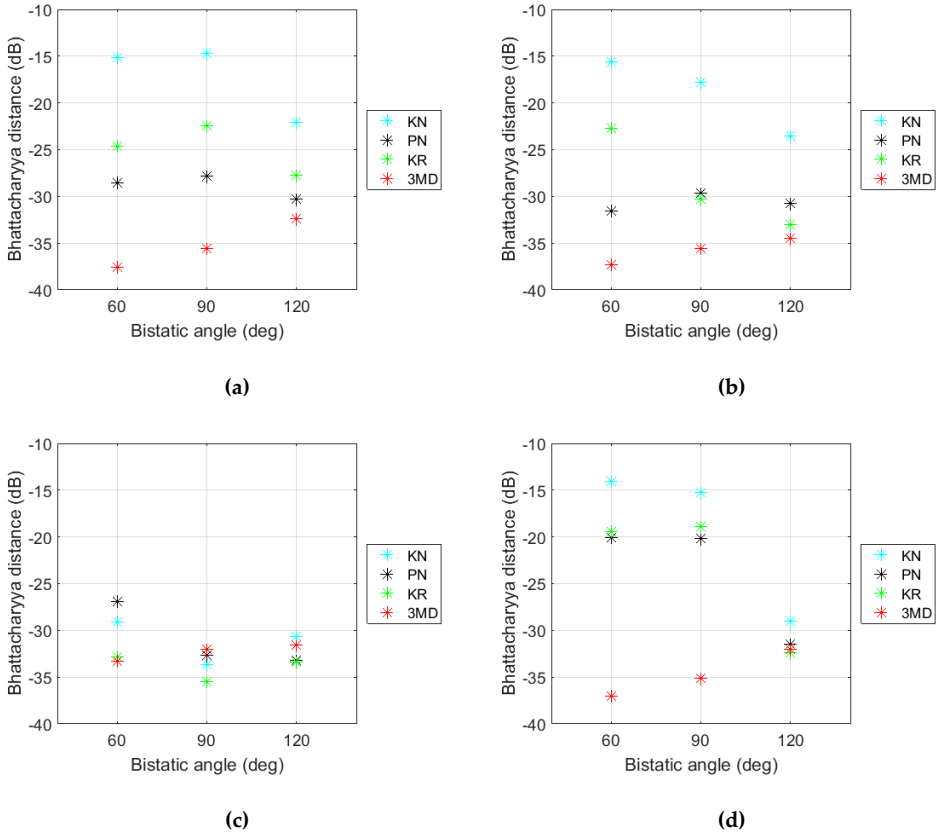

Figure 10. NetRAD S-band: Bhattacharyya distance (in dBs) for the NetRAD data. (**a**) HH polarization, monostatic, (**b**) HH polarization, bistatic, (**c**) VV polarization, monostatic, (**d**) VV polarization, bistatic.

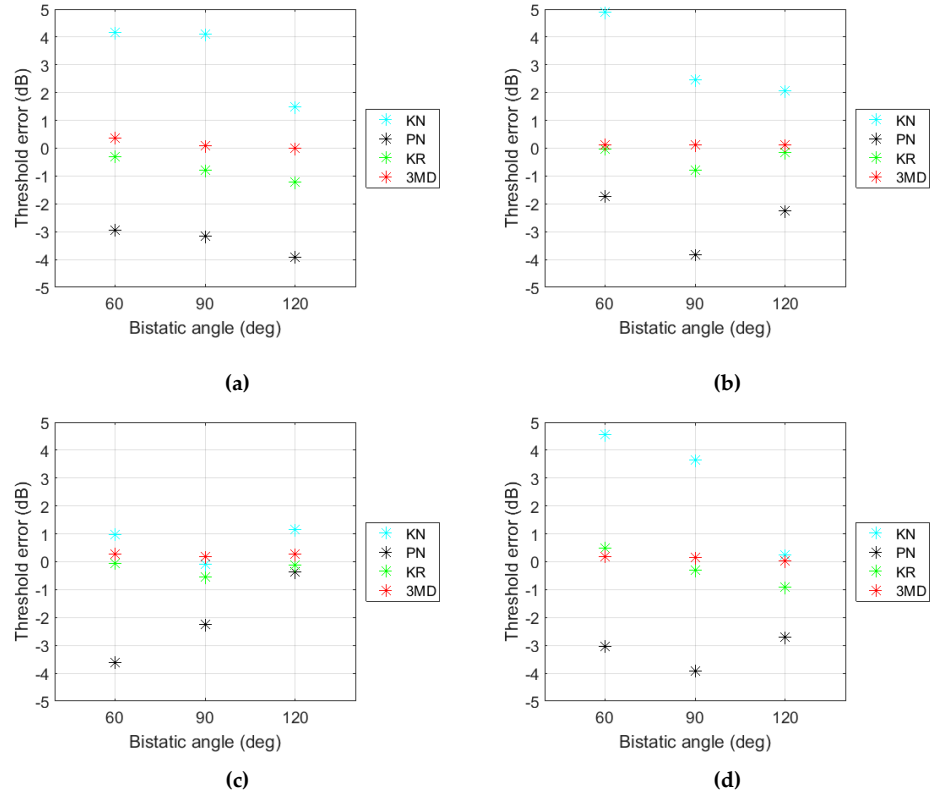

Figure 11. NetRAD S-band: Threshold error for a CCDF of 10^{-4}. (**a**) HH polarization, monostatic, (**b**) HH polarization, bistatic, (**c**) VV polarization, monostatic, (**d**) VV polarization, bistatic.

5.1.3. Summary

Analysis of the NetRAD S-band monostatic and bistatic sea clutter dataset demonstrates that both the KN and PN distributions fail to match the data in many cases and would provide degraded detection performance if used in a detection scheme. However, the KR and 3MD distributions show a good match in the tail region, making them a good choice. When considering the total fit to both the body and distribution tail, it is only the 3MD model that is able to consistently provide good results, but at the cost of a higher number of parameters to be estimated.

5.2. Analysis of the INGARA Dataset

We now consider how the different distributions can model the INGARA sea clutter data set. Firstly, we give some illustrations of the proposed models with an example run. We then study the behavior of the texture for the 3MD model over a range of geometries. Finally, we look at the model accuracy for fitting each distribution to the INGARA dataset.

Two example datasets, Runs 3 and 9 are first considered with the respective sea conditions given in Table 2. Figure 12 shows the model fits for Run 3 in the upwind direction and 30° grazing. These results show the KN under fitting the HH polarization and the PN over fitting for each result. The KR model has a good fit until a CCDF value of 10^{-4}, while the 3MD shows an excellent fit for all results. The estimated model parameters and goodness of fit metrics are given in Tables 7 and 8 respectively.

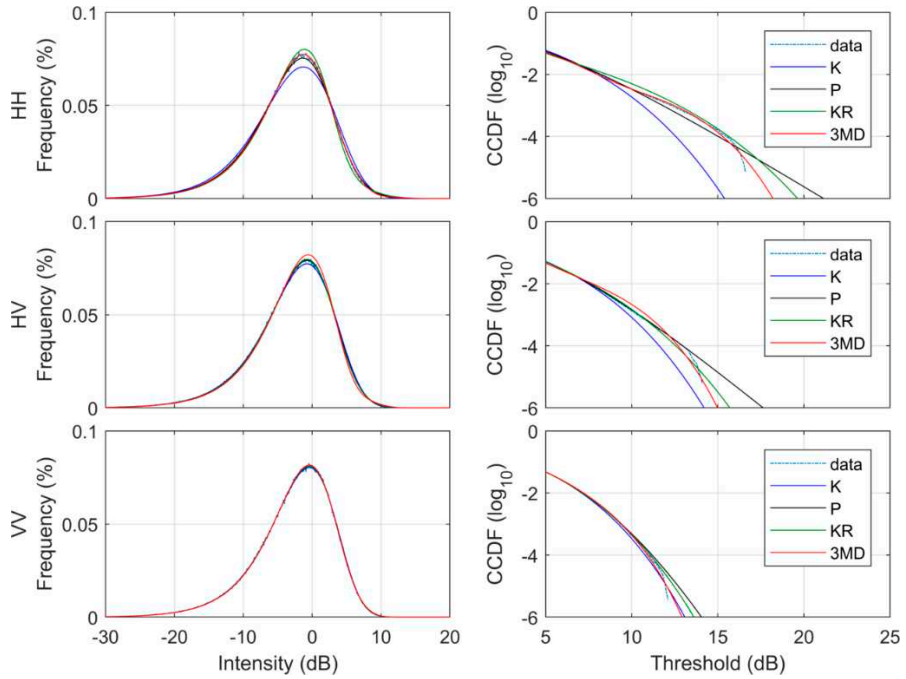

Figure 12. Amplitude distributions for the INGARA dataset (Run 3), upwind, grazing angle 30°. Illustrations show the (**left**) PDF and (**right**) CCDF results.

Table 7. Parameter estimates for the model fits in Figure 12.

Run 3	Polarization		
	HH	**HV**	**VV**
CNR (dB)	11.7	6.5	21.6
KN shape	2.3	3.5	7.0
PN shape	3.4	4.7	8.0
K+Rayleigh shape	0.34	1.9	7.1
K+Rayleigh k_r—value	0.49	0.19	0
3MD mode 1 (a, c)	(0.70, 0.49)	(0.82, 0.74)	(0.82, 0.55)
3MD mode 2 (a, c)	(1.12, 0.47)	(1.42, 0.26)	(1.19, 0.45)
3MD mode 3 (a, c)	(2.11, 0.038)	-	-

Table 8. Goodness of fit metrics for the model fits in Figure 12. Threshold error is measured at a CCDF of 10^{-4}.

	BD (dB)			Threshold Error (dB)		
	HH	**HV**	**VV**	**HH**	**HV**	**VV**
KN	−30.7	−36.5	−36.0	1.6	0.2	−0.3
PN	−36.1	−35.1	−34.9	−0.8	−1.1	−0.9
KR	−35.1	−36.6	−36.0	−0.2	−0.1	−0.3
3MD	−36.5	−35.0	−36.0	0.1	0.2	0.1

5.2.1. Parameter Variation for the 3MD Distribution

In order to further study the modes of the 3MD model, we compare the product of the texture locations a_n and the proportion c_n [17]. For INGARA Runs 3 and 9, Figures 13 and 14 show this result for each polarization, over all azimuth angles and grazing angles from 15° to 45°. The dashed lines indicate either missing data or regions where no mode was required for the model fit. To achieve a BD lower than −30 dB, at least two modes were required for each polarization, with 53% and 20% of the HH data blocks requiring three. These latter data blocks are primarily in the low grazing angle region in the HH polarization where there is an even proportion spread between the first two modes ($a_n c_n \sim 0.5$). Although not shown here, this result matches where the KR shape value is lowest indicating the spikiest clutter [26].

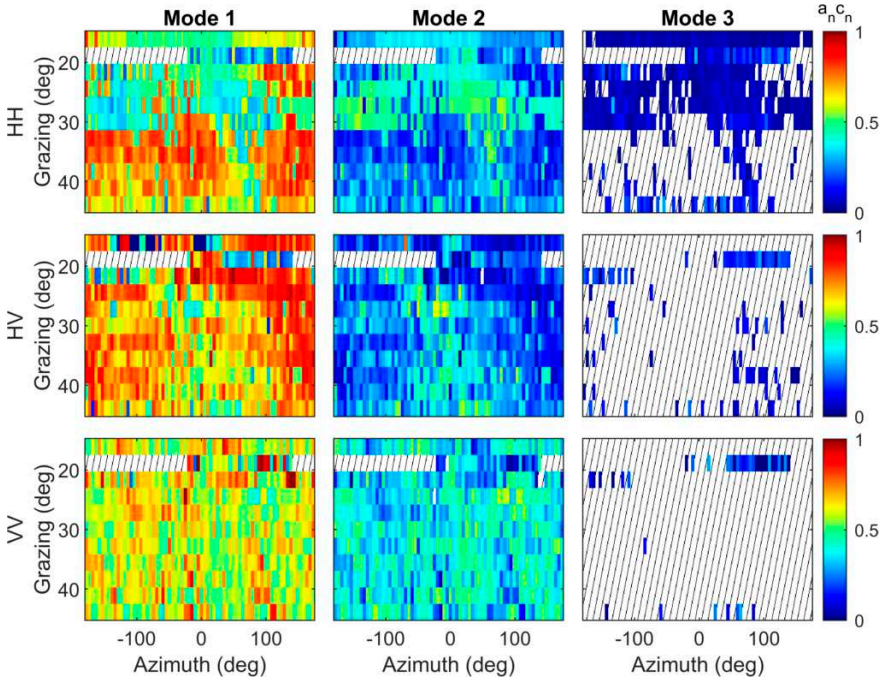

Figure 13. 3MD distribution parameters ($a_n c_n$) for the INGARA dataset, Run 3.

5.2.2. Analysis of Model Accuracy

To determine the accuracy of the model fits over the two data runs, the BD and threshold errors at a CCDF value of 10^{-4} have been measured for all data blocks with the results shown as histograms in Figures 15 and 16. For the BD, the biggest variation is seen for the HH polarization with the KN distribution having the highest value (worst fit) for Run 3 followed closely by the 3MD distribution. Note that the BD values for the 3MD distribution are nearly always less than −30 dB which is our stopping criteria for the model fit. The other two distributions, KR and PN have very similar results spread between −40 to −30 dB.

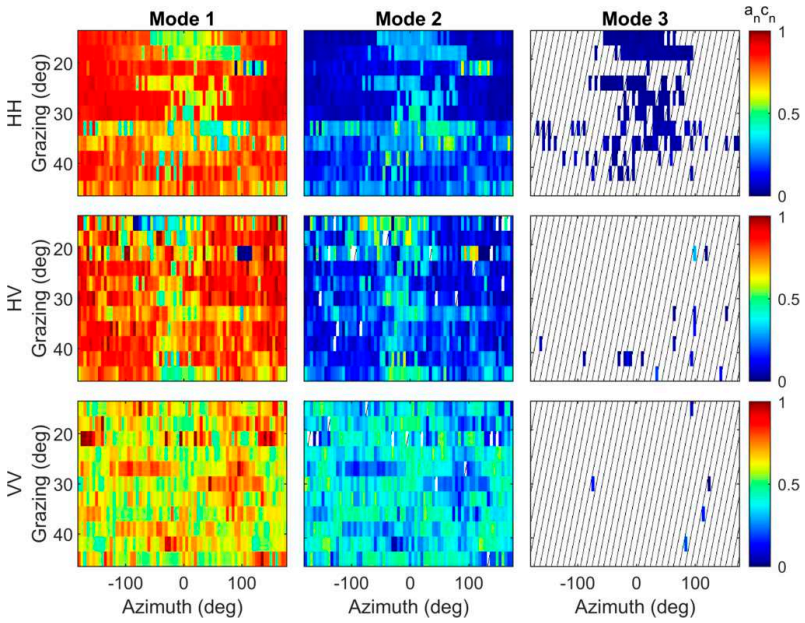

Figure 14. 3MD distribution parameters ($a_n c_n$) for the INGARA dataset, Run 9.

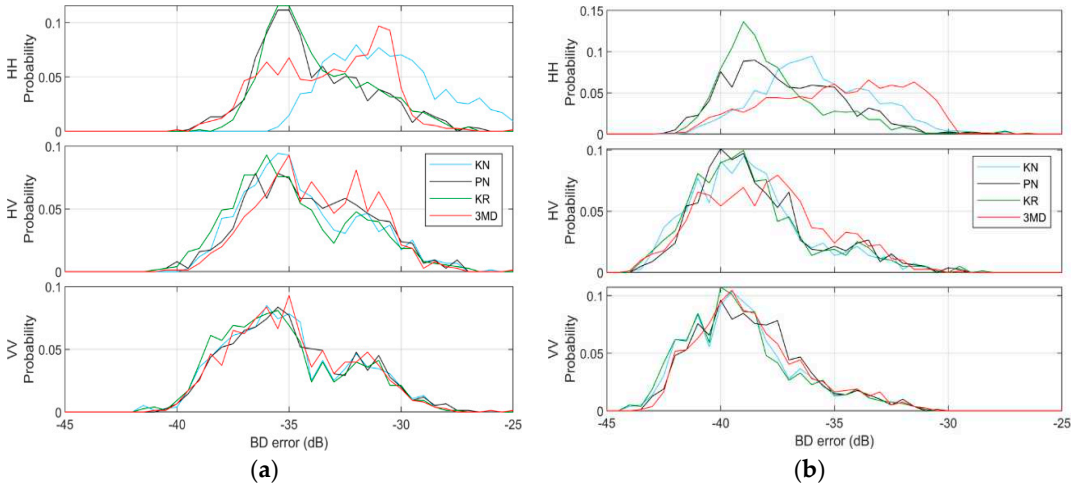

Figure 15. BD histograms for INGARA Runs 3 and 9. (**a**) Run 3, (**b**) Run 9.

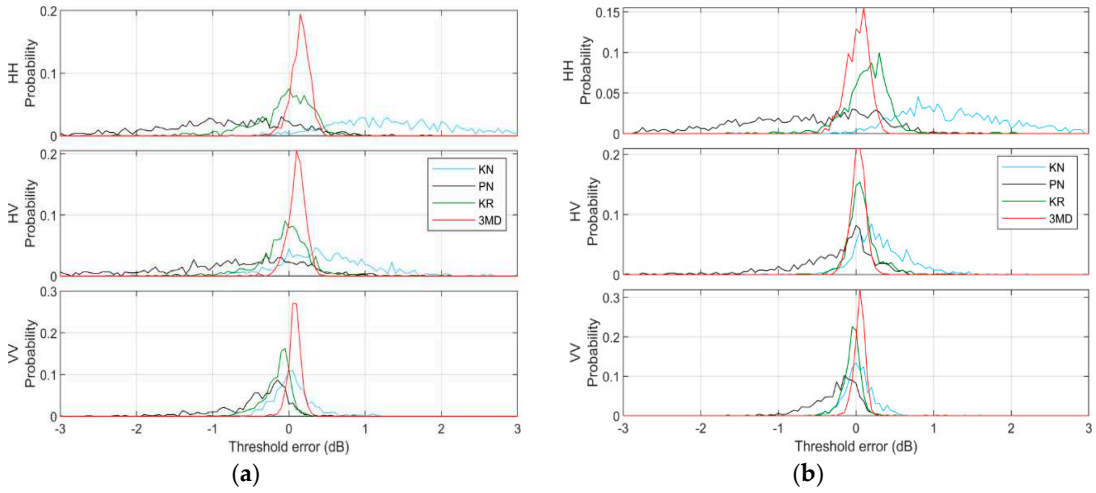

Figure 16. Threshold error histograms for INGARA Runs 3 and 9. Threshold error is measured at a CCDF of 10^{-4}. (**a**) Run 3, (**b**) Run 9.

For the threshold error in Figure 16, the 3MD distribution clearly has the lowest error with very little bias around 0 dB. The KR distribution also has a low error spread, while the KN and PN show a wide range of threshold errors. Figure 17 then shows the threshold errors over the 12 different days/wind speeds in the upwind direction for grazing angles of 15°, 30°, and 45°. The same spread of errors are observed here with a large mismatch for the KN and PN distributions with mean absolute values of 0.76 and 0.89 dB respectively, while the KR and 3MD models show the lowest absolute mean errors of 0.30 and 0.11 dB. The largest errors were observed within the HH polarization at the lowest grazing angles for the PN and KN models, while data from the VV polarization showed a significantly reduced threshold error across all grazing angles.

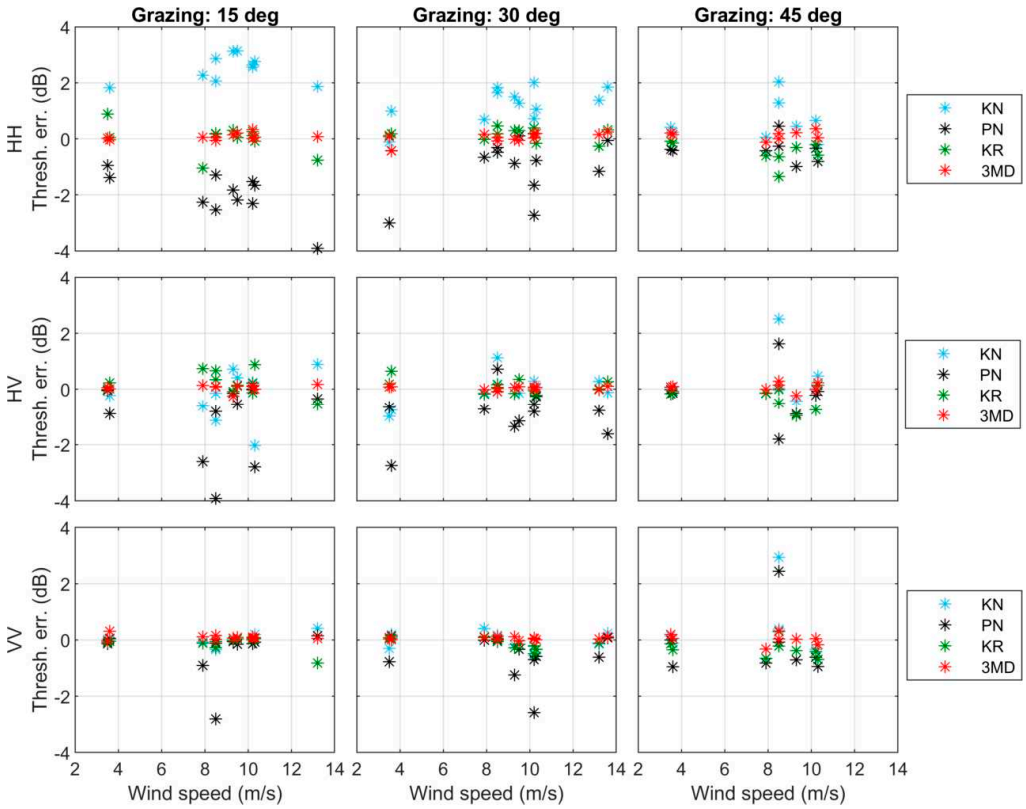

Figure 17. Threshold error against windspeed in the upwind direction for the INGARA dataset. Threshold error is measured at a CCDF of 10^{-4}.

5.2.3. Summary

The results for the INGARA sea clutter data set show that the 3MD distribution produces the best match with the data set over a wide range of collection geometries and sea conditions, with at most three modes required. The KR distribution provides a reasonable match in the body of the distribution, but has a slightly higher threshold error and hence mismatch in the tail of the distribution. The PN and KN distributions produce the worst match, particularly in the HH polarization.

5.3. Analysis of the SETHI Dataset

This section now looks at results from the SETHI SAR dataset. We first show illustrations of model fitting with X-band SAR data and then study the model accuracy when representing real SAR data with varying geometry and sea state.

Examples of the model fits are shown in Figure 18 from Run 1 (see Table 3) at a grazing angle of 10° and a high sea state (wind speed of 17 m/s). For the HH polarization, the KN distribution deviates from the data PDF, while the PN, KR, and 3MD models show close agreeement to the real data (Figure 18a). In the tail of the distribution (Figure 18b), the KR and 3MD models show a good

match the data, while the KN and PN both show mismatch. For the VV polarization (Figure 18c–d), we observe an overall good agreement between the data and the models, except for the PN distribution which over estimates the distribution tail (Figure 18d). Tables 9 and 10 show the model parameters and goodness of fit metrics for these results.

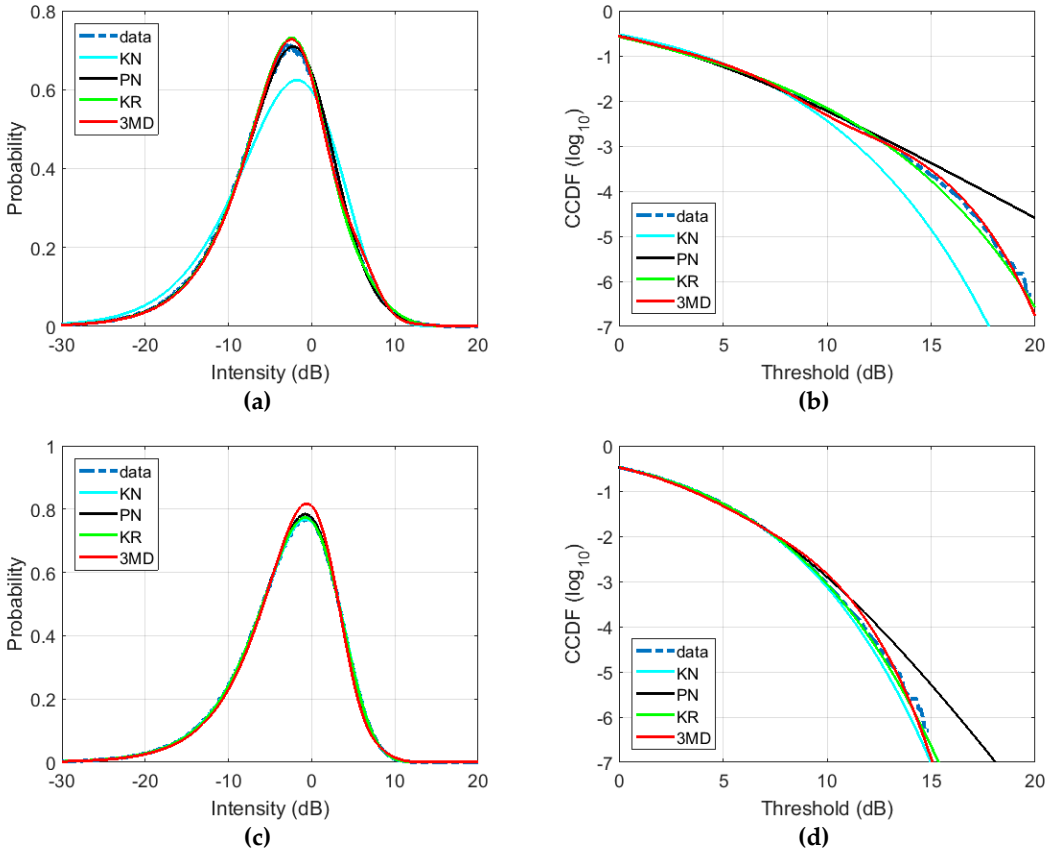

Figure 18. Amplitude distributions of the SETHI dataset, (Run 1), grazing angle 10°, wind speed 17 m/s. (**a**) HH polarization PDF, (**b**) HH polarization CCDF, (**c**) VV polarization PDF, (**d**) VV polarization CCDF.

Table 9. Parameter estimates for the models in Figure 18.

Run 3	Polarization	
	HH	VV
CNR (dB)	12.08	16.70
KN shape	1.45	5.56
PN shape	2.44	6.56
K+Rayleigh shape	0.19	2.69
K+Rayleigh k_r—value	0.47	0.27
3MD mode 1 (a, c)	(0.68, 0.65)	(0.88, 0.795)
3MD mode 2 (a, c)	(1.29, 0.33)	(1.39, 0.205)
3MD mode 3 (a, c)	(2.92, 0.02)	-

Table 10. Goodness of fit metrics for the model fits in Figure 18. Threshold error is measured at a CCDF of 10^{-4}.

	BD (dB)		Threshold Error (dB)	
	HH	VV	HH	VV
KN	−24.5	−41.0	2.88	0.23
PN	−38.0	−39.4	−1.27	−0.68
KR	−33.5	−41.5	0.22	−0.02
3MD	−36.5	−36.1	0.15	−0.06

5.3.1. Grazing and Azimuth Angle Variation

We now look at the goodness of fit for the SETHI data as a function of grazing and azimuth angles. The first set of results are for Runs 3 to 5 (see Table 3) with grazing angles of 10°, 20°, and 30° and a wind speed of 7 m/s. Table 11 shows the Bhattacharyya distance for the four models with good results (BD ≤ -30 dB) observed. Figure 19 then shows the threshold errors for CCDF values of 10^{-4}. For the HH data, the threshold errors obtained with the KN and PN distributions decrease when the grazing angle increases, while KR and the 3MD distributions show a consistently low error. For the VV polarized radar data, the threshold errors are less than or equal to 1 dB for each model.

Table 11. SETHI X-band Run 3 (grazing 10°), Run 4 (grazing 20°), and Run 5 (grazing 30°). Bhattacharyya distance (values in dB) between experimental and fitted PDFs.

Polarization	Grazing Angle	KN	PN	KR	3MD
HH	10°	−29.9	−36.4	−36.2	−38.4
	20°	−30.4	−34.5	−38.0	−39.0
	30°	−29.2	−35.9	−36.9	−37.6
VV	10°	−40.7	−49.9	−51.7	−35.2
	20°	−37.5	−39.4	−39.7	−38.1
	30°	−34.3	−37.5	−37.9	−38.4

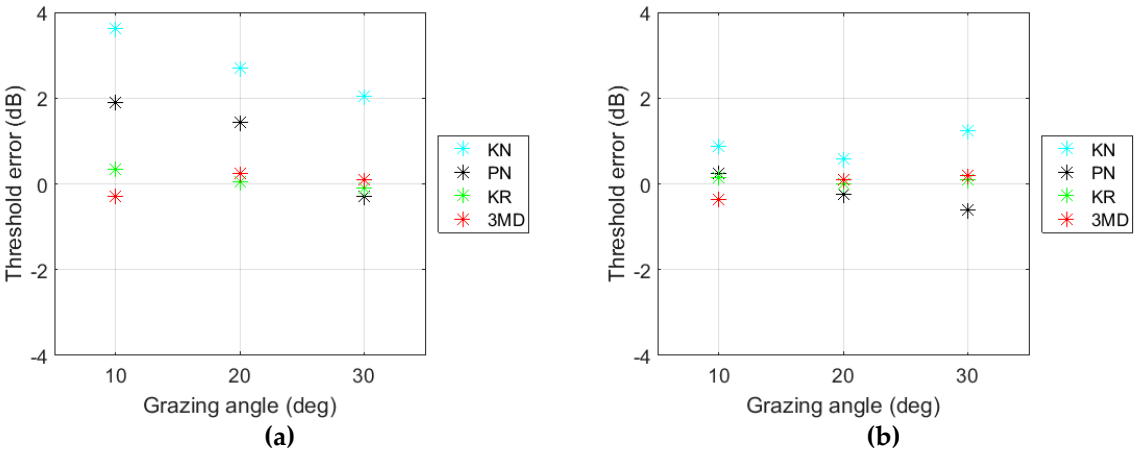

Figure 19. Threshold error with increasing grazing angle for SETHI X-band Runs 3 to 5 (wind speed 7 m/s). Threshold error is measured at a CCDF of 10^{-4}. (**a**) HH, (**b**) VV.

As with the INGARA results, there are no clear trends with the goodness of fit metrics as a function of wind direction. The next results consider the dual-frequency SAR data collected at 45° grazing and over the full 360° azimuth range (Run 8). For both the L and X-band datasets, histograms of the BD and threshold errors are shown in Figures 20 and 21 at a CCDF value of 10^{-4}. For the L-band data, the BD is low (≤ -30 dB) for the four investigated models suggesting that they all match closely to the body of distribution, regardless of the polarization state. For the X-band data, the mean BD values increase for each model with the KN distribution showing the largest increase. There is also an increase in the spread of BD values at X-band. For the threshold error results, the 3MD distribution clearly has the lowest error at both frequencies with no bias around 0 dB. We find that the KN model has under fitted both data sets, while the PN and KR histograms show an over fitting. For the KN, PN, and KR models, the threshold error increases at X-band, probably due to data being spikier.

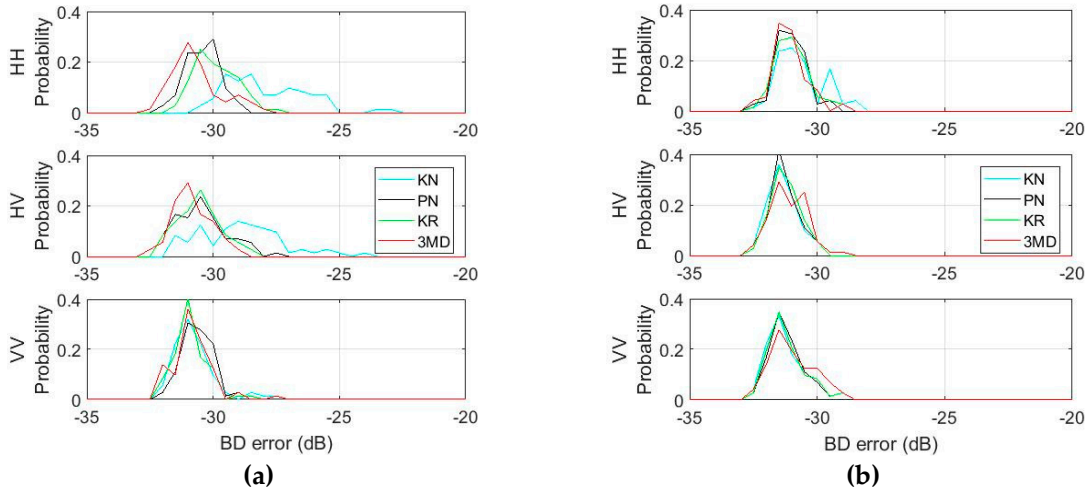

Figure 20. BD histogram for SETHI, Run 8. (**a**) X-band, (**b**) L-band.

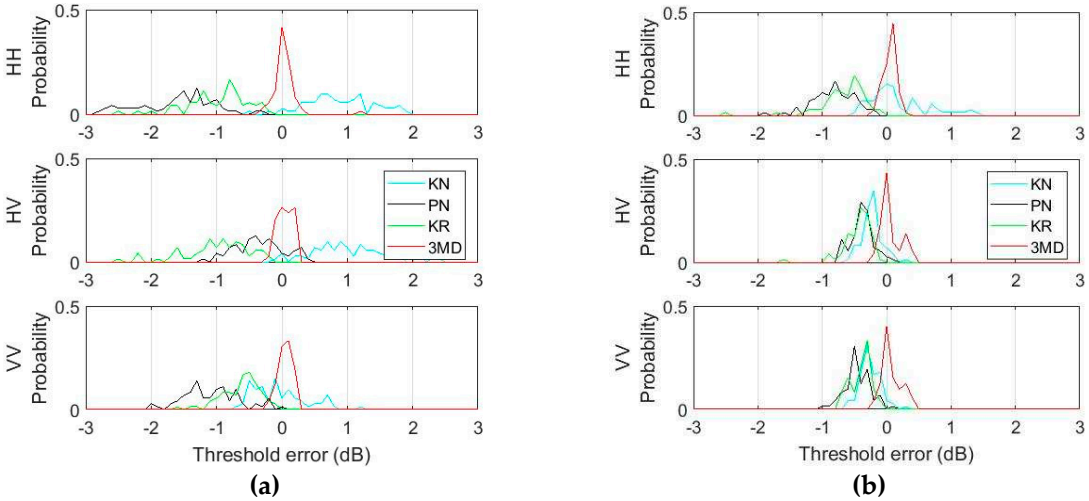

Figure 21. Threshold error histogram for SETHI, Run 8. Threshold error is measured at a CCDF of 10^{-4}. (**a**) X-band, (**b**) L-band.

5.3.2. Wind Speed Variation

The final section looks at the fitting accuracy as the wind speed varies for the SETHI dataset. For this analysis, we consider three runs with grazing angles of 10° and 20° (see Table 3) and wind speeds of 7 m/s (Runs 3 and 4), 10 m/s (Runs 6 and 7) and 17 m/s (Runs 1 and 2). As with previous results, the BD is quite low, indicating a good fit to the distribution body. There is no observed trend or increase of the BD with the wind speed and the relative ordering of the four models are also similar to the previous results with the PN, KR, and 3MD distributions all having lower values than the KN model for the HH polarization, while all four models have similar BD values close to -40 dB for the VV polarization.

The threshold error for a CCDF of 10^{-4} is shown in Figure 22 for the HH and VV polarizations and both grazing angles. These results show quite similar errors for the KR and 3MD distributions with values typically below ± 0.5 dB. There is one exception for the VV polarization with the higher wind speed and 20° grazing, where the KR model has overfitted the data. In this case, the 3MD model still produces a good fit with a low threshold error. No significant variation of the threshold error with the wind speed is observed.

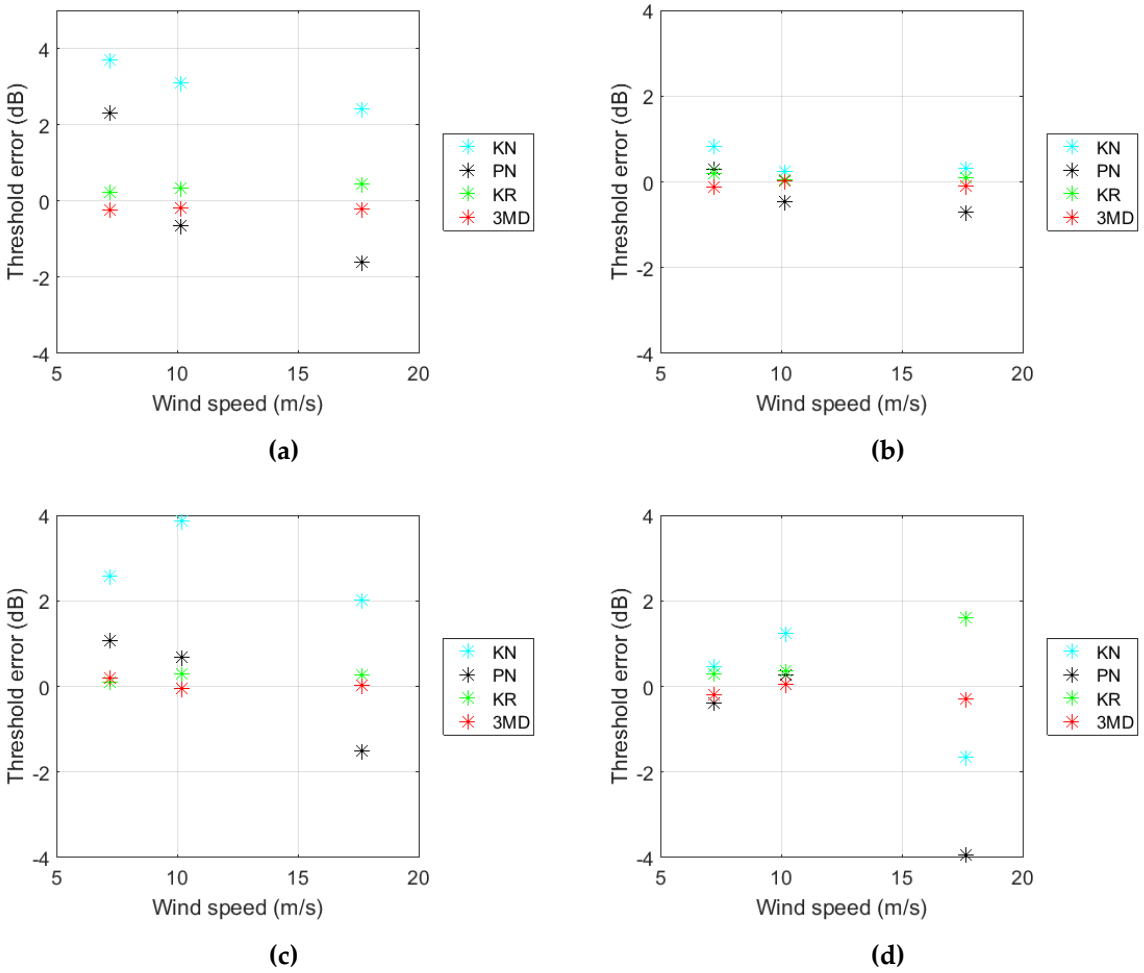

Figure 22. Threshold error against windspeed for the SETHI X-band dataset. Threshold error is measured at a CCDF of 10^{-4}. (**a**) HH polarization, 10° grazing; (**b**) VV polarization, 10° grazing; (**c**) HH polarization, 20° grazing; (**d**) VV polarization, 20° grazing.

5.3.3. Summary

Analysis of SETHI airborne SAR dataset presented in this section shows that the BD is always very low for the four investigated models, indicating that they can all accurately model the distribution body of the data. However, when we focus on the tail of the distribution, both the KR and 3MD distributions produce superior fits to the experimental data, especially for the HH polarization. Moreover, no significant variation of the threshold error with the wind speed and the angles of observation (grazing and azimuth) can be inferred from these results.

6. Conclusions

Accurately modeling the amplitude distribution of sea clutter is key to ensure good detection performance in the maritime domain. This can be a challenging task due to the wide variety of environmental conditions, collection geometries, and radar configurations. In this paper, we have evaluated the accuracy of four key amplitude distributions, the K+Noise, P+Noise, K+Rayleigh, and 3MD, in matching experimental high spatial resolution data from three different radar sensors. These include a ground-based radar collecting S-band mono- and bi-static data at very low grazing angles, an airborne sensor acquiring X-band full-polarized real aperture data and a second airborne fully-polarized SAR operating simultaneously at L- and X-band. The model accuracy was assessed using two goodness of fit measures: the Bhattacharyya distance which considered the body of the distribution, and the threshold error which focused on the tail.

The originality of the analysis is a quantitative evaluation of PDF models to represent actual radar sea clutter. This extends an earlier study [11] by expanding the range of frequency bands, collection geometries and amplitude distribution models. In Tables 12 and 13 below, a summary of the average Bhattacharyya distance and the threshold error measured at a CCDF of 10^{-4} is illustrated for each dataset. They demonstrate that both the KR and 3MD models provide a good match to the datasets studied, while the KN and PN distributions often show a mismatch. When focusing on the tail of the distribution, only the 3MD model consistently matches well, while the KR model has a slightly higher threshold error. The tradeoff with using the 3MD model is the larger number of parameters which require estimating.

Table 12. Mean values of the Bhattacharyya distance for each dataset investigated in this study.

Dataset	Polarization	Bhattacharyya Distance (Mean Value—dB)			
		KN	PN	KR	3MD
NetRAD	HH	−15.4	−23.7	−30.1	−37.5
	VV	−21.5	−23.5	−26.2	−35.2
INGARA	HH	−32.0	−34.1	−34.3	−32.8
	VV	−35.5	−35.3	−35.6	−35.4
SETHI	HH	−28.5	−37.7	−37.8	−33.2
	VV	−38.1	−40.2	−40.5	−35.2

Table 13. Mean values of the threshold error at a CCDF of 10^{-4} for each dataset investigated in this study.

Dataset	Polarization	Threshold Error (Mean Value—dB)			
		KN	PN	KR	3MD
NetRAD	HH	4.7	−2.4	−0.2	0.2
	VV	2.7	−3.3	0.2	0.1
INGARA	HH	1.4	−0.8	0.0004	0.1
	VV	0.03	−0.3	−0.1	0.05
SETHI	HH	2.7	0.7	0.3	0.1
	VV	0.3	−1.3	0.4	0.1

Since the reported data covered such a wide range of frequencies, collection geometries, and sea conditions, these conclusions give confidence that these models would be applicable over a much wider range of conditions and with different radar sensors. In future work, we will focus on the improving the usefulness of the 3MD model. This can be achieved by speeding up the parameter estimation and understanding how the model parameters can be related to our understanding of the ocean scattering.

Author Contributions: S. Angelliaume processed and analyzed the SETHI dataset; L. Rosenberg processed and analyzed the INGARA dataset; M. Ritchie processed the NetRAD dataset; S. Angelliaume analyzed the NetRAD dataset; L. Rosenberg developed the fitting methods; S. Angelliaume, L. Rosenberg, and M. Ritchie wrote and revised the paper.

Funding: This research received no external funding.

Acknowledgments: Part of this work is funded by the French Ministry of Armed Forces (DGA) under the COMAREM project run by the French Defense Procurement Agency (DGA—Direction Générale de l'Armement). One part of this project aims to improve statistics and physical modeling of the sea clutter. Research presented herein was also carried out in part under the NATO SET-185 program. The authors would like to thank all those involved with the NetRAD measurement campaign, with particular thanks to W. Al-Ashwal, S. Sandenbergh, M. Inggs and H. Griffiths.

Conflicts of Interest: The authors declare no conflict of interest.

References

1. Crisp, D.J. *The State-of-the-Art in Ship Detection in Synthetic Aperture Radar Imagery*; Research Report DSTO-RR-0272; Defence Science and Technology Organisation Australia: Fairbairn, Canberra, Australia, May 2004.
2. Rosenberg, L. Sea-spike detection in high grazing angle X-band sea clutter. *IEEE Trans. Geosci. Remote Sens.* **2013**, *51*, 4556–4562. [CrossRef]
3. Ward, K.D.; Tough, R.J.A.; Watts, S. *Sea Clutter: Scattering, the K-Distribution and Radar Performance*, 2nd ed.; The Institute of Engineering Technology UK: London, UK, 2013.
4. Posner, F.L. Spiky sea clutter at high range resolutions and very low grazing angles. *IEEE Trans. Aerosp. Electron. Syst.* **2002**, *38*, 5872. [CrossRef]
5. Fingas, M.F.; Brown, C.E. Review of ship detection from airborne platforms. *Can. J. Remote Sens.* **2001**, *27*, 379–385. [CrossRef]
6. Angelliaume, S.; Ceamanos, X.; Viallefont-Robinet, F.; Baqué, R.; Déliot, P.; Miegebielle, V. Hyperspectral and Radar Airborne Imagery over Controlled Release of Oil at Sea. *Sensors* **2017**, *17*, 1772. [CrossRef] [PubMed]
7. Jakeman, E.; Pusey, P. A model for non-Rayleigh sea echo. *IEEE Trans. Antennas Propag.* **1976**, *24*, 806–814. [CrossRef]
8. Trunk, G.V.; George, S.F. Detection of targets in non-Gaussian sea clutter. *IEEE Trans. Aerosp. Electron. Syst.* **1970**, *5*, 620–628. [CrossRef]
9. Schleher, D.C. Radar detection in Weibull Clutter. *IEEE Trans. Aerosp. Electron. Syst.* **1976**, *12*, 736–743. [CrossRef]
10. Dong, Y. *Distribution of X-Band High Resolution and High Grazing Angle Sea Clutter*; Research Report, DSTO-RR-0316; Defence Science and Technology Organisation Australia: Fairbairn, Canberra, Australia, 2006.
11. Fiche, A.; Angelliaume, S.; Rosenberg, L.; Khenchaf, A. Analysis of X-Band SAR Sea-Clutter Distributions at Different Grazing Angles. *IEEE Trans. Geosci. Remote Sens.* **2015**, *53*, 4650–4660. [CrossRef]
12. Balleri, A.; Nehorai, A.; Wang, J. Maximum likelihood estimation for compound-Gaussian clutter with inverse gamma texture. *IEEE Trans. Aerosp. Electron. Syst.* **2007**, *43*, 775–779. [CrossRef]
13. Weinberg, G.V. Assessing Pareto fit to high-resolution high-grazing angle sea clutter. *IET Electron. Lett.* **2011**, *47*, 516–517. [CrossRef]
14. Rosenberg, L.; Bocquet, S. Application of the Pareto plus noise distribution to medium grazing angle sea-clutter. *IEEE J. Sel. Top. Appl. Earth Obs. Remote Sens.* **2015**, *8*, 255–261. [CrossRef]
15. Lamont-Smith, T. Translation to the normal distribution for radar clutter. *IEE Proc. Radar Sonar Navig.* **2000**, *147*, 17–22. [CrossRef]
16. Rosenberg, L.; Watts, S.; Bocquet, S. Application of the K+Rayleigh distribution to high grazing angle sea-clutter. In Proceedings of the International Radar Conference, Lille, France, 13–17 October 2014; pp. 1–6.
17. Gierull, C.H.; Sikaneta, I. A Compound-Plus-Noise Model for Improved Vessel Detection in Non-Gaussian SAR Imagery. *IEEE Trans. Geosci. Remote Sens.* **2018**, *56*, 1444–1453. [CrossRef]
18. Kil, D.H.; Shin, F.B. *Pattern Recognition and Prediction with Applications to Signal Processing*; Springer: New York, NY, USA, 1998.
19. Rosenberg, L.; Bocquet, S. Non-coherent radar detection performance in medium grazing angle X-band sea-clutter. *IEEE Trans. Aerosp. Electron. Sens.* **2017**, *53*, 669–682. [CrossRef]
20. Bocquet, S. Parameter estimation for Pareto and K distributed clutter with noise. *IET Radar Sonar Navig.* **2015**, *9*. [CrossRef]
21. Ward, K.D. Compound representation of high resolution sea clutter. *Electron. Lett.* **1981**, *17*, 561–563. [CrossRef]
22. Derham, T.; Doughty, S.; Woodbridge, K.; Baker, C. Design and evaluation of a low-cost multistatic netted radar system. *IET Radar Sonar Navig.* **2007**, *1*, 362–368. [CrossRef]
23. Ritchie, M.; Stove, A.; Woodbridge, K.; Griffiths, H. NetRAD: Monostatic and Bistatic Sea Clutter Texture and Doppler Spectra Characterization at S-Band. *IEEE Trans. Geosci. Remote Sens.* **2016**, *54*, 5533–5543. [CrossRef]
24. Rosenberg, L.; Watts, S. *High Grazing Angle Sea-Clutter Literature Review*; General Document; DSTO-GD-0736; Defence Science and Technology Organisation Australia: Fairbairn, Canberra, Australia, March 2013.

25. Valenzuela, G.R. Theories for the interaction of electromagnetic and oceanic waves—A review. *Bound. -Layer Meteorol.* **1978**, *13*, 61–82. [CrossRef]
26. Rosenberg, L.; Angelliaume, S. Characterisation of the Tri-Modal Discrete Sea Clutter Model. In Proceedings of the International Radar Conference, Brisbane, Australia, 27–30 August 2018; pp. 1–6.

Modeling the Polarization Ratio in the Upper Microwave Band for Sea Clutter Analysis

Floriane Madeleine Schreiber, Sébastien Angelliaume, *Member, IEEE*, and Charles-Antoine Guérin, *Member, IEEE*

***Abstract*— The two-scale model (TSM) based on Bragg tilting is widely employed to model the normalized radar cross section (NRCS) from the sea surface in the microwave bands. It also leads to the compound distribution model when used to represent the distribution of intensity in high-resolution sea clutter. While the TSM satisfactorily describes the dynamical behavior of the polarized NRCS at moderate incidence angles for various sea states and radar frequencies, it fails to consistently describe the polarized sea clutter distribution in the upper microwave band. The hidden reason is an overestimation of the Bragg polarization ratio (PR) at larger local incidence angles. Following the concept of universal analytical scattering models and based on the experimental evidence of two independent X-band airborne data sets, we propose a simple correction to the facet NRCS which brings the PR in closer agreement to the observations and makes it analytically very close to the popular Thompson empirical model. This amended model preserves the simple structure of Bragg scattering; it admits one single extra parameter which makes a dynamical transition between the asymptotic Bragg and Kirchhoff regime depending on the sea state and the radar frequency. This allows to correctly describe the angular variations of the PR in the upper microwave regime (C-, X-, and Ku-bands) with minimal *a priori* information regarding the sea surface. Once this correction is incorporated in the TSM, a consistent modeling of the polarized sea clutter statistics can be obtained with the compound distribution model.**

***Index Terms*— Radar clutter, radar polarimetry, sea surface, synthetic aperture radar (SAR).**

I. Introduction

RADAR remote sensing is a unique tool for global ocean surface monitoring in many applications such as ship detection, search-and-rescue operations, etc. For these tasks which are related to target identification in a complex environment, sea clutter discrimination is a key issue. With an imaging radar operating at metric spatial resolution the pixel intensity, which is proportional to the backscattered sea surface signal on each radar cell, is known to follow an exponential probability distribution; if one considers the signal amplitude rather than the signal intensity as it is often the case, this corresponds to a Rayleigh distribution. However, as the resolution increases, the backscattered intensity of sea clutter deviates from this distribution and is better represented by heavy tail distributions such as Pareto, Weibull, or K distributions (see e.g., [1]). Now, even though these distributions provide consistent fits with the observations using a limited number of tuning parameters (typically, the "shape" and "scale" parameter), they are purely empirical and there is no analytical formulation which links the parameters of the distributions with the sea state.

Nevertheless, there are both experimental evidences and theoretical arguments to support the fact that the mere intensity distribution at a single incidence carries rich information on the sea state, a relation which calls for a physical model to describe sea clutter. Valenzuela and Laing [2] were the first to use the idea of a compound probability distribution based on a two-scale model (TSM) to account for the non-Rayleigh statistics of sea clutter amplitude. They attributed the latter to the modulation of the pixel amplitude (the so-called texture) by the tilting effect of long waves. This idea was subsequently pursued by other authors and compared to either experimental measurements [3] or numerical simulations [4] of radar backscatter; in particular [3] showed that, assuming a perfectly conducting surface, the compound model could explain analytically the log-normal shape of the sea clutter amplitude distribution in the horizontal polarization.

Our work was originally driven by an attempt to use the TSM to describe the sea clutter distribution (Section II) obtained with a X-band synthetic aperture radar (SAR) system at medium incidence during the airborne campaign POLLUPROOF conducted by the French AeroSpace Lab [Office National d'Études et de Recherches Aérospatiales (ONERA)] a few years ago over the Mediterranean ([5]). Well-calibrated fully polarimetric images at high-resolution (50 cm) were processed to obtain the normalized radar cross section (NRCS) as a function of the incidence angle in vertical (σ^0_{VV}) and horizontal (σ^0_{HH}) copolarization as well as the distribution of pixel intensity at fixed incidence angle. This last distribution was seen to deviate significantly from the Exponential function in vertical as well as horizontal polarization (Section III). This was found contradictory with the prediction of the compound probability distribution, for which only a small deviation from the Exponential distribution and a weak sensibility to the sea state was observed for the vertical polarization. After many unsuccessful attempts to tune the model parameters, it has become clear that it is the model itself that should be revised to obtain consistent estimates

Manuscript received April 10, 2020; revised June 30, 2020 and September 11, 2020; accepted September 14, 2020. The work of Floriane Madeleine Schreiber was supported by the Région Sud - Provence-Alpes-Côte d'Azur and the Office National d'Études et de Recherches Aérospatiales (ONERA). *(Corresponding author: Charles-Antoine Guérin.)*

Floriane Madeleine Schreiber and Sébastien Angelliaume are with the Département Electromagnétisme et Radar, Office National d'Études et de Recherches Aérospatiales, DEMR, Office National d'Études et de Recherches Aérospatiales (ONERA), 13661 Salon cedex Air, France (e-mail: floriane.schreiber@onera.fr; sebastien.angelliaume@onera.fr).

Charles-Antoine Guérin is with the Mediterranean Institute of Oceanography (MIO), Université de Toulon, Aix Marseille Univ, Centre National de la Recherche Scientifique (CNRS), Institut de Recherche pour le Développement (IRD), 83041 Toulon, France (e-mail: guerin@univ-tln.fr).

Color versions of one or more of the figures in this article are available online at http://ieeexplore.ieee.org.

Digital Object Identifier 10.1109/TGRS.2020.3025683

of the sea clutter in the two copolarization states. The main outcome of our analysis (Section IV-A) is that the inadequacy of the TSM to describe sea clutter distribution is related to the failure of the Bragg model in evaluating properly the polarization ratio (PR) of rough facets, which is defined as the ratio of the vertically to horizontally copolarized NRCS ($\mathrm{PR} = \sigma^0_{\mathrm{VV}}/\sigma^0_{\mathrm{HH}}$). The inadequacy of pure or composite Bragg model to represent the PR has been known for long (e.g., [6], [7]) and becomes apparent in the upper microwave band (C-, X-, and Ku-band) and is far less pronounced in lower frequency bands (L- or P-band) or at coarse image resolution where the distribution is close to exponential. In seeking to correct the compound distribution model in the upper microwave band, we were led to devise an improved but still elementary facet scattering model on the basis of general theoretical considerations following the rationale of universal scattering models (Section V-A). This NRCS model has the same functional form as the Bragg scattering model, with a modified geometrical kernel, however, resulting from an hybridization between the Bragg and Kirchhoff kernels and will therefore be referred to as the "hybrid Bragg model" in the following. It as some differences and similarities with the popular model [7] based on correcting the pure or composite Bragg NRCS with an additive unpolarized "breaking wave contribution" (Section IV-B). It is also compared with empirical (Section IV-C) as well as analytical (Section IV-D) models from the literature. Its main strength is to restore the correct order of magnitude for NRCS and PR with help of a single parameter (or two parameters if a directional description is required). For the PR, it yields a roughness-independent formula which has been found *a posteriori* extremely close to the popular empirical model proposed by Thompson *et al.* [6] two decades ago (Section V-C). Its analytical dependence on the incidence angle has been further confirmed by experimental evidence of two independent X-band data sets (Section V-D). The hybrid Bragg scattering model can be used either *per se* or to describe rough facet scattering in the framework of the TSM (Section VI). This improved TSM has been evaluated in the light of a series of C-, X-, and Ku-band data from the literature and found to yield significant improvement for the NRCS, PR and polarization difference with respect to the classical TSM based on Bragg scattering (Section VII). At last we show that the use of this corrected TSM reconciles the vertical and horizontal polarization in the derivation of sea clutter intensity according to the compound distribution model (Section VIII).

II. Sea Clutter Distribution

A. Compound Model

In high-resolution radar imaging the pixel size is typically of the order of a few radar wavelengths. It is therefore natural to describe the radar reflectivity in terms of a TSM ([8]–[10]) in which the elementary rough facets coincide with image pixels. In this model, the NRCS from the sea surface is obtained through incoherent average of the rough facet backscattered intensity according to the facet slope distribution [$\mathrm{pdf}(\boldsymbol{s})$]

$$\sigma^0(\theta) = \int \mathrm{pdf}(\boldsymbol{s})\sigma^0_L(\theta;\boldsymbol{s})d\boldsymbol{s}. \tag{1}$$

Here $\sigma^0_L(\theta;\boldsymbol{s})$ is the NRCS expressed in the *local* frame of reference attached to one facet but projected onto the polarization basis attached to the *global* frame of reference. For a single look image, the fluctuations of pixel intensity I (the *speckle*) are exponentially distributed about a mean quantity $\sigma^0_L(\theta;\boldsymbol{s})$ referred to as the *texture*, which is the local NRCS attributed to a tilted facet of size L and slope $\boldsymbol{s}$. The conditional probability distribution function (pdf) of facet intensity for a given facet slope vector $\boldsymbol{s}$ is therefore

$$\mathrm{pdf}(I|\boldsymbol{s}) = \frac{1}{\sigma^0_L(\theta;\boldsymbol{s})}\exp\left(-\frac{I}{\sigma^0_L(\theta;\boldsymbol{s})}\right), \quad u \geq 0 \tag{2}$$

where θ is the incidence angle. The unconditional pdf of facet intensity is obtained by further integration over the facet slope distribution

$$\mathrm{pdf}(I) = \int \mathrm{pdf}(I|\boldsymbol{s})\mathrm{pdf}(\boldsymbol{s})d\boldsymbol{s}. \tag{3}$$

It is noted that due to facet tilting the local incidence angle can exceed 90°. In that case, the corresponding local NRCS is set to zero (or to the instrument noise floor in case of experimental data) to correct this effect. It is often advantageous to express the clutter distribution in terms of a dimensionless intensity $\tilde{I}$ such that $I = \sigma^0(\theta)\tilde{I}$, where $\sigma^0(\theta)$ is the NRCS of the infinite surface, assumed to be statistically homogeneous. The resulting compound distribution for the normalized intensity is given by

$$\mathrm{pdf}(\tilde{I}) = \int \frac{1}{\mathcal{T}(\theta;\boldsymbol{s})}\exp\left(-\frac{\tilde{I}}{\mathcal{T}(\theta;\boldsymbol{s})}\right)\mathrm{pdf}(\boldsymbol{s})d\boldsymbol{s} \tag{4}$$

where $\mathcal{T}(\theta;\boldsymbol{s}) = \sigma^0_L(\theta;\boldsymbol{s})/\sigma^0(\theta)$ is a dimensionless quantity which we refer to as the "texture" parameter. In the absence of long wave tilt this parameter reduces to unity and the exponential distribution is recovered in (4). On the contrary, the occurrence of strong facet slope increases the deviation from the latter. The facet slope distribution is usually assumed to be a 2-D Gaussian, discarding skewness and peakedness effects as well as extreme slopes related to breaking events.

B. Sea Clutter Distribution Under Bragg Tilting

The classical way to describe scattering by small-scale roughness within the TSM is the small-perturbation method ([11]), also known as Bragg scattering model in the oceanic context (henceforth simply referred to as the "Bragg model"). At first order in roughness, the copolarized components of the NRCS are given by [9]

$$\sigma^0(\theta) = 16\pi K_0^4 \cos^4\theta\ \mathcal{B}(\theta)\ S(\boldsymbol{q}_H) \tag{5}$$

where $K_0 = 2\pi/\lambda$ is the radar wavenumber and θ is the incidence angle, S is the 2-D wavenumber spectral density of ocean roughness (with normalization $\int d\boldsymbol{k}S(\boldsymbol{k}) = \langle\eta^2\rangle$) and $\mathcal{B}$ is the first-order Bragg scattering kernel depending on the incidence angle, sea surface relative permittivity ϵ, and polarization (see the Appendix). The ocean surface spectrum S is only involved through a single wavenumber $\boldsymbol{q}_H$, referred to as the Bragg resonant wave vector and equal to twice the horizontal projection of the incident wave vector (so that

$q_H = 2K_0 \sin\theta$ in norm). The local NRCS of a rough facet expressed in its local frame of reference takes the form

$$\sigma_L^0(\theta; s) = 16\pi K_0^4 \cos^4\theta_s \ \mathcal{B}_s \ S(\boldsymbol{q}_{H,s}) \tag{6}$$

where s is the facet slope, θ_s and $\boldsymbol{q}_{H,s}$ are the local incidence angle and Bragg resonant wave vector attached to this facet, respectively, and $\mathcal{B}_s$ is the tilted Bragg kernel obtained by projection of the horizontally and vertically components of the Bragg kernel onto the polarization basis see (5.1) and (5.2) in [9].

III. Experimental X-Band Sea Clutter Distribution

The compound probability distribution has been calculated under a Bragg scattering assumption and compared with experimental distributions extracted from two independent airborne X-band data sets, namely the INGARA and POLLUPROOF data sets.

INGARA is a polarimetric real aperture radar (RAR) system maintained and operated within the Defense Science and Technology Group in Australia [12]. During the ocean backscatter experiments in 2004 and 2006, sea clutter data were collected at X-band (10.1 GHz carrier frequency) with a 200-MHz bandwidth giving a 0.75 m range resolution. Alternate pulses transmitted horizontal and vertical polarizations resulting in a nominal pulse-repetition frequency (PRF) of 300 Hz. The radar was operated in a circular spotlight-mode covering 360° of azimuth angles and each day, the radar platform performed at least six full orbits around the same patch of ocean to cover a large portion of grazing angles between 15° and 45°.

SETHI [13], the airborne remote-sensing imaging system developed by ONERA, has collected quad-pol SAR data at X-band over the Mediterranean sea with a range (across-track) resolution of 50 cm (bandwidth from 9.6 to 9.9 GHz) during the POLLUPROOF campaign [5]. Images are processed with an azimuth (along-track) resolution equal to the range resolution, which implies an integration time equal to 1.1 s. Imaged area is 9.5 km in azimuth and 1.5 km in range, with incidence angles from 34° to 52°.

The measured wind speed was about 8 m/s for the POLLUPROOF data set in the crosswind radar look direction. Similar wind speeds (7.9 and 10.3 m/s) were available with the INGARA data set in upwind radar look direction. We calculated the distribution of normalized intensity according to the compound model (4), where the texture parameter was evaluated using classical tilted Bragg scattering with an Elfouhaily omnidirectional spectrum by 8 m/s wind speed to describe the resonant Bragg frequency. The facet slope distribution was assumed to be a centered 2-D Gaussian distribution parameterized by the directional mean-square slope (mss); we denote mss_x the mss in the radar look direction and mss_y the mss in the cross-look direction. For small slopes, the effect of the out-of-plane tilting is negligible and thus the distribution of facet NRCS is quasi-insensitive to the radar cross-look direction mss_y, which was therefore assumed to be equal to the mss_x in the numerical simulations. Given the dynamical range of the backscattered intensity, it is convenient to express it in decibels providing a simple change of variable for the corresponding pdf

$$\text{pdf}(\tilde{I}_{\text{dB}}) = \frac{\log(10)}{10}\tilde{I}\,\text{pdf}(\tilde{I}). \tag{7}$$

This function was evaluated using different values of the mss_x in the expected range of this parameter (0.005–0.03). The directional mss of a 50 cm facet should indeed be of the order of half the total slick mss of Cox and Munk [14] or half the total mss obtained by integration of the Elfouhaily spectrum with wavenumber cut-off. It turns out that the experimental intensity distributions obtained in each copolarization channel [vertical transmit and vertical receive (VV) or horizontal transmit and horizontal receive (HH)] are inconsistent with the tilted Bragg model as they cannot be fit simultaneously using the same value of mss_x. We found systematically with the POLLUPROOF data that it takes a larger value to match the VV data than the HH data (for example $\text{mss}_x = 0.02$ versus $\text{mss}_x = 0.008$). The higher value of mss needed to fit the VV data in the tilted Bragg model can be explained by either the insufficient sensitivity of the VV Bragg kernel or the exaggerated sensitivity of the HH Bragg kernel to the tilt angle. This can be seen by comparing the angular dependence of the geometrical factors $\cos^4\theta\mathcal{B}_{\text{VV}}(\theta)$ and $\cos^4\theta\mathcal{B}_{\text{HH}}(\theta)$ of the Bragg model (see the Appendix). While the HH factor can vary by about 20 dB when the local incidence angle changes from 0° to 60°, the VV undergoes only weak variations (less than 3 dB over the same angular domain). It seems therefore that the Bragg kernels do not have the appropriate dependence to the local incidence angle to account for the distribution of facet intensities.

IV. Scattering Models

A. Failure of Bragg Tilting

The "classical" TSM based on Bragg scattering (henceforth referred to as the "tilted" or "composite" Bragg model) has been for long the most popular model for ocean scattering [9] and has been shown to give correct qualitative trends of ocean backscatter and fair quantitative agreement with experimental data at medium incidences, especially in the lower part of the microwave frequency band (L- or P-band). In particular, it is able to provide a (slight) dependence on roughness of the PR contrarily to the original Bragg scattering model. Another interesting feature of the tilted Bragg model in ocean backscatter modeling is that it involves only a limited knowledge of the sea surface spectrum, namely a small wavenumber interval around the Bragg resonant frequency (due to the variation of the local incidence angle) and is simple to implement. However, the tilted Bragg model has some acknowledged limitations; it is dependent on the facet size, which makes the latter choice somewhat arbitrary, and it fails at low incidence angles. In this respect, the use of the first-order Bragg model for the local facet cross section can be advantageously replaced by the use of the first-order small-slope approximation (SSA, [15]), leading to the cut-off invariant TSM [10], henceforth simply referred to as geometrical optics (GO)-SSA. This last model has a wider angular domain of validity as it holds at low incidence angles and is robust to the choice of the cut-off scale. Nevertheless, these three models from the "Bragg

family" (Bragg model, tilted Bragg model, GO-SSA) yield close results when employed at mid-incidence for copolarized components. In particular, the PRs predicted by models of the "Bragg family" are way too large when applied at mid- or large incidence and compared to data acquired in the upper part of the microwave frequency band (C, X, Ku, Ka). By inspecting the available data, we found that typically, even the most accurate model (GO-SSA) overestimates the PR by at least 2 dB at 50° incidence in X-band by moderate wind speed.

This effect is systematic and does not depend on the choice of the ocean spectrum nor on the wind direction. We have tested various spectral models at several wind speed: the omnidirectional and directional Elfouhaily spectrum [16], the omnidirectional Kudryavtsev spectrum [17], and the omnidirectional Bringer spectrum [18], with virtually no difference for the resulting PR. This quasi-insensitivity of the PR to the spectral model is plain from the expression of the tilted Bragg model since the NRCS is proportional to the wave spectrum in the vicinity of the Bragg frequency. The same is verified for the GO-SSA model which is very close to the tilted Bragg model at medium incidences. Now, a few dB difference might be acceptable when trying to model the large dynamics of the copolarized NRCS over a large span of incidence angles and sea states. However, having an accurate PR is crucial when it comes to the modeling of sea clutter intensity distribution. The reason is, the distribution of facet intensity is primarily accounted for by the sensibility of the local NRCS to the tilt angle. Whereas in the global NRCS the main contributing facets are those with small and positive slopes, the entire set of facet slopes must be taken into account to model the distribution of intensity. Hence, a good estimation of the total NRCS can be obtained with less stringent conditions on the PR which need only be accurate at small and moderate incidence angles. On the contrary, the PR must remain accurate over a large range of incidence to allow for a correct modeling of the clutter distribution especially at the tail which is usually the most critical part.

B. Non-Bragg Corrections

The overestimation of the PR assuming Bragg scattering in the upper microwave bands has been known for long. Several authors starting with the pioneering work of O.M. Phillips ([19]) attribute the failure of pure or composite Bragg models to the missing, nonpolarized, contribution of breaking waves which becomes increasingly important at large incidence angles and large wind speeds. In a series of articles ([7], [20]–[24]), the NRCS is obtained by combining a pure surface model based on a "Bragg term" (σ^0_B) with an additional "non-Bragg" (σ^0_{NB}), nonpolarized, term which accounts for scattering by "zones of enhanced roughness associated with breaking waves" [7]. As the relative correction is stronger in HH than VV polarization, this has the effect to reduce the PR and to bring it in closer agreement to the observations. A coverage fraction parameter q is used to govern the weight of the non-Bragg component

$$\sigma^0 = (1-q)\sigma^0_B + q\sigma^0_{\mathrm{NB}}. \tag{8}$$

The Bragg term is computed using the classical TSM ([7]) or the first-order SSA ([23]). The non-Bragg term is calculated with a GO approximation using some further approximation on the geometry of the breaking zone. In the following, we will refer to this still unnamed model as the "Bragg+breaking" model. Even though this model provide satisfactory fits with observed NRCS at moderate and large wind speeds, we found it not adapted to the modeling of sea clutter distribution. The first reason is that the use of a breaking model requires the tuning of a certain number of parameters (probability of occurrence, mean square slope of breaking roughness, tilt of breaking zone, ratio of vertical to horizontal scales, etc) which cannot be measured directly and introduce further degree of arbitrariness when trying to characterize a sea state from a reduced number of observations. The second reason is that this approach is purely statistical whereas the modeling of sea clutter from SAR images requires a "pixel by pixel" approach. In addition, it is unlikely to account for the observed sea clutter at low wind speed, where breaking is rare and its contribution negligible.

C. Empirical Models for the PR

Many alternative, empirical approaches leading to an improved PR have been proposed in the literature. A very popular model is the heuristic formulation used two decades ago by Thompson *et al.* [6] to fit the C- and Ku-band PR

$$\mathrm{PR}_{\mathrm{Th}} = \frac{(1+2\tan^2\theta)^2}{(1+\alpha\tan^2\theta)^2}. \tag{9}$$

This model depends solely on the incidence angle and a tuning parameter α which is frequency-dependent. With $\alpha = 0$, it recovers the Bragg PR in the conducting case (see the Appendix)

$$\mathrm{PR}_{\mathrm{Bragg}} = \frac{(1+\sin^2\theta)^2}{\cos^4\theta} \tag{10}$$

while for $\alpha = 1$ it reaches the PR predicted by the physical optics (PO) or Kirchhoff approximation in the conducting case

$$\mathrm{PR}_{\mathrm{Kirch}} = \frac{1}{\cos^4\theta}. \tag{11}$$

This empirical model was found in very good agreement with experimental PR at medium incidences (20°–50°) in C- and Ku-band with estimated values $\alpha = 0.6$ and $\alpha = 0.95$, respectively. Later on, empirical PR were developed in conjunction with geophysical model functions (GMFs) for describing the observed NRCS in different microwave bands as a function of wind speed, such as the C-band model (CMOD)5 ([25]), X-band model (XMOD) ([26]), and L-band model (LMOD) ([27]) GMFs for C-, X-, and L-band data, respectively. As many GMFs have been developed from airborne or spaceborne mono-polarized acquisition, empirical PR models were proposed to allow estimation of the NRCS in the other copolarized channel. By construction, these models provide a better representation of the PR. However, they cannot be used to correct the copolarized NRCS independently of one another and hence cannot be used within the TSM to model the sea clutter distribution.

D. Unified Analytical Scattering Models

Another approach to improve the PR relies on a better choice of analytical scattering models. The essential reason for the failure of the TSM in this respect is that it misses the PO limit, obtained at moderate incidence for very rough seas or high radar frequencies as well as the GO limit obtained in the same conditions at very low incidence. In the PO model, the NRCS is given by a Kirchhoff integral involving the surface auto-correlation function ρ rather than the roughness power spectral density S

$$\sigma^0(\theta) = 16\pi K_0^4 \cos^4\theta \frac{\mathcal{K}}{q_z^2} \frac{1}{4\pi^2} \int_{\mathbb{R}^2} d\boldsymbol{r}\ e^{i\boldsymbol{q_H}\cdot\boldsymbol{r}} e^{-q_z^2\rho(\boldsymbol{r})} \quad (12)$$

where $q_z = 2K\cos\theta$ is twice the vertical projection of the incident wave vector and $\mathcal{K}$ is a geometrical kernel referred to as the *Kirchhoff kernel*, depending only on the incidence angle and sea surface permittivity (but not on the polarization). For small roughness or for large angles ($q_z\rho \ll 1$), the surface integral reduces to the Fourier Transform of the autocorrelation function and brings the PO NRCS to a form similar to the Bragg NRCS (5), with a different kernel, however ($\mathcal{K} \neq \mathcal{B}$)

$$\sigma^0(\theta) \to 16\pi K_0^4 \cos^4\theta\ \mathcal{K}\ S(\boldsymbol{q}_H). \quad (13)$$

It is noted that we have singled out the geometrical factor $16\pi K_0^4 \cos^4\theta$ in the expression of the Kirchhoff kernel, which therefore differs from its customary expression given in the literature. A wealth of modern analytical models referred to as "universal" (see e.g., [28] for a review) are known to extend the domain of validity of Bragg scattering and to comply to the PO limit in appropriate conditions. Many of these models perform a dynamical transition between the PO and Bragg regime, depending on sea state, incidence, and radar frequency. This is usually done through the summation of two terms, one being one reference asymptotic model (PO, Bragg or SSA1), the other being a Kirchhoff integral with a roughness-dependent kernel that allows to recover the other asymptotic model in the appropriate limit. This is for example the case with the "resonant curvature approximation" (RCA, [29], [30]), the "local curvature approximation" (LCA, [31]), the "weighted curvature approximation" (WCA, [32], [33]), and the Green's function method ([34]) which seek to correct a PO NRCS, or the second-order small-slope approximation (SSA2, [15]), which complements the SSA1 to reach the PO in the appropriate limit [35]. In all these methods (except SSA2), the corrective kernel is built from a difference between the Kirchhoff and the Bragg kernel, a property which is necessary to ensure the dynamical transition between the Bragg and Kirchhoff regime.

V. Hybrid Bragg Scattering Model

A. Heuristic Derivation

The universal analytical methods proceed via an integration of a Kirchhoff integral, which is in general a delicate numerical task and requires the full knowledge of the ocean spectrum together with some simplifying assumptions on the statistical nature of the random fields of wave elevations. Now it turns out that the Kirchhoff integral (12) rapidly converges to its "Bragg-like" approximation (13) as the incidence angle is increased above, say, 30°–40°. This can be seen in Fig. 1, where the X-band PO NRCS is calculated with an isotropic Elfouhaily spectrum at 8 m/s and compared with its approximation (13) as well as with its "GO-like" approximation at low incidence angles using a filtered mss. The difference between the exact Kirchhoff integral (12) and its approximation (13) using the Bragg resonant spectrum is less than 1 dB beyond 40°. The same holds true for other types of Kirchhoff integrals involving derivatives of the surface correlation function (such as those encountered with the WCA), a result which was termed as "the Kirchhoff filtering formula" [33]. Building on the idea of balancing a pure Bragg contribution and a PO like correction we devise a simple heuristic correction to the Bragg scattering model which captures the essence of a universal scattering model by seeking the rough facet NRCS in the form

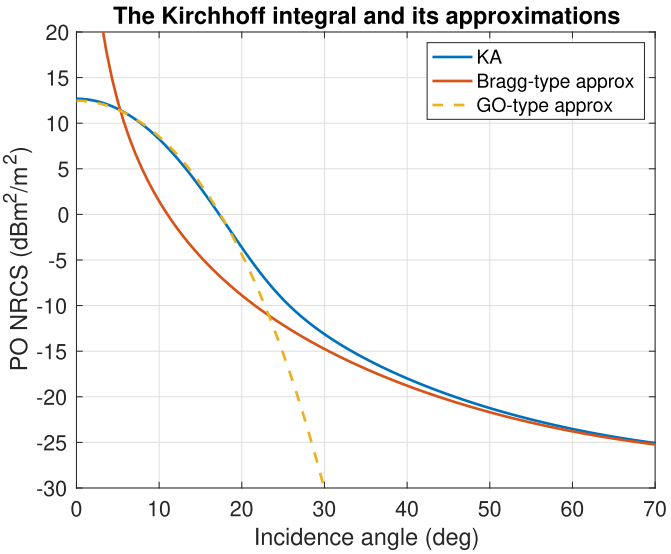

Fig. 1. PO X-band NRCS for an isotropic Elfouhaily spectrum with 8 m/s wind speed as a function of the incidence angle and comparison with its GO-like and Bragg-like approximations.

$$\sigma^0(\theta) = 16\pi K_0^4 \cos^4\theta(\mathcal{B} + \beta(\mathcal{K} - \mathcal{B}))S(\boldsymbol{q}_H) \quad (14)$$

for some dynamical parameter β which is expected to be small and depends primarily on sea state and radar frequency. Such a correction is expected to hold at low and moderate incidence only as the corrective term must remain small whereas the difference between the Kirchhoff and Bragg kernels diverges rapidly at large incidences, especially in VV polarization. However, the form of (14) suggests an equivalent correction with a wider angular domain of validity and another parameter α

$$\sigma^0 = 16\pi K_0^4 \cos^4\theta\mathcal{B}(1 - \varepsilon\alpha\sin^2\theta)S(\boldsymbol{q}_H) \quad (15)$$

with $\varepsilon = 1$ in VV and $\varepsilon = -1$ in HH. This is based on the observation that at low incidence angle

$$\frac{\mathcal{K} - \mathcal{B}}{\mathcal{B}} \simeq -\varepsilon A \sin^2\theta \quad (16)$$

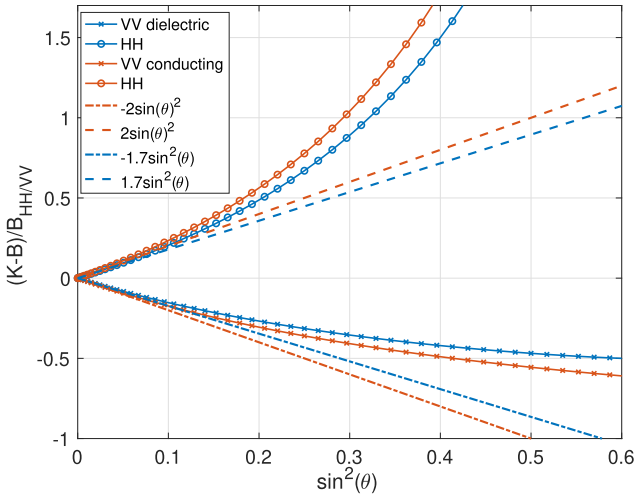

Fig. 2. Relative difference between the Kirchhoff and Bragg kernels $((K-B)/B)$ as a function of the squared sinus of the incidence angle ($\sin^2\theta$) for the VV and HH polarization; infinite ("conducting") as well as finite ("dielectric") sea surface permittivity are considered.

for some $A > 0$. Equation (16) can be easily checked both analytically and numerically with a value $A = 2$ in the conducting case and $A \simeq 1.7$ for the sea surface permittivity. Fig. 2 illustrates this approximation and confirms its validity at small incidence angle. The additive symmetrical correction $\pm A \sin^2\theta$ mitigates the divergence of the left-hand side of (16) in vertical polarization and slightly enhances it in horizontal polarization. The NRCS model (14) for rough facet scattering will be referred to as "hybrid" as it combines Bragg and Kirchhoff kernels in the form of Bragg scattering.

B. Comparison With the Bragg + Breaking Scattering Model

There are some similarities between the hybrid Bragg model and the aforementioned "Bragg + breaking" scattering model-based (Section IV-B). In both approaches, the Bragg component that produces overestimated PR is mitigated by a nonpolarized incoherent contribution having the flavor of a PO or GO mechanism. In the hybrid Bragg model, the parameter $\alpha > 0$ controls the amplitude of the required correction with respect to pure Bragg scattering and plays the same role as the coverage parameter q in the Bragg + breaking model; both parameters are expected to grow with the radar frequency and wind speed. The essential conceptual difference, however, is that the "Bragg + breaking" model makes uses of a spatial compounding of Bragg and non-Bragg mechanisms to obtain a statistically relevant NRCS model. It thus assumes that the sea patches can be separated in two distinct populations that obey drastically different scattering mechanisms. The hybrid Bragg model does not make such distinction and assumes the same non-Bragg correction for each rough facet. In addition, it has the advantage to reduce the required knowledge of the sea surface to one single parameter (α) while the "Bragg + breaking model" needs the double input of the breaking coverage and breaking mss at the risk of a more ambiguous parametrization. Another notable difference pertains to the PR. Under the hybrid Bragg model, it does not depend on the spectral model and is simply given by

$$\mathrm{PR} = (\mathrm{PR})_{\mathrm{Bragg}} \frac{1-\alpha\sin^2\theta}{1+\alpha\sin^2\theta} \tag{17}$$

where $(\mathrm{PR})_{\mathrm{Bragg}} = \mathcal{B}_{\mathrm{VV}}/\mathcal{B}_{\mathrm{HH}}$ denotes the Bragg PR with the kernels $\mathcal{B}_{\mathrm{VV}}$ and $\mathcal{B}_{\mathrm{HH}}$ are recalled in the Appendix. Again, this is in contradistinction with the "Bragg + breaking model" where the PR depends on the spectral model. Lastly, it is interesting to consider the polarization difference

$$\mathrm{PD} = \sigma^0_{\mathrm{VV}} - \sigma^0_{\mathrm{HH}} \tag{18}$$

which has been recognized as an important quantity to measure polarization sensibility [36]. While the PD eliminates the additive nonpolarized "breaking" contribution in the "Bragg + breaking model," it maintains a nontrivial expression with the hybrid Bragg model

$$\mathrm{PD} = \mathrm{PD}_{\mathrm{Bragg}} - \alpha\sin^2\theta \mathrm{PS}_{\mathrm{Bragg}} \tag{19}$$

where $\mathrm{PS} = \sigma^0_{\mathrm{VV}} + \sigma^0_{\mathrm{HH}}$ is the polarization sum.

C. Comparison With the Thompson Empirical Model

To elucidate the nature of this hybrid Bragg model, it is interesting to compare the modified PR in the perfectly conducting case with Thompson's formula (9) for the same values α

$$\frac{\mathrm{PR}}{\mathrm{PR}_{\mathrm{Th}}} = \frac{(1-\alpha\sin^2\theta)(1+\alpha\tan^2\theta)^2}{1+\alpha\sin^2\theta}. \tag{20}$$

Some elementary algebraic manipulations show that

$$\frac{\mathrm{PR}}{\mathrm{PR}_{\mathrm{Th}}} = 1+\rho(\theta) \tag{21}$$

where

$$\rho(\theta) = \frac{\alpha\sin^2\theta\tan^2\theta}{1+\alpha\sin^2\theta}\left(2+\frac{\alpha(1-2\cos^2\theta)}{\cos^2\theta}-\alpha^2\tan^2\theta\right) \tag{22}$$

is a remainder which remains small for intermediate incidence angles regardless of the value of α. Fig. 3 shows the evolution of ρ with the incidence angle in the conducting case (where there is a perfect analytical match at small angles) and for the actual sea surface permittivity (taken to be $\epsilon = 57+36i$). In this last case, the maximum absolute value of the remainder is 0.1 even though the analytical match at small angle is not perfectly reached. Hence, the proposed correction (17) can be seen as an analytical version of Thompson empirical model.

D. Experimental Evidence of the Proposed Correction

The proposed correction (17) for the PR ratio was established on the basis of general theoretical considerations regarding the expected structure of a universal facet model. However, it has also been experimentally confirmed by the two available data sets. For the relation (17) to hold, the ratio $p(\theta) = \mathrm{PR}/(\mathrm{PR})_{\mathrm{Bragg}}$ should satisfy the following relation:

$$Q(\theta) = \frac{1-p(\theta)}{1+p(\theta)} = \alpha\sin^2\theta \tag{23}$$

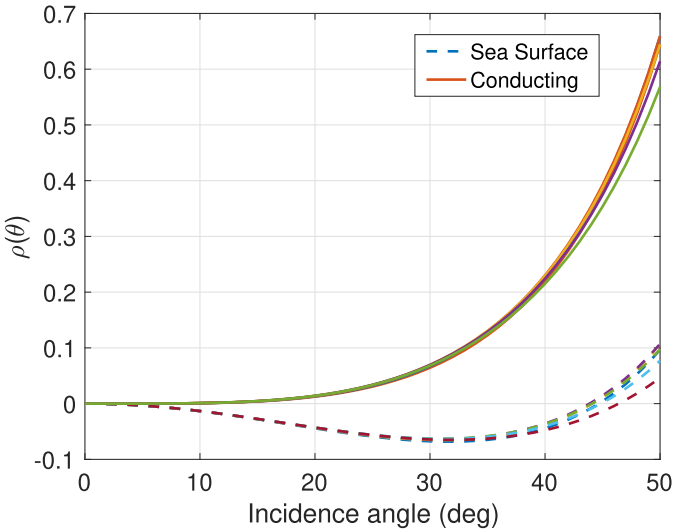

Fig. 3. Evolution of the relative difference $\rho = (\mathrm{PR} - \mathrm{PR_{Th}})/\mathrm{PR}$ in (21) as a function of the incidence angle for 9 values of the parameter α between 0.6 and 0.95. The solid lines correspond to the conducting case and the dashed lines to the sea surface dielectric constant.

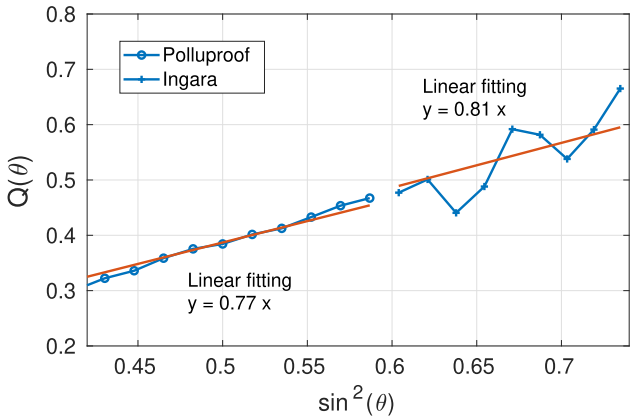

Fig. 4. Experimental evidence of relation (23) in X-band with the POLLUPROOF (8 m/s) and INGARA (7.9 m/s) data set.

TABLE I

SEA STATES CONDITIONS FOR THE X-BAND AIRBORNE MEASUREMENTS POLLUPROOF AND INGARA: WIND SPEED (WIND), RADAR AIM DIRECTION WITH RESPECT TO THE WIND VECTOR (DIR.), AND SIGNIFICANT WAVE HEIGHT (HS). THE VALUE OF α IS ESTIMATED FROM THE BEST LINEAR FIT $Q(\theta) = \alpha \sin^2\theta$

data set	wind (m/s)	dir.	Hs (m)	α
POLLUPROOF	8	cross	0.5	0.77
INGARA	10.3	up	2.6	0.89
INGARA	9.3	up	2.5	0.93
INGARA	7.90	up	3.5	0.81
INGARA	9.5	up	3.0	0.88

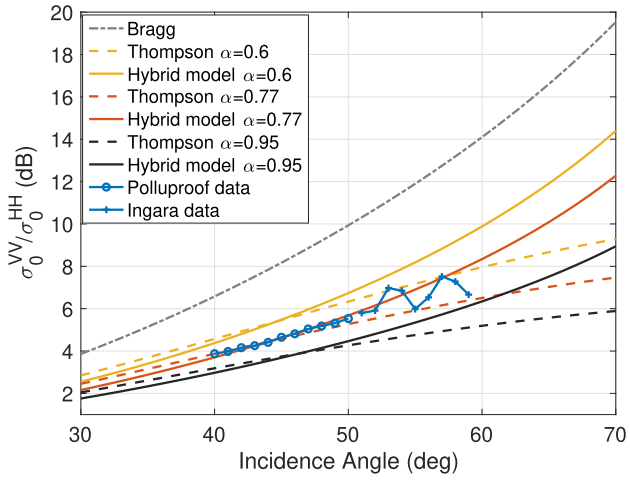

Fig. 5. Corrected PR as a function of incidence in different bands for a moderate wind speed and comparison with X-band data.

that is the variables Q and $\sin^2\theta$ should be linearly related by the coefficient α. This observation provides a mean to both check the existence of the relation (17) and evaluate the parameter α. This operation was performed with the X-band POLLUPROOF and INGARA airborne data sets, where the full-polarized NRCS was available on a sufficient range of incidence angles for various sea states. Fig. 4 shows the function $Q(\theta)$ obtained with the X-band POLLUPROOF (wind speed 8 m/s) and INGARA data sets (wind speed 7.9 m/s). A good linear fitting $Q = \alpha \sin^2\theta$ is found for the two data sets with $\alpha = 0.77$ and $\alpha = 0.81$, respectively. For the INGARA data set, several days of calibrated data were available, with a slight variation of α depending on sea states and wind direction (see Table I).

After evaluation of the coefficient α from the linear regression of $Q(\theta)$, the corrected PR model (17) is found in excellent agreement with the X-band data. This is shown in Fig. 5, where the evolution of the X-band PR with the incidence angle is given for moderate wind speeds (8–10 m/s) and compared with the experimental measurements. Superimposed on this figure is given by the PR after Thompson model in C- ($\alpha = 0.6$), X- ($\alpha = 0.77$), and Ku-band ($\alpha = 0.95$) when fit in the upwind direction. As seen, the corrected PR (17) is very consistent with the POLLUPROOF and INGARA data set over their joined angular coverage (40°–60°) and corrects the underestimation of the Thompson model at larger incidences (50°–60°). As expected, the X-band PR is intermediate between the C- and Ku-band PR. Since the PR decreases with increasing wind speed and radar frequency, the fitting value of α is expected to increase with these last parameters, as already seen on Fig. 5 for the radar band. As we will see in the following, it also depends on wind direction so that the general formula (17) only gives a coarse evaluation of the omnidirectional PR for a given wind speed and radar frequency.

VI. HYBRID TSM

A. Incorporating the Hybrid Bragg Model in the TSM

As was seen in Section II, the TSM is the natural theoretical framework to express the clutter intensity distribution. It was observed experimentally that in the upper microwave band,

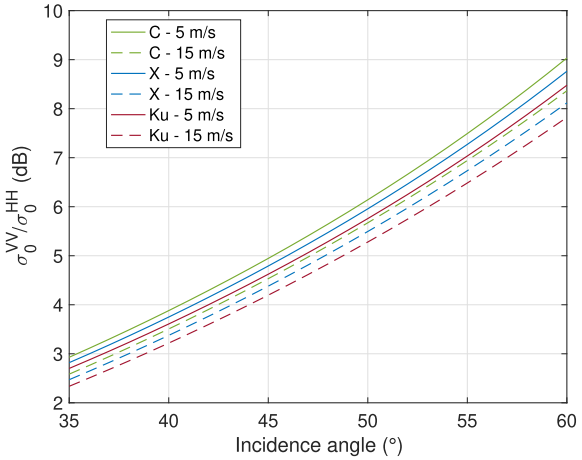

Fig. 6. Omnidirectional PR obtained under the hybrid TSM model in different bands and wind speeds with the universal value $\alpha = 0.6$.

a rough facet scattering model based on Bragg scattering yields erroneous PR and conflicting intensity probability distributions for the horizontal and vertical polarizations. This led us to devise an improved but still tractable facet scattering model, which we referred to as the hybrid Bragg model.

When employed in the framework of the TSM, the α-parameter of the hybrid Bragg scattering model should be reevaluated since part of the correction is already taken into account by the large-scale tilting process. To estimate the relevant value of α in the light of the experimental data sets, we applied the same methodology as in Section V-D with the replacement of the Bragg PR by the tilted Bragg PR (i.e., the classical TSM) in (23). This operation was made not only for the aforementioned data sets (POLLUPROOF, INGARA) but also for other available data set that can be found in the literature. Our numerical investigations on the combined TSM and hybrid Bragg model (henceforth simply referred to as the "hybrid TSM") and our comparisons with the available experimental data led to several conclusions. Most importantly, the value $\alpha \simeq 0.6$ is a common value to adequately fit the omnidirectional C-, X-, and Ku-band data for various sea states under the hybrid TSM. This means that the sea state and radar frequency dependence that were observed for the α parameter in the hybrid Bragg scattering model is canceled by the facet tilting process, which is also dependent on these parameters through the facet slope distribution.

Fig. 6 shows the PR obtained in the omnidirectional hybrid TSM model with the universal value $\alpha = 0.6$ for different frequency bands and wind speeds. As seen, the model consistently follows the observed trends and magnitude of the PR. A wind dependence is observed with the model even though the value of the hybridization parameter α has been kept constant. This is purely due to the tilting effect, which is driven by the wind-dependent facet mss.

We also found that the resulting PR is virtually independent on the chosen oceanic spectrum and the chosen type of facet slope distribution in the range of admissible models (Gaussian distribution and its weak deviations).

Fig. 7 shows the angular dependence of the X-band PR under the TSM + hybrid Bragg scattering model ($\alpha = 0.6$) for three types of omnidirectional wavenumber spectra at 10 m/s wind speed ("Bringer" [18], "Elfouhaily" [16], and "Kudryavtsev" [17]). The facet slope distribution has been taken to be a 2-D Gaussian with its mss given by the integrated Elfouhaily spectrum with a high-frequency cut-off corresponding to the facet size (here, 50 cm, that is 17λ.) As seen, the resulting PR is quasi-independent on the spectral model. On the same plot we have represented the classical TSM (corresponding to $\alpha = 0$), for which the same conclusion holds with a much stronger level of PR. The effect of the type of facet slope distributions is shown in Fig. 7, where two popular weakly non-Gaussian distributions have been compared to the Gaussian omnidirectional distribution with same mss as previously: the Gram-Charlier "slick" distribution [14] and an heavy-tail distribution in the form of a Levy alpha-stable distribution [37] with parameter 1.7. Again, the exact shape of the facet slope distribution has little influence as long as it remains a realistic, weakly non-Gaussian distribution.

B. Azimuthal Variations

The anisotropy of the NRCS in most analytical models is in general rendered by the use of a directional spectrum, which can be combined with a directional facet slope distribution when a tilting process is involved. A natural question is whether the hybrid Bragg and hybrid TSM models are able to capture the azimuthal variability of PR which is observed in the literature and customarily described by the upwind-crosswind asymmetry (UCA) and the upwind-downwind asymmetry. The typical observation is that the NRCS at moderate incidence has a quasi-sinusoidal variation with the wind direction; it is maximum in upwind and minimum in cross-wind with a few dB amplitude; it has a secondary maximum in the downwind direction and the difference between the upwind and downwind direction (UDA) is more pronounced in HH polarization [22]. As to the PR, it has a primary maximum in downwind and secondary maximum in upwind and is minimum in crosswind; the contrast between the crosswind and downwind direction can be as high as 2–3 dB at middle incidence and wind speed [see e.g., Fig. 3(a) of [30] at 40° incidence and 11 m/s wind speed] while the UDA is of the order of 1–2 dB. The same pattern is observed for the PD. Several physical mechanisms have been invoked in the literature to account for the UDA such as the hydro-dynamical modulation of small-scale roughness by long waves, the asymmetry of the tilt angle distribution of facet slopes in the UDA and the nonpolarized contribution of "breaking patterns." Comparisons between models and observations suggest that the first two invoked mechanisms are too weak to explain the observations and that the steep waves and breaking zone play a major role in the azimuthal anisotropy [22]. However, the description of backscattering by the breaking zone requires the knowledge of several breaking parameters whose determination introduces further arbitrariness. Therefore, it seems desirable to simplify and absorb as much as possible this breaking contribution in the hybrid Bragg model which has a reduced number of degrees of freedom.

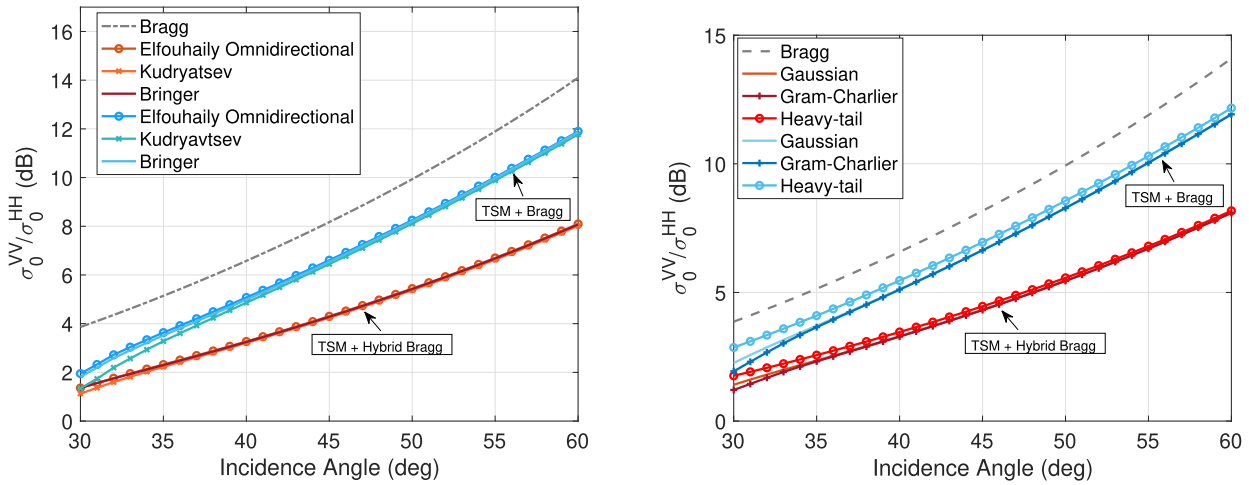

Fig. 7. X-band PR under the TSM and hybrid TSM ($\alpha = 0.6$) obtained at 10 m/s wind speed with 1) different omnidirectional wave spectrum models and a Gaussian facet slope distribution (top panel) and 2) Elfouhaily omnidirectional wave spectrum and different types of isotropic facet slope distributions with equal mss: Gaussian, Gram-Charlier, or alpha-stable with parameter 1.7 (bottom panel). The pure Bragg PR is given for reference.

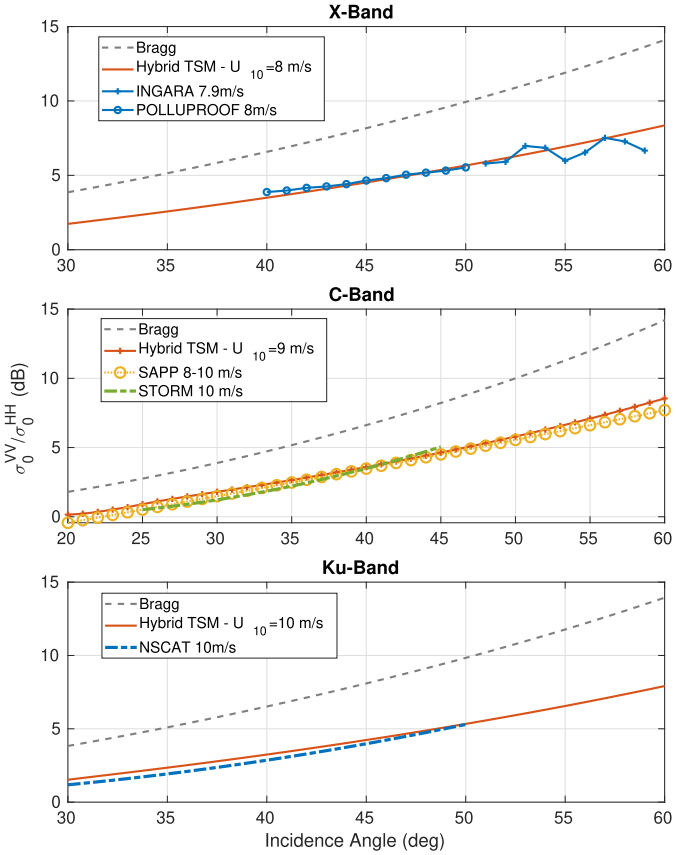

Fig. 8. Comparison of the modeled PR in the TSM+hybrid Bragg model with isotropic Elfouhaily spectrum and the measured omnidirectional NRCS in C-, X-, and Ku-bands for moderate wind speeds.

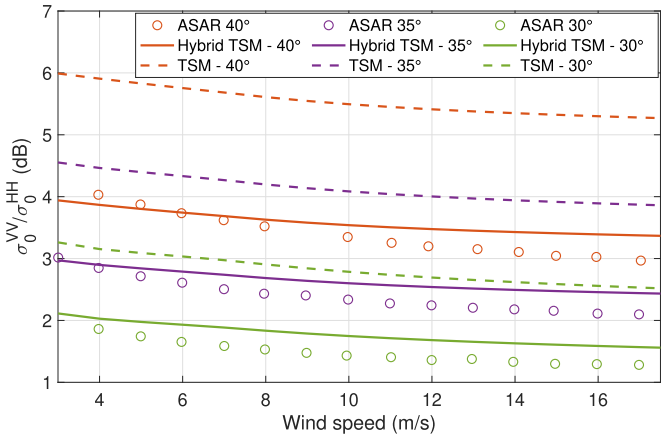

Fig. 9. Evolution of the omnidirectional C-band PR with wind speed according to the TSM and TSM+hybrid Bragg model between 30° and 40° incidence. A comparison is given with ASAR observations taken from Fig. 5(a) of [36].

By construction, the hybrid Bragg model eliminates the spectral dependence in the PR and therefore any anisotropy originating from the spectrum. When it is used within a TSM, the tilting process by facet slopes restore some azimuthal dependence but not sufficiently. Hence, assuming a constant value of α does not allow the PR model to describe the sensitivity to the wind direction. To be compliant with the directional observations, it therefore seems necessary to introduce a further dependence of the α parameter on the wind direction. The UCA of the PR can be restored by assuming a small azimuthal variation of α in the form of one single even harmonic

$$\alpha = \alpha_0 - \alpha_2 \cos(2\varphi) \tag{24}$$

where φ is the wind direction with respect to the radar direction and $\alpha_2 > 0$ is a small parameter of anisotropy. This correction to the hybrid Bragg model is perfectly consistent with the azimuthal variations of the copolarized NRCS which are mainly driven by the directional spectrum $S_0(\boldsymbol{q}_H) + \cos(2\varphi) S_2(\boldsymbol{q}_H)$ and only slightly influenced by the marginal modification of the amplitude factor $(1 \pm \alpha \sin^2\theta)$.

The observed UDA for the PR and PD could be accounted for by the introduction of an additional odd harmonic $\alpha_1 \cos(\varphi)$ in (24). However, this would lead to a nonphysical behavior of the VV NRCS after (15) with a maximum

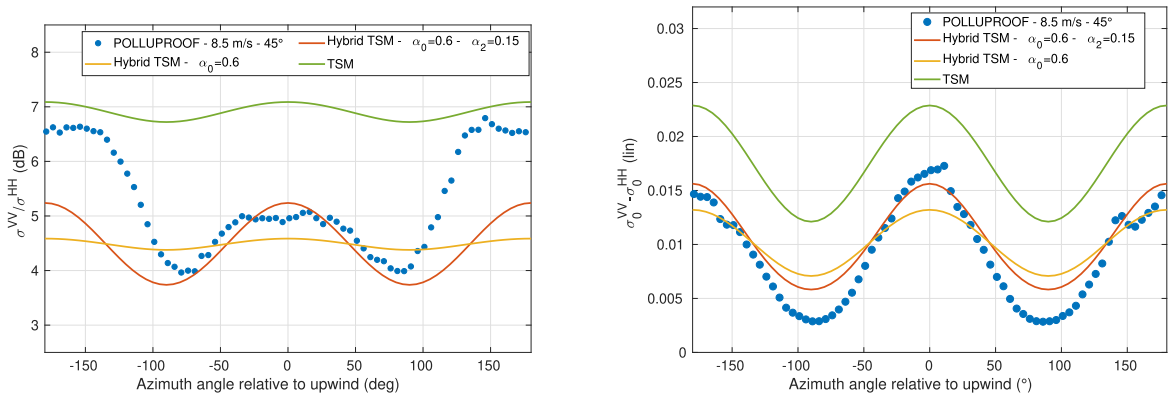

Fig. 10. X-band PR (upper panel) and PD (lower panel) at 45° incidence by 8.5 m/s wind speed. The POLLUPROOF data (blue dots) are compared with the isotropic (yellow dashed line) and anisotropic (red solid line) hybrid TSM. The classical TSM ($\alpha = 0$) is given for reference.

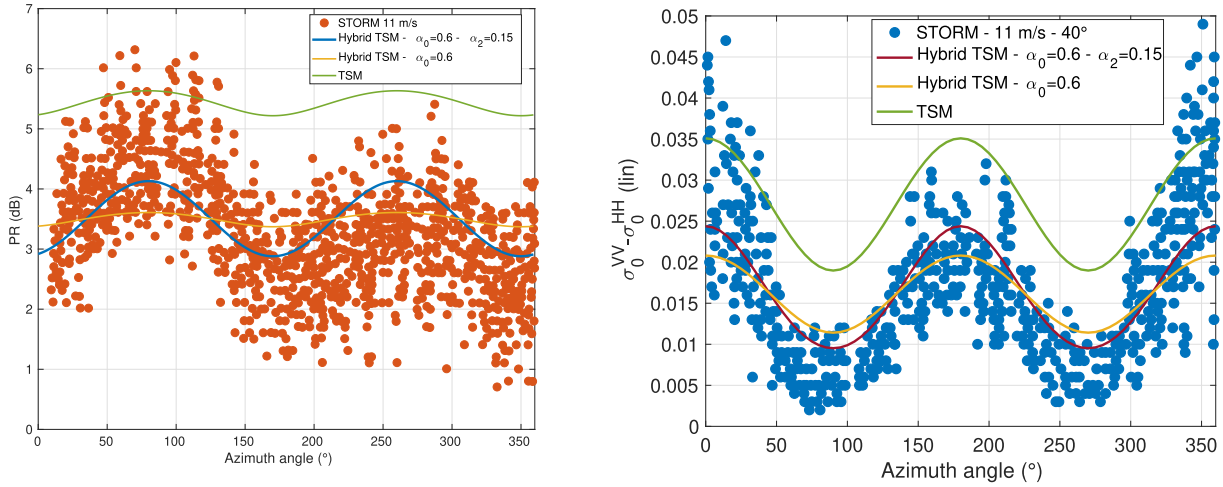

Fig. 11. Same as Fig. 10 for the C-band at 40° incidence by 11 m/s wind speed. The STORM data are compared with the isotropic and anisotropic hybrid TSM.

in downwind. Another way to introduce some UDA in the model is to use a skewed facet slope distribution. However, we found that weakly non-Gaussian distribution such as Cox and Munk Gram-Charlier expansions have only a marginal effect in the TSM (a few tenth of dB UDA) and strong asymmetric slopes resulting from near-breaking waves would be necessary to account for the observed level of UDA (as investigated in [38]). As the tail of facet slope distribution is only poorly known, we chose to ignore these non-Gaussian effects to preserve the degree of simplicity of the model and limit the number of unknown or questionable parameters. As it stands the hybrid Bragg model (as well as its tilted version, the hybrid TSM model) is not able to incorporate the complex scattering mechanisms which are at the origin of the UDA. It can drive the dynamical transition between the Bragg and Kirchhoff surface scattering regime but is not able to render the hydrodynamical modulation of small roughness (which implies a modified spectrum on rear and front side of rough facets) nor volume and wedge scattering resulting from breaking. However, it provides the correct order of magnitude of the PR (within one dB or so) at moderate incidence angles at the cost of only one (or two if the azimuthal description is needed) extra parameter.

VII. Experimental Assessment

A. Reference Data Sets

We have investigated the hybrid TSM at different frequencies in the upper microwave band (C, X, and Ku) and evaluated its ability to follow the correct trends and magnitude of the PR by comparison with various experimental data sets.

1) X-band airborne POLLUPROOF and INGARA data sets (see above).
2) Airborne C-band fully polarized data set from [39] which provides measurements from 20° to 60° for moderate to strong wind speeds.
3) STORM airborne C-band scatterometer ([22], [30], [40], [41]) which provides dual-polarized NRCS at medium incidence angles (10°–55°) for a variety of wind speeds between 5 and 15 m/s as well as the azimuthal dependence of the NRCS thanks to circular flights.
4) C-band advanced SAR (ASAR) ENVISAT copolarized NRCS as processed in [36].
5) Fully polarized Ku-band spaceborne NSCAT scatterometer (13.6 GHz), covering medium incidence angles from 18° to 54° for a rich variety of wind and sea conditions (e.g., [42]).

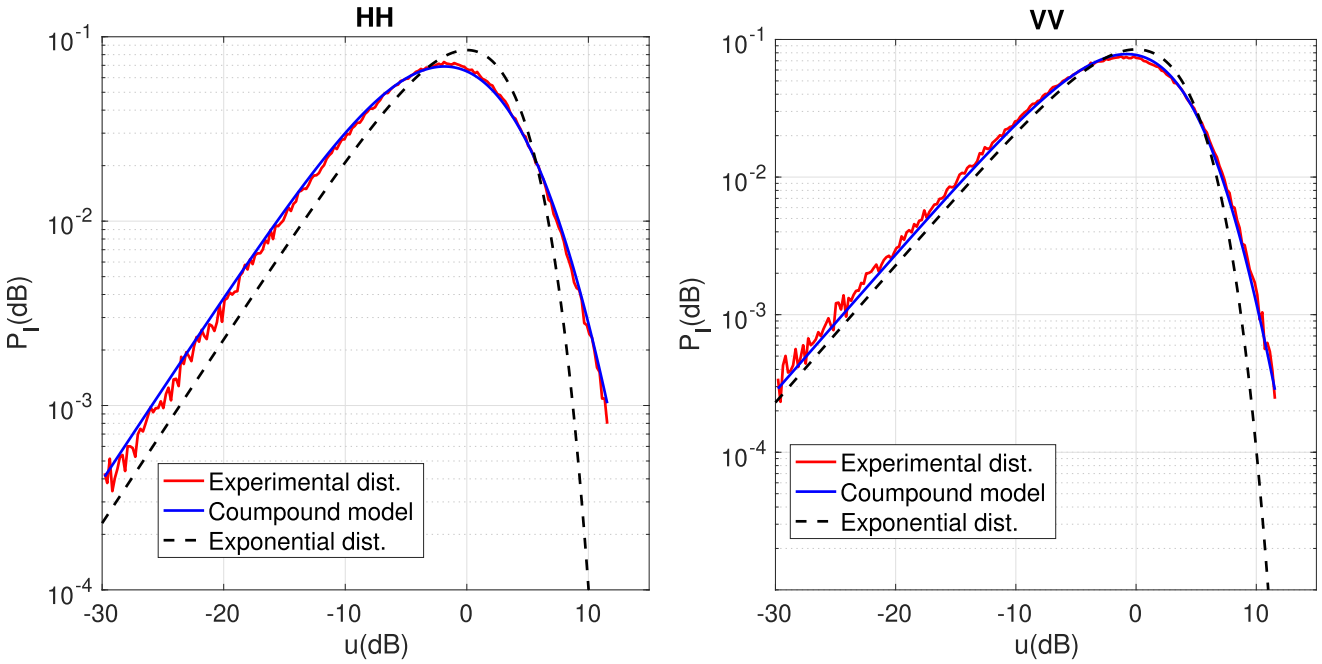

Fig. 12. Normalized intensity distribution (in logarithmic scale) from (7) according to the compound distribution model with corrected PR ($\alpha = 0.6$) at 45° incidence with $\text{mss}_x = 0.0113$ for the horizontal (HH, left panel) and vertical (VV, right panel) polarization. An excellent agreement with the POLLUPROOF experimental data is obtained simultaneously for the two copolarization states with the same value of mss_x. The exponential distribution is given for reference.

B. Omnidirectional Quantities

We first focused the comparison on omnidirectional quantities. Whenever the data NRCS GMF are fit in the form of 2-harmonic azimuthal expansion $a_0 + a_1 \cos\varphi + a_2 \cos 2\varphi$, this corresponds to the isotropic term a_0. The hybrid TSM was evaluated using the same value $\alpha = 0.6$ for the C-, X-, and Ku-band and a common small-scale cut-off of 17 λ (corresponding to facet sizes of 85, 50, and 34 cm, respectively). An omnidirectional Elfouhaily spectrum was employed to describe the small-scale roughness as well as the facet slope mss, which was obtained by integration of the ocean spectrum up to the facet cut-off wavenumber. Fig. 8 shows a comparison of the PR based on the hybrid TSM and the PR obtained as the ratio of the omnidirectional NRCS from SAPP and STORM airborne experiments (C-band) and the NSCAT satellite data (Ku-band) as well as the PR obtained from the X-band POLLUPROOF & INGARA transects. The omnidirectional PR for these last data is not available but is expected to be within 1 dB of the upwind/cross wind values. As seen, the hybrid TSM is able to follow quite accurately the observed angular dependence of the PR in the different bands. The sea state dependence of the omnidirectional PR is illustrated in Fig. 9 with the help of the omnidirectional ASAR data. Again, a major improvement is obtained and the estimated PR is within 0.5 dB of the measurements.

C. Directional Dependence

Next we evaluated the ability of the hybrid TSM to follow the azimuthal variations of the PR. For this we used the STORM and POLLUPROOF data for which some circular flights were available at 40° and 45° incidence, respectively. The hybrid TSM was run using the directional Elfouhaily spectrum combined with an anisotropic Gaussian facet slope distribution. The directional mss were calculated by integration of the directional spectrum with the same facet cut-off as previously. A sinusoidal variation of the hybridization parameter (24) was assumed by keeping the omnidirectional value $\alpha_0 = 0.6$. The value $\alpha_2 = 0.15$ was found in best agreement with the majority of observations.

Fig. 10 shows the smoothed variations of the PR and PD with respect to the wind direction φ in the X-band at 45° incidence for 8.5 m/s wind speed. The aforementioned upwind/downwind marked asymmetry is confirmed, with a difference of about 2.5 dB. The amplitude of variation between the crosswind and upwind direction has a smaller value, of the order of 1 dB. The hybrid TSM is able to follow quite closely the azimuthal variations of the PR except near the downwind direction where it is underestimated by about 1 dB. Once again, this is due to the acknowledged inability of the hybrid TSM to cope with the UDA which calls for a more complex description of the breaking wave scattering mechanisms. It is noted that a slight azimuthal variation of the PR is observed even with an isotropic α. This is due to the tilting effect of anisotropic facet slopes. The classical TSM (corresponding to $\alpha = 0$) is given for reference. Likewise, the estimation of the PD is greatly improved by resorting to the anisotropic hybrid TSM. The same comparisons have been made with the Storm C-band data on Fig. 11. The data have been replicated from Figs. 3 and 8 of [30]. The anisotropic hybrid TSM has been used with the same values $\alpha_0 = 0.6$ and $\alpha_2 = 0.15$ and the same directional Elfouhaily spectrum with the only difference that the C-band facet cut-off is employed. The same conclusions hold as previously.

VIII. Corrected Sea Clutter Distribution

The hybrid TSM (14) has been implemented and used to calculate the sea clutter intensity distribution and compared with the experimental measurements from the POLLUPROOF airborne X-band data over the Mediterranean Sea (8 m/s wind speed). Fig. 12 shows the obtained distribution for an Elfouhaily omnidirectional spectrum by wind speed 8 m/s using a directional facet $\mathrm{mss}_x = 0.0113$, which is the large-scale mss in the radar look direction. With the corrected PR model, the intensity distributions in the two polarizations VV and HH are now consistently fit with the same value of the mss and are in very good agreement with the experimental distributions of the POLLUPROOF campaign. We investigated other cases with different wind speeds (not shown here) to reach the same conclusion. The clutter intensity distribution from the two copolarized signals can be consistently fit with the compound distribution model when using the hybrid Bragg facet scattering model but not the classical Bragg model. This holds also at small wind speeds, thereby showing that the hybrid Bragg correction is necessary even in the absence of breaking.

IX. Conclusion

The distribution of sea clutter intensity is classically modeled by the compound probability model, wherein the local exponential distribution of intensity is integrated over the image with a varying texture parameter. In the case of high-resolution images where one pixel is of the order of a few wavelengths, the texture is given by the local facet NRCS, which is usually assumed to be a tilted-Bragg component. The resulting intensity distribution has been simulated and compared with a high-resolution, dual-polarization, X-band SAR data set at medium incidences. While the experimental distribution can be well reproduced with the compound probability model, it is at the price of inconsistent facet mss in vertical and horizontal polarization. This contradiction can only be explained by the inability of the Bragg kernels to evaluate correctly the PR in the upper microwave band. This failure of the scattering models based on Bragg or tilted-Bragg scattering has been known for long and many alternative empirical as well as analytical models have been proposed in the last two decades to rectify it. To retain the simplicity and the minimal sea state knowledge requirements which are offered by the tilted-Bragg model, we have proposed on heuristic grounds and experimental evidence an elementary single parameter correction referred to as the hybrid Bragg model. When used without tilting, the resulting PR is found in its analytical form very close to the empirical PR model by Thompson, with a parameter α which is strongly dependent on the radar frequency (from about 0.6 in C-band to 0.95 in Ku-band) and weakly dependent on sea state; it renders correctly the observed variation of the omnidirectional PR with incidence over a wide span of medium angles (30°–60°). When combined within a two-scale tilting process, the hybrid Bragg model is found to greatly improve the evaluation of the PR with respect to the classical composite model. For this, it is found that a universal parameter $\alpha_0 = 0.6$ can be best employed in the hybrid TSM. The observed azimuthal variations of the PR can be rendered to some extent (that is, including the UCA but not the UDA) by assuming a simple sinusoidal dependence of the α parameter on the wind direction. The performances of the hybrid TSM in estimating the PR and the polarization difference have been thoroughly investigated in the light of various experimental data sets from the literature. The hybrid Bragg scattering ultimately satisfies its original need, that is to provide consistent estimation of the sea clutter distribution for the copolarized intensity.

Appendix

The dielectric Bragg kernels are given by

$$\mathcal{B}_{\mathrm{HH}} = \left| \frac{\epsilon - 1}{(\cos(\theta_i) + \sqrt{\epsilon - \sin^2(\theta_i)})^2} \right|^2$$
$$\mathcal{B}_{\mathrm{VV}} = \left| \frac{(\epsilon - 1)[\epsilon(1 + \sin^2(\theta_i)) - \sin^2(\theta_i)]}{[\epsilon \cos(\theta_i) + \sqrt{\epsilon - \sin^2(\theta_i)}]^2} \right|^2. \quad (25)$$

The dielectric Kirchhoff kernel [43] is given by

$$\mathcal{K} = \left| \frac{\sqrt{\epsilon} - 1}{\sqrt{\epsilon} + 1} \right|^2 \frac{1}{\cos^4 \theta} \quad (26)$$

and is common to the vertical and horizontal polarization. In the perfectly conducting limit ($\epsilon \to \infty$), these kernels reduce to

$$\mathcal{B}_{\mathrm{HH}} = 1, \ \mathcal{B}_{\mathrm{VV}} = \frac{(1 + \sin^2 \theta)^2}{\cos^4 \theta}, \quad \mathcal{K} = \frac{1}{\cos^4 \theta}. \quad (27)$$

Acknowledgment

The authors are very grateful to L. Rosenberg from the Australian Defense Science and Technology Group for providing the INGARA data set.

References

[1] K. D. Ward, R. J. A. Tough, and S. Watts, *Sea Clutter: Scattering, the K-Distribution and Radar Performance*, 2nd ed. Herts, U.K.: The Inst. Eng. Technol., 2013.

[2] G. Valenzuela and M. Laing, "On the statistics of sea clutter," Naval Res. Lab Washington, Washington, DC, USA, Tech. Rep. NRL Report 7349, 1971.

[3] B. L. Gotwols and D. R. Thompson, "Ocean microwave backscatter distributions," *J. Geophys. Res.*, vol. 99, no. C5, pp. 9741–9750, 1994.

[4] H. Li and J. T. Johnson, "On the amplitude distributions of bistatic scattered fields from rough surfaces," *IEEE Trans. Geosci. Remote Sens.*, vol. 55, no. 12, pp. 6883–6892, Dec. 2017.

[5] S. Angelliaume, B. Minchew, S. Chataing, P. Martineau, and V. Miegebielle, "Multifrequency radar imagery and characterization of hazardous and noxious substances at sea," *IEEE Trans. Geosci. Remote Sens.*, vol. 55, no. 5, pp. 3051–3066, May 2017.

[6] D. R. Thompson, T. M. Elfouhaily, and B. Chapron, "Polarization ratio for microwave backscattering from the ocean surface at low to moderate incidence angles," in *Proc. Sens. Manag. Environ. IEEE Int. Geosci. Remote Sensing. Symp. IGARSS*, Jul. 1998, pp. 1671–1673.

[7] V. Kudryavtsev, "A semiempirical model of the normalized radar cross-section of the sea surface 1. Background model," *J. Geophys. Res.*, vol. 108, no. C3, p. 8054, 2003.

[8] J. Wright, "A new model for sea clutter," *IEEE Trans. Antennas Propag.*, vol. AP-16, no. 2, pp. 217–223, Mar. 1968.

[9] G. R. Valenzuela, "Theories for the interaction of electromagnetic and oceanic waves ? A review," *Boundary-Layer Meteorol.*, vol. 13, nos. 1–4, pp. 61–85, Jan. 1978.

[10] G. Soriano and C.-A. Guérin, "A cutoff invariant two-scale model in electromagnetic scattering from sea surfaces," *IEEE Geosci. Remote Sens. Lett.*, vol. 5, no. 2, pp. 199–203, Apr. 2008.

[11] S. O. Rice, "Reflection of electromagnetic waves from slightly rough surfaces," *Commun. Pure Appl. Math.*, vol. 4, nos. 2–3, pp. 351–378, Aug. 1951.

[12] L. Rosenberg and S. Watts, "High grazing angle sea-clutter literature review," Defence Sci. Technol. Organisation, Edinburgh, Scotland, Tech. Rep. DSTO-GD-0736 and AR-015-559, 2013.

[13] S. Angelliaume, X. Ceamanos, F. Viallefont-Robinet, R. Baqué, P. Déliot, and V. Miegebielle, "Hyperspectral and radar airborne imagery over controlled release of oil at sea," *Sensors*, vol. 17, no. 8, p. 1772, Aug. 2017.

[14] C. Cox and W. Munk, "Measurement of the roughness of the sea surface from photographs of the sun's glitter," *J. Opt. Soc. Amer.*, vol. 44, no. 11, pp. 838–850, 1954.

[15] A. G. Voronovich, "Small-slope approximation for electromagnetic wave scattering at a rough interface of two dielectric half-spaces," *Waves Random Media*, vol. 4, no. 3, pp. 337–368, 1994.

[16] T. Elfouhaily, B. Chapron, K. Katsaros, and D. Vandemark, "A unified directional spectrum for long and short wind-driven waves," *J. Geophys. Res., Oceans*, vol. 102, no. C7, pp. 15781–15796, Jul. 1997.

[17] V. N. Kudryavtsev, V. K. Makin, and B. Chapron, "Coupled sea surface-atmosphere model: 2. spectrum of short wind waves," *J. Geophys. Res., Oceans*, vol. 104, no. C4, pp. 7625–7639, Apr. 1999.

[18] A. Bringer, B. Chapron, A. Mouche, and C.-A. Guérin, "Revisiting the short-wave spectrum of the sea surface in the light of the weighted curvature approximation," *IEEE Trans. Geosci. Remote Sens.*, vol. 52, no. 1, pp. 679–689, Jan. 2014.

[19] O. M. Phillips, "Radar returns from the sea surface—Bragg scattering and breaking waves," *J. Phys. Oceanogr.*, vol. 18, no. 8, pp. 1065–1074, Aug. 1988.

[20] V. Kudryavtsev, "A semiempirical model of the normalized radar cross section of the sea surface, 2. Radar modulation transfer function," *J. Geophys. Res.*, vol. 108, no. C3, p. 8055, 2003.

[21] V. N. Kudryavtsev, B. Chapron, A. G. Myasoedov, F. Collard, and J. A. Johannessen, "On dual co-polarized SAR measurements of the ocean surface," *IEEE Geosci. Remote Sens. Lett.*, vol. 10, no. 4, pp. 761–765, Jul. 2013.

[22] A. A. Mouche, D. Hauser, and V. Kudryavtsev, "Radar scattering of the ocean surface and sea-roughness properties: A combined analysis from dual-polarizations airborne radar observations and models in C-band," *J. Geophys. Res.*, vol. 111, no. C9, 2006, Art. no. C09004.

[23] A. G. Voronovich and V. U. Zavorotny, "Theoretical model for scattering of radar signals in Ku- and C-bands from a rough sea surface with breaking waves," *Waves Random Media*, vol. 11, no. 3, pp. 247–269, Jul. 2001.

[24] P. A. Hwang and F. Fois, "Surface roughness and breaking wave properties retrieved from polarimetric microwave radar backscattering," *J. Geophys. Res., Oceans*, vol. 120, no. 5, pp. 3640–3657, May 2015.

[25] H. Hersbach, A. Stoffelen, and S. de Haan, "An improved C-band scatterometer ocean geophysical model function: CMOD5," *J. Geophys. Res.*, vol. 112, no. C3, 2007, Art. no. C03006.

[26] X.-M. Li and S. Lehner, "Algorithm for sea surface wind retrieval from TerraSAR-X and TanDEM-X data," *IEEE Trans. Geosci. Remote Sens.*, vol. 52, no. 5, pp. 2928–2939, May 2014.

[27] O. Isoguchi and M. Shimada, "An L-band ocean geophysical model function derived from PALSAR," *IEEE Trans. Geosci. Remote Sens.*, vol. 47, no. 7, pp. 1925–1936, Jul. 2009.

[28] T. M. Elfouhaily and C.-A. Guérin, "A critical survey of approximate scattering wave theories from random rough surfaces," *Waves Random Media*, vol. 14, no. 4, pp. R1–R40, Oct. 2004.

[29] A. A. Mouche, B. Chapron, and N. Reul, "A simplified asymptotic theory for ocean surface electromagnetic wave scattering," *Waves Random Complex Media*, vol. 17, no. 3, pp. 321–341, Jun. 2007.

[30] A. A. Mouche, B. Chapron, N. Reul, D. Hauser, and Y. Quilfen, "Importance of the sea surface curvature to interpret the normalized radar cross section," *J. Geophys. Res.*, vol. 112, no. C10, 2007, Art. no. C10002.

[31] T. Elfouhaily, S. Guignard, R. Awadallah, and D. R. Thompson, "Local and non-local curvature approximation: A new asymptotic theory for wave scattering," *Waves Random Media*, vol. 13, no. 4, pp. 321–337, Oct. 2003.

[32] C.-A. Guérin, G. Soriano, and T. Elfouhaily, "Weighted curvature approximation: Numerical tests for 2D dielectric surfaces," *Waves Random Media*, vol. 14, no. 3, pp. 349–363, Jul. 2004.

[33] C.-A. Guérin, G. Soriano, and B. Chapron, "The weighted curvature approximation in scattering from sea surfaces," *Waves Random Complex Media*, vol. 20, no. 3, pp. 364–384, Aug. 2010.

[34] W. Shaw and A. Dougan, "Half-space green's functions and applications to scattering of electromagnetic waves from ocean-like surfaces," *Waves random media*, vol. 5, no. 3, p. 341, 1995.

[35] C.-A. Guérin and M. Saillard, "On the high-frequency limit of the second-order small-slope approximation," *Waves Random Media*, vol. 13, no. 2, pp. 75–88, Apr. 2003.

[36] A. Mouche and B. Chapron, "Global C-b and E nvisat, Radarsat-2 and S entinel-1 SAR measurements in copolarization and cross-polarization," *J. Geophys. Res., Oceans*, vol. 120, no. 11, pp. 7195–7207, Nov. 2015.

[37] M. Joelson, M. C. Néel, G. Soriano, and M. Saillard, *Sur la Distribution Alpha Stable de la Pente des Vagues de Vent*. Marseille, France: Ème Congrès Français de Mécanique, 2009.

[38] Z. Guerraou, S. Angelliaume, and C.-A. Guérin, "Physical modeling of the upwind-downwind asymmetry in microwave return from the sea surface," in *Proc. IEEE Int. Geosci. Remote Sens. Symp. IGARSS*, Jul. 2018, pp. 228–231.

[39] J. W. Sapp, S. O. Alsweiss, Z. Jelenak, P. S. Chang, S. J. Frasier, and J. Carswell, "Airborne co-polarization and cross-polarization observations of the ocean-surface NRCS at C-band," *IEEE Trans. Geosci. Remote Sens.*, vol. 54, no. 10, pp. 5975–5992, Oct. 2016.

[40] H. Danièle, T. Podvin, M. Dechambre, G. Caudal, A. Mouche, and J. Daloze, "Polarimetric measurements over the sea-surface with the airborne storm radar in the context of the geophysical validation of the envisat asar," in *Proc. Eur. Space Agency (POLinSAR)*, Jan. 2003.

[41] A. A. Mouche, D. Hauser, J.-F. Daloze, and C. Guérin, "Dual-polarization measurements at C-band over the ocean: Results from airborne radar observations and comparison with ENVISAT ASAR data," *IEEE Trans. Geosci. Remote Sens.*, vol. 43, no. 4, pp. 753–769, Apr. 2005.

[42] Y. Quilfen, B. Chapron, A. Bentamy, J. Gourrion, T. El Fouhaily, and D. Vandemark, "Global ERS 1 and 2 and NSCAT observations: Upwind/crosswind and upwind/downwind measurements," *J. Geophys. Res., Oceans*, vol. 104, no. C5, pp. 11459–11469, May 1999.

[43] A. Stogryn, "Electromagnetic scattering from rough, finitely conducting surfaces," *Radio Sci.*, vol. 2, no. 4, pp. 415–428, Apr. 1967.

Multifrequency Radar Imagery and Characterization of Hazardous and Noxious Substances at Sea

Sébastien Angelliaume, Brent Minchew, Sophie Chataing, Philippe Martineau, and Véronique Miegebielle

***Abstract*— The increase in maritime traffic, particularly the transport of hazardous and noxious substances (HNSs), requires advanced methods of identification and characterization in environmental chemical spills. Knowledge about HNS monitoring using radar remote sensing is not as extensive as for oil spills; however, any progress on this issue would likely advance the monitoring of both chemical and oil-related incidents. To address the need for HNS monitoring, an experiment was conducted in May 2015 over the Mediterranean Sea during which controlled releases of HNS were imaged by a multifrequency radar system. The aim of this experiment was to establish a procedure for collecting evidence of illegal maritime pollution by noxious liquid substances using airborne radar sensors. In this paper, we demonstrate the ability of radar imagery to detect and characterize chemicals at sea. A normalized polarization difference parameter is introduced to quantify both the impacts of released product on the ocean surface and the relative concentration of the substance within the spill. We show that radar imagery can provide knowledge of the involved HNS. In particular, one can distinguish a product that forms a film on the top of the sea surface from another that mixes with seawater, the information that is critical for efficient cleanup operations.**

***Index Terms*— Chemical, hazardous and noxious substance (HNS), ocean, oil, oil and water mixing index, multifrequency, normalized polarization difference (NPD), polarimetry, pollution, sea surface, slick, spill, synthetic aperture radar (SAR).**

I. Introduction

AIRBORNE and spaceborne remote sensing techniques are of great interest for monitoring maritime pollution [1], [2]. Slicks are often detected using real aperture radar or synthetic aperture radar (SAR) because radar can be used any time and in almost any weather conditions [3]–[7]. For remote sensing applications, the ocean surface is usually modeled as the superposition of waves of different scales. At high frequency (microwave domain) and at moderate incidence angles (30°–60°), slick-free sea surface scattering calls for Bragg or tilted-Bragg scattering: the electromagnetic (EM) wave resonates with ocean waves with wavelengths comparable to the transmitted radar wavelength [8]. The slick layer on top of the sea surface damps these waves [9], [10], which are the main contributors to backscattered EM signal. Reduced backscatter causes slick-covered areas to appear as dark patches in the radar image.

Traditionally, SAR slick observation is based on single-polarization amplitude images, often vertically polarized transmit and receive (VV) radar waves. While algorithms have been developed to facilitate automatic slick detection, manual inspection is often needed [11]. Studies published in the literature have suggested the use of polarimetric SAR (POLSAR) parameters to improve the detection capability of slicks [12] and to attempt to characterize the observed pollution [13]–[17]. Nevertheless, some issues remain unresolved, such as the quantification of the spilled product or the distinction between polluted areas and look-alikes, which can arise in areas with relatively low winds, biogenic substances, or other natural sources [2].

Several parameters influence the capability of a radar sensor to detect maritime pollution. The sensor itself must be well adapted (high frequency is preferable to lower frequency [9]). Acquisitions must be made under low-to-moderate wind conditions (e.g., 2–12 m/s at C-band [5]) to ensure enough contrast between polluted and clean areas (lower limit) and to avoid too fast mixing of the product into the water column (upper limit). Under high wind speed conditions, wind-generated waves may receive enough energy to counterbalance the damping effect [18] and breaking-wave events can disperse slicks [19].

The nature of the involved substance is likewise a key issue. Marine slicks can be composed of mineral oils, including petroleum-based material, natural hydrocarbon seeps, or films from biological processes (called look-alike). However, they can also come from any other liquid substance produced by human activity, such as hazardous and noxious substances (HNSs). An HNS is defined by the International Maritime Organization (IMO) as any substance other than oil, which if introduced into the marine environment is likely to create hazards to human health, to harm living resources and marine life to damage amenities, or to interfere with other legitimate uses of the sea [20]. The effectiveness of radar remote sensing for HNS monitoring depend on the imaged product, the latter impacting the sea surface differently depending on its physical and chemical properties. In order to quickly evaluate the behavior of chemical substances

Manuscript received June 15, 2016; revised October 4, 2016 and December 21, 2016; accepted January 9, 2017. Date of publication March 6, 2017; date of current version March 17, 2017. This work was supported by the French National Research Agency through the POLLUPROOF research program under Grant ANR-13-ECOT-007.

S. Angelliaume and P. Martineau are with the Electromagnetism and Radar Department, ONERA, 13661 Salon-de-Provence, France (e-mail: sebastien.angelliaume@onera.fr; philippe.martineau@onera.fr).

B. Minchew is with the British Antarctic Survey, Cambridge, UK (e-mail: bremin15@bas.ac.uk).

S. Chataing is with the Research and Development Department, CEDRE, 29200 Brest, France (e-mail: sophie.chataing.pariaud@cedre.fr).

V. Miegebielle is with the Research and Development Department, TOTAL, 64018 Pau, France (e-mail: veronique.miegebielle@total.com).

Digital Object Identifier 10.1109/TGRS.2017.2661325

when released at sea, the Standard European Behavior Classification (SEBC) was created in the framework of the Bonn Agreement in 1994. Based on physical and chemical properties, i.e., specific gravity, water solubility, and vapor pressure, this classification enables a first estimation of short-term chemical substances behaviors: floating (F), sinking (S), evaporating (E), and dissolving (D), with the combinations represented as floater and dissolver (FD), ED, FED, and so on. Over the frequency range of 1 to 10 GHz (approximately L- to X-band), the penetration depth (i.e., skin depth) of seawater is between 0.1 cm and 1.0 cm [21]. Due to the shallow penetration of EM signal into seawater, radar remote sensing should be effective for monitoring only floating product, classified as F or a combination of F with another behavior such as floater and evaporator (FE). In the case of floating substance, the speed of evaporation or dissolution and the amount of released product are important because they strongly influence how the sea surface will be affected.

For decades, initiatives implemented by both the oil/shipping industry and governments have been largely focused on the fight against oil spills, which had the effect of drastically reducing the quantities discharged in oceans. For a period of 40 years (between 1970 and 2010), the average number of oil spills observed per year has fallen by more than 85% [22], [23], despite a steady increase in oil transported by sea. Similarly, the increase in marine transportation of HNS increases the risk that a marine HNS-related incident occurs. In response, the IMO has adopted a protocol aimed at providing a global framework for international cooperation in combating major incidents or threats of marine pollution from ships carrying HNS, such as chemicals. The Protocol on Preparedness, Response and Co-operation to Pollution Incidents by Hazardous and Noxious Substances (OPRC-HNS Protocol) was adopted in 2000 [20], following the principles of the International Convention on Oil Pollution Preparedness, Response and Co-operation (OPRC) adopted 10 years earlier [20]. Its objectives are to advance the adoption of adequate response measures in the event that an oil pollution incident does occur and to provide for mutual assistance and cooperation between states.

In addition to this international awareness, previous accidents that have resulted in marine pollution by chemicals have highlighted the need for the use of remote sensing assets to detect various HNS at sea. A complete database of spill incidents and threats in waters around the world can be found in [24] and [25]. Use or adaptation of sensors that have been successfully employed for oil spill monitoring needs to be investigated and any progress in this issue would likely advance both the monitoring of oil and chemical pollution [26].

Despite the utility of airborne and spaceborne radar systems for detecting chemicals at sea, less effort have been devoted to HNS monitoring with radar remote sensing than to oil slicks monitoring [22]. To address this knowledge gap, an experimental campaign of measurements (called POLLUPROOF) was conducted in May 2015 in the Mediterranean Sea (off the French coast). Controlled releases of six chemical and nonhydrocarbon oil products were carried out in collaboration with the French Navy and Customs. SETHI, the ONERA (French aerospace laboratory) airborne SAR system [27], acquired POLSAR data over the released products simultaneously at X- (9.75 GHz) and L-band (1.325 GHz). While beyond the scope of this paper, we note that optical imagery data (LWIR, SWIR, and UV) were also acquired during this campaign.

Our goals in this paper are to better understand the capability of high-resolution multifrequency SAR imagery to detect HNS at sea and the potential of radar remote sensing to relatively quantify the concentration of released product and to distinguish between different substances. This paper is organized as follows. Section II describes the experimental measurement campaign at sea, Section III presents the methodology for detecting and characterizing liquid substances discharged at sea, and Section IV presents some original results and demonstrates the relevance of radar imagery for monitoring HNS-related pollution over maritime surface.

II. Experimentation at Sea

A. Airborne Radar Imagery

SETHI is an airborne remote sensing imaging system developed by ONERA [27]. It integrates a new generation of radar and optronic payloads and can operate over a wide range of frequency bands from UHF and VHF to X-band, including L-band, with long-range and very high-resolution polarimetric and interferometric capabilities. SETHI is a pod-based system operating onboard a Falcon 20 Dassault aircraft, which is owned by AvDEF.

For the POLLUPROOF campaign, quad-pol SAR data were acquired at X- and L-band, with a range (across-track) resolution of 0.5 m (bandwidth from 9.6 to 9.9 GHz) and 1.0 m (bandwidth from 1.25 to 1.4 GHz), respectively. Images are processed with an azimuth (along-track) resolution equal to the range resolution at both X- and L-band, which implies an integration time equal to 1.1 s at X-band and 4.1 s at L-band. Imaged area is 9.5 km in azimuth and 1.5 km in range, with incidence angles from 34° to 52°. The instrument noise floor has been estimated using the method proposed in [28] and the results are shown in the Appendix. The estimated Noise Equivalent Sigma^0 (NESZ) is very low, ranging from around -37 to -50 dB at X-band and from around -51 to -53 dB at L-band, allowing a sufficient signal-to-noise ratio (SNR) over polluted areas for efficient analysis.

B. Chemicals Products

Six chemical substances have been chosen to evaluate the capability of remote sensing sensors: rapeseed oil, fatty acid methyl ester (FAME), toluene, heptane, xylene, and methanol. These chemicals are among the most transported substances by maritime freight in Europe. Methanol and liquid chemicals represent 46% of the 165 million tons annually transported by chemical carriers while vegetable oil accounts for 29% [22]. Some of these chemicals are classified as the most noxious substances in the IBC Code [20], which provides an international standard for the safe carriage by sea of HNS in bulk. Those chemicals have already been involved in accidents at sea, e.g., *Poona* sank in 1971 with 600 T of rapeseed

oil, *Grape On*e sank in 1993 with 3000 T of xylene, and *Cape Horn* carrying a cargo of 14 000 T of methanol was seriously damaged by an explosion in the port of Leghorn in 2003 [24], [25].

Rapeseed oil and FAME are in the vegetal oil family, while toluene, heptane, and xylene are petrochemical products and methanol is a member of the family of alcohols and derivates. Their main properties are described below and their values come from the supplier of each HNS, which agree with values found in [29] and [30].

1) *Rapeseed Oil:* Rapeseed or colza oil is vegetal oil obtained from crushed colza seeds. At ambient pressure and temperature, rapeseed oil is a viscous liquid with a specific gravity of 0.910. Rapeseed oil is insoluble in water and does not evaporate (vapor pressure below 0.01 kPa at 25 °C); these characteristics classify rapeseed oil as a floater F in the SEBC.
2) *FAME:* FAMEs are biofuel directly added in conventional fuels such as diesel. At ambient pressure and temperature, they are a liquid with a specific gravity of 0.888. This product is virtually insoluble in water (solubility of 0.023 $mg \cdot L^{-1}$ at 20 °C) and has relatively low evaporative potential (vapor pressure of 0.42 kPa at 25 °C) making it a floater F in the SEBC.
3) *Toluene:* Toluene, also named methylbenzene or phenylmethane, is an aromatic hydrocarbon that is commonly used as chemical reagent or solvent, particularly in the industrial sector. Toluene is a liquid at ambient pressure and temperature and has a specific gravity of 0.867. Toluene is nearly insoluble in water (535 $mg \cdot L^{-1}$ at 25 °C) and tends to evaporate relatively easily (vapor pressure of 2.91 kPa at 20 °C). Considering the SEBC classification, toluene is a floating and evaporating FE substance.
4) *Heptane:* Heptane is the generic term to identify one of the nine isomers of C_7H_{16} and is a saturated hydrocarbon of the linear alkane family. This is a constituent of fuel and is used as extraction solvent, synthesis intermediate in chemical industry, and solvent for glues, inks, rubbers and plastics. At ambient pressure and temperature, heptane is a volatile liquid (6 to 7.7 kPa at 20 °C) and nearly insoluble in water (<2 $mg \cdot L^{-1}$ at 20 °C). With a specific gravity of 0.710, heptane is lighter than water and floats. According to the SEBC classification, heptane is considered as evaporator E.
5) *Xylene:* Xylene, or dimethylbenzene, is a group of aromatic hydrocarbons with one methyl derivative on benzene. It is naturally present in oil, xylene is observed in (diesel) engine exhaust gases, either a residual oil chemical or formed during incomplete combustion. Xylene is also produced from oil in the petrochemical industry and is one of the 30 most produced chemicals in the USA. It is used in the printing industry, rubber, and leather industries mainly as a solvent. Xylene is an inflammable liquid with a pleasant fragrance. Chemical properties are similar from one isomer to another. Its specific gravity of 0.87 makes it float on water. Xylene is slightly soluble in water (146 $mg \cdot L^{-1}$ at 25 °C) and is not likely to evaporate (vapor pressure of 0.89 kPa at 20 °C). Due to these characteristics, xylene is considered as FE (floater and evaporator) in the SEBC classification.
6) *Methanol:* Methyl alcohol or methanol is the simplest alcohol of chemical formula CH_3OH. At ambient temperature, this polar liquid is used as antifreeze, solvent, or fuel (e.g., in aeromodelling). Methanol is not present in large amounts in nature and is industrially produced. Methanol is mainly used as basic material for chemical synthesis of more complex chemical products. Nearly 40% of methanol is converted in formaldehyde to be then transformed into plastics, synthetic resins, paints, explosives, or fabrics. Methanol is a light liquid (specific gravity of 0.791), volatile (vapor pressure of 12.3 kPa at 20 °C), miscible in water, inflammable and toxic with a characteristic odor. These properties enable the classification of methanol as DE, a dissolving and evaporating substance.

If one considers only the SEBC classification, we can expect to monitor rapeseed oil (classified as floater F), FAME (classified as floater F), toluene (classified as FE) and xylene (classified as FE) from radar remote sensing. For the last two, the speed of evaporation should be crucial. Thus, delays between releases and radar imagery must be short enough to allow efficient detection and analyses. For methanol and heptane, other remote sensing systems like infrared or ultraviolet sensors are expected to be more efficient [31].

During the POLLUPROOF experiment, 1 m^3 of each of these six products was released at sea and imaged by radar and optical airborne sensors. Optical remote sensing results are beyond the scope of this paper and we focus here on SAR observations. Vegetal oils (like plant oil or rapeseed oil) have already been imaged by SAR sensors (plant oil is often used to simulate a natural monomolecular biogenic slick) and are observable in radar imagery [32]. Radar remote sensing of the five other HNS has not been as extensively studied as mineral or vegetal oils, especially in the case of experimental releases at sea, and we consider these in detail below.

C. Planning of Measurements

For the POLLUPROOF campaign, airborne multifrequency POLSAR acquisitions have been conducted over chemicals presented before (Section II-B) and discharged by the French Navy in the Mediterranean Sea. Experimentation took place in May 2015 over the French coast where three flights were performed, with two releases per flight:

The first flight took place on 18 May from 16:40 to 17:30 UTC. The sea was calm. Heptane and toluene were released from 2 semisubmersible 1 m^3 tanks at 16:30 and 16:35 UTC, respectively. Heptane and toluene were released at known positions (separated by about 100 m). SAR acquisitions began 10 min after the first release (heptane) and 5 min after the second release (toluene).

The second flight took place on 22 May from 13:25 to 13:55 UTC. There was a heavy swell, restricting any activity at sea, and hence products were discharged directly from the back

TABLE I
ENVIRONMENTAL CONDITIONS

Date	TIME (UTC)	Wind speed (m/s)	Wind direction (from-deg)	Wave height (m)	Wave direction (from-deg)
18 may, 2015	17:00	8	255	0.5	240
22 may, 2015	13:00	7	315	2	270
22 may, 2015	16:00	7	315	1.75	270

TABLE II
FLIGHT $n°1$ (18 MAY, 2015)

Run number	Time (UTC)	Radar look direction (deg)
	16:27	**Heptane release**
	16:34	**Toluene release**
1	16:40	250°
2	16:48	250°
3	16:57	250°
4	17:06	250°
5	17:16	340°
6	17:25	340°
7	17:30	340°

TABLE III
FLIGHT $n°2$ (22 MAY, 2015)

Run number	Time (UTC)	Radar look direction (deg)
	12:35-12:46	**Methanol release**
	12:53-13:25	**Xylene release**
1	13:25	270°
2	**13:29**	**0°**
3	13:36	180°
4	13:45	270°
5	13:56	180°

of the boat (French Navy) advancing toward the east at a speed of 1 knot. Methanol was released from 12:35 to 12:45 UTC and xylene from 12:55 to 13:25 UTC. SAR acquisitions began 40 min after the end of the first release (methanol) and at the end of the second release (xylene).

The third flight took place on 22 May from 15:20 to 16:50 UTC. Because of the swell, products were also released directly from the back of the boat advancing toward the east at a speed of 1 knot. Rapeseed oil was discharged from 15:00 to 15:30 UTC and FAME from 15:25 to 15:40 UTC. SAR acquisitions were synchronized with releases.

Sea and weather conditions during experimentation are presented in Table I. A description of each run of SAR acquisition is given in Tables II–IV (Flights 1–3), respectively. In Tables III–IV, the lines in bold correspond to the acquisitions mainly analyzed in the following. In this paper, we focus on cross-wind observation because in this case the spill is well centered in the image, oriented parallel to the azimuth axes. For upwind or downwind acquisitions, the spill is across the swath and variations with incidence angle can add other effects. Note that sea conditions are not exactly the same for Flight 1 and for Flights 2 and 3. Due to weather conditions, methods of release also differ between Flight 1 and Flights 2 and 3. Since each chemical was released only once and since each spilled product is different from one flight to each other's, in this paper monitoring of HNS is studied regardless of sea conditions.

TABLE IV
FLIGHT $n°3$ (22 MAY, 2015)

Run number	Time (UTC)	Radar look direction (deg)
	15:01-15:28	**Rapeseed oil release**
	15:24-15:40	**FAME release**
1	15:22	270°
2	15:33	270°
3	15:43	270°
4	15:56	270°
5	**16:07**	**180°**
6	16:20	180°
7	16:33	0°
8	16:43	315°
9	16:49	270°

III. METHODOLOGY

A. Scattering From Ocean Surface

Ocean surfaces can be modeled as a composition of slightly rough tilted facets, each of which has superimposed small-scale surface roughness that creates a Bragg scattering [8]. Small-scale roughness is randomly distributed on the scattering surface and responds to the strength of local wind, i.e., gravity capillary waves, whose wavelength is of order centimeters to decimeters with periods less than 1 s [33]. The tilt of the facet is caused by larger scale gravity waves on the ocean surface that changes the local orientation, or tilt, of the short waves [34]. The orientation of the facet normal in the radar reference frame is defined by two angles ψ, which is the angle between local up and the projection of the facet normal onto the radar scattering plane, and ξ, the angle between local up and the projection of the facet normal onto the vertically oriented plane perpendicular to the scattering plane [35]. The resulting local incidence angle of the EM wave is

$$\theta_i = \cos^{-1}\left[\cos\left(\theta + \psi\right)\cos\xi\right] \tag{1}$$

where θ is the EM angle of incidence relative to local untilted up. The copolarized radar backscattered power is proportional to the normalized radar cross section (NRCS), which is defined as [8]

$$\sigma^0_{pp} = 4\pi\, k^4_{EM} \cos^4\theta_i \Gamma_{pp}\, W \tag{2}$$

where the subscript p denotes either H (horizontal) or V (vertical) polarization, $k_{EM} = 2\pi/\lambda_{EM}$ is the EM wavenumber corresponding to wavelength λ_{EM}, W is the spectral density of the ocean surface roughness, and Γ_{pp} is the reflectivity. The spectral density of the ocean surface describes the shape or directionality of the radar signal scattered by the ocean surface [21], while the reflectivity describes the total power scattered from the surface. Copolarized reflectivity is a function of the facet tilt, EM wave incidence angle, and the electrical properties of the seawater such that

$$\Gamma_{pp} = \left| \left(\frac{\sin(\theta + \psi)\cos\xi}{\sin\theta_i} \right)^2 \alpha_{pp} + \left(\frac{\sin\xi}{\sin\theta_i} \right)^2 \alpha_{qq} \right|^2 \quad (3)$$

where the subscript p $(p \neq q)$ denotes either H or V polarization. The Bragg scattering coefficients, defined as [8]

$$\alpha_{HH} = \frac{\cos\theta_i - \sqrt{\varepsilon_r - \sin^2\theta_i}}{\cos\theta_i + \sqrt{\varepsilon_r - \sin^2\theta_i}} \quad (4)$$

$$\alpha_{VV} = \frac{(\varepsilon_r - 1)(\sin^2\theta_i - \varepsilon_r(1 + \sin^2\theta_i))}{(\varepsilon_r \cos\theta_i + \sqrt{\varepsilon_r - \sin^2\theta_i})^2} \quad (5)$$

depend only on the local incidence angle of the EM wave θ_i and the relative dielectric constant ε_r. For a given viewing geometry (fixed incidence angle) and assuming that the ocean surface is homogeneous over a sufficiently large area, the NRCS is a function of only the EM wavelength, the relative dielectric constant and the sea surface roughness.

In the case of an ocean surface covered by slicks, the product surface layer will damp the gravity-capillary waves, thereby attenuating the radar backscattered power. The relative dielectric constant can also be reduced in the case of a product that is mixed with seawater, because the relative dielectric constant of released product is low compared to seawater. See [35] in the case of oils and dielectric properties of HNS studied during the experiment have been measured to be similar of those of oil (authors are not allowed to publish the actual values). The resulting NRCS will be lower for a product mixed with water than for clean sea surface.

This study is based on the principle that in the case of a thin layer, only the short gravity-capillary waves will be damped. When the layer gets thicker, longer gravity capillary waves should also be damped (see Figs. 1 and 3 [36]). These phenomena should be observable in the case of multifrequency SAR data acquired simultaneously over the same surface. Moreover, this should be enhanced when using sufficiently different EM wavelengths (e.g., X- and L-band) since the EM signal will simultaneously interact with hydrodynamic mechanisms of different scales.

From the above model of the sea surface and interactions with the EM signal, we propose two methods. The first method allows for detection and relative quantification of the impact of a released product on the ocean surface (Section III-B). The second method allows for characterization of the behavior of the involved substance discharged in the marine environment (Section III-C).

B. Detection and Relative Quantification

Many studies have suggested using POLSAR parameters to improve slick detection capability. A useful review of those parameters has been proposed in [11], wherein most of the methods published in the literature for oil slicks detection are presented. A comprehensive comparison of those parameters was undertaken in [37]. Following [38], [37] quantitatively demonstrates the effectiveness of the polarization difference (PD) for oil slick detection on the ocean surface. PD is defined such as

$$\mathrm{PD} = \sigma^0_{VV} - \sigma^0_{HH} \quad (6)$$

where σ^0_{PP} is the NRCS (in linear units) and the subscript p denotes either H or V polarization.

The interest in this parameter for a marine pollutant detection application is that PD is proportional to the spectral density of the ocean surface roughness W [39]. As discussed in [38] and [40], the nonpolarized part of the backscattered signal is removed using PD, and thus it mostly contains contribution due to short wind waves around the Bragg wavenumber. This is precisely the scale of waves that will be mainly affected by the presence of a liquid substance on the sea surface; which makes PD an attractive parameter for slick detection at sea [38]. To enhance its use, we propose in this paper a normalized variant of PD. We note that PD ranges from a maximum value that occurs in the case of a clean sea surface ($\mathrm{PD_{water}}$) and goes to 0 as the impact of the substance on the surface increases, since both VV and HH reflectivity tend to 0 over a perfectly smooth surface. Hence, we define the normalized PD (NPD) as

$$\mathrm{NPD} = 1 - \frac{\mathrm{PD}}{\mathrm{PD_{water}}} \quad 0 \leq \mathrm{NPD} \leq 1. \quad (7)$$

Following (2) and (6), NPD can be written in terms of spectral density and reflectivity as

$$\mathrm{NPD} = 1 - \frac{W^{\mathrm{slick}}\left(\Gamma^{\mathrm{slick}}_{VV} - \Gamma^{\mathrm{slick}}_{HH}\right)}{W^{\mathrm{water}}\left(\Gamma^{\mathrm{water}}_{VV} - \Gamma^{\mathrm{water}}_{HH}\right)} \quad (8)$$

where superscripts *water* and *slick* correspond to uncontaminated and contaminated water, respectively. The NPD depends on two contrasts between contaminated and uncontaminated water, one contrast on the spectral density of the surface (W), which is driven by the difference of roughness between the two surfaces, and the other on the polarimetric reflectivity difference. Assuming that the tilt angles are constant regardless of the presence of slick [41], the latter contrast depends on the difference in the dielectric constant between the clean sea surface and the polluted water. NPD is equal to 0 over clean sea area and goes to 1 as the concentration or the impact of the product on the ocean increases. Hence, NPD can be interpreted as an indication of the presence and the relative concentration of a substance on the sea surface. It can be used directly or with a threshold to produce a binary detection map. Therefore, a detection map and a relative quantification map can be computed simultaneously based on NPD. This information is valuable for both identifying polluted sea surfaces and locating the most contaminated areas, thus guiding cleaning operations.

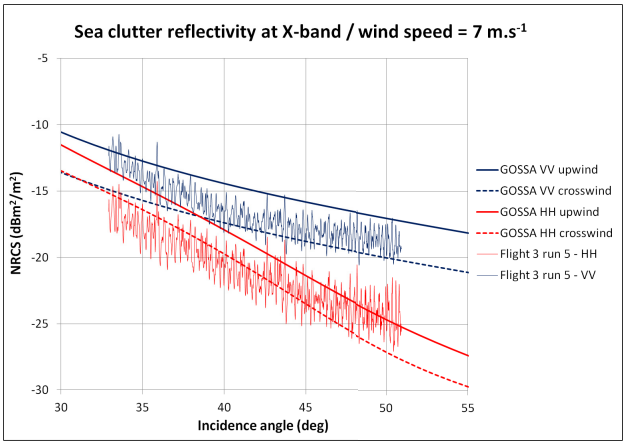

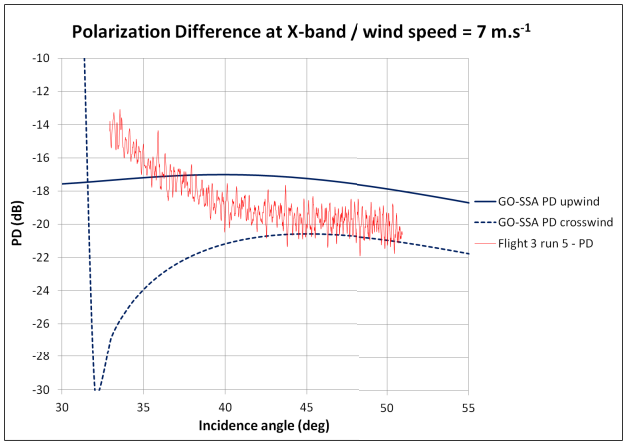

X-band: sea clutter reflectivity (left) and Polarization Difference (right)

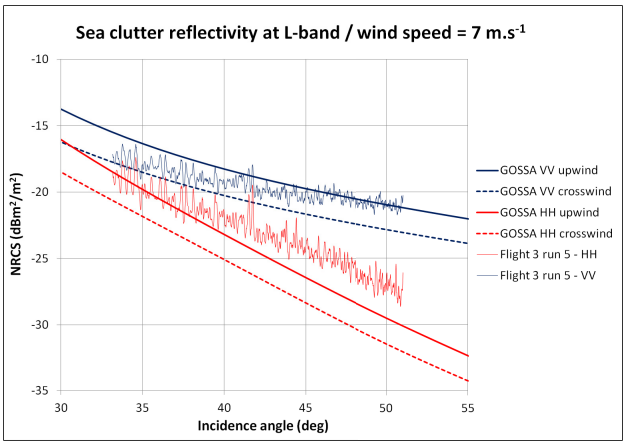

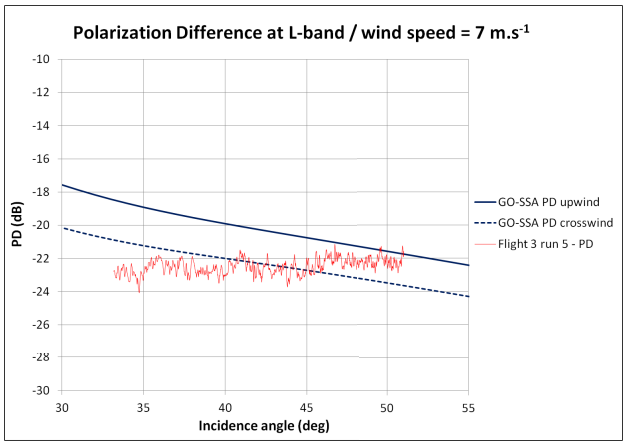

L-band: sea clutter reflectivity (left) and Polarization Difference (right)

Fig. 1. Comparison between the measured and theoretical sea clutter reflectivities (left) and PD (right) at X-band (top) and L-band (bottom).

In (7), PD_{water} is the PD value obtained in the case of a clean sea surface. It can be computed directly from the dual copolarized channels (HH and VV) over uncontaminated area of water imaged by the radar, most likely selected by visual inspection. If an automatic process is needed, PD_{water} can be estimated through a model. This latter method requires only wind speed and wind direction information, but uncertainties induced by the chosen model and the meteorological parameters can introduce some differences between the estimated and the measured PD_{water} values. The selection of the model should be done judiciously and in the following, the GO-SSA physical two-scale model [42] is used to estimate the PD over clean sea surface with the wind information given in Table I.

A comparison between theoretical values obtained with the GO-SSA model and values measured over uncontaminated areas of SAR data are shown in Fig. 1. Experimental data used for this comparison were acquired during the third flight for a crosswind observation (fifth run). The PD values are plotted in decibel scale to enhance interpretation. We can observe an overall agreement between the physical two-scale model and experimental measurements, especially at X-band. At L-band, estimated values are slightly lower than measured, and so estimated PD_{water} is underestimated by only 1 or 2 dB. We assume that this difference is due to the presence of a strong swell, not taken into account in the GO-SSA model, with a stronger effect at low frequency than at high frequency. Nevertheless, those discrepancies will weakly impact the exploitation of the data while making it more automatic, since it does not require manual selection of a clean sea area through the entire swath of an image.

C. Characterization

When a pollutant spills into a marine environment, the selection of the appropriate response requires detailed knowledge of the physical and chemical properties of the involved substance. It has been demonstrated in [41] that for the case of an oil-related offshore pollutant, SAR imagery can indicate whether the spilled product behaves like a viscoelastic film that is more or less homogenous and floating on the surface or if the spilled product is mixed with seawater within the upper few centimeters of the water column. The basic premise of this method, which yields the oil–water mixing index (M), is that radar backscattered power is diminished by oil slicks through

mechanical damping of Bragg wavelength gravity capillary waves and reductions in the relative dielectric constant of the upper few centimeters near the sea surface [35], [41]. By decoupling the relative contribution to signal attenuation of mechanical damping of surface roughness and changes in dielectric constant, we can define the characteristics of the slick along a spectrum ranging from thin surface films to a product mixed with seawater within the water column [41].

In addition to the assumptions underlying the NRCS model (2), the process of decoupling the mechanical and EM attenuation mechanisms is based on the following assumptions.

1) The long-wavelength tilting of the sea surface [as described by angles ψ and ξ in (1)] is unaffected by the presence of an oil slick [35].
2) The dielectric constant of uncontaminated seawater is well constrained [21].

These assumptions allow for inferences of the long-wavelength tilting of the sea surface over the entire radar image (so long as the radar images ample areas of uncontaminated water), the dielectric constant of contaminated water, and the small-scale roughness spectrum of both contaminated and uncontaminated water. As described in detail in [41], the salient parts of the process of decoupling the mechanical and EM attenuation mechanisms can be summarized as follows.

1) Use the copolarized ratio over uncontaminated seawater and an assumed value for the dielectric constant of pure seawater, $\varepsilon_r^{\text{water}}$, to infer the long-wavelength tilting of the ocean surface. In the following, $\varepsilon_r^{\text{water}}$ is taken to be $80 - \text{i}70$ [21].
2) Calculate the short-wavelength roughness spectrum over uncontaminated water, W^{water}, by applying the tilt angles estimated in 1).
3) For each pixel of contaminated water, infer the local (effective) relative dielectric constant, $\varepsilon_r^{\text{slick}}$, from the copolarized ratio and the estimated long-wavelength tilt angles deduced from 1).
4) Calculate the short-wavelength roughness spectrum over contaminated water, W^{slick}, using the dielectric constant inferred in 3) and the tilt angles obtained in 1).

Once 1)–4) are complete, we can calculate M as

$$M = M_W - M_\alpha \tag{9}$$

where

$$M_W = \frac{W^{\text{water}} - W^{\text{slick}}}{W^{\text{water}}} \tag{10}$$

$$M_\alpha = \frac{|\alpha_{VV}^{\text{water}}|^2 - |\alpha_{VV}^{\text{slick}}|^2}{|\alpha_{VV}^{\text{water}}|^2}. \tag{11}$$

M_W ($0 \leq M_W \leq 1$) is the *normalized damping factor* and M_α ($0 \leq M_\alpha \leq 1$) is the *normalized power attenuation factor*. M_W is a measure of how much the product will damp the sea surface roughness (0 indicates no damping and 1 indicates total damping), while M_α is a measure of how much the backscattered signal is attenuated due to a lower relative dielectric constant (0 indicates no attenuation and 1 indicates total attenuation).

M ($-1 \leq M \leq 1$) is the oil–water mixing index introduced in [41] that we will apply here in the case of HNS-related incident. Negative values indicate that reduced EM amplitudes are due more to reduced relative dielectric constants than to damped surface roughness, meaning that the product is largely mixed with seawater. On the other hand, positive values indicate that the decreasing of the EM signal is mainly due to smoothing of the ocean surface, and thus product is primarily present as a film on the sea surface. In an operational context, this information may be valuable to identify the behavior of the pollutant and guide response activities.

IV. Results and Discussion

We applied the methodologies described in the previous section to identify and characterize HNS released during the POLLUPROOF experiment. We first analyze which of the six chemicals discharged are detectable with radar imagery. Then we discuss the efficiency of multifrequency POLSAR imagery for HNS-related maritime pollution monitoring.

A. Observation of Hazardous and Noxious Substances at Sea

During the first data acquisitions, heptane and toluene were discharged at sea and the slick areas were imaged by SETHI. Neither chemical was detected in SAR acquisitions at either X-band or L-band. The lack of radar detection is likely due to the extreme volatility of heptane and toluene. As previously noted, heptane and toluene were released only 5 and 10 min before acquisitions, and despite the short time lag between discharge and measure, it is likely that evaporation is important enough so that the chemicals are not observed in SAR imagery.

Methanol was released during the second exercise. Given that methanol is both extremely volatile substance and soluble in water and that SAR imagery occurred 40 min after the end of its release, methanol was never observed in SAR acquisitions at either X-band or L-band.

SAR observations collected over released xylene show that this chemical is observable as an area of reduced amplitude on SAR images (Fig. 2). As for oil, the contrast is enhanced using VV polarization compared with HH (not shown here) and the impact of the product is more pronounced at X-band than at L-band. The approximate area extent of the spill was 0.26 km^2, and the bright point just at the end of the spill is the ship (53 m length) from which the discharges were performed. One can observe a strong impact of xylene on the sea surface imaged at X-band. At L-band, the slick is not easily observable, probably due to a low effect of this HNS on the sea surface damping only short gravity capillary waves corresponding mainly to the X-band Bragg wavelength. SAR images over xylene were acquired up to 30 min after the end of the release and the HNS is still observable even on the later acquisition. Both toluene and xylene are classified as floating and evaporating FE substance according to the SEBC classification. However, toluene (whose vapor pressure at 20 °C is 2.91 kPa) was not observed (SAR imagery started 40 min after the end of the release), while xylene (whose vapor pressure at 20 °C is 0.89 kPa) is detectable on all SAR data, acquired up to 30 min after the end of the release.

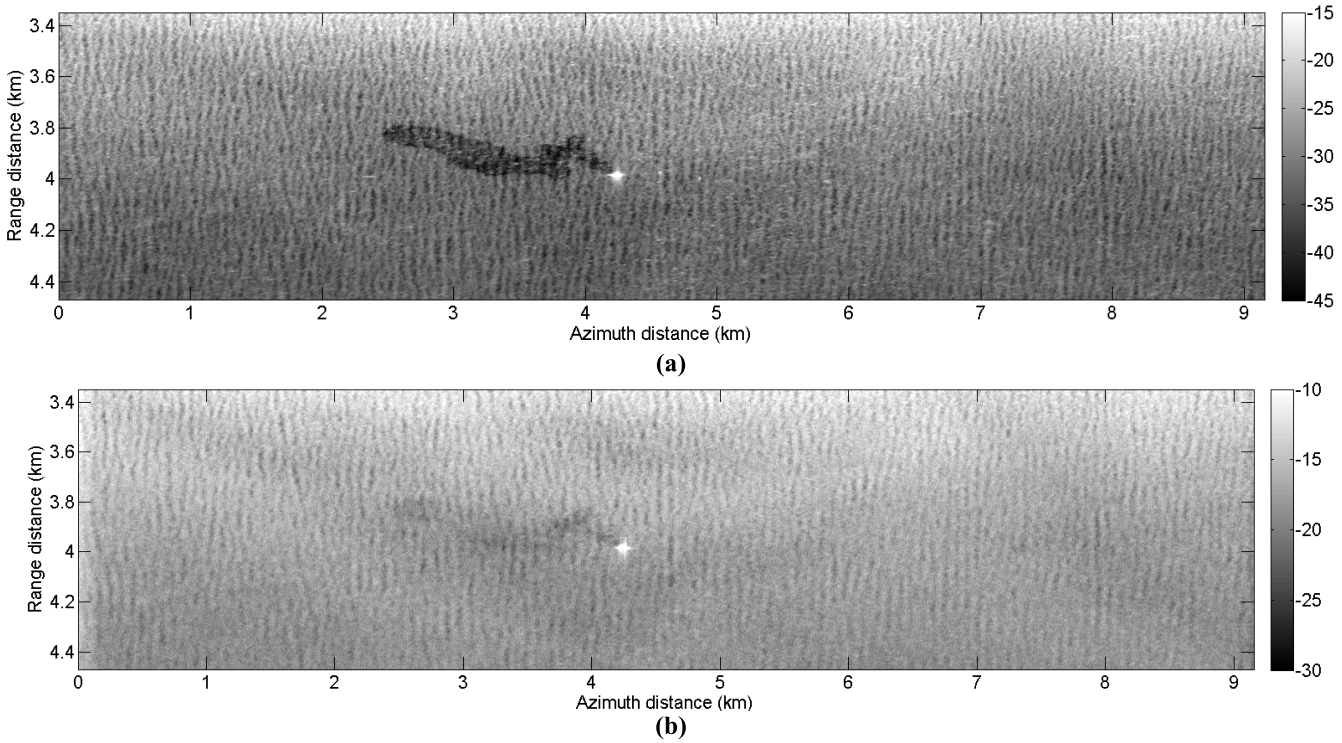

Fig. 2. SAR images over xylene for (a) X-VV and (b) L-VV taken on May 22, 2015 at 13:29 UTC (multilook 7×7), crosswind observation.

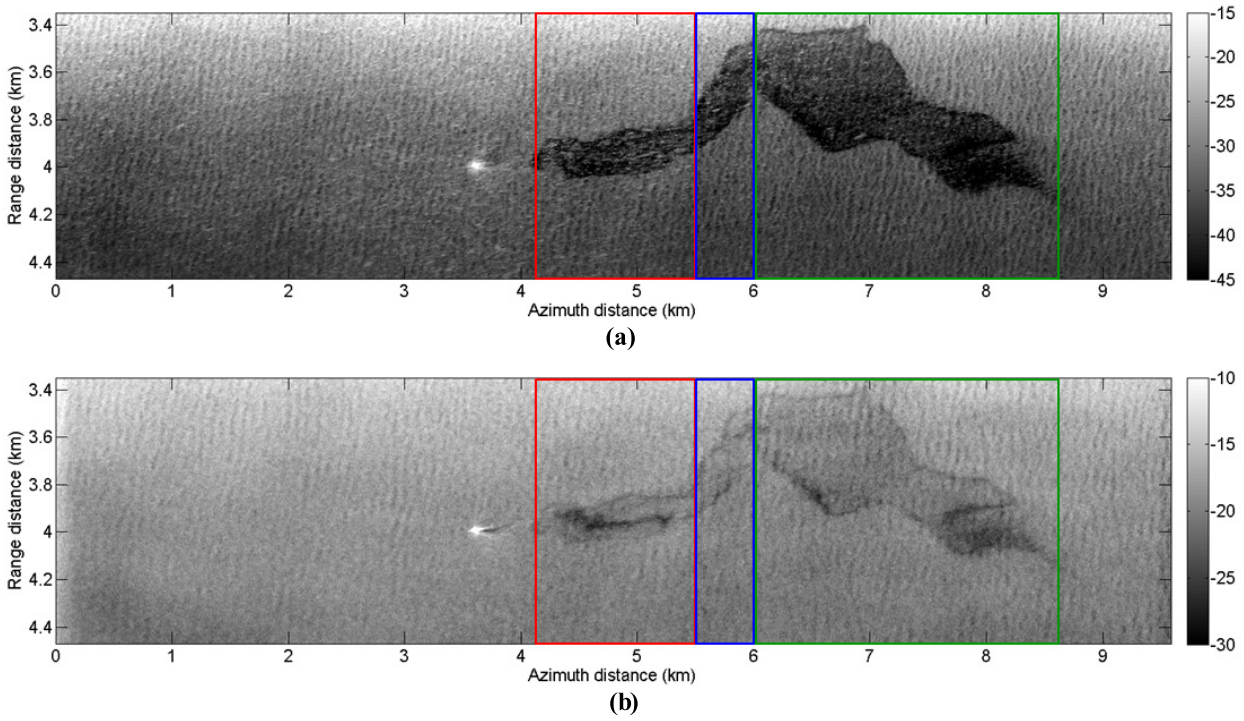

Fig. 3. SAR images over rapeseed oil and FAME for (a) X-VV and (b) L-VV taken on May 22, 2015 at 16:07 UTC (multilook 7×7), crosswind observation. FAME is indicated by the red box, rapeseed oil by the green box, and the blue box corresponds to a mixture between the two chemicals.

SEBC enables only a first estimation of chemical behaviors, here it is observed that *a priori* detection of HNS using SAR remote sensing cannot be based only on this classification, the importance of the evaporation rate of a chemical when monitored by remote sensing is also a key parameter.

The two more persistent HNS, classified as a floater F in the SEBC, have been studied during the last flight. Both rapeseed oil and FAME are observable on SAR images acquired at X- and L-band. VV polarized images for crosswind observation over the two releases forming a single spill are shown (Fig. 3). Data have been acquired at 16:07 UTC, namely, 40 min after the end of the rapeseed oil release and 30 min after the FAME release. Rapeseed oil, having been discharged first, corresponds to the right part of the spill while FAME to

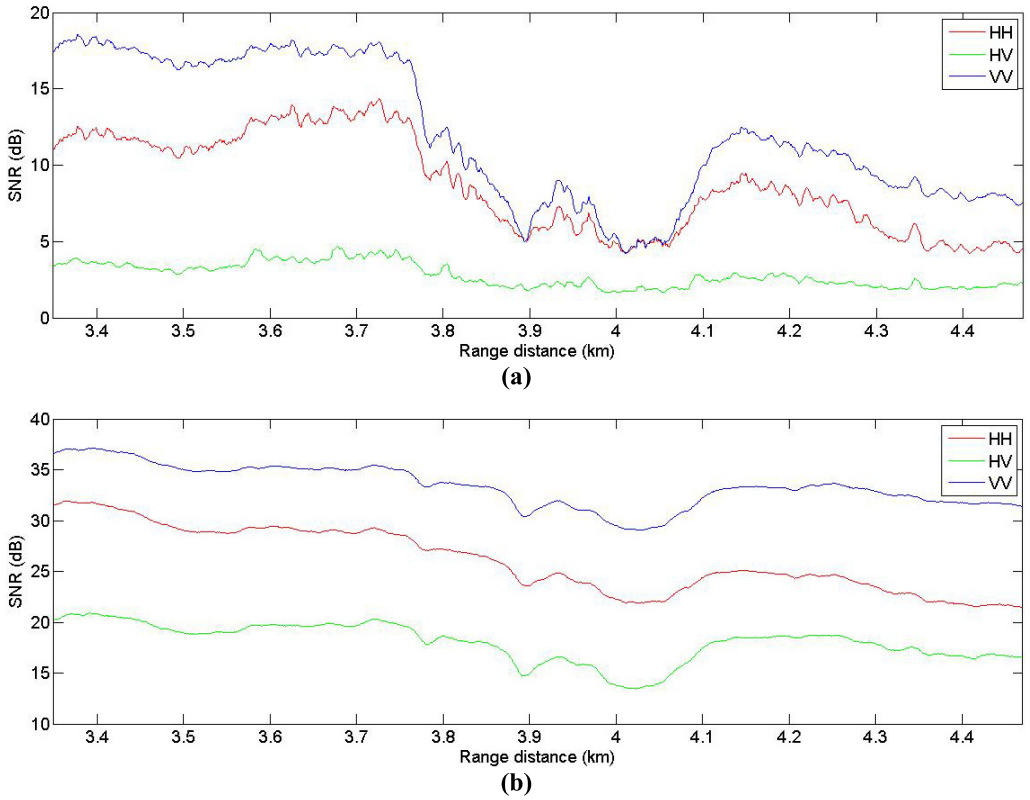

Fig. 4. SNR at X-band (a) and L-band (b) for polarization HH (red curve), HV (green curve), and VV (blue curve) taken on May 22, 2015 at 16:07 UTC. Range transect for azimuth 8 km (see Fig. 3).

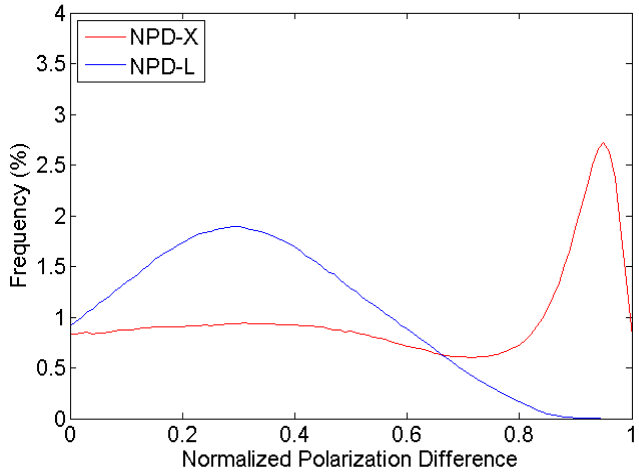

Fig. 5. Histograms of NPD at X-band (red curve) and L-band (blue curve) over full area (uncontaminated and contaminated seawater).

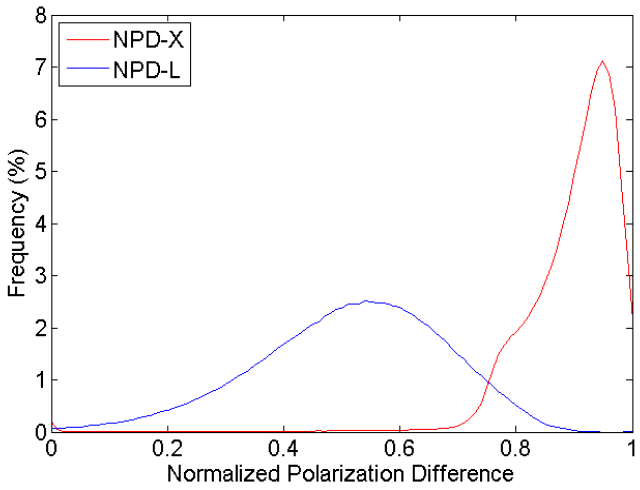

Fig. 6. Histograms of NPD at X-band (red curve) and L-band (blue curve) over contaminated seawater.

the left. The overall surface of the spill is 1.745 km^2. From *in situ* information, we know that FAME ranges from azimuth 4100 to 5500 m (covering a surface of 0.29 km^2; see the red box in Fig. 3), and that rapeseed oil is from azimuth 6000 to 8500 m (which corresponds to a surface of 1.26 km^2; see the green box in Fig. 3). In between, we have a mixture of the two products (surface of 0.195 km^2; see the blue box in Fig. 3). These amplitude images do not allow us to distinguish the two chemicals that form the spill because their respective impact on the backscattered signal appears similar, in terms of amplitude.

The SNRs computed for SAR data acquired during the third flight (run 5 at 16:07 UTC) are shown in Fig. 4. The range transect is computed for the azimuth 8000 m; the spill is between range 3750 and 4100 m (see Fig. 3). For polarization HH and VV, the SNR is greater than 5 dB at X-band and 20 dB at L-band. This allows for an efficient analysis of copolarized channels, even over polluted areas, for both frequency bands. Note that the SNR for the cross polarization at L-band is also very high.

The HV channel is never used in this paper, but the high value of SNR suggests interesting perspectives for the exploitation of the cross polarization.

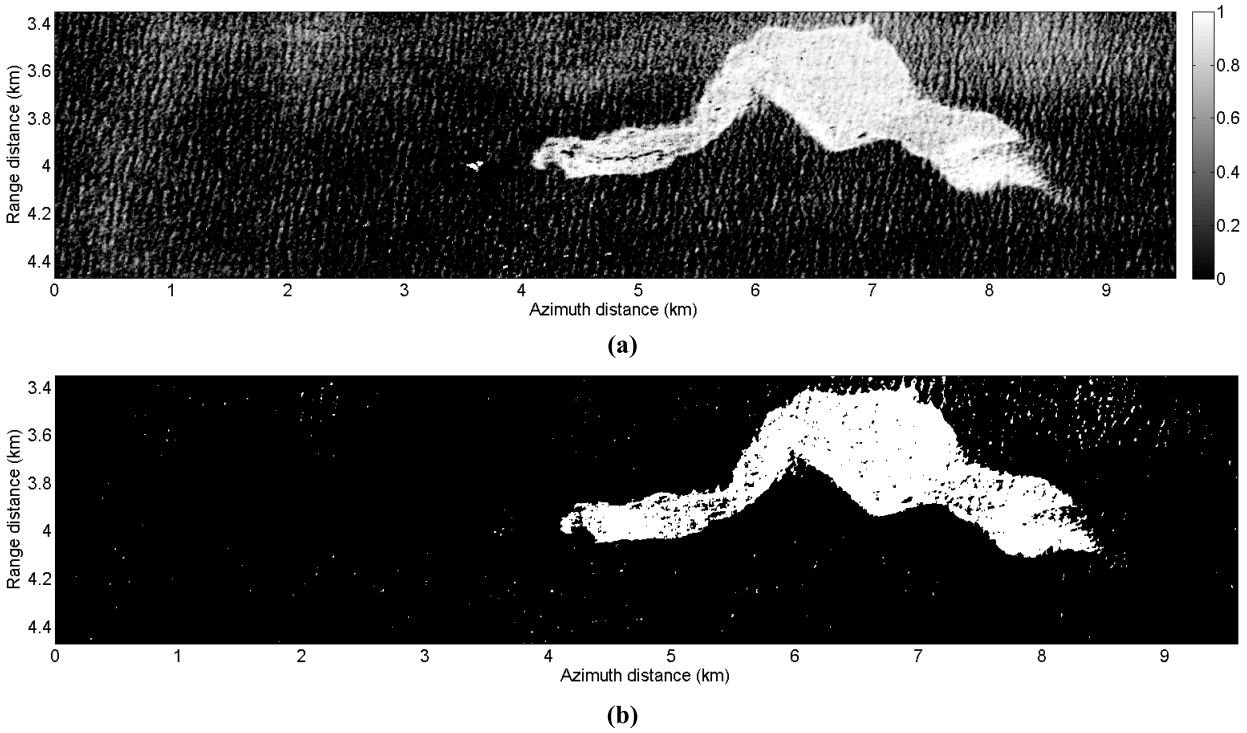

Fig. 7. NPD at (a) X-band and (b) detection mask taken on May 22, 2015 at 16:07 UTC for FAME and rapeseed oil (multilook 7×7), crosswind observation.

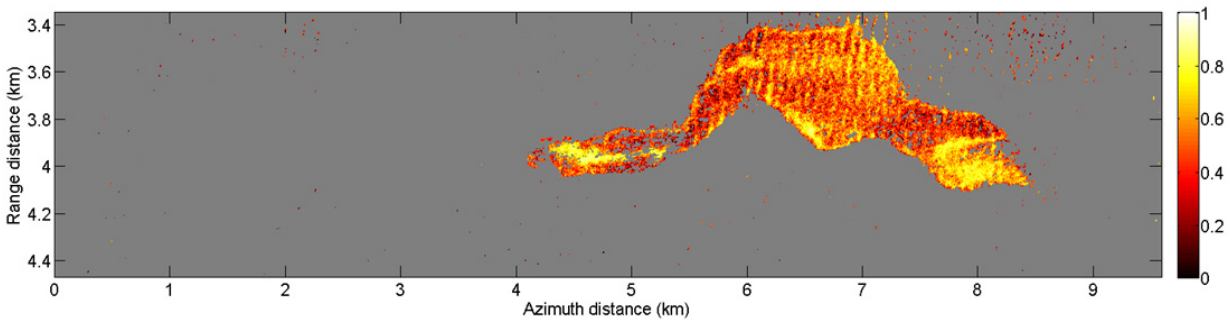

Fig. 8. NPD at L-band taken on May 22, 2015 at 16:07 UTC for FAME and rapeseed oil (multilook 7×7).

At X-band polarization VV, we measure a contrast of 5–10 dB between pure seawater and sea polluted by HNS, while at L-band, the contrast is lower than 5 dB. Contrast between the spill and the clean sea surface is more significant at X-band than at L-band, which support the use of high frequencies compared with low frequencies for maritime pollution monitoring [9], even in the case of HNS-related incident. While at X-band, the spill seems homogeneous [Fig. 3(a)], at L-band [Fig. 3(b)], we observe strong variations of the EM signal into the spill with dark patches. We can assume that short gravity capillary waves, corresponding to the X-band Bragg wavelength, are more or less damped anywhere within the spill, which implies, at this wavelength, a uniformly low response over the contaminated area. At L-band, the spill looks heterogeneous and a high SNR allows us to identify areas within the spill where HNS as a stronger impact than elsewhere, probably due to a higher concentration of the chemical. These observations support previous results [9], [43] and the NRCS model, which all show that the characteristics of EM backscatter over contaminated seawater are wavelength dependent. Thus by using different frequency bands, we should be able to better characterize the contaminant.

B. Detection and Quantification of Impact on the Ocean Surface

We now undertake a quantitative study of the added value of multifrequency POLSAR imagery for monitoring chemical pollution at sea. As presented in Section III-B and based on previous work done about oil-related incident, the NPD is proposed to detect HNS at sea and quantify their relative concentration on the ocean surface.

Histograms of NPD values at X- and L-band computed over data acquired during the last flight (FAME and rapeseed oil releases) are shown in Figs. 5 and 6 (histograms obtained over the entire image scene and histograms computed only over the contaminated area), respectively. At X-band (see the red curve in Fig. 5), the histogram shown in Fig. 5 has a strong maximum at 0.95, corresponding to seawater contaminated by FAME or rapeseed oil. Lower values are those of

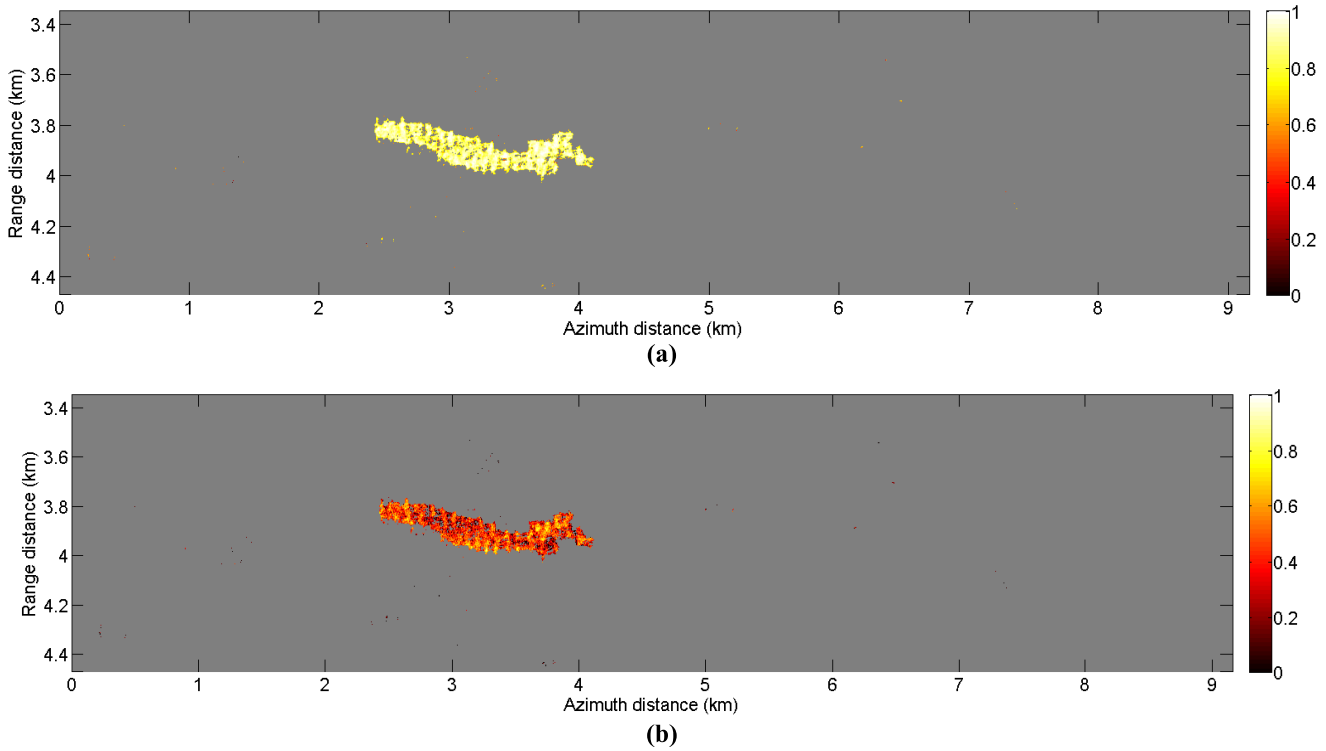

Fig. 9. NPD at (a) X-band and (b) L-band taken on May 22, 2015 at 13:29 UTC for xylene (multilook 7×7), crosswind observation.

clean seawater (see the red curve in Fig. 5). The distinction between slick and slick-free areas is thus clear. Interestingly, at L-band (see the blue curve in Fig. 6), one can observe more variation of the NPD parameter within the spill, with values ranging mainly from 0.2 to 0.8. These variations make detecting HNS more challenging with L-band than with X-band but suggest that with a sufficiently high SNR and with a well-adapted frequency, EM signal allows for measurements of the relative impact of product within the spill. This impact should be related to the concentration of product.

From these observations, the proposed method to detect and relatively quantify maritime pollution is as follows.

1) First, a detection mask is calculated by thresholding the NPD map at X-band.
2) Then, the L-band NPD parameter is computed over detected pixels from the previous step.

This methodology was applied on data acquired during the releases of FAME and rapeseed oil (third flight). The NPD map at X-band and the detection mask obtained by thresholding the NDP values at X-band for values greater than 0.7 are shown in Fig. 7. The empirical value of 0.7 was manually chosen from the results obtained with this experiment. Automatic selection of a threshold is a subject for future studies. The ship, from which the discharges were performed, has been filtered by thresholding the copolar phase, assumed to be null over sea surface and nonzero over ships. The NPD map at L-band, to which the detection mask is applied, is shown in Fig. 8. One can observe that the spill is well detected using this method. A wave pattern is observable in the upper part of the rapeseed oil spill, which corresponds to the impact of the swell on the radar reflectivity (Fig. 3) and should not be interpreted as a local variation of the HNS concentration. On the other hand, an evolution of the concentration is clearly observable on the right part of the spill (range: 7.2–8.5 km). Then, we can observe that information provided by the two frequencies is effectively different: at X-band values of NPD within the spill are almost always close to 1.0 (between 0.8 and 1.0), whereas at L-band, much more fluctuations are observed. Similar results are obtained with X- and L-band SAR data acquired over xylene release (Fig. 9). At X-band, response is saturated by the presence of the liquid substance. This frequency is perfectly suited for detection but does not seem to provide information on the thickness (for the SNR with which SAR data were acquired). At lower frequency (L-band in our case), the EM signal backscattered by the spill fluctuates with the concentration of the HNS within the contaminated area. Information provided by NPD and simultaneous use of two frequency bands allow us to detect HNS at sea and to quantify their impact on the ocean surface in terms of relative concentration. However, results shown in Fig. 8 do not enable us to distinguish between the two products that form the spill (rapeseed oil and FAME). The oil–water mixing index (M) is then required to achieve this.

C. Characterization

In the third exercise, two chemicals were successively discharged: rapeseed oil and FAME, forming a single spill. The right part of the spill is rapeseed oil and the left part is FAME. Both products are classified as floater F in the SEBC, but from the physical and chemical properties of each HNS (see Section II-B), one can expect different behaviors of each product on the sea surface. Indeed, rapeseed oil is supposed to

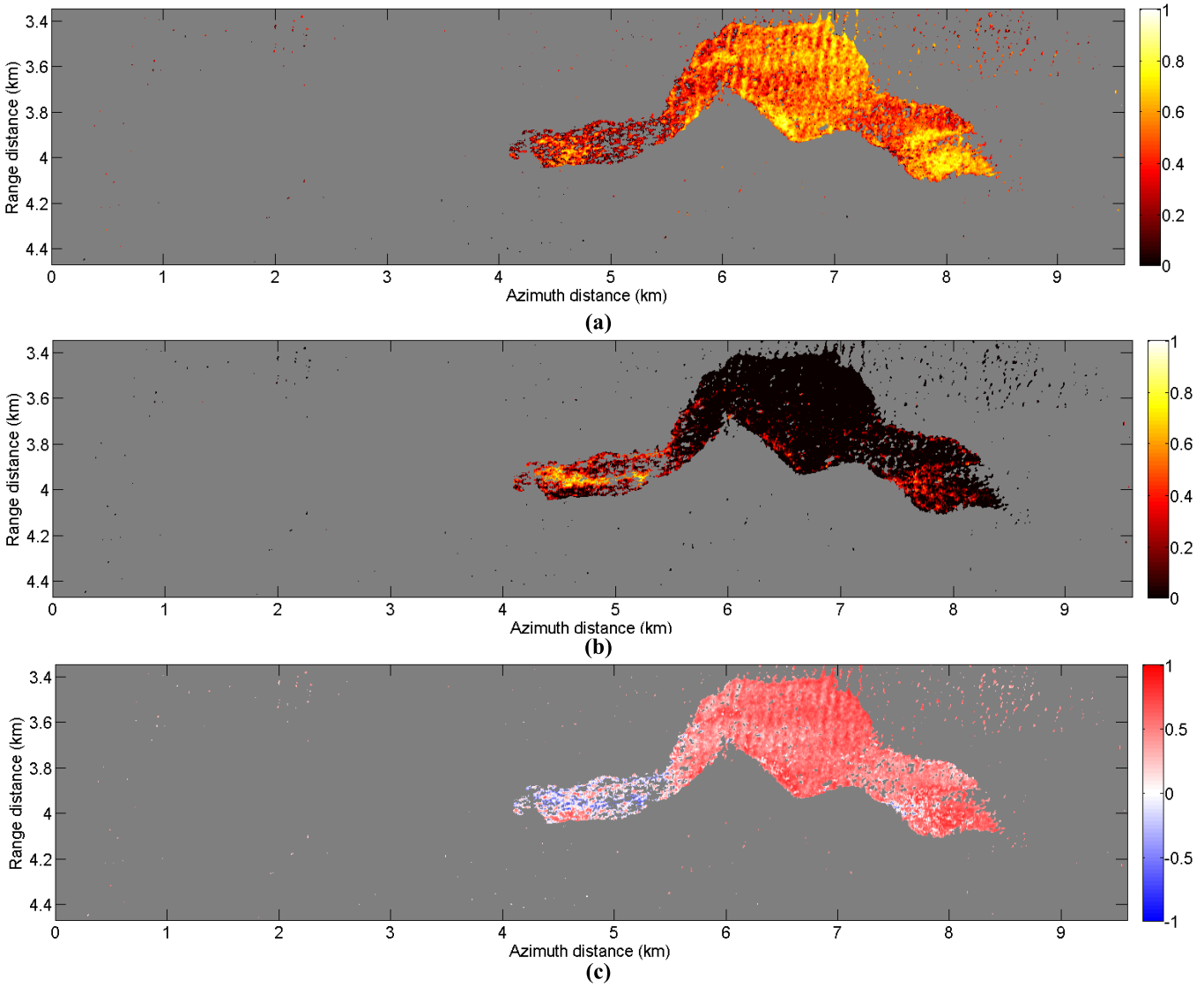

Fig. 10. (a) M_W, (b) M_α, and (c) M in the case of L-band acquisitions taken on May 22, 2015 at 16:07 UTC for FAME and rapeseed oil (multilook 7×7), crosswind observation.

remain above the surface and produce a film, while FAME will form a cloud in the water column composed of microdroplets. This is confirmed by observations made from the ship during the releases. These behaviors should be observable with SAR imagery as they impact the ocean surface in different ways.

Following the results presented in Section IV-B, we focus on L-band data and compute M_W, M_α, and M parameters using the method presented in Section III-C and initially published in [41]. As for NPD map (see Section IV-B), a detection map has been used beforehand and values have been computed for each pixel detected as contaminated using X-band data.

Fig. 10 shows the maps obtained over the releases for the normalized damping factor (M_W), the normalized power attenuation factor (M_α), and the mixing index (M). First, gravity capillary waves are more damped on the right side of the spill than on the left side (lower M_W values on average for the last than for the former). Inversely, the signal attenuation due to a decrease in the dielectric constant is higher on the left part than on the right part (M_α close to 0). Finally, by combining these two pieces of information, we observe in the M map the separation between the two chemicals constituting the spill [see Fig. 10(c)]. On average, M is equal to 0.6 on the right part of the spill, which reveals the presence of a film on the sea surface, and M is negative on the left part, meaning that the HNS is mixed with seawater with lower effect on the ocean surface roughness than on the right part. These behaviors match visual observations made during rapeseed oil and FAME discharges and are consistent with behaviors predicted by chemical and physical properties of each chemical (see Section II-B). L-band SAR data acquired at 16:20 UTC have also been investigated. The same results are generally obtained as for data acquired 13 min before, which confirms that the measured variation (between FAME and rapeseed oil) of M_α, M_w, and M parameters is related to the HNS and not caused by a temporal effect.

Maps of M_W, M_α, and M parameters obtained over the xylene release are shown in Fig. 11. The results presented in Figs. 10 and 11 show a similar behavior of xylene and rapeseed oil once released at sea. These two HNS form a

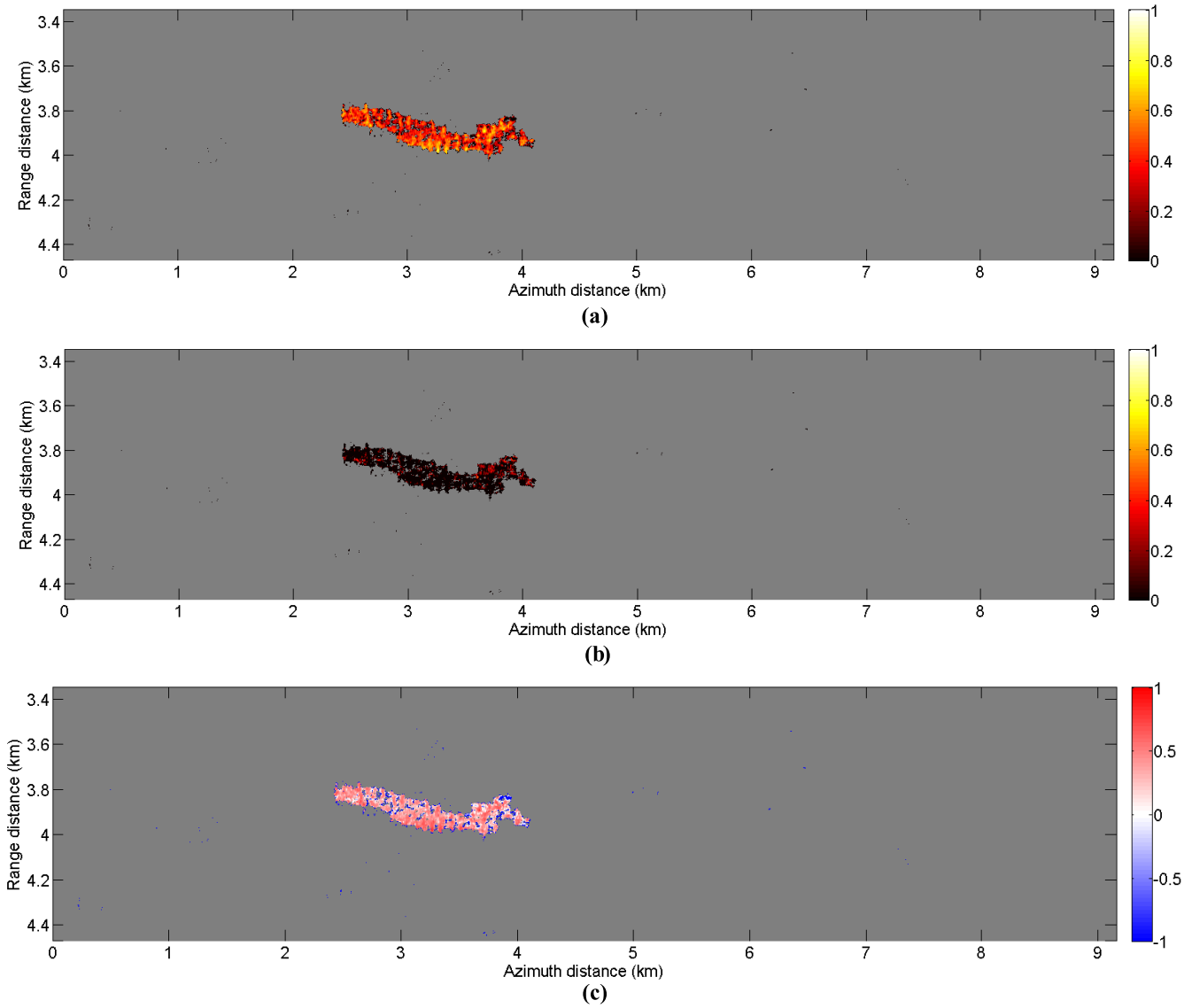

Fig. 11. (a) M_W, (b) M_α, and (c) M in the case of L-band acquisitions taken on May 22, 2015 at 13:29 UTC for xylene (multilook 7 × 7), crosswind observation.

film on the sea surface, while the FAME mixes in the water column.

Thus, analysis of NPD, M_W, M_α, and M parameters can be used to specify the behavior of the chemical product. Histograms of NPD, M_W, M_α, and M parameters computed with SAR data acquired at L-band over xylene (second flight), rapeseed oil, and FAME (third flight) are shown in Fig. 12. As discussed above, xylene and rapeseed oil have similar responses: M_α is close to 0, which means that there is limited mixing with seawater, and M_W and NPD at L-band are very similar and significantly high, indicating that signal attenuation is mainly due to the damping of the wind-driven sea surface waves and M is equal to 0.4–0.6, which corresponds to the presence of a film on the sea surface that damped the short waves. FAME has a different behavior: M_W is lower than for the two other chemicals, M_α is no longer negligible, and thus M takes positive and negative values, which means that, as expected, mixing is more present over FAME than over rapeseed oil and xylene. Note that these behaviors deduced from radar imagery analysis are not correlated with the SEBC classification. Indeed, FAME and rapeseed oil are classified as floater F in the SEBC, whereas in SAR, the FAME behavior is more like an FD with the presence of droplets into the water column, which is confirmed by visual observations made during the releases. Due to the variability of each parameter within the polluted area, the approach proposed in this paper could only be a region-based approach. Therefore, the use of M_W, M_α, and M parameters allows to distinguish an area contaminated by a substance that forms a film on the top of the sea surface from another area polluted by a product that mixes with seawater.

For the three chemicals, NPD at X-band is always significantly high (greater than 0.9). Over the FAME, NPD at L-band allows us to distinguish two areas (two peaks in the histogram located at 0.5 and 0.8) corresponding to two different concentrations, as it can be seen in Figs. 3 and 8. Interestingly, one can also observe a bimodal histogram for the M_α parameter, which confirms the presence of two different mixing.

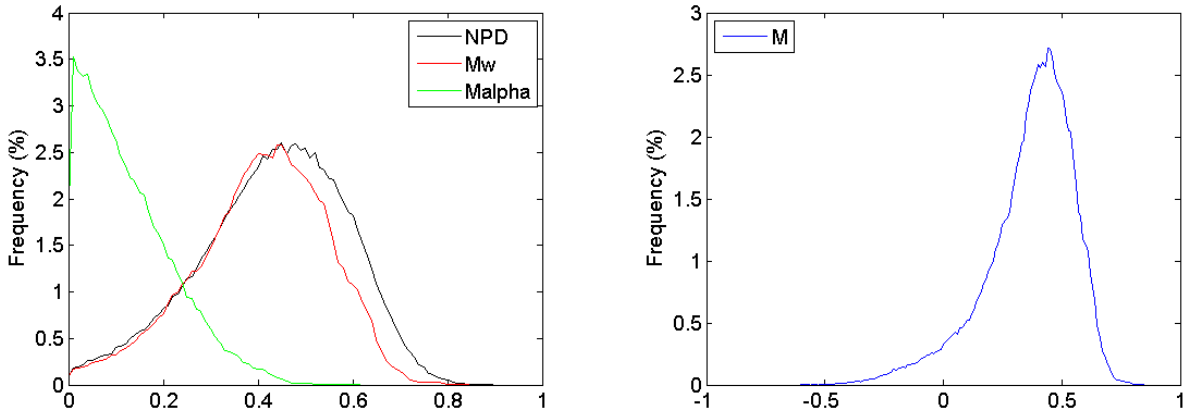

(a)

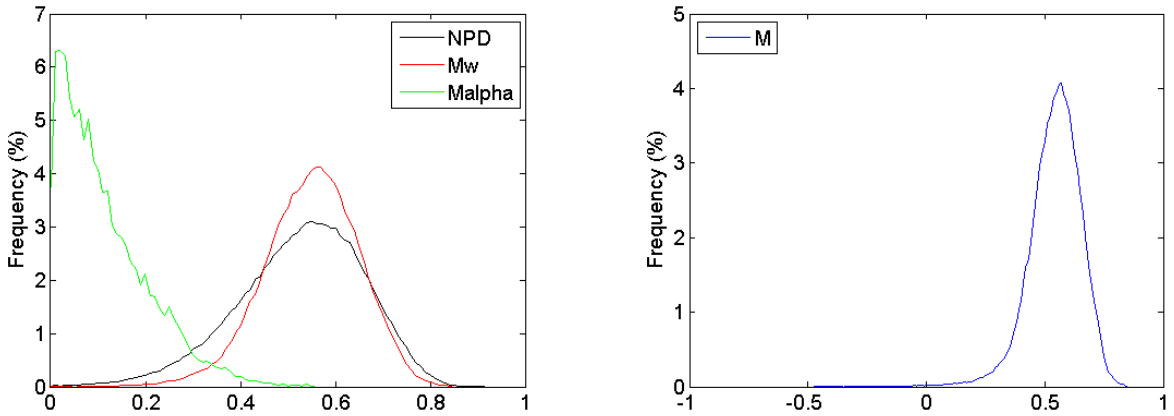

(b)

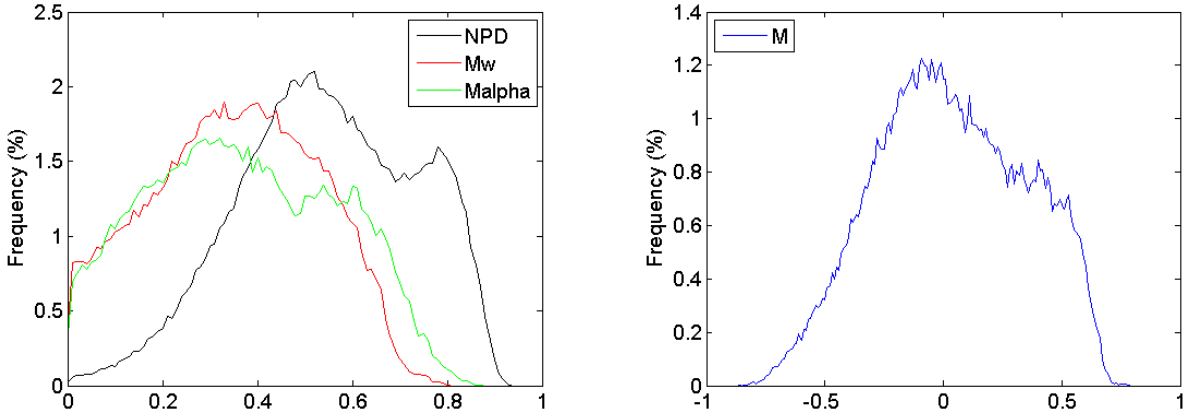

(c)

Fig. 12. Histograms over (a) xylene on 22 May 2015, 13:29 UTC, (b) rapeseed oil on 22 May 2015, 16:07 UTC, and (c) FAME on 22 May 2015, 16:07 UTC for L-band SAR data NPD (black curve), M_W (red curve), M_α (green curve), and M (blue curve).

V. Conclusion

Motivated by the need for remote sensing technique to locate and characterize the HNS at sea, we developed the NPD, a metric for distinguishing contaminants from surrounding clean water, and demonstrated in a controlled experiment the utility of POLSAR data for quantifying chemical relative concentration and distinguishing between HNS that is manifest as a thin film and the HNS that mixes with seawater near the surface. The experiment, called POLLUPROOF, was conducted in May 2015 over the Mediterranean Sea and focused on the release and subsequent observation of several HNS products that are meant to represent the majority of commonly transported chemicals. The primary goal of this experiment is to establish a procedure for collecting evidence of illegal maritime pollution by HNS using airborne sensors.

Of the six products tested during this experimentation at sea, we unambiguously detected three using SAR imagery. These detectable substances are rapeseed oil, FAME and xylene. For the three others, the nondetectability seems to be caused by a high volatility of tested products and a relatively long time lag between discharge and observations (especially for methanol release).

Using data collected over the detectable substances, we developed a methodology using X- and L-band radar imagery to detect and quantify the relative concentration of chemical products at sea. X-band is used to detect the slick and L-band is then used to quantify the relative concentration. A NPD parameter is then introduced for this purpose. NPD is a normalized parameter that, by design, provides only relative information about the impact of a liquid product released on the sea surface. We show that at L-band, the NPD parameter takes a wide range of values within the slick, a variation that is related to the impact of the released substance on the ocean surface. This impact depends on the concentration of chemical and can manifest itself in two different ways on the sea surface: smoothing of the sea surface due to the damping of the gravity capillary waves and a decrease in the dielectric constant compared with clean seawater due to a mix between HNS and pure seawater. Then we show that the distinction between two HNS within the same spill is possible with radar imagery by calculating the oil–water mixing index (M). We conclude that, SAR data can allow us to define the characteristics of a spill along a spectrum ranging from thin surface films to natural dispersion (droplets in suspension in the water column). In summary, multifrequency POLSAR data can provide crucial information for efficient cleanup operations during HNS- or oil-related maritime pollution. The proposed methodology is as follows: NPD parameters, at X- and L-band, are recommended to detect and quantify the relative concentration of the involved substance and then the oil–water mixing parameters (M_W, M_α, and M) are recommended to characterize the behavior of the pollutant. Those pieces of information should be seen as a means of improving decision making by experts or operational staff. Automation of decisions is not guaranteed, as artifacts may appear, and a human intervention is usually necessary.

APPENDIX

The noise of the radar instrument, usually called NESZ, is a key parameter when studying maritime pollution as it appears on SAR images as dark patches, with low backscattered value and hence a potentially low SNR.

As discuss in Section II-A, SETHI instrument noise floor has been estimated using the method proposed in [28] and the results are shown in Fig. 13. At X-band, one can recognize the characteristic modulation induced by the antenna pattern with a minimum value corresponding to the maximum of illumination. At L-band, as half-power beamwidth is larger than that at X-band (33° and 16° respectively) and as the imaged area is the same for the two frequency bands, the effect of the antenna pattern is less pronounced. The estimated NESZ is very low, ranging from around −37 to −50 dB at X-band and from around −51 to −53 dB at L-band, allowing a sufficient signal to noise ratio (see Fig. 4) over polluted areas for efficient analysis.

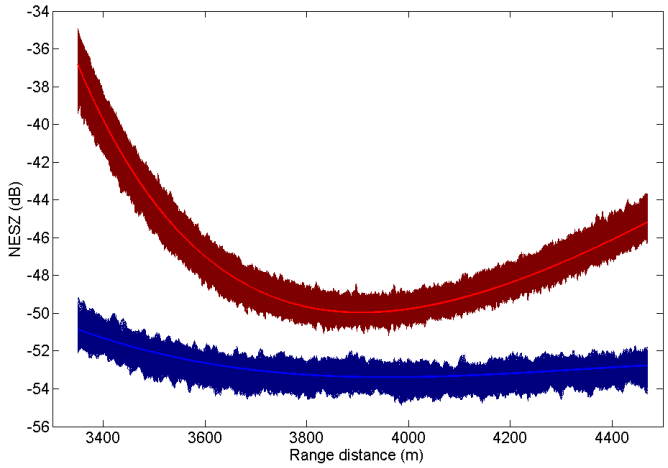

Fig. 13. SETHI instrumental noise floor at X-band (red curve) and L-band (blue curve).

ACKNOWLEDGMENT

The authors would like to thank everyone involved in the experiment at sea (ONERA–CEDRE–AVDEF–DGDDI–French Navy) and those who participated in the SAR data processing. They would also like to thank G. Soriano and C.-A. Guerin for the GO-SSA modeling and P.-D. Fernandez and H. Oriot from ONERA for the successful discussions.

REFERENCES

[1] M. Fingas and C. Brown, "Review of oil spill remote sensing," *Marine Pollution Bull.*, vol. 83, no. 1, pp. 9–23, 2014.
[2] C. Brekke and A. H. S. Solberg, "Oil spill detection by satellite remote sensing," *Remote Sens. Environ.*, vol. 95, no. 1, pp. 1–13, 2005.
[3] M. Gade and W. Alpers, "Using ERS-2 SAR images for routine observation of marine pollution in European coastal waters," *Sci. Total Environ.*, vols. 237–238, pp. 441–448, Sep. 1999.
[4] O. Garcia-Pineda, B. Zimmer, M. Howard, W. Pichel, X. Li, and I. R. MacDonald, "Using SAR images to delineate ocean oil slicks with a texture-classifying neural network algorithm (TCNNA)," *Can. J. Remote Sens.*, vol. 35, no. 5, pp. 411–421, Oct. 2009.
[5] F. Girard-Ardhuin, G. Mercier, F. Collard, and R. Garello, "Operational oil-slick characterization by SAR imagery and synergistic data," *IEEE J. Ocean. Eng.*, vol. 30, no. 3, pp. 487–495, Jul. 2005.
[6] A. Gambardella, G. Giacinto, M. Migliaccio, and A. Montali, "One-class classification for oil spill detection," *Pattern Anal. Appl.*, vol. 13, no. 3, pp. 349–366, 2010.
[7] H. A. Espedal, O. M. Johannessen, J. A. Johannessen, E. Dano, D. R. Lyzenga, and J. C. Knulst, "COASTWATCH'95: ERS 1/2 SAR detection of natural film on the ocean surface," *J. Geophys. Res.*, vol. 103, no. C11, pp. 24969–24982, 1998.
[8] G. R. Valenzuela, "Theories for the interaction of electromagnetic and oceanic waves—A review," *Boundary-Layer Meteorol.*, vol. 13, nos. 1–4, pp. 61–85, Jan. 1978.
[9] V. Wismann, M. Gade, W. Alpers, and H. Huhnerfuss, "Radar signatures of marine mineral oil spills measured by an airborne multi-frequency radar," *Int. J. Remote Sens.*, vol. 19, no. 18, pp. 3607–3623, 1998.
[10] W. Alpers and H. Hühnerfuss, "The damping of ocean waves by surface films: A new look at an old problem," *J. Geophys. Res.*, vol. 94, no. C5, pp. 6251–6265, 1989.
[11] A. H. S. Solberg, "Remote sensing of ocean oil-spill pollution," *Proc. IEEE*, vol. 100, no. 10, pp. 2931–2945, Oct. 2012.
[12] M. Migliaccio, A. Gambardella, and M. Tranfaglia, "SAR polarimetry to observe oil spills," *IEEE Trans. Geosci. Remote Sens.*, vol. 45, no. 2, pp. 506–511, Feb. 2007.
[13] M. Migliaccio, A. Gambardella, F. Nunziata, M. Shimada, and O. Isoguchi, "The PALSAR polarimetric mode for sea oil slick observation," *IEEE Trans. Geosci. Remote Sens.*, vol. 47, no. 12, pp. 4032–4041, Dec. 2009.

[14] B. Zhang, W. Perrie, X. Li, and G. P. Pichel, "Mapping sea surface oil slicks using RADARSAT-2 quad-polarization SAR image," *Geophys. Res. Lett.*, vol. 38, no. 10, pp. 1–5, 2011.

[15] S. Skrunes, C. Brekke, and T. Eltoft, "A comprehensive analysis of polarimetric features for oil spill characterization," in *Proc. SeaSAR*, vol. 2012. pp 203–210, 2012.

[16] R. Shirvany, M. Chabert, and J.-Y. Tourneret, "Ship and oil-spill detection using the degree of polarization in linear and hybrid/compact dual-pol SAR," *IEEE J. Sel. Topics Appl. Earth Observ. Remote Sens.*, vol. 5, no. 3, pp. 885–892, Jun. 2012.

[17] F. Nunziata, A. Gambardella, and M. Migliaccio, "On the degree of polarization for SAR sea oil slick observation," *ISPRS J. Photogramm. Remote Sens.*, vol. 78, pp. 41–49, Apr. 2013.

[18] B. T. Demin, S. A. Ermakov, E. N. Pelinovsky, T. G. Talipova, and A. I. Sheremeteva, "Study of the elastic properties of sea surface-active films," *Izvestiya, Atmos. Ocean. Phys.*, vol. 21, no. 4, pp. 312–320, 1985.

[19] H. A. Espedal, "Satellite SAR oil spill detection using wind history information," *Int. J. Remote Sens.*, vol. 20, no. 1, pp. 49–65, 1999.

[20] *International Maritime Organization*. accessed on Feb. 15, 2015. [Online]. Available: http://www.imo.org

[21] F. T. Ulaby, R. K. Moore, and A. K. Fung, *Microwave Remote Sensing: Active and Passive*. Dedham, MA, USA: Artech House, 1986.

[22] K. Purnell, "Are HNS spills more dangerous than oil spills?" in *Proc. White Paper Interspill Conf. 4th IMO R&D Forum*, Marseille, France, May 2009. [Online]. Available: http://www.imo.org/en/OurWork/Environment/PollutionResponse/Documents/White%20paper%20Interspill%202006%20R%20and%20D%20Forum.pdf

[23] *International Tanker Owners Pollution Federation Limited*, accessed on Feb. 15, 2015. [Online]. Available: http://www.itopf.com

[24] *Database of Spill Incidents and Threats in Waters Around the World*, accessed on Feb. 15, 2015. [Online]. Available: http://wwz.cedre.fr/en/Our-resources/Spills

[25] *Database of Hazardous and Noxious Substances Spill Incidents*, accessed on Feb. 15, 2015. [Online]. Available: http://www.ciimar.up.pt/hns/incidents.php

[26] S. Le Floch, "HNS detection and monitoring recent incidents and future considerations," in *Proc. Interspill*, 2009. [Online]. Available: http://www.interspill.org/previous-events/2009/12-May/pdf/1530_floch.pdf

[27] G. Bonin *et al.*, "The new ONERA multispectral airborne SAR system in 2009," in *Proc. IEEE Radar Conf.*, Pasadena, CA, USA, May 2009, pp. 1–3.

[28] I. Hajnsek, E. Pottier, and S. R. Cloude, "Inversion of surface parameters from polarimetric SAR," *IEEE Trans. Geosci. Remote Sens.*, vol. 41, no. 4, pp. 727–744, Apr. 2003.

[29] D. Mackay, W.-Y. Shiu, K.-C. Ma, and S. C. Lee, *Handbook of Physical-Chemical Properties and Environmental Fate for Organic Chemicals*, vol. 1. Boca Raton, FL, USA: CRC Press, 2006.

[30] D. Mackay, W.-Y. Shiu, K.-C. Ma, and S. C. Lee, *Handbook of Physical-Chemical Properties and Environmental Fate for Organic Chemicals*, vol. 3. Baco Raton, FL, USA: CRC Press, 2006.

[31] J. Harrison, N. D. C. Allen, and P. F. Bernath, "Infrared absorption cross sections for methanol," *J. Quant. Spectrosc. Radiat. Transf.*, vol. 113, no. 17, pp. 2189–2196, Nov. 2012.

[32] S. Skrunes, C. Brekke, and T. Eltoft, "Characterization of marine surface slicks by RADARSAT-2 multipolarization features," *IEEE Trans. Geosci. Remote Sens.*, vol. 52, no. 9, pp. 5302–5319, Sep. 2014.

[33] B. Holt, "SAR imaging of the ocean surface," in *Synthetic Aperture Radar (SAR) Marine User's Manual*, C. R. Jackson and J. R. Apel, Eds. Silver Spring, MD, USA: NOAA, 2004, pp. 263–275.

[34] K. Hasselmann *et al.*, "Theory of synthetic aperture radar ocean imaging: A MARSEN view," *J. Geophys. Res.*, vol. 90, no. C3, pp. 4659–4686, 1985.

[35] B. Minchew, C. E. Jones, and B. Holt, "Polarimetric analysis of backscatter from the deepwater horizon oil spill using L-band synthetic aperture radar," *IEEE Trans. Geosci. Remote Sens.*, vol. 50, no. 10, pp. 3812–3830, Oct. 2012.

[36] N. Pinel, C. Bourlier, and I. Sergievskaya, "Two-dimensional radar backscattering modeling of oil slicks at sea based on the model of local balance: Validation of two asymptotic techniques for thick films," *IEEE Trans. Geosci. Remote Sens.*, vol. 52, no. 5, pp. 2326–2338, May 2014.

[37] S. Angelliaume, P. Dubois-Fernandez, V. Miegebielle, and D. Dubucq, "Polarimetric parameters for oil slicks detection using SAR data remote sensing—An evaluation," in *Proc. IEEE Int. Geosci. Remote Sens. Symp. (IGARSS)*, Milan, Italy, Jul. 2015, pp. 3794–3797.

[38] V. N. Kudryavtsev, B. Chapron, A. G. Myasoedov, F. Collard, and J. A. Johannessen, "On dual co-polarized SAR measurements of the ocean surface," *IEEE Geosci. Remote Sens. Lett.*, vol. 10, no. 4, pp. 761–765, Jul. 2013.

[39] C.-A. Guérin, G. Soriano, and B. Chapron, "The weighted curvature approximation in scattering from sea surfaces," *Waves Random Complex Media*, vol. 20, no. 3, pp. 364–384, 2010.

[40] A. Mouche and B. Chapron, "Global C-band ENVISAT, RADARSAT-2 and Sentinel-1 SAR measurements in copolarization and cross-polarization," *J. Geophys. Res. Oceans*, vol. 120, no. 11, pp. 7195–7207, 2015.

[41] B. Minchew, "Determining the mixing of oil and sea water using polarimetric synthetic aperture radar," *Geophys. Res. Lett.*, vol. 39, no. 16, p. L16607, 2012.

[42] G. Soriano and C.-A. Guérin, "A cutoff invariant two-scale model in electromagnetic scattering from sea surfaces," *IEEE Geosci. Remote Sens. Lett.*, vol. 5, no. 2, pp. 199–203, Apr. 2008.

[43] M. Gade, W. Alpers, H. Hühnerfuss, H. Masuko, and T. Kobayashi, "Imaging of biogenic and anthropogenic ocean surface films by the multifrequency/multipolarization SIR-C/X-SAR," *J. Geophys. Res.*, vol. 103, no. C9, pp. 18851–18866, 1998.

Sébastien Angelliaume received the B.E. degree from the Ecole Nationale Supérieure d'Ingénieur de Constructions Aéronautiques, Toulouse, France, in 2003, and the M.S. degree from the Ecole Nationale Supérieure d'Electrotechnique, d'Electronique, d'Informatique, d'Hydraulique et des Télécommunications, Toulouse, in 2003.

Since 2006, he has been with Electromagnetism and Radar Department, Office National d'Etudes et de Recherches Aérospatiales (ONERA)–The French Aerospace Laboratory, Salon de Provence, France. He has been involved in the ONERA synthetic aperture radar airborne platform RAMSES and SETHI, developing science applications. His research interests focuses mainly on remote sensing over the ocean surface.

Brent Minchew received the B.S. and M.S. degrees in aerospace engineering from The University of Texas at Austin, Austin, TX, USA, in 2008 and 2010, respectively, and the Ph.D. degree in geophysics from the California Institute of Technology, Pasadena, CA, USA, in 2016.

He is currently an NSF Earth Sciences Post-Doctoral Fellow with British Antarctic Survey, Cambridge, U.K. His research interests include glacier dynamics, with an emphasis on remote sensing applications.

Sophie Chataing received the B.E. degree from the Ecole d'ingénieurs en Chimie, Physique et Electronique, Lyon, France, in 2011, and the M.S. degree in marine chemistry from the University of Brittany, Brest, France, in 2012.

She was a Chemical Engineer with the Research and Technological Developments Department, Ifremer, Brest, France, she joined Cedre's Research Department in 2014. She is mainly involved in studies on the short, medium, and long term behavior of chemical products: laboratory-based, in-situ experiments, and analysis techniques demonstrating weathering processes.

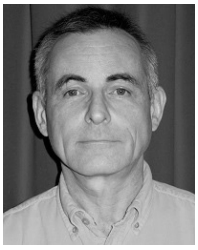

Philippe Martineau received the B.E. degree from the Institut de Science et Technique, University Pierre et Marie Curie, Paris, France, in 1984.

Since 1984, he has been with the Electromagnetism and Radar Department, Office National d'Etudes et de Recherches Aérospatiales (ONERA)–The French Aerospace Laboratory, Palaiseau, France. He has been involved in the ONERA synthetic aperture radar airborne platform RAMSES and SETHI, in charge of SAR image processing.

Véronique Miegebielle received the Ph.D. degree in geology from the University of Pau et Pays de l'Adour, Pau, France, in 1993.

She spent the first 15 years of her career involved with geology and environmental subjects. In 2009, she was with Total Company Remote Sensing Service, Pau. Since 2011, she has been in charge of the Remote Sensing Offshore Research Project.

SAR Imagery for Detecting Sea Surface Slicks: Performance Assessment of Polarization-Dependent Parameters

Sébastien Angelliaume, Pascale C. Dubois-Fernandez, *Senior Member, IEEE,* Cathleen E. Jones, Benjamin Holt, Brent Minchew, Emna Amri, and Véronique Miegebielle

***Abstract*— Remote sensing technology is an essential link in the global monitoring of the ocean surface, and radars are efficient sensors for detecting marine pollution. When used operationally by authorities, a tradeoff must usually be made between the covered area and the quantity of information collected by the radar. To identify the most appropriate imaging mode, a methodology based on receiver operating characteristic curve analysis has been applied to an original data set collected by two airborne systems operating at L-band, both characterized by a very low instrument noise floor. The data set was acquired during controlled releases of mineral and vegetable oil at sea. Various polarization-dependent quantities are investigated, and their ability to detect slick-covered areas is assessed. A relative ordering of the main polarimetric parameters is reported in this paper. When the sensor has a sufficiently low noise floor, HV is recommended because it provides the strongest slick–sea contrast. Otherwise, VV is found to be the most relevant parameter for detecting slicks on the ocean surface. Among all the investigated quad-polarimetric settings, no significant added value compared to single-polarized data was found. More specifically, it is demonstrated, by increasing the instrument noise level, that the studied polarimetric quantities which combine the four polarimetric channels have performances of detection mainly driven by the instrument noise floor, namely, the noise equivalent sigma zero. This result, obtained by progressively adding noise to the raw synthetic aperture radar (SAR) data, indicates that the polarimetric discrimination between clean sea and polluted area results mainly from the differentiated behavior between single-bounce scattering and noise. It is thus demonstrated, using SAR data collected with a low instrument noise floor, that there is no deviation from Bragg scattering for radar scattering from ocean surface covered by mineral and vegetable oil.**

***Index Terms*— Bragg, detection, instrument noise, marine pollution, noise, noise equivalent sigma zero (NESZ), noise floor, ocean, oil, polarimetric discrimination, polarization, probability of detection (Pd), probability of false alarm (Pfa), radar, ranking, receiver operating characteristic (ROC) curves, synthetic aperture radar (SAR), sea, slick, spill.**

I. Introduction

SPACEBORNE and airborne remote sensing sensors are commonly used in the offshore domain for monitoring natural and anthropogenic oil slicks [1]–[3]. These sensors allow the authorities and the petroleum companies to monitor sea shipping lanes to identify possible fuel releases, respond to incidents occurring at surface or subsurface oil and gas facilities, and identify the occurrence of natural hydrocarbons (seeps) on the sea surface [4]–[6], testifying to the presence of mature source rock on the ocean bottom.

Because of the constraints linked mainly to weather conditions and the risk of significant cloud cover, the use and programming of synthetic aperture radar (SAR) data is usually favored over optical imagery for oil slick detection over the ocean surface [6]–[8]. SAR is a powerful tool for detecting hydrocarbons or chemicals on the sea surface because of the sensitivity of the electromagnetic (EM) scattering to surface roughness. In calm seas, most of the transmitted energy is reflected away from the radar and the backscattered signal toward the instrument is very low. Wind-driven roughness increases the total backscattered energy from the surface. Oil films on the sea surface damp the capillary and short gravity waves [9], [10], which are the main source of sea surface roughness. As a consequence, slicks appear as dark areas in the SAR image (low backscattered signal), which makes the presence of an oil slick on the sea surface detectable in radar imagery.

Several major issues are identified in the success of hydrocarbon detection in the offshore domain, the first of which remains today, namely, the revisit time. Indeed, in an emergency situation, obtaining quick information from spaceborne sensors is decisive. The latency is constrained by the repeat orbit interval of SAR satellite systems, the trajectory of the orbits, the location of the area of interest (e.g., there are more possibilities of acquisition daily at high latitudes than that toward the equator), the data recording and downlink system, and the SAR viewing geometry agility [11]. Thus, very large swath modes are often selected by maritime surveillance services to the detriment of the spatial resolution or to the amount of information potentially collected over the area of interest, for example, with polarimetric modes. Monitoring

Manuscript received October 11, 2017; revised December 20, 2017 and January 26, 2018; accepted January 28, 2018. Date of publication March 14, 2018; date of current version July 20, 2018. This work was supported in part by the French National Research Agency (ANR) through the POLLUPROOF Research Program under Grant ANR-13-ECOT-007 and in part by the New Advanced Observation Method Integration Project, a common research program between Total (the French Petroleum Company) and ONERA (the French Aerospace Lab). *(Corresponding author: Sébastien Angelliaume.)*

S. Angelliaume, P. C. Dubois-Fernandez, and E. Amri are with ONERA, DEMR, 13661 Salon de Provence, France (e-mail: sebastien.angelliaume@onera.fr).

C. E. Jones and B. Holt are with the Jet Propulsion Laboratory, California Institute of Technology, Pasadena, CA 91109 USA.

B. Minchew is with British Antarctic Survey, Cambridge CB3 0ET, U.K.

V. Miegebielle is with the Remote Sensing Department, Total, 64018 Pau, France.

Color versions of one or more of the figures in this paper are available online at http://ieeexplore.ieee.org.

Digital Object Identifier 10.1109/TGRS.2018.2803216

services exploit mainly radar remote sensing data acquired in a single-polarization mode, maximizing the covered surface of the ocean. Due to a higher backscattered signal level from the sea surface for vertically (V) polarized waves than that for horizontal (H) polarization [12], the VV channel is often preferred to HH for ocean studies. Because most of the spaceborne SAR systems available today have a moderate noise floor (between -20 and -35 dBm^2/m^2 [13]), the cross-polarization (HV or VH) channels have not been used for operational ocean slick detection.

The second major issue affecting the success of offshore hydrocarbon detection concerns the speed of data analysis coupled with the reliability of hydrocarbon detection. Operationally, the analysis of SAR images is mostly based on the visual identification of dark areas corresponding to oil slicks [14]. Many oceanic and atmospheric phenomena can occur over the sea surface and manifest themselves on radar images in the same way as areas covered by hydrocarbons. These are called look-alikes, and they can originate from several sources [15]: 1) natural biogenic surface films produced by fish or plankton; 2) young and thin sea ice; 3) low-wind areas; and 4) upwelling of cold water. For decades, Alpers *et al.* [15], Migliaccio *et al.* [16], and Hansen *et al.* [17] have attempted to develop methodologies to differentiate ocean areas covered by hydrocarbon from look-alikes. Today, the discrimination between biogenic films and mineral oil slicks remains an active area of research [15]. The method of conventional operational SAR analysis is mainly based on the experience and expertise of the image interpreter. In order to facilitate visual inspection, there have been many studies of the SAR signature of hydrocarbons observed in different acquisition configurations in order to identify the optimal detection method. Regarding the choice of sensor, the reliability of detection depends mainly on the frequency band and the sensor noise floor. For example, it has been demonstrated in [18] that SAR images acquired at high frequency (e.g., X- or C-band) are preferable to those acquired at lower frequency (e.g., L-band) for mineral oil slick detection. In parallel with system considerations, it is essential to know what information is most relevant for detection, especially information that can be obtained from the polarization of the EM waves. Because many studies published in the literature have suggested that multipolarization (dual-polarization or quad-polarization) or polarimetric (POLSAR, i.e., using both amplitude and phase information) parameters improve the detection capability of slicks compared to single-polarization data [19]–[26], exploring various polarization-dependent SAR parameters accessible in the range of possible SAR acquisition configurations is a valuable aid to operational teams in ranking the acquisition modes that can be used.

The aim of this paper is to present a prioritization of SAR parameters to enhance and facilitate slick detection in the offshore domain. The originality of the proposed method lies in the definition and quantitative evaluation of parameters calculated using data obtained in quad-polarimetric mode by two airborne SARs operating at L-band (1.275 and 1.325 GHz) with very high signal-to-noise ratio (SNR) over controlled releases of mineral and vegetable oil at sea. These two sensors are Système Expérimental de Télédétection Hyperfréquence Imageur (SETHI) operated by ONERA [27], the French Aerospace Lab, and Uninhabited Aerial Vehicle Synthetic Aperture Radar (UAVSAR) operated by National Aeronautics and Space Administration (NASA)/Jet Propulsion Laboratory (JPL) [28].

This paper is organized as follows. Section II presents the basis of the radar scattering from the ocean surface. Section III summarizes the state-of-the-art POLSAR parameters proposed in the literature for slick detection. Section IV describes the airborne SAR data used in this paper. Section V presents the methodology used to evaluate the studied parameters and gives the results, and main discussions are presented in Section VI.

II. Radar Scattering From the Ocean Surface

Over a rough sea surface where Bragg scattering is dominant (incidence angles in the so-called "plateau region" [29], ranging from around 30° to 60°), the co-polarized channels (HH and VV) have higher backscattered power than that of the cross-polarized (HV and VH) channels. Higher backscattered power means higher SNR, which makes these channels more attractive for slick detection on the sea surface where typical backscattered power can be low [17]. The co-polarized radar backscattered power is proportional to the normalized radar cross section (NRCS), which is defined in the Bragg scattering theory [12] as

$$\sigma^0_{\mathrm{pp}} = 4\pi k^4_{\mathrm{EM}} \cos^4\theta_i \Gamma_{\mathrm{pp}} W(k_B) \tag{1}$$

$$k_B = 2k_{\mathrm{EM}} \sin\theta_i \tag{2}$$

where subscript p denotes either H (horizontal) or V (vertical) polarization; $k_{\mathrm{EM}} = 2\pi/\lambda_{\mathrm{EM}}$ is the EM wavenumber corresponding to the radar wavelength λ_{EM}; Γ_{pp} is the reflectivity; $W(k_B)$ is the spectral density of ocean surface roughness evaluated at the Bragg wavenumber k_B; and θ_i is the radar local incidence angle. The spectral density of the sea surface describes the components of the ocean wave spectrum that contribute to the scattering of the radar pulses [30], while the reflectivity describes the total power scattered from the surface.

This formulation of the NRCS (1) does not fully explain the EM signal backscattered by a rough sea surface because it takes into account only the polarized components of the backscattering from the ocean surface. Deviations between model estimation (Bragg theory) and real observation [31], [32] are often explained through nonresonant mechanisms, called non-Bragg or nonpolarized effects [33]. Those mechanisms are generally associated with breaking waves or whitecaps, and they contribute to the total backscattered energy from the sea surface. However, the contribution of non-Bragg scattering to the total NRCS is frequency dependent, and it has been reported in [34] that at low EM frequency (e.g., L-band), the relative contribution of this non-polarized component with respect to the total power scattered from the ocean surface is negligible. For this reason, we do not consider nonpolarized effects in the rest of this paper.

The local incidence angle of the EM wave θ_i is defined [12] as

$$\theta_i = \cos^{-1}[\cos(\theta + \psi)\cos\xi] \tag{3}$$

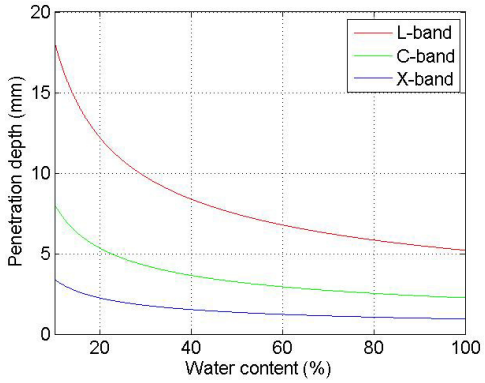

Fig. 1. Penetration depth as a function of water content (volumetric percentage) based on a linear mixing model for the dielectric constant at L-band (red), C-band (green), and X-band (blue); dielectric constants are specified in Table I.

where θ is the EM angle of incidence relative to the local, untilted surface vertical direction and ψ and ξ are defined in the following paragraph.

The sea surface is modeled as a set of slightly rough tilted facets that contributes to the backscattering of the incident radiation. Each facet has superimposed small-scale surface roughness that creates a Bragg scatterer when the roughness scale is commensurate with the radar wavelength. Small-scale roughness is randomly distributed on the scattering surface and responds to the strength of local wind, which generates capillary and short gravity waves whose wavelengths are of the order centimeters to decimeters with periods less than 1 s [35]. The tilt of the facet is caused by larger scale gravity waves on the ocean surface that change the local orientation, or tilt, of the short waves [36]. The orientation of the facet of the sea surface is defined by two angles: ψ, which is the angle between local up and the projection of the facet normal onto the radar scattering plane (in-plane tilt), and ξ, which is the angle between local up and the projection of the facet normal onto the vertically oriented plane perpendicular to the scattering plane (out-of-plane tilt) (see [37, Fig. 1]).

The co-polarized reflectivity Γ_{pp} is a function of the local geometry and the electrical properties of the scattering surface (e.g., seawater and films) such that

$$\Gamma_{pp} = \left| \left(\frac{\sin(\theta+\psi)\cos\xi}{\sin\theta_i} \right)^2 \alpha_{pp} + \left(\frac{\sin\xi}{\sin\theta_i} \right)^2 \alpha_{qq} \right|^2 \quad (4)$$

where subscript $q(p \neq q)$ denotes either H or V polarization. The co-polarized Bragg scattering coefficients, introduced in (4), are defined [12] as

$$\alpha_{\mathrm{HH}} = \frac{\cos\theta_i - \sqrt{\varepsilon_r - \sin^2\theta_i}}{\cos\theta_i + \sqrt{\varepsilon_r - \sin^2\theta_i}} \quad (5)$$

$$\alpha_{\mathrm{VV}} = \frac{(\varepsilon_r - 1)(\sin^2\theta_i - \varepsilon_r(1+\sin^2\theta_i))}{(\varepsilon_r\cos\theta_i + \sqrt{\varepsilon_r - \sin^2\theta_i})^2}. \quad (6)$$

They depend only on the local incidence angle of the EM wave θ_i and the complex-valued relative dielectric constant of the imaged surface ε_r.

TABLE I
DIELECTRIC CONSTANT OF SEAWATER FROM [38] AND MINERAL OIL FROM [39] AND [40]

Material	L-BAND [1.3 GHz]	C-BAND [5.0 GHz]	X-BAND [10 GHz]
Seawater (15°C 35 PSU)	73.0+65.1i	66.8+35.7i	52.9+39.0i
Mineral oil	2.3+0.01i	2.3+0.01i	2.3+0.01i

The relative dielectric constant ε_r defined as the ratio between the material dielectric constant and the electric constant in a vacuum is a complex number. Its value is material dependent and varies with the radar frequency. The imaginary part characterizes how far an EM wave can penetrate into a conducting medium. The penetration depth δ_p is defined as the depth where the power of the propagating EM wave is attenuated by a factor of $1/e$ such that

$$\delta_p = \frac{1}{2k_{\mathrm{EM}}\mathrm{Im}(\sqrt{\varepsilon_r})} \quad (7)$$

where Im(.) selects the imaginary part of a complex number. Typical values of dielectric constant of seawater [38] and mineral oil [39], [40] are given in Table I. Note that the value of the dielectric constant for mineral oil is nearly constant in the range 1–10 GHz, with a loss factor (imaginary component) close to 0, suggesting a nonnegligible penetration of the EM wave through this medium.

Assuming a linear mixing model, the effective dielectric constant of a water-in-oil emulsion ($\varepsilon_{\mathrm{em}}$) is given by

$$\varepsilon_{\mathrm{em}} = \upsilon\varepsilon_w + (1-\upsilon)\varepsilon_{\mathrm{oil}} \quad (8)$$

where υ, ranging from 0 to 1, is the water content by volume of the oil–water mixture, and ε_w and $\varepsilon_{\mathrm{oil}}$ are the relative dielectric constants of seawater and oil, respectively. It follows from (8) that the effective dielectric constant of a mixture of oil and seawater is lower than that of seawater alone [41]. From values given in Table I and from (7) and (8), it is seen that the penetration depth decreases with increasing frequency and water content, with typical penetration depth of the order of millimeters for water content greater than 50% (Fig. 1).

When hydrocarbons are spilled into a marine environment, the oil can be mixed with seawater within the upper few centimeters of the water column or can behave like a viscoelastic film floating on the surface. In the first case, mixing of oil with seawater will lead to a reduction of the relative dielectric constant of the contaminated sea surface compared to the surrounding slick-free area. This will contribute to a decrease in the total radar backscattered power, along with suppression of the Bragg-wavelength gravity–capillary waves that are present due to the difference in surface tension and density. In the second case (thin film), radar-backscattered power is mainly diminished through mechanical damping of Bragg-wavelength gravity–capillary waves. The capability of radar imagery to distinguish between varying substances that manifest as a thin film on the sea surface or that mix with seawater near the surface has already been demonstrated in the case of

mineral oil [42] and chemicals [43]. If the thickness of the film on the top of the sea surface is thin compared to the penetration depth δ_p, the EM wave is not altered and will penetrate the film to scatter from the seawater below the film, so the effective dielectric constant will remain that of seawater, and not be changed by different, generally lower, dielectric constants of that product which forms the film. When the film becomes thicker (relative to the penetration depth), the dielectric properties of the film/seawater mixture will be reduced compared to seawater itself, with the mixture acting as a separate layer on the ocean surface with intermediate dielectric values that will also impact the power of the backscattered signal.

Mineral oil films can form multilayers, whose thickness can vary considerably within oil patches, from less than 1 μm to more than 1 mm [44]–[46]. When released at sea, mineral oil mixes quickly with seawater under the action of wind and waves and will result in water-in-oil mixture (emulsion) with water content generally between 50% and 75% [47].

Results shown in Fig. 1 suggest that the backscattered signal from ocean surface covered by a mineral oil film will only be impacted by the dielectric properties of the medium in the case of very thick slick, with greater effect on high-frequency imaging radar. Otherwise, damping of the sea surface roughness will be the primary mechanisms for decreasing radar-backscattered power. Because the dielectric constants of biogenic films and mineral oil are similar [48], [49] and because biogenic films can be observed on the ocean surface only in the form of monolayers [15], [18], i.e., they are only one molecular layer thick (typical thickness of 2.4–2.7 nm), the same phenomena will be observed as in the case of mineral oil film, namely, reduced backscattered power caused by mechanical damping of the Bragg-wavelength surface waves with little dependence on the effective dielectric constant.

III. State-of-the-Art POLSAR Parameters

Radar remote sensing techniques are of great interest for monitoring slick-covered ocean surface for two primary reasons. First, EM waves are sensitive to the modification of the sea surface induced by oil. Second, SAR sensors can be used any time of day or year and in almost any weather conditions [50]. The physical interaction between an EM wave and a slick-covered area has been established by analyzing airborne and spaceborne data acquired over ocean surfaces covered by mineral oil and biogenic film [18], [51], [52]. Many studies [19]–[26] have analyzed the added value of polarimetric SAR data for slick monitoring. A review of SAR parameters used for this purpose is given in [14], where most of the methods published in the literature for oil slick detection are presented. Since this publication in 2012, many researchers have attempted to assess the utility of POLSAR parameters for slick detection. These works exploit either accidental events [53] or controlled releases of pollutant at sea, the latter of which includes experiments managed by the Norwegian Clean Seas Association for Operating Companies (NOFO) in the North Sea [17], [25], [26], [54]–[57] or the POLLUPROOF experiment whose objective is to establish a procedure for collecting evidence of illegal maritime pollution by chemicals using remote sensing sensors [43]. In the following, we focus on polarization-dependent parameters that have been found to be efficient for slick detection in the offshore domain [13], [14] and we organize them by input data type. These are separated into categories that use backscattered amplitudes only (incoherent systems) and those that use both amplitude and phase of the backscattered signals (coherent systems, i.e., POLSAR modes of operation), and into systems that acquire dual-polarization data (HH/HV, VV/VH, or HH/VV acquisitions) and those that acquire quad-polarization data (HH/VV/HV/VH). Here we consider only linearly polarized systems, which are currently the most common in remote sensing.

A. Dual-Polarized Synthetic Aperture Radar

1) Incoherent Dual-Co-Polarized Radar Imaging System: For slick-detection methods using a dual-co-polarized (HH and VV) radar remote sensing system, the two relevant parameters that use amplitude data only [33] are the Polarization Ratio (PR) and the Polarization Difference (PD), respectively, defined within the Bragg model (in linear units) as

$$\mathrm{PR} = \frac{\sigma^0_{\mathrm{HH}}}{\sigma^0_{\mathrm{VV}}} \approx \frac{\alpha_{\mathrm{HH}}}{\alpha_{\mathrm{VV}}} \quad 0 \le \mathrm{PR} \le 1 \tag{9}$$

$$\mathrm{PD} = \sigma^0_{\mathrm{VV}} - \sigma^0_{\mathrm{HH}} \quad \mathrm{PD} \ge 0. \tag{10}$$

As backscattered power over the sea surface in the Bragg regime is stronger in VV polarization than that in HH [12], it follows that PR varies between 0 and 1 and PD takes positive values. As reflectivities at VV and HH are always different when the SNR is greater than 0 dB, there is no realistic scenario in which backscattered power is nonzero and PD is equal to 0. It follows from (9) that PR, commonly referred to as the Bragg ratio when written in this simplified form, is independent of sea surface roughness (W) and depends only on the local incidence angle and the relative dielectric constant [41], [42]. Because the relative dielectric constant is lower for slick-covered areas than for uncontaminated seawater [41], the Polarization Ratio (PR) can detect sea surface slicks through the decrease in the relative dielectric constant. It is also considered an effective parameter to distinguish between slick-covered sea surface and oceanographic phenomena [17].

When the ocean surface is covered by a thin film (like biogenic or thin mineral oil film), the surface layer is transparent to the EM waves, and thus the radar will sense the dielectric constant of the seawater under the film, which will have no effect on the Polarization Ratio [58]. However, for thick oil film (relative to the radar wavelength) or emulsions, the dielectric constant of the imaged product will affect the radar backscattering and its effect will manifest itself on the Polarization Ratio. Thus, Polarization Ratio could be used to discriminate between thin film and emulsion/thick film. However, at least one major issue occurs when using the Polarization Ratio for slick characterization at sea. The contrast, which is defined as the ratio of the values obtained over contaminated and uncontaminated areas, is low. This limitation is evident in Fig. 2 where, for example, there is little difference

in PR between pure seawater (line labeled 100%) and a 50–50 or a 25–75 mixture of seawater and oil.

The PD parameter is of interest for slick detection at sea [17], [33], [43] because it is proportional to the spectral density of the ocean surface roughness [59], which is altered even by thin films [9], [10]. As discussed in [33], the non-polarized part of the backscattered signal (see Section II) is removed using PD. Therefore, the Polarization Difference mostly contains contributions due to the presence of short wind-driven waves around the Bragg wavenumber (2), making PD an attractive parameter for slick detection at sea [33], [43].

2) Coherent Dual-Co-Polarized Radar Imaging System: The Polarization Difference (PD) and the Polarization Ratio (PR), introduced above, use only the backscattered power of the complex dual-polarized signals. With a remote sensing system collecting coherent acquisitions, the phase between the two co-polarized channels is measured. In this case, the following parameters are generally recommended in the literature for slick detection over the ocean surface: the modulus of the co-polarized complex coherence (ρ_{HHVV}) [22], [25] and the Bragg likelihood ratio (BLR) [25], [26]

$$\rho = \frac{\langle S_{\mathrm{HH}} S_{\mathrm{VV}}^{*} \rangle}{\sqrt{\langle |S_{\mathrm{HH}}|^2 \rangle \cdot \langle |S_{\mathrm{VV}}|^2 \rangle}} = \rho_{\mathrm{HHVV}} e^{j\,\Delta\phi} \qquad 0 \le \rho_{\mathrm{HHVV}} \le 1 \tag{11}$$

$$\mathrm{BLR} = \max\{0, \mathrm{Re}(\rho)\} \quad 0 \le \mathrm{BLR} \le 1. \tag{12}$$

In (11) and (12), superscript * denotes the complex conjugate, $\langle . \rangle$ denotes spatial averaging, Re(.) denotes the real part of a complex number, and S_{pp} represents the complex scattering coefficient. In the case of an EM signal backscattered by rough surface, the co-polarized channels (HH and VV) are correlated and in phase [12], [60]. It follows that the complex correlation of the co-polarized channels is a real number (imaginary part close to 0) and the modulus (ρ_{HHVV}) takes values close to 1. Thus, these two parameters have the same behavior, namely, the value is high (close to 1) when the Bragg scattering mechanism is dominant and the value is low (close to 0) otherwise. However, when the backscattered signal is corrupted by noise, the phase between the co-polar channels becomes uniformly distributed between 0 and π and the modulus of the co-polarized coherence reaches 0. The polarimetric coherence between the co-polarized channels can be written as the product of three terms

$$\rho_{\mathrm{HHVV}} = \rho_{\mathrm{Scattering}}\, \rho_{\mathrm{Temp}}\, \rho_{\mathrm{SNR}} \tag{13}$$

where $\rho_{\mathrm{Scattering}}$ denotes the correlation between HH and VV due to scattering mechanism (close to 1 over ocean surface) and ρ_{Temp} and ρ_{SNR} denote temporal decorrelation and decorrelation due to noise, respectively. The decorrelation time of a moving sea surface is of the order of 1×10^{-2} s at X-band [61] and 1×10^{-1} s at L-band [62]. For sensors operating at low pulse repetition interval (PRI), the decorrelation due to time lag between transmitted pulses (alternatively polarized H and V) can be neglected. For the two sensors investigated in Sections IV-A and IV-B, the PRIs are equal to 1×10^{-7} s for SETHI and 2.3×10^{-6} s for UAVSAR, which are both orders of magnitude smaller than the surface decorrelation time and assure no temporal decorrelation between HH and VV (ρ_{Temp} close to 1). Thus, the only remaining decorrelation term is that induced by the noise defined as

$$\rho_{\mathrm{SNR}} = \frac{1}{1 + \mathrm{SNR}^{-1}}. \tag{14}$$

Equation (14) exhibits the strong dependence of the modulus of the co-polarized complex coherence (ρ_{HHVV}), as well as the BLR, on the SNR. Following (14), an SNR equal to 10 or 5 dB induces a decorrelation between the two co-polarized channels of 10% and 25%, respectively.

In addition to their strong dependence on the SNR, being normalized by the amplitude of the co-polarized backscattering coefficient, both ρ_{HHVV} and BLR are more strongly affected by the noise (low SNR) than the intensities alone. To overcome this limitation while exploiting the potential of these parameters, we propose in this paper to use the Hermitian product (HP) between the two co-polarized channels, defined as

$$\mathrm{HP} = \langle S_{\mathrm{HH}} S_{\mathrm{VV}}^{*} \rangle. \tag{15}$$

3) Coherent Dual-Polarized Radar Imaging System: A way to represent polarimetric information collected by a coherent dual-polarized (HH and HV or VV and VH) remote sensing system is the Stokes formalism [63]–[65]. The Stokes parameters are a set of four values (S_0, S_1, S_2, and S_3) describing the polarization state of an EM wave

$$S_0 = \langle |E_H|^2 + |E_V|^2 \rangle \tag{16}$$

$$S_1 = \langle |E_H|^2 - |E_V|^2 \rangle \tag{17}$$

$$S_2 = 2\mathrm{Re}\big(\langle E_H E_V^{*} \rangle\big) \tag{18}$$

$$S_3 = 2\mathrm{Im}\big(\langle E_H E_V^{*} \rangle\big) \tag{19}$$

where Re(.) and Im(.) select the real and the imaginary values, respectively, of a complex number. E is the measured complex scattering coefficient in the subscripted polarization and is independent of the polarization state of the transmitted wave. Using this formalism, Touzi *et al.* [19], Shirvany *et al.* [23], and Nunziata *et al.* [24] have proposed to use the degree of polarization (DoP) for ship or marine pollution detection

$$\mathrm{DoP} = \frac{\sqrt{S_1^2 + S_2^2 + S_3^2}}{S_0} \quad 0 \le \mathrm{DoP} \le 1. \tag{20}$$

Over ocean surface, the EM wave is well polarized [60] and the DoP is close to 1 [23]. When the received signal is dominated by the noise, as in the case for slicked surfaces imaged by most of spaceborne SARs available today, the measured signals appear depolarized and the DoP reaches values close to 0.

These last four parameters (ρ_{HHVV}, BLR, HP, and DoP), derived from co-polarized coherent acquisitions, are recommended in the literature for oil slick detection and the proposed justification comes from their ability to distinguish Bragg scattering (over clean sea surface) to another scattering mechanism that may occur over slick-covered area [19], [22]–[25]. However, the impact of the noise on these parameters is often omitted even though, as we have just seen, it can have a predominant effect. An analysis of the impact of the noise is presented in Section V-D.

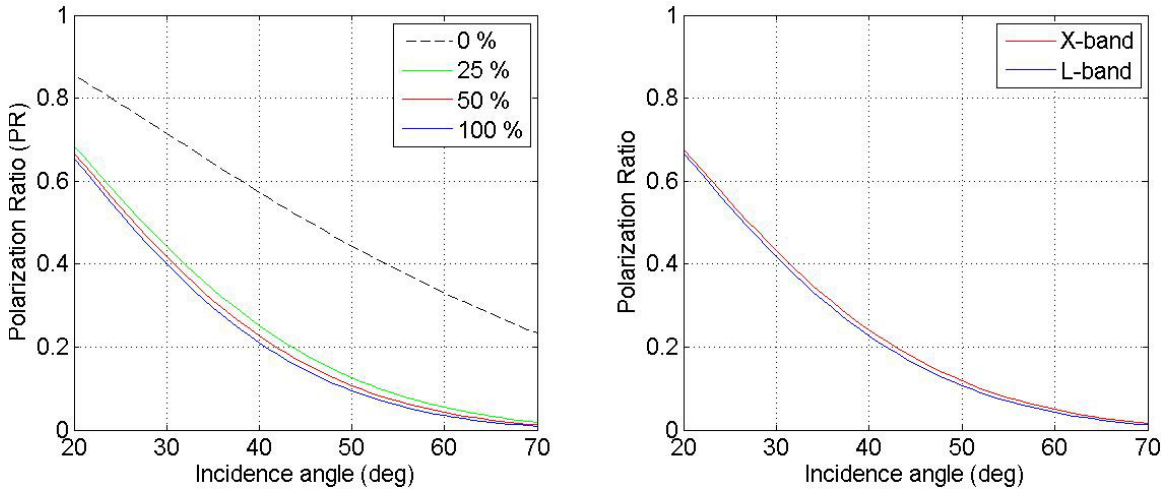

Fig. 2. PR (Bragg theory) as a function of incidence angle (a) at L-band for a water content of 0% (black dashed line), 25% (green line), 50% (red line), and 100% (blue line) and (b) at X-band (red line) and L-band (blue line) for a water content of 50%. A linear mixing is assumed between mineral oil and seawater. Values of dielectric constants are from Table I.

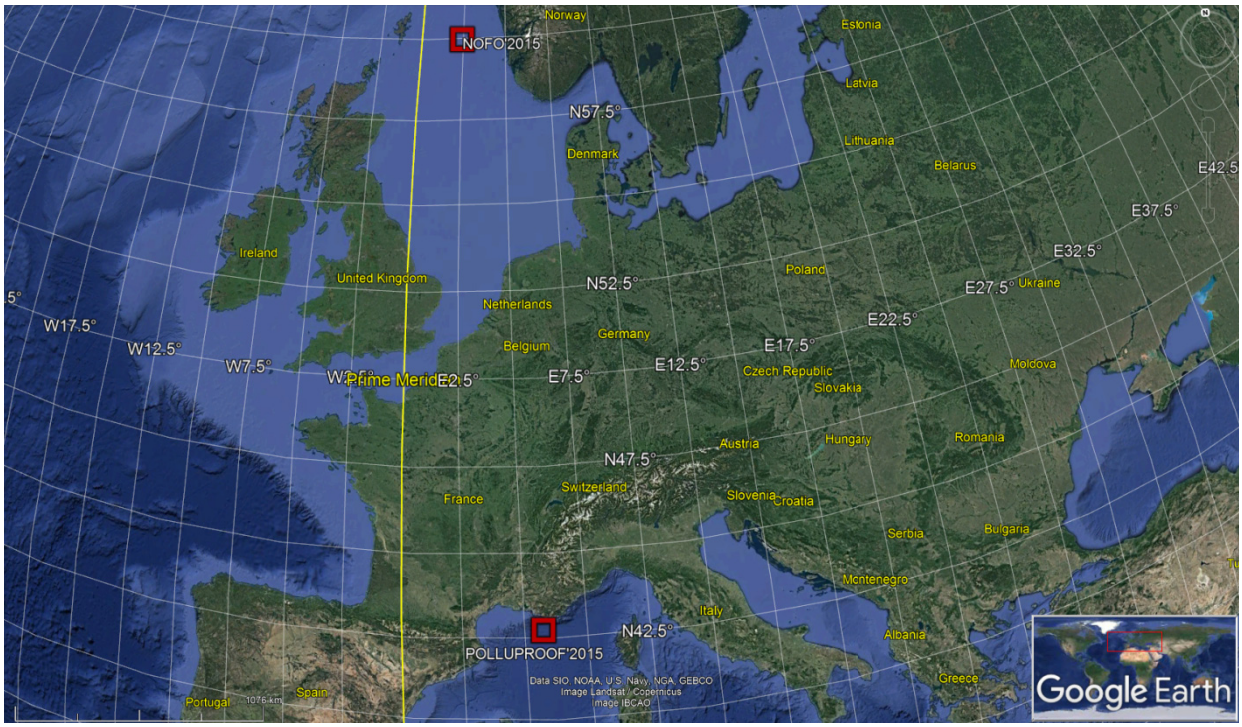

Fig. 3. Map of the POLLUPROOF'2015 and NOFO'2015 experimental sites.

B. Coherent Quad-Polarized Synthetic Aperture Radar

Many methods using quad-polarized remote sensing data are proposed in the literature to detect ocean surface covered by a slick. For a review, the reader is referred to [13] and [14]. Here we consider a few parameters dependent on all polarizations, namely, the Conformity Coefficient (μ) [66], originally proposed in [67] for remote sensing application over land surfaces, the first eigenvalue (λ_1) [41], and the Entropy (H) [25], [66] based on the eigenvalue decomposition of the covariance matrix C [68], [69]

$$\mu \approx \frac{2\left(\mathrm{Re}\left(S_{\mathrm{HH}}S_{\mathrm{VV}}^{*}\right)-|S_{\mathrm{HV}}|^{2}\right)}{|S_{\mathrm{HH}}|^{2}+2|S_{\mathrm{HV}}|^{2}+|S_{\mathrm{VV}}|^{2}} \quad -1\leq\mu\leq 1 \tag{21}$$

$$C=\begin{bmatrix} \langle|S_{\mathrm{HH}}|^{2}\rangle & \sqrt{2}\langle S_{\mathrm{HH}}S_{\mathrm{HV}}^{*}\rangle & \langle S_{\mathrm{HH}}S_{\mathrm{VV}}^{*}\rangle \\ \sqrt{2}\langle S_{\mathrm{HV}}S_{\mathrm{HH}}^{*}\rangle & 2\langle|S_{\mathrm{HV}}|^{2}\rangle & \sqrt{2}\langle S_{\mathrm{HV}}S_{\mathrm{VV}}^{*}\rangle \\ \langle S_{\mathrm{VV}}S_{\mathrm{HH}}^{*}\rangle & \sqrt{2}\langle S_{\mathrm{VV}}S_{\mathrm{HV}}^{*}\rangle & \langle|S_{\mathrm{VV}}|^{2}\rangle \end{bmatrix}. \tag{22}$$

Over the ocean, because the cross-polarized signal is very low, the Conformity Coefficient can be interpreted in the same way as the co-polarized coherence (11) or the BLR (12). A simple algorithm with a threshold equal to 0 is proposed in [66] for oil slick detection. The Entropy has similar interpretation to that of the Degree of Polarization (DoP), but with values near 0 corresponding to one dominant scattering mechanism and values close to 1 when multiscattering occurs or when the signal is corrupted by noise [68], [69].

TABLE II
ENVIRONMENTAL CONDITIONS AND PROPERTIES OF RELEASED SUBSTANCES

Date of release	Time of release (UTC)	Amount of release	Released substance	Time of imaging (UTC)	Wind speed (m/s)	Wind direction (from-deg)	Wave height (m) at time of imaging
22 May, 2015	15:00-15:30	1 m^3	Rapeseed oil	16:07	7	315	2
22 May, 2015	15:25-15:40	1 m^3	FAME	16:07	7	315	2
09 June, 2015	06:30-08:00	45 m^3	Mineral oil	09:56 10:01	5	255	1

TABLE III
PROPERTIES OF SAR SCENES INVESTIGATED IN THIS PAPER. INCIDENCE ANGLE AND NESZ VALUES ARE THE MINIMUM AND MAXIMUM ACROSS THE IMAGING SWATH

Sensor	Frequency band	Polarization mode	Experiment	Date	Time (UTC)	Incidence angle (deg)	NESZ (dBm^2/m^2)
SETHI	L	Quad-Pol	POLLUPROOF	22 May, 2015	16:07	34 / 52	-51 / -53
SETHI	L	Quad-Pol	NOFO	09 June, 2015	10:01	34 / 52	-51 / -53
UAVSAR	L	Quad-Pol	NOFO	09 June, 2015	09:56	19 / 68	-35 / -51

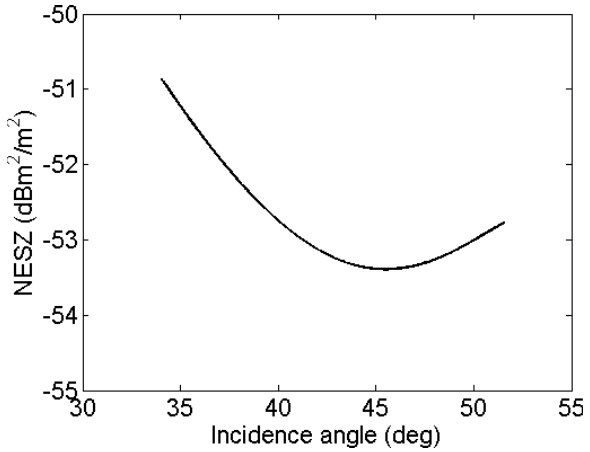

Fig. 4. SETHI—POLLUPROOF'2015 and NOFO'2015 experiments—instrument noise floor (NESZ) plotted by increasing incidence angle.

The main issue when working with quad-polarized SAR data is the low power of the backscattered signal in the cross-polarization channels (HV and VH). For most of spaceborne SAR sensors available today, the backscattered signal measured in cross-polarization over slick-covered area is close to or below the instrument noise floor [17]. This low SNR values strongly impact the values of the polarimetric parameters measured over oil slicks.

IV. EXPERIMENTAL DATA

Two experimental campaigns of measurements are used in this paper: NOFO'2015 and POLLUPROOF'2015 (see Fig. 3). POLLUPROOF'2015 was conducted in May 2015 over the Mediterranean Sea (off the French coast, near 42°45′ N, 5°45′ E) and focused on the release and subsequent observation of several hazardous and noxious substances (HNS) that are meant to represent the majority of chemicals commonly transported by sea. The primary goal of this experiment is to establish a procedure for collecting evidence of illegal marine pollution by HNS using airborne sensors [43]. SAR images of controlled releases of fatty acid methyl esters (FAME) and rapeseed oil, conducted during the POLLUPROOF'2015 experiment, are investigated in this paper (Table II). Vegetable oils (like plant oil or rapeseed oil) have already been imaged by SAR sensors as they are often used to simulate a natural monomolecular biogenic slick [15], [18], [25]. NOFO'2015 was conducted from June 8, 2015 to June 14, 2015, during NOFO's oil-on-water exercise. This experiment aims at testing recovering systems of pollution at sea by hydrocarbons. During the exercise, airborne and spaceborne acquisitions were collected over the offshore spill areas (North Sea, near 59°59′ N, 2°27′ E—see Fig. 3 and [56, Fig. 2]). In the following, we use SAR images collected by the French and American airborne sensors on June 9, 2015. For the investigated experiment, the released product is an emulsion of mineral oil in water, with a water content of 60% (Table II). It consists of a mixture of seawater, Oseberg crude oil, and a small addition of intermediate fuel oil (IFO) 380 (IFO or marine diesel oil, with a viscosity of 380 $mm^2 \cdot s^{-1}$). For the trial, 45 m^3 of mineral oil emulsion was discharged at sea. Large swath remote sensing data collected by UAVSAR (see Section IV-B) imaged the full extent of the hydrocarbon-covered area, namely, 5.4 km^2. Assuming all the 45 m^3 of mineral oil emulsion released at sea was on

TABLE IV
SIGNAL-TO-NOISE RATIO—SETHI, NOFO'2015 EXPERIMENT, JUNE 09, 2015, 10:01 UTC

Region	Incidence angle (deg)	HH MEAN [MIN MAX]	HV MEAN [MIN MAX]	VV MEAN [MIN MAX]
Clean sea	44.5°	26.5 [25.8 27.4] dB	16.4 [15.6 17.2] dB	34.1 [33.3 34.9] dB
Oil slick	44.5°	21.5 [19.7 23.0] dB	10.2 [8.6 12.3] dB	28.0 [26.3 29.3] dB

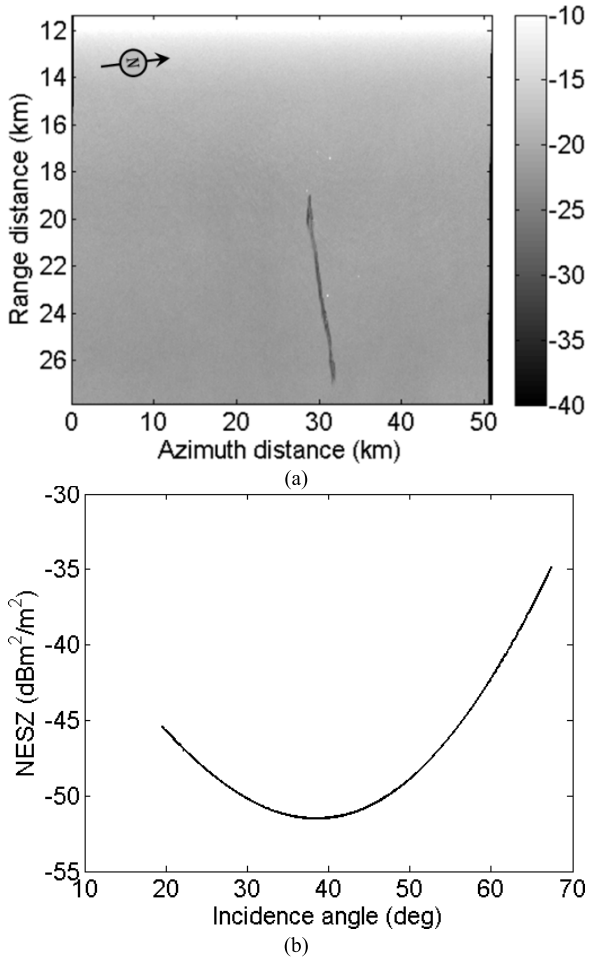

Fig. 5. UAVSAR—NOFO'2015 experiment, June 09, 2015, 09:56 UTC. (a) VV image and (b) instrument noise floor (NESZ) plotted by increasing incidence angle for the corresponding acquisition. The oil slick is located across the range of incidence angles from ∼56° to 67° in the image.

the surface, the upper limit of the average slick thickness is greater than 1 μm. The actual thickness is likely to be lower, shown through modeling of slicks released in the same area on June 10 during another spill experiment and under higher wind conditions that indicate only ∼50% of the released oil was on the surface a few hours after the release [70].

Wind and waves information was obtained from Météo-France, the French national meteorological service (POLLUPROOF'2015 campaign), and from the Norwegian Meteorological Institute (NOFO'2015 campaign) and is given in Table II.

The methodologies and the results presented in the following are based on SAR data collected by SETHI [27], the remote sensing imaging system developed by ONERA,

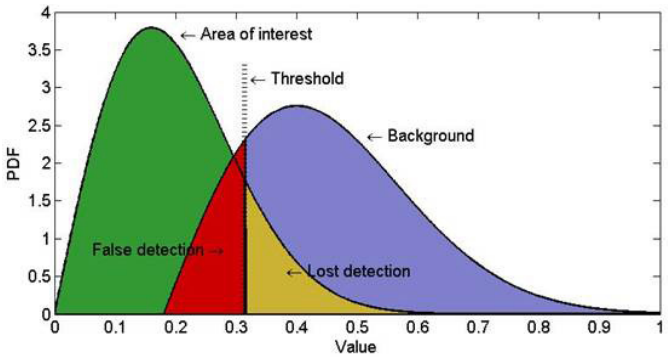

Fig. 6. Overview of histogram thresholding for ROC curve computation based upon separation of two classes.

as well as experimental data acquired by UAVSAR [28], the airborne sensor of JPL/NASA. Sections IV-A and IV-B briefly present the two SAR systems used here. Table III summarizes all SAR scenes investigated in this paper.

A. SETHI: Airborne Quad-Polarized SAR Sensor

SETHI is the ONERA airborne remote sensing laboratory designed to explore the science applications of remote sensing [27]. It is a pod-based system operating onboard a Falcon 20 Dassault aircraft flying at an altitude of 9000 ft. For both POLLUPROOF'2015 and NOFO'2015 campaigns, POLSAR data were acquired by SETHI at L-band, with a range resolution of 1 m (bandwidth from 1.25 to 1.4 GHz). Images are processed with an azimuth (along track) resolution equal to the range resolution. Imaged area is 9.5 km in azimuth and 1.5 km in range, with incidence angles from 34° to 52°. The instrument noise floor has been estimated using the method proposed in [71], and the results are shown in Fig. 4. The estimated noise equivalent sigma zero (NESZ) is very low, ranging from around -51 to -53 dBm^2/m^2, allowing a sufficiently high SNR over slick-covered areas for valid analysis of surface characteristics. Examples of high-resolution polarization-dependent images acquired by SETHI at L-band are shown in Section V.

B. UAVSAR: Airborne Quad-Polarized SAR Sensor

During the NOFO'2015 experiment, UAVSAR (developed by NASA [28]) acquired POLSAR data at L-band over controlled releases of mineral oil at sea, flying at an altitude of 35 100 ft. The data used in this analysis were acquired on June 9, 2015, within 5 min of SETHI and over the same area. They are processed with a resolution of 5 m in range and 7.2 m in azimuth (multilook format). The incidence angle ranges from 19.5° to 67.5° across the swath. The instrument

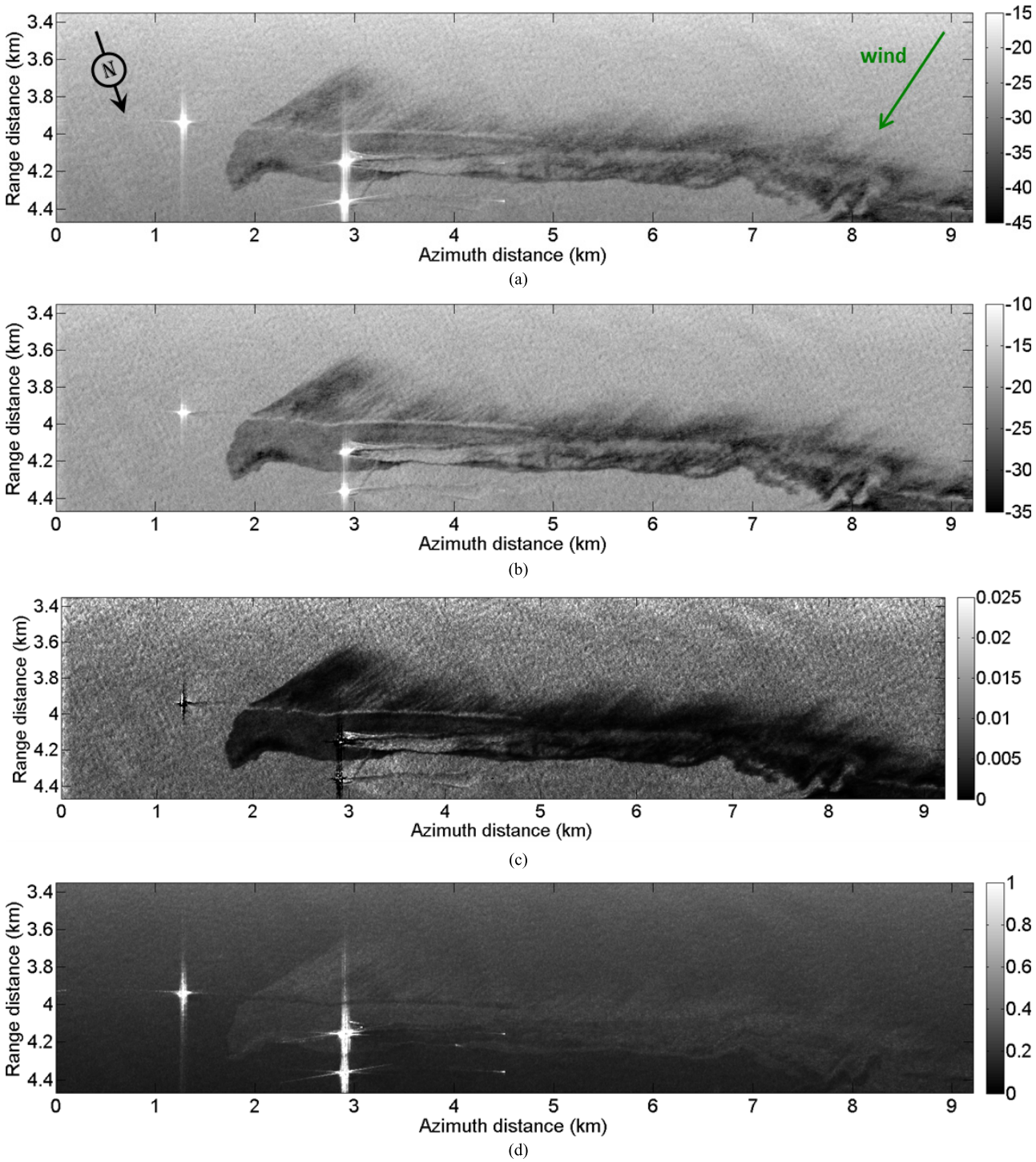

Fig. 7. SETHI NOFO'2015—L-band SAR data acquired over mineral oil released at sea—June 09, 2015, 10:01 UTC. (a) HH, (b) VV, (c) PD, and (d) PR quantities. Multilook 7 m × 7 m.

noise floor has been estimated using the same methodology as that used for the SETHI one [71], and it is shown in Fig. 5. The NESZ is very low, ranging from around -35 to -51 dBm^2/m^2, allowing a sufficient SNR over sea surface covered by slicks for valid analysis of surface properties.

V. Methodology and Performance Assessment

We use receiver operating characteristic (ROC) [72] curves to characterize the detection capabilities of the parameters discussed in Section III. This is an extension of the methodology published in [26] using a much larger data set and a more comprehensive set of parameters. ROC curves are obtained by plotting the probability of detection (Pd) against the probability of false alarm (Pfa), which quantifies the performance of a detector as its discrimination threshold is varied. In other words, ROC graphs depict the tradeoff between hit rates and false alarm rates of detectors [72]. The procedure, shown in Fig. 6, is as follows: we manually select areas of

clean sea surface (i.e., the background) and slick (i.e., the area of interest) and compute for each investigated parameter the histograms of values within the two regions. Then, for all possible values of the detection threshold, we calculate Pd as the fraction of samples within the area of interest that are below the threshold and Pfa as the fraction of samples in the background that are below the threshold. We will use these results to develop an instrument-independent ranking of the detection capabilities of each investigated parameter.

A. Sea Surface Slick Observation

We begin by evaluating the quad-pol SAR data acquired by SETHI (Fig. 7) over a controlled release of mineral oil (NOFO'2015 experiment). In Fig. 7, images of HH and VV channels are given as well as the PD and the PR maps. Visually, there is no significant difference between the cross-polarized and the co-polarized images, so the HV channel is not shown here. For these images, the wind direction is from the top right (see green arrow in Fig. 7(a); black arrow indicates the north direction). Wind information was obtained from the Norwegian Meteorological Institute and is given in Table II. The oil slick is observable as a dark area, with a ship's wake running through the slick. Within the lower part of the slick, the passage of a mechanical recovery boom (MOS sweeper [73]) appears to have left a relatively clean sea surface. Images show a feathered structure along the top of the slick (upwind) and a smooth edge on the downwind side of the slick, the expected appearance of the slick based on the wind direction.

Interestingly, while the upper limit of the slick thickness (greater than 1 μm) has been estimated to be at least one-hundredth of the penetration depth at L-band (typically of the order of millimeters for water content greater than 50%—see Fig. 1), the mineral oil slick is observable in the PR images [Fig. 7(d)]. An explanation could be that there is a dielectric change due to the presence of oil in the water column that will impact the Polarization Ratio.

Low backscattering values from slick-covered areas can lead to low SNR values. Therefore, it is critical that we ensure sufficiently high SNR values before undertaking any analysis. SNR values along a transect through data obtained by SETHI during the NOFO'2015 experiment are shown in Fig. 8. The curves have been computed across a range transect at azimuth 2.1 km. The slick is between 3.85 km (incidence angle 44.2°) and 4.2 km (incidence angle 49.4°). The SNR values are high (even in cross-polarization), which enables polarimetric analysis of the surface properties.

B. Evaluation of Polarimetric Parameters for Slick Detection: Mineral Oil

We first focus on SAR data collected by SETHI over mineral oil spill (NOFO'2015 experiments). Fig. 9 shows areas selected for ROC curves computation where the uncontaminated sea surface (background) is outlined by the blue box and the contaminated area of interest is outlined by the red box. Note that the average SNR computed over the two regions (Table IV) is greater than 10 dB.

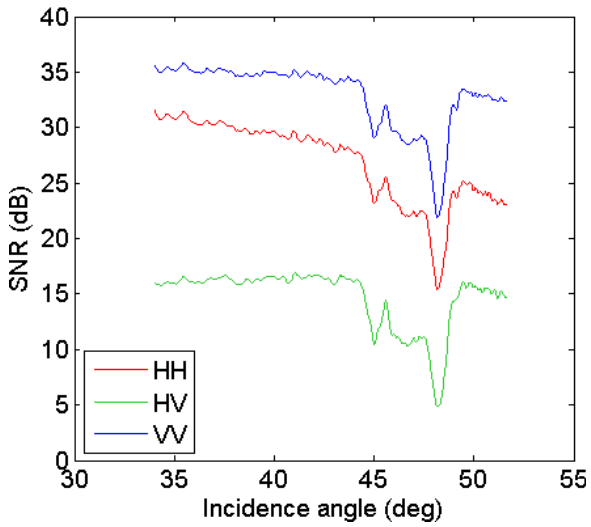

Fig. 8. SETHI signal-to-noise ratio (SNR) in polarization HH (red), HV (green), VV (blue)—range transect for azimuth 2.1 km (see Fig. 7)—June 09, 2015, 10:01 UTC.

ROC curves (Fig. 10) show that the Polarization Difference and VV are the most efficient parameters for mineral oil slick detection (i.e., for a given value of Pfa, they exhibit the greater value of Pd). The first eigenvalue (λ_1) is also very efficient for detecting slick-covered area, as it gives a performance of detection similar (slightly lower for low values of Pfa) to that obtained with VV and PD. They are then followed by the Hermitian Product between HH and VV (HP) and HH and HV. HV has good performance of detection and is even better than that of HH for low values of Pfa. This result for HV, which is consistent with the results obtained with UAVSAR data in stronger wind conditions obtained one day later (June 10) [57], is possible because of high SNR over the entire image. Then, we found that the Polarization Ratio and the studied quad-polarimetric parameters have low Pd values for all Pfa values. So, the co-pol coherence, the Bragg Likelihood Ratio, the Degree of Polarization, the Entropy, and the Conformity Coefficient are the parameters that give the worst performances of detection. These results seem to indicate that the same main scattering mechanism occurs over both contaminated and uncontaminated sea surface, namely, surface reflection and Bragg scattering [41]. To confirm this, we note that the polarimetric entropy, computed with a high SNR even over the polluted area, is low over both the clean sea surface and the slick; the mean entropy values are, respectively, equal to 0.18 and 0.17. This indicates that only one dominant scattering mechanism occurs, which confirms previous observations [56], [57] for the NOFO'2015 exercise and the original observation based on UAVSAR L-band data acquired over the Deepwater Horizon oil spill accident [41].

We now investigate SAR data collected with UAVSAR during the same NOFO'2015 experiment (mineral oil). As for SETHI, the UAVSAR instrument is characterized by a very low noise floor, which suggests a good complementarity of the results obtained with the two airborne sensors. The imaged ocean surface is the same as for the previous SETHI analysis (Fig. 9), and the time lag between the two

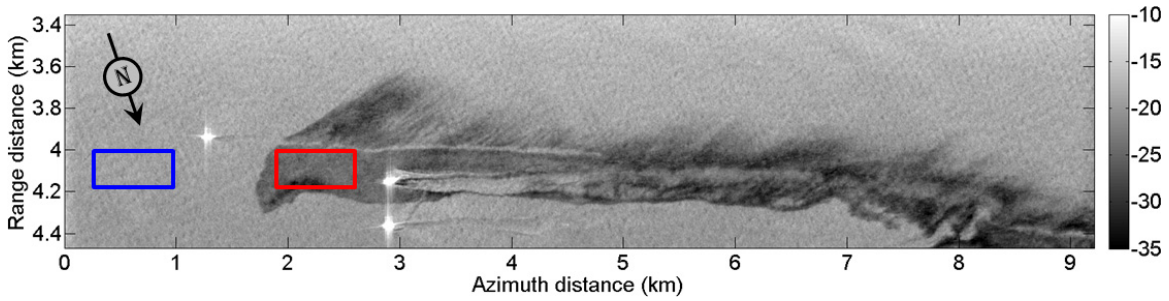

Fig. 9. Areas selected for ROC curve computation—blue box: clean sea surface and red box: slick area. SETHI, NOFO'2015 experiment, June 09, 2015, 10:01 UTC; VV channel; multilook 7 m × 7 m.

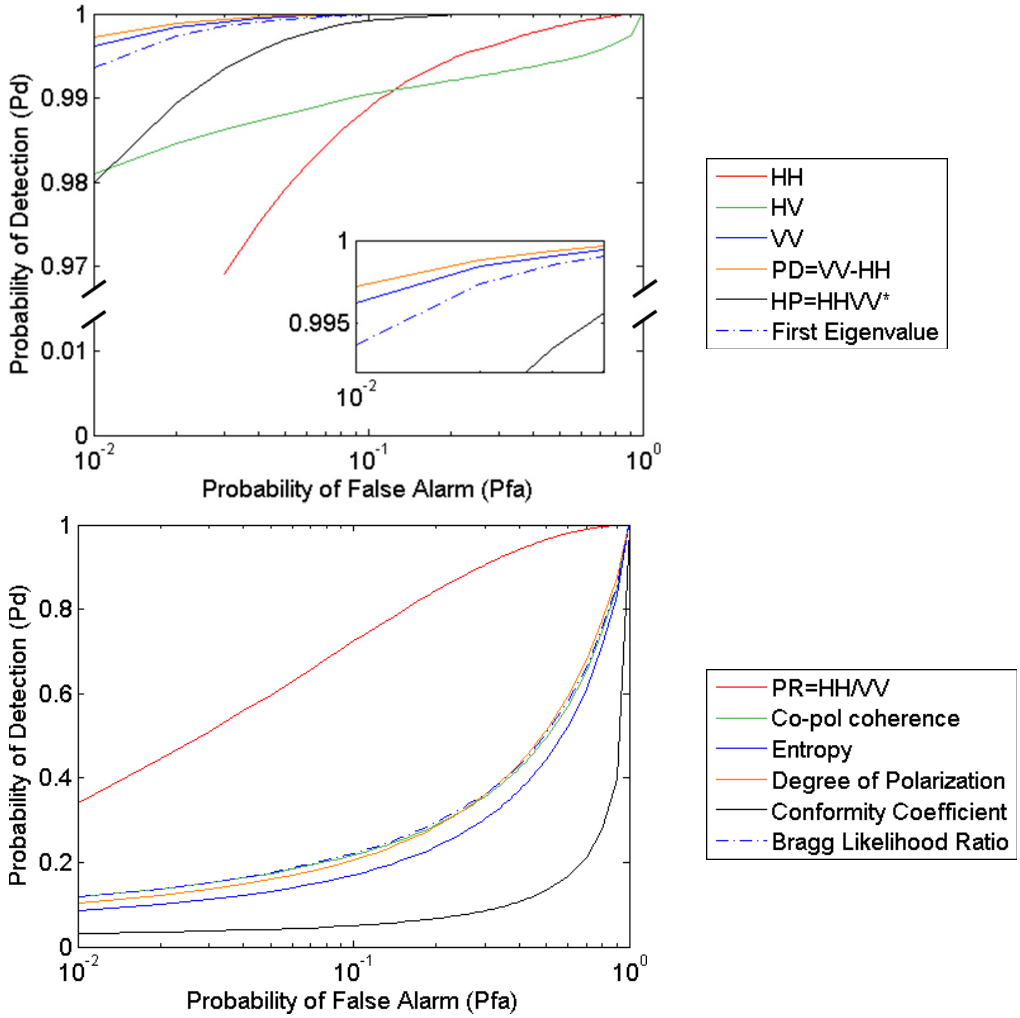

Fig. 10. SETHI, NOFO'2015 experiment, June 09, 2015, 10:01 UTC—Pd versus Pfa computed for all investigated parameters. Note the cut of the vertical axis on the top figure.

TABLE V
SIGNAL-TO-NOISE RATIO—UAVSAR, NOFO'2015 EXPERIMENT, JUNE 09, 2015, 09:56 UTC

Region	Incidence angle (deg)	HH MEAN [MIN MAX]	HV MEAN [MIN MAX]	VV MEAN [MIN MAX]
Clean sea	56.8°	14.8 [14.4 15.1] dB	9.4 [9.1 9.6] dB	23.7 [23.3 24.0] dB
Oil slick	56.8°	10.2 [10.0 10.4] dB	4.8 [4.5 5.0] dB	17.0 [16.7 17.4] dB

acquisitions is 5 min. For UAVSAR ROC graph analysis, the contaminated sea surface is close to that selected for SETHI (Figs. 9 and 11). Clean sea regions are selected to be at the same range as the selected oil-covered areas, but they are in different places for SETHI and UAVSAR due to different flight directions. For the chosen regions of interest, the NESZ is

TABLE VI
SIGNAL-TO-NOISE RATIO—SETHI, POLLUPROOF'2015 EXPERIMENT, MAY 22, 2015, 16:07 UTC

Region	Incidence angle (deg)	HH MEAN [MIN MAX]	HV MEAN [MIN MAX]	VV MEAN [MIN MAX]
Clean sea	42.5°	30.7 [29.6 31.7] dB	18.7 [17.5 19.7] dB	36.6 [35.6 37.5] dB
Oil slick	42.5°	26.7 [25.9 27.5] dB	14.6 [13.5 15.8] dB	33.1 [32.2 33.8] dB

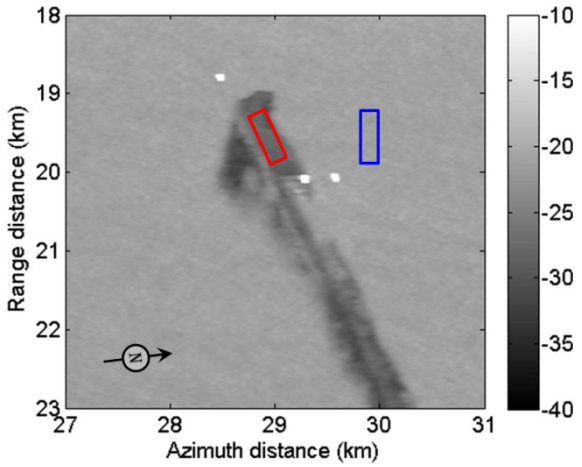

Fig. 11. Areas selected for ROC curve computation. Blue box: clean sea surface and red box: slick area. UAVSAR, NOFO'2015 experiment, June 09, 2015, 09:56 UTC—VV channel.

around -45 dBm^2/m^2 (incidence angle around 57°). The SNR in the selected regions are given in Table V. As for SETHI, the levels are high (>5 dB), which ensures a reliable analysis of surface backscatter over both slick-free and oil-covered sea surfaces. ROC graphs shown in Fig. 12 demonstrate that the best performance of detection is given by the cross-polarized channel (HV), followed by VV, the Polarization Difference, and the first eigenvalue (λ_1), then HH and the Hermitian Product between HH and VV (HP), and finally the conventional quad-polarimetric parameters of Entropy, Polarization Ratio, Degree of Polarization, dual-pol coherence, Bragg Likelihood Ratio and Conformity Coefficient. These results are very close to those obtained by SETHI.

C. Evaluation of Polarimetric Parameters for Slick Detection: Vegetable Oil

We now investigate Fatty Acid Methyl Esters (FAME) and rapeseed oil releases imaged by SETHI during the POLLUPROOF'2015 experiment (Fig. 13). Because of their physicochemical properties, these two substances have different behaviors once released into the ocean. FAME forms a cloud in the water column composed of microdroplets, and rapeseed oil forms a film on the surface [43]. These two behaviors have been highlighted in [43], using the oil–water mixing index introduced in [42].

The slick contains both substances. FAME appears on the left part of the spill and covers a surface of 0.29 km^2 [see red box in Fig. 13(a)]. Rapeseed oil corresponds to the right part of the spill [green box in Fig. 13(a)] and covers a surface of 1.26 km^2. In between, there is a mixture of the two products [blue box in Fig. 13(a)]. From the amount released product (1 m^3) and the area covered by the spill, the average thickness of the rapeseed oil spill is estimated to be equal to 0.8 μm. This is approximately three orders of magnitude thinner than the penetration depth at L-band. Thus, the relative dielectric constant measured by the radar should be unaffected by the oil slick, and no signature of the rapeseed oil is observed in the Polarization Ratio image [Fig. 13(d)]. FAME, which mixes in the seawater column [43], slightly appears on the Polarization Ratio image, probably due to a decrease of the effective dielectric constant of this mixture compared to that of the surrounding clean sea area.

Clean sea surface and surface covered by rapeseed oil have been chosen and ROC curves computed for the selected areas. As for mineral oil analysis, the SNR is high (see Table VI), at least 14 dB, over both covered and free sea surfaces.

Similar to the results from mineral oil slicks, we observe (see Fig. 14) that for the rapeseed oil release, most of quad-polarimetric parameters (BLR, Entropy, and co-polarized coherence) give very poor performance of detection while amplitude channels are very powerful: HV gives the best performance of detection, followed closely by VV, the first eigenvalue (λ_1), HH, the Hermitian Product between HH and VV (HP), and the Polarization Difference (PD). As obtained above for mineral oil, we find here again that the Polarization Ratio (PR) and the conventional quad-polarimetric parameters (co-pol coherence, Bragg Likelihood Ratio, Degree of Polarization, Entropy and Conformity Coefficient) give the worst detection performance. We note finally that an identical ordering of the investigated parameters is obtained when selected sea surface contaminated by FAME instead of rapeseed oil (ROC curves not shown here).

This analysis, based on ROC graphs obtained with SAR data acquired by two airborne remote sensing sensors, both characterized by a very low instrument noise floor, demonstrate that, in the three cases shown, the VV and HV amplitude channels provide the best overall performance of detection. Sometimes, a slight improvement could be obtained with polarization-dependent parameters like the Polarization Difference.

Speckle affects the performances of detection, and multi-looking is the most common method to reduce its effect. In this paper, we study the performances of detection offered by several polarization-dependent parameters, all calculated with the same window size, namely, multilooking by 7×7 in range and azimuth directions. The size of the window influences the detection performance of each of the parameters, but since the same window size is always used, the result obtained herein can be generalized to other window sizes.

When SAR data are collected with a very low NESZ, the backscattered signal is not corrupted by noise, the EM wave is well polarized, and only one scattering mechanism

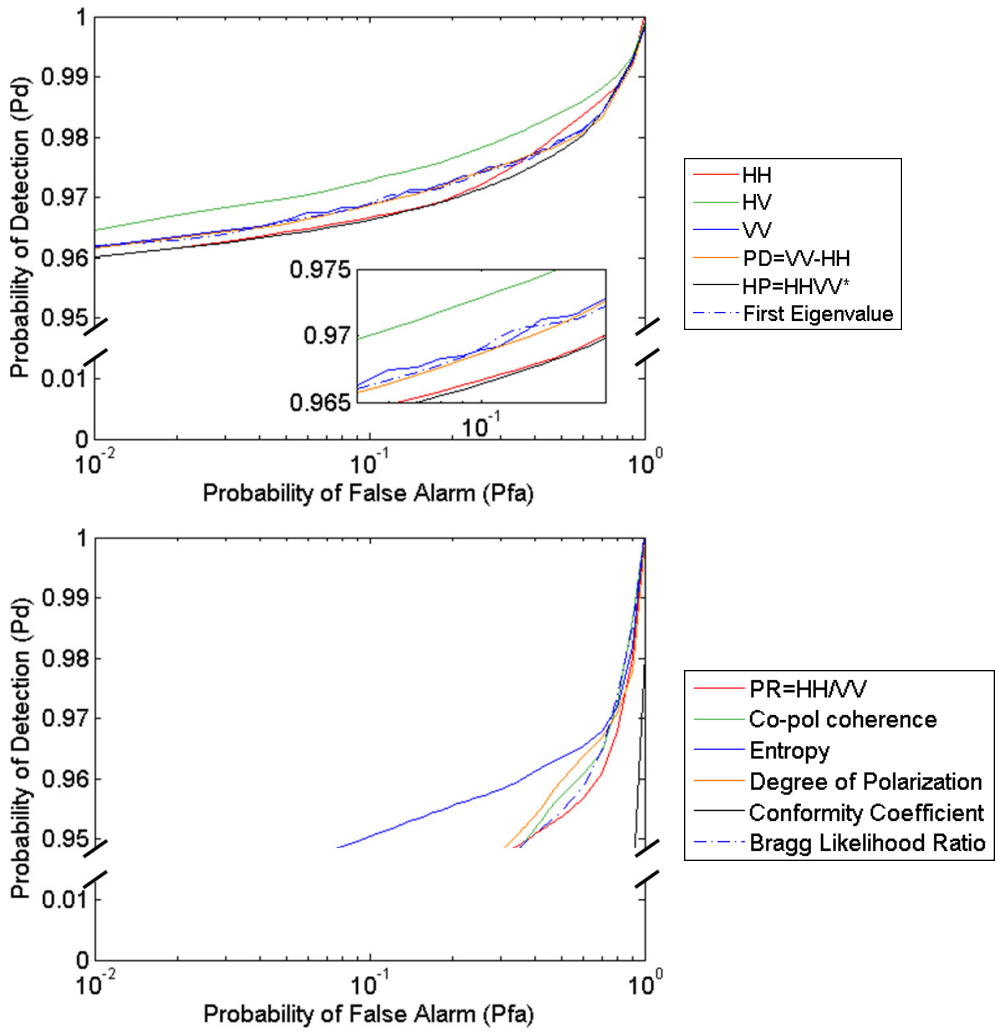

Fig. 12. UAVSAR, NOFO'2015 experiment, June 09, 2015, 09:56 UTC—Pd versus Pfa computed for all investigated parameters. Note the cut of the vertical axis on both figures.

occurs over both clean and contaminated sea surface (low entropy values over both surfaces). When the SNR over slick-covered area is not as high as with the airborne acquisitions analyzed here, as for the spaceborne SARs available today, the instrument noise must be considered when evaluating the performance of detection of polarimetric parameters. Section V-D focuses on the influence of instrument noise.

D. Instrument Noise Effect

To study how the NESZ impacts the ROC curves obtained for the investigated features, we added increasing levels of Gaussian white noise, from 5 to 30 dB, to the raw SAR data collected by SETHI during the NOFO'2015 experiment. We then processed the noisier data using the standard processing software (Fig. 15). We note that when the noise is increased by 15 dB [Fig. 15(d)], its detrimental effect in the VV image is apparent. When 30 dB of noise is added, the slick is no longer observable in the VV image [Fig. 15(f)].

We now assess the detection performance for all simulated instrument noise levels. ROC curves are computed over the areas shown in Fig. 9. The results for some selected radar quantities are given in Fig. 16, and conclusions are as follows.

1) For a given Pfa, Pd for HH, VV, and HV decreases as SNR decreases. When the additive noise is less than or equal to 10 dB, the ROC curves are largely unchanged.
2) For a given Pfa, Pd increases for the polarimetric parameters for additive noise values less than 20 dB. Then, performance of detection decreases with greater levels of additive noise.

Thus, in contrast to the amplitude values, the Pd for the polarimetric parameters increases with the instrument noise so long as the SNR is sufficiently high over clean sea surface (∼15 dB added noise) and then decreases for decreasing SNR. As the SNR decreases, the received signal is increasingly corrupted by noise and the combined noise plus scattered EM signal becomes randomly randomly polarized (DoP goes to 0 and Entropy goes to 1 as the total signal approaches noise only). With sufficiently high noise levels, both contaminated and uncontaminated sea surfaces will appear randomly polarized and no further separation between the two regions is possible. SNR values as well as mean values of DoP and Entropy over

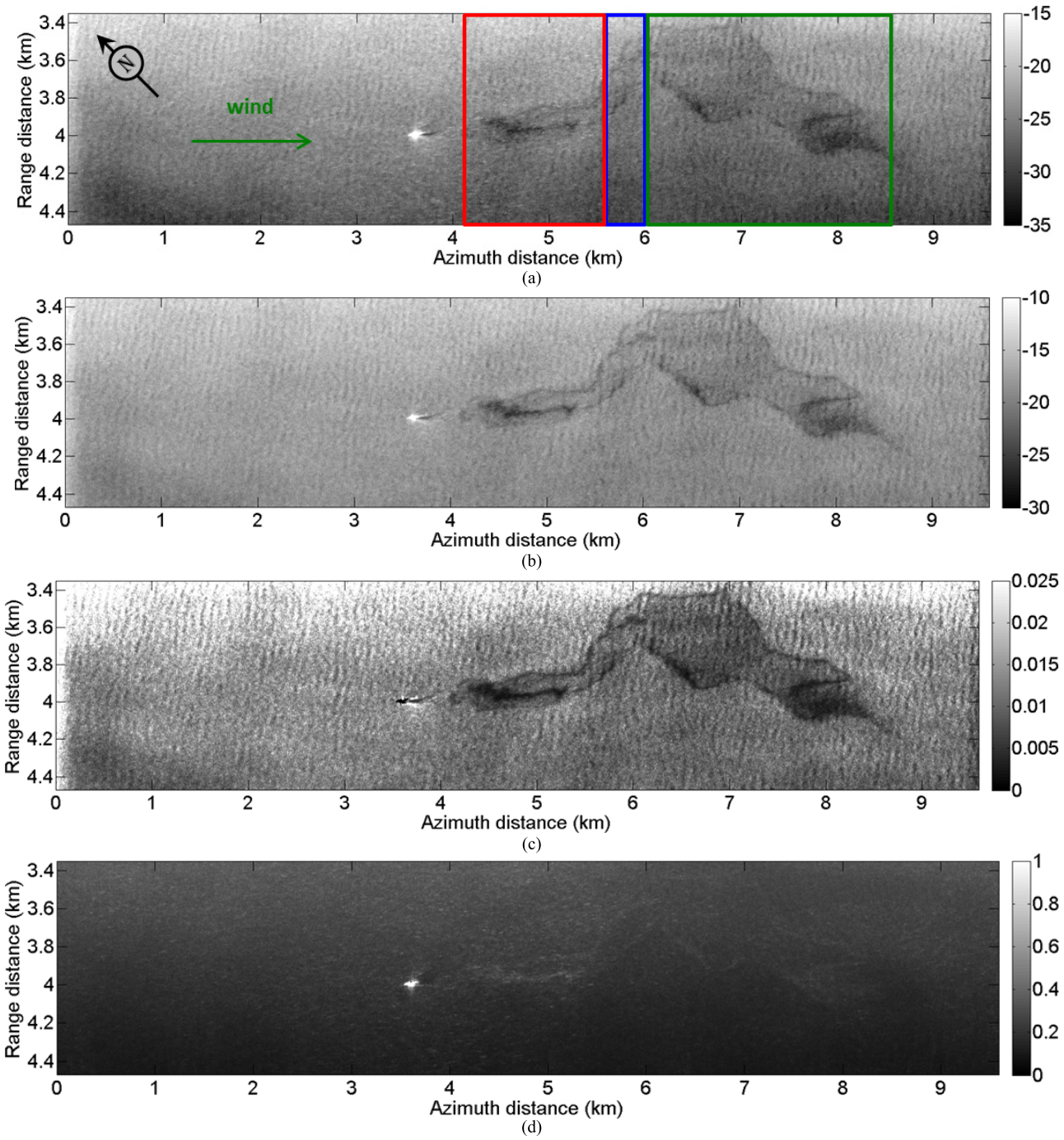

Fig. 13. SETHI POLLUPROOF'2015—L-band SAR data—May 22, 2015, 16:07 UTC. (a) HH, (b) VV, (c) PD, and (d) PR quantities—multilook 7 m × 7 m. FAME is indicated by the red box and rapeseed oil by the green box, and the blue box corresponds to a mixture between the two products.

clean sea and the oil slick are given in Tables VII and VIII. Despite the increase in Pd with increasing noise component for the polarimetric parameters, the Pd remains highest for the single-polarization HH and VV parameters at any given level of added noise. For a noise level increased by less than 20 dB, HV has higher Pd than all polarimetric parameters.

VI. Discussion

Our analysis of L-band SAR data collected by SETHI and UAVSAR, two airborne sensors that have low instrument noise floor, allows us to formulate the following ordering of polarization-dependent parameters for region-based slick detection, whether vegetable films or mineral oil slicks.

1) *Group 1:* VV, HV, the Polarization Difference (PD), and the first eigenvalue (λ_1).
2) *Group 2:* HH and the Hermitian Product between HH and VV (HP).
3) *Group 3:* The Entropy (H), the Polarization Ratio (PR), the Degree of Polarization (DoP), the co-polarized coherence (ρ_{HHVV}), the Bragg Likelihood Ratio (BLR), and the Conformity Coefficient (μ).

The parameters in the first group all provide high performance of detection based on the ROC curve results. The presence

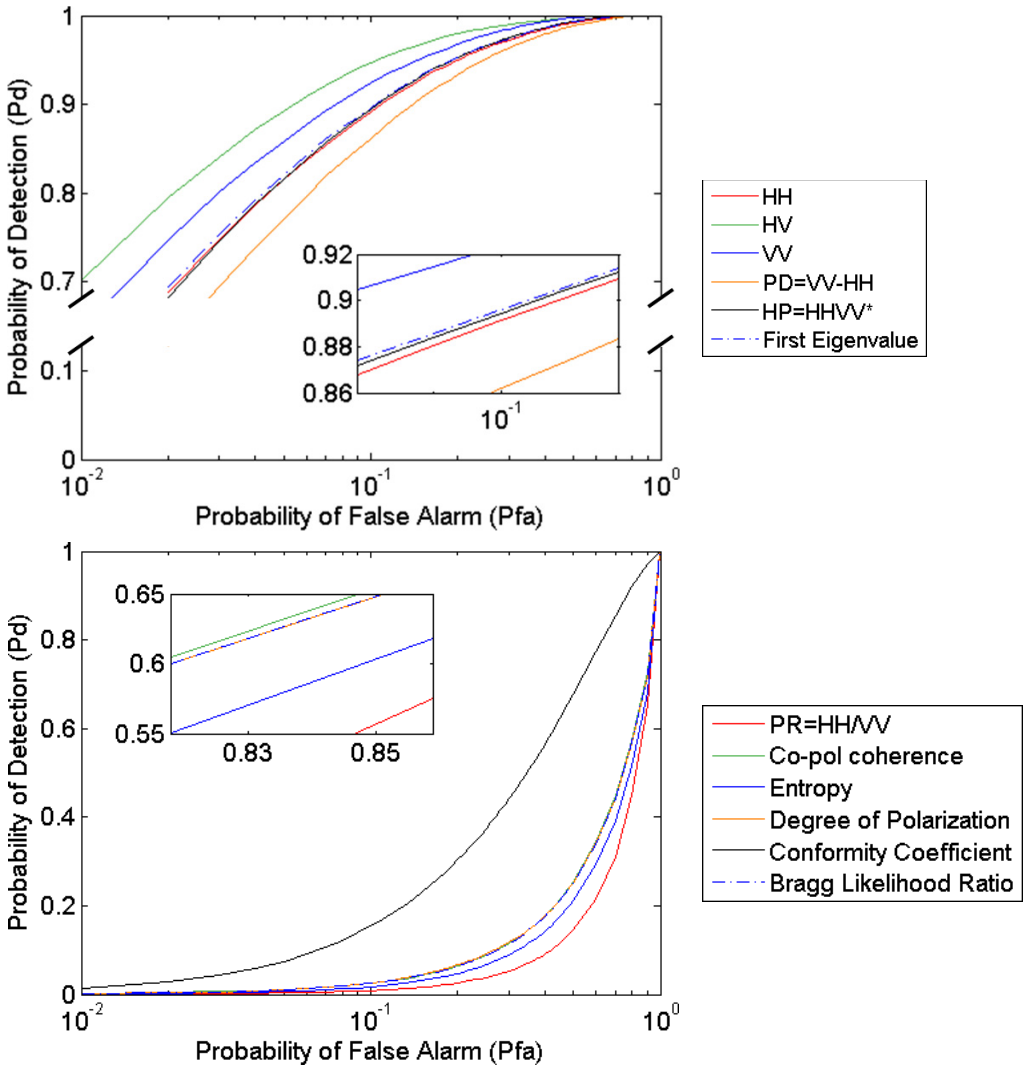

Fig. 14. SETHI, POLLUPROOF'2015 experiment, May 22, 2015, 16:07 UTC—Pd versus Pfa computed for all investigated parameters. Note the cut of the vertical axis on the top figure.

TABLE VII
SIGNAL-TO-NOISE RATIO—SETHI, NOFO'2015 EXPERIMENT, JUNE 09, 2015, 10:01 UTC

Region	Noise added	HH	HV	VV
Clean sea	Original data	26.5 dB	16.4 dB	34.1 dB
	5 dB	21.5 dB	11.4 dB	29.1 dB
	10 dB	16.5 dB	6.4dB	24.1 dB
	15 dB	11.5 dB	1.4 dB	19.1 dB
	20 dB	6.5 dB	-3.6 dB	14.1 dB
	30 dB	-3.5 dB	-13.6 dB	4.1 dB
Oil slick	Original data	21.5 dB	10.2 dB	28.0 dB
	5 dB	16.5 dB	5.2 dB	23.0 dB
	10 dB	11.5 dB	0.2 dB	18.0 dB
	15 dB	6.5 dB	-4.8 dB	13.0 dB
	20 dB	1.5 dB	-9.8 dB	8.0 dB
	30 dB	-8.5 dB	-19.8 dB	-2.0 dB

of each parameter in group 1 can be understood through the Bragg scattering model. In this framework, VV always has the highest amplitude and HH and VV have different reflectivities, ensuring that PD takes positive values. In the tilted-Bragg-scattering model, HV can have a nonzero amplitude that is always less than both HH and VV. As a result, the first eigenvalue of the covariance matrix is dominated by VV and, to a lesser extent, HH. The control

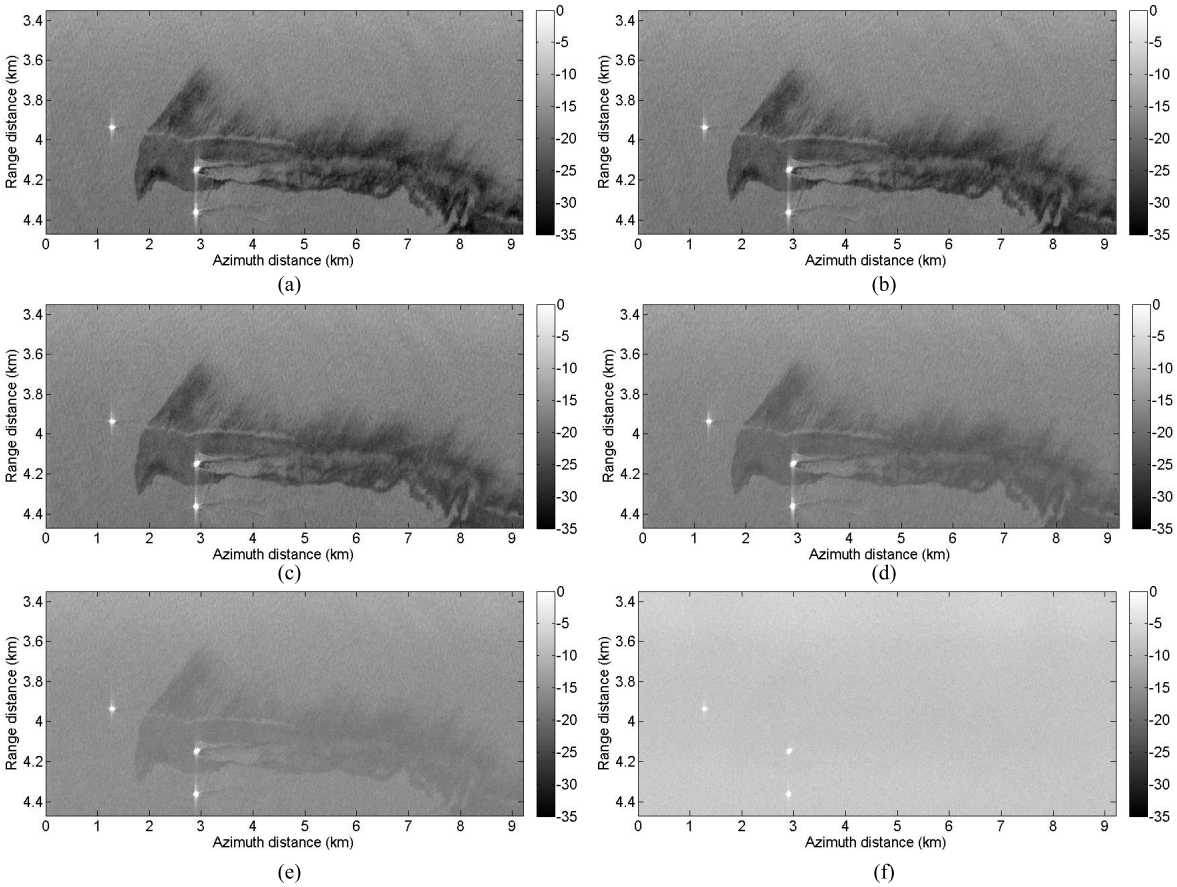

Fig. 15. Noise effect—SETHI polarization VV. (a) Original data and instrument noise increased by (b) 5 dB, (c) 10 dB, (d) 15 dB, (e) 20 dB, and (f) 30 dB—NOFO'2015 experiment, June 09, 2015, 10:01 UTC.

TABLE VIII
DoP AND ENTROPY—SETHI, NOFO'2015 EXPERIMENT, JUNE 09, 2015, 10:01 UTC

Region	Noise added	DoP	Entropy
Clean sea	Original data	0.94	0.17
	5 dB	0.93	0.19
	10 dB	0.9	0.24
	15 dB	0.84	0.34
	20 dB	0.75	0.46
	30 dB	0.67	0.56
Oil slick	Original data	0.92	0.18
	5 dB	0.88	0.25
	10 dB	0.81	0.36
	15 dB	0.72	0.48
	20 dB	0.67	0.55
	30 dB	0.66	0.57

of VV on the value of the first eigenvalue explains why the first eigenvalue is a high-performing parameter. As previously reported in [57], HV performs well where the instrument noise floor is low because, to a good approximation in the tilted-Bragg model, the HV amplitude is proportional to PD.

The second group of parameters, composed of HH and the Hermitian Product between HH and VV channels, gives good performance of detection, although slightly lower than the performance of group 1. We show that HH channel is slightly less effective than VV for slick detection. However, we emphasize that HH is effective for distinguishing slicks from relatively clean sea surfaces. HP suffers from the decrease in detection performance of HH compared to that of VV.

We place all remaining parameters in group 3, which has the worst capabilities of detection. The parameters in group 3 are the Polarization Ratio (PR), the co-polarized coherence (ρ_{HHVV}), the Bragg Likelihood Ratio (BLR), the Entropy (H), the Degree of Polarization (DoP) and the Conformity Coefficient (μ). For these parameters, detection performance seems to be very strongly correlated with the instrument noise and their applicability in a sea pollution detection scheme is instrument dependent. For a sufficiently high SNR, the EM wave backscattered by the slick-free sea surface remains well polarized (DoP close to 1 and Entropy close to 0). It becomes less polarized over the contaminated area (DoP decreases and Entropy increases) and the performances of detection increase. When the instrument noise becomes a significant fraction of the measured signal (low SNR), the apparent backscattered signal becomes randomly polarized for contaminated and uncontaminated sea surfaces, and no further separation between the two regions is possible. The instrument noise issue for oil spill detection using quad-polarimetric SAR data has been recently addressed in [15]. In this paper, the authors hypothesize that the often-stated claims that non-Bragg scattering occurs over slick-covered areas is due to a misinterpretation of SAR images collected with too low an SNR. Our study presented in this paper is in agreement with this hypothesis and goes even further since,

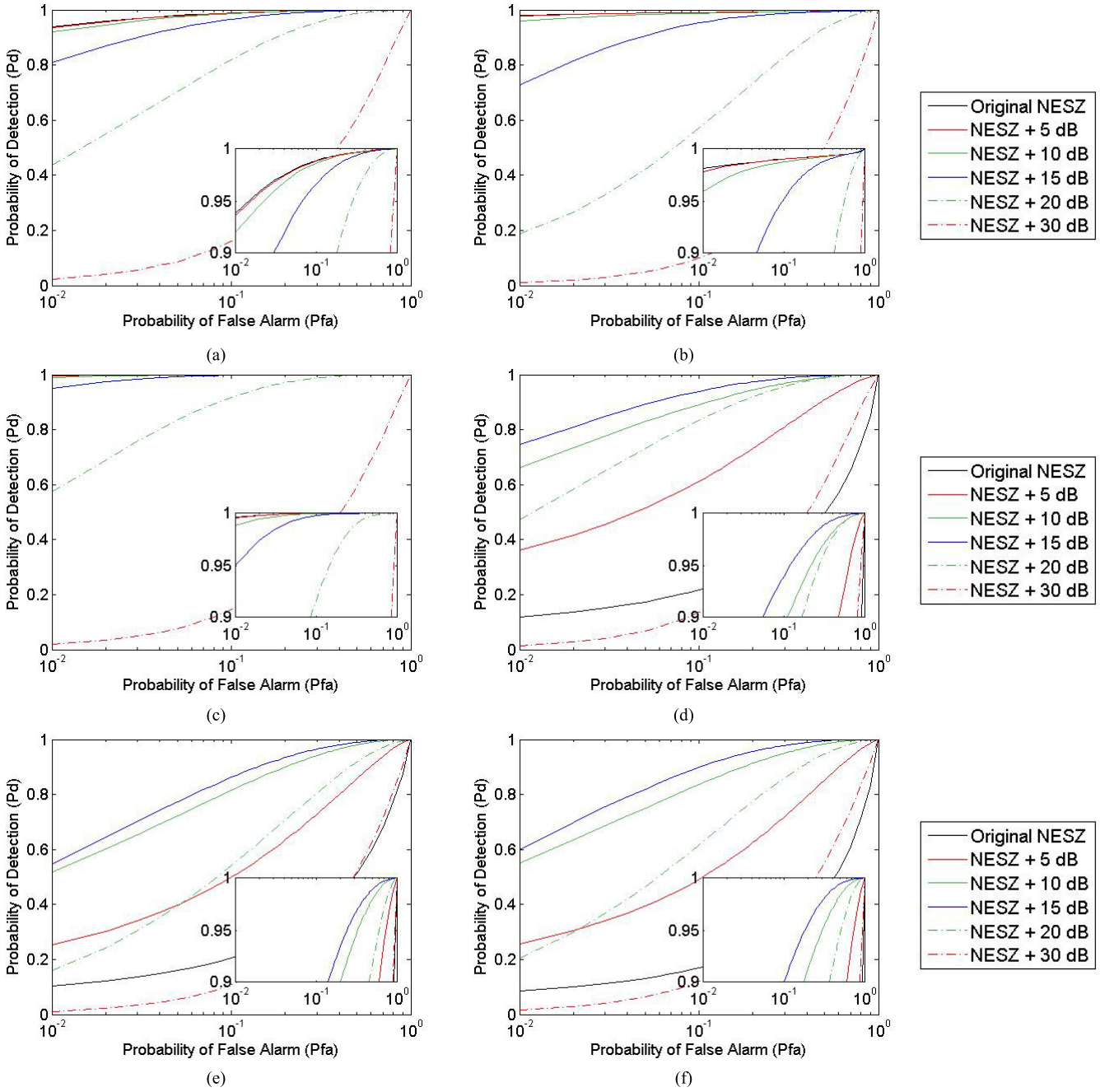

Fig. 16. Noise effect on ROC curves—SETHI (a) HH, (b) HV, (c) VV, (d) dual-pol coherence, (e) DoP, and (f) Entropy—NOFO'2015 experiment, June 09, 2015, 10:01 UTC.

for the first time, we quantify in a systematic way the effect of instrument noise on polarization-dependent SAR parameters when applied to oil spill detection. As previously reported in [15] and [41], we demonstrate that there is no deviation from Bragg scattering for radar scattering from ocean surface covered by mineral and vegetable oil.

The hierarchy that we propose here is obtained from L-band airborne SAR data collected over vegetable and mineral oil slick released during moderate wind conditions. A similar study is proposed in [56] and [57], with [57] evaluating the parameters during transport and evolution of mineral and plant slicks. The major differences between all these studies are the proposed method of measuring the capabilities of detection of different quantities investigated and the fact that the slicks studied in [56] and [57] were thinner, formed from the release of 0.2–0.5 m^3 of material rather than 45 m^3 as the slick in our study. In [56], SAR data acquired by UAVSAR, TerraSAR-X, and RADARSAT-2 at nearly the same time over mineral oil spills under high-wind conditions are investigated using many of the same parameters as herein. They found likewise that VV intensity is the most efficient parameter for the detection of oil slick on sea surface. The HV channel was not investigated in [56] because of the low SNR of the satellite data. The UAVSAR image investigated in [56] is also studied in [57], combined with 17 other images covering the evolving slicks over an 8-h period. In the latter, the proposed methodology

to order the polarimetric parameters is slightly different than in [56], and the authors also found that VV intensity is very efficient for slick–sea discrimination. The HV channel was studied in [57] and, similar to our results, those authors found that the cross-polarized channel is attractive for slick detection over ocean surface when employed SAR data are acquired with a very low instrument noise floor. Comparing [56], [57], and the results that we report here, there is a clear consensus on the use of VV or HV channels for slick detection at sea. The main difference between results obtained in this paper and those reported in [56] and [57] concerns the performances of detection given by the Polarization Difference. Indeed, we found here, and as already reported in [17], [33], [43], and [54], that the Polarization Difference is one of the most efficient parameters for slick–sea discrimination. This difference could be due to different wind conditions, sea state, or slick thicknesses, and highlights the complexity of slick detection across a range of variables under which they can occur.

VII. Conclusion

To guide the selection of the most appropriate SAR imaging mode for marine pollution detection, a methodology based on the analysis of ROC curves has been reported in this paper. The ROC analysis accounts for the non-Gaussian tails of the probability distribution of parameter values, which are particularly important for the slick-covered areas. We compare the probabilities of detecting a slick with the probabilities of a false alarm for a range of detection thresholds to rank various polarization-dependent parameters in the order of slick-detection performance, from best to worst. A key aspect of the results reported in this paper lies in the analysis of the instrument noise effect on the performance of detection offered by the studied parameters. This is done by progressively adding Gaussian white noise directly to the raw SAR data and then processing the noisier data using the standard processing software. The other important aspects of this paper derive from three factors: the quantitative evaluation of a dozen common parameters used for detecting marine slicks; the uniqueness of the studied data set collected by two airborne sensors operating at L-band, both of which are characterized by an instrument noise floor that is much lower than the one that is currently available from spaceborne SARs; and the evaluation of detectability of both vegetable and mineral oil slicks with the same low-noise instrument. Low noise makes the parameters more sensitive to the surface properties and less influenced by the sensor.

We find that HV amplitude can outperform all other investigated amplitudes and polarimetric settings whenever the instrument noise is sufficiently low (at least 5 dB in this paper). However, as instrument noise increases, HV amplitude and all polarimetric parameters that rely on HV become corrupted by the noise and their slick-detection performance diminishes. HV is closely followed by the investigated co-polarized settings (ordered as follows: VV, the Polarization Difference, HH, and the Hermitian Product between HH and VV), while being more robust to a lower SNR than the cross-polarized channel.

We note that this relative ordering is determined from a single combined set of sea state, meteorological conditions, and slick properties, and further work is needed to expand to other conditions, in particular lower wind speeds and different slick thicknesses.

For detecting slicks on the sea surface, we propose that VV parameter offers the best tradeoff between the benefit of detection performance and the instrument and data requirements.

We find that the co-pol amplitudes (HH and VV) and two polarimetric parameters, the Polarization Difference and the first eigenvalue of the quad-pol covariance matrix, are more robust in the presence of instrument noise than the cross-pol (HV) amplitude and quad-polarimetric parameters. This disparity in robustness is due to higher co-pol amplitudes relative to the cross-pol amplitude and the strong impact of instrument noise on POLSAR parameters. This implies that polarimetric quantities which combine the four polarimetric channels have performances of detection mainly driven by the instrument noise level (NESZ).

Acknowledgment

The authors would like to thank the Norwegian Clean Seas Association for Operating Companies (NOFO), Norway, for allowing them to participate in the oil-on-water exercise, which was carried out during June 8, 2015–June 14, 2015. They would like to thank everyone involved in the experiment at sea and those who participated in SAR data processing. They would also like to thank H. Oriot from ONERA, Palaiseau, France, for his thoughtful discussions about receiver operating characteristic curve computation. This research was carried out in part at the Jet Propulsion Laboratory, California Institute of Technology, Pasadena, CA, USA, under contract with the U.S. National Aeronautics and Space Administration (NASA). The UAVSAR data are courtesy of the NASA/Jet Propulsion Laboratory and are openly available through the Alaska Satellite Facility (http://asf.alaska.edu).

References

[1] M. Fingas and C. Brown, "Review of oil spill remote sensing," *Marine Pollution Bull.*, vol. 83, no. 1, pp. 9–23, 2014.
[2] C. Brekke and A. H. S. Solberg, "Oil spill detection by satellite remote sensing," *Remote Sens. Environ.*, vol. 95, no. 1, pp. 1–13, 2005.
[3] O. Garcia-Pineda *et al.*, "Detection of floating oil anomalies from the Deepwater Horizon oil spill with synthetic aperture radar," *Oceanography*, vol. 26, no. 2, pp. 124–137, 2013.
[4] H. A. Espedal, "Satellite SAR oil spill detection using wind history information," *Int. J. Remote Sens.*, vol. 20, no. 1, pp. 49–65, Jan. 1999.
[5] H. A. Espedal, O. M. Johannessen, J. A. Johannessen, E. Dano, D. R. Lyzenga, and J. C. Knulst, "COASTWATCH'95: ERS 1/2 SAR detection of natural film on the ocean surface," *J. Geophys. Res.*, vol. 103, no. C11, pp. 24969–24982, 1998.
[6] M. Gade and W. Alpers, "Using ERS-2 SAR images for routine observation of marine pollution in European coastal waters," *Sci. Total Environ.*, vols. 237–238, pp. 441–448, Sep. 1999.
[7] O. Garcia-Pineda, B. Zimmer, M. Howard, W. Pichel, X. Li, and I. R. MacDonald, "Using SAR images to delineate ocean oil slicks with a texture-classifying neural network algorithm (TCNNA)," *Can. J. Remote Sens.*, vol. 35, no. 5, pp. 411–421, Oct. 2009.
[8] F. Girard-Ardhuin, G. Mercier, F. Collard, and R. Garello, "Operational oil-slick characterization by SAR imagery and synergistic data," *IEEE J. Ocean. Eng.*, vol. 30, no. 3, pp. 487–495, Jul. 2005.

[9] A. D. Jenkins and K. B. Dysthe, "The effective film viscosity coefficients of a thin floating fluid layer," *J. Fluid Mech.*, vol. 344, pp. 335–337, Aug. 1997.

[10] A. D. Jenkins and A. S. Jacobs, "Wave damping by a thin layer of viscous fluid," *Phys. Fluids*, vol. 9, no. 5, pp. 1256–1264, 1997.

[11] K. P. Singh, A. L. Gray, R. K. Hawkins, and R. A. O'Neil, "The influence of surface oil on c-and ku-band ocean backscatter," *IEEE Trans. Geosci. Remote Sens.*, vol. GE-24, no. 5, pp. 738–744, Sep. 1986.

[12] G. R. Valenzuela, "Theories for the interaction of electromagnetic and oceanic waves—A review," *Boundary-Layer Meteorol.*, vol. 13, nos. 1–4, pp. 61–85, Jan. 1978.

[13] M. Migliaccio, F. Nunziata, and A. Buono, "SAR polarimetry for sea oil slick observation," *Int. J. Remote Sens.*, vol. 36, no. 12, pp. 3243–3273, 2015.

[14] A. H. S. Solberg, "Remote sensing of ocean oil-spill pollution," *Proc. IEEE*, vol. 100, no. 10, pp. 2931–2945, Oct. 2012.

[15] W. Alpers, B. Holt, and K. Zeng, "Oil spill detection by imaging radars: Challenges and pitfalls," *Remote Sens. Environ.*, vol. 201, pp. 133–147, Nov. 2017.

[16] M. Migliaccio, F. Nunziata, and A. Gambardella, "On the co-polarized phase difference for oil spill observation," *Int. J. Remote Sens.*, vol. 30, no. 6, pp. 1587–1602, 2009.

[17] M. W. Hansen, V. Kudryavtsev, B. Chapron, C. Brekke, and J. A. Johannessen, "Wave breaking in slicks: Impacts on C-band quad-polarized SAR measurements," *IEEE J. Sel. Topics Appl. Earth Observ. Remote Sens.*, vol. 9, no. 11, pp. 4929–4940, Nov. 2016.

[18] M. Gade, W. Alpers, H. Hühnerfuss, H. Masuko, and T. Kobayashi, "Imaging of biogenic and anthropogenic ocean surface films by the multifrequency/multipolarization SIR-C/X-SAR," *J. Geophys. Res.*, vol. 103, no. C9, pp. 18851–18866, 1998.

[19] R. Touzi, F. J. Charbonneau, R. K. Hawkins, and P. W. Vachon, "Ship detection and characterization using polarimetric SAR," *Can. J. Remote Sens.*, vol. 30, no. 3, pp. 552–559, 2004.

[20] F. Nunziata, A. Gambardella, and M. Migliaccio, "On the Mueller scattering matrix for SAR sea oil slick observation," *IEEE Geosci. Remote Sens. Lett.*, vol. 5, no. 4, pp. 691–695, Oct. 2008.

[21] M. Migliaccio, A. Gambardella, F. Nunziata, M. Shimada, and O. Isoguchi, "The PALSAR polarimetric mode for sea oil slick observation," *IEEE Trans. Geosci. Remote Sens.*, vol. 47, no. 12, pp. 4032–4041, Dec. 2009.

[22] D. Velotto, M. Migliaccio, F. Nunziata, and S. Lehner, "Dual-polarized TerraSAR-X data for oil-spill observation," *IEEE Trans. Geosci. Remote Sens.*, vol. 49, no. 12, pp. 4751–4762, Dec. 2011.

[23] R. Shirvany, M. Chabert, and J. Y. Tourneret, "Ship and oil-spill detection using the degree of polarization in linear and hybrid/compact dual-pol SAR," *IEEE J. Sel. Topics Appl. Earth Observ. Remote Sens.*, vol. 5, no. 3, pp. 885–892, Jun. 2012.

[24] F. Nunziata, A. Gambardella, and M. Migliaccio, "On the degree of polarization for SAR sea oil slick observation," *ISPRS J. Photogramm. Remote Sens.*, vol. 78, pp. 41–49, Apr. 2013.

[25] S. Skrunes, C. Brekke, and T. Eltoft, "Characterization of marine surface slicks by radarsat-2 multipolarization features," *IEEE Trans. Geosci. Remote Sens.*, vol. 52, no. 9, pp. 5302–5319, Sep. 2014.

[26] A.-B. Salberg, O. Rudjord, and A. H. S. Solberg, "Oil spill detection in hybrid-polarimetric SAR images," *IEEE Trans. Geosci. Remote Sens.*, vol. 52, no. 10, pp. 6521–6533, Oct. 2014.

[27] S. Angelliaume, X. Ceamanos, F. Viallefont-Robinet, R. Baqué, P. Déliot, and V. Miegebielle, "Hyperspectral and radar airborne imagery over controlled release of oil at sea," *Sensors*, vol. 17, no. 8, p. 1772, 2017.

[28] S. Hensley *et al.*, "The UAVSAR instrument: Description and first results," in *Proc. IEEE Radar Conf.*, Rome, Italy, May 2008, pp. 1–6.

[29] K. D. Ward, R. J. A. Tough, and S. Watts, *Sea Clutter: Scattering, the K Distribution and Radar Performance*, 2nd ed. Herts, U.K.: IET, 2013.

[30] F. T. Ulaby, R. K. Moore, and A. K. Fung, *Microwave Remote Sensing: Active and Passive: Radar Remote Sensing and Surface Scattering and Emission Theory*, vol. 2. Dedham, MA, USA: Artech House, 1986.

[31] Y. Quilfen, B. Chapron, A. Bentamy, J. Gourrion, T. El Fouhaily, and D. Vandemark, "Global ERS 1 and 2 and NSCAT observations: Upwind/crosswind and upwind/downwind measurements," *J. Geophys. Res. Oceans*, vol. 104, no. C5, pp. 11459–11469, May 1999.

[32] J. Horstmann, W. Koch, S. Lehner, and R. Tonboe, "Wind retrieval over the ocean using synthetic aperture radar with C-band HH polarization," *IEEE Trans. Geosci. Remote Sens.*, vol. 38, no. 5, pp. 2122–2131, Sep. 2000.

[33] V. N. Kudryavtsev, B. Chapron, A. G. Myasoedov, F. Collard, and J. A. Johannessen, "On dual co-polarized SAR measurements of the ocean surface," *IEEE Geosci. Remote Sens. Lett.*, vol. 10, no. 4, pp. 761–765, Jul. 2013.

[34] V. Kudryavtsev, D. Hauser, G. Caudal, and B. Chapron, "A semiempirical model of the normalized radar cross section of the sea surface, 2. Radar modulation transfer function," *J. Geophys. Res.*, vol. 108, no. C3, pp. 2156–2202, 2003.

[35] B. Holt, "SAR imaging of the ocean surface," in *Synthetic Aperture Radar (SAR) Marine User's Manual*, C. R. Jackson and J. R. Apel, Eds. Silver Spring, MD, USA: NOAA, 2004, pp. 263–275.

[36] K. Hasselmann *et al.*, "Theory of synthetic aperture radar ocean imaging: A MARSEN view," *J. Geophys. Res.*, vol. 90, no. C3, pp. 4659–4686, 1985.

[37] G. R. Valenzuela, "Scattering of electromagnetic waves from a tilted slightly rough surface," *Radio Sci.*, vol. 3, no. 11, pp. 1057–1066, Nov. 1968.

[38] T. Meissner and F. J. Wentz, "The complex dielectric constant of pure and sea water from microwave satellite observations," *IEEE Trans. Geosci. Remote Sens.*, vol. 42, no. 9, pp. 1836–1849, Sep. 2004.

[39] K. Folgerø, "Bilinear calibration of coaxial transmission/reflection cells for permittivity measurement of low-loss liquids," *Meas. Sci. Technol.*, vol. 7, no. 9, pp. 1260–1269, 1996.

[40] T. Friisø, Y. Schildberg, O. Rambeau, T. Tjomsland, H. J. Førdedal, and J. Sjøblom, "Complex premittivity of crude oils and solutions of heavy crude oil fractions," *J. Dispersion Sci. Technol.*, vol. 19, no. 1, pp. 93–126, 1998.

[41] B. Minchew, C. E. Jones, and B. Holt, "Polarimetric analysis of backscatter from the Deepwater Horizon oil spill using L-band synthetic aperture radar," *IEEE Trans. Geosci. Remote Sens.*, vol. 50, no. 10, pp. 3812–3830, Oct. 2012.

[42] B. Minchew, "Determining the mixing of oil and sea water using polarimetric synthetic aperture radar," *Geophys. Res. Lett.*, vol. 39, no. 16, p. L16607, 2012.

[43] S. Angelliaume, B. Minchew, S. Chataing, P. Martineau, and V. Miegebielle, "Multifrequency radar imagery and characterization of hazardous and noxious substances at sea," *IEEE Trans. Geosci. Remote Sens.*, vol. 55, no. 5, pp. 3051–3066, May 2017.

[44] *Bonn Agreement Aerial Surveillance Handbook*, Bonn Agreement, London, U.K., 2004, p. 96.

[45] *Bonn Agreement Aerial Surveillance Handbook*, Bonn Agreement, London, U.K., 2009, p. 106.

[46] I. Leifer *et al.*, "State of the art satellite and airborne marine oil spill remote sensing: Application to the BP *Deepwater Horizon* oil spill," *Remote Sens. Environ.*, vol. 124, pp. 185–209, Sep. 2012.

[47] M. Fingas and B. Fieldhouse, "Studies on water-in-oil products from crude oils and petroleum products," *Marine Pollution Bull.*, vol. 64, no. 2, pp. 272–283, 2012.

[48] Z. H. Shah and Q. A. Tahir, "Dielectric properties of vegetable oils," *J. Sci. Res.*, vol. 3, no. 3, pp. 481–492, Aug. 2011.

[49] U. Erle, M. Regier, C. Persch, and H. Schubert, "Dielectric properties of emulsions and suspensions: Mixture equations and measurement comparisons," *J. Microw. Power Electromagn. Energy*, vol. 35, no. 3, pp. 185–190, 2000.

[50] W. Alpers and H. A. Espedal, "Oils and surfactants," in *Synthetic Aperture Radar Marine User's Manual*, C. R. Jackson and J. R. Apel, Eds. Washington, DC, USA: U.S. Department of Commerce, National Oceanic and Atmospheric Administration, 2004, ch. 11, pp. 263–275.

[51] V. Wismann, M. Gade, W. Alpers, and H. Huhnerfuss, "Radar signatures of marine mineral oil spills measured by an airborne multi-frequency radar," *Int. J. Remote. Sens.*, vol. 19, no. 18, pp. 3607–3623, 1998.

[52] M. Gade, W. Alpers, H. Hühnerfuss, V. Wismann, and P. Lange, "On the reduction of the radar backscatter by oceanic surface films: Scatterometer measurements and their theoretical interpretation," *Remote Sens. Environ.*, vol. 66, no. 1, pp. 52–70, Oct. 1998.

[53] D. Latini, F. Del Frate, and C. E. Jones, "Multi-frequency and polarimetric quantitative analysis of the Gulf of Mexico oil spill event comparing different SAR systems," *Remote Sens. Environ.*, vol. 183, pp. 26–42, Sep. 2016.

[54] D. V. Ivonin, S. Skrunes, C. Brekke, and A. Y. Ivanov, "Interpreting sea surface slicks on the basis of the normalized radar cross-section model using RADARSAT-2 copolarization dual-channel SAR images," *Geophys. Res. Lett.*, vol. 43, no. 6, pp. 2748–2757, 2016.

[55] S. Skrunes, C. Brekke, T. Eltoft, and V. Kudryavtsev, "Comparing near-coincident C- and X-band SAR acquisitions of marine oil spills," *IEEE Trans. Geosci. Remote Sens.*, vol. 53, no. 4, pp. 1958–1975, Apr. 2015.
[56] S. Skrunes, C. Brekke, C. E. Jones, and B. Holt, "A multisensor comparison of experimental oil spills in polarimetric SAR for high wind conditions," *IEEE J. Sel. Topics Appl. Earth Observ. Remote Sens.*, vol. 9, no. 11, pp. 4948–4961, Nov. 2016.
[57] M. M. Espeseth, S. Skrunes, C. E. Jones, C. Brekke, B. Holt, and A. P. Doulgeris, "Analysis of evolving oil spills in full-polarimetric and hybrid-polarity SAR," *IEEE Trans. Geosci. Remote Sens.*, vol. 59, no. 7, pp. 4190–4210, Jul. 2017.
[58] M. Gade, W. Alpers, H. Hühnerfuss, and P. A. Lange, "Wind wave tank measurements of wave damping and radar cross sections in the presence of monomolecular surface films," *J. Geophys. Res.*, vol. 103, no. C2, pp. 3167–3178, 1998.
[59] C.-A. Guérin, G. Soriano, and B. Chapron, "The weighted curvature approximation in scattering from sea surfaces," *Waves Random Complex Media*, vol. 20, no. 3, pp. 364–384, 2010.
[60] H. A. Zebker, J. J. van Zyl, and D. N. Held, "Imaging radar polarimetry from wave synthesis," *J. Geophys. Res.*, vol. 92, no. B1, pp. 683–701, Jan. 1987.
[61] W. J. Plant, E. A. Terray, R. A. Petitt, Jr., and W. C. Keller, "The dependence of microwave backscatter from the sea on illuminated area: Correlation times and lengths," *J. Geophys. Res.*, vol. 99, no. C5, pp. 9705–9723, May 1994.
[62] A. S. Milman, A. O. Scheffler, and J. R. Bennett, "A theory of the synthetic aperture radar images of time-dependent scenes," *J. Geophys. Res.*, vol. 98, no. C1, pp. 911–925, Jan. 1993.
[63] W. Born and E. Wolf, *Principles of Optics*. New York, NY, USA: Pergamon, 1959.
[64] W.-M. Boerner *et al.*, "Polarimetric in radar remote sensing: Basic and applied concepts," in *Principles and Applications of IMAGING RADAR*, vol. 2. Hoboken, NJ, USA: Wiley, 1998.
[65] R. Touzi, W.-M. Boerner, J.-S. Lee, and E. Lueneburg, "A review of polarimetry in the context of synthetic aperture radar: Concepts and information extraction," *Can. J. Remote Sens.*, vol. 30, no. 3, pp. 380–407, 2004.
[66] B. Zhang, W. Perrie, X. Li, and W. B. Pichel, "Mapping sea surface oil slicks using RADARSAT-2 quad-polarization SAR image," *Geophys. Res. Lett.*, vol. 38, no. 10, p. L10602, 2011.
[67] M.-L. Truong-Loi, P. Dubois-Fernandez, A. Freeman, and E. Pottier, "The conformity coefficient or how to explore the scattering behaviour from compact polarimetry mode," in *Proc. IEEE Radar Conf.*, Pasadena, CA, USA, May 2009, pp. 1–6.
[68] S. R. Cloude and E. Pottier, "A review of target decomposition theorems in radar polarimetry," *IEEE Trans. Geosci. Remote Sens.*, vol. 34, no. 2, pp. 498–518, Mar. 1996.
[69] S. R. Cloude and E. Pottier, "An entropy based classification scheme for land applications of polarimetric SAR," *IEEE Trans. Geosci. Remote Sens.*, vol. 35, no. 1, pp. 68–78, Jan. 1997.
[70] C. E. Jones *et al.*, "Measurement and modeling of oil slick transport," *J. Geophys. Res. Oceans*, vol. 121, no. 10, pp. 7759–7775, 2016.
[71] I. Hajnsek, E. Pottier, and S. R. Cloude, "Inversion of surface parameters from polarimetric SAR," *IEEE Trans. Geosci. Remote Sens.*, vol. 41, no. 4, pp. 727–744, Apr. 2003.
[72] J. P. Egan, *Signal Detection Theory and ROC Analysis* (Cognition and Perception). New York, NY, USA: Academic, 1975.
[73] *MOS Sweeper—Egersund Group*. Accessed: Jan. 23, 2018. [Online]. Available: http://www.egersundgroup.no/oilspill/mos-sweeper

Sébastien Angelliaume received the Engineering degree from the Ecole Nationale Supérieure d'Ingénieur de Constructions Aéronautiques, Toulouse, France, and the M.S. degree from the Ecole Nationale Supérieure d'Electrotechnique, d'Electronique, d'Informatique, d'Hydraulique et des Télécommunications, Toulouse, both in 2003.

Since 2006, he has been with the Electromagnetism and Radar Department, Office National d'Etudes et de Recherches Aérospatiales (ONERA—the French Aerospace Lab), Salon de Provence, France, where he has been involved in the ONERA synthetic aperture radar airborne platforms RAMSES and SETHI, developing science applications. Since 2010, his research at ONERA has focused mainly on remote sensing over the ocean surface.

Pascale C. Dubois-Fernandez (A'04–M'04–SM'04) received the Diplôme d'Ingenieur degree from the Ecole Nationale Supérieure d'Ingénieur de Constructions Aéronautiques, Toulouse, France, in 1983, and the M.S. and Eng. degrees from the California Institute of Technology, Pasadena, CA, USA, in 1984 and 1986, respectively.

She was with the Radar Science and Technology Group, Jet Propulsion Laboratory, Pasadena, CA, USA, where she stayed for ten years, participating in numerous programs such as Magellan, AIRSAR, and SIR-C. She then moved back to France, where she focused on cartographic applications of satellite data. In 2000, she joined the Electromagnetism and Radar Department, Office National d'Etudes et de Recherches Aérospatiales (ONERA—the French Aerospace Lab), Salon de Provence, France, where she has been involved in the ONERA synthetic aperture radar (SAR) airborne platform, RAMSES, developing science applications as the SAR civilian remote sensing expert.

Cathleen E. Jones received the B.S. degree in physics from Texas A&M University, College Station, TX, USA, and the Ph.D. degree in physics from the California Institute of Technology, Pasadena, CA, USA.

She is currently a Radar Scientist with NASA's Jet Propulsion Laboratory, California Institute of Technology, Pasadena, CA, USA, where her main research is focused on using radar remote sensing for studying natural disasters and monitoring critical infrastructure, primarily using high-resolution L-band PolSAR and InSAR based on UAVSAR data. Her research interests include development of methods for determining oil slick characteristics and identifying levee deformation, seepage, and general subsidence rates using synthetic aperture radar (SAR), and detection of sinkhole precursors in InSAR-challenged areas.

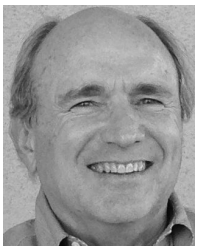

Benjamin Holt received the B.S. degree from Stanford University, Stanford, CA, USA, in 1972, and the M.S. degree in physical oceanography from the University of Southern California, Los Angeles, CA, USA, in 1988.

In 1978, he joined the Ocean Circulation Group, Earth Science Section, Jet Propulsion Laboratory, California Institute of Technology, Pasadena, CA, USA, where he is currently a Research Scientist. His research interests include using multisensor remote sensing data to examine the geophysical state of polar sea ice and snow, coastal oceanography and circulation, the detection of marine pollutants, new instrument development, and techniques for microwave measurement of sea ice thickness.

Brent Minchew received the B.Sc. and M.Sc. degrees in aerospace engineering from the University of Texas at Austin, Austin, TX, USA, in 2008 and 2010, respectively, and the Ph.D. degree in geophysics from the California Institute of Technology, Pasadena, CA, USA.

From 2016 to 2018, he was an NSF Postdoctoral Fellow at the British Antarctic Survey, Cambridge, U.K. He is currently an Assistant Professor with the Department of Earth, Atmospheric and Planetary Sciences, Massachusetts Institute of Technology, Cambridge, MA, USA. His research interests include remote sensing applications and environmental fluid dynamics, with an emphasis on glacier mechanics.

Emna Amri was born in Tunis, Tunisia, in 1990. She received the Engineering degree in computer science and the master's degree in intelligent systems in imaging and artificial vision from the University of Tunis El Manar, Tunis, in 2015 and 2017, respectively.

Her research interests include computer vision, machine learning, and remote sensing.

Véronique Miegebielle received the Geology Doctorate degree with a specialization in remote sensing from Pau and Pays de l'Adour University, Pau, France, in 1993.

She spent the first 15 years of her career, dealing with geology and environmental subjects. In 2009, she moved on to take care of Remote Sensing Service at Total, Pau. Since 2011, she has been in charge of remote sensing offshore research project.

remote sensing

MDPI

Article

Dual-Polarized L-Band SAR Imagery for Temporal Monitoring of Marine Oil Slick Concentration

Sébastien Angelliaume [1,*], Olivier Boisot [1] and Charles-Antoine Guérin [2]

[1] DEMR, ONERA, F-13661 Salon Air CEDEX, France; Olivier.Boisot@onera.fr
[2] Université de Toulon, Aix Marseille Université, CNRS IRD, MIO UM110, La Garde, France; Charles-Antoine.Guerin@univ-tln.fr
* Correspondence: Sebastien.Angelliaume@onera.fr; Tel.: +33-4-9017-6512

Received: 7 May 2018; Accepted: 20 June 2018; Published: 25 June 2018

Abstract: SAR sensors are usually used in the offshore domain to detect marine oil slicks which allows the authorities to guide cleanup operations or prosecute polluters. As radar imagery can be used any time of day or year and in almost any weather conditions, the use and programming of such remote sensing data is usually favored over optical imagery. Nevertheless, images collected in the optical domain provide access to key information not accessible today by SAR instruments, such as the thickness or the amount of pollutant. To address this knowledge gap, a methodology based on the joint use of a scattering model (U-WCA) and remote sensing data collected by a low frequency (e.g., L-band) imaging radar over controlled release of mineral oil spill is reported in this paper. The proposed method allows estimation of the concentration of pollutant within an oil-in-water mixture as well as the temporal variation of this quantity due to weathering processes.

Keywords: SAR; radar imagery; polarimetry; ocean; marine environment; oil; spill; slick; quantification; modelling; surface properties; Universal Weighted Curvature Approximation

1. Introduction

The authorities and petroleum companies usually use airborne and spaceborne SAR (Synthetic Aperture Radar) images to detect and monitor marine slicks [1,2]. In an operational context, radar images are favored over optical ones because radar can be used any time and in almost any weather conditions [3–5]. In the microwave regime, the ocean surface is modelled as a set of slightly rough tilted facets that contributes to the backscattering of the Electromagnetic (EM) wave. Each facet has superimposed small-scale surface roughness that creates a Bragg scatterer when the wind-driven roughness scale is commensurate with the radar wavelength [6]. When oil is released in the marine environment, these scales of roughness, namely the capillary and short gravity waves, are damped, and slick-covered surface appears as a low backscattering area in the SAR image [7].

While remote sensing instruments operating in the microwave domain are of great interest for detecting and monitoring maritime pollution, some issues remain unresolved when using SAR images only, such as the characterization and the quantification of the detected substance [2,7]. Characterization aims at distinguishing between anthropic and biogenic oil slicks. Quantification is the estimation of the amount of pollutant within the spilled area and is investigated in this paper.

The EM frequency is of primary importance when imaging the ocean surface and particularly for remotely sensed slick-covered area [8–10]. High-frequency imaging radars (e.g., X- or C-band) are preferable to those operating at lower frequency (e.g., L-band) for mineral oil slick detection [8]. SAR data collected at L-band allows definition of the characteristics of a marine slick along a level ranging from thin surface films to oil-in-water emulsion [10,11]. In any case, the instrument noise is a

key factor and estimating the slick surface properties must be achieved with a sufficiently low noise floor instrument [12], otherwise strong misinterpretation may occur [7].

The relative contribution of the different scattering mechanisms that participate to the total backscattering energy from the ocean surface is also frequency-dependent. Bragg scattering is the dominant mechanism that occurs over the ocean surface, whether covered or not by hydrocarbons [7,12,13]. Non-Bragg scattering [14] also contributes to the total power but its actual impact on the backscattered signal is more difficult to estimate [15–17]. As a result, a discrepancy between Bragg modelling and experimental measurements collected by spaceborne SARs that operate at high frequency (X- or C-band) is usually observed [18,19]. This deviation as well as the use of images collected with insufficient Signal to Noise Ratio (SNR) over slick-covered sea surface [7], is a major issue when trying to derive the surface properties of marine slick from remote sensing SAR data.

However it has been previously reported in [12,20] that for radar operating at low EM frequency (e.g., L-band) the relative contribution of the non-polarized component with respect to the total power scattered from the ocean surface is negligible. This key result, which will also be experimentally validated in this paper, offers the opportunity to accurately predict the radar quantities that could be measured over free seawater and marine slick and to propose a novel methodology to estimate their properties, namely the quantity of oil within a mixture of oil and seawater. For this purpose, the SAR data used to estimate the slick properties must be collected by a radar sensor with an extremely low Noise Equivalent Sigma Zero (NESZ) to ensure a sufficiently high SNR over both covered and uncovered sea surface [7,12].

In an earlier work [21], the authors have developed a novel model-based approach to estimate the oil concentration within an oil-in-water mixture from L-band dual-pol SAR images. It is based on the pixel by pixel, numerical inversion of the surface properties from the polarization ratio inferred by the Universal Weighted Curvature Approximation (U-WCA) scattering model [22]. In this paper, the authors report on a simplification of the original method, which makes it less time-consuming and no longer dependent on a reference clean sea image. This simplification, however, is made at the expense of the accuracy of the oil concentration estimate, especially for low percentages values of oil.

The methodology reported herein is based on the joint use of a rigorous scattering model to predict the ratio between the dual-co-polarized channels (HH and VV) and L-band SAR images collected by a very low noise floor instrument. It is applied to a dataset obtained during an oil spill cleanup exercise managed by the NOFO (Norwegian Clean Seas Association for Operating Companies) in June 2015. We demonstrate how remote sensing SAR data can estimate the proportion of oil within an oil-in-water marine slick mixture as well as its application to the temporal monitoring of the oil concentration due to weathering processes.

Once mineral oil is released into the marine environment, it will first spread on the sea surface and forms an approximately homogeneous film, which will attenuate the surface roughness. The spatial abundance of mineral oil can be quantified by the oil areal fraction [23], that is, the cover fraction of the mineral oil in a given pixel. Then, the weathering processes mix the released product in the water column and form a mixture between sea water and mineral oil (emulsion). In this paper, we focus on quantifying the oil content (volume percentage) in an emulsion. If the investigated ocean area is partially impacted, at the resolution cell scale, the estimated oil content will be that of the whole emulsion plus clean sea water.

The paper is organized as follows: Section 2 gives the basis of the radar backscattering from the ocean surface, Section 3 describes the oil spill cleanup exercise and the airborne campaign, Section 4 presents the method to estimate the oil concentration, Section 5 gives the results and uncertainties are discussed in Section 6.

2. Radar Backscattering from the Ocean Surface

2.1. Bragg Scattering Theory

In the microwave regime, the ocean surface, when imaged by a remote sensing system with incidence angles ranging from around 30 to 60°, is considered to be a rough surface for which the dominant scattering mechanism is Bragg scattering [6]. In that case, the EM signal backscattered by the sea depends strongly on the polarization state of the transmitted wave [24]. The dual-co-polarized radar backscattered power is proportional to the normalized radar cross-section (NRCS), which is defined in the Bragg scattering theory [6] as

$$\sigma^0_{pp} = 4\pi k^4_{EM} \cos^4 \theta_i \Gamma_{pp} W(k_B) \tag{1}$$

$$k_B := 2k_{EM} \sin \theta_i \tag{2}$$

where the subscript p denotes either H (horizontal) or V (vertical) polarization; $k_{EM} = 2\pi/\lambda_{EM}$ is the *EM* wavenumber corresponding to the radar wavelength, λ_{EM}; Γ_{pp} is the reflectivity; $W(k_B)$ is the spectral density of the ocean surface roughness evaluated at the so-called Bragg wavenumber, k_B; and θ_i is the radar local incidence angle. In the Bragg scattering theory, the backscatter power is higher in vertical polarization than in horizontal, ensuring a polarization ratio (PR) smaller than unity.

$$PR = \frac{\sigma^0_{HH}}{\sigma^0_{VV}} \; 0 \leq PR \leq 1 \tag{3}$$

Although dominant, Bragg scattering is not the only scattering mechanism which contributes to the total backscattered energy from the ocean surface. Non-resonant mechanisms generally associated with large-scale events (e.g., breaking waves, whitecaps . . .) contribute to the signal backscattered by the sea surface. Those events are frequency-dependent and explain the deviation commonly observed between experimental observations and model estimations [18,19], mainly in high-frequency imaging radar (e.g., X- and C-band). At lower frequency (e.g., L-band), it has been reported that the relative impact of those non-Bragg mechanisms with respect to the total power scattered from the ocean surface is negligible [20].

Thus, at L-band the EM signal backscattered by the ocean surface is well modeled by the Bragg theory and it comes from (1)–(3) that the polarization ratio depends mainly on the local incidence angle and the dielectric properties of the sea surface [6,11,21].

2.2. Impact of Oil on the Sea Surface

When oil is released in the marine environment, it can behave in two different ways: it can either manifest as a film on the top of the sea surface or mix with the seawater within the water column. In the first case (film or sheen), the product surface layer will damp the gravity-capillary waves, which are the main contributors to backscattered EM signal, thereby attenuating the radar backscattered power. As discussed above, this attenuation of the surface roughness should not have significant impact on the polarization ratio at L-band (see [12] Figure 13d). Moreover, as the film thickness usually encountered (µm to mm [5]) is small compared to the penetration depth [12], the EM wave is not attenuated and penetrates the film to scatter from the seawater underneath. Therefore, the effective dielectric constant remains that of seawater and is not changed by the different dielectric constant of the oil film. As a result, at low EM frequency, the measured polarization ratio over film-covered sea surface is close to that measured over the surrounding uncovered sea surface.

In the second case (oil-in-water emulsion), the mixture between oil and seawater modifies the dielectric properties of the remotely sensed surface, thus impacting the reflection coefficients of the scattering process as well as the value of the polarization ratio with respect to the surrounding clean-sea surface.

Please note that an oil layer at sea is quickly spread and mixed within the water column by weathering processes such as natural wind stress and waves motion. At the resolution cell scale, an emulsion and a partially covered surface have a similar impact on the Polarization Ratio. In this paper, it is assumed that the slick is homogeneous at the pixel scale (metric in this experiment) and the distinction between covered, partially covered and uncovered surface can be done using a detection method based on, for example, the Polarization Difference [10,14] which is mostly impacted by the sea surface roughness.

The polarization ratio of low-frequency imaging radars allows measurement of the dielectric properties of both seawater and oil-in-water mixture. For slick-free or slick-covered area, those properties are described by the complex relative dielectric constant, ε, defined as

$$\varepsilon = \varepsilon' + i\varepsilon'' \tag{4}$$

The dielectric constant is material-dependent. Typical values are given in Table 1, taken from [25] for seawater and from [26,27] for mineral oil. Values for mineral oil are nearly constant in the range 1–10 GHz, with a loss factor (imaginary component) close to zero, suggesting a non-negligible penetration of the EM wave through this medium.

Table 1. Dielectric Constant of seawater from [25] and mineral oil from [26,27].

Surface	L-BAND [1.3 GHz]	C-BAND [5.0 GHz]	X-BAND [10 GHz]
Seawater (15 °C 35 PSU)	73.0 + 65.1i	66.8 + 35.7i	52.9 + 39.0i
Mineral oil	2.3 + 0.01i	2.3 + 0.01i	2.3 + 0.01i

A linear mixing model is often employed [11,12] between mineral oil and seawater (5) to estimate the effective dielectric constant of an oil-in-water mixture, ε_{eff}. However, a more relevant approach from the Effective Medium Theory [28] advocates the use of the Bruggeman formula (6) to estimate the effective complex dielectric constant of such a mixture [21]:

$$\varepsilon_{eff} = v\varepsilon_{oil} + (1 - v)\varepsilon_w \tag{5}$$

$$\varepsilon_{eff} = \frac{1}{4}\left\{\varepsilon_w - (1 - 3v)(\varepsilon_{oil} - \varepsilon_w) + \sqrt{[\varepsilon_w - (1 - 3v)(\varepsilon_{oil} - \varepsilon_w)]^2 + 8\varepsilon_w\varepsilon_{oil}}\right\} \tag{6}$$

where v, ranging from 0 to 1, is the oil content (in volume) of the oil-water mixture, and ε_w and ε_{oil} are the relative dielectric constant of seawater and oil, respectively (Table 1). The real and imaginary parts of the effective dielectric constant of an oil-in-water emulsion are displayed in Figure 1 as a function of the oil content (in percentage) for both linear (blue curve) and Bruggeman's model (red curve). One can observe a strong overestimation of both real and imaginary parts of the effective dielectric constant with the linear model compared to the Bruggeman formula. This overestimation is more pronounced at high concentration of oil (oil content~60–80%). In the following, the Bruggeman formula will be adopted to estimate the effective dielectric constant of an oil-in-water emulsion.

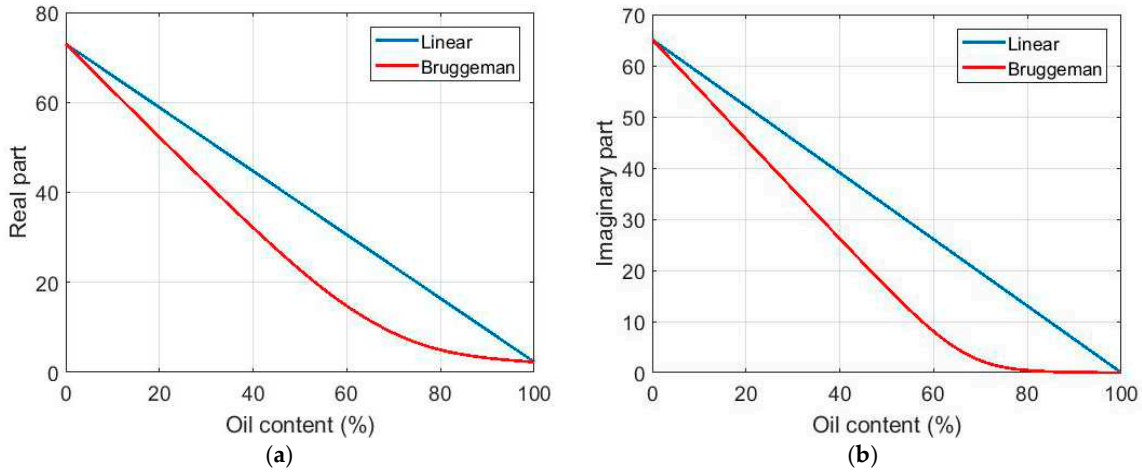

Figure 1. Effective dielectric constant of an oil-in-water emulsion plotted by increasing oil content using a linear model (blue) and the Bruggeman's model (red): (**a**) real part; (**b**) imaginary part.

3. Airborne Campaign of Acquisition over Controlled Releases of Mineral Oil at Sea

3.1. NOFO'2015 Oil-on-Water Exercise

In June 2015, the NOFO (Norwegian Clean Seas Association for Operating Companies) has managed controlled releases of mineral oil at sea to test mechanical recovery systems. The oil spill cleanup exercise was carried out in the North Sea between the Norway and the United Kingdom within 10 Nautical Miles of position 59°59'N, 02°27'E. In the following we will focus on the 9 June exercises, during which the MOS Sweeper [29] and DESMI Boom [30] systems were tested at sea (Figure 2). For both experiments, hydrocarbons were released by a floating pump at the sea surface towed by a leading vessel (Stril Mariner) and recovered by a second vessel (Stril Luna), at only a few hundred meters. Figure 3 shows an illustration of the offshore spill area taken from a balloon during the MOS Sweeper experiment.

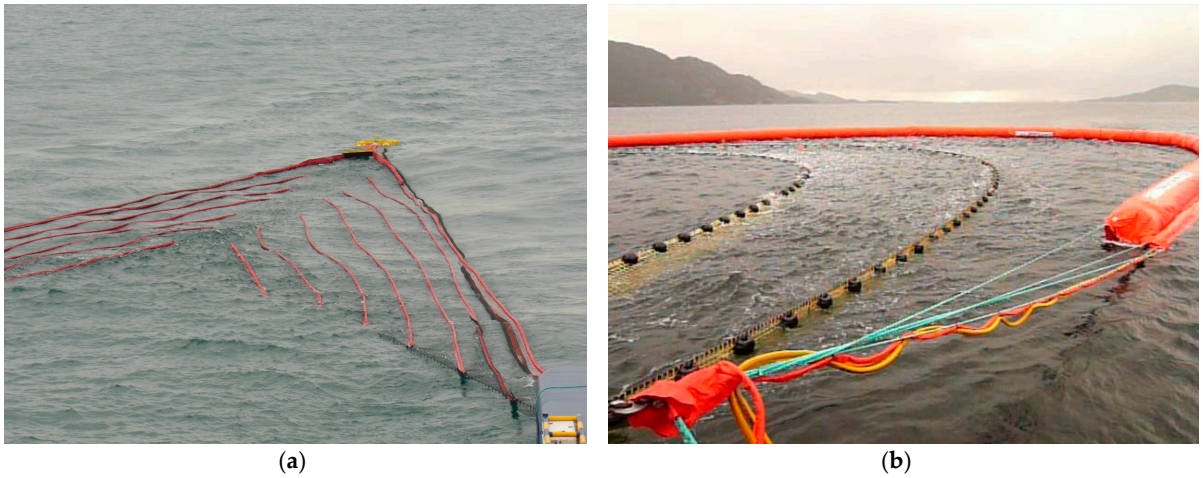

Figure 2. NOFO'2015 oil spill cleanup exercise: (**a**) MOS Sweeper and (**b**) DESMI Boom recovery systems tested on 9 June 2015 (photographs provided by NOFO).

Figure 3. NOFO'2015—MOS Sweeper oil spill cleanup exercise (photograph provided by NOFO).

Trials with MOS Sweeper and DESMI Boom were conducted, respectively, in the morning (from 06:00 until 10:30 UTC) and in the afternoon (from 12:30 until 15:00 UTC) of June 9, using 45 m^3 of mineral oil for MOS Sweeper and 35 m^3 for DESMI Boom. The released product is an emulsion of mineral oil-in-water, with a water content of 60%. It consists of a mixture of seawater, Oseberg crude oil and a small addition of IFO 380 (Intermediate Fuel Oil or marine diesel oil, with viscosity of 380 $mm^2 \cdot s^{-1}$). The emulsion was prepared onshore by the NOFO several weeks before the exercises at sea. The stability and the exact constitution of the spilled product at the time of the exercise is therefore not precisely known.

Wind and waves information during the oil spill cleanup exercises was obtained from the Norwegian Meteorological Institute and is given in Table 2.

Table 2. Environmental Conditions during the experiments.

Date	Time (UTC)	Experiment	Wind Speed at 10 m ($m \cdot s^{-1}$)	Wind Direction (from-deg)	Significant Wave Height (m)
9 June 2015	06:00	MOS Sweeper	5	250	1
	09:00		5	250	1
	12:00	DESMI Boom	7	250	1
	15:00		7	250	1

3.2. *Airborne SAR Acquisitions*

Polarimetric SAR (POLSAR) images were recorded during the oil-in-water exercise by SETHI, the airborne remote sensing system developed by ONERA [23]. POLSAR data in linear basis (HH, HV, VH, VV) were collected at L-band (EM frequency of 1.325 GHz) with a transmitted bandwidth equal to 150 MHz (range resolution of 1 m) and processed with an azimuth resolution of 1 m. The imaged area is 9.5 km in azimuth and 1.5 km in range, with incidence angles from 34° to 52°. SETHI is a high-resolution imaging radar characterized by a low instrument noise floor, see Figure 4 reproduced from [12], allowing a sufficiently high SNR over marine slick for efficient surface properties estimation.

The SETHI remote sensing system flew over the oil spill area during the two cleanup exercises and collected SAR images throughout the 9 of June. In the following, four SAR scenes are investigated: three collected during the MOS Sweeper experiment at 09:37, 10:02 and 10:27 UTC and one at 13:30 UTC during the DESMI Boom exercise, cf. Table 3. The last one (run 4) was acquired 3 h after the last image of the MOS Sweeper exercise (run 3). Nevertheless, this image still contains part of the spill released during the morning experiment, MOS Sweeper, cf. Figure 5—red box. A 4-h temporal monitoring of this spill is then possible, between 09:37 UTC and 13:30 UTC.

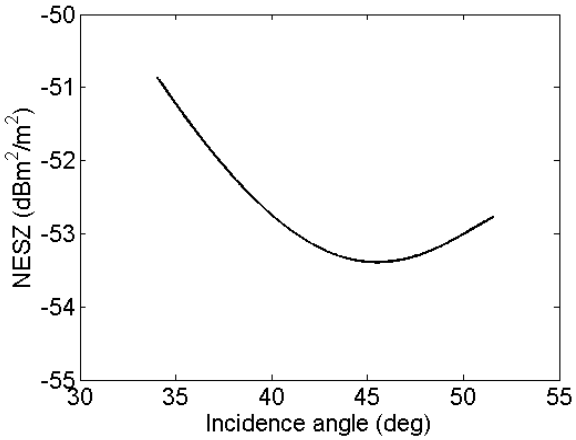

Figure 4. SETHI instrument noise floor (NESZ) plotted by increasing incidence angle—reproduced from [12].

Table 3. Properties of the SETHI L-band POLSAR scenes investigated in this study.

Date	Run Number	Time of Imaging (UTC)	Cleanup Exercise	Flight Heading (deg)
9 June 2015	1	09:37	MOS Sweeper	105
	2	10:02	MOS Sweeper	290
	3	10:27	MOS Sweeper	105
	4	13:30	DESMI Boom	250

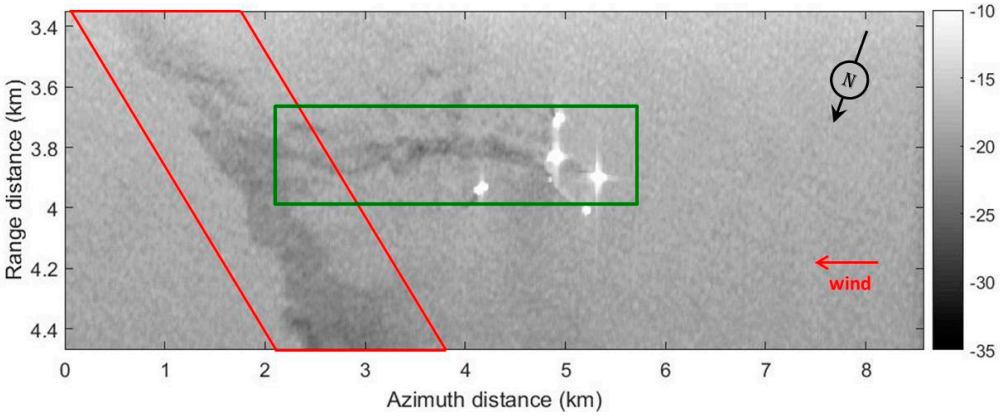

Figure 5. SETHI L-band SAR data, VV-polarization, 13:30 UTC. Red box: MOS Sweeper spill. Green box: DESMI Boom spill—multi-look 21 × 21.

The four SAR scenes investigated in this paper have been projected from the slant range to the ground range geometry (Figure 6). The spilled area has been automatically detected using the polarization difference (in linear unit) between VV and HH channels [10,12,14,31] and the temporal evolution of the detected area is pictured on Figure 7 in a false color representation: drifting of the MOS Sweeper spill for one hour (from 09:37 to 10:27 UTC) in the morning of 9 June (Figure 7a) and drifting of the spill for four hours (from 09:37 to 13:30 UTC), Figure 7b. The spilled product during the MOS Sweeper exercise has drifted in the North-East direction, under the influence of wind (coming from 250°, cf. Table 2). The distance traveled by the spill between the first (09:37) and the last acquisition (13:30) is about 1.8 km in 4 h, which corresponds to a drift speed of about 0.125 m·s^{-1}.

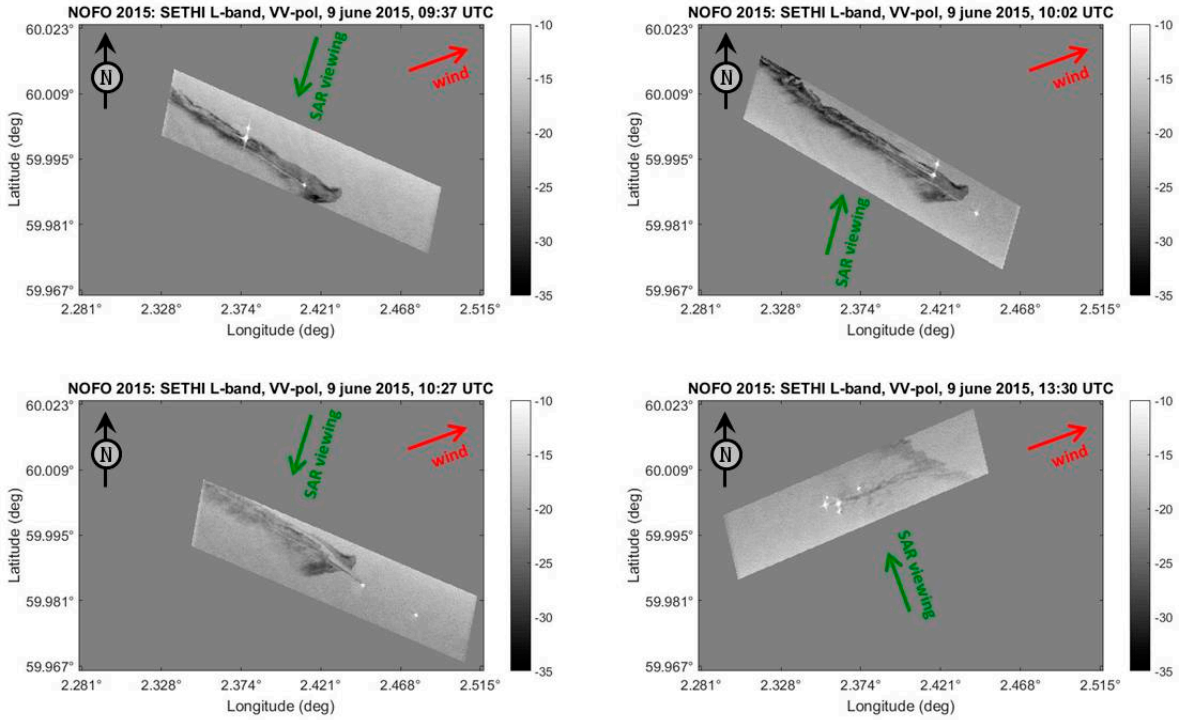

Figure 6. SETHI L-band SAR data, VV-polarization, collected at 09:37 UTC (run 1—upper left panel), 10:02 UTC (run 2—upper right panel), 10:27 UTC (run 3—lower left panel) and 13:30 UTC (run 4—lower right panel)—multi-look 21 × 21—ground geometry.

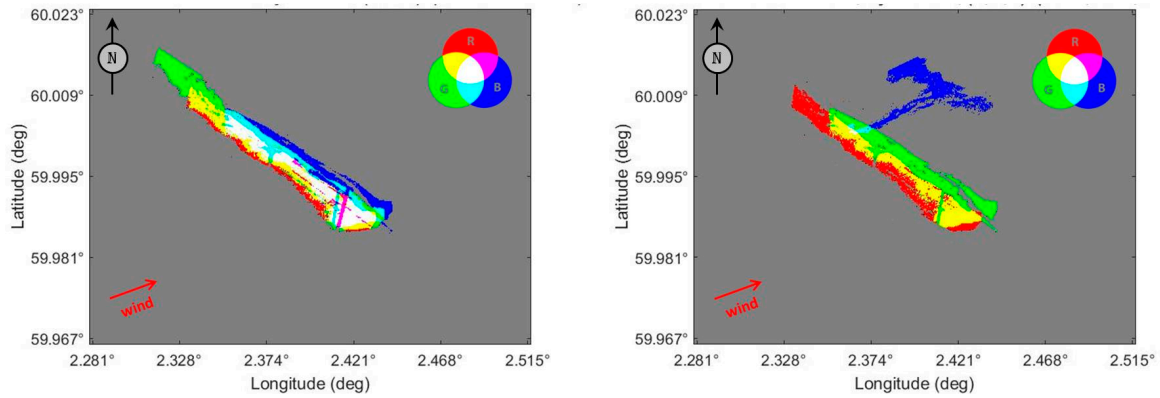

(**a**) (**b**)

Figure 7. SETHI L-band SAR data, detection masks in false color representation—ground geometry. (**a**) (Red,Green,Blue) = (09:37,10:02,10:27); (**b**) (Red,Green,Blue) = (09:37,10:27,13:30).

4. Estimation of Oil Concentration in an Oil-in-Water Slick Emulsion

As discussed in Paragraph 2, the ratio between the two dual-co-polarized channels (3), at low frequency (e.g., L-band), is a useful quantity for measuring the concentration of oil within a marine slick [21]. The approach presented in this paper is based on the comparison between the polarization ratio measured by a radar operating at L-band and the values estimated by an analytical scattering model, namely the Universal Weighted Curvature Approximation (U-WCA), [22].

4.1. The Universal Weighted Curvature Approximation Scattering Model

With a remote sensing imaging radar collecting data at L-band, PR is only slightly impacted by changes in surface roughness but is mainly varying with the local incidence angle and the dielectric properties of the surface [11,12,21]. The proposed methodology for estimating the proportion of oil in an oil-in-water mixture is based on the comparison between the experimental value of PR with a scattering model, the Universal Weighted Curvature Approximation.

The U-WCA scattering model [22] belongs to the family of so-called "unified models" [32], such as the Two Scale Models (TSM) [6,33] or the Small-Slope Approximation [34], that is models which are able to cope with both large scales and small ripples at the sea surface. The U-WCA model leads to non-trivial roughness-dependent PR but has the considerable advantage of a simple formulation involving the nominal incidence angle only and requiring no facet decomposition. The expression of the co-polarized NRCS given by the U-WCA model is as follows

$$\sigma^0_{pp} = 4\pi \left|\mathrm{B}_{pp}\right|^2 W(k_B) + |\mathrm{K}|^2 [I_s - 4\pi\, W(k_B)] \tag{7}$$

where Is is proportional to the classical Kirchhoff integral and Bpp and K are the Bragg and the Kirchhoff kernels [32], respectively.

In the Two Scale approach, ocean surfaces are usually modelled as a composition of slightly rough tilted facets, each of which has superimposed small-scale surface roughness that creates a Bragg scattering [6]. Small-scale roughness is randomly distributed on the scattering surface and responds to the strength of local wind, i.e., gravity-capillary waves. The tilt of the facet is caused by larger-scale waves on the ocean surface that changes the local orientation, or tilt, of the short waves [35]. The orientation of the facet changes the value of the local incidence angle of the EM wave interacting with the surface and therefore the levels of the backscattered signal and the polarization ratio. In general, a precise knowledge of the local incidence angle is not available; an approximation from SAR data can be obtained from an uncovered area close to the oil slick assuming homogeneous large-scale phenomena over the entire imaged area [11]. To overcome this strong limitation, the use of the U-WCA scattering model allows estimation of the polarization ratio without requiring the knowledge of the locale incidence angle [21,22], resulting from the local tilt of the facets composing the sea surface. In this paper, the polarization ratio measured by a radar sensor is compared to those estimated by the U-WCA model, the difference over slick covered area being linked to the modification of the effective dielectric constant compared to the surrounding clean sea surface.

PR values estimated with the U-WCA scattering model at 1.325 GHz are shown Figure 8. The simulation has been carried out in the upwind direction with the U-WCA scattering model using the classical Elfouhaily [36] sea surface directional spectrum. As expected, we observe strong variations of PR with the incidence angle but few variations with the sea surface roughness (Figure 8a). On the contrary, for a given value of incidence angle, PR values are strongly varying with the oil content into the oil-in-water mixture, especially for high oil concentration rates (Figure 8b). One can also note the strong difference between the Bragg theory (Figure 8a—black dotted line) and the U-WCA model (Figure 8a—colored full line). By construction, the U-WCA model, which is a weighted summation of Bragg and Kirchhoff kernels (see Equation (7)), produces higher PR than the pure Bragg model (recall that the Kirchhoff PR is one). This explains the discrepancy between the PR values computed using the Bragg theory (Equations (1)–(3)) and the U-WCA scattering model (Equation (3) with the HH and VV NRCS given by Equation (7)).

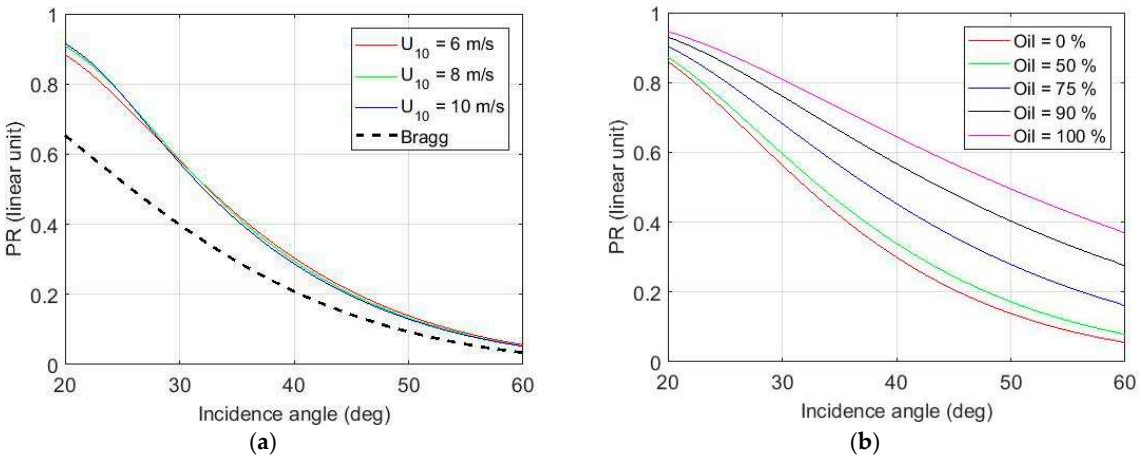

Figure 8. Bragg theory and U-WCA scattering model. Polarization Ratio (PR) as a function of the incidence angle (**a**) for various wind speeds and (**b**) for various oil contents using the Bruggeman formula to estimate the effective dielectric constant of an oil-in-water mixing with a wind speed of 5 m/s. Values of the dielectric constant are taken from Table 1.

4.2. Comparison with L-Band Remote Sensing Data

A comparison between experimental and theoretical values of the polarization ratio at L-band is of primary importance and is displayed in Figure 9 with environmental conditions given in Table 2. Experimental values over slick-free (Figure 9a—blue line) and slick-covered (Figure 9a—red line) are computed over a range transect of L-band SAR data collected by SETHI during the NOFO'2015 experiment at 10:02 UTC (Table 3, run 2). We found a very good agreement between the PR values estimated by U-WCA (Figure 9a—black dotted line) and those measured by the SAR sensor over uncovered sea surface (Figure 9a—blue line). This confirms that at low EM frequency (e.g., L-band) the relative contribution of the non-polarized component with respect to the total power scattered from the ocean surface is negligible and hence that the scattering model can be used as a reference. The impact of mineral oil on the PR values is obvious, with a marked difference between histograms computed over free sea surface (Figure 9b—blue line) and covered area (Figure 9b—red line). This difference is due to the variation of the dielectric properties between the mineral oil slick and the surrounding clean sea surface. The quantitative estimation of the proportion of oil in an oil-in-water emulsion is made possible by comparing the PR measured by the remote sensing SAR data at L-band and the values estimated by the U-WCA scattering model, using a previously calculated data sheet (Figure 10a) allowing quick oil concentration estimation to meet operational constraints. For a given value of incidence angle, the unicity of the estimate is ensured by the monotonic variation of PR with the oil concentration (Figure 10a).

The data sheet of PR values estimated at L-band with the Bragg theory is displayed in Figure 10b. Compared to the U-WCA reference map (Figure 10a), the use of the Bragg model results in a strong overestimation of the oil concentration of a marine slick: an incidence angle of 45° and an actual value of PR value of 0.3 lead to an oil concentration estimate of 65% and 77% using the U-WCA (Figure 10a) and the Bragg model (Figure 10b), respectively.

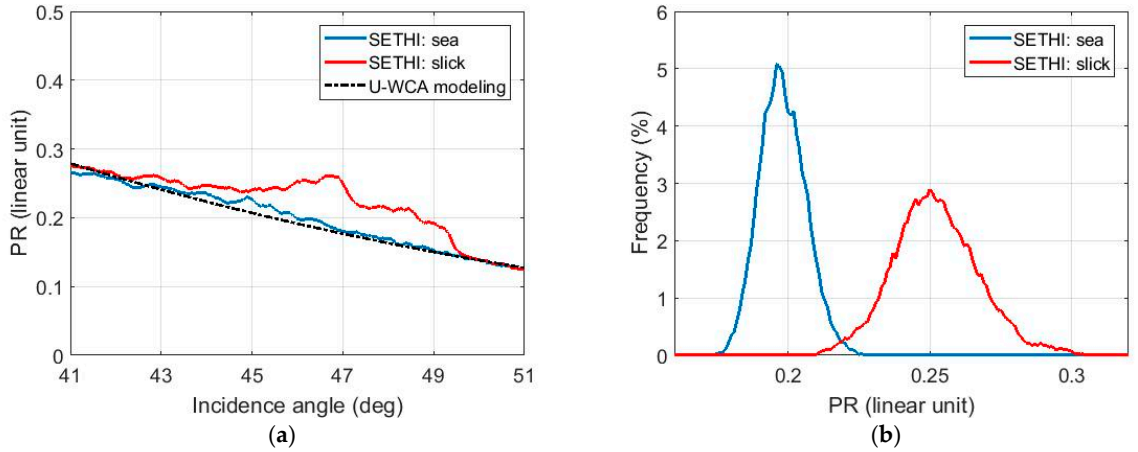

Figure 9. PR at L-band (**a**) estimated with the U-WCA scattering model (dotted black) and measured with experimental SAR data (SETHI NOFO'2015 10:02 UTC) across a range transect over a clean sea surface (blue) and a slick-covered surface (red); (**b**) Normalized histograms of experimental PR values measured at L-band (SETHI NOFO'2015 10:02 UTC) over clean sea (blue) and slick (red) surface with an incidence angle of 46°.

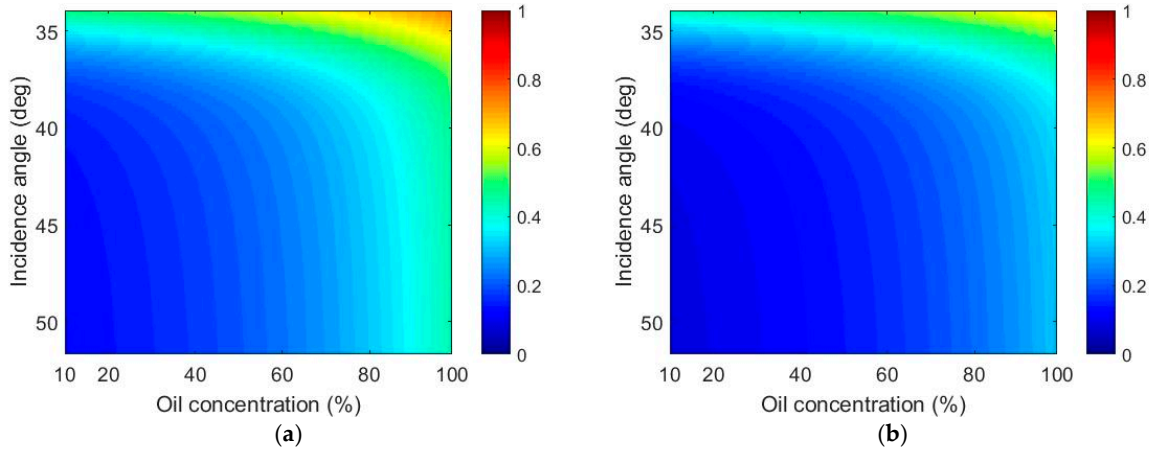

Figure 10. Reference map of PR values at L-band estimated with (**a**) the U-WCA scattering model and (**b**) the Bragg theory.

5. Quantifying the Concentration of Oil within a Marine Slick with Real Airborne SAR Data

The methodology described in Section 4 has been first applied to L-band SAR data collected by SETHI at 10:02 during the MOS Sweeper oil spill exercise (Table 3, run 2). A VV polarized image is displayed in Figure 11 together with the experimental PR and the estimated oil concentration maps. A detection mask has first been applied, based on the thresholding of the polarization difference [10,12,14,31]. The ranges of variation of PR values and oil concentrations have been reduced to 0.15–0.35 and 20–80%, respectively, to enhance the visualization.

On the PR map (Figure 11b), one can observe strong variations of the PR values in the range direction due to the incidence angle changes across the swath. The second-order variation is due to the modification of the dielectric properties of the surface related to the oil content within the oil-in-water mixture. The oil concentration is estimated by firstly, selecting, for each pixel, the closest value between the actual PR and those given by the U-WCA data sheet (Figure 10a) and then by finding the concentration rate corresponding to the modelled PR value. The result is displayed in Figure 11c. The mean value of oil content within the emulsion is equal to 52% and more than 80% of the pixels

within the slick have a concentration between 40 and 65%. Usually, the water content of marine oil slick lies between 50 and 75% [37], that is oil concentration between 50 and 25%. The values obtained in this experiment are slightly higher, which could be due to the relative short time lag between the release of oil by NOFO at sea and the scene acquisition by the radar sensor.

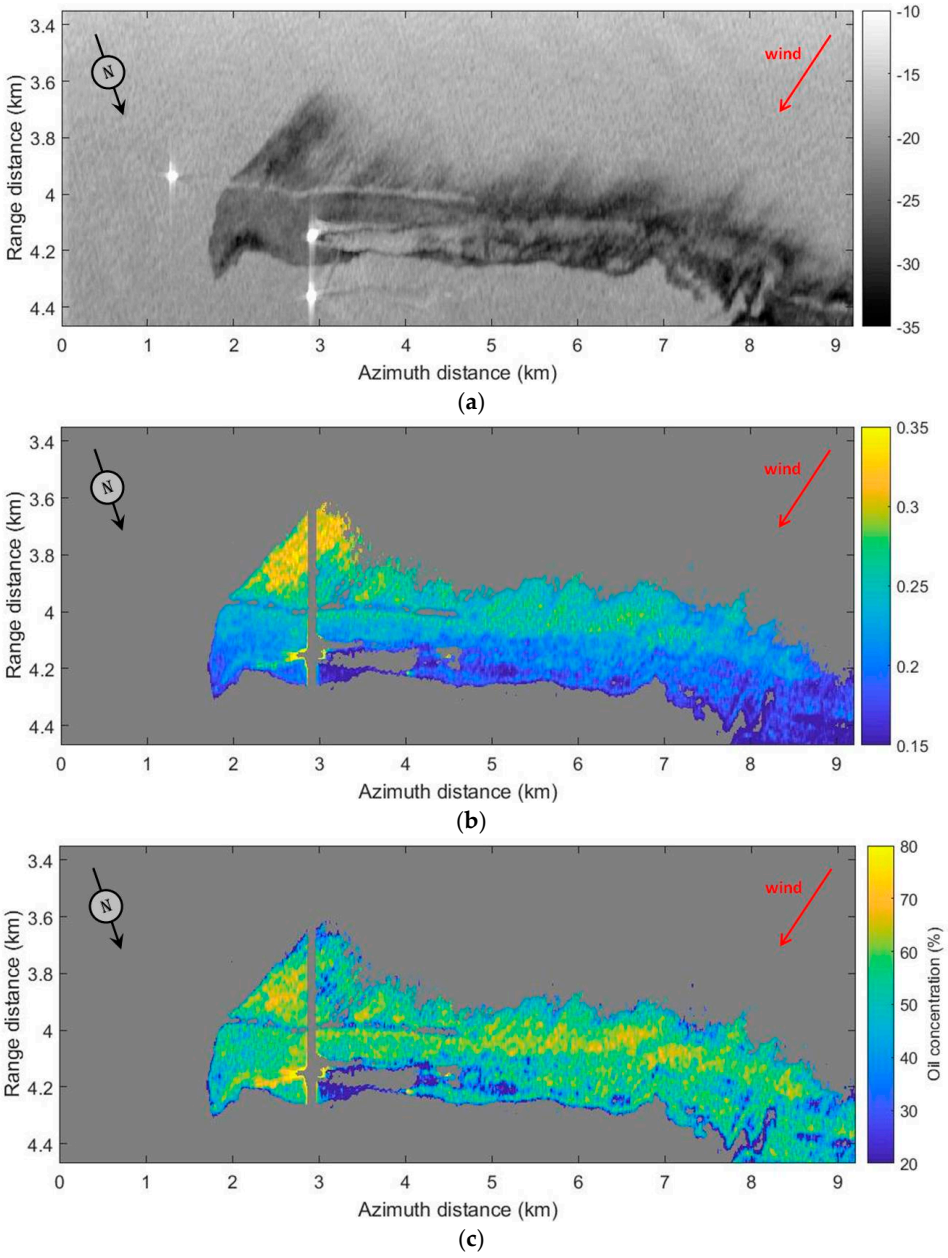

Figure 11. SETHI NOFO'2015 10:02 UTC. (**a**) L-band VV-pol image; (**b**) polarization ratio [0.15 0.35]; (**c**) oil concentration map [20 80%]—multi-look 21 × 21.

The same methodology has been applied to the other SAR scenes collected during the NOFO'2015 experiment and investigated in this paper (Table 3). All oil concentration maps have been projected in the ground geometry and are displayed in Figure 12 as well as the corresponding normalized histograms in Figure 13. The oil concentration underwent little change between 09:37 and 10:27 UTC (only 50 min) and no significant variation can be seen between the three histograms (Figure 13—blue, red and green curves). The average value of the oil concentration is 52%, 52% and 49% for the acquisitions of 09:37, 10:02 and 10:27 UTC, respectively. Compared to the first three histograms,

the last histogram (acquisition at 13:30 UTC, 3-h later) is shifted to the lower values of oil content (Figure 13—black curve), with an average value of oil concentration of 43%. This decrease of oil concentration is due to weathering processes (wind, waves, evaporation . . .) whose impact is clearly highlighted on the oil concentration histograms.

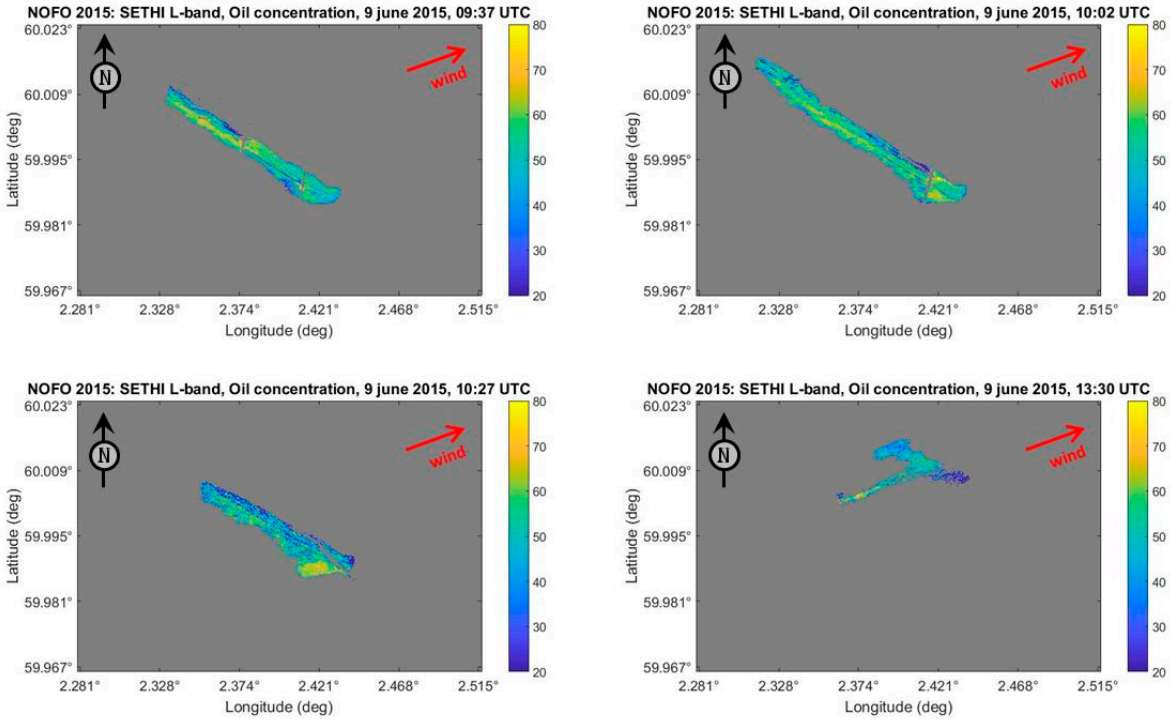

Figure 12. SETHI NOFO'2015 oil concentration map [20 80%] corresponding to the SAR data collected at 09:37 UTC (run 1—upper left panel), 10:02 UTC (run 2—upper right panel), 10:27 UTC (run 3—lower left panel) and 13:30 UTC (run 4—lower right panel)—multi-look 21 × 21—ground geometry.

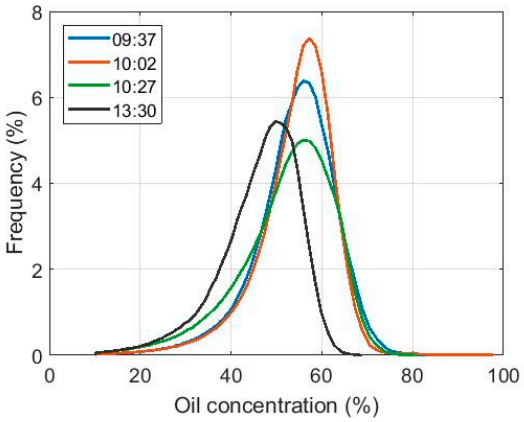

Figure 13. Normalized histograms of oil concentration estimated within the mineral oil slick released during the MOS Sweeper exercise. Temporal measurements at 09:37 (blue), 10:02 (red), 10:27 (green) and 13:30 UTC (black).

6. Confidence in Oil Concentration Estimate

The quantification method proposed in this paper is based on the U-WCA scattering model and the Bruggeman formula for estimating the oil concentration from the effective dielectric constant of the oil-in-water mixture. Usually, a simple linear mixing between mineral oil and seawater is

employed [11,12]. This important simplification leads to a significant error in the estimate of the oil concentration within an oil slick. The Figure 14 below shows two histograms of the oil concentration (run 2—10:02 UTC) obtained using a linear (blue curve) and the Bruggeman model (red curve). With a linear mixing, the histogram is shifted to the higher values of oil concentration, resulting in a strong overestimation of the average oil concentration (75% against 52%). These results show that the selection of the dielectric mixing model is a key aspect. The Bruggeman model has proven [28] to accurately reproduce the effective dielectric constant of an emulsion-type mixture and is highly recommended against the linear one when investigating the surface properties of marine slick from SAR imagery.

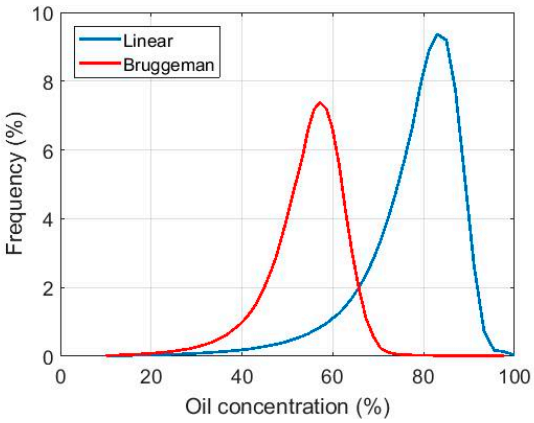

Figure 14. Normalized histograms of oil concentration estimated within the mineral oil slick released during the MOS Sweeper exercise (10:02 UTC) using the linear mixing model (blue) and the Bruggeman formula (red).

The second source of errors comes from the wind information which is one of the inputs of the U-WCA scattering model. This information usually comes from large-scale forecast models, which cannot describe local variations. According to the Norwegian Meteorological Institute, the wind speed (U_{10}) was 5 m/s during SAR data acquisition at 10:02 UTC (run 2). The oil concentration has been estimated in a wind speed interval of $+/-$ 2 m/s around the reported value. Histograms of oil concentration estimated from dual-pol SAR data collected at 10:02 UTC and for an input wind speed of 3, 5 and 7 m/s are shown in Figure 15. As discussed in Paragraph 4.1, at low EM frequency the polarization ratio has a weak dependence on surface roughness and therefore modelling with the U-WCA scattering model varies only slightly with wind speed. Hence, wind speed uncertainties induce little errors on the estimate of the oil content into the oil-in-water mixing. For the investigated SAR data collected at 10:02 UTC, the mean oil concentration is estimated to be 51.9%, 52.4% and 50.8% for a wind speed of 3, 5 and 7 m/s, respectively.

Since the remote sensing dataset explored in this study was not collected with validation data, no comparison between oil concentration estimate and in situ sampling within the spill areas can be performed. Even if the method reported in this paper is based on physical justifications, it cannot be formally validated. However, all the results presented herein are consistent with the expected behavior of an oil slick imaged area. First, the values of the oil concentration estimate are close to the concentration usually observed [37]. Then, we observe no trend of the estimation in the range direction, which suggests that the incidence angle variation across the swath as well been considered. Moreover, SAR data collected with a small time gap (09:37, 10:02 and 10:27 UTC) give similar oil content maps, despite the polluted area is differently positioned in the swath between the images, which ensures the robustness of the proposed methodology. Finally, the estimated maps covering the evolving spill over a 4-h period indicates a decrease of the average oil concentration, which can be attributed to weathering processes.

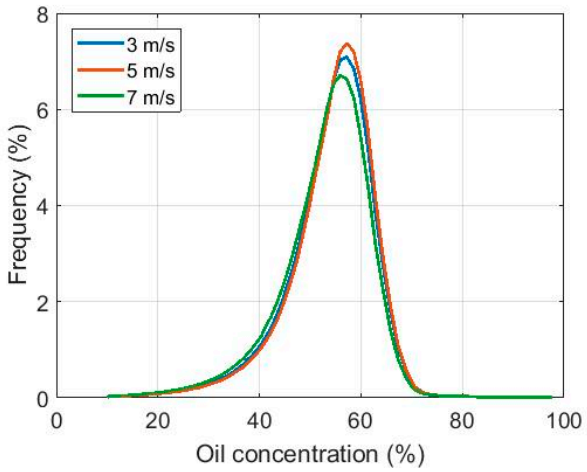

Figure 15. Normalized histograms of oil concentration estimated within the mineral oil slick released during the MOS Sweeper exercise (10:02 UTC) for an input wind speed of 3 m/s (blue), 5 m/s (red) and 7 m/s (green).

7. Conclusions

A methodology to estimate the proportion of oil within an oil-in-water marine slick mixture has been reported in this paper as well as its application to the temporal monitoring of the oil concentration. The key aspects of this study rely on three elements: the use of a rigorous surface scattering model to estimate the polarization ratio; the estimation of the volume fraction of oil from the Bruggemann formula; and the uniqueness of the dataset collected from controlled releases of mineral oil by an airborne SAR sensor operating at L-band, characterized by an instrument noise floor that is much lower than is currently available from spaceborne SARs.

At low frequency imaging radar (e.g., L-band), the relative contribution of non-resonant scattering with respect to the total backscattered energy from the ocean surface is negligible. For this reason, the polarization ratio measured by a radar sensor can be well approximated by a simple analytical scattering model such as U-WCA (see Figure 9a), which provides a non-trivial PR but depends only on the incidence angle of the incident radiation. Another advantage of using low frequency SAR images is that the ratio between the two co-polarized channels is only slightly dependent on the sea surface roughness but strongly affected by the dielectric properties of the imaged surface. This is not the case for higher frequency remote sensing radar, operating at C- or X-band. The volume fraction of oil within an oil-in-water mixture can then be retrieved from an Effective Medium Theory using the Bruggeman formula, by comparing the actual and the modelled polarization ratio at L-band.

The proposed methodology has been applied to an original set of L-band SAR scenes collected in June 2015 during an oil spill cleanup exercise carried out in the North Sea by the NOFO. Polarimetric SAR images have been acquired over controlled releases of mineral oil at sea by an airborne sensor characterized by a low instrument noise floor allowing a sufficiently high SNR over both slick-free and slick-covered areas for valid analysis of surface properties. Over freshly spilled mineral oil emulsion, the average oil concentration has been estimated to be above 50% with values ranging mainly from 40 to 65%. SAR data collected 4-h later permit to monitor the temporal behavior of the oil content and a decrease from around 50% to less than 45%, due to weathering processes, has been highlighted.

As shown in this paper, a combined utilization of an analytical scattering model and L-band SAR images collected with a sufficiently high SNR allows efficient estimation the concentration of oil within a marine oil slick (mixture between seawater and mineral oil). This estimation is shown to be robust to the uncertainties related to the sea state. Although no in situ measurements were collected with the remote sensing data, all the results presented herein are consistent with the expected behavior of an oil slick imaged area.

Author Contributions: S.A. conceived, design and performed the airborne experiments; S.A. analyzed the radar data; O.B., S.A. and C.-A.G. developed the methodology; S.A., O.B. and C.-A.G. wrote and revised the paper.

Funding: This work is funded by TOTAL (the French Oil and Gas Company) and ONERA (the French Aerospace Lab) under the NAOMI (New Advanced Observation Method Integration) project.

Acknowledgments: Research presented in this paper is part of the NAOMI (New Advanced Observation Method Integration) project funded by TOTAL (the French Oil and Gas Company) and ONERA (the French Aerospace Lab). The authors would like to thank all people involved in the NAOMI project, and especially Pierre-Yves Foucher from ONERA and Véronique Miegebielle and Dominique Dubucq from TOTAL for supporting this work. The authors are also very grateful to the NOFO (Norwegian Clean Seas Association for Operating Companies) for allowing them to participate in the Oil-on-Water exercise, which was carried out from the 8th to the 14th June 2015. Authors are very thankful for everyone involved in the experiment at sea and colleagues who participated to data processing.

Conflicts of Interest: The authors declare no conflict of interest.

References

1. Fingas, M.; Brown, C. Review of oil spill remote sensing. *Mar. Pollut. Bull.* **2014**, *83*, 9–23. [CrossRef] [PubMed]
2. Brekke, C.; Solberg, A. Oil spill detection by satellite remote sensing. *Remote Sens. Environ.* **2005**, *95*, 1–13. [CrossRef]
3. Gade, M.; Alpers, W. Using ERS-2 SAR images for routine observation of marine pollution in European coastal waters. *Sci. Total Environ.* **1999**, *237–238*, 441–448. [CrossRef]
4. Girard-Ardhuin, F.; Mercier, G.; Collard, F.; Garello, R. Operational oil-slick characterization by SAR imagery and synergistic data. *IEEE J. Ocean. Eng.* **2005**, *30*, 487–495. [CrossRef]
5. Leifer, I.; Lehr, W.J.; Simecek-Beatty, D.; Bradley, E.; Clark, R.; Dennison, P.; Hu, Y.; Matheson, S.; Jones, C.E.; Holt, B.; et al. State of the art satellite and airborne marine oil spill remote sensing: Application to the BP Deepwater Horizon oil spill. *Remote Sens. Environ.* **2012**, *124*, 185–209. [CrossRef]
6. Valenzuela, G.R. Theories for the interaction of electromagnetic and oceanic waves—A review. *Bound.-Layer Meteorol.* **1978**, *13*, 61–85. [CrossRef]
7. Alpers, W.; Holt, B.; Zeng, K. Oil spill detection by imaging radars: Challenges and pitfalls. *Remote Sens. Environ.* **2017**, *201*, 133–147. [CrossRef]
8. Wismann, V.; Gade, M.; Alpers, W.; Huhnerfuss, H. Radar signatures of marine mineral oil spills measured by an airborne multi-frequency radar. *Int. J. Remote Sens.* **1998**, *19*, 3607–3623. [CrossRef]
9. Gade, M.; Alpers, W.; Hühnerfuss, H.; Masuko, H.; Kobayashi, T. Imaging of biogenic and anthropogenic ocean surface films by the multifrequency/multipolarization SIR-C/X-SAR. *J. Geophys. Res.* **1998**, *103*, 18851–18866. [CrossRef]
10. Angelliaume, S.; Minchew, B.; Chataing, S.; Martineau, P.; Miegebielle, V. Multifrequency Radar Imagery and Characterization of Hazardous and Noxious Substances at Sea. *IEEE Trans. Geosci. Remote Sens.* **2017**, *55*, 3051–3066. [CrossRef]
11. Minchew, B. Determining the mixing of oil and seawater using polarimetric synthetic aperture radar. *Geophys. Res. Lett.* **2012**, *39*, L16607. [CrossRef]
12. Angelliaume, S.; Dubois-Fernandez, P.C.; Jones, C.E.; Holt, B.; Minchew, B.; Amri, E.; Miegebielle, V. SAR Imagery for Detecting Sea Surface Slicks: Performance Assessment of Polarization-Dependent Parameters. *IEEE Trans. Geosci. Remote Sens.* **2018**, *PP*, 1–21. [CrossRef]
13. Minchew, B.; Jones, C.E.; Holt, B. Polarimetric Analysis of Backscatter from the Deepwater Horizon Oil Spill Using L-Band Synthetic Aperture Radar. *IEEE Trans. Geosci. Remote Sens.* **2012**, *50*, 3812–3830. [CrossRef]
14. Kudryavtsev, V.; Chapron, B.; Myasoedov, A.G.; Collard, F.; Johannessen, J.A. On Dual Co-Polarized SAR Measurements of the Ocean Surface. *IEEE Geosci. Remote Sens. Lett.* **2013**, *10*, 761–765. [CrossRef]
15. Plant, W.J.; Irisov, V. A joint active/passive physical model of sea surface microwave signatures. *J. Geophys. Res. Oceans* **2017**, *122*, 3219–3239. [CrossRef]
16. Makhoul, E.; López-Martínez, C.; Broquetas, A. Exploiting Polarimetric TerraSAR-X Data for Sea Clutter Characterization. *IEEE Trans. Geosci. Remote Sens.* **2016**, *54*, 358–372. [CrossRef]

17. Ivonin, D.V.; Skrunes, S.; Brekke, C.; Ivanov, A.Y. Interpreting sea surface slicks on the basis of the normalized radar cross-section model using RADARSAT-2 copolarization dual-channel SAR images. *Geophys. Res. Lett.* **2016**, *43*, 2748–2757. [CrossRef]
18. Quilfen, Y.; Chapron, B.; Bentamy, A.; Gourrion, J.; Elfouhaily, T.M.; Vandemark, D. Global ERS 1 and 2 and NSCAT observations: Upwind/crosswind and upwind/downwind measurements. *J. Geophys. Res. Oceans* **1999**, *104*, 11459–11469. [CrossRef]
19. Horstmann, J.; Koch, W.; Lehner, S.; Tonboe, R. Wind retrieval over the ocean using synthetic aperture radar with C-band HH polarization. *IEEE Trans. Geosci. Remote Sens.* **2000**, *38*, 2122–2131. [CrossRef]
20. Kudryavtsev, V.; Hauser, D.; Caudal, G.; Chapron, B. A semiempirical model of the normalized radar cross section of the sea surface, 2, Radar modulation transfer function. *J. Geophys. Res.* **2003**, *108*, 2156–2202. [CrossRef]
21. Boisot, O.; Angelliaume, S.; Guerin, C.-A. Marine Oil Slicks Quantification from L-band dual-polarization SAR imagery. *IEEE Trans. Geosci. Remote Sens.*. Submitted.
22. Guerin, C.-A.; Soriano, G.; Chapron, B. The weighted curvature approximation in scattering from sea surfaces. *Waves Random Complex Media* **2010**, *20*, 364–384. [CrossRef]
23. Angelliaume, S.; Ceamanos, X.; Viallefont-Robinet, F.; Baqué, R.; Déliot, P.; Miegebielle, V. Hyperspectral and Radar Airborne Imagery over Controlled Release of Oil at Sea. *Sensors* **2017**, *17*, 1772. [CrossRef] [PubMed]
24. Zebker, H.A.; van Zyl, J.; Held, D.N. Imaging radar polarimetry from wave synthesis. *J. Geophys. Res.* **1987**, *92*, 683–701. [CrossRef]
25. Meissner, T.; Wentz, W.J. The complex dielectric constant of pure and sea water from microwave satellite observations. *IEEE Trans. Geosci. Remote Sens.* **2004**, *42*, 1836–1849. [CrossRef]
26. Folgerø, K. Bilinear calibration of coaxial transmission/reflection cells for permittivity measurement of low-loss liquids. *Meas. Sci. Technol.* **1996**, *7*, 1260–1269. [CrossRef]
27. Friisø, T.; Schildberg, Y.; Rambeau, O.; Tjomsland, T.; Førdedal, H.; Sjøblom, J. Complex premittivity of crude oils and solutions of heavy crude oil fractions. *J. Dispers. Sci. Technol.* **1998**, *19*, 93–126. [CrossRef]
28. Sihvola, A. *Electromagnetic Mixing Formulas and Applications*; IEE Electromagnetic Waves Series; Institution of Engineering and Technology: London, UK, 1999.
29. MOS Sweeper. Available online: http://www.egersundgroup.no/oilspill/mos-sweeper (accessed on 20 April 2018).
30. DESMI Boom. Available online: https://www.desmi.com/news-(3)/nofo-accelerates-spill-recovery-with-desmi-speed-sweep.aspx#1 (accessed on 20 April 2018).
31. Hansen, M.W.; Kudryavtsev, V.; Chapron, B.; Brekke, C.; Johannessen, J.A. Wave Breaking in Slicks: Impacts on C-Band Quad-Polarized SAR Measurements. *IEEE J. Sel. Top. Appl. Earth Obs. Remote Sens.* **2016**, *9*, 4929–4940. [CrossRef]
32. Elfouhaily, T.; Guérin, C.-A. A critical survey of approximate scattering wave theories from random rough surfaces. *Waves Random Media* **2004**, *14*, R1–R40. [CrossRef]
33. Soriano, G.; Guérin, C.-A. A cutoff invariant two-scale model in electromagnetic scattering from sea surfaces. *IEEE Geosci. Remote Sens. Lett.* **2008**, *5*, 199–203. [CrossRef]
34. Voronovich, A.G. Small-slope approximation in wave scattering from rough surfaces. *J. Exp. Theor. Phys.* **1985**, *62*, 65–70.
35. Hasselmann, K.; Raney, R.K.; Plant, W.J.; Alpers, W.; Shuchman, R.A.; Lyzenga, D.R.; Rufenach, C.L.; Tucker, M.J. Theory of synthetic aperture radar ocean imaging: A MARSEN view. *J. Geophys. Res.* **1985**, *90*, 4659–4686. [CrossRef]
36. Elfouhaily, T.; Chapron, B.; Katsaros, K.; Vandemark, D. A unified directional spectrum for long and short wind-driven waves. *J. Geophys. Res.* **1997**, *102*, 15781–15796. [CrossRef]
37. Fingas, M.; Fieldhouse, B. Studies on water-in-oil products from crude oils and petroleum products. *Mar. Pollut. Bull.* **2012**, *64*, 272–283. [CrossRef] [PubMed]